Disaster Resilience and Green Growth
Series Editors: Anil Kumar Gupta · SVRK Prabhakar · Akhilesh Surjan

Manish Pandey
Hazi Azamathulla
Jaan H. Pu *Editors*

River Dynamics and Flood Hazards

Studies on Risk and Mitigation

Springer

Disaster Resilience and Green Growth

Over the years, the relationship between environment and disasters has received significant attention. This is largely due to the emerging recognition that environmental changes - climate change, land-use and natural resource degradation make communities more vulnerable to disaster impacts. There is a need to break this nexus through environment based and sustainability inclusive interventions. Science – technology and economic measures for disaster risk management, hence, need to adapt more integrated approaches for infrastructure and social resilience. Environmental and anthropogenic factors are key contributors to hazard, risk, and vulnerability and, therefore, should be an important part of determining risk-management solutions.

Green growth approaches have been developed by emphasizing sustainability inclusion and utilizing the benefits of science-technology interventions along policy-practice linkages with circular economy and resource efficiency. Such approaches recognize the perils of traditional material-oriented economy growth models that tend to exploit natural resources, contribute to climate change, and exacerbate disaster vulnerabilities, Green growth integrated approaches are rapidly becoming as preferred investment avenue for mitigating climate change and disaster risks and for enhancing resilience. This includes ecosystem-based and nature-based solutions with potential to contribute to the resilience of infrastructure, urban, rural and peri-urban systems, livelihoods, water, and health. They can lead to food security and can further promote people-centric approaches.

Some of the synergistic outcomes of green growth approaches include disaster risk reduction, climate change mitigation and adaptation, resilient livelihoods, cities, businesses and industry. The disaster risk reduction and resilience outcome of green growth approaches deserve special attention, both for the academic and policy communities. Scholars and professionals across the domains of DRR, CCA, and green growth are in need of publications that fulfill their knowledge needs concerning the disaster resilience outcomes of green growth approaches. Keeping the above background in view, the book series offers comprehensive coverage combining the domains of environment, natural resources, engineering, management and policy studies for addressing disaster risk and resilience in the green growth context in an integrated and holistic manner. The book series covers a range of themes that highlight the synergistic outcomes of green growth approaches.

The book series aims to bring out the latest research, approaches, and perspectives for disaster risk reduction along with highlighting the outcomes of green growth approaches and including Science-technology-research-policy-practice interface, from both developed and developing parts of the world under one umbrella. The series aims to involve renowned experts and academicians as volume-editors and authors from all the regions of the world. It is curated and developed by authoritative institutions and experts to serve global readership on this theme.

Manish Pandey • Hazi Azamathulla • Jaan H. Pu
Editors

River Dynamics and Flood Hazards

Studies on Risk and Mitigation

Springer

Editors
Manish Pandey
Civil Engineering
National Institute of Technology Warangal
Warangal, Telangana, India

Hazi Azamathulla
Civil and Environmental Engineering
University of West Indies
Trinidad, Trinidad and Tobago

Jaan H. Pu
Civil and Structural Engineering
University of Bradford
Bradford, UK

ISSN 2662-4885 ISSN 2662-4893 (electronic)
Disaster Resilience and Green Growth
ISBN 978-981-19-7099-3 ISBN 978-981-19-7100-6 (eBook)
https://doi.org/10.1007/978-981-19-7100-6

This Springer imprint is published by the registered company Springer Nature Singapore Pte Ltd.
The registered company address is: 152 Beach Road, #21-01/04 Gateway East, Singapore 189721, Singapore

Contents

About the Editors

Manish Pandey graduated in Civil Engineering from Uttarakhand Technical University, India. He completed his master's and doctorate from Indian Institute of Technology Roorkee, India. Presently, Dr Pandey is Assistant Professor at NIT Warangal. He has more than 5 years teaching and research experience in experimental hydraulics and water resources engineering. He has authored more than 40 peer-reviewed journal papers and 10+ book chapters and conference proceeding papers. He has guided one PhD and five M.Tech students. Presently he is guiding four PhD and five M.Tech students. He was also awarded MOST postdoctoral research grant in the year 2018. He is a member of the editorial board of journals such as *Journal of Water Management Modeling* and *Larhyss Journal*. He has also handled guest editorship for *Frontiers in Environmental Science Journal* and *SI: The Urban Fluvial and Hydro-Environment System*. Dr. Pandey is an active reviewer for several reputed peer-reviewed journals.

Hazi Azamathulla is Professor of Civil and Environmental Engineering at the University of the West Indies at St. Augustine, Trinidad. He has a degree in Civil Engineering from SKD University (India), master's degree in Water Resources from Devi Ahilya University (India), and a doctorate in Hydraulic Engineering from Indian Institute of Technology, Bombay. His research interests and activities are in the fields of physical hydraulic model studies and hydroinformatics. He has authored more than 100 peer-reviewed journal papers and book chapters. He has guided 7 PhD students and 16 master's students. He has been a member of the editorial board of several high ranked journals: *Water Science and Technology*, *Water Science and Technology: Water Supply*, *Journal of Pipeline Systems Engineering*—ASCE (2009–2013), *Dam Engineering* journal. He is the Associate Editor of *Journal of Hydrology* (Elsevier).

Jaan H. Pu is an Associate Professor at the University of Bradford, UK. His research concentrates on modeling and laboratory approaches to represent various water engineering applications which include naturally compounded riverine flows, sediment transport, water quality, and vegetated flow. His research outputs have led to several journal articles (50+), conference proceedings (10+), edited books (2), and book chapters (2). He has/is supervising 7 PhD students at Bradford (5 as their principal supervisor) to investigate river hydrodynamics, sediment transport, and water quality challenging applications. He has been appointed as the Associate Editor by *Frontiers in Environmental Science* (IF 4.581); and Leading/Guest Editing various Special Issues for MDPI *Fluids*, MDPI *Water*, and *Frontiers in Environmental Science*. He is also currently Visiting Scientist to Tsinghua University, China, and Nanyang Technological University, Singapore.

Part I
Introduction to River Hazards and Their Management

Chapter 1
Natural River Hazards: Their Impacts and Mitigation Techniques

Guguloth Saikumar, Manish Pandey, and Pratibha Kumari Singh Dikshit

Abstract Natural hazards occur due to the interactions between extreme natural events and anthropogenic activity that have the potential to inflict damage, disruption, death, or injury. The escalating anthropogenic influence on the natural processes of the fluvial stream has polluted the water, altered the transit capacity due to the increase in suspended loads, and there by leading fluvial hazards. River-related natural hazards are broadly categorized as (a) flooding and (b) lateral erosion. Floods are natural disasters that occur either due to waterlogging and spreading induced by heavy rains or due to collapse of hydraulic structures caused by rising water levels in the river channel. The flood management process in India is extremely complicated due to the influence of numerous socio-hydro climatological elements such as climate change, sea level rise, and socioeconomic dynamics. In this article, the unique geomorphic patterns of three major recent flood-affected sites in India such as Uttarakhand flood in Upper Ganga Valley in June 2013, Kashmir flood in Jhelum River occurred in September 2014, and Chennai flood happened on December 2015 were briefly explained. Consequently, the activities of Indian flood management agencies were also discussed with a focus on current flood management techniques. River bank erosion has long-term implications for human life leading to economic crisis and forced relocation of victims. The alterations in the flow of rivers due to bank erosion have a profound impact on river ecology. The impacts of river bank erosions in four zones of India viz., (a) North West region, (b) central India and Deccan region, (c) Brahmaputra region, and (d) Ganga (Ganges) region were presented in this study.

Keywords Hydrological hazards · Floods · NDMA

G. Saikumar (✉) · M. Pandey
Department of Civil Engineering, National Institute of Technology Warangal, Warangal, India
e-mail: gs712006@student.nitw.ac.in; mpandey@nitw.ac.in

P. K. S. Dikshit
Department of Geography, C.M.P. College, Allahabad University, Allahabad, India

M. Pandey et al. (eds.), *River Dynamics and Flood Hazards*, Disaster Resilience and Green Growth, https://doi.org/10.1007/978-981-19-7100-6_1

1.1 Introduction

Rivers are the lifeline of the human race across the world. Many of the villages, towns, hamlets and cities in the world are located along the river banks. However, the intervention of humans with the natural process of the fluvial streams has contaminated the water, damaged the ecology, altered the transit capacity, raised the suspended load, and triggered the fluvial hazards (Singh and Kumar 2017; Jain et al. 2021; Pu et al. 2021; Shankar et al. 2021; Chaudhuri et al. 2022). For instance, due to rapid growth of population and raising demand for land, humans began to live within the valleys and flood plains of rivers. Consequently, these inhabitants are constantly threated during high- and low-discharge intervals (Singh and Singh 2011; Shivashankar et al. 2022). The most prevalent fluvial risks encountered in river systems are generally classified as follows: floods, lateral erosion, strainers, and undercuts. Floods are the most common, widespread, and devastating natural disaster, causing significant social, economic, and environmental damage in both developing and wealthy countries (Mohapatra and Singh 2003; Singh et al. 2022; Wallwork et al. 2022). Developing nations, particularly South Asian countries, are predominantly exposed to flood hazards occurs due to heavy rainfalls, dynamic terrain forms, and high population density (Saleem Ashraf et al. 2017). In recent years, flooding has claimed more lives in these regions than any other natural calamity. From 1976 to 2005, the total number of people impacted by floods in South Asia was close to one billion, and in Bangladesh more than half of the country's population is affected due to flood in 1988 (Wahiduzzaman 2021). The economic losses due to floods across the globe stood at a humongous $58.7 billion. In India, floods accounting for over 68% of total economic losses due to natural hazards. Some of the widely recognized major floods occurred in Huang Ho, China, 1931 and Bangladesh, 1987 and 1988 in the USA, 1998 in Mozambique, are all widely recognized. Floods in India affected around 100 million people in the states of Assam, Madhya Pradesh, Haryana, Jammu and Kashmir, Gujarat, Punjab, Himachal Pradesh, Chandigarh, and Rajasthan in 1993 (Shrestha and Takara 2008). Along with Bangladesh, India is one of the countries that has been severely impacted by river hazards on several occasions.

Aside from floods and stream bank erosion during periods of high flow, lateral migration has been found to act as an independent hazard during low-discharge periods (Singh and Awasthi 2011). Lateral migration of the river bank occurs due to the movement of a stream channel, fluctuations in fluid flow, and sediment discharges (Dekaraja and Mahanta 2021; Pandey and Md Azamathulla 2021). The combination of distinct sediments, inadequate compaction, scouring action, and the development of fractures causes the river bed configurations to change, forcing the river channel to migrate laterally. Many studies reported that increased urbanization and changes in land use land cover patterns increase the frequency and intensity of such disasters in the future (Ali et al. 2019). Lateral erosion and shifting of channel dimensions are geomorphological processes that have been investigated by a number of researchers in recent years (Bordoloi et al. 2020; Das et al. 2007; Pati

et al. 2008; Phillips 1991; Sarma 2013). The important river hazards that affect the lives of human being and their resources are floods, lateral erosion, strainers, and undercuts. In this paper, a detailed introduction to river hazards, their impacts on human being and mitigation techniques have been explained considering some of the case studies.

1.2 Natural Hazards

1.2.1 Floods

Floods are the outcome of imbalances in natural forces and processes and are inevitable in the scheme of nature and that occur with a predictable frequency year after year, causing widespread morbidity and mortality over the continent (Subrahmanyam 1988). Floods have a significant influence on the global population because of their location and geography, as well as human demographics and built-environment features (Tripathi 2015). The majority of India's population lives in the riverine and coastal plains. Because of their topography, certain places are frequently prone to flooding. As a result, a great number of individuals and their livelihoods have been severely impacted. The main causes of river floods are shown in Fig. 1.1. When flow exceeds the capacity of the river, flooding occurs in neighbouring places, which can be disastrous. It is caused by two factors: (a) Waterlogging and spreading as a result of severe rainfall and (b) Hydraulic structure failure as a result of rising water levels in the river channel. We briefly describe the distinct geomorphic configurations of three significant recent flood-affected locations in India: Uttarakhand flood in Upper Ganga Valley in June 2013 (Rana et al. 2013), Kashmir flood in Jhelum River occurred in September 2014, and Chennai flood happened on December 2015.

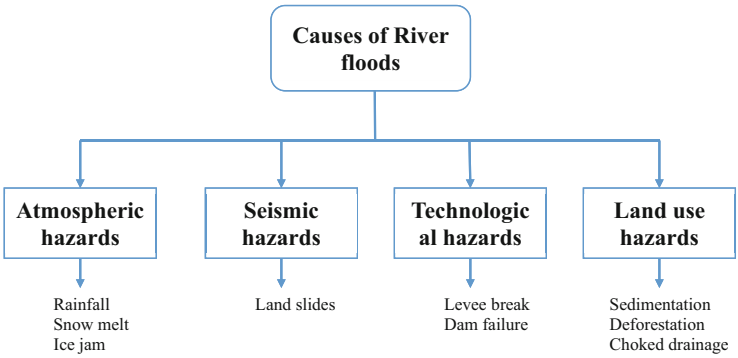

Fig. 1.1 Causes of river floods

1.2.1.1 Uttarakhand Flood (2013)

In June 2013, the banks of the Chorabari Lake in Kedarnath fell owing to a cloudburst that caused a large flash flood in Uttarakhand, inflicting widespread devastation and becoming the country's greatest natural catastrophe (Martha et al. 2015). The Kedarnath valley is built on the glacial outwash plain. The disaster struck Kedarnath on the morning of the 17th, with the immediate cause being torrential rain (375% more than average) and abrupt overflow from the Chorabari glacier lake on the upstream of the Kedarnath valley, followed by a landslide on another slope a few hours before. Ten feet of flood water carrying a massive load of muck, trash, and rocks suddenly inundated Kedarnath and the surrounding valley, destroying everything but the main shrine. The flood waters proceeded downstream via the Mandakini, Alkananda, and Bhagirathi rivers, wreaking havoc on a huge region of 40,000 km^2 across Chamoli, Rudraprayag, Pithoragarh, and Uttarkashi districts. Nearly 6054 people died as a result of the flood, and 4550 communities have been damaged (Rana et al. 2013). Because of the extreme flooding, bridges, towers, poles, and roads were destroyed. A total of 2052 homes were demolished, 147 bridges were damaged, and 1307 roads were devastated.

1.2.1.2 Kashmir Flood (2014)

The Jammu and Kashmir area saw severe floods over the bulk of its districts during the first week of September 2014, triggered by multi-day heavy rainfall storms. Flooding in Kashmir caused by heavy rain, mismanagement, unplanned development, and a lack of readiness (Alam et al. 2018). This flood caused localized devastation of property and public infrastructure, as well as a significant impact on life, communities, and communication. According to statistics released by India's Home Ministry, several thousand villages were impacted across the state, with 390 villages entirely inundated. The early estimate of property loss ranged from INR 50,000 million to INR 60,000 million. Approximately 277 individuals were killed.

1.2.1.3 Chennai Flood (2015)

Heavy rains in Tamil Nadu and Andhra Pradesh in early December 2015 caused significant flooding. A deep tropical depression passed over the Bay of Bengal and impacted India's south-eastern coast, pouring torrential rain. From December 1 to 2, Chennai got nearly 33 cm of rain in a 24-h period, causing significant flooding and damage. The catastrophic calamity was exacerbated by a sudden and uncontrolled discharge of water from the Chembaramkkam reservoir (Gupta and Nair 2011). In Tamil Nadu, the districts of Chennai, Cuddalore, Kanchipuram, and Tiruvallur were the most damaged. Unfortunately, as a result of this tragic disaster, over 500 people

have died in Tamil Nadu. Flooding has impaired the educational system, food availability, transportation, and access to electricity in Chennai (Vishnu and Sridharan 2016). There were 500 confirmed deaths in the flooding catastrophe, and almost 1.8 million people were affected. The primary cause of this predicament is Chennai's unscientific urbanization and growth. Many studies have issued warnings against converting marshy area to concrete infrastructure, which exacerbated the situation.

1.2.1.4 Kerala Flood (2018)

Due to abnormally heavy rainfall during the monsoon season, major floods struck the South Indian state of Kerala on August 16, 2018. The extreme rainfall in the monsoon season resulted in flooding, which is significantly higher than the capacity of reservoirs. The total rainfall is received by Kerala during the period 1 June 2018 to 19 August 2018 is 42% higher than the average monsoon rainfall for the same period. The return period of extreme rainfall is about 145 years and the occurrence of the extreme rainfall is due to the monsoon depressions over the Bay of Bengal as per India Meteorological Department (IMD). Approximately a million people were evacuated, primarily from Chengannur, Pandanad, Edanad, Aranmula, Kozhencherry, Ayiroor, Ranni, Pandalam, Kuttanad, Malappuram, Aluva, Chalakudy, Thrissur, Thiruvalla, Eraviperoor, Vallamkulam, North Paravur, Chellanam, and 483 casualties were reported. According to the Kerala government, the floods and related occurrences directly affected one-sixth of the state's entire population.

In a warming climate, extreme weather events such as convective storm rainfalls are projected to cause an increase in the number of floods that endanger minor catchments. Despite this, the government always appears to treat these issues as a matter of crisis management rather than taking early actions to reduce the factors that lead to the crises (Singh and Kumar 2017). Moreover, there is a dearth of substantial national planning for surface water management, such as water storage, the construction of check dams, desiltation, and assuring seepage of water into the ground rather than runoff. Several entities at the state and national levels have attempted to lessen flood susceptibility by employing a variety of techniques (Abbas et al. 2016). Significant afforestation is also required in the higher portions of river systems to act as a buffer against excessive rainfall and to prevent silt and boulders from becoming dislodged and rushing down to clog water channels, resulting in siltation. Desiltation efforts should engage not only the government, but the entire community who benefits from this.

1.2.2 Flood Management and Control

The flood hazard management system in the country has been developed over the years. It helps states to develop, implement, and maintain all water resource management plans in accordance with their requirement (Ranjan 2017). After an exceptional and disastrous flood occurrence in Bihar in 1954, the importance of flood prevention and the necessity for an action plan to safeguard floodplains were recognized (Khan and Sharma 2020). Since then, major flood-prevention efforts have focused on controlling riverine floods, with significant expenditures in building structural measures such as river embankments and detention reservoirs, as well as improving river basin drainage. These solutions have not proven to in the long run, as the number of flood-prone areas in the country has expanded over the previous five decades. For the floods with a return period higher than the design return period of the structure, in the long run we have to adapt for non-structural measures such as enhancing catchment storage, flood plain zoning, flood forecasting and early warning system, awareness-raising, etc., serves as an alternative to structural measures for effective flood management (Jain et al. 2018; Kundzewicz and Menzel 2005; WMO 2011). Although flood management comes under water resources management, the responsibilities of construction and maintenance of flood control systems are linked with state government and state agencies. The federal government establishes numerous committees, task groups, and policies to assist states in developing an effective flood control system (Bhattacharjee and Behera 2017). According to the directives of several committees, various agencies of the central government operate as a catalyst to provide financial and technical aid to the states through qualified initiatives.

1.2.2.1 National Level Organizations

It is the role of the central government to oversee the country's catastrophe management procedure. The central ministries coordinate with other agencies to execute disaster preventive and mitigation measures. Flood control is a multi-disciplinary process that necessitates collaboration and coordination among several entities. The primary co-ordinator/supervising department is the Ministry of Jal Shakti, Department of Water Resources, River Development, and Ganga Rejuvenation (MoWR; http://mowr.gov.in/). However, the Central Government has formed a multitude of distinct agencies and expert committees to more thoroughly monitor the flood concerns. The following sections describe the various organizations and their roles in flood management.

1.2.2.2 Central Water Commission (CWC)

Central Water Commission (CWC) (http://cwc.gov.in/), the country's nodal body for water resource management, has decades of experience in water resource development planning, management, and design. It was established to promote flood management methods and to assist in policy-related matters as a technical advisory body to the MoWR and the states. It is in charge of developing infrastructure, maintaining information, and developing a flood forecasting system, as well as disseminating it to various end-users. It also conducts and coordinates research on water-related issues and provides guidance on different development initiatives involving river basins, such as flood control techniques. To give special attention to two of India's largest river basins, the Ganga and Brahmaputra, the MoWR established the Ganga Flood Control Commission (GFCC), and the Brahmaputra Board as statutory entities to handle flood control initiatives in their respective basins.

1.2.2.3 National Disaster Management Authority (NDMA)

The National Disaster Management Authority (NDMA) (https://ndma.gov.in/en/) is in charge of initiating a comprehensive and accelerated response to floods or other disasters. It is responsible for conception of national policies and action plans for disaster management. It offers guidelines to implement the plans and conduct essential disaster preparedness and capacity building setups by collaborating with the states and other agencies. These recommendations aim to improve post-flood response, relief, and rehabilitation methods while also enhancing existing flood preparedness and mitigation measures.

1.2.2.4 Other Organizations

Although the India Meteorological Department (IMD; https://mausam.imd.gov.in/), the National Remote Sensing Centre (NRSC; https://www.nrsc.gov.in/), and the National Institute of Disaster Management (NIDM; https://nidm.gov.in/) are not subsidiary bodies for flood management, their assistance is critical. For instance, IMD's frequent weather predictions give critical information for flood forecasting. At the same time, the NRSC's remote sensing capabilities are important for a variety of observational research and flood mapping projects. NIDM's flood management research is primarily concerned with policy formulation and capacity building through the development of training modules.

1.3 River Bank Erosion

River bank erosion is a major natural hazard and a major source of concern. It originates from the sediment composition, which is mostly made of different proportions of sediment materials such as clay, silt, and sand. According to granulometric studies, geomorphological and facies, the lower and middle regions of the Sand and silt assist compensate for stream banks and ridges that are prone to erosion, scouring, and mass movement, resulting in lateral erosion. The abandoned river route has a sandy bottom, which leads to lateral erosion. The spatio-temporal migration of river channel is critical to many geomorphological and river management challenges (Shah 1995). Every year, it brings unspecified misery to hundreds of individuals who live along river banks. Only erosion has displaced millions of people and has become a significant societal disaster. People who live along riverbanks suffer from erosion, forcing them to shift their livelihood and society. The majority of riverbank erosion victims end up living in slums in towns and metropolitan cities (Hasnat et al. 2018). From the literature survey, the contributing factors to riverbank erosion are: excessive flood, extreme precipitation in the upstream, increased flow of water with strong wind, and insufficient land cover along the line (Das et al. 2017).

River bank erosion has several effects, including social, economic, health, education shown in Fig. 1.2. The first and most evident social consequence is homelessness caused by soil erosion, which drives people to migrate. They face economic catastrophe as a result of forced migration, including loss of work and property, and they experience poverty (Iqbal 2010). For these displaced people, identity crises is inescapable because their membership in any specific neighbourhood, state, or nation is routinely denied.

1.3.1 River Bank Erosion in India

The river bank erosion across four regions of India is explained in the following sections.

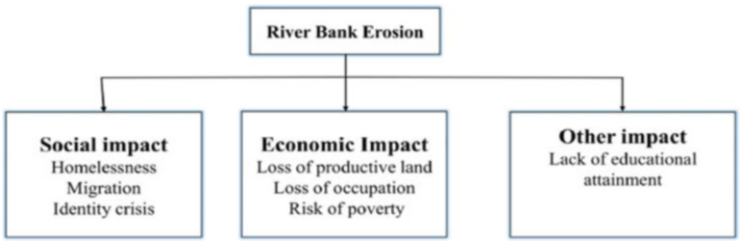

Fig. 1.2 Impacts of River bank erosion

1.3.1.1 North West Region

There are five main rivers in this region, namely Sutlej, Ravi, Chenab, Beas, and Jhelum, all of which are the tributaries of the Indus river that originates from the Himalayas (Sarma and Acharjee 2012). Flood and erosion hazards are quite modest in this region when compared to the Ganges and Brahmaputra regions. The biggest concern is insufficient surface drainage, that causes flooding and water logging across large regions.

1.3.1.2 Central India and Deccan Region

The major rivers in this region includes Krishna, Godavari, Cauvery, Tapi, Narmada, and Mahanadi. These rivers' courses are typically well-defined and steady. Except in the delta area, they have sufficient capacity inside the natural banks for carrying the flood runoff. The lower portions of the East Coast's major rivers have been embanked, essentially alleviating flood and erosion concerns. Orissa is another state where river banks are eroding. The state's largest river, the Mahanadi, and its two branches, the Kathajodi and the Kuakhai, are continually expanding and altering their path. These rivers devour a few settlements every year. Many people have already been affected by erosion or are at risk of being swept away by these three rivers. These individuals have no other option except to relocate, and the government refuses to acknowledge the erosion problem.

1.3.1.3 Brahmaputra Region

This region includes seven states: Arunachal Pradesh, Assam, Mizoram, Meghalaya, Tripura, Northern West Bengal, Nagaland, and Manipur as well as the rivers Barak and Brahmaputra and their tributaries. Islam and Guchhait (2017) demonstrated the effects of river bank erosion in Brahmaputra floodplain zones. For this study, an interview, field observation, secondary data sources, focus group discussion, and a semi-structured questionnaire were used. There are ten unions in Gauripur upazila, with Bhangnamari union mainly destroyed by riverbank erosion between 1988 and 2015 (Bhuiyan et al. 2017). Recent riverbank erosion has mostly impacted Bhangnamari, Kashiar Char, Bhatipara, and Gazariapara villages in Gauripur upazilla Bhangnamari union.

According to Guchhait et al. (2016), there was considerable evidence of frequent and rapid erosion rate along the Jamuna and Brahmaputra rivers between 1973 and 1992, the average width of the Brahmaputra River in 1830 was 6.2 km, and by 1992, it had expanded to 10.6 km. The canal extended at a pace of 27 metres per year on average between 1830 and 1914. The eroded area (ha) of the Brahmaputra River's left and right banks from 1995 to 2020 is depicted in Fig. 1.3. The results suggest that more than 1000 ha of land are eroded every 5 years on the left bank, while more

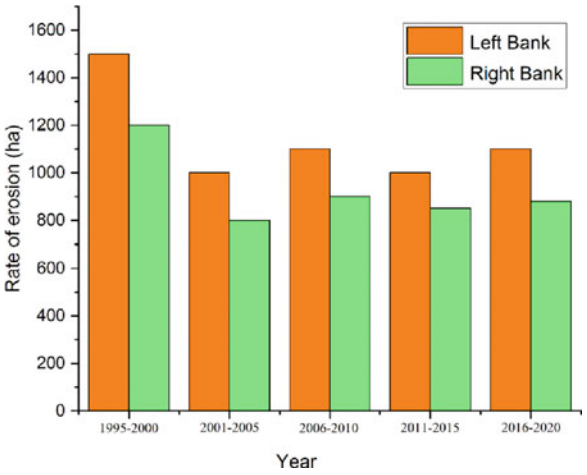

Fig. 1.3 Eroded areas of banks of Brahmaputra River during past decades

than 800 ha are degraded on the right bank. According to the findings, the communities located along the river's left bank are prone to lateral erosion.

1.3.1.4 Ganga (Ganges) Region

The Ganges and its various tributaries drain Uttaranchal, Delhi, Uttar Pradesh, Madhya Pradesh, Bihar, South and Rajasthan, Himachal Pradesh, and Haryana. Despite the fact that the Ganges is a lengthy river with a streamflow up to 70,000 m^3/s, only a few locations are susceptible to erosion (Thakur et al. 2012). Flooding and erosion are major issues in the lower Ganges area, notably in West Bengal. Chatterjee and Mistri (2013) investigated the socioeconomic impacts of river bank erosion in various communities in the Shantipur block of West Bengal's Nadia district. Methiadanga was formerly a community in Shantipur block that had been gradually submerged by the river. As the river inundates the settlement, the people who lived there were migrated. The population of this community is being altered by the river bank erosion for every 20 years from the date of the census.

1.4 Mitigation

Recent hazards data show an ominous trend of rising hazard losses. The primary causes of this phenomenon are land use and climate change. This factor increases vulnerability to natural catastrophes. It is suggested that internal variables such as catastrophe-related science and policy are partly to blame for the inability to stop or reverse the growing trend in disaster damage (Birkland et al. 2003).

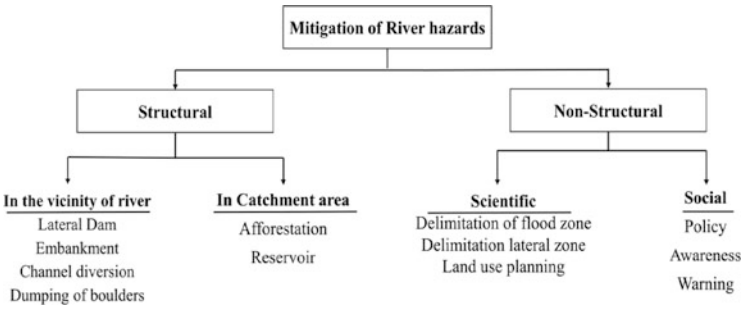

Fig. 1.4 Mitigation of River Hazards

Nature causes floods and river bank erosion, but the anthropogenic interference are making them lethal. While there is no known way to avoid flooding and lateral erosion, much may be done to minimize the effects of river hazards (Mehta 2007). Increasing urbanization creates new difficulties in decreasing catastrophe risk. However, calamities are usually ignored until they happen, at which stage the damage is done and relief is the only solution. There should be a perceptible shift in policy, with a greater emphasis on loss reduction through mitigation, preparedness, and recovery.

Flooding and river bank erosion could be reduced by assessing structural and non-structural measures shown in Fig. 1.4. The construction of embankments, lateral dams to regulate the flow of the river, vegetation, and the dumping of sand and cement bags and boulders are all examples of structural control. Plants are utilized to stabilize and reduce the erosion of stream banks by reducing stream flow velocity and trapping sediments, vegetation lowers stream bank erosion. Controlling deforestation, denudation, and soil erosion, as well as adequate planning, are the primary ways to tackle stream bank erosion and the growing flood threats.

The non-structural factors such as emergency security, flood and lateral erosion zone delimitation, land use planning, forecasting, palaeocurrent and facies research, and warning systems are examples of non-structural variables. Policy should be implemented to prevent people from settling near the river's danger zone.

1.5 Conclusions

The research work presented in this paper explains the various types of river hazards such as floods, lateral erosion, and their impacts on human resources along with their mitigation techniques. The river channel, water, sediment, and nutrient flows have all changed as a result of human ecologically disruptive activities. When the river's capacity is exceeded, flooding occurs in nearby areas, which can be devastating. Despite decades of catastrophic flooding and numerous flood-prevention initiatives, the exposure to disasters has not decreased to projected levels. For effective flood

management and mitigation, both structural and non-structural measures are being adapted to reduce flood risk and disaster relief preparedness. However, due to the feasibility issues related to structural measures, a paradigm shift to non-structural measures such as flood forecasting and warning systems has been witnessed in recent times. Moreover, non-structural flood protection measures are reversible and economically feasible. The scientific advancements in remote sensing and instrumentation aids in generating more observables such as soil moisture, evapotranspiration, and other earth surface and atmospheric variables. These variables are useful in data assimilation of Numerical Weather Prediction models, land surface models, and hydrological models for improving the forecast quality. Many of the existing flood forecasting systems across the world are using deterministic forecasts for shorter lead times (ranging from few hours to 3 days). A probabilistic approach (ensemble flood forecasting) for medium range lead times (up to 15 days) is suggested for improved flood preparedness. An active federal role is anticipated for taking effective actions to mitigate floods and carry out disaster relief duties in coordination with local authorities. However, the implementation highly depends on regional governments. The coordination between regional water resource councils is important as watersheds do not respect any political boundaries. Adequate training of communities is necessary for maintenance and operation purposes.

The growing frequency of disasters is seen as a sign of unsustainable development, according to the researchers. The majority of river-borne tragedies are caused by humans. As the human population has grown, people have begun to live in the river's danger zone. As a result, lateral erosion is a dangerous concern. To protect civilization from natural hazards, the trend of erosional pattern, river channel shifting, river discharge, and facies association should be studied. The mitigation of river-borne disasters requires a thorough understanding of river dynamics. Improved floodplain and river valley management, flood and lateral erosion mitigation strategies, greater disaster readiness, and the implementation of a forecasting and warning system can all assist to lessen damage effects. Hydrographic data and a digital elevation model of flood plain can be utilized for hydraulic and sedimentation prediction of Indian river reach; future flood and riverbank erosion risk maps may be developed and are extremely valuable for future mitigation and hazard preparation programmes to be conducted by government authority.

References

Abbas A, Amjath-Babu TS, Kächele H, Usman M, Müller K (2016) An overview of flood mitigation strategy and research support in South Asia: implications for sustainable flood risk management. Int J Sustain Dev World Ecol 23(1):98–111

Alam A, Bhat MS, Farooq H, Ahmad B, Ahmad S, Sheikh AH (2018) Flood risk assessment of Srinagar city in Jammu and Kashmir, India. Int J Disaster Resil Built Environ 9:114–129

Ali H, Modi P, Mishra V (2019) Increased flood risk in Indian sub-continent under the warming climate. Weather Clim Extremes 25:100212

Bhattacharjee K, Behera B (2017) Forest cover change and flood hazards in India. Land Use Policy 67:436–448
Bhuiyan MAH, Islam SM, Azam G (2017) Exploring impacts and livelihood vulnerability of riverbank erosion hazard among rural household along the river Padma of Bangladesh. Environ Syst Res 6(1):1–15
Birkland TA, Burby RJ, Conrad D, Cortner H, Michener WK (2003) River ecology and flood hazard mitigation. Nat Hazar Rev 4(1):46–54
Bordoloi K, Nikam BR, Srivastav SK, Sahariah D (2020) Assessment of riverbank erosion and erosion probability using geospatial approach: a case study of the Subansiri River, Assam, India. Appl Geomat 12(3):265–280
Chatterjee S, Mistri B (2013) Impact of river bank erosion on human life: a case study in Shantipur block, Nadia District, West Bengal. Population 66(26.009):7–17
Chaudhuri S, Pandey M, Debnath K, Oliveto G (2022) A comparative study on equilibrium scour volume around circular cylinders in clay-sand mixed cohesive beds, at near threshold velocity of sand–an experimental approach. Water Supply 22:6777–6791. https://doi.org/10.2166/ws.2022.250
Das JD, Dutta T, Saraf AK (2007) Remote sensing and GIS application in change detection of the Barak river channel, NE India. J Indian Soc Remote Sens 35(4):301–312
Das TK, Haldar SK, Sarkar D, Borderon M, Kienberger S, Gupta ID, Kundu S, Guha-Sapir D (2017) Impact of riverbank erosion: a case study. Australas J Disaster Trauma Stud 21(2):73–81
Dekaraja D, Mahanta R (2021) Riverbank erosion and migration inter-linkage: with special focus on Assam, India. Environ Syst Res 10(1):1–10
Guchhait SK, Islam A, Ghosh S, Das BC, Maji NK (2016) Role of hydrological regime and floodplain sediments in channel instability of the Bhagirathi River, Ganga-Brahmaputra Delta, India. Phys Geography 37(6):476–510
Gupta AK, Nair SS (2011) Urban floods in Bangalore and Chennai: risk management challenges and lessons for sustainable urban ecology. Curr Sci:1638–1645
Hasnat GNT, Kabir MA, Hossain MA (2018) Major environmental issues and problems of South Asia, particularly Bangladesh. In: Handbook of environmental materials management. Springer, pp 1–40. https://doi.org/10.1007/978-3-319-58538-3_7-1
Iqbal S (2010) Flood and erosion induced population displacements: a socio-economic case study in the Gangetic riverine tract at Malda district, West Bengal, India. J Hum Ecol 30(3):201–211
Islam A, Guchhait SK (2017) Search for social justice for the victims of erosion hazard along the banks of river Bhagirathi by hydraulic control: a case study of West Bengal, India. Environ Dev Sustain 19(2):433–459
Jain R, Lodhi AS, Oliveto G, Pandey M (2021) Influence of cohesion on scour at piers founded in clay–sand–gravel mixtures. J Irrig Drain Eng 147(10):04021046
Jain SK, Mani P, Jain SK, Prakash P, Singh VP, Tullos D, Kumar S, Agarwal SP, Dimri AP (2018) A brief review of flood forecasting techniques and their applications. Int J River Basin Manag 16(3):329–344. https://doi.org/10.1080/15715124.2017.1411920
Khan WA, Sharma RA (2020) Study on flood management in India. J Crit Rev 7(3):1–13
Kundzewicz ZW, Menzel L (2005) Natural flood reduction strategies–a challenge. Int J River Basin Manag 3(2):125–131
Martha TR, Roy P, Govindharaj KB, Kumar KV, Diwakar PG, Dadhwal VK (2015) Landslides triggered by the June 2013 extreme rainfall event in parts of Uttarakhand state. India Landslides 12(1):135–146
Mehta M (2007) Gender matters: lessons for disaster risk reduction in South Asia. The International Centre for Integrated Mountain Development (ICIMOD), Lalitpur
Mohapatra PK, Singh RD (2003) Flood management in India. In: Flood problem and Management in South Asia. Springer, Berlin, pp 131–143
Pandey M, MdAzamathulla H (2021) Discussion of "gene-expression programming, evolutionary polynomial regression, and model tree to evaluate local scour depth at culvert outlets" by Mohammad Najafzadeh and Ali Reza Kargar. J Pipeline Syst Eng Pract 12(2):07021001

Pati JK, Lal J, Prakash K, Bhusan R (2008) Spatio-temporal shift of western bank of the ganga river, Allahabad city and its implications. J Indian Soc Remote Sens 36(3):289–297
Phillips JD (1991) Fluvial sediment budgets in the North Carolina Piedmont. Geomorphology 4(3–4):231–241
Pu JH, Wallwork JT, Khan M, Pandey M, Pourshahbaz H, Satyanaga A, Hanmaiahgari PR, Gough T (2021) Flood suspended sediment transport: combined modelling from dilute to hyper-concentrated flow. Water 13(3):379
Rana N, Singh S, Sundriyal YP, Juyal N (2013) Recent and past floods in the Alaknanda valley: causes and consequences. Curr Sci 105(9):1209–1212
Ranjan R (2017) Flood disaster management. In: River system analysis and management. Springer, Berlin, pp 371–417
Saleem Ashraf ML, Iftikhar M, Ashraf I, Hassan ZY (2017) Understanding flood risk management in Asia: concepts and challenges. In: Flood risk management. InTech, p 177. https://doi.org/10.5772/intechopen.69139
Sarma D (2013) Rural risk assessment due to flooding and riverbank erosion in Majuli, Assam. University of Twente, India
Sarma JN, Acharjee S (2012) A GIS based study on bank erosion by the river Brahmaputra around Kaziranga National Park, Assam. India Earth Syst Dyn Discuss 3(2):1085–1106
Shah NM (1995) Emigration dynamics from and within South Asia. Int Migr 33(3–4):559–625
Shankar MS, Pandey M, Shukla AK (2021) Analysis of existing equations for calculating the settling velocity. Water 13(14):1987
Shivashankar M, Pandey M, Zakwan M (2022) Estimation of settling velocity using generalized reduced gradient (GRG) and hybrid generalized reduced gradient–genetic algorithm (hybrid GRG-GA). Acta Geophys:1–11
Shrestha MS, Takara K (2008) Impacts of floods in South Asia. J South Asia Disaster Study 1(1):85–106
Singh UK, Jamei M, Karbasi M, Malik A, Pandey M (2022) Application of a modern multi-level ensemble approach for the estimation of critical shear stress in cohesive sediment mixture. J Hydrol 607:127549
Singh O, Kumar M (2017) Flood occurrences, damages, and management challenges in India: a geographical perspective. Arab J Geosci 10(5):1–19
Singh RB, Singh S (2011) Rapid urbanization and induced flood risk in Noida. India Asian Geographer 28(2):147–169
Singh DS, Awasthi A (2011) Natural hazards in the Ghaghara river area, ganga plain. India Nat Hazard 57(2):213–225
Subrahmanyam VP (1988) Hazards of floods and droughts in India. In natural and man-made hazards. Springer, Berlin, pp 337–356
Thakur PK, Laha C, Aggarwal SP (2012) River bank erosion hazard study of river ganga, upstream of Farakka barrage using remote sensing and GIS. Nat Hazards 61(3):967–987
Tripathi P (2015) Flood disaster in India: an analysis of trend and preparedness. Interdiscip J Contemp Res 2(4):91–98
Vishnu CR, Sridharan R (2016) A case study on impact of Chennai floods: supply chain perspective. Ind Eng J 9(8):12–16
Wahiduzzaman M (2021) Major floods and tropical cyclones over Bangladesh: clustering from ENSO timescales. Atmos 12(6):692
Wallwork JT, Pu JH, Kundu S, Hanmaiahgari PR, Pandey M, Satyanaga A, Pandey M, Satyanaga A, Amir Khan M, Wood A (2022) Review of suspended sediment transport mathematical modelling studies. Fluids 7(1):23
WMO (2011) Manual on flood forecasting and warningWMO-No. 1072. World Meteorological Organisation, Geneva

Chapter 2
Assessment of Sediment Hazard and Associated Measurement

Navam Shrivastava and Anant Kumar Rai

Abstract The uncontrolled excess sediment transport into farm fields and river reaches can have disastrous effects leading to hazards and mitigation of these serious issues need extensive study. Sediment hazards, a threat to different biotic and abiotic factors of the ecosystem take place due to either the transportation of sediment or its deposition. Various causes, effects, and mitigation strategies for the sediment hazard along with respective case studies are presented in this article. A natural physical phenomenon like rainfall, melting of glaciers as well as human activities like mining, construction of roads, and railway tracks can increase the availability of sediment and its transport results in landslides. The sediment carrying trace metals and harmful chemicals, when enters the river, can disturb the aquatic life and society dependent on the river. The sediment transport is also responsible for the hydro-abrasive erosion of the hydraulic components. In addition to sediment transport, sediment deposition is also a big issue as it reduces the reservoir capacity affecting various factors like irrigation, hydropower generation, etc. depending on it. From analyzing various case studies, it is inferred that the chance of sediment hazard is more where other natural hazards like floods, earthquakes, and volcanic eruptions are frequent as in the Himalayan regions, Japan, Colorado, etc. Various sediment measurement techniques are also discussed in the article, which includes the measurement of suspended sediment and bed load. In various mitigation measures, the reinforced synthetic fiber-based river bank stabilization is found to be the most durable method due to its high strength and non-biodegradable nature. Furthermore, the laser diffraction-based instrument is found to be the best method at the moment for measuring suspended sediments continuously as it can provide both size and concentration information with good accuracy. For bed load measurement, the radioactive tracer method is found to be the most flexible option as it can be used for in situ measurements and can also measure fine sediment particles. Knowing the sediment discharge and suspended sediment concentration (SSC) with a proper mitigation technique to tackle the sediment hazard can be selected or developed

N. Shrivastava · A. K. Rai (✉)
Department of Mechanical Engineering, National Institute of Technology Warangal, Warangal, India
e-mail: ns720040@student.nitw.ac.in; anant@nitw.ac.in

M. Pandey et al. (eds.), *River Dynamics and Flood Hazards*, Disaster Resilience and Green Growth, https://doi.org/10.1007/978-981-19-7100-6_2

effectively and this will improve the living condition of flora, fauna, society, etc. during hazardous situations in addition to enhancing the efficiency of hydraulic structures and machinery. A land slide early warning system (LEWS) based on the rainfall forecast model is found effective in determining the threshold limit for evacuations in different national systems. In the future, the number of computational software to predict the flow pattern and intensity of sediment transport will increase.

Keywords Sedimentation · Hazard · Landslides · Measurement · Suspended sediment concentration · Bed load · Sediment transport

2.1 Introduction

The event or incidence which could cause serious damage to the surrounding environment or even result in loss of health and life is termed as a hazard. To tackle a specific hazard, a deep understanding including its causes, effects, and remedies is required. Some hazards can be man-made like the 1993 Bhopal gas tragedy and the 1986 Chernobyl disaster, while others can be categorized as natural like earthquakes, floods, volcanic eruptions, etc. Sediment hazards can be natural or man-made depending on their causes. Sediment transport and deposition play an important role in hydrology. Sediment hazard is associated with its adverse effect and is a threat to flora, fauna, human life, environment, hydraulic machinery, etc. Some of the main phenomena causing sediment-related disasters include debris flow, slope failure, and landslides. Debris flow is the movement of sediment caused by rainfall, melting of glaciers, heavy wind, etc. Slope failure and landslides occur due to the movement of sediment along the slope under gravity, these occur when soil above the slope gets weakened due to rainfall. Slope failure is usually a slow process and the possibility of reoccurrence is high, whereas a landslide occurs abruptly and the reoccurrence chance is less. Other than rainfall, an increase in temperature can also cause landslides, with rising temperature, glacier melts causes stream flow resulting in landslides (Pu et al. 2021). Sediment transport can be caused by human intervention as well as by natural physical processes. Human activities triggering sediment transport involves mining, agriculture, deforestation, construction of road, railway track, building, hydraulic structures, etc. whereas the natural causes include stream flow, rainfall, heavy wind, melting of glaciers, earthquake, flood, volcanic eruption, and gravity. The process of sediment transport and deposit due to rainfall in the upland is shown in Fig. 2.1.

The movement of harmful chemicals with sediments due to its transport has adverse effects on humans, aquatic, and wildlife. Along with this, it can cause abrasive erosion to hydraulic machinery. Sediment gets settled in the reservoir, lakes, rivers, and groundwater lowering their water level, this creates socio-economic losses. Improper and excess irrigation can remove the top soil, affecting the vegetation and polluting the water (Trout and Neibling 1993). Water flowing near the bank of rivers erodes the soil which gets transported along the river resulting in the loss of land and water contamination (Prosser et al. 2001). Roots of the trees

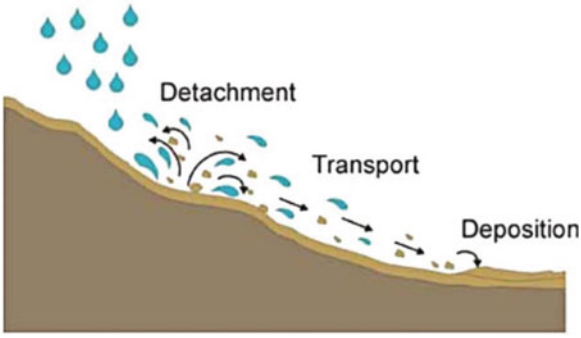

Fig. 2.1 Transportation of sediment due to rainfall along a sloppy land (Huertos 2020)

hold up the soil, deforestation results in loosening of the soil, increasing the rate of sediment transport and triggering landslides (Vasantha Kumar and Bhagavanulu 2008).

In India, the sub-Himalayans region near Shiwaliks is a prone region affected by sediment transportation due to heavy rainfall, cultivation in sloppy lands, and road construction. Another cause of the high rate of sediment transfer in the Himalayan region is the frequent occurrence of floods which bring a large amount of sediment along with it (Kothyari 2011). Sediment concentration in the melting stream of the Dokrian glacier, Uttarakhand varied from 80 ppm to 3830 ppm (Singh et al. 2003). Nepal is one of the countries highly affected by sediment hazards. The main reason for this is heavy rainfall causing floods, which result in frequent landslides, resulting in economic loss and loss of life. In the sediment disaster of 1993 in Nepal, more than 1400 people died, nearly 5 lakhs people were affected and about 60 thousand acres of fertile lands were lost (Joshi et al. 1998). Japan is also extensively affected by sediment disaster, which includes steep slope failure, debris flow, and landslides. Japan witnesses around 1241 average cases of sediment disaster every year, in which cases due to steep slope failure are more compared to debris flow and landslides as shown in Fig. 2.2. This is due to the geographic location of Japan which is prone to the volcanic eruptions, earthquakes, and heavy rainfall provoking sediment hazards. Between the years 2000 and 2019, about 678 people were missing or dead due to sediment (Junichi and Naoki 2020).

In 1996, 7000 cubic yards of sediment was released while draining a reservoir in the Poudre River, Larimer causing a river hazard. In Conejos County, a high amount of sediment yield in the Alamosa River decreased the depth of the river. The problem can also occur due to a decrease in sediment transport. In Pueblo County, initially, infiltration of an irrigation ditch was 15% as fine sediment particles fills the cracks reducing the loss of water. With the construction of a reservoir, infiltration reached 45% as sediment particles get settled in the reservoir, restricting the flow of fine particles in the irrigation ditch. This causes the government an economic loss of one million dollars to line the ditch with cement to fill cracks (Wohl et al. 1998). One of the main purposes of reservoirs is to store excess available water during peak flow periods which can be utilized during lean flow periods to handle the shortage of

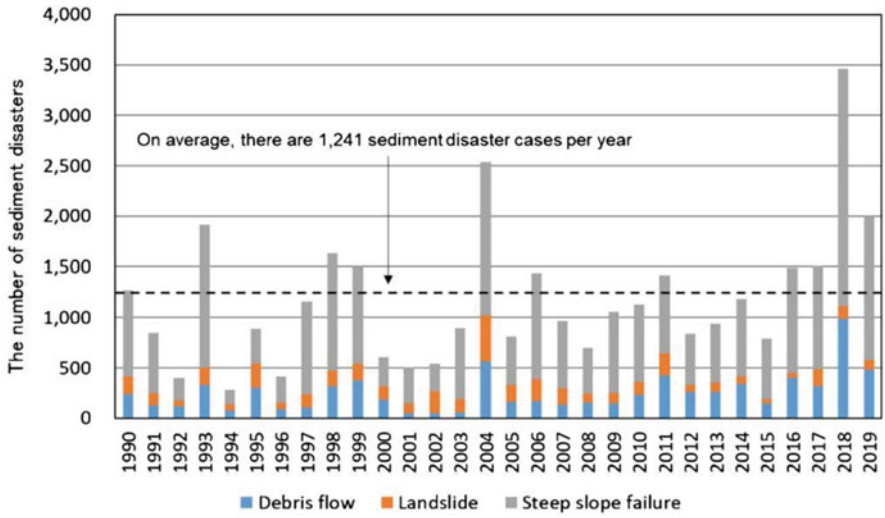

Fig. 2.2 Sediment hazard in Japan between 1990 and 2019 (Junichi and Naoki 2020)

water. The main problem encountered in a reservoir is the loss of its storage capacity due to sedimentation over a period of time. In the year 2003, International Commission on Large Dams (ICLD) estimated a huge loss of 45 billion m^3 of water due to sedimentation causing a 0.75% loss of storage capacity of the reservoir in a year (Zhide and Yuling 2010). In the span of 11 years since the construction of the Manwan reservoir, China, 21.5%–22.8% storage capacity was lost affecting the life of the reservoir (Fu et al. 2008).

Massive debris flow and about 2395 landslides due to heavy rainfall are some of the main reasons for the Kedarnath tragedy in 2013. More than 15,000 human and animal lives were lost, around 4200 villages were affected and huge economic losses were encountered (Deen and Sharma 2020). Sediment-related parameters like sedimentation rate, size, concentration, shape, and hardness of sediment play an important role in deciding the life span of hydraulic structures and machines, and the economic loss related to it. Therefore, a proper measurement technique is required for the effective functioning of the mitigation measures and will help in estimating the optimum design of reservoirs as well as hydraulic machinery. In order to reduce the loss due to sediment transportation and deposition, proper sediment traps design for hydraulic structures and machines is required. Though many articles are available on sediment transport; however, a study containing a concise review of case studies based on causes, effects, and mitigation of sediment hazards along with sediment measurement techniques is not collectively available yet making it necessary to conduct this study. The present article is distributed in five sections. The first section introduces the topic of sediment hazards, their causes, and various case studies related to them. The second section contains effects and menace due to sediment hazards. The third section describes the measurement techniques for sediment-related parameters, the fourth section gives details of different ways to mitigate the

effect of sediment hazards and the last section summarizes the important points of the article in a lucid manner.

2.2 Major Impacts of Sediment Hazard

In this section, some of the major areas affected by sediment hazards due to sediment transport and deposition are discussed.

2.2.1 Aquatic Life

Sediment particles coming to water bodies get settled down over a period of time. During the deposition, these particles can stick to the gills of fish affecting their life as shown in Fig. 2.3. Many times, trace metals, and harmful chemicals come along with sediment in water bodies. When aquatic animals and plants come in contact with the sediments, a serious threat to their life can happen. Sediment in water increases its turbidity, reducing the penetration of sunlight required by aquatic plants for photosynthesis as shown in Fig. 2.3. This stops their growth reducing the oxygen level in the water, which has a negative impact on aquatic animals. Sediment containing phosphorus can boost algae production which will consume oxygen and blocks the sunlight from entering the water body. With sediment present in water, the average temperature of the water will increase due to heat retention by sediment. This will reuse the dissolved oxygen, causing a threat to aquatic life (John et al. 202).

Around 4000 fish lost their life due to the sudden release of sediment while draining the Halligan reservoir situated in Larimer country. In a Sheep creek, excessive grazing by cows makes sediment particles finer, which eventually blocks the fish eggs when entering in water, reducing the supply of water and oxygen to embryos resulting in their demise. During the spring run-off season, the concentration of sediment carrying heavy meats increases. This contaminates the river, resulting in a reduction in the diversity and population of aquatic animals. Bed sediment in the Upper Colorado River contains a high concentration of trace metals due to the mining process taking place near it. Sediment carries these metals downstream, increasing the level of metals in fish bodies. This has resulted in a decline in the fish population due to adverse effects caused to them. A similar situation is also observed in Alamos River, Conejos (Wohl et al. 1998).

Along with the sediment concentration, the size and shape of sediment present in water also affect aquatic life. It is observed that the fatality rate of Sockeye Salmon present in Fraser River is increased due to an increase in the size of sediments. Furthermore, it was observed that angular sediment has more chance to cause a lethal effect on aquatic life than spherical sediment. The high angularity of volcanic ash particles entering a river in Washington was one of the major reasons contributing to

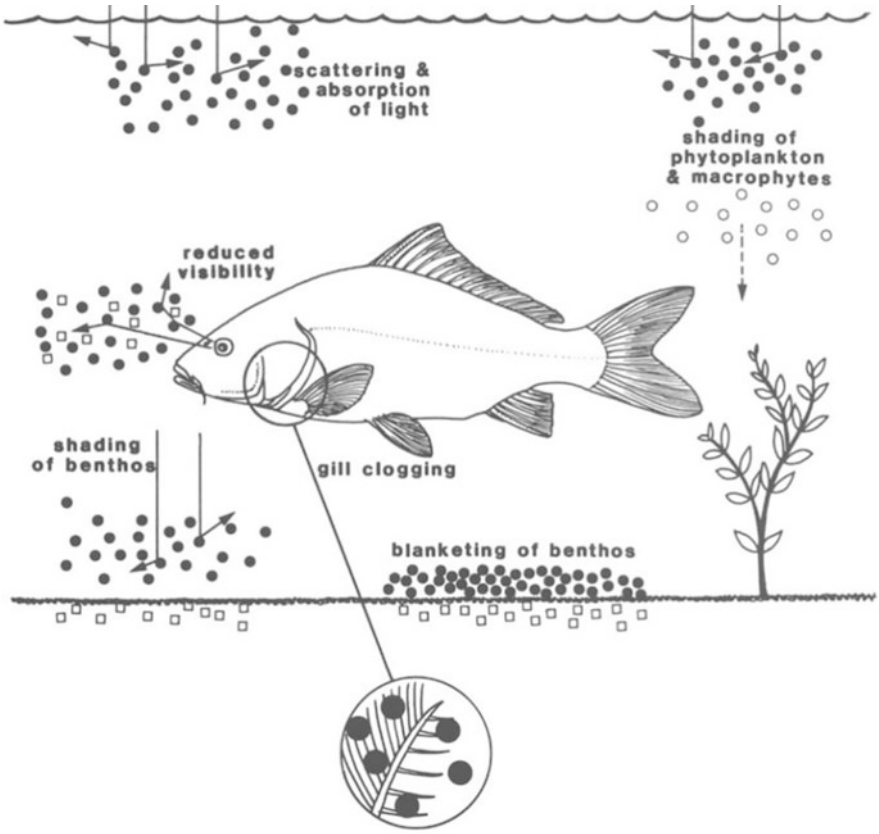

Fig. 2.3 Various effects of sediment on aquatic life (Bruton 1985)

mortality of fish (DFO 2000). In some cases, sediment concentration can also have a negative impact on aquatic life. Due to sediment deposition in reservoirs, sediment supply to water bodies containing important nutrients reduces, badly affecting fish breeding (Liu et al. 2017).

2.2.2 Environment

Sedimentation, landslides, and debris flow can destroy the ecosystems, majorly forest, agricultural land, and water stream. About 1500 hectares of agricultural land were destroyed by landslides in Ethiopia (Woldearegay 2013). Sedimentation in Dongting Lake of China has produced a serious impact on the ecosystem. As a result, the size and capacity of the reservoir were reduced by 172 km^2 and 12,600 million m^3, respectively, in a span of 49 years. Furthermore, flood protection dikes made of sand and mud get outburst several times a year causing the flow of sand in

paddy fields near it, resulting in the desertification of the agricultural land (Li et al. 2009). Forests are frequently affected by landslides and debris flow across the globe. In Papua-New-Guinea, huge landslides occur along the Torricelli range which has completely destroyed the vegetation of that region. About 5000 to 10,000 meters cube of topsoil is lost to Mogoro River every year due to landslides affecting the cultivation (Schuster and Highland 2007). About 250 km^2 of forest in Chile was destroyed due to landslides triggered by the earthquake. Debris flow due to volcanic eruption has modified the flow of the Toutle River and partially blocks the Columba River for about 1 year (Geertsema et al. 2009).

High deposition of sediment in the river decreases its cross-section and induces the risk of flood occurrence. Random flow of high concentrated sediment present in the river can change the river flow pattern which disturbs the ecosystem near to river by altering the levels of the different nutrients. Landslides can destroy the terrace farming land by removing the top soil causing desertification. Though the intensity of landslides gets reduced due to terrace vegetation eventually, it will result in the loss of agricultural land. Due to sediment transport in sloppy land being much higher than in flat land, the chances of soil erosion are higher in sloppy lands. In Nigeria, the rate of soil erosion measured in tonnes of soil lost per hectare of land in a year was 73.66 times more in sloppy land compared to flat land due to sediment movement in sloppy lands. In another case of sloppy land, rainfall has caused the sediment flow which eventually leads to the loss of 400 tonnes of soil per hectare in a year. One of the main causes of the "The great flood of 1993" was high sediment deposition in Mississippi and Missouri Rivers (Pimentel and Kounang 1998).

2.2.3 Urban Areas

Transportation and deposition of sediments in different water resources affect the lifestyle and health of the public. Harmful chemicals and metal absorbed in sediment can contaminate the water used by society. Sediment deposition partially or fully chokes the water and sewer pipes which can cause flooding of roads and property, hampering the socio-economic life of the public. A partially blocked stormwater pipe due to sediment deposition is shown in Fig. 2.4. Settlement of sediment on topsoil can act as a seal to the infiltration of water from the surface to underground reducing the groundwater recharging rate. Salalah city of Oman mostly depends on groundwater for its daily water requirement. The city reported a reduction in infiltration rate from 16 cm/h in 1988 to 0.18 cm/h due to the deposition of sediment in top soil (Prathapar and Bawain 2014). Improper or insufficient filtration of water taken from the river to fill the municipal water tank can reduce its storage capacity due to the sedimentation of fine particles. This will cause economic loss and cut-off of water supply during the maintenance period.

Otamiri River is the major source of water for the people near it. With the addition of sediment in the river, pathogens and iron content were increased to 100% and 50%, respectively, exceeding the permissible level set by World Health Organization

Fig. 2.4 Deposition of sediment in a stormwater pipe (Weeks et al. 2013)

(WHO). Excessive iron can cause vomiting, stomach pain, etc. whereas pathogens can cause intestine infection, dysentery, etc. Sediment having arsenic can contaminate drinking water. If present at more than the critical level set by WHO, i.e. 10 µg/L, it can cause cancer of the cervical, skin, liver, kidney, and lungs. In 1998, in Brazil 126 school children were found to have a very high arsenic concentration of 25.7 µg/L. In another case, sediment with an excess of arsenic coming from the Danube River in Hungarian contaminated the groundwater. As a result of this, thousands of people get affected with skin cancer, melanosis, bronchitis, etc. (Rai et al. 2017).

2.2.4 Hydraulic Structures and Machinery

Reservoirs are built for serving multipurpose activities like water storage, water supplying for irrigation, hydropower generation, development of aquatic and wildlife, navigation, soil conservation, flood control, etc. Sediment entering a reservoir can reduce its storage capacity and useful life, which will further affect the resources depending on it. Sumi et al. (2004) observed that with the current global sediment rate, by the end of the year 2100 global reservoir storage capacity will be halved. El-Girba reservoir of Sudan lost half of its storage capacity within 13 years of its construction due to sedimentation this has resulted in drought and loss of cultivated land. A similar drastic effect of sedimentation was observed in the Hongshan reservoir situated along the Liaohe River in which 36.8% of storage capacity was lost in a span of 37 years (Liu et al. 2017). Surveys were conducted on Jor reservoir, Malaysia in the years 2007 and 2010. It was observed that a 14.3% loss in storage capacity occur due to sedimentation over the span of 3 years. Elevation of bed height due to sedimentation in Dez reservoir, causing a reduction in its storage is shown in Fig. 2.5 (Trimble and Wilson 2012).

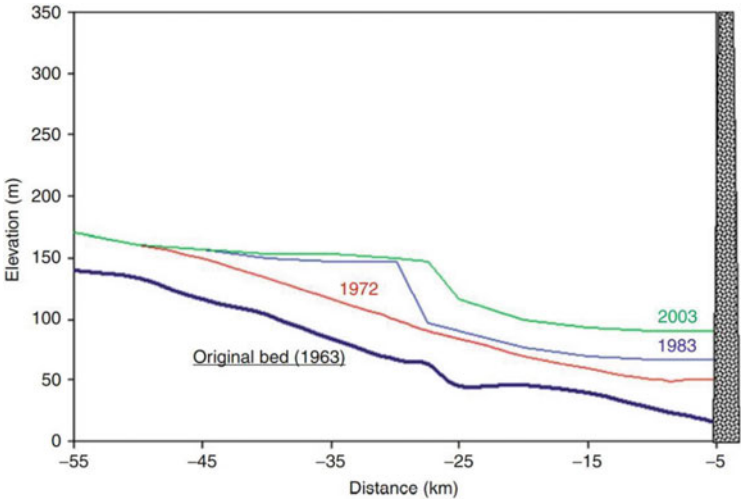

Fig. 2.5 Elevation in bed height of Dez reservoir, between 1963 and 2003 (Trimble and Wilson 2012)

Due to the loss of storage capacity of the reservoir from sedimentation, optimum discharge to hydropower plants (H.P.P.) cannot be maintained resulting in the loss of power. In Brazil, Taquaracu H.P.P. was not able to generate power equivalent to 4000 to 5000 US dollars in 1992, due to a loss of storage capacity because of sedimentation (de Miranda and Mauad 2015). Other than the loss of storage capacity, hydro-abrasive erosion of hydraulic structures is also reported in many cases due to sediment transport. Some major examples include hydro-abrasive erosion of the sluiceway of Yellowtail Afterbay sluiceway and spillway of Milburn diversion dam (Adamo et al. 2021).

The effects of the sediment hazard can also be observed in hydraulic machinery like hydraulic turbines and centrifugal pumps. When sediment with higher hardness minerals like quartz and feldspar present in water strikes the hydraulic machinery components, it leads to hydro-abrasive erosion degrading their life and performance. The impeller of the centrifugal pump used in the Jingtai Yellow River irrigation project was found to be heavily eroded (Fig. 2.6) which has dropped the performance of the pump. This is due to the high sediment concentration of Yellow River whose sediment concentration reaches up to 61,547 ppm during monsoon season, i.e. July to October (Shen et al. 2019).

In Chenani H.P.P., volume of material loss due to hydro-abrasive erosion in the nozzle and needle of the Pelton turbine was 5% and 3.71%, respectively, between May to September 2017. The eroded nozzle and needle of Chenani H.P.P. are shown in Fig. 2.7 (Din and Harmain 2020). From continuous monitoring of Toss H.P.P. from May to October 2015, Rai et al. (2017) observed a change in the profile of the Pelton bucket at the end of the observation period. Each turbine unit of H.P.P. handled 1240 tons of suspended sediment. As a result, abrasion in the

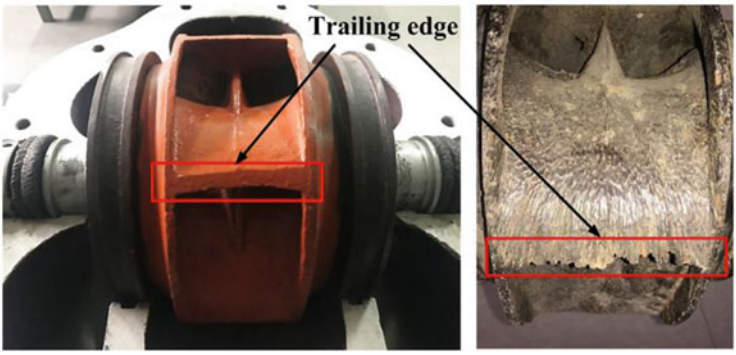

Fig. 2.6 Impeller of centrifugal pump before (left) and after (right) hydro-abrasive (Shen et al. 2019)

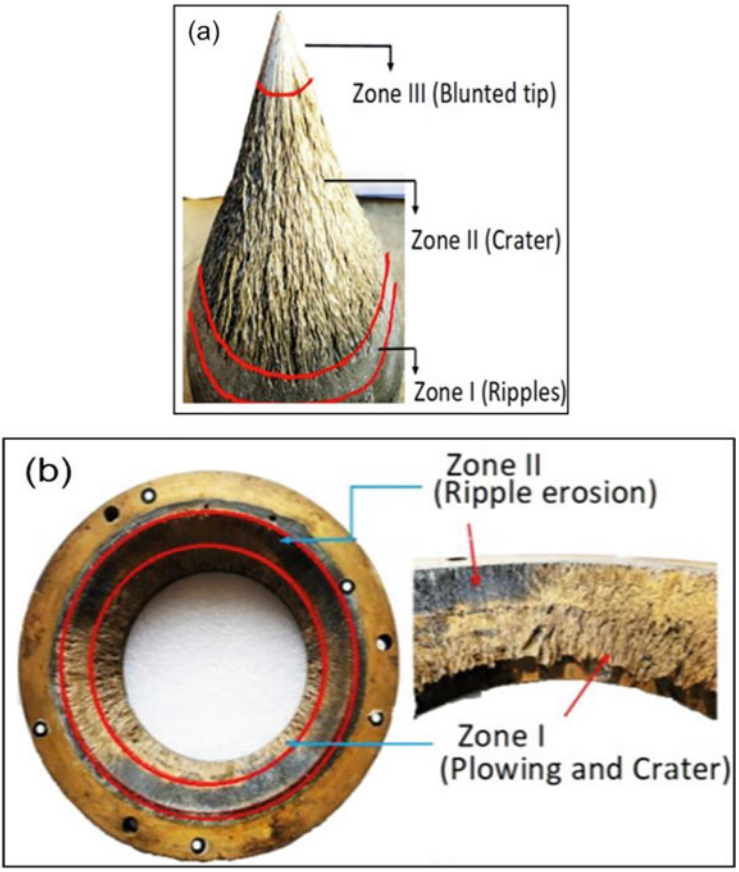

Fig. 2.7 Eroded Pelton turbine injector of Chenani H.P.P. (**a**) Needle and (**b**) Nozzle (Din and Harmain 2020)

Fig. 2.8 Eroded Pelton Bucket of Toss H.P.P. (Rai et al. 2017)

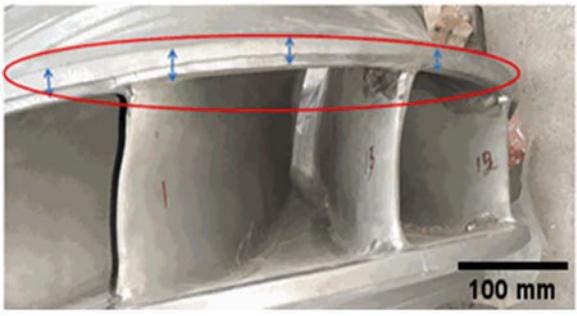

Fig. 2.9 Eroded Francis runner of Francis of Bhilangana H.P.P. (Sharma et al. 2021)

cut-out region and reduction in splitter of height were 5% and 3% of bucket width, respectively. The eroded Pelton bucket of Toss H.P.P. is shown in Fig. 2.8. In Bhilangana H.P.P., about 1.99% of the mass of the Francis turbine runner was lost in 6993.12 h of operation due to excessive sediment transportation of 29,291 megatons. Runner shroud and the trailing edge of the blades were heavily eroded. The eroded Francis runner of Bhilangana H.P.P. is shown in Fig. 2.9 (Sharma et al. 2021).

2.3 Sediment Measurement Techniques

The parameters associated with the water quality and sediments, which has potential hazardous influences, require measurement of temperature, salinity and related parameters, suspended sediments and turbidity, pH, dissolved oxygen, nutrients,

viz. nitrogen, phosphorus, organic carbon, organics as measured by oil and grease, volatile solids and biochemical oxygen demand, chlorophyll-a and pheophytin, coliforms, metals (total and dissolved), and trace organics, including pesticides, herbicides, PAH's, PCB's, and priority pollutants. However, the measurement of sediments in this present section is discussed from the aspect of sediment transport modes and different properties of sediment like sediment load, sediment discharge, suspended sediment concentration (SSC), particle size distribution, etc. because, before applying the mitigation strategy to tackle sediment hazards, proper sediment measurement needs to be done. Total sediment load comprises suspended sediment load and bed load, suspended load travel due to turbulence in water whereas bed load gets transported by sliding along the streambed due to tractive force from the water. This section comprises measurement techniques for suspended sediment load and bed load as well as accuracy and reliability related to sediment measurement.

2.3.1 Measurement of Suspended Sediment

Suspended sediment can be measured in a conventional way or by in situ method using special gauges. The details of the sediment measurement techniques, in general, are provided in this section.

2.3.1.1 Conventional Method

In conventional methods, the sediment sample is collected from the river and taken to a field laboratory for obtaining sediment-related properties, this process is known as sediment sampling. The measurement of sediment discharge can be done by distributing the cross-section of the river into different vertical sections and performing sediment sampling along this vertical. Sampling in vertical can be done either by point integration method or by depth integration method.

2.3.1.1.1 Point Integration Sampling

In point integration sampling, points are selected along the vertical to distribute the section and sediment sampling is done at these points. While sampling, a sampler is held stationary at a particular point and the sampler is moved to another specific point for sampling after sampling at the initial point. The SSC at each point in vertical is obtained in the field laboratory from which the average sediment discharge per unit width of the river is calculated. The ratio of average sediment discharge per unit width to water discharge per unit width will give average sediment concentration considering weighted discharge (Yuqian 1989).

2.3.1.1.2 Depth Integration Sampling

Depth integration sampling is performed using a specially designed depth integration sampler as shown in Fig. 2.10. Here, the sampler is lowered and raised with a controlled transit rate such that ambient flow velocity is almost equal to flow velocity at the inlet of the sampler. The sediment concentration obtained from the laboratory from this method is itself discharged weighted sediment concentration. It reduces the cost involved in the sampling process since only a one-time sample is procured in the field conditions in a vertical compared to point integration where sampling is done at multiple points in a vertical. However, for depth integration sampling, the depth of sampling is limited to 9 m for single trip and 4.5 m for round trips (Yuqian 1989).

According to the mode of operation, a sediment sampler can be classified as a manual operating sampler or an automatic sampler. The manually operated sampler can further be divided into an instantaneous sampler and an isokinetic sampler. An isokinetic sampler is a time-integrated sampler used for depth integration sampling. In this type of sampler, the magnitude and direction of flow velocity remain unaltered while entering the sampler. When frequency sampling is required or the site is not safe to operate manually then automatic samplers are used which are controlled using a microprocessor installed in the sampler.

After the sediment sample is collected, it is taken to the laboratory for measuring sediment properties like SSC and sediment size. Sediment concentration is obtained from the weight of dried sediment to the volume of a sediment-water mixture. Sediment can be separated from the sediment-water mixture by evaporation, filtration, and displacement method. In the evaporation method, sediment is dried at a constant temperature of 110 °C after separating it from clear water. It is preferred for

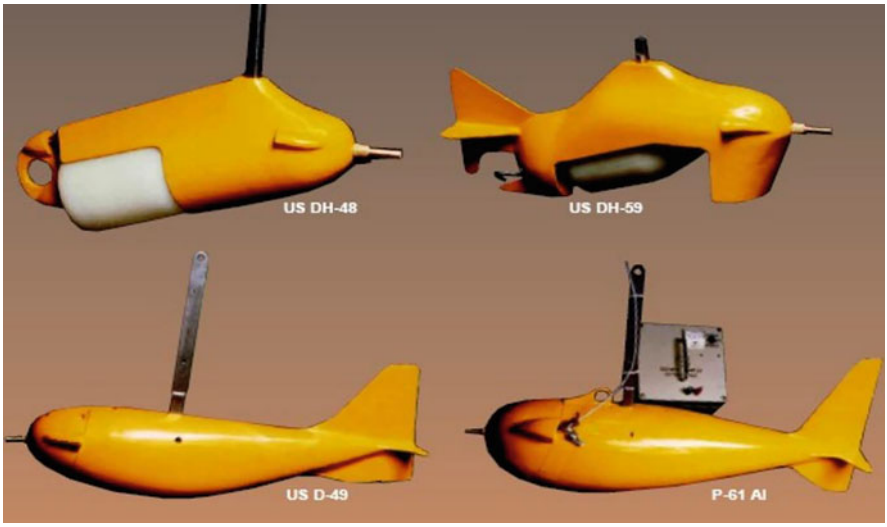

Fig. 2.10 Depth integration samplers (Msadala et al. 2010)

low sediment concentration. The filtration method is used for the medium sediment concentration, filter material is selected such that the leakage of sediment should not increase by 2% of the total sediment. In the displacement method, the difference in weight of the sediment-water mixture and clear water of the same volume is taken into consideration for determining the weight of the sediment. It is preferred when sediment concentration is very high. Measurement methods involved in the estimation of sediment size are selected according to the size of sediment. The sediment with a size lower than 2 mm is separated from the rest sample using a sieve. For sediment size less than 2 mm a method based on the settling principle of sediments like visual accumulation and pipette method is used for sediment size measurement by investigating the settling velocity of sediment. For sediment size greater than 2 mm sieve analysis is performed (Yuqian 1989).

2.3.1.2 In Situ Measurement

Measurement of suspended sediment concentration (SSC) and particle size distribution (PSD) can also be performed without collecting the sediment sample from the river. This can be achieved through continuous sediment monitoring and measurement in which the sensor of the instrument is submerged in the river, known as in situ methods. All the in situ instruments need to be calibrated within a regular time interval as the accuracy of the measurement depends on the validity of instrument calibration. Different in situ measurement techniques are discussed below.

2.3.1.2.1 Turbidity Based In Situ Technology

Turbidimeters are based on either the transmissometry principle or the scattering phenomenon. In transmissometry principle, light coming from a source gets transmitted through the sediment-water sample and is attenuated due to the absorption of some light photons by sediment. The turbidimeter detects the intensity of the attenuated light and gives the measure for SSC. Some of the initial source light striking the sediment gets scattered in a different direction. The turbidimeter based on scattering phenomena like nephelometer shown in Fig. 2.11 and optical backscatter detector (OBS) shown in Fig. 2.12 detects the intensity of scattered light and gives the measure for SSC. Since turbidity depends on the size of the sediment, this technique of measurement is valid when the range of particle size is minimal (Rai and Kumar 2015).

2.3.1.2.2 Acoustic-Based In Situ Technology

Hydro-acoustics can also be considered for measuring SSC and PSD. In this technique, an acoustic transducer sends the acoustic signal. The signal, after striking the sediment present in water, gets attenuated due to viscous and scattering loss and

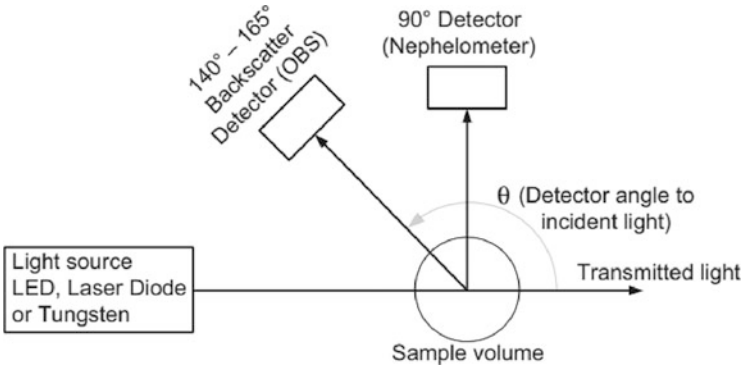

Fig. 2.11 Scattering principle of turbidimeter (Rai and Kumar 2015)

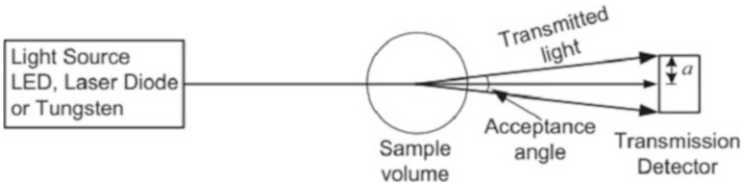

Fig. 2.12 Transmissometry principle of turbidimeter (Rai and Kumar 2015)

returns back to the transducer (acoustic backscatter detector) as shown in Fig. 2.13. Measuring the backscatter signal strength gives the SSC and PSD. Similar to a turbidimeter, the use of an acoustic backscatter detector is limited to small variations in the size of sediment (Rai and Kumar 2015).

2.3.1.2.3 Laser Diffraction-Based In Situ Technology

This method is based on the diffraction principle of optics, in which definite size sediment will diffract the light at a specific signal. The larger the sediment size, the smaller will be the angle of diffraction of light. Monochromatic light is made to pass through suspended sediment after which light is diffracted and reaches a receiver lens, through which it is passed and detected by a different detector placed at the focus of the receiving lens as shown in Fig. 2.14. Light energy recorded by the detector gives the volumetric SSC and PSD. Though the cost involved in LISST is higher than other in situ measurement techniques, it is the most reliable and accurate in situ technique (Rai and Kumar 2015).

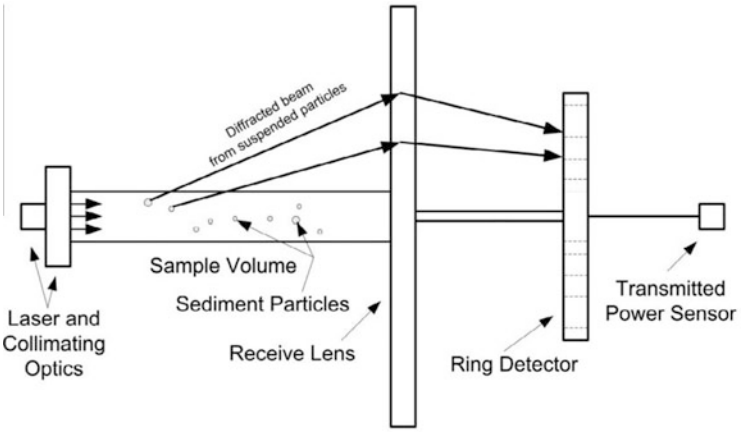

Fig. 2.13 Acoustic-based sediment measurement (Rai and Kumar 2015)

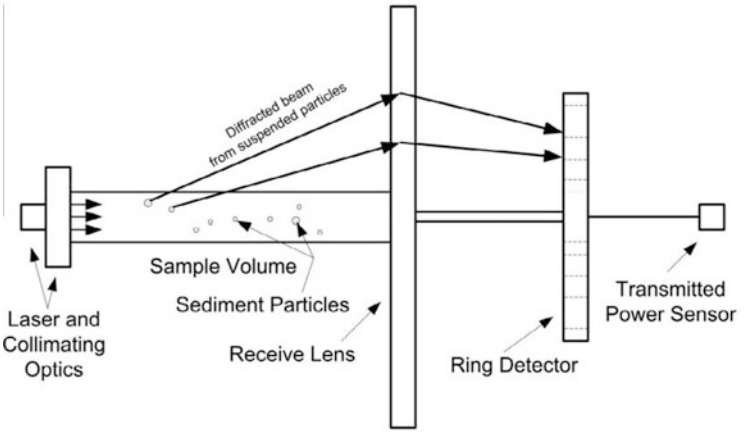

Fig. 2.14 Laser diffraction-based sediment measurement (Rai and Kumar 2015)

2.3.1.2.4 Nuclear-Based In Situ Technology

In a nuclear-based technique to measure sediment concentration, monochromatic radiation is transmitted from radioisotopes like cadmium-109 and americium-241. These isotopes should have low energy otherwise small variation in SSC will not be detected by the nuclear gauge and the half-life of the isotope should be long so that frequent calibration of the nuclear gauge is not required. The principle for measuring SSC in this method is based on the detection of attenuated nuclear radiation transmitted or scattered after interacting with sediment. In scattering type measurement, a reduction in the number of photons after striking the sediment is sensed by the detector which gives the SSC. In transmission type measurement, when nuclear radiation passes through the sediment, some of it gets absorbed by it. Attenuated

nuclear radiation transmitted through the sediment is detected by the nuclear gauge. Variation in the intensity of attenuated nuclear radiation coming through sediment and nuclear radiation coming through pure water after traveling the same distance and reaching the detector is the basis for determining the SSC (Pu et al. 2021).

2.3.2 Measurement of Bed Load

Bed load is part of total sediment load other than suspended sediment load. Measurement of bed load can be carried out either by using a direct method or an indirect method.

2.3.2.1 Direct Method

In the direct method, a sample of bed load is taken with a specially designed bed load sampler and is taken to the field laboratory for a further investigation similar to the conventional method of suspended sediment measurement. Some of the bed load samplers are discussed below.

2.3.2.1.1 Basket Type Sampler

The basket type sampler consists of a box for collecting sediment samples. In such samplers, metallic sides with a mesh structure and a steering fin as shown in Fig. 2.15 are used for positioning and the sampler is rested in the stream bed. Almost half of the sediment coming toward the sampler is dropped out at entranced of the sampler due to a reduction in flow velocity because of the sampler.

2.3.2.1.2 Pressure Difference Sampler

The pressure difference sampler has overcome the problem of basket type sampler due to a reduction in flow velocity at the inlet of the sampler. Here, a pressure drop is created by making the container in diverging section as shown in Fig. 2.16. This inlet velocity remains almost equal to undisturbed stream velocity. Sediment samples are collected at the rear end of the sampler.

2.3.2.1.3 Pan Type Sampler

In a pan type sampler, baffles or strip is provided in the collector region to trap the sediment as shown in Fig. 2.17. It is made similar to a pressure difference sampler with diverging section to maintain the stream flow.

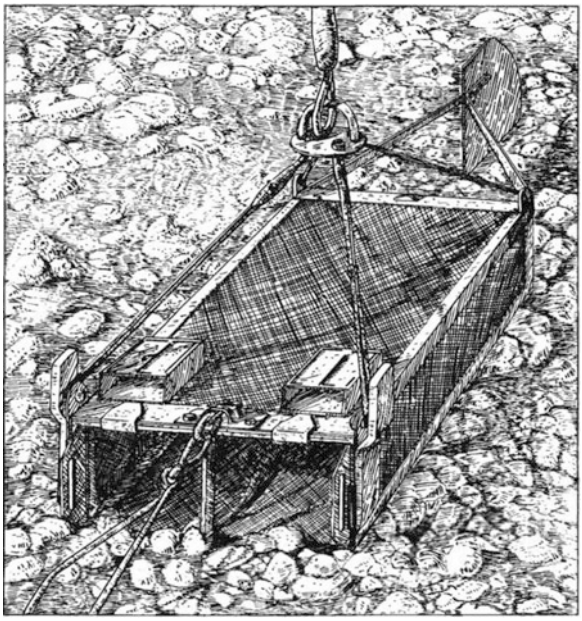

Fig. 2.15 Basket type bed load sampler (Hubbell 1964)

Fig. 2.16 Pressure difference type bed load sampler (Erskine et al. 2011)

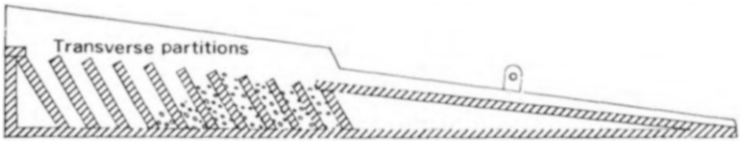

Fig. 2.17 Pan type bed load sampler (Hubbell 1964)

2.3.2.1.4 Slot Type Sampler

A slot type sampler is placed inside the sediment bed with an opening at the top such that moving sediment drops in the slot as shown in Fig. 2.18 and it is generally preferred for small streams.

2.3.2.2 Indirect Method

2.3.2.2.1 Sedimentation Process

In the sedimentation process, water containing sediment enters a reservoir where it is allowed to completely settle down. After the sediment settlement, the already calculated suspended sediment load before the water enters the reservoir is deducted from the total deposited load to get the bed load.

2.3.2.2.2 Dune Tracking

In the dune tracking method, the dune created by the movement of bed load in flow direction is analyzed. Longitudinal profiles of the dunes are investigated by repetitive measure for up to 25 dunes using an echo sounder. It is generally used for an alluvial river in which it is difficult to measure bed load due to the presence of fine sand.

2.3.2.2.3 Tracer Method

In the tracer method, the movement of the bed load is investigated using the tracer. The entire process involves the selection of a correct tracer, the introduction of the tracer to bed load, and the detection. This process eventually gives bed load discharge. Generally, stable isotope tracer, fluorescent tracer, and radioactive tracer are used for this purpose. Among all three tracers, only a radioactive tracer can be used for in situ measurement and in measuring fine sediment particles. Stable isotope tracer and fluorescent tracer investigate the sediments sample in the field laboratory.

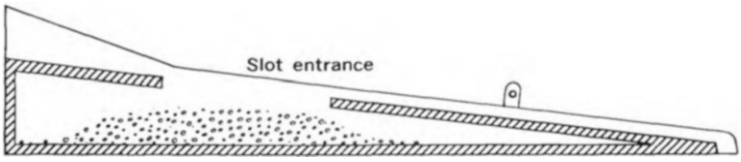

Fig. 2.18 Slot type bed load sampler (Hubbell 1964)

2.3.3 Accuracy and Reliability in Sediment Measurement

For correct measurement of the sediment load, an assessment of reliability and accuracy need to be performed as measurements are affected by systematic and random error. Accuracy of measurement can be increased by increasing the number of observations if only a random error is present; but, if the systematic error is also present, there liability of the measurement reduces with observations. Improper selection or incorrect use of instruments can generate systematic errors. If the transit rate of a sampler in the depth integration sampling is more than 0.4 times the average velocity in the vertical, it can result in an inaccurate result. Error in the calibration of the instrument is another reason for the systematic error. For in situ-based instruments, if the counting rate at which signal is received by the sensor is less, it can result in a higher chance of error in the measurement. A minimum weight or volume of sediment sample is required in laboratory measurements. If minimum sample quantity criteria are not fulfilled, a systematic error can be generated.

While measuring the sediment discharge error is more for coarser sediment due to the involvement of high non-uniformity. Thus, measurement of bed load discharge is less accurate than suspended sediment load discharge due to higher coarser sediment in bed load. Also due to spatially and temporally variation of bed load, it is very difficult to obtain a reliable result of sediment measurement. In point sampling of suspended sediment, the depth of the sample cannot be exactly equal to stream depth. It induces negative systematic error while measurement. The ignorance of suspended sediment variation/distribution in the vertical and transport of sediment in the unmeasured zone can also result in systematic errors (Yuqian 1989). If the measurement section is not enough or the site of measurement is not properly selected, measurement can deviate from accurate values. SSC measurement used for designing hydraulic machinery would be unreliable if continuous measurement is not taken throughout the year, especially during the rainy monsoon season when the maximum SSC is expected.

2.4 Mitigation Strategies for Sediment Hazard

With such a ravaging effect of sediment hazards on different elements of an ecosystem, strategies to manage and mitigate the hazard need to be considered. Some of those techniques are discussed here.

The chance for the occurrence of landslides can be reduced by removing heavy rocks and debris from the top of the sloppy land, reducing the slope of the land by digging the top surface or filling the bottom surface, and preserving trees and tall grasses present along the slope, terrace farming, etc. Constructing a proper drainage system to avoid water run-off entering loose clay, sand, gravel, etc. can also diminish the chances of landslides. Sediment entering the river from its bank can be reduced by stabilizing river bank erosion. This can be done by having dense vegetation near

Fig. 2.19 Stabilization of river bank using (**a**) Turf reinforcement matrix (**b**) Coir logs (Aditi 2020)

the river banks, constructing retention walls and riprap, placing coir logs and synthetic fiber mats along the river bank, etc. as shown in Fig. 2.19, among them synthetic fiber mats are more long lasting due to its non-biodegradable nature. Sedimentation at reservoirs can be prevented or reduced by implementing three different steps. The first step is to prevent sediment from entering the reservoir, the second step is to prevent sediment deposition in the reservoir, and the third step is by removing the sediment already deposited in the reservoir.

Sediment entering the reservoir can be prevented by stabilizing the river bank, improving farming techniques, afforestation, constructing check dams and desilting basins, etc. In the Yellow river basin, more than 1 lakh of check dams are constructed to restrict the sediment entering the reservoir (Liu et al. 2017). The initial sedimentation rate in the Tungabhadra reservoir was 50.47 million m^3 per year which was reduced to 16 million m^3 after the construction of the Bhadra dam and by afforestation in an area of 223 km^2. In order to reduce the high sedimentation rate of 70 million m^3 per year of the Guanting reservoir, more than 300 small reservoirs were constructed in the catchment. This has significantly reduced the sedimentation rate of the Guanting reservoir to 6.6 million m^3 per year (Batuca and Jordaan 2000). About 90% of sediment coming to the Hongshan reservoir of China was restricted by the vegetation screen of Typha Latifolia and Scirpus Yagara plants (Brabben 1998).

Sediment can be prevented from settling down in the reservoir by constructing a bypass tunnel which will divert the sediment flow as shown in Fig. 2.20. This technique is quite effective during floods when the sediment discharge rate is high. The Hushan reservoir of China has lost 54% of its storage capacity within seven years of its construction due to the high sedimentation rate. Later a sediment bypass tunnel has been constructed, which resulted in reducing the annual sedimentation rate of the reservoir by approximately 92%. Amsteg and Palagnedra reservoirs of Switzerland have reported almost no sedimentation after the construction of a bypass tunnel for diverting the sediments (Trimble and Wilson 2012). In the Nunobiki dam of Japan, sediment entering the reservoir was reduced by 95% after the completion of a bypass tunnel. Asahi dam of Japan faced a huge sedimentation problem as about 85 thousand m^3 of sediment gets deposited in the reservoir every year. With the construction of a sediment bypass tunnel, only 10% to 20% of sediment was able to

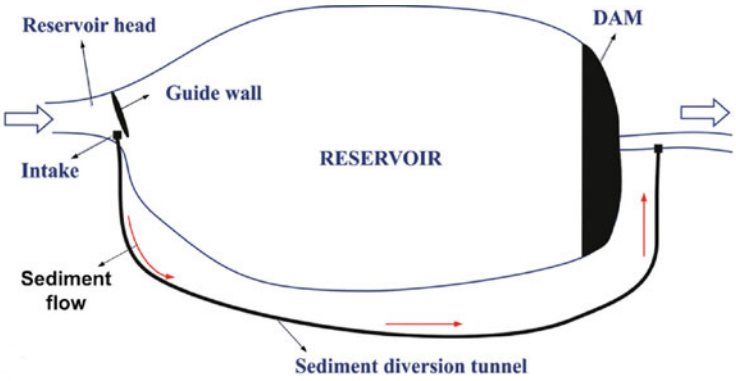

Fig. 2.20 Diversion of sediment flow by bypass tunnel (Hauer et al. 2018)

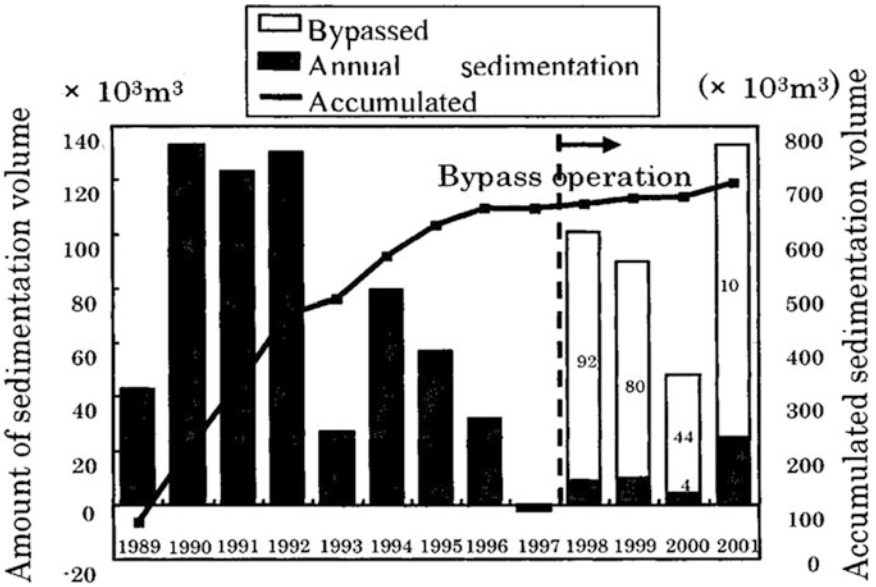

Fig. 2.21 Reduction in sediment accumulation in Asahi dam due to bypass tunnel (Sumi et al. 2004)

enter the reservoir, rest was diverted by the bypass tunnel as shown in Fig. 2.21 (Sumi et al. 2004). When high-density sediment carrying water enters the low-density clear water present in the reservoir, a turbidity current is formed. Proper monitoring and releasing the turbidity current through the bottom outlet vent can also prevent the settlement of sediment. During flood seasons huge amount of sediment was transported to Mapragg reservoir along with the formation of a turbidity current. By venting the turbidity current from the bottom outlet, about 6000 tons of sediments have been released (Trimble and Wilson 2012). More than

60% of sediment entering the Nebeur reservoir of Tunesia is prevented from settling down by venting turbidity current (Rai et al. 2017).

Already deposited sediment can be removed from the reservoir by flushing and dredging. The opening of the sluice gate present at the bottom outlet of the reservoir releases water along with the deposited sediments. This process is known as sediment flushing. In the years 2002 and 2003, sediment flushing was carried out on the Xiaolangdi reservoir of Yellow River from which 66.4 million tonnes and 120.7 million tonnes of sediment were flushed out (Liu et al. 2017). About 3.19 million m^3 of sediment was deposited in the Hengshan reservoir of China in 8 years since its construction. After two times flushing, the sediment deposited was reduced to 2.62 million m^3. In absence of a flushing process, 60% storage capacity of the Gen Shan Pei reservoir of Taiwan was lost in 19 years due to a high sedimentation rate of 0.224 million m^3 per year. With the adoption of the flushing process at a regular time interval, the sedimentation rate is reduced to 0.0012 million m^3 per year (Batuca and Jordaan 2000). Removal of sediment through machines or an external source like a strong water jet to regain the lost storage capacity of reservoirs, lakes, ponds, etc. is known as dredging. It is a costly process and is done when flushing and construction of a bypass tunnel are not possible or uneconomic. 160 million US dollars were spent on the Shihmen reservoir in the dredging process for removing 8.1 Million m^3 of sediment (Wang et al. 2018). Lilly lake was restored by dredging 6.65 lakh m^3 of sediment. In another case, dredging has increased the storage capacity of the Shunshine Spring pond by 300% (Peterson 1982).

The disastrous effects of hydro-abrasive erosion on hydraulic machinery due to sediment flow can be mitigated by placing a desilting basin upstream of the H.P.P. Generally very fine sediment particles with a size less than 200 μm cannot be filtered and are responsible for hydro-abrasive erosion (John et al. 2021). Optimizing the design and flow condition in hydraulic machinery using CFD can also help in reducing hydro-abrasive erosion. Furthermore, coating the base material with hydro-abrasive erosion-resistant material can be done for decreasing the erosion rate. Making components of centrifugal pumps with materials like nickel-chromium-based stainless steel, and cobalt-based super-alloys can reduce the hydro-abrasive erosion rate due to their high abrasive resistant property. Variation in velocity around the blade of the impeller is a major cause of hydro-abrasive erosion in a centrifugal pump. This can be done by producing a swirling flow around the convex dome of the bionic blade (Pokharel et al. 2022). One of the main reasons for the hydro-abrasive erosion of the runner in the Francis turbine is the high relative velocity across it. Reducing the curvature of the blade at the outlet or increasing the thickness of the blade at the trailing edge can reduce the hydro-abrasive erosion in the Francis turbine by reducing the magnitude of relative velocity (Eltvik 2009). Rai et al. (2020) compared the hydro-abrasive behavior in Pelton turbine buckets for six different materials. They observed that 13 Cr-4Ni steel coated with HVOF tungsten carbide is most resistive to hydro-abrasive erosion and bronze is the least resistive. Messa et al. (2019) observed a decrease in hydro-abrasive erosion in the Pelton injector with an increase in needle vertex angle. A landslides early warning system (LEWS) can be useful in reducing the adverse effects of sediment hazards by evacuating lives at the

right time. Guzzetti et al. (2020) observed LEWS based on the rainfall forecast model, beneficial in giving early alerts for landslides in different regional and national systems. Furthermore, CFD-based technologies can be used in the future to predict flow patterns and intensity of sediment transport, which can help in selecting and optimizing mitigation strategies.

2.5 Conclusion

In this article, sediment hazards occurring naturally or through human activity have been discussed in detail. Various causes, case studies along with the effects of the sediment hazard are provided. Sediment measurement which plays an important role in deciding mitigation techniques is also discussed along with strategies for reducing the disastrous effects of sediment hazards. Sediment hazards due to either transportation or by deposition of the sediment can occur due to natural phenomena like rainfall, heavy wind flow, etc., or by man-made activities like mining, farming, etc. Sediment hazard is a threat to abiotic factors like hydraulic structures and hydraulic machinery as well as biotic factors like fishes, humans, etc. Sedimentation in reservoirs is one of the biggest menaces of the sediment hazard affecting the hydropower generation, irrigation, and development of aquatic life depending on the reservoir.

The study of sediment measurement techniques helps in selecting a proper mitigation strategy. Separate measurements of suspended sediment load from sampling, in situ technology, and bed load from the direct and indirect methods will provide the total sediment load present in the stream. By investigating the accuracy and reliability of the measurement chance of systematic error can be reduced. The sedimentation problem of the reservoirs can be controlled by afforestation, construction of check dams, bypass tunnels, sediment flushing, and dredging. Hydro-abrasive erosion caused by striking sediment particles can be mitigated by selecting proper material, optimum flow conditions, and the design of hydraulic components.

References

Adamo N, Al-Ansari N, Sissakian V, Laue J, Knutsson S (2021) Dam safety: sediments and debris problems. J Earth Sci Geotech Eng 11(1):27–63

Aditi U River Bank erosion ,Causes, River Bank Erosion Control Methods in Detail. 2020. https://civildigital.com/river-bank-erosion-causes-river-bank-erosion-control-methods-in-detail/. Accessed 23 May 2022

Batuca DG, Jordaan JM (2000) Silting and desilting of reservoirs. Taylor and Francis, Netherlands

Brabben T. Reservoir desilting methods. 1998. https://eprints.hrwallingford.com/180/. Accessed 22 May 2022

Bruton MN (1985) The effects of suspensoids on fish. Perspect Southern Hemisphere Limnol 28: 221–241

de Miranda RB, Mauad FF (2015) Influence of sedimentation on hydroelectric power generation: case study of a Brazilian reservoir. J Energy Eng 141(3):04014016
Deen S, Sharma S (2020) Impact of Kedarnath flood tragedy on ecological and socio-economic setup: a geographical study. Sodhsanchar Bull 10(40):128–133
DFO (2000) Effects of sediment on fish and their habitat. In: DFO Pacific Region Habitat Status Report 2000/01
Din MZ, Harmain GA (2020) Assessment of erosive wear of Pelton turbine injector: nozzle and spear combination–a study of Chenani hydro-power plant. Eng Fail Anal 116:104695
Eltvik M. Sediment erosion in Francis turbines. 2009. http://hdl.handle.net/11250/235485. Accessed May 22 2022
Erskine WD, Saynor MJ, Evans KG, Moliere DR (2011) Bedload transport, hydrology and river hydraulics in the Ngarradj Creek catchment. In: Jabiluka, Northern Territory, Australia Supervising scientist report, p 199
Fu KD, He DM, Lu XX (2008) Sedimentation in the Manwan reservoir in the upper Mekong and its downstream impacts. Quat Int 186(1):91–99
Geertsema M, Highland L, Vaugeouis L (2009) Environmental impact of landslides. In: Landslides–disaster risk reduction. Springer Science & Business Media, New York
Guzzetti F, Gariano SL, Peruccacci S, Brunetti MT, Marchesini I, Rossi M et al (2020) Geographical landslide early warning systems. Earth Sci Rev 200:102973
Hauer C, Wagner B, Aigner J, Holzapfel P, Flödl P, Liedermann M, Tritthart M, Sindelar C, Pulg U, Klosch M, Haimann M (2018) State of the art, shortcomings and future challenges for a sustainable sediment management in hydropower: a review. Renew Sust Energ Rev 98:40–55
Hubbell DW. Apparatus and techniques for measuring bedload. US Govt Print Off 1964. https://pubs.er.usgs.gov/publication/wsp1748. Accessed 22 May 2022
Huertos ML (2020) Water Quality and catchments. In: Ecology and management of inland waters. Elsevier Science, Amsterdam, pp 315–358
John CK, Pu JH, Pandey M, Hanmaiahgari PR (2021) Sediment deposition within rainwater: case study comparison of four different sites in Ikorodu, Nigeria. Fluids 6(3):124
Joshi J, Bhattarai TN, Sthapit KM, Omura H (1998) Soil erosion and sediment disaster in Nepal-a review. J Fac Agric Kyushu Univ 42:491–502
Junichi K, Naoki I (2020) Outline of measures for sediment disaster by the Sabo department of MLIT. Japan Landslides 17(11):2503–2513
Kothyari UC (2011) Sediment problems and sediment management in the indian sub-himalayan region. In: Sediment Problems and Sediment Management in Asian River Basins, vol 349. IAHS Press, Wallingford
Li J, Yin H, Chang J, Lu C, Zhou H (2009) Sedimentation effects of the Dongting Lake area. J Geogr Sci 3:287–298
Liu C, Walling DE, Spreafico M, Ramasamy J, Thulstrup HD, Mishra A. Sediment problems and strategies for their management: experience from several large river basins. United Nations Educational, Scientific and Cultural Organization, Paris 2017. https://unesdoc.unesco.org/ark:/48223/pf0000258795. Accessed 21 May 2022
Messa GV, Mandelli S, Malavasi S (2019) Hydro-abrasive erosion in Pelton turbine injectors: a numerical study. Renew Energy 130:474–488
Msadala V, Gibson L, Le Roux J, Rooseboom A, Basson GR (2010) Sediment yield prediction for South Africa: 2010th edition. Pretoria, South Africa, South African Water Research Commission
Peterson SA (1982) Lake restoration by sediment removal 1. J Am Water Resour Assoc 18(3):423–435
Pimentel D, Kounang N (1998) Ecology of soil erosion in ecosystems. Ecosystems 1(5):416–426
Pokharel N, Ghimire A, Thapa B, Thapa BS (2022) Wear in centrifugal pumps with causes, effects and remedies: a review. Earth Environ Sci 1037:012042
Prathapar SA, Bawain AA (2014) Impact of sedimentation on groundwater recharge at SahalanowtDam, Salalah. Oman Water Int 39(3):381–393

Prosser IP, Rutherfurd ID, Olley JM, Young WJ, Wallbrink PJ, Moran CJ (2001) Large-scale patterns of erosion and sediment transport in river networks, with examples from Australia. Marine and Freshwater Research. 52(1):81–99

Pu JH, Wallwork JT, Khan MA, Pandey M, Pourshahbaz H, Satyanaga A, Hanmaiahgari PR, Gough T (2021) Flood suspended sediment transport: combined modelling from dilute to hyper-concentrated flow. Water 13(3):379

Rai AK, Kumar A, Staubli T (2020) Effect of concentration and size of sediments on hydro-abrasive erosion of Pelton turbine. Renew Energy 145:893–902

Rai AK, Kumar A, Staubli T (2017) Hydro-abrasive erosion in Pelton buckets: classification and field study. Wear 392:8–20

Rai AK, Kumar A (2015) Continuous measurement of suspended sediment concentration: technological advancement and future outlook. Measurement 76:209–227

Schuster RL, Highland LM (2007) Overview of the effects of mass wasting on the natural environment. Environ Eng Geosci 13(1):25–44

Sharma S, Gandhi BK, Pandey L (2021) Measurement and analysis of sediment erosion of a high head Francis turbine: a field study of Bhilangana-III hydropower plant, India. Eng Failure Anal 122:105249

Shen Z, Chu W, Li X, Dong W (2019) Sediment erosion in the impeller of a double-suction centrifugal pump–a case study of the Jingtai Yellow River irrigation project, China. Wear 422: 269–279

Singh P, Ramasatri KS, Kumar N, Bhatnagar NK (2003) Suspended sediment transport from the Dokriani glacier in the Garhwal Himalayas. Hydrol Res 34(3):221–244

Sumi T, Okano M, Takata Y (2004) Reservoir sedimentation management with bypass tunnels in Japan. In: 9th International symposium on river sedimentation, pp 1036–1043

Trimble SW, Wilson B (2012) Reservoir and lake trap efficiency. Encyclopedia of Earth Sciences Series 1:619–626

Trout TJ, Neibling WH (1993) Erosion and sedimentation processes on irrigated fields. J Irrig Drain Eng 119(6):947–963

Vasantha Kumar S, Bhagavanulu DV (2008) Effect of deforestation on landslides in Nilgiris district—a case study. J Indian Soc Remote Sens 36(1):105–108

Wang HW, Kondolf M, Tullos D, Kuo WC (2018) Sediment management in Taiwan's reservoirs and barriers to implementation. Water 10(8):1034

Weeks W, Witheridge G, Rigby E, Barthelmess A, O Loughlin Project 11: blockage of hydraulic structures. Engineers Australia 2013. https://arr.ga.gov.au/arr-guideline/revision-projects/project-list/projects/project-11. Accessed 21 May 2022

Wohl EE, McConnell R, Skinner J, Stenzel R. Inheriting our past: river sediment sources and sediment hazards in Colorado. 1998

Woldearegay K (2013) Review of the occurrences and influencing factors of landslides in the highlands of Ethiopia: with implications for infrastructural development. Momona Ethiop. J. Sci 5(1):3–31

Yuqian L (1989) Manual on operational methods for the measurement of sediment transport. World Meteorological Organization, Geneva

Zhide Z, Yuling T (2010) Sediment in Rivers-origin and challenges. Stockholm Water Front 4:8–10

Chapter 3
Modeling Approach to Study the Riverine Flood Hazard of Lower Damodar River

Ravindra Kumar Singh, Ravi Prakash Tripathi, Shweta Singh, Srinivas Pasupuleti, and Vasanta Govind Kumar Villuri

Abstract Flood is the hydraulic response of the river to the rainfall excess runoff generated in the natural watershed due to high rainfall events. The accuracy of flood damage evaluations depends on the understanding of the occurrence of flood events and the areas that are vulnerable to flood damage. Hydraulic and hydrologic models have gained significant importance among hydrologists for flood study. The objective of this study is to identify the locations along the lower Damodar river which are susceptible to flood. One dimensional hydrodynamic model using MIKE HYDRO RIVER was prepared for flood of 20 year return period in the lower Damodar river. For the Manning's n value of 0.03, the model output data (water depth) match closed to observed water depth at three gauge station. Furthermore, NSE, PBIAS, and RSR were used for determining the model performance. A good agreement was detected between the model output and the observed data at the gauging stations. The finding of the study indicated that majority of river discharge (65% to 70%) is carried by Mundeswari river and 30% to 35% carried by Amta Damodar in lower part of the Damaodar river. Encroachment in the riverine system for agricultural purposes,

R. K. Singh (✉)
Department of Civil Engineering, Maharishi University of Information Technology, Lucknow, India

R. P. Tripathi
Department of Civil Engineering, Rajkiya Engineering College, Sonbhadra, India
e-mail: ravipt.rs.civ15@itbhu.ac.in

S. Singh
Department of Electrical Engineering, Maharishi University of Information Technology, Lucknow, India

S. Pasupuleti
Department of Civil Engineering, Indian Institute of Technology (Indian School of Mines), Dhanbad, Jharkhand, India
e-mail: srinivas@iitism.ac.in

V. G. K. Villuri
Department of Mining Engineering, Indian Institute of Technology (Indian School of Mines), Dhanbad, Jharkhand, India
e-mail: vgkvilluri@iitism.ac.in

M. Pandey et al. (eds.), *River Dynamics and Flood Hazards*, Disaster Resilience and Green Growth, https://doi.org/10.1007/978-981-19-7100-6_3

changes in the LULC due to recent developments, and activation of local minor distributaries during the peak monsoon season with inadequate capacity in these low-lying areas aid the spatial extent of the flooding.

Keywords Flood · Hydrodynamic Model · MIKE HYDRO RIVER · Remote Sensing

3.1 Introduction

Disasters are as ancient as human civilization. Disasters are events of severe disruption that causes monetary, material, human, and environmental losses, and they also adversely affect the progress of a country. Disasters can be natural or man-made. Natural disasters include floods, cyclones, cloudbursts, snow avalanches, earthquakes, hailstorms, and landslides, whereas man-made disasters refer to railroad accidents, fires, and leakages of chemicals/ nuclear installations, among others. The phases of all disasters are the same, whether such disasters are natural or man-made. India as a nation is highly vulnerable to cyclones, floods, droughts, and earthquakes. Every year, food security, health infrastructure, agriculture, economy, and environment are adversely affected by natural disasters. The nation's infrastructure encounters a wide range of direct and indirect losses due to various disasters. The productivity of crops and agricultural land suffers huge losses due to droughts. Floods and cyclones cause immense damage to infrastructure, whereas damage to agriculture depends on the relative agricultural cycle. India as a nation is highly vulnerable to cyclones, floods, droughts, and earthquakes. Every year, food security, health infrastructure, agriculture, economy, and environment are adversely affected by natural disasters. The nation's infrastructure encounters a wide range of direct and indirect losses due to various disasters. The productivity of crops and agricultural land suffers huge losses due to droughts. Floods and cyclones cause immense damage to infrastructure, whereas damage to agriculture depends on the relative agricultural cycle.

Flood is the hydraulic response of the river to the rainfall excess runoff generated in the natural watershed due to high rainfall events. It is extensively destructive natural disasters causing massive societal and monetary loss to several nations globally (Mosavi et al. 2018). In present time floods become a huge problem due to fast land use change, channel blockages in low-lying areas, sedimentation in river, urban sprawl in areas prone to flooding and population growth (Pramanik et al. 2010; Singh et al. 2020). The distinctive circumstances of information are vital to learning about flood occurrence (e.g., hydrological aspect means the intensity and frequency of rain, hydraulics aspect refers to the response of river to rainfall, geographical aspect pertains to flood zone, environmental aspect is the damage to the system, and civil engineering aspect denotes the response of a structure to the flood hazard). The accuracy of flood damage evaluations depends on the understanding of the occurrence of flood events and the areas that are vulnerable to flood damage. Thus,

gaining an understanding of the catchment area response to river discharge during rainfall is critically important.

The primary aim of flood risk analysis is to evaluate the probable consequences related to the incidence of flooding in an area. During earlier periods, flood risk was primarily related to the prospect of hazard incidence. However, flood risk nowadays is also associated with the susceptibility of the system to damage. To develop a flood control system, obtaining knowledge regarding the occurrence of flood and its after effects is crucial. Although flood cannot be wholly evaded, its hazardous effects can be weakened usually by structural or non-structural approaches. On the one hand, structural modes involve designing and building a river embankment or a reservoir structure to safeguard the flood vulnerable areas. On the other hand, non-structural methods entail defining the flood zoning area and developing an early flood warning system that can help with shifting the affected individuals during a flooding. Non-structural approaches nowadays have become more popular than flood protection works because earlier is a cost-effective system.

Hydraulic and hydrologic models have gained significant importance among hydrologists for river basin management in situations involving the investigation of real-time prediction (Bates and De Roo 2000; Hsu et al. 2003; Pappenberger et al. 2005; Jung and Merwade 2011; Pappenberger et al. 2006; Quiroga et al. 2016; Noh et al. 2019; Nyaupane et al. 2018). Abdella and Mekuanent (2021) applied hydrodynamic models on Kulfo river in southern Ethiopia for riverine flood mitigation. The simulation of real flood events using factual hydrological data along with geometric data for specific river system is performed in the flood model. Based on the simulation of the flood model, the characteristics of flood risk can be determined at a particular instant of time. With the advancement of technology, computational time has significantly reduced during flood mapping. In hydrological modeling, remote sensing (RS) data are frequently used for the preparation of geometric data and a thematic map in the absence of field data. Geospatial technologies provide powerful capabilities for natural hazard planning, monitoring, and mitigation. Geographic Information System (GIS) is used for identifying vulnerable areas; moreover, the representation of existing terrain is possible through spatial tools and modeling techniques (Saraf and Choudhury 1998; Chowdhury et al. 2010; Meyer et al. 2009). The use of computer-based systems in support of decision making in different phases of disaster management has dramatically increased over the past decade. With advances in computer technology, this computational limitation is being resolved (Morales-Hernández et al. 2020). Enhanced computing power has enabled large-scale flood modeling applications ranging from regional to national scales (Ashrafi et al. 2017; Yu et al. 2017; Wing et al. 2019). Spatial decision support system (SDSS) has gained importance among decision makers that incorporates the computational capabilities of computers to understand the response of complex physical systems during a disaster (Shankar and Mohan 2005; Sinha et al. 2008; Boroushaki and Malczewski 2010).

3.2 Rational of the Study

Floods and cyclones cause immense damage to infrastructure, whereas damage to agriculture depends on the relative agricultural cycle. The EM-DAT is a global database formed by the funding of the WHO and the Belgian government. According to Emergency Events Database (EM-DAT), in the past four decades on a worldwide level, floods caused maximum economic damage among natural disasters, except for a few years in which earthquakes predominated, as shown in Fig. 3.1. Keeping in view aforementioned issue present work prepared a 1-D hydrodynamic model for lower Damodar river using high resolution RS data. The purpose of this study is to identify the locations along the lower Damodar river which are susceptible to flood. Present study used MIKE HYDRO RIVER software developed by DHI to prepare 1-D model. Thus, the aim of this study is to boost the understanding of the flooding problem of the lower Damodar river by preparing a hydrodynamic model. Study area map is shown in Fig. 3.2.

3.3 Limitations of the Study

In this study 1-D hydrodynamic model was considered for riverine flood of the Damodar river in which geometric data of river cross-section was extracted from high resolution remote sensing data. 1-D model is better for river flow but for floodplain areas analysis its results will be conservative.

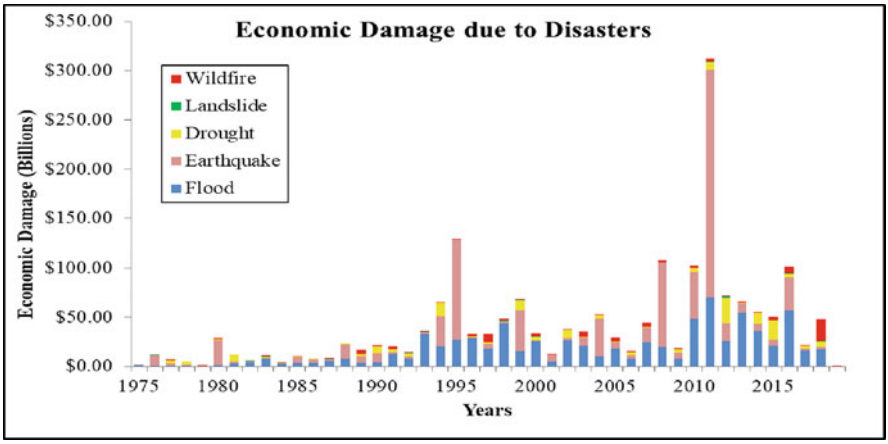

Fig. 3.1 Representation of economic damage by the different types of natural disaster (Source: EM-DAT 2018)

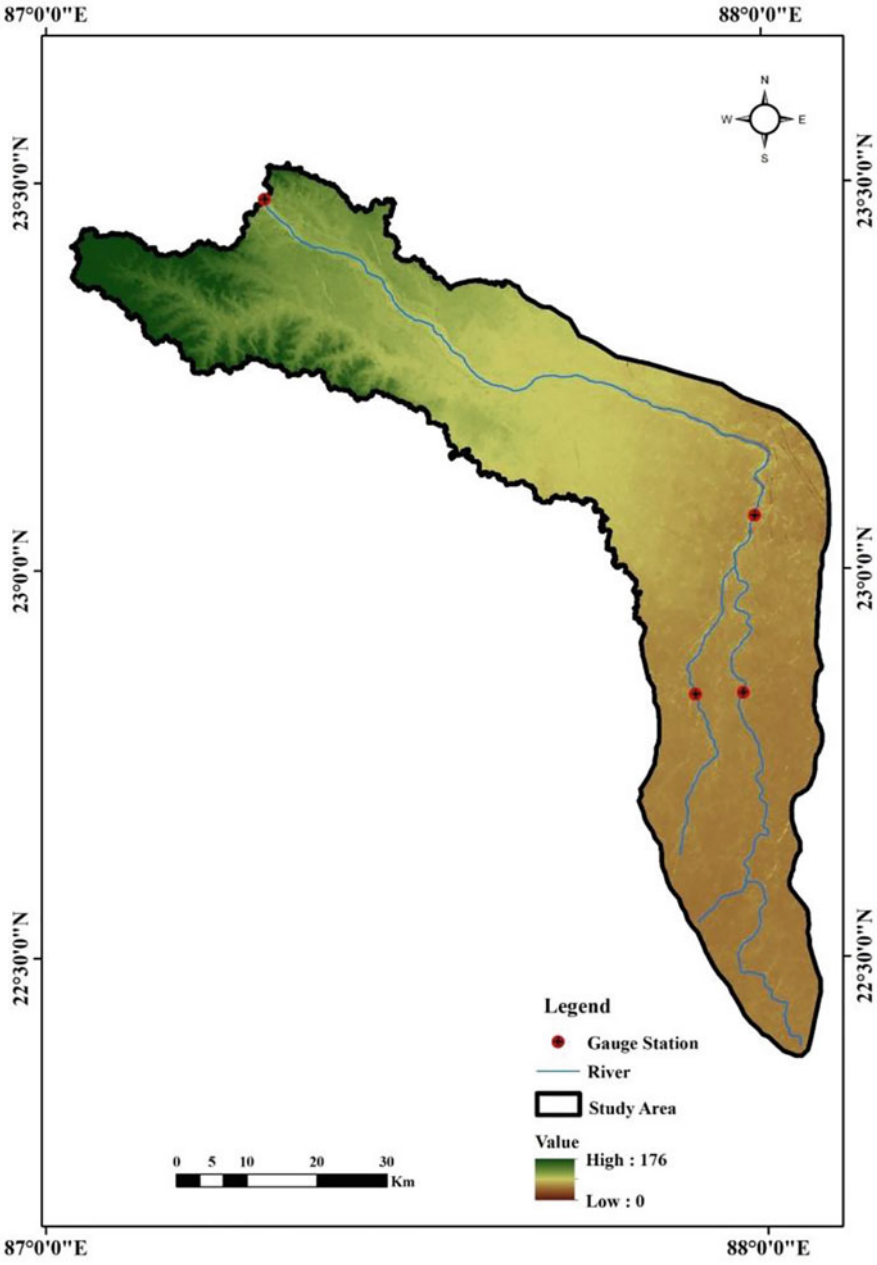

Fig. 3.2 Location map of the study area

3.4 Materials and Methods

The methodology of the study field consists of three phases, namely data collection, data processing, and preparation of the hydrodynamic model. River discharge data were collected from concerned government office. High resolution RS data were acquired from the National Remote Sensing Centre Hyderabad for the input data preparation of the model. In the field visit, data such as base flow depth, LULC, river depth, cross-section width, and settlement location near the river were collected to validate the model setup. At 15 cross-sections location width of the river and water depth were measured in field. Total station, handheld GPS, distometer, measuring tape, and other accessories were used during a field survey. Flowchart of the applied methodology is shown in Fig. 3.3.

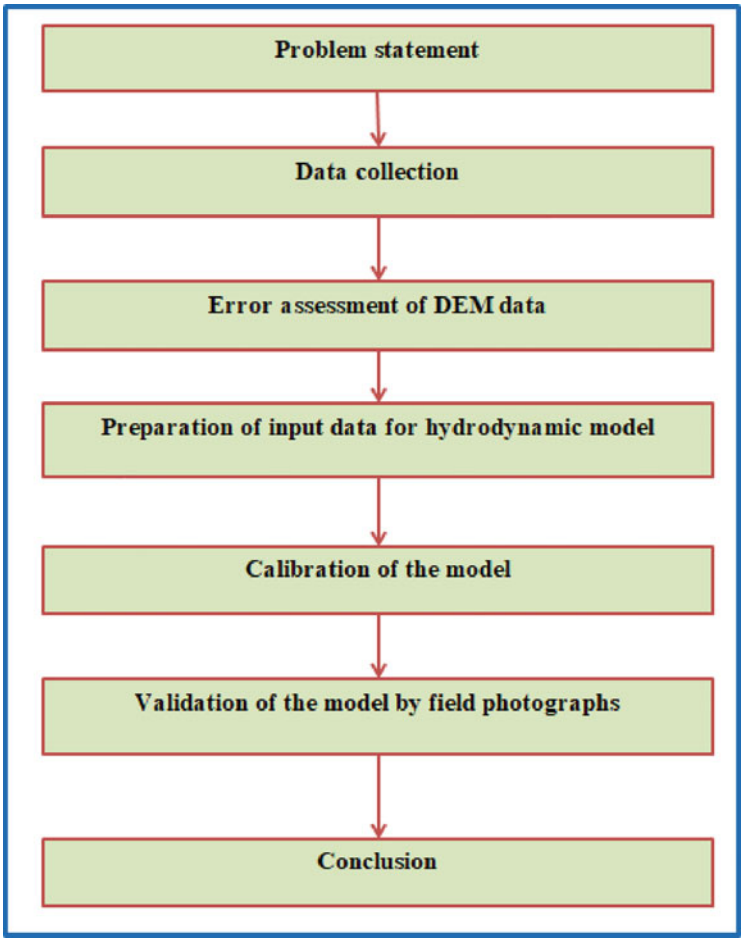

Fig. 3.3 Flowchart of the applied methodology

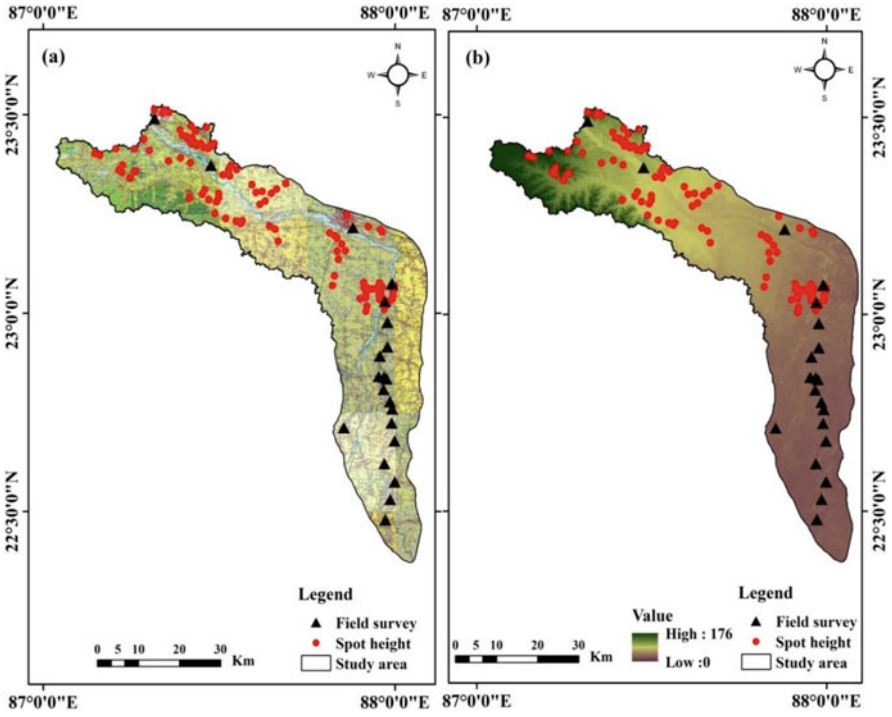

Fig. 3.4 (**a**) Location of spot height point in toposheet. (**b**) Location of elevation point in DEM

River network shapefiles and river cross-section files were prepared in ArcGIS 10.5 using high resolution Cartosat-I (spatial resolution of 2.5 m) satellite imagery and imported in the MIKE HYDRO RIVER model. Cartosat DEM was used for extracting the river geometry. Modification of DEM was conducted by subtracting the RMSE (Eq. 3.1) value from the original DEM elevation value to bring the extracted geometrics as close as possible to the ground value. Location point of spot height in toposheet and DEM elevation point is shown in Fig. 3.4a, b. Comparison of both data is shown in Fig. 3.5.

$$\mathrm{RMSE} = \sqrt{\frac{1}{n}\sum_{i=1}^{n}\left(Z_s - Z_{\mathrm{DEM}}\right)^2} \tag{3.1}$$

where

Z_s = spot height from toposheet.
Z_{DEM} = elevation height from DEM.

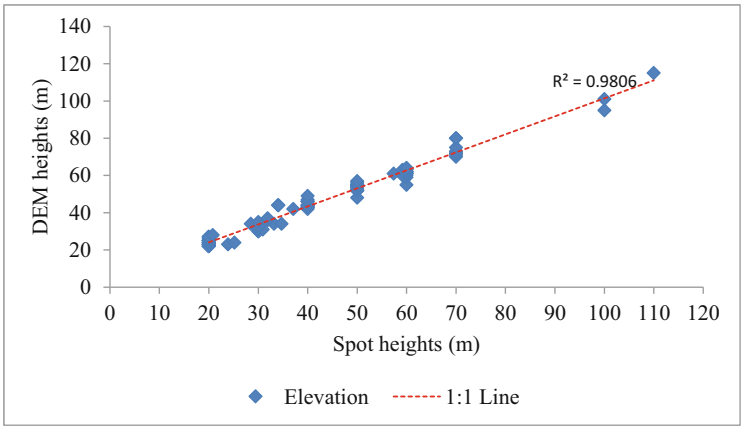

Fig. 3.5 Comparison between spot height and DEM elevation

3.5 Results and Discussion

One-dimensional hydrodynamic modeling was carried out to identify weak levee point along the lower Damodar river which is susceptible to flooding. A 1-D model is best for representing the flows inside the interconnected systems of channels. MIKE HYDRO RIVER is extensively used for the 1-D modeling of rivers, streams, and channels. The St. Venant Equation is the core of a 1-D hydrodynamic model. Peak flood event of 20 years return period was selected for simulation of the model. All the input geometry files were generated in GIS-compatible format using high resolution RS data. For Upstream boundary condition of the model daily discharge data and for downstream Q/h curve was utilized. Model was run from the July 1 to October 15, 2009 period. For model calibration Manning's roughness coefficient (n) was used as a calibrating parameter.

In modeling studies, calibration is required for identifying key factors by matching the model output data with the observed data for a given set of assumed conditions. The key target of calibration is to increase the accuracy of the model. Multiple statistics index that covers all the aspects of the hydrograph is used for assessing the performance of the model (Boyle et al. 2000). In the present study, Nash–Sutcliffe efficiency (NSE), percent bias (PBIAS), and RMSE–observations standard deviation ratio (RSR) were used for determining model performance. The value of NSE varies between $-\infty$ and 1.0, and the best value is represented by NSE = 1. PBIAS evaluates the normal inclination of the predicted data of the model to be greater or lesser than their corresponding observed data (Gupta et al. 1998). RSR integrates the assistance of error index statistics. Equations of statistics index are presented below from Eqs. 3.2–3.4.

Nash–Sutcliffe efficiency (NSE)

$$\mathrm{NSE} = 1 - \frac{\sum_{i=1}^{n}\left(Y_{i_{\mathrm{obs}}} - Y_{i_{\mathrm{sim}}}\right)^2}{\sum_{i=1}^{n}\left(Y_{i_{\mathrm{obs}}} - Y_{\mathrm{mean}}\right)^2} \tag{3.2}$$

Percent Bias (PBIAS)

$$\mathrm{PBIAS} = \frac{\sum_{i=1}^{n}\left(Y_{i_{\mathrm{obs}}} - Y_{i_{\mathrm{sim}}}\right) \times 100}{\sum_{i=1}^{n}\left(Y_{i_{\mathrm{obs}}}\right)} \tag{3.3}$$

RMSE–observations standard deviation ratio (RSR)

$$\mathrm{RSR} = \frac{\mathrm{RMSE}}{\text{Standard deviation}} = \frac{\left[\sqrt{\sum_{i=1}^{n}\left(Y_{i_{\mathrm{obs}}} - Y_{i_{\mathrm{sim}}}\right)^2}\right]}{\left[\sqrt{\sum_{i=1}^{n}\left(Y_{i_{\mathrm{obs}}} - Y_{\mathrm{mean}}\right)^2}\right]} \tag{3.4}$$

$Y_{i_{\mathrm{obs}}} = i$th observed field data, $Y_{i_{\mathrm{sim}}} = i$th model simulated data, Y_{mean} = observed mean data, n = total number of observations.

Selection of initial roughness coefficient (n) in the model for the channel is based on the guidelines mentioned in the available literature (i.e., Chow 1959) and in model it varied from 0.02 to 0.045 during calibration process. Simulated water depth from the model compared with the observed water depth which shows both the data were close for roughness's (n) value of 0.03 at gauging station. Observed data and the simulated data of water depth was plotted around 1:1 line to estimate the deviation in both values. In this study, the residual plots for all three gauge stations for 2009 were plotted. The residual is the difference between individual observed and model values. The residual plot suggests an opportunity to improve the model. For the years 2009 all the graphs were plotted simultaneously for each gauge station as shown in Figs. 3.6, 3.7, 3.8, 3.9, 3.10. Performance of the model based on three statistics is given in Table 3.1.

Water level difference error occurred as the model used DEM-extracted river cross-sections. As simulation period proceed variation of input discharge reflected in the water depth curve at selected gauge stations, but the curve not self-attuned as quickly as the observed water depth curve due to the frequency of flow data. From the residual plot, water depth predicted by the model was observed to be on the higher side. In the residual plot, some data points showed a higher residual value due to the lag of time, as the frequency of flow was moderate, which could be minimized by increasing the frequency of flow data. The absence of a sufficient amount of observed data due to the lack of gauge stations in certain important locations reduced the accuracy of the model. The frequency of the observed data has a vital role in enhancing the accuracy of the model which means whether the data are available on an hourly, daily, or monthly basis.

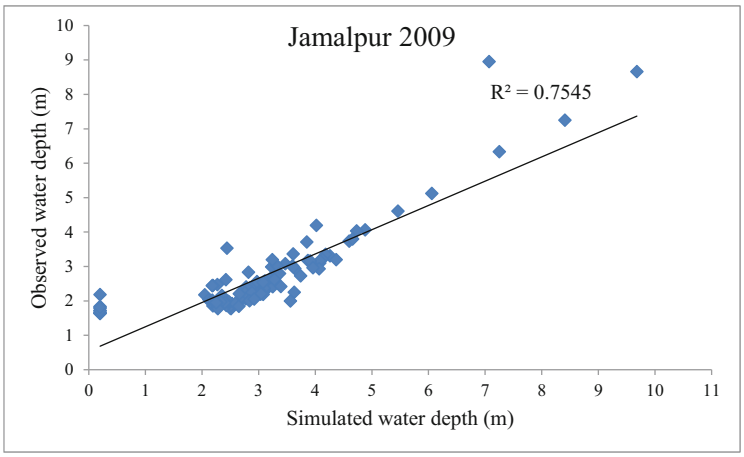

Fig. 3.6 Observed and Simulated water depth around 1:1 line at Jamalpur in 2009

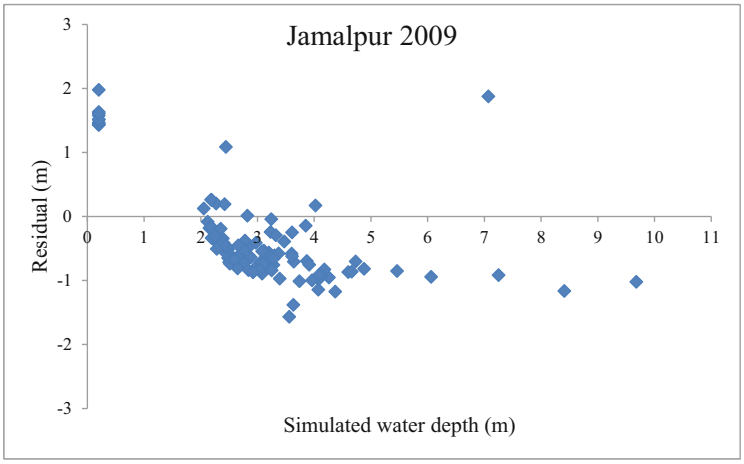

Fig. 3.7 Residual plot of water depth at Jamalpur in 2009

3.5.1 Validation

The validation of the model comprises a simulation of the model using input parameters estimated by the calibration process. For the validation of the model in this study, information collected by local people's experiences about the flood-affected areas during past flood events, field visit photographs at key sites were utilized. The questions posed to the local people in flood-affected areas during the field survey are as follows: When did you arrive at these area? What was the extent of the increase in water level during flood times?

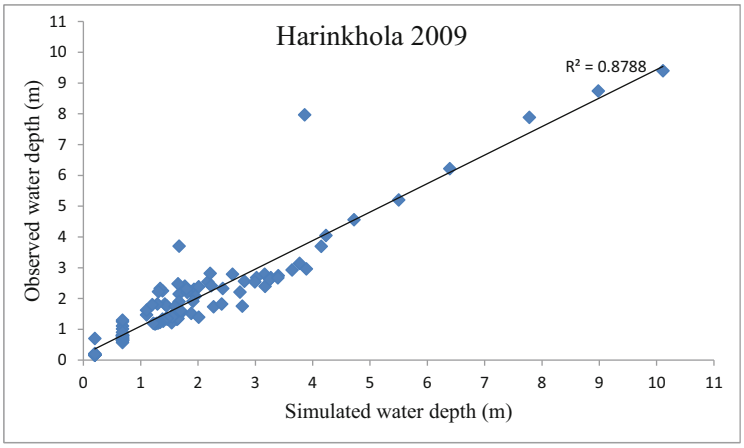

Fig. 3.8 Observed and Simulated water depth around 1:1 line at Harinkhola in 2009

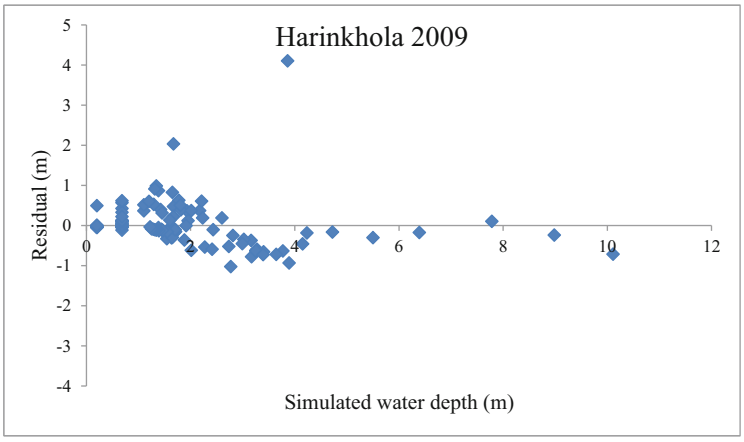

Fig. 3.9 Residual plot of water depth at Harinkhola in 2009

Figures 3.11 and 3.12 shows the field validation of model predicted water depth at Amarpur, and Joynagar along with chainage. In the validation map, the blue line shows the water level, the red line represents the left levee bank, and the green line shows the right levee bank. We obtained the information on the extent of water raise point at flood times by interacting with the local people in flood-affected areas. This information was implemented during the validation of the model and verification of whether that point was attained by the model output or not. At Amarpur location, the cross-section was extended to the nearest high elevation point, which was a road and flood water level in the field indicated by blue line (Fig. 3.13). At Joynagar (Fig. 3.11) flood water touched up to nearest road and building as shown by blue line. Field validation photographs were shown with the model output. We

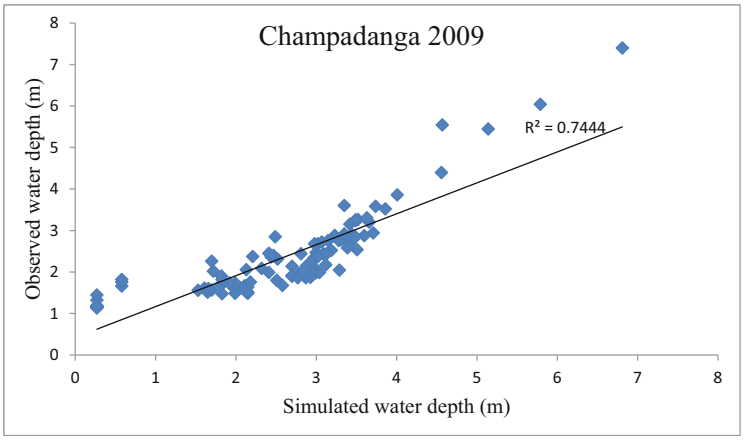

Fig. 3.10 Observed and Simulated water depth around 1:1 line at Champadanga in 2009

Table 3.1 Performance of the model

Statistical performance measures	Jamalpur	Harinkhola	Champadanga
NSE	0.81	0.90	0.66
PBIAS	−13.17	1.76	−9.86
RSR	0.43	0.31	0.58

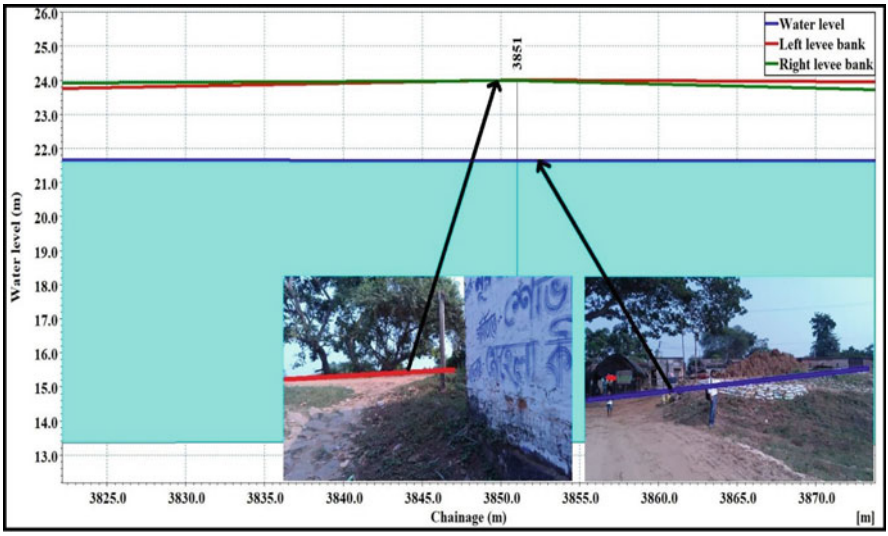

Fig. 3.11 Map showing field validation with model output at Amarpur

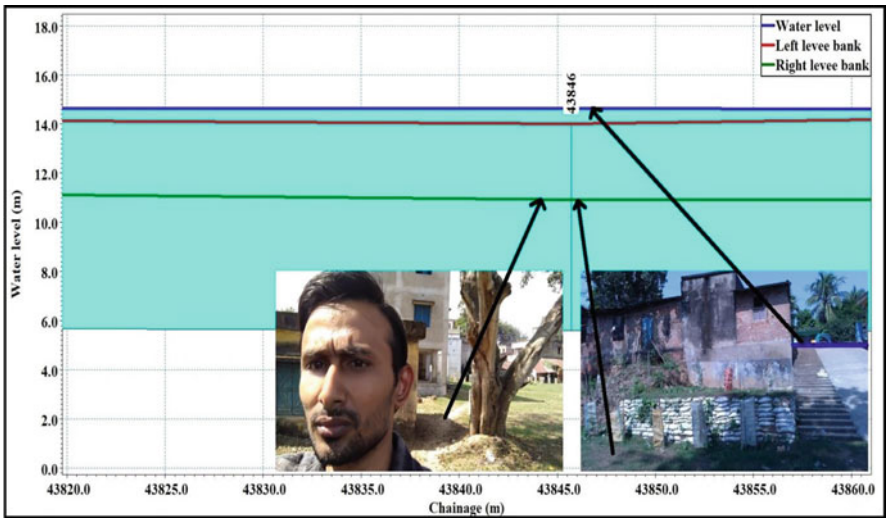

Fig. 3.12 Map showing field validation with model output at Joynagar

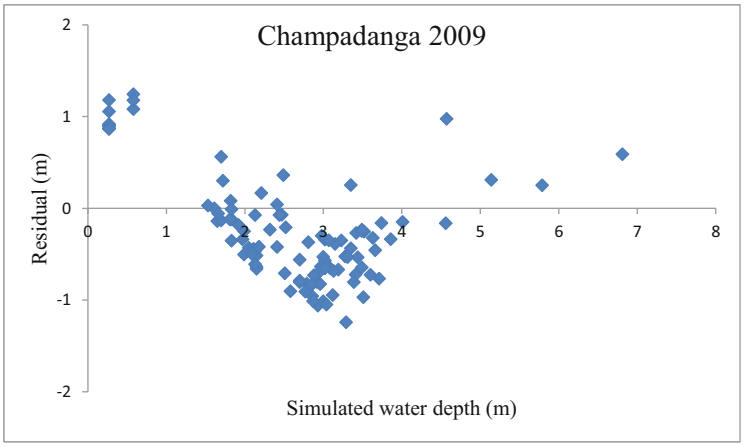

Fig. 3.13 Residual plot of water depth at Champadanga in 2009

endeavored to validate the model as accurately as possible; however, we could not obtain the accuracy up to that level due to some limitations in the same manner that we acquired the accuracy in current flood events and actually measured the experimentation works. From model simulated water depth profile (Fig. 3.14) it was found that due to narrower river cross-section and reduced carrying capacity of the river overtopping of water mostly takes place in downstream section of the river.

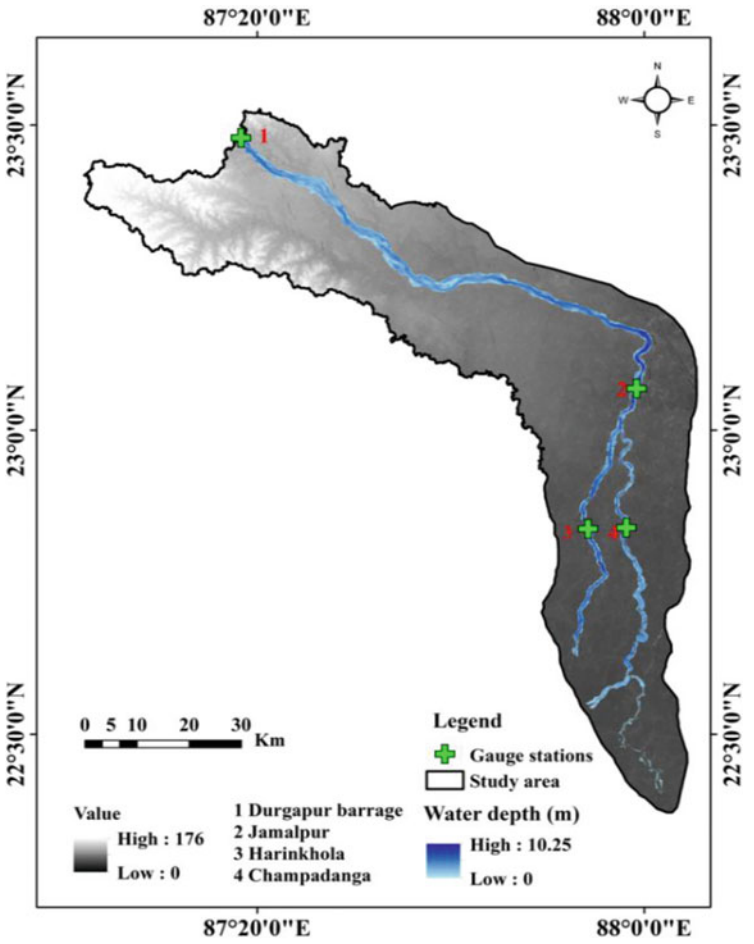

Fig. 3.14 Predicted Water depth map by the model overlaid on DEM

3.6 Recommendations

To minimize flood problems in the lower Damodar basin, desilting should be carried out in the main river and distributary channels that are active during floods. Land encroachments and illegal constructions in the flood plains of the Damodar River should be removed to minimize flood damage. As predicted by the model, embankments of less strength should be repaired and earthen banks parallel to the river's path at flood vulnerable points should be reconstructed. Also, the height of existing embankments at critical locations should be raised. Confining the river's path frees large areas from floods and consequently reduces damage intensity.

3.7 Conclusions

Present study used one dimensional hydrodynamic model (MIKE HYDRO RIVER) to study the riverine flood problem of the lower Damodar river. This study study used high resolution satellite data for this riverine flood affected area. The purpose of the study to identify the weak levee location along the river which is susceptible to the flood. One-dimensional hydrodynamic model was prepared for flood of 20-year return period in the lower Damodar river. High resolution RS data were used for input geometry data in the model. For simulation of the model daily discharge data used as input in in the model. Model output data (water depth) match closed to observed water depth at three gauge station for the Manning's n value of 0.03. Furthermore, NSE, PBIAS, and RSR were used for determining the model performance which shows good agreement between the model output and the observed data at the gauging stations. Output of model indicates that water overtopping from river bank of lower Damodar river mostly occurred in the downstream area which is more susceptible to flooding.

Acknowledgments The present work was funded by FRS project (FRS (120)/2017-18/ME) of Dr. Vasanta Govind Kumar Villuri, Indian Institute of Technology (Indian School of Mines), Dhanbad. Authors thankful to Central Water Commission, Irrigation and Waterways Directorate, West Bengal for giving the data for the study.

References

Abdella K, Mekuanent F (2021) Application of hydrodynamic models for designing structural measures for river flood mitigation: the case of Kulfo River in southern Ethiopia. Model Earth Syst Environ 7(4):2779–2791

Ashrafi M, Chua LHC, Quek C, Qin X (2017) A fully-online neuro-fuzzy model for flow forecasting in basins with limited data. J Hydrol 545:424–435

Bates PD, De Roo APJ (2000) A simple raster-based model for flood inundation simulation. J Hydrol 236(1–2):54–77

Boroushaki S, Malczewski J (2010) Using the fuzzy majority approach for GIS-based multicriteria group decision-making. Comput Geosci 36(3):302–312

Boyle DP, Gupta HV, Sorooshian S (2000) Toward improved calibration of hydrologic models: combining the strengths of manual and automatic methods. Water Resour Res 36(12): 3663–3674

Chow VT (1959) Open-channel hydraulics. McGraw-Hill, New York

Chowdhury A, Jha MK, Chowdary VM (2010) Delineation of groundwater recharge zones and identification of artificial recharge sites in West Medinipur district, West Bengal, using RS, GIS and MCDM techniques. Environ Earth Sci 59(6):1209

EMDAT 2018: OFDA/CRED International Disaster Database, Université catholique de Louvain—Brussels—Belgium http://www.emdat.be/

Gupta HV, Sorooshian S, Yapo PO (1998) Toward improved calibration of hydrologic models: multiple and noncommensurable measures of information. Water Resour Res 34(4):751–763

Hsu MH, Fu JC, Liu WC (2003) Flood routing with real-time stage correction method for flash flood forecasting in the Tanshui River, Taiwan. J Hydrol 283(1-4):267–280

Jung Y, Merwade V (2011) Uncertainty quantification in flood inundation mapping using generalized likelihood uncertainty estimate and sensitivity analysis. J Hydrol Eng 17(4):507–520

Meyer V, Scheuer S, Haase D (2009) A multicriteria approach for flood risk mapping exemplified at the Mulde river, Germany. Nat Hazards 48(1):17–39

Morales-Hernández M, Sharif MB, Gangrade S, Dullo TT, Kao SC, Kalyanapu A, Ghafoor SK, Evans KJ, Madadi-Kandjani E, Hodges BR (2020) High-performance computing in water resources hydrodynamics. J Hydroinf 22(5):1217–1235

Mosavi A, Ozturk P, Chau KW (2018) Flood prediction using machine learning models: literature review. Water 10(11):1536

Noh SJ, Lee JH, Lee S, Seo DJ (2019) Retrospective dynamic inundation mapping of hurricane Harvey flooding in the Houston metropolitan area using high-resolution modeling and high-performance computing. Water 11(3):597

Nyaupane N, Bhandari S, Rahaman MM, Wagner K, Kalra A, Ahmad S, Gupta R (2018) Flood frequency analysis using generalized extreme value distribution and floodplain mapping for hurricane Harvey in Buffalo Bayou. In: World Environmental and Water Resources Congress 2018, pp 364–375

Pappenberger F, Matgen P, Beven KJ, Henry JB, Pfister L (2006) Influence of uncertain boundary conditions and model structure on flood inundation predictions. Adv Water Resour 29(10): 1430–1449

Pappenberger F, Beven K, Horritt M, Blazkova S (2005) Uncertainty in the calibration of effective roughness parameters in HEC-RAS using inundation and downstream level observations. J Hydrol 302(1-4):46–69

Pramanik N, Panda RK, Sen D (2010) One-dimensional hydrodynamic modeling of river flow using DEM extracted river cross-sections. Water Resour Manag 24(5):835–852

Quiroga VM, Kure S, Udo K, Mano A (2016) Application of 2D numerical simulation for the analysis of the February 2014 Bolivian Amazonia flood: application of the new HEC-RAS version 5. RIBAGUA-Revista Iberoamericana del agua 3(1):25–33

Saraf AK, Choudhury PR (1998) Integrated remote sensing and GIS for groundwater exploration and identification of artificial recharge sites. Int J Remote Sens 19(10):1825–1841

Singh RK, Villuri VGK, Pasupuleti S, Nune R (2020) Hydrodynamic modeling for identifying flood vulnerability zones in lower Damodar river of eastern India. Ain Shams Eng J 11(4): 1035–1046

Sinha R, Bapalu GV, Singh LK, Rath B (2008) Flood risk analysis in the Kosi river basin, North Bihar using multi-parametric approach of analytical hierarchy process (AHP). J Indian Soc Remote Sens 36(4):335–349

Shankar MR, Mohan G (2005) A GIS based hydrogeomorphic approach for identification of site-specific artificial-recharge techniques in the Deccan Volcanic Province. J Earth Syst Sci 114(5): 505–514

Wing OE, Sampson CC, Bates PD, Quinn N, Smith AM, Neal JC (2019) A flood inundation forecast of hurricane Harvey using a continental-scale 2D hydrodynamic model. J Hydrol X 4: 100039

Yu PS, Yang TC, Chen SY, Kuo CM, Tseng HW (2017) Comparison of random forests and support vector machine for real-time radar-derived rainfall forecasting. J Hydrol 552:92–104

Chapter 4
Field Measurement of Accumulated Surface Water and Infiltration Depth in a Flood-Prone Langol Catchment of Manipur Valley Region

Sochanphi Kashung and Thiyam Tamphasana Devi

Abstract The cause of flooding in the Manipur valley (where the study area is located in the North Eastern region of India) is mainly due to poor urban drainage, deforestation, vanishing traditional recharge structures, heavy runoff, and less infiltration in the degraded watershed in the upper reach of the river during the rainy season. The aim and objectives of this study are to determine the accumulated inundated water in the Langol catchment area and to get information on predicted floods to facilitate early preparation and planning before flood events. Then infiltration depth is also measured to understand the water holding capacity in the region where the study area is majorly covered by clay and clay loam soil, which has less infiltration capacity. The measurements were taken at different site locations (15 locations for surface water depth and 03 locations for infiltration depth) on a weekly basis (August to September, 2021 for surface water depth and February to September, 2022 for infiltration depth). The maximum accumulated water depth measured was 45 cm, and the minimum was 0.3 cm in the catchment area during the measurement time. In February 2022, maximum infiltration depth was observed at 0.39 cm, with an average of 0.2 cm. From the results, it was concluded that soil in the NIT campus has less infiltration capacity and, therefore, the only means for preventing the frequent inundation of surface water is through the provision of a proper drainage system considering the low-lying landscape of the catchment area.

Keywords Accumulated water depth · Flood-prone zone · Infiltration depth · Langol catchment · Manipur valley

S. Kashung · T. T. Devi (✉)
Department of Civil Engineering, National Institute of Technology, Langol, Manipur, India

M. Pandey et al. (eds.), *River Dynamics and Flood Hazards*, Disaster Resilience and Green Growth, https://doi.org/10.1007/978-981-19-7100-6_4

4.1 Introduction

Flood hazards can be divided into primary, secondary, and tertiary effects. Primary effects occur due to direct contact of flood water with direct contact of flood water and some of the effects are erosion, damage to furniture, walls, floors, automobiles, and equipment; loss of crops and livestock; and also health hazards. Secondary effects occur because of the primary effects. The effects include pollution of drinking water, which may cause health effects. Electricity and transportation may be disrupted. Tertiary effects are the long-term changes, which include changes in the location of river channels, destruction of wildlife habitats, economic growth, people may get traumatized and experience psychological effects (Pu et al. 2021; Wallwork et al. 2022).

Runoff results from rain flow into the river, utilizing drains and streams. The water in the river spills over when heavy rainfall occurs as it increases the discharge of that river. Thus, a flood in a river is caused by excessive precipitation in the catchment of that river. It can cause damage to people, materials, and also valuable properties (Jain et al. 2021; Shankar et al. 2021; Shivashankar et al. 2022; Singh et al. 2022). A flood is an inundation of dry land from the overflow of an accumulation of runoff. Floods in India occur mainly during the wet season or monsoon season because the rainfall is concentrated 3–4 months of the year and because it also occurs quite often. Therefore, due to the runoff from this heavy rainfall, floods occur as it exceeds the capacity of the river and it spills over to the flood plains. As humans cannot control excessive precipitation, it is managed by adopting different measures and methods, which we call flood control methods or flood control measures. The soil saturated conductivity indicates how quickly it infiltrates the soil. And determining the hydraulic conductivity is of great importance in various applications like drainage system designing, seepage measurement in the canal, distention basin, and also for monitoring the movement of leachates and in the prediction of soil erosion and soil compaction. Therefore, it is an essential parameter in in situ measurement and results can give us insight on methods to be used in dealing with hydraulic conductivity. For longer period of accumulated surface water as well as soil properties (Reynolds and Elrick 1991) contributes to flooding situation in a particular catchment and its understanding has become one of the most important information for flood prevention measures. Several authors used various techniques, e.g., satellite data integrated with Geographical Information System, GIS (Forkuo 2013) and instruments to understand the surface water and soil hydraulic profile. One of the widely used instruments is Mini Disk Infiltrometer (MDI) for measuring the infiltration rate as well as soil hydraulic conductivity (Latorrea et al. 2013; Kargas et al. 2018; Naik et al. 2019; John et al. 2021).

Naik et al. (2019) conducted an experimental study to characterize the soil infiltration properties using MDI and results were also compared with numerical study. They selected such study location where four soil types (sand, loamy sand, loam, and silt) were involved. Cumulative infiltration were measured using MDI and near saturated hydraulic conductivity were determined. They found that numerical

simulation accurately predicts for loamy sand soil but for sandy and loamy soils, numerical simulated results were under predicted. Basri and Chandra (2021) determines the infiltration rate in the Lawe Menggamat sub-watershed, Aceh Province, Indonesia and find that the Lawe Manggamat sub-watershed has been degraded due to the increase in flood frequency over the years. Since surface runoff increases, the infiltration process gets hampered. It uses a descriptive method (survey) called Land Map Unit (LMU). Infiltration was observed using a double ring infiltrometer. The dominant factors affecting the infiltration rate are texture, C-organic, bulk density, soil type, and land use. Management of cover crops and organic matter, as well as forest and land rehabilitation, is expected to improve infiltration in these areas. One type of land use can play a role in accelerating the infiltration rate, but another type of land use may inhibit it. Soil types that have a certain texture will respond differently to the infiltration rate than other soil types. Seong Seong et al. (2020) carried out an experimental study on analysis of urban flood inundation patterns according to rainfall intensity using a rainfall simulator in the Sadang area of South Korea. It shows that the rainwater is mostly accumulated in low-lying areas. They wrote that high-intensity rainfall due to climate change and rapid urbanization increases flood damage in the areas. This work was carried out to give a demonstration on inundation and also talks about the vulnerability of human activities during flood events. Mangala et al. (2016) discussed how the magnitude and distribution of surface runoff is affected by infiltration. Here, in the estimation of infiltration, single-ring and double-rings were used. Infiltration is the measure of the rate at which the soil absorbs rainfall or irrigation, which is measured by infiltration. Capillary action and gravity are the two forces that cause infiltration. The water infiltrates into the pores of the large soil through gravity force, and for the smaller surface, the water is taken into the pores through capillarity. The downward moving water is also sucked in by capillary pores. The gravitational water moves towards the ground water following the path of least resistance. From a design calculation point of view, soil testing plays an important role in effective storm water management. It also helps in investigating the subsurface conditions of soils, their historic conditions, and also their limiting conditions. Abichou and Fatehnia (2014) use the Tension Disc Infiltrometer (type of MDI) for the measurement of infiltration properties. The cumulative infiltration curve and hydraulic conductivity were obtained from derived information and hydraulic conductivity was estimated by eight different methods. Hermas et al. (2021) conducted a study to investigate the impact of an urban flash flood (October 2016 flash floods on the urban area's catchment along the Nile valley and Red Sea region) in Egypt using GIS techniques. Several satellite data were used to map the urban areas, active channels of the drainage system, accumulated water ponds of the flash flood, and the status of the road network. The absence of in situ measurements of rainfall is one of the major challenges, and to date, it has not accurately estimated the rainfall required for a given runoff as mentioned in their study.

The expected outcome of the study is to get information on predicted floods to extend to facilitate early preparation and planning before flood events. As the NIT Langol campus is frequently flooded during the monsoon season, it was required to calculate the amount of rainfall accumulated in the Langol catchment area as well as

water holding capacity in terms of infiltration. For these inundation problems, we can propose a plan on drainage to drain away the accumulated water. It will give early preparation for minimizing and mitigating the after-flood effect. The Langol catchment is frequently inundated during the rainy season, which leads to flooding. Most of the time, it affects the property, especially in NIT Manipur, and also the livestock in the catchment area is also affected. The water accumulation in the catchment is observed to know how long the rainwater gets inundated and how it will affect people and the surroundings. This is a preliminary study which is for the observation of the accumulation of surface water during the flooding periods and so it does not intend to provide an in-depth technical study.

4.2 Background of the Study

The Langol catchment is taken into consideration as the study area because during the monsoon season, the area always gets inundated. The catchment area is covered by agricultural land, settlement areas, institutions, etc. During the flood, great loss occurred to institute infrastructure where the laboratory instruments were submerged, inhabitants of animals were displaced, and settlements of people were also severely affected in and around the catchment area. As the cause of floods in the Manipur valley is mainly due to poor drainage, deforestation, and heavy precipitation as well as rapid urbanization (rapid change in land use pattern), it is imperative to understand the accumulated surface water profile as well as the holding capacity of soil in the region. The inundated water is measured to know when the depth of the inundated water is highest and when it is lowest. The volume of the inundated water is also calculated to know how much water in the catchment has accumulated during the observation periods. It is an important parameter if we want to diverge this accumulated water. It also gives information and precautions about these events to the people, especially those residing in the area where the inundation occurs every year. One of the reasons for inundation in the Langol catchment area during the monsoon season could possibly be the poor infiltration capacity of the soil. Therefore, the infiltration depth was measured for a better understanding of the soil in the catchment area. The infiltration is measured using the MDI by measuring the volume of water infiltrated during the specific time interval. The infiltration rate is also calculated. The field measurement of the infiltration rate is calibrated with Horton's equation. After the calibration is done, the infiltration capacity in the study area is obtained.

4.3 Limitation of the Study

The recording of the accumulated depth of the rainfall water should have been taken in the entire region of the catchment, but due to less rainfall during the measurement periods (August to November, 2021), it was observed only in and around the NIT Manipur campus as it is located at the lowest level of any part of the region. The depth of all the locations when recorded is taken as the same elevation, but the elevation of all the locations may not be the same. Also, the temperature cannot be incorporated in determining the measurement in the field record, but it can be useful in studying and analyzing the infiltration of the soil as it is one of the factors affecting the infiltration capacity. For the field measurement, simple tools were used. Therefore, the accuracy may not be efficient. While measuring the depth of the inundated water, there is some disturbance in the water level, so the readings may not be accurate. Due to time constraints, recording of the depth of the accumulated water was not taken for the whole year. If the recording for the whole year was taken, important information on the inundation like when the starting accumulation started and around which month it dries up could be obtained with better results.

4.4 Study Area

The study area is the Langol catchment area (Fig. 4.1). It is in Imphal West district and is mostly a valley region. The average temperature ranges from 11 °C to 36 °C. The soil type for this area is mostly clay and clay loam with alluvial soil (Fig. 4.2). The output for this catchment area is defined at the coordinates of 93° 55′ 31.613″ E and 24° 48′ 16.725″ N. The catchment area covers an area of 14.02 km^2. The Langol catchment area is mostly a valley area that is surrounded by hills. So, the catchment area gets inundated easily due to the nature of the soil types, which have low infiltration capacity and also discharge the water from the hilly region when there is high-intensity rainfall. The outlet for the catchment area is taken from the Nambul river. The location of the outlet point is at Uripok. It is located near the overpass. It is between Meino bridge and Bijoy Govinda bridge.

The rainy season in the study area starts in May and extends up to October. Some of the flood events in Manipur, which are collected from the report of the Manipur Science and Technology Council, are: September–October in 1916, June 1929 (3 days), June 1941, September 1952, June–July 1966, July–August 1989, October 1992, September 1997, 1998, September 1999, September 2000, 2001, 2002, July 2017 (cyclone MORA), July 2015 (experienced heavy rain on July 28, which led to the worst flood in 200 years), June 2018 (Flood Report 2002).

The types of soil in the Langol catchment area are mostly clay and clayey loam. Figure 4.2 shows the soil type in the Langol catchment area. Mostly catchment area is covered by clay and very small part by clayey loam.

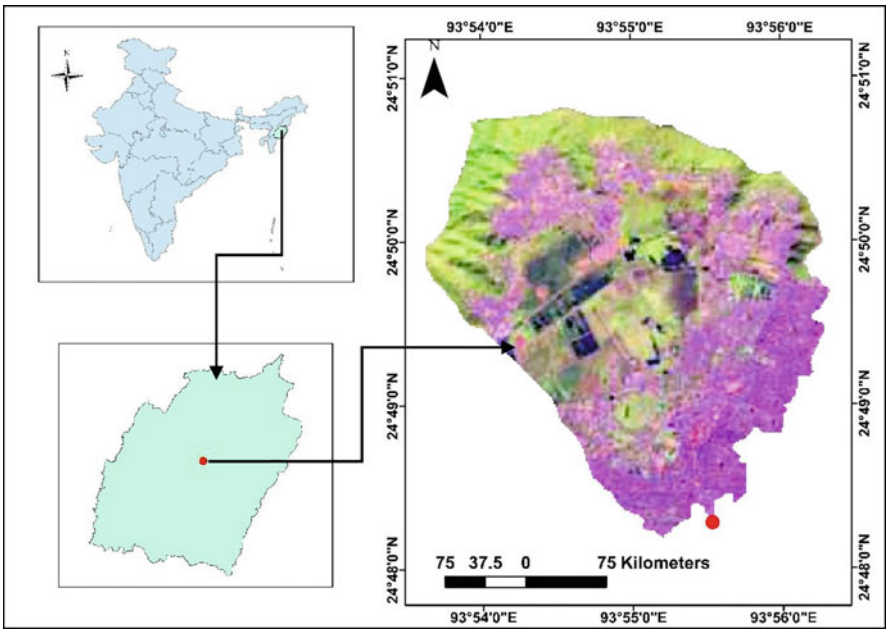

Fig. 4.1 Location of study area (Langol catchment)

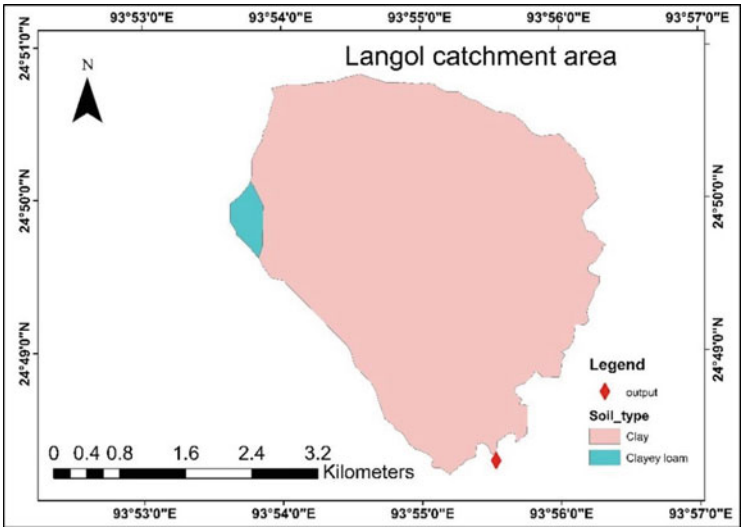

Fig. 4.2 Soil type in the Langol catchment area

4.5 Data Used and Methodology

4.5.1 Data Used

The satellite data, i.e., ALOS_PALSAR (Advanced Land Observing Satellite-1_Phased Array type L-band Synthetic Aperture Radar) & SENTINEL 2 and software tools (ArcGIS 10.3 and Sigma plot) used in this study are briefly described in this section.

4.5.1.1 PALSAR, ALOS

For shapefile extraction of the Langol catchment area, The ALOS_PALSAR_DEM (Digital Elevation Model) of resolution 12.5 m is used to extract the boundary of the catchment area. The data is from multiple observation modes with variable polarization, resolution, swath width, and off-nadir angle. It was one of three instruments on the Advanced Land Observing Satellite-1 (ALOS), also known as DAICHI, developed to contribute to the fields of mapping, precise regional land-coverage observation, disaster monitoring, and resource surveying.

4.5.1.2 Sentinel 2

Sentinel 2 has multispectral data with 13 bands of spectrum. The revisiting period of sentinel 2 is 10 of the same viewing angles. The spatial resolution of the data is 20 m. The watershed delineation of the catchment area is shown using Sentinel images, which reflect the natural landscape of the study region.

4.5.1.3 ArcGIS 10.3

ArcGIS is geographic software for working with maps and geographic information. It is used for creating and using maps, compiling geographic data, analyzing mapped information, and managing the geographic information in a database.

4.5.1.4 Sigma Plot

Sigma plot is proprietary software for scientific graphing and data analysis. It is designed for scientific applications and includes a variety of tools and plots for working with experimental data. Sigma plot allows users to insert images, graphs, or color cells into any of the worksheet cells, which helps in presenting data and results more efficiently as compared to excel.

4.5.2 Methodology

4.5.2.1 Methodology Flow Chart

The proposed methodology for the determination of accumulated water and infiltration is shown in Fig. 4.3.

First, the catchment area of the study area is obtained using ArcGIS® 10.3. The satellite data, which is the ALOS PALSAR DEM data, is downloaded, then using the arc GIS tools, the DEM data is used in delineating the watershed and also extracting the shape file for the catchment area of the study area. Before starting the delineation, it is necessary to define the outlet point. The outlet point for the study area is the Nambul river. After defining the outlet point, the accumulation flowline of NIT Manipur is selected when the catchment area is defined. Then, the catchment area of the study is delineated and, in order to show the natural landscape and topographical characteristics on the surface, sentinel 2 is used. After the catchment area was

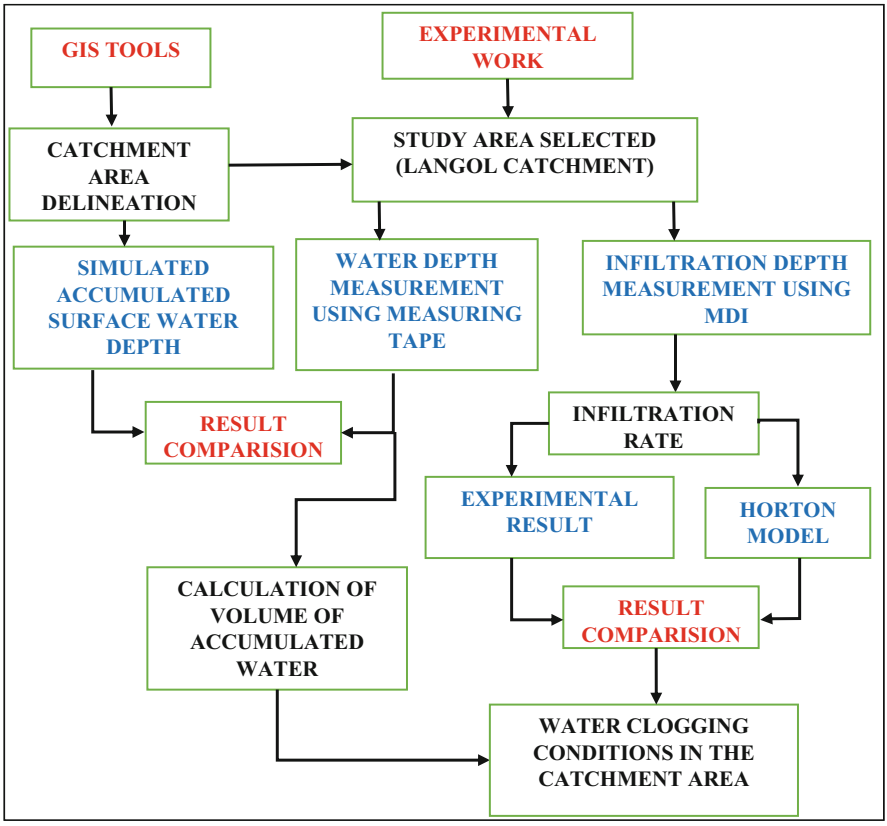

Fig. 4.3 Flow chart of methodology

Fig. 4.4 Instruments used for the measurement in the field (**a**) GPS, (**b**) measuring tape, and (**c**) infiltrometer

delineated, the field observations to measure the inundated water were selected at different locations.

First, the location of the study area was determined with the help of GPS (Global Positioning System) (Fig. 4.4a). From the GPS, the position of the location is taken. The coordinates of the location are given in degrees, minutes, and seconds. The depth of the water accumulated is then measured using a measuring tape (Fig. 4.4b). The scale of the measuring tape for finding out the depth of accumulated water is given in centimeters. The measurement is taken on random days (some on a daily basis, a few on 3-day intervals, and a few on a weekly basis). After taking the field measurement, the average depth of water for the different locations was plotted using Excel and Sigma plot. Then, multiplying average water depth with catchment area (14.02 km^2), the volume of the accumulated water is accordingly plotted. Then, the infiltration depth of the soil in the catchment area is also measured using a MDI, which is shown in Fig. 4.4c. From the measured infiltration depth, the corresponding infiltration rate was calculated and also compared with Horton's equation.

The infiltrometer works by first filling the upper and lower chambers with water. The upper chamber controls the suction, and the lower chamber contains a volume of water that infiltrates into the soil at a rate determined by the suction control tube in the upper chamber. The reservoir is labeled as a graduated cylinder with the volume shown in milliliters. Once the infiltrometer is on the soil, water begins to leave the lower chamber and infiltrate into the soil at a rate determined by the hydraulic properties of the soil. We continue to take the reading of the volume of water in lower chamber at regular intervals until it reaches 40 mL to 30 mL. The data is placed in the excel sheet and it automatically calculates the cumulative infiltration and the square root from the predetermined equations. Then the measured infiltration rate is calculated. After the calculation of the infiltration rate, it is calibrated by using Horton's equation. To understand the flooding situation in the catchment area (NIT campus), some of the photographs taken from the field are presented in Fig. 4.5.

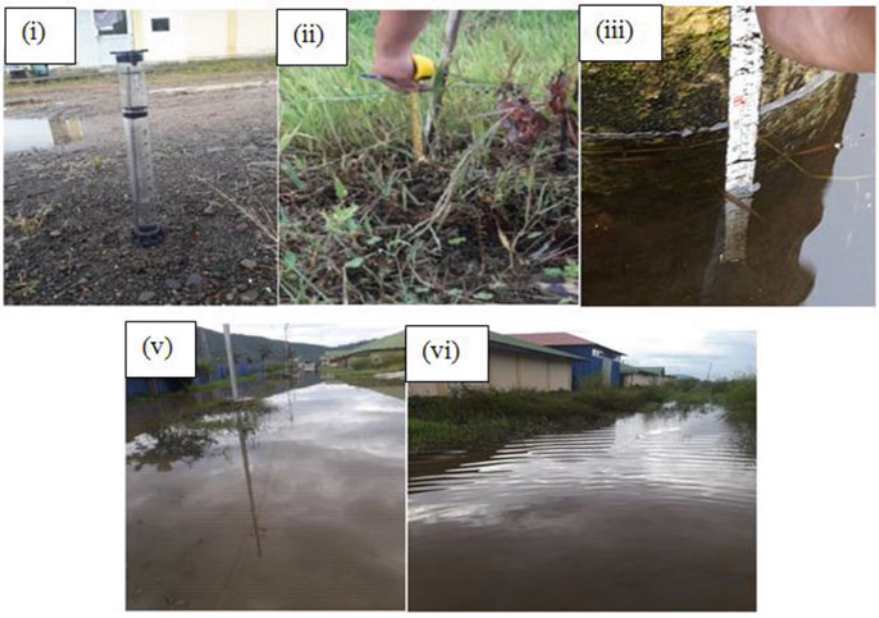

Fig. 4.5 Photographs taken during the field measurement (September, 2021): (i) Soil condition on rainy day measuring infiltration depth using infiltrometer, (ii) measuring accumulated water depth using measuring tape in a vegetated site, (iii) measurement of accumulated water depth in a flooded site, and (iv) and (v) flood in NIT Campus

4.5.2.2 Horton's Equation

When the water flows into the soil, part of it seeps into the soil while part of it flows over the surface as overland flow. This movement of water through soil is known as infiltration. Infiltration is essential for the rainfall and runoff process. Rainwater enters the soil surface at full capacity only during the rainfall period. The prevailing rate at which water will enter the given soil at any given time is known as the infiltration rate. The infiltration rate depends on soil structure. The amount of groundwater stored in the underground soil is primarily determined by the number of voids present in the soil, which is determined by the arrangement compaction degree rather than the size of the soil particle. The maximum rate at which a soil in any given condition is capable of absorbing water is called its infiltration capacity. For the calibration of the experimental data of the infiltration rate, Horton's equation (Horton 1933) is used. Table 4.1 shows the infiltration capacity for the different types of soil. Horton expressed the decay of infiltration capacity with time as an exponential decay given by Eq. (4.1).

$$f_p = f_c + (f_o - f_c)\, e^{-kt} \text{ for } 0 \geq t \leq t_c \tag{4.1}$$

where f_p = infiltration capacity at any time t from the start of the rainfall.

Table 4.1 Infiltration capacity of different types of soil (Subramanya 2015)

Infiltration class	Infiltration capacity (cm/h)	Remarks
Very low	<2.5	Highly clayey soils
Low	2.5 to 25	Shallow soils, clay soil, soil in low organic matter
Medium	12.5 to 25	Sandy loam, silt
High	>25	Deep sands, well drained aggregated soils

f_o = initial infiltration capacity at $t = 0$.
f_c = final steady-state infiltration capacity occurring at $t = t_c$.
k = Horton 's decay coefficient which depends on soil characteristic and vegetation cover.

4.6 Results and Discussion

Accumulated water depth (cm) at different locations for the duration of 47 days (August to November 2021) was measured and the average of the measured results were compared with simulated results. The infiltration depth (cm) was measured at three (3) locations during February 2022 to understand the water holding capacity in the catchment area and compare the measured infiltration rate with Horton's model.

4.6.1 Accumulated Surface Water Depth

The measurement of water accumulation is taken in 15 locations in the morning on random days (measured values with climatic conditions are provided in Table 4.2 of the Appendix) and is plotted in Fig. 4.6. It is required to be noted that inside the catchment area, NIT Manipur is located and is at the lowest level compared to other parts in the study region. Therefore, it was observed while taking the measurements that accumulated water is only in and around the NIT Manipur campus, which made us take the measurements inside the campus. This is due to less rainfall during the measurement period (August to November 2021), as rainfall is the most significant contributor to flooding in the region.

It is evident from the graph of average water depth measured (Fig. 4.6) that during the four months of field observation, the highest accumulation is during August and September. The graph slowly decreases till 07/09/2021, then rises again, then suddenly increases till 27/09/2021, and then it decreases till 15/10/2021. After that, only small changes can be observed. The average inundated water depth recorded in the month of August is 16.54 cm, and for the month of September it is 13.4 cm. For the month of October, the inundated water depth is 3.79 cm, and for the month of November (first week), it is 2.15 cm.

Table 4.2 Measured water depth with climatic condition at various locations (August–November 2021)

Location	**1**	**2**	**3**	**4**	**5**	**Climatic condition**
Latitude	**24°49′ 58.28″**	**24°49′ 58.374″**	**24°49′ 57.466″**	**24°49′ 58.44″**	**24°49′ 57.60″**	
Longitude	**93°54′ 47.73″**	**93°54′ 48.455″**	**93°54′ 47.118″**	**93°54′ 47.9″**	**93°54′ 46.91″**	
Date	**Water depth (cm)**	**Water depth (cm)**	**Water depth (cm)**	**Water depth (cm)**	**Water depth (cm)**	
21/08/2021	11.9	17	18.4	8.4	14.4	Sunny day
23/08/2021	9.8	15.3	13.5	7	2.8	Cloudy
24/08/2021	8.8	16.6	13.8	2	1.5	Sunny day with light rainfall in the morning
25/08/2021	7.8	15.6	12.7	1.5	0.4	Sunny day but light rainfall in the evening
26/08/2021	6.8	14.8	11.7	1.3	0	Sunny day
27/08/2021	7.5	15.5	12.5	2.1	0.2	Rainy day (normal rainfall)
28/08/2021	7.8	14.9	11.2	2.1	0	Sunny day
30/08/2021	7.8	5.2	12.5	1.5	0.3	Cloudy and heavy rainfall in the evening
07/09/2021	6	14	0	0	1	Sunny day
08/09/2021	4.3	12.9	8.9	0	0	Sunny day
09/09/2021	6.9	15	11	0.5	0	Cloudy (rainy)
10/09/2021	8.8	16	12.4	2.5	1.1	Sunny day
11/09/2021	7.2	15.9	11.8	1.4	0.2	Sunny day
13/09/2021	3.6	9.4	7.9	0	0	Sunny day with rainfall in the evening
14/09/2021	4.5	8.4	7.3	0	0	Sunny day
15/09/2021	3.4	7.6	6	0	0	Cloudy and rainy
16/09/2021	3.2	6.3	5.4	0	0	Sunny day

(continued)

Table 4.2 (continued)

17/09/2021	3.4	5.5	3.8	0	0	Cloudy with heavy rainfall during the day
18/09/2021	4.3	8.8	7.5	0	0	Rainy day (normal rainfall)
21/09/2021	6	12.3	10.1	0.3	0	Rainy day
22/09/2021	6.1	11.6	10	0	0	Rainy day and cloudy
27/09/2021	9.2	14.8	13.9	3.3	2	Sunny day
28/09/2021	7.9	14	12.8	1.6	1	Sunny day
30/09/2021	5.2	11.5	9.8	0	0	Sunny day
05/10/2021	0	5.8	0	0	0	Rainy day (light)
08/10/2021	0	0	0	0	0	Cloudy
11/10/2021	0	0	0	0	0	Sunny
13/10/2021	0	0	0	0	0	Sunny
15/10/2021	0	0	0	0	0	Sunny
20/10/2021	0	0	0	0	0	Cloudy and rainy
26/10/2021	0	0	0	0	0	Cloudy
29/10/2021	0	0	0	0	0	Rainy
03/11/2021	0	0	0	0	0	Sunny
Location	**6**	**7**	**8**	**9**	**10**	**Climatic condition**
Latitude	**24°49′ 57.199″**	**24°49′ 57.067″**	**24°49′ 56.44″**	**24°49′ 56.273″**	**24°49′ 56.56″**	
Longitude	**93°54′ 46.973″**	**93°54′ 46.176″**	**93°54′ 45.83″**	**93°54′ 45.979″**	**93°54′ 45.17″**	
Date	**Water depth (cm)**	**Water depth (cm)**	**Water depth (cm)**	**Water depth (cm)**	**Water depth (cm)**	
21/08/2021	26.5	11.4	20.8	25.5	12.5	Sunny day
23/08/2021	24.4	19.3	18.7	25.9	19.8	Cloudy
24/08/2021	23.8	8.3	17.6	23.5	18.3	Sunny day with light rainfall in the morning

(continued)

Table 4.2 (continued)

25/08/2021	22.4	7.3	17	21.4	17.6	Sunny day but light rainfall in the evening
26/08/2021	21.5	6	16.3	21.8	16.6	Sunny day
27/08/2021	22.5	7.6	17.2	22.5	17.5	Rainy day (normal rainfall)
28/08/2021	11.7	7.6	17.5	20.3	16.8	Sunny day
30/08/2021	22.5	6.9	18.5	19	17.5	Cloudy and heavy rainfall in the evening
07/09/2021	20.8	6.1	25.7	26.1	15.6	Sunny day
08/09/2021	19.5	4	14.5	15.8	14.4	Sunny day
09/09/2021	21	6.5	15.8	19.2	16.5	Cloudy (rainy)
10/09/2021	22.9	8.5	16	19	18	Sunny day
11/09/2021	22.3	7	16	19.4	16.6	Sunny day
13/09/2021	18.5	2.1	12.1	16.5	13.4	Sunny day with rainfall in the evening
14/09/2021	18	2	11.3	16.9	13	Sunny day
15/09/2021	6.7	1.8	9.7	9.9	11.8	Cloudy and rainy
16/09/2021	5.9	0.7	9.8	13.6	10.4	Sunny day
17/09/2021	15	0	8.4	13.1	10	Cloudy with heavy rainfall during the day
18/09/2021	18	3.2	10.2	16.7	13	Rainy day (normal rainfall)
21/09/2021	20.8	6.1	13.6	17.3	15.9	Rainy day
22/09/2021	21	5.9	14.3	17.4	16	Rainy day and cloudy
27/09/2021	15.5	9.6	17.2	21	19.3	Sunny day
28/09/2021	23.9	7.1	16	21.9	18.3	Sunny day
30/09/2021	21.7	6	13.2	20.9	15.5	Sunny day
05/10/2021	14.7	0	7.8	20	9.9	Rainy day (light)

(continued)

Table 4.2 (continued)

08/10/2021	10	0	3.2	13.8	5	Cloudy
11/10/2021	0	0	0	7	0	Sunny
13/10/2021	0	0	0	7.1	0	Sunny
15/10/2021	0	0	0	3	0	Sunny
20/10/2021	0	0	0	8	0	Cloudy and rainy
26/10/2021	4.4	0	0	8	0	Cloudy
29/10/2021	0	0	0	5.9	0	Rainy
03/11/2021	0	0	0	4.9	0	Sunny
Location	**11**	**12**	**13**	**14**	**15**	**Climatic condition**
Latitude	**24°49′ 56.06″**	**24°49′ 55.91″**	**24°49′ 55.844″**	**24°49′ 56.073″**	**24°49′ 56.6094″**	
Longitude	**93°54′ 44.465″**	**93°54′ 44.546″**	**93°54′ 43.729″**	**93°54′ 46.821″**	**93°54′ 47.688″**	
Date	**depth (cm)**	**depth (cm)**	**depth (cm)**	**depth (cm)**	**depth (cm)**	
21/08/2021	17.1	21.8	15.3	44	45	Sunny day
23/08/2021	15.5	11.7	12.8	41.8	41	Cloudy
24/08/2021	13.3	10.9	10.6	40.9	37.7	Sunny day with light rainfall in the morning
25/08/2021	14	10.2	9.9	39.5	42.2	Sunny day but light rainfall in the evening
26/08/2021	12	9.3	8.8	39.5	40.3	Sunny day
27/08/2021	13.8	10	9	40.7	40.1	Rainy day (normal rainfall)
28/08/2021	10.9	9.8	8.7	39.8	41.2	Sunny day
30/08/2021	12.3	10	9.2	38.8	41.3	Cloudy and heavy rainfall in the evening
07/09/2021	10.7	8.5	7.3	38.2	39.8	Sunny day
08/09/2021	10	7	6.1	36.7	37.5	Sunny day

(continued)

Table 4.2 (continued)

09/09/2021	11.2	9.6	9.3	39.8	40.1	Cloudy (rainy)
10/09/2021	14.1	10.2	9.8	40.3	41.9	Sunny day
11/09/2021	13.1	10	8.7	39	41.2	Sunny day
13/09/2021	9.3	6.1	5	36	37.4	Sunny day with rainfall in the evening
14/09/2021	8.8	5.8	4.4	35.2	36.2	Sunny day
15/09/2021	7.7	4.3	4	33.1	35.8	Cloudy and rainy
16/09/2021	6.6	3.5	2.8	33.1	35.6	Sunny day
17/09/2021	6	3	2.6	32.6	33.9	Cloudy with heavy rainfall during the day
18/09/2021	8.5	6	4.1	35.3	37.1	Rainy day (normal rainfall)
21/09/2021	11.9	8.8	8.5	38.2	40.1	Rainy day
22/09/2021	11.2	8.5	8.3	38.6	39.2	Rainy day and cloudy
27/09/2021	15	12	10.5	41	42.5	Sunny day
28/09/2021	12.3	10.7	10.3	40.5	41.9	Sunny day
30/09/2021	11	7.9	8.3	37.5	39.2	Sunny day
05/10/2021	5	0	0	32	33.9	Rainy day (light)
08/10/2021	0	0	0	27.8	29.2	Cloudy
11/10/2021	0	0	0	18	19.3	Sunny
13/10/2021	0	0	0	11.7	12.8	Sunny
15/10/2021	0	0	0	8.3	10	Sunny
20/10/2021	0	0	0	17.8	18.3	Cloudy and rainy
26/10/2021	0	0	0	19.2	21.3	Cloudy
29/10/2021	0	0	0	18	19.3	Rainy
03/11/2021	0	0	0	13.1	14.3	Sunny

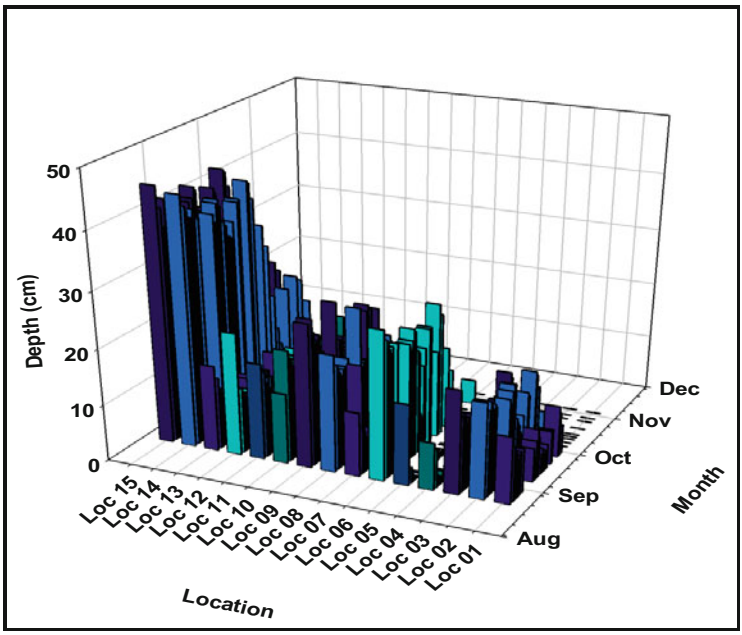

Fig. 4.6 Accumulated water depth (cm) at different sites on different days (duration of 47 days)

The simulated surface runoff depth is calculated using the SCS-CN (Soil Conservation Services-Curve Number) method (Rallison 1980, Jun et al. 2015, Satheeshkumar et al. 2017). Four types of hydrological soil groups are obtained for the study area. The CN (curve number, which depends on landuse/landcover and hydrological soil group) values of the study area are 90, 64, 86.5, and 93, respectively. It is calculated for each month from August to October. The following equation is used for the surface runoff depth (Q) as (USDA 1972):

$$Q = \frac{(P - 0.3S)^2}{P + 0.7S} \tag{4.2}$$

where Q is the surface runoff depth (mm), P is total precipitation (mm), and S is the potential maximum retention after runoff begins and is calculated as:

$$S = \frac{25400}{\text{CN}} - 254 \tag{4.3}$$

(Table 4.3 of the Appendix contains simulated and measured (experimental) data on surface runoff depth.) Figure 4.7 shows the comparison of the surface runoff of the simulated and measured data. For the month of August, simulated Q is 197.59 mm and experimental Q is 165.45 mm. For the month of September, simulated Q is 159.63 mm and experimental Q is 131.48 mm. For the month of

Table 4.3 Comparison of simulated and measured surface runoff depth

Month	P (mm)	Surface water depth (Q), mm		Error percentage (%)
		Simulated	Measured	
August 2021	248	197.59	165.45	16.27
September 2021	208.9	159.63	131.48	17.63
October 2021	77.7	38.25	37.96	0.77

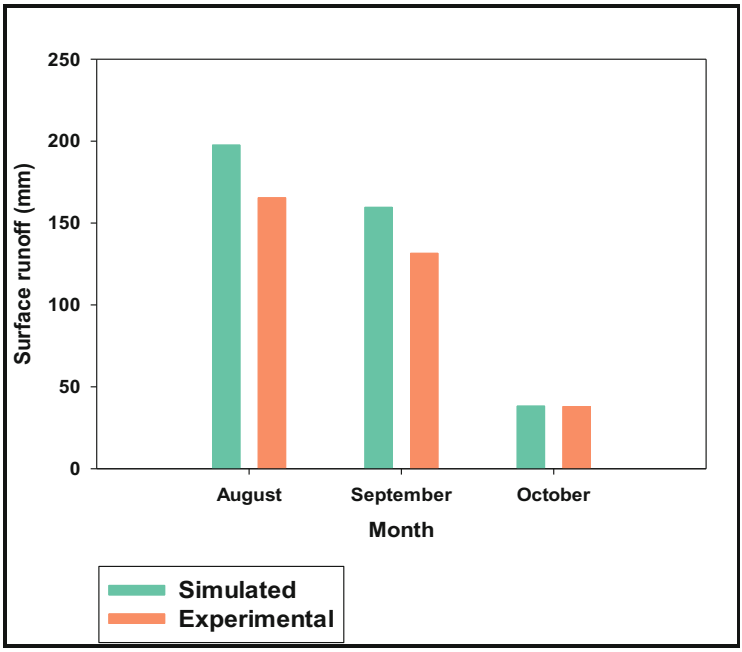

Fig. 4.7 Comparison of simulated and measured surface runoff depth

October, simulated Q is 38.25 mm and experimental Q is 37.96 mm. The corresponding percentage of error between the simulated and measured for the months of August, September, and October is 16.27%, 17.63%, and 0.77%, respectively.

4.6.2 Volume of Accumulated Water

The average volume of the accumulated water in the catchment area is shown in Fig. 4.8 (measured values with climatic conditions were provided in Table 4.4 of the Appendix). The area of the catchment is 14.02 km^2 and the volume of the accumulated water in the catchment is calculated by multiplying the average depth of the inundated water. The average volume of the inundated water for each month is

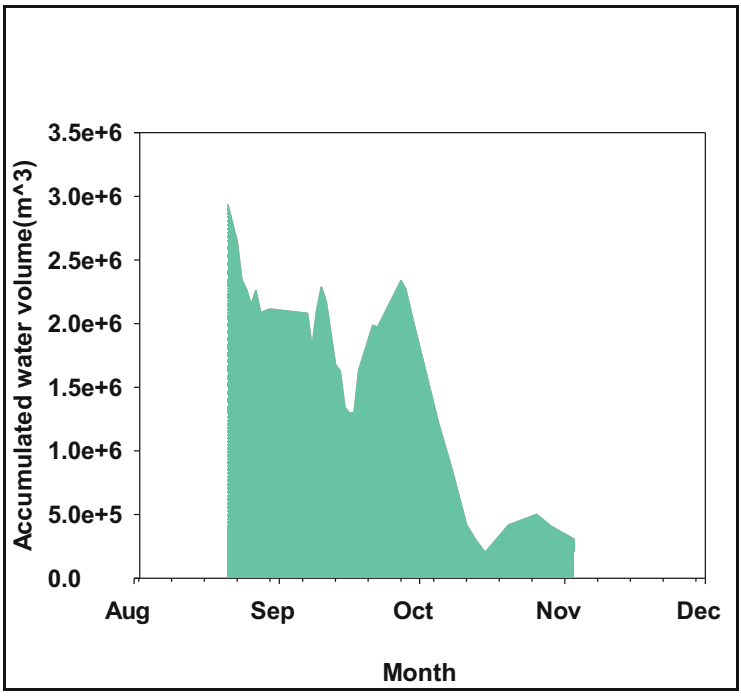

Fig. 4.8 Accumulated volume of water (m^3) in the catchment area during August–November 2021

2.38×10^6 m^3 in the month of August, 1.867×10^6 m^3 in the month of September, 0.539×10^6 m^3 in the month of October, and 0.306×10^6 m^3 in the month of November. There is a trend of decreasing the accumulated water volume from August to November.

4.6.3 Infiltration Depth

The infiltration depth (cm) was measured at three locations (measured values are provided in Table 4.5 of the Appendix) to understand the water holding capacity in the catchment area. It was measured during the month of February 2022 using MDI. After the readings were recorded, the data was plotted in the excel spreadsheet using predetermined equations. The spread sheets, which have predetermined equations, calculate the value of cumulative infiltration from the measured time (min) with the measured volume (mL). After obtaining the value of the cumulative infiltration, we calculate the incremental infiltration (cm).

From Fig. 4.9, at location 1, it was observed that the highest value of infiltration is 0.188 cm, the lowest value is 0.125 cm, and the average value is 0.171 cm. The infiltration depth at location 02 is 0.314 cm, the lowest value is 0.125 cm, and the

Table 4.4 Measured volume of accumulated water (August–November 2021)

Date	Average depth (m)	Volume (m^3)
21/08/2021	0.207	2934666.667
23/08/2021	0.186	2644040.000
24/08/2021	0.165	2343946.667
25/08/2021	0.160	2267266.667
26/08/2021	0.151	2146093.333
27/08/2021	0.159	2259693.333
28/08/2021	0.147	2085506.667
30/08/2021	0.149	2113906.667
07/09/2021	0.147	2080773.333
08/09/2021	0.128	1813813.333
09/09/2021	0.148	2105386.667
10/09/2021	0.161	2286200.000
11/ 09/2021	0.153	2175440.000
13/09/2021	0.118	1678440.000
14/09/2021	0.115	1626373.333
15/09/2021	0.095	1342373.333
16/09/2021	0.091	1295986.667
17/09/2021	0.092	1299773.333
18/09/2021	0.115	1634893.333
21/09/2021	0.140	1987053.333
22/09/2021	0.139	1970013.333
27/09/2021	0.165	2336373.333
28/09/2021	0.160	2273893.333
30/09/2021	0.138	1966226.667
05/10/2021	0.086	1222146.667
08/10/2021	0.059	842533.333
11/10/2021	0.030	419373.333
13/10/2021	0.021	299146.667
15/10/2021	0.014	201640.000
20/10/2021	0.029	417480.000
26/10/2021	0.035	500786.667
29/10/2021	0.029	408960.000
03/11/2021	0.022	305773.333

average value of infiltration is 0.217 cm. Similarly, at location 03, the highest value of infiltration depth is 0.39 cm, the lowest value is 0.188 cm, and the average value of infiltration is 0.234 cm. The highest infiltration depth recorded was 0.39 cm, and the average depth observed for all the locations was 0.2 cm.

Table 4.5 Measured infiltration (February 2022)

Location 1		Location 2		Location 3	
Time (h)	Infiltration (cm)	Time (h)	Infiltration (cm)	Time (h)	Infiltration (cm)
0.000	0.000	0	0	0	0
0.167	0.126	0.1	0.314	0.083	0.377
0.333	0.189	0.2	0.126	0.167	0.252
0.500	0.189	0.3	0.189	0.250	0.252
0.667	0.126	0.4	0.252	0.333	0.252
0.833	0.189	0.5	0.189	0.417	0.252
1.000	0.189	0.6	0.189	0.500	0.189
1.167	0.189	0.7	0.252	0.583	0.252
1.333	0.189	0.8	0.189	0.667	0.252
1.500	0.189	0.9	0.252	0.750	0.126
1.667	0.189	1	0.189	0.833	0.252
1.833	0.189	1.1	0.189	0.917	0.252
2.000	0.126	1.2	0.252	1.000	0.189
2.167	0.189	1.4	0.252	1.083	0.189
2.333	0.189				
2.5	0.126				

4.6.4 Infiltration Rate

From the measured incremental infiltration depth, the infiltration rate of the different soil types at different locations was calculated. For the calibration of the Horton's infiltration model, the minimum square error equation is used. Then, a solver equation is applied to the equations from excel to obtain an automatic value for the minimum total square error, and the calculated values to be used in Horton's model are provided in Table 4.1. It is plotted for each location and is shown in Fig. 4.10. For location 01, the initial infiltration rate for the measured data is 0.754 cm/h and for Horton's equation it is 0.566 cm/h. The steady infiltration rate for the measured data is around 0.08 cm/h and for the Horton model it is around 0.06 cm/h. For location 02, the initial infiltration rate for the measured data is 3.14 cm/h and for Horton's equation it is 1.05 cm/h. The steady infiltration rate for the measured data is around 0.17 cm/h and for the Horton model it is around 0.17 cm/h. For location 03, the initial infiltration rate for the measured data is 4.52 cm/h and for Horton's equation it is 2.79 cm/h. The steady infiltration rate for the measured data is around 0.18 cm/h and for Horton's model it is around 0.2 cm/h.

Table 4.6 shows the values of f_o (cm/h), f_c (cm/h), and k (h^{-1}), where f_o is the initial infiltration capacity, f_c is the final steady infiltration capacity, and k is the Horton decay coefficient, which depends on soil characteristics. These values are the calculated values of Horton's model. The average value of f_o is 2.21 cm/h. The average value of f_c is 0.13 cm/h. The average value of Horton decay, k, is 3.65 h^{-1}.

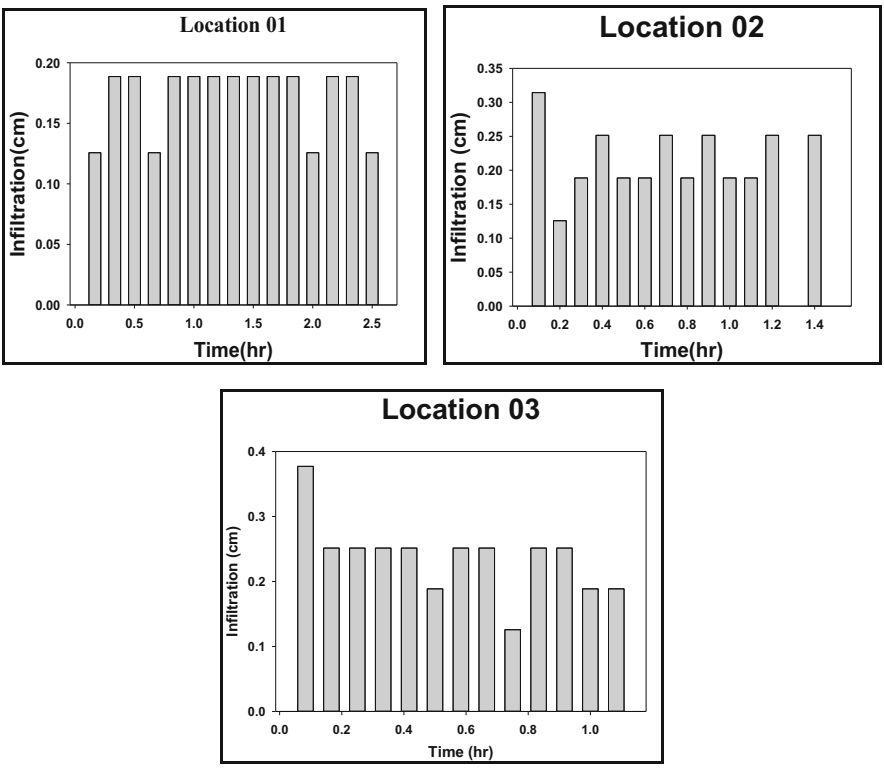

Fig. 4.9 Measured infiltration depth (cm) at location 1, 2 and 3

4.7 Conclusion and Recommendations

4.7.1 Conclusion

The depth of the inundated water was observed during the month of August–November 2021 and the measured results were compared with simulated results and observed in good agreement (maximum error is 17.63%). During the observation period the depth was recorded highest at 45 cm. The average inundated water depth recorded highest in the month of August is 16.54 cm. The volume calculated from the field measurement was calculated using the field measurement and the volume for August comes out highest at 2.38×10^6 m^3. Since the depth of the water accumulated during these months are high, normal activities carried out by people or animals were disturbed and also, as the volume of accumulated water were high it is better to plan for minimizing these flood water from the catchment. The infiltration for the soil in the catchment area was measured during the month of February 2022. The highest depth recorded was 0.39 cm and the average depth observed for all the locations was 0.2 cm. The average value of f_o is 2.21 cm/h. The average value of f_c is

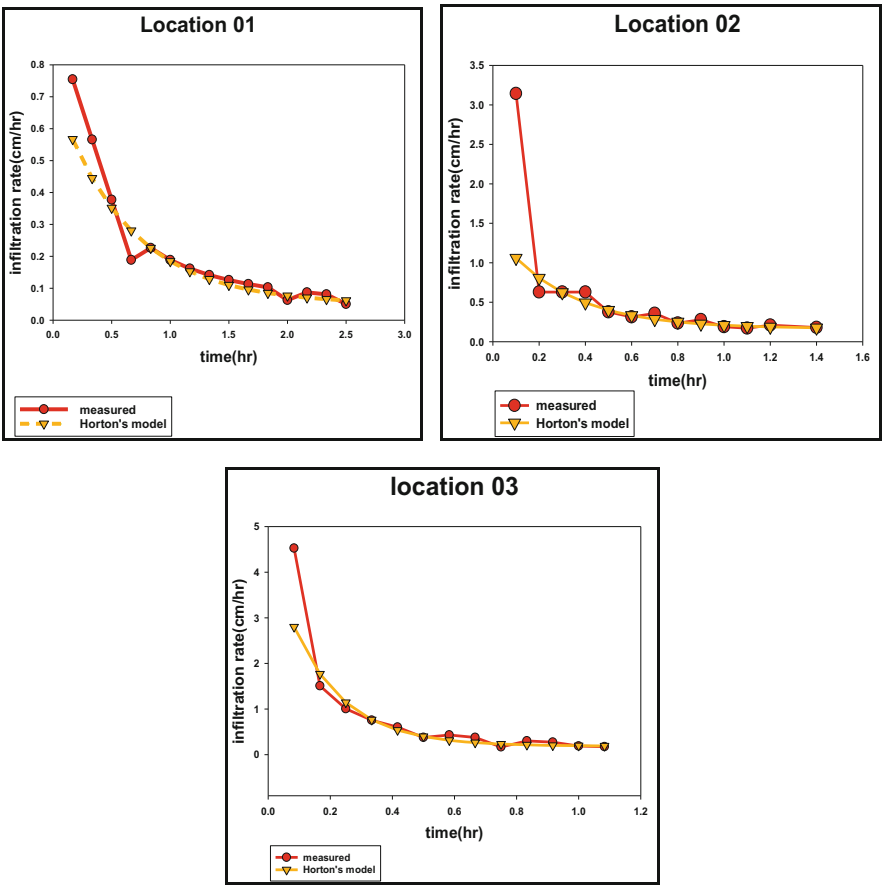

Fig. 4.10 Comparison of measured infiltration rate (cm) with Horton's model

Table 4.6 Values of f_o, f_c, and K of Horton's model for each location

Location	Lat/Long	f_o (cm/h)	f_c (cm/h)	$K(h^{-1})$
1	24°49′55.661″N,93°54′44.80″E	0.727	0.050	1.616
2	24°49′55.356″N,93°54′44.968″E	1.414	0.164	3.331
3	24°49′54.635″N,93°54′45.8865″E	4.505	0.186	6.028
	Average	2.215	0.133	3.658

0.13 cm/h. The average value of Horton decay, k is 3.65 h^{-1}. The infiltration class for different infiltration capacity is shown and infiltration capacity less than 2.5 cm/h is considered having very low infiltration class. The study area has an average infiltration capacity 0.13 cm/h, so we can say that the soil in the catchment area have a very low infiltration class. We can say that the inundation of the rainfall water

during the monsoon is affected by the infiltration capacity of the soil in the catchment area.

4.7.2 Recommendations

It is recommended to observe the accumulated depth for a period of whole year to get better efficiency in the result and understanding. It is also recommended to record the elevation of the site; velocity can also be recorded if we want to know about discharge of these accumulated water. The infiltration of the soil in the Langol catchment area was observed during the month of February 2022. It is recommended to take temperature of the location site when taking the measurement as it is one of the factors that affects the infiltration capacity of the soil. It is also recommended to take readings in other parts of the catchment area for better accuracy of the results. Also, high-intensity rainfall and continuous rainfall without proper drainage system contributes to the inundation of these water. We can use this information to extend to facilitate early preparation and planning before flood events. In view of such findings, it is recommended to provide proper drainage system to quickly drain out the accumulated surface water from NIT campus while considering the low laying landscape of the catchment area.

Appendix

References

Abichou T, Fatehnia M (2014) Comparison of the methods of hydraulic conductivity estimation from mini disk infiltrometer. Electron J Geotech Eng 19:1047–1061

Basri H, Chandra SY (2021) Assessment of infiltration rate in the Lawe Menggamat sub-watershed, Aceh Province, Indonesia, in. IOP Conference Series: Earth and Environmental Science 667(1): 012069

Flood Report (2002). Flood Hazard Zonation in Manipur (2022), Manipur Science & Technology Council. https://www.yumpu.com/en/document/view/24250287/final-report-mastec

Forkuo EK (2013) The use of digital elevation models for water-shed and flood hazard mapping. Int J Remote Sens Geosci 2(2):56–65

Hermas ES, Gaber A, Bastaswery ME (2021) Application of remote sensing and GIS for assessing and proposing mitigation measures in flood-affected urban areas, Egypt. Egypt J Remote Sens Space Sci 24(1):119–130

Horton RE (1933) An approach toward a physical interpretation of infiltration-capacity 1. Soil Sci Soc Am J 5(C):399–417

Jain R, Lodhi AS, Oliveto G, Pandey M (2021) Influence of cohesion on scour at piers founded in clay–sand–gravel mixtures. J Irrig Drain Eng 147(10):04021046

John CK, Pu JH, Pandey M, Hanmaiahgari PR (2021) Sediment deposition within rainwater: case study comparison of four different sites in Ikorodu, Nigeria. Fluids 6(3):124

Kargas G, Londra P, Anastasiou K, Kerkides P (2018) A note on one- and three-dimensional infiltration analysis from a mini disc infiltrometer. Water 10:1783

Latorrea B, Moret-Fernándeza D, Peñaa C (2013) Estimate of soil hydraulic properties from disc infiltrometer three-dimensional infiltration curve: theoretical analysis and field applicability. Procedia Environ Sci 19:580–589

Mangala OS, Toppo P, Ghoshal S (2016) Study of infiltration capacity of different soils. International Journal of Trend in Research and Development 3(2):388–390

Naik AP, Ghosh B, Sreeja P (2019) Estimating soil hydraulic properties using mini disk infiltrometer. J Hydraul Eng 25(1):62–70

Pu JH, Wallwork JT, Khan M, Pandey M, Pourshahbaz H, Satyanaga A, Hanmaiahgari PR, Gough T (2021) Flood suspended sediment transport: combined modelling from dilute to hyper-concentrated flow. Water 13(3):379

Rallison RE (1980) Origin and evolution of the SCS runoff equation, proceeding of the symposium on watershed management 80 American Society of Civil Engineering Boise ID

Reynolds WD, Elrick DE (1991) Determination of hydraulic conductivity using a tension infiltrometer. Soil Sci Soc Am J 55:633–639

Satheeshkumar S, Venkateswaran S, Kannan R (2017) Rainfall–runoff estimation using SCS–CN and GIS approach in the Pappiredipatti watershed of the Vaniyar sub basin, South India. Model Earth Syst Environ 3:24

Seong H et al (2020) Analysis of urban flood inundation patterns according to rainfall intensity using a rainfall simulator in the Sadang area of South Korea. Appl Sci 10(3):1158

Shankar MS, Pandey M, Shukla AK (2021) Analysis of existing equations for calculating the settling velocity. Water 13(14):1987

Shivashankar M, Pandey M, Zakwan M (2022) Estimation of settling velocity using generalized reduced gradient (GRG) and hybrid generalized reduced gradient–genetic algorithm (hybrid GRG-GA). Acta Geophys:1–11

Singh UK, Jamei M, Karbasi M, Malik A, Pandey M (2022) Application of a modern multi-level ensemble approach for the estimation of critical shear stress in cohesive sediment mixture. J Hydrol 607:127549

Subramanya K (2015) Engineering hydrology. Mc Graw Hill Education, New Delhi

Wallwork JT, Pu JH, Kundu S, Hanmaiahgari PR, Pandey M, Satyanaga A, Pandey M, Satyanaga A, Amir Khan M, Wood A (2022) Review of suspended sediment transport mathematical modelling studies. Fluids 7(1):23

USDA (1972) Soil conservation service, National Engineering Handbook, hydrology section 4. Chapters 4-10. USDA, Washington, D.C

Chapter 5
Soil Erosion Analysis with Respect to Land Use/Land Cover Change in Godavari Basin

S. Srinithisathian and J. Brema

Abstract Soil erosion is a major concern to the environment which leads to the loss of fertility of the soil, initiating sedimentation, clogging and polluting the water bodies. The goal of this study is to develop a GIS-based soil erosion model of the Godavari basin along with LULC changes. In this study, the popular method of Universal Soil Loss equation (USLE) is coupled with GIS. To get total soil erosion USLE needs to multiply six factors: rainfall erosivity (R) factor, soil erodibility (K) factor, slope length (L) factor, slope gradient (S) factor, crop cover or crop management (C) factor and conservation practices (P) factor. From the analysis, the magnitude of USLE model obtained corresponding to the parameter R, K, LS, C and P factors is varied between 90 to 140 MJ mm ha^{-1} h^{-1} $year^{-1}$, 0.1–1.0 Mg h MJ^{-1} mm^{-1}, 0–215, 0.002–1.00 and 0.39–1.00, respectively. Soil erosion on the basin ranges from 0 to 2360 t/ha/year. It is identified that LULC change is the more predominant factor compared to rainfall for soil erosion. Based on the findings, 2015 has the highest net soil erosion (97993275.32 ton/year) compared to previous years.

Keywords Godavari basin · LULC · Soil erosion · GIS · Remote sensing · USLE

5.1 Introduction

This paper estimates soil erosion for the entire Godavari basin from 1985 to 2015 and identifies the districts which are vulnerable to soil erosion. Soil erosion due to water is a global concern of this century mostly in all developing/developed countries (Asfaw et al. 2021). Soil is one of the primary resources of nature, yet it is subjected to degradation in an enormous amount especially in the river basin areas. The removal of topsoil is a result of soil erosion in the watershed which leads to the gradual decrease in the fertility of the soil (Islam et al. 2020). Continuous expansion of the cultivated land and unsustainable agricultural practices are one of the major

S. Srinithisathian · J. Brema (✉)
Department of Civil Engineering, Karunya Institute of Technology and Sciences, Coimbatore, Tamil Nadu, India
e-mail: srinithisathian@karunya.edu.in; brema@karunya.edu

M. Pandey et al. (eds.), *River Dynamics and Flood Hazards*, Disaster Resilience and Green Growth, https://doi.org/10.1007/978-981-19-7100-6_5

reasons for the land degradation which initiates the soil erosion in a particular region (Kidane et al. 2019). Even though soil erosion has been identified as a serious concern, in India the number of related studies on this problem are very limited (Devatha et al. 2015). Siltation and sedimentation contribute towards land degradation and low water quality and this has necessitated a good soil loss management (Devatha et al. 2015). The Universal Soil Loss Equation (USLE) predicts the long-term average annual rate of erosion (Stone 2012). USLE can be derived from topography of the area, soil characteristics, rainfall distribution over the area, land use and land cover and support conservation practices (Vemu and Pinnamaneni 2012). The terms land use and land cover are often used in many environmental related studies. For monitoring and managing the environment and natural resources, land use and land cover (LULC) change has become an elementary tool (Twisa and Buchroithner 2019). LULC change in an area possibly affects the soil properties by increasing or by decreasing the soil stability. Recent studies prove that urbanisation causes soil erosion and on the other hand studies show that forests play an important role in reducing topsoil erosion.

The aim of this study is to analyse the effect of land use land cover change on soil erosion in the Godavari basin. This study has two main objectives, i.e., to find land use land cover change in the basin for four respective years (1985, 1995, 2005 and 2015) with 10 years interval and to analyse the soil loss for the entire basin for the above-mentioned years.

5.2 Study Area

Godavari basin extends over eight states of India, namely, Andhra Pradesh, Maharashtra, Chhattisgarh, Odisha, Telangana, Karnataka, Chhattisgarh, Madhya Pradesh and Union territory of Puducherry. The basin includes 56 districts with a total area of 307816.72 Km^2. It lies between 73° 24′ to 83° 4′ E Latitude 16° 19′ to 22° 34′ N Longitude. The basin is surrounded by Satmala hills, Ajantha range and Mahadeo hills in the north, by the Eastern ghats and Western ghats in the eastern and western directions, respectively. The southwest monsoon contributes to 84% of annual rainfall spreading over June to September. Western ghats experiences the heaviest rainfall and the dampest climate in the basin. The climate is hot and humid with mean dry temperature between 35 °C and 40 °C during summer and 25 °C and 30 °C during winter. Agriculture and deciduous forest are the prime land use classes covering most of the area of the basin. The Godavari River originates from Trimbakeshwar in the Nashik district of Maharashtra, having 12 main tributaries. The Pranhita River is the largest tributary of the Godavari with about 34.87% coverage of the total drainage area. Figure 5.1 shows the boundary and the Digital Elevation Model (DEM) of Godavari basin.

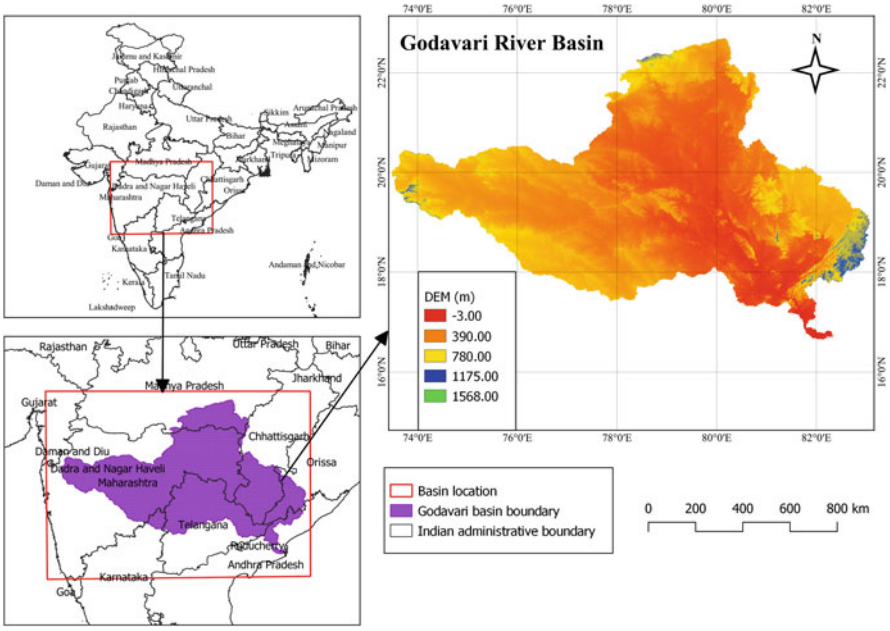

Fig. 5.1 Study area with Digital Elevation Model (DEM)

5.3 Materials and Methodology (Table 5.1)

Figure 5.2 explains about the methodology followed for the estimation of soil loss based on USLE and GIS. Table 5.1 shows the data used for generation of each of the map corresponding to the factors applicable to USLE equation. Table 5.2 exhibits various USDA textural classes of soil.

Table 5.1 Data source

S. No	Data type	Source	Description
1	Digital elevation model (DEM)	https://earthexplorer.usgs.gov/	SRTM 1 arc second global (30 m resolution)
2	Land use/land cover (LULC)	https://daac.ornl.gov/VEGETATION/guides/Decadal_LULC_India.html and https://bhuvan-app1.nrsc.gov.in/thematic/thematic/index.php	1985, 1995, 2005 and 2015 LULC maps
3	Soil data	http://worldmap.harvard.edu/data/geonode:DSMW_RdY	Soil map
4	Rainfall data	https://power.larc.nasa.gov/data-access-viewer/	Rainfall data for the periods of 1985–2015 with 13 rainfall stations

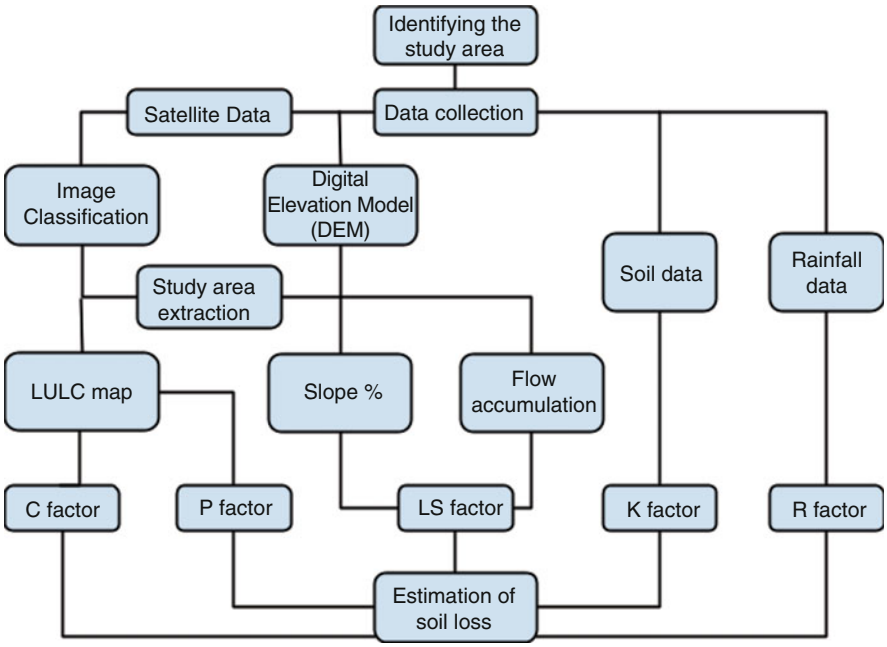

Fig. 5.2 Methodology

Table 5.2 USDA textural classes of soil

Common names of soils (General texture)	Sand	Silt	Clay	Textural class
Sandy soils (coarse texture)	86–100	0–14	0–10	Sand
	70–86	0–30	0–15	Loamy sand
Loamy soils (moderately coarse texture)	50–70	0–50	0–20	Sandy loam
Loamy soils (medium texture)	23–52	28–50	7–27	Loam
	20–50	74–88	0–27	Silty loam
	0–20	88–100	0–12	Silt
Loamy soils (moderately fine texture)	20–45	15–52	27–40	Clay loam
	45–80	0–28	20–35	Sandy clay loam
	0–20	40–73	27–40	Silty clay loam
Clayey soils (fine texture)	45–65	0–20	35–55	Sandy clay
	0–20	40–60	40–60	Silty clay
	0–45	0–40	40–100	Clay

Note. Based on the USDA particle-size classification (https://www.fao.org/fishery/docs/CDrom/FAO_Training/FAO_Training/General/x6706e/x6706e06.htm)

5.3.1 USLE Model Description

In this study, the total soil loss was predicted using the USLE model where all the respective parameters were multiplied using raster calculator in QGIS software.

$$\text{Total soil loss } (A) = R \times K \times L \times S \times C \times P.$$

where A is the soil loss in t/ha/year, R is the rainfall-runoff erosivity factor in MJ (mm/ha/year); K is the soil erodibility factor (t h/(MJ mm)); L is the slope length factor; S is the slope steepness factor; C is the cover and management factor; and P is the supporting conservation practices factor.

5.3.1.1 Rainfall Erosivity Factor (R)

The rainfall erosivity is calculated by multiplying the kinetic energy by the maximum rainfall intensity during a period of 30 min for each rainstorm. The R factor accumulates the rainfall erosivity of individual rainstorm events and averages this value over multiple years. Rainfall data for various stations were collected from power access data viewer website and the mean annual rainfall for the years 1985, 1995, 2005 and 2015 were calculated. R factor is calculated using the following equation (Singh et al. 1981):

$$R = 79 + 0.363 \times X.$$

where R is a rainfall erosivity factor, X is the mean annual precipitation in mm. The rainfall erosivity map for the basin is shown in Fig. 5.3.

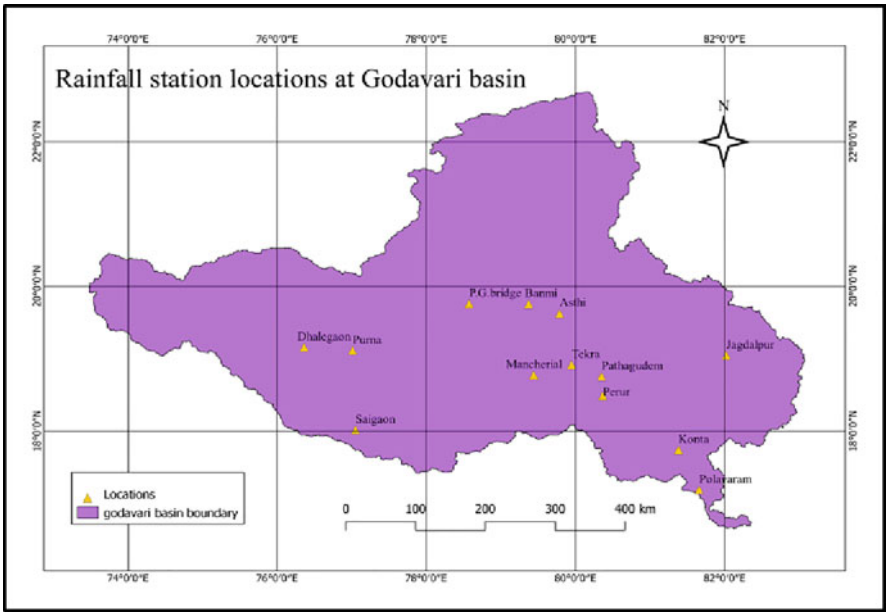

Fig. 5.3 Rainfall station locations at Godavari basin

5.3.1.2 Soil Erodibility Factor (K)

The impact of raindrop on soil and the shearing action of runoff between lumped earthy materials on the water bodies like small streams are the main factors which define the erodibility of the soil. Soil map was downloaded from the World map website where the soils are classified based on the classification developed by FAO (Food and Agricultural Organisation). Godavari basin contains 13 types of FAO soil classes (Food and Agricultural Organisation of the United Nations, Land and Water Division 2003) (Tables 5.2 and 5.3). The soil texture is classified based on USDA textural classes of soil (FAO 1985) (Table 5.2). Soil erodibility factor (k) is calculated by using the equation (Al Rammahi and Khassaf 2018),

$$K_{\text{usle}} = f_{\text{csand}} \times f_{\text{cl}-\text{si}} \times f_{\text{orgc}} \times f_{\text{hisand}}$$

where

K_{usle}: USLE model soil erodibility factor.

$f_{\text{csand}} = [0.2 + 0.3 \times \exp.(-0.256 \times m_s \times (1 - \frac{m\text{silt}}{100}))]$.

$f_{\text{cl-si}} = [m_{\text{silt}}/(m_c + m_{\text{silt}})]^{0.3}$.

$f_{\text{orgc}} = (1 - \frac{0.25 \times \text{orgC}}{\text{orgC} + \exp\ [3.75 - 2.95 \times \text{orgC}]})$.

$f_{\text{hisand}} = (1 - \frac{0.75 \times \left(1 - \frac{m_s}{100}\right)}{\left(1 - \frac{m_s}{100}\right) + \exp\ \left[-5.51 + 22.9 \times \left(1 - \frac{m_s}{100}\right)\right]})$.

m_s: the percentage of sand fraction content (0.5–2 mm particle diameter) [%].

m_{silt}: the percentage of silt fraction content (0.002–0.05 mm particle diameter) [%].

Table 5.3 Soil classification and K factor

Soil type	Soil unit symbol	Textural properties	K factor
Plinthis Acrisols	AP	Sandy clay loam	0.13
Eutric Cambisols	BE	Loam	0.15
Vertic Cambisols	BV	Caly	0.13
Haplic Phaeozem	HH	Clay loam	0.15
Lithosols	I	Sandy clay loam	0.14
Calcaric Fluvisol	JC	Loam	0.17
Chromic Luvisols	LC	Sandy clay loam	0.14
Ferric Luvisols	LF	Loamy sand	0.13
Plinthic luvisols	LP	Sandy loam	0.13
Eutric Nitosols	NE	Sandy clay loam	0.14
Dystric Regosols	RD	Loamy sand	0.10
Chromic Vertisols	VC	Clay	0.14
Pellic Vertisols	VP	Clay	0.11
Water	WA	–	1.0

Note. Taken from "Digital Soil Map of the World. [computer file]. v3.6. Food and Agricultural Organisation of the United Nations, Land and Water Division, 2003"

m_c: the percentage of clay fraction content (<0.002 mm particle diameter) [%].
orgC: the percentage of organic carbon fraction content) [%].

5.3.1.3 Slope Length and Steepness Factor (LS)

The slope length and slope steepness can be used in a single index, which expresses the ratio of soil loss as defined by (Wischmeier and Smith 1978).

Slope Gradient Factor (S): Soil loss increases with steepness of the slope. The density of the vegetation and the size of the soil particles influences the soil loss of the region. Slope of the basin was derived from DEM (digital elevation model).

Slope Length Factor (L): The rate of soil erosion is affected by the slope length, since in a larger slope length a higher concentration of overland flow with a higher velocity of flow will occur accelerating the rate of soil erosion (Das 2004). *L* is the actual unbroken slope length in metres, where *m* is the ratio of the soil loss from the field plot length to soil loss from the unit plot provided with a slope length of 22.1 m. Values of "m" corresponding to different slopes are given in Table 5.4.

Estimation of slope length and steepness factor: In the case of LS factor, the effect of slope length on erosion is accounted by the slope length factor *L*. Whereas, the effect of slope steepness is considered by the slope steepness factor *S*. To calculate LS factor, we need slope percentage and flow accumulation of the basin. Flow accumulation is derived from DEM using the Accumulation function tool in QGIS.

$$\mathrm{LS} = (\text{Flow accumulation} \times \text{Cell size}/22.1)^{m} \times \left(0.065 + 0.045\ \mathrm{s} + 0.0065\ \mathrm{s}^2\right).$$

In the raster calculator the following expression were used,

$$\mathrm{LS} = \Big(\left(\text{Flow accumulation} \times 100/22.1\right)^{0.2}\Big) \times (0.065 + 0.045 \times \text{slope percent} + 0.045 \times \text{slope percent} + 0.0065 \times (\text{slope percent} \times \text{slope percent})).$$

5.3.1.4 Crop Cover Management Factor (C)

C factor is used to estimate the effect of land cover, cropping and management practices on soil loss. Landuse/landcover image data is collected from various satellites corresponding to the years 1985, 1995, 2005 and 2015. A total of

Table 5.4 *m* value of slope

m value	Slope in %
0.5	>5
0.4	3–5
0.3	1–3
0.2	<1

Table 5.5 *C* factor and *P* factor

Land use	*C* factor	*P* factor
Deciduous Forest	0.004	1
Cropland	0.38	0.39
Built-up land	0.002	1
Mixed Forest	0.004	1
Shrubland	0.38	0.39
Barren land	1	1
Fallow land	1	1
Wasteland	1	1
Water bodies	1	1
Plantations	0.38	0.39
Mangrove Forest	0.4	1
Grassland	0.38	0.39
Evergreen Forest	0.004	1

Note. Adapted from "Shinde, V., Tiwari K. N. and Singh, M.: Prioritisation of micro watersheds on the basis of soil erosion hazard using remote sensing and geographic information system. International Journal of Water Resources and Environmental Engineering. 2 (2010), 130–136." and "Priya, S. and Shibasaki, R. Quantification of soil loss and its detection using GIS and remote sensing technology. Asian-Pacific Remote Sensing Journal, 10 (1998), 33–38"

13 landuse categories were identified from the satellite imageries with the help of training data for carrying out supervised classification. The classes are Deciduous Forest, Evergreen Forest, Mangrove Forest, Mixed Forest, Built-up land, Crop land, Fallow land, Shrub land, Waste land, Barren land, Grassland, Plantations and Water bodies. The values for *C* Factor (Shinde et al. 2010) corresponding to various landuse categories are given in Table 5.5.

5.3.1.5 Supporting Conservation Practice Factor (P)

The support conservation practice factor is called the *P* factor. Since water is playing a major role on the soil erosion *P* factor indicates the practices that reduce the soil erosion by reducing runoff. LULC data is reclassified with the *P* factor data taken from the previous work. Values for *P* Factor were taken from the literature (Priya and Shibasaki 1998) and are given in Table 5.5.

5.4 Results and Discussion

5.4.1 *Landuse/Landcover Change*

Landuse/landcover map of the Godavari basin for the years 1985,1995, 2005 and 2015 has been created and classified into 13 classes using QGIS software. Among these 13 classes, cropland covers more than 50% of the basin area for all the mentioned years (Table 5.6). Deciduous forests cover a large amount of area next to cropland. Table 5.7 and Fig. 5.4a–d show the average annual rate of change (%) in the area for years 1985–1995, 1995–2005 and 2005–2015. Positive sign indicates the increase in areal extent and negative sign indicates reduction in area. The average annual rate of change for built-up areas is 75.51%.

This shows the enormous rate of increase in the built-up area indicates rapid urbanisation in the past 30 years. The study shows that there exist a negative growth in all the types of forest stating that deforestation is happening over the basin. The area for water bodies does not show a significant change in the years of 1985 and 1995 but it rapidly reduced in 2005 and increased in the next 10 years. The increase in areal extent of water bodies is due to the conservation activities carried out in the basin. Mangroves did not show a significant rate of change, yet it has decreased over the years.

5.4.2 *Rainfall Erosivity Factor (R)*

Rainfall erosivity increases with the increase in the rainfall in a particular area. As per the data, for all the years during the study period it was observed that a very high rainfall occurred in the east of the Godavari basin which naturally leads to a high rainfall erosivity in that area (Tables 5.8 and 5.9). Hence the eastern part of the basin is vulnerable to high rainfall erosivity. Western part of the basin has low rainfall erosivity compared to other regions. For all the four years (1985, 1995, 2005 and 2015) rainfall erosivity varies from 90 to 140 MJ mm ha^{-1} h^{-1} $year^{-1}$. A very high rainfall happened in the year of 2015 in the eastern part of the basin exhibiting high rainfall erosivity of 132.06 MJ mm ha^{-1} h^{-1} $year^{-1}$. Likewise, a very low rainfall of 94.71 MJ mm ha^{-1} h^{-1} $year^{-1}$ takes place in the west of the basin during the year, 1985. Moderate rainfall prevails in the north and middle region of the basin.

The Fig. 5.5a–d show that the rainfall erosivity is high in the eastern part of the basin which happened to be of higher elevation also. From Fig. 5.6 it was observed that the rainfall was high during the year 2005.

Table 5.6 Area under different categories

	1985		1995		2005		2015	
LULC	Area (km^2)	%	Area (km^2)	%	Area (km^2)	%	Area (km^2)	%
Deciduous Forest	80152.71	26.04	79363.09	25.78	78985.41	25.66	74076.12	24.05
Cropland	178009.98	57.83	179270.32	58.24	186867.91	60.71	183929.28	59.72
Built-up land	1583.46	0.51	2269.81	0.74	2441.44	0.79	6671.86	2.17
Mixed Forest	10971.26	3.56	10780.69	3.50	10729.25	3.49	6232.61	2.02
Shrubland	18154.95	5.90	15909.72	5.17	14849.43	4.82	11806.31	3.83
Barren land	548.56	0.18	567.87	0.18	568.31	0.18	559.60	0.18
Fallow land	6823.52	2.22	7248.68	2.35	7796.45	2.53	12627.77	4.10
Wasteland	425.19	0.14	410.76	0.13	495.1	0.16	259.69	0.08
Water bodies	9369.84	3.04	10345.98	3.36	3356.75	1.09	9942.34	3.23
Plantations	1406.52	0.46	1277.87	0.42	1356.57	0.44	1534.42	0.50
Mangrove Forest	38.91	0.01	40.59	0.01	39.06	0.01	28.81	0.01
Grassland	57.33	0.02	62.35	0.02	62.21	0.02	122.17	0.04
Evergreen Forest	274.49	0.09	268.99	0.09	268.83	0.09	185.31	0.06
Total area	307×10^3	100	307×10^3	100	307×10^3	100	307×10^3	100

Table 5.7 Average annual rate of change in percentage

	Rate of change of area in %			
LULC	1985–1995	1995–2005	2005–2015	Avg annual rate of change in %
Deciduous Forest	−1.00	−0.47	−6.27	−2.58
Cropland	0.71	4.24	−1.63	1.11
Built-up land	45.10	6.76	174.68	75.51
Mixed Forest	−1.69	−0.29	−42.12	−14.70
Shrubland	−12.37	−6.77	−20.54	−13.23
Barren land	0.00	0.00	0.00	0.00
Fallow land	5.86	7.66	62.06	25.19
Wasteland	−7.14	23.08	−50.00	−11.36
Water bodies	10.53	−67.56	196.33	46.43
Plantations	−8.70	4.76	13.64	3.23
Mangrove Forest	0.00	0.00	0.00	0.00
Grassland	0.00	0.00	100.00	33.33
Evergreen Forest	0.00	0.00	−33.33	−11.11

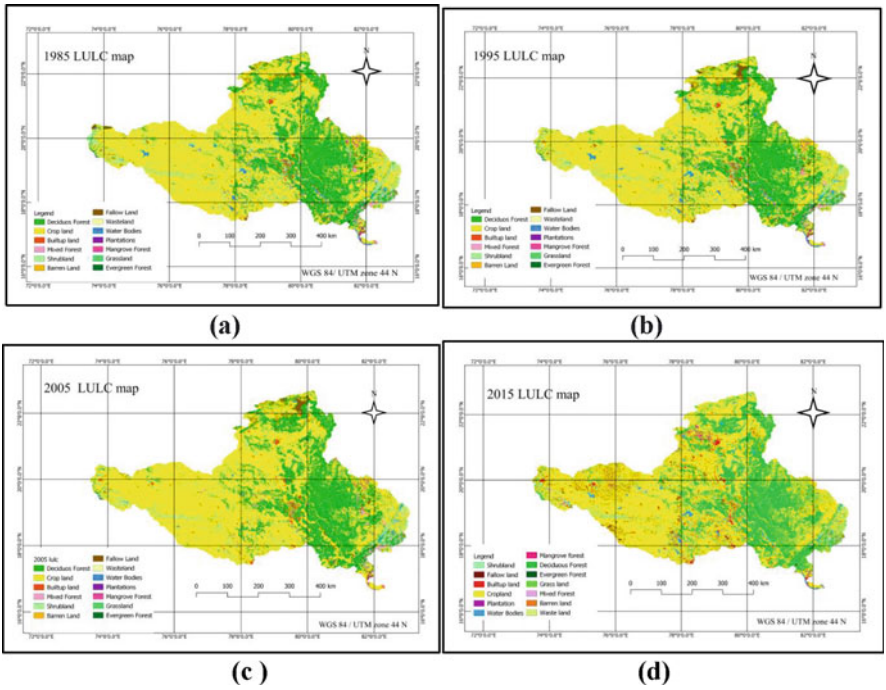

Fig. 5.4 Landuse Landcover change map—(**a**) 1985; (**b**) 1995; (**c**) 2005; (**d**) 2015

Table 5.8 Average rainfall in Godavari basin

Year	Average rainfall (mm)
1985	76.434
1995	105.846
2005	108.627
2015	80.500

Table 5.9 Mean annual rainfall

			Mean annual rainfall (mm)			
Site	Latitude	Longitude	Year 1985	Year 1995	Year 2005	Year 2015
Polavaram	17.246	81.660	84.11	140.811	117.248	97.19
Konta	17.800	81.383	90.393	137.976	122.071	100.313
Perur	18.550	80.367	87.678	112.129	115.792	79.684
Pathagudem	18.817	80.350	87.678	112.129	115.792	79.684
Jagdalpur	19.108	82.025	112.443	133.867	128.859	146.181
Tekra	18.978	79.947	76.257	101.363	107.524	62.832
Banmi	19.815	79.379	78.217	103.13	109.258	85.912
P.G.bridge	19.818	78.578	65.134	91.078	98.478	77.183
Asthi	19.687	79.787	91.183	114.093	121.246	95.299
Mancherial	18.836	79.445	67.137	93.974	99.968	53.713
Saigaon	18.076	77.053	57.646	94.057	96.208	48.259
Purna	19.176	77.014	52.499	81.528	94.138	59.873
Dhalegaon	19.220	76.364	43.272	59.866	85.578	60.383

5.4.3 Soil Erodibility Factor (K)

Soil erodibility factor depends on the soil classification or type of soil. There are 13 types of soils available in Godavari basin (Fig. 5.7a). Soil erodibility factor in the basin ranges from 0.1 to 0.17 t ha^{-1} MJ^{-1} mm^{-1} (excluding water having *K* factor as 1). More than 70% of the basin area has a soil erodibility of 0.14 t ha^{-1} MJ^{-1} mm^{-1} as shown in Fig. 5.7b.

5.4.4 Slope Length and Steepness Factor (LS)

Higher elevation prevails in the north, west and eastern parts of the basin. It is because Godavari basin is surrounded by Satmala hills at north, western ghats at west and eastern ghats at east of the basin. As the slope is steeper and longer, the rate of soil erosion is high. Godavari basin has a LS factor ranging from 0 to 213 with most of the area having the value of 0 as shown in Fig. 5.8. Even though the maximum coverage of LS factor of the basin is 0, still the other factors made the particular regions in the basin vulnerable to soil erosion.

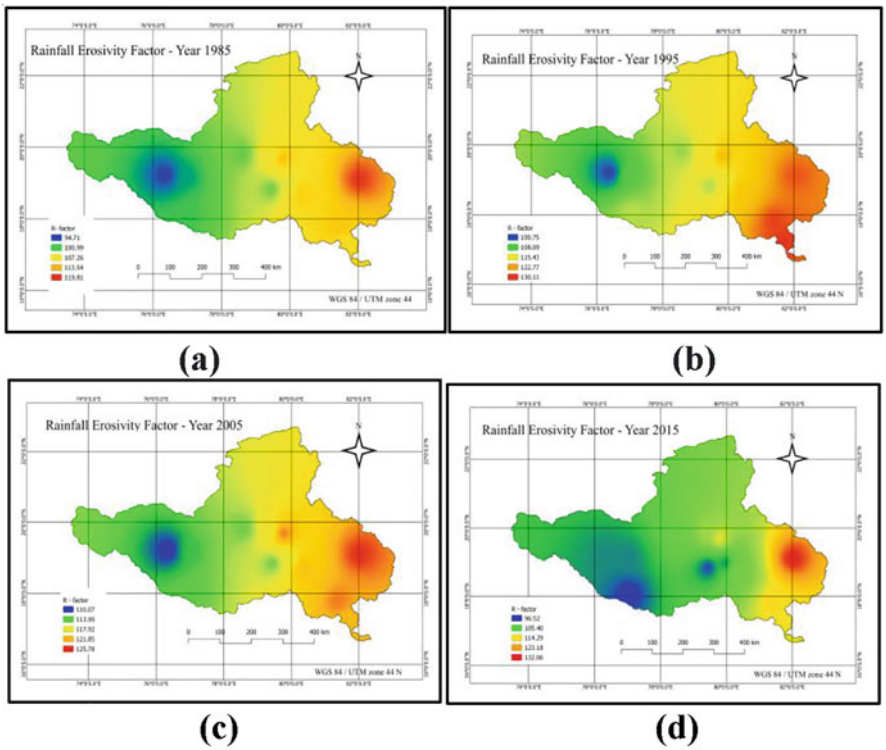

Fig. 5.5 Rainfall erosivity factor map—(**a**) 1985; (**b**) 1995; (**c**) 2005; (**d**) 2015

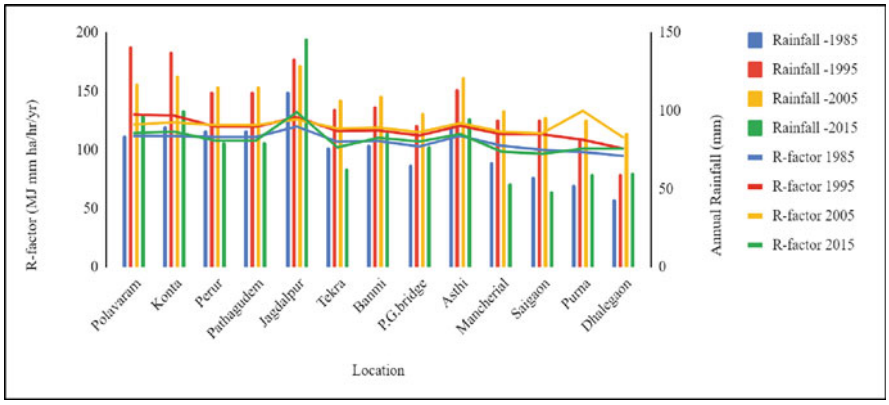

Fig. 5.6 Spatial variation of rainfall and erosivity in Godavari River basin

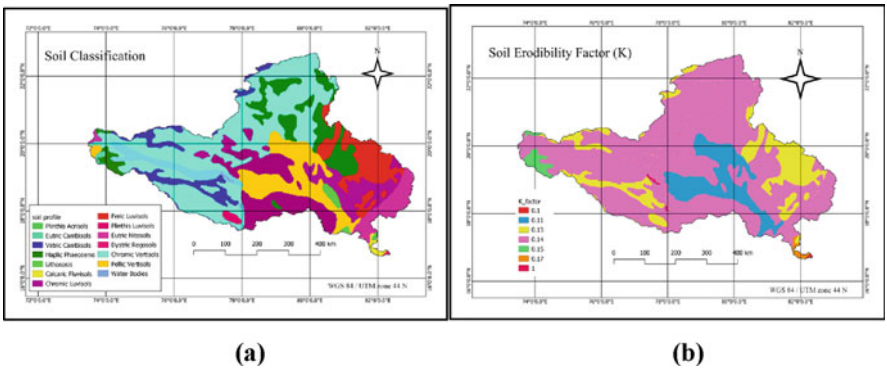

Fig. 5.7 (**a**) Soil classification and (**b**) Soil erodibility of Godavari basin

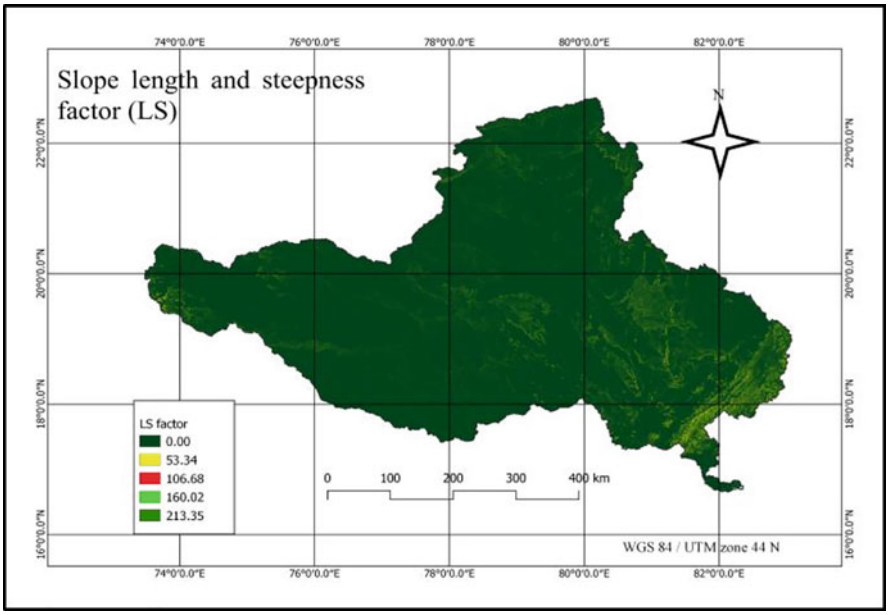

Fig. 5.8 Slope length and Steepness factor

5.4.5 Crop Cover Management Factor (C)

Crop cover management factor is one of the most important factors considered for estimating the soil loss. The barren land, i.e., with no vegetation, and with tillage along the slope has been considered as a reference condition, with a *C* factor value of 1. The value of *C* factor ranges from 0.004 to 1. The study assigned lowest value for forest and highest value for cultivated land along with water and lands with no vegetation which pointed out that the highest value of *C* factor accelerates soil

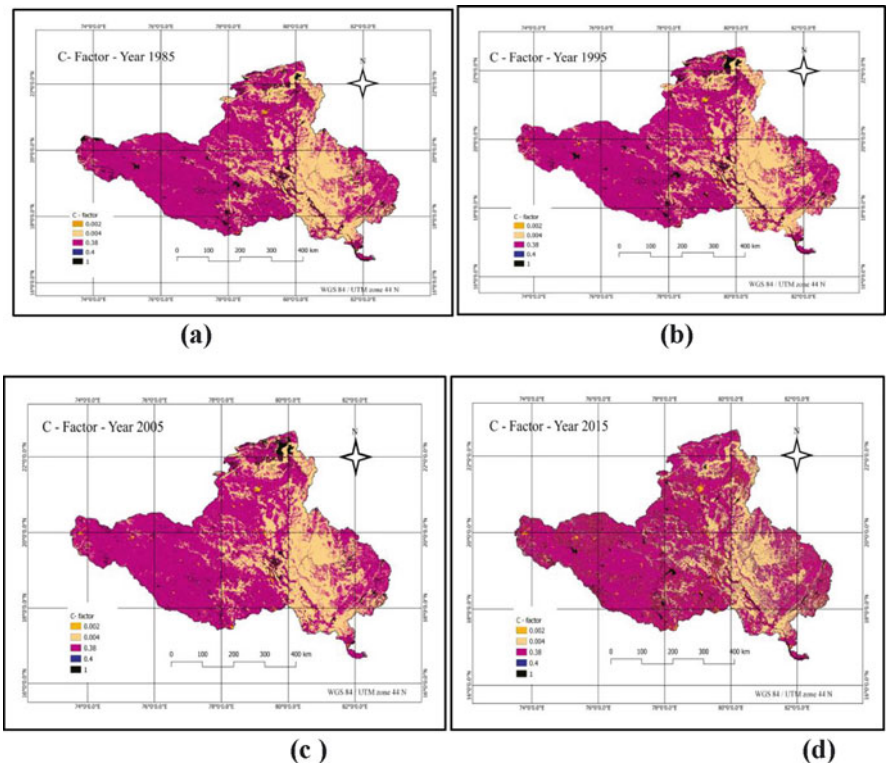

Fig. 5.9 Crop cover management factor map—(**a**) 1985; (**b**) 1995; (**c**) 2005; (**d**) 2015

Table 5.10 *C* factor in the Godavari basin

	Year 1985	Year 1995	Year 2005	Year 2015
C factor	% of area	% of area	% of area	% of area
0	0.03	0.05	0.05	0.05
0.002	5.34	0.74	0.79	0.51
0.004	22.36	29.36	29.22	29.68
0.38	60.95	63.81	65.96	64.17
0.4	3.15	0.01	0.01	0.01
1	8.16	6.03	3.97	5.57

erosion. *C* factor value 0.38 covers more than 60% of the basin area which corresponds to the cultivation area indicating possible soil erosion in the cropland. The low *C* factor values that take place in the forest areas shows that forests can reduce the soil loss. The variations in the *C* factor across the basin are shown in Fig. 5.9a–d. Table 5.10 illustrates the variations in percentage of area under various *C* factor values.

5.4.6 Supporting Conservation Practice Factor (P)

P factor ranges from 0.39 to 1 in the basin, where 0.39 is the most dominant value corresponds to cultivation or cropland. Lower value of *P* factor indicates good conservation practices in that area whereas higher *P* factor indicates that there is a need for conservation practice inured to reduce the soil erosion. Figure 5.10a–d shows the variations in *P* factor across the basin. The maps show that the conservation practices are sufficiently good in the middle reach of the basin.

5.4.7 Soil Loss Estimation (A)

The estimated quantity of soil loss in Godavari basin was estimated for all four years (1985, 1995, 2005, 2015) and it seems that the most of the area of the basin is having a low amount of soil erosion (0–1 ton/ha/year), particularly the area covered with forests and vegetation. Soil erosion was observed as high in the eastern, western and the northern parts of the basin. From the soil erosion map (Fig. 5.11), it has been observed that out of 56 districts in Godavari basin 7 of them (Ahmednagar,

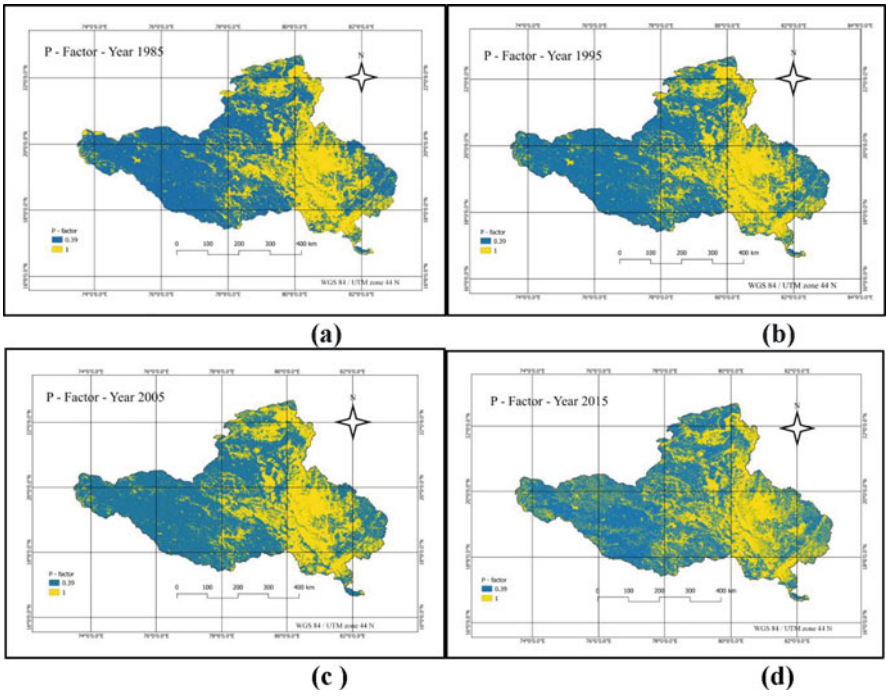

Fig. 5.10 Supporting conservation practice factor map (**a**) 1985; (**b**) 1995; (**c**) 2005; (**d**) 2015

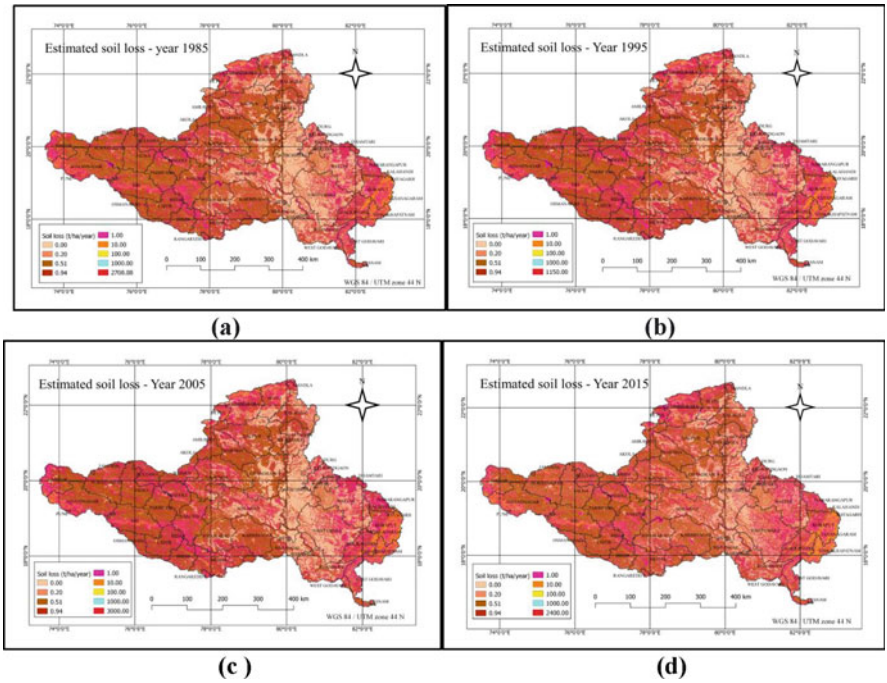

Fig. 5.11 Soil loss map—(**a**) 1985; (**b**) 1995; (**c**) 2005; (**d**) 2015

Chhindwara, East Godavari, Koraput, Nasik, Malkangiri and Visakhapatnam) are prone to more soil erosion (Fig. 5.12).

Table 5.11 shows the net soil erosion in the seven districts and the erosion percentage with the total soil loss in the basin for the respective years. These districts are responsible for more than 40% of the net soil loss of the basin. It seems that Koraput district is having a higher amount of net soil loss among the seven districts. Table 5.12 shows the rate of change of soil loss in districts in percentage. The positive sign indicates the increase in the rate of change of soil loss in % and the negative sign indicates the reduction in the rate of change of soil loss in %. During the decades, 1985–1995 and 2005–2015 East Godavari district showed an increase in the rate of change and during 1995–2005 the soil loss was reduced to 60%. Though Nashik district initially showed a reduction in the rate of change in the soil loss in the decade 1985–1995, there is an increase in the rate of change of soil loss during the decades 1995–2005 and 2005–2015.

It has to be noted that even though the average annual rainfall during the year 2015 is lower compared to other years, the changes in the C and P factor are the major factors that influence the soil loss over the area. This indicates that though rainfall is a major factor for soil loss, LULC change is a prime factor that largely impacts soil erosion. This gives the reason for the drastic rate of change of soil erosion in the Chhindwara district (Figs. 5.13a–g, 5.14 and Table 5.12). The

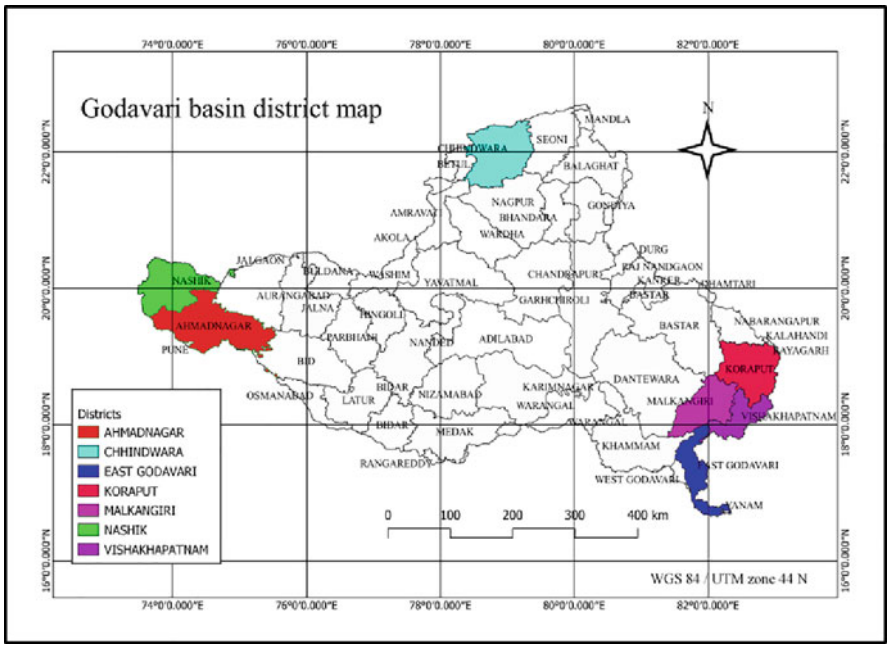

Fig. 5.12 Godavari basin district map

estimated result shows that the net soil loss of the basin in the year 2015 is very high (97993275.35 tonnes/year) compared for another 3 years. This change in the soil loss may be due to the increase of built-up lands, Fallow lands and decrease amount of forest area in 2015. Table 5.13 gives the net soil loss in the basin over the years.

The Fig. 5.15a–d shows the soil erosion in the districts such as Malkangiri, East Godavari, Ahmednagar and Koraput districts respectively.

5.5 Conclusion

The present continuing changes in LULC followed by the high rate of soil erosion in Godavari basin highlights the need for implementation of sustainable soil conservation practices. If the control measures are not considered to revert the present scenario, the whole Godavari basin area would be facing the risk of siltation, excess nutrient pollution and loss of water quality. Even though the rate of erosion is high, conservation measures carried out on a prioritisation basis will definitely bring down the severity of soil erosion in this region. In the Godavari basin, in particular regions located in the hilly areas of the basin require intensive soil and water conservation practices. As per the study, Koraput district is severely affected among the seven identified districts due to soil erosion. More importantly, appropriate conservation

Table 5.11 Net soil loss in the districts with Percentage of area

Net soil loss (tonnes/year)								
Site	Year 1985	%	Year 1995	%	Year 2005	%	Year 2015	%
Chhindwara	2493427.51	4.93	2738210.73	4.88	2842896.18	5.34	2777876.53	2.83
Nashik	1691017.53	3.35	1503795.79	2.68	1473595.68	2.77	3265499.92	3.33
East godavari	953250.04	1.89	1233391.28	2.20	728911.55	1.37	2655186.66	2.71
Visakhapatnam	4107832.79	8.13	4422035.57	7.88	4256781.87	8.00	10100364.18	10.31
Malkangiri	4127082.07	8.16	4492494.34	8.01	4338138.34	8.16	10179733.69	10.39
Koraput	5948544.52	11.77	6716912.88	11.97	6686326.72	12.57	11768741.27	12.01
Ahmadnagar	3770248.16	7.46	3962621.9	7.06	3862960.37	7.26	5826954.72	5.95

Table 5.12 Rate of change of soil loss in the districts

Rate of change of soil loss in %			
Site	1985–1995	1995–2005	2005–2015
Chhindwara	−1.06	8.69	−88.54
Nashik	−24.80	3.25	16.86
East Godavari	14.22	−60.42	49.42
Visakhapatnam	−3.10	1.52	22.36
Malkangiri	−1.96	1.82	21.49
Koraput	1.71	4.76	−4.67
Ahmednagar	−5.60	2.75	−22.14

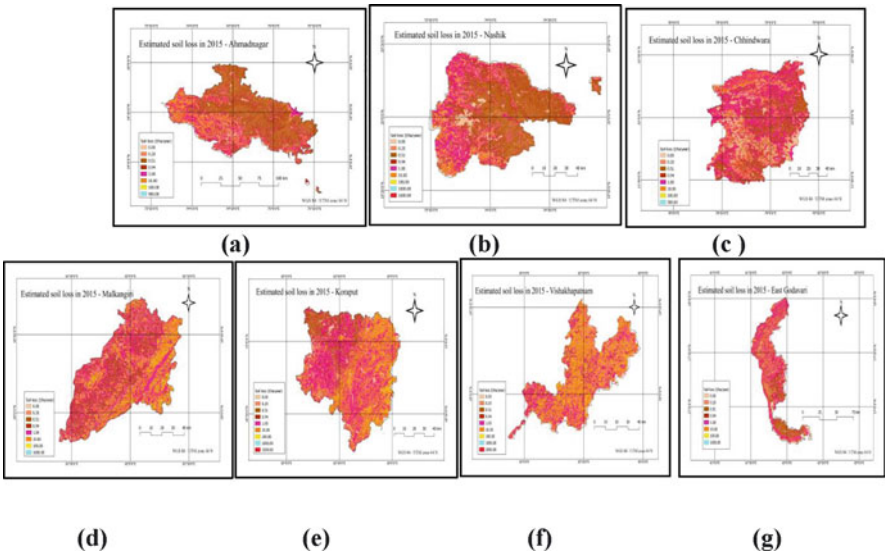

Fig. 5.13 Districts which are vulnerable to soil erosion—(**a**) Ahmednagar, (**b**) Nashik, (**c**) Chhindwara, (**d**) Malkangiri, (**e**) Koraput, (**f**) Visakhapatnam, (**g**) East Godavari

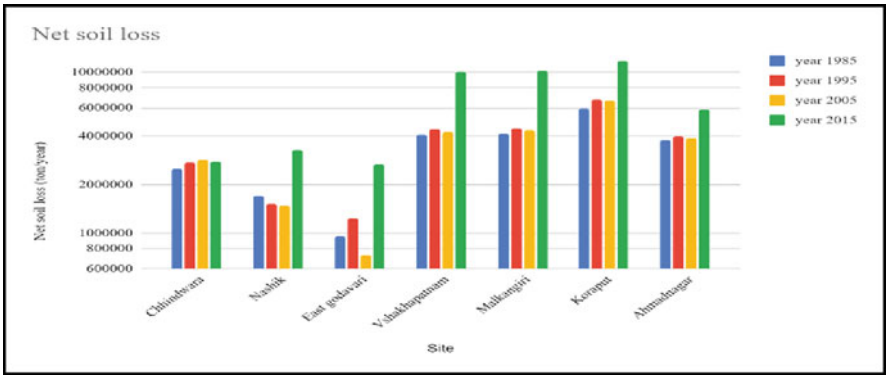

Fig. 5.14 Net soil loss in the districts

Table 5.13 Net soil loss

Year	Net soil loss (tonnes/year)
1985	50552005.93
1995	56105079.79
2005	53190150.30
2015	97993275.32

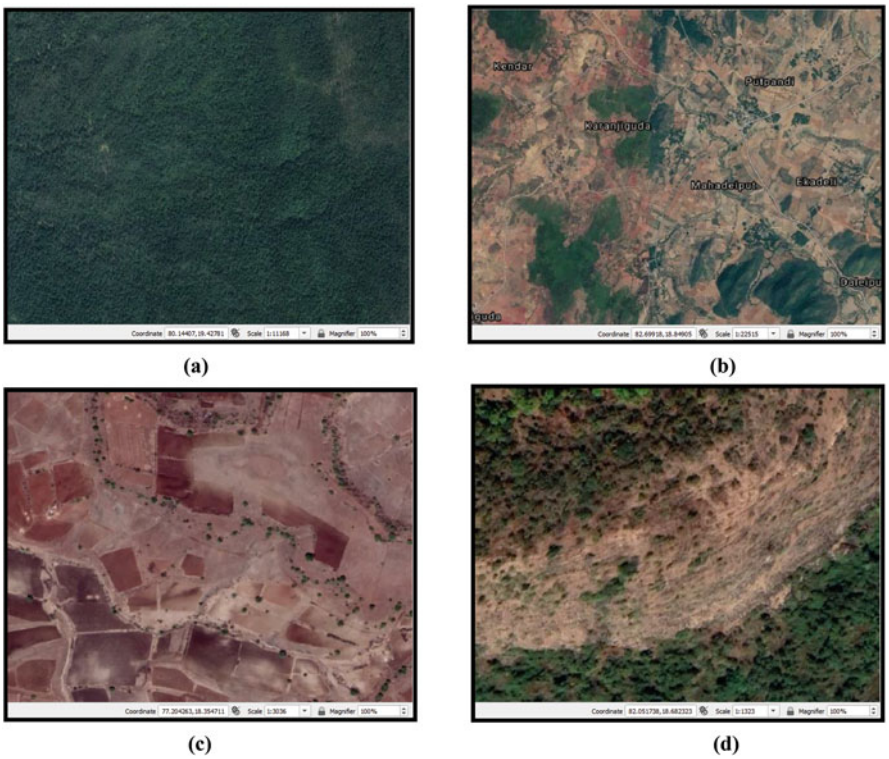

Fig. 5.15 Satellite imageries showing the areas of soil erosion within the Godavari basin (**a**) Areas with soil loss between 0 and 1 (t/ha/year); (**b**) 1 and 10 (t/ha/year); (**c**) 10 and 100 (t/ha/year); (**d**) 100 and 2400 (t/ha/year)

practices should be adapted to enhance soil productivity and food security in the basin.

References

Al Rammahi AHJ, Khassaf SI (2018) Estimation of soil erodibility factor in RUSLE equation for Euphrates river watershed using GIS. Int J Geomate 18(46):164–169

Asfaw D, Gella GW, Asfaw M (2021) Modeling landscape dynamics, erosion risk, and annual sediment yield in Guna-tana watershed: a contribution for micro watershed level conservation priority area identification. Springer, Cham, pp 73–91

Das G (2004) Hydrology and soil conservation engineering. PHI Learning Private Limited, New Delhi, p 539 S

Devatha CP, Deshpande V, Renukaprasad MS (2015) Estimation of soil loss using USLE model for Kulhan watershed, Chattisgarh- A case study. Aquatic Procedia 4:1429–1436

FAO (1985). https://www.fao.org/fishery/docs/CDrom/FAO_Training/FAO_Training/General/x6706e/x6706e06.htm

Food and Agricultural Organisation of the United Nations, Land and Water Division (2003) Digital soil map of the world. [computer file]. v3.6

Islam MR, Wan Jaafar WZ, Hin LS, Osman N, Karim MR (2020) Development of an erosion model for Langat River basin, Malaysia, adapting GIS and RS in RUSLE. Appl Water Sci 10

Kidane M, Bezie A, Kesete N, Tolessa T (2019) The impact of land use and land cover (LULC) dynamics on soil erosion and sediment yield in Ethiopia. Heliyon 5:e02981

Priya S, Shibasaki R (1998) Quantification of soil loss and its detection using GIS and remote sensing technology. ASian Pac Remote Sens J 10:33–38

Shinde V, Tiwari KN, Singh M (2010) Prioritization of micro watersheds on the basis of soil erosion hazard using remote sensing and geographic information system. Int J Water Resour Environ Eng 2:130–136

Singh G, Babu R, Chandra S (1981) Soil loss and prediction research in India, Central Soil and Water Conservation Research Training Institute (Bulletin No. T-12/D9)

Stone RP (2012) Universal Soil Loss Equation (USLE), Ministry of Agriculture, Food and Rural Affairs

Twisa S, Buchroithner MF (2019) Land-use and land-cover (LULC) change detection in Wami River basin, Tanzania. Land 8:136

Vemu S, Pinnamaneni UB (2012) Sediment yield estimation and prioritization of watershed using remote sensing and GIS. International Archives of the Photogrammetry, Remote Sensing and Spatial Information Sciences, Volume XXXIX-B8, XXII ISPRS congress, 25 August – 01 September 2012, Melbourne, Australia. 529–533

Wischmeier WH, Smith D (1978) Predicting rainfall erosion losses – a guide to conservation planning. ESDA handbook, vol 537. USDA, Washington DC

Part II
Stability of Hydraulic Structures and Sediment Transport

Chapter 6
Stability of Hydraulic Structures Against Erosion and Scour Due to Water Jets

Ankit Chakravarti, Z. Ahmad, R. K. Jain, and Umesh K. Singh

Abstract In rivers and streams, one of the most challenging problems is to minimize and to know the depth of scour due to changes in flow pattern around the hydraulic structures for its stability and economical design consideration.

This chapter presents a critical review of the investigations on scour due to submerged water jets. A vast amount of literature exists on the topic of scour by water jets in soils, however, less attention has been focused on the mixture of sediment, i.e., sand-silt-gravel mixtures. Various aspects of scour process, role of different parameters on equilibrium scour depth, dimensional analysis, change in scour depth with respect to time, scour hole profiles, and equations for scour depth estimation are discussed herein. Scour processes have been studied from time to time by many scientists and researchers. The detailed review of literatures related to scour in cohesionless sediments is presented. The brief descriptions about the important parameters in the process of scour by jets were discussed and how these parameters can help in identifying the practical problem were shown with real time examples for safety of hydraulic structures against erosion and scour due to water jets.

Keywords Hydraulics · Laboratory experiment · Erosion and scour · Water jets · Cohesionless sediment · Hydraulic structures

A. Chakravarti
School of Civil & Engineering, Ambo University, Ambo, Ethiopia

Z. Ahmad
Hydraulic Engineering Division, Civil Engineering Department, IIT Roorkee, Roorkee, Uttarakhand, India

R. K. Jain
Hydraulic Engineering Division, Civil Engineering Department, L.D. College of Engineering, Ahmedabad, Gujarat, India

U. K. Singh (✉)
Civil Engineering Department, Koneru Lakshmaiah Education Foundation, Vaddeswaram, Andhra Pradesh, India

M. Pandey et al. (eds.), *River Dynamics and Flood Hazards*, Disaster Resilience and Green Growth, https://doi.org/10.1007/978-981-19-7100-6_6

6.1 Introduction

Scour is a process of lowering of river bed by the removal of bed material in the vicinity of water structures by erosive action of the flowing water. Scour around the hydraulic structures may lead to failure of the structures (Ahmad et al. 2018). For example, degradation leads to failure of Islam weir on the Sutlej River (Singh 2018; Bhave et al. 2020; Pandey et al. 2022a, b; Singh et al. 2022). Scour around hydraulic structures exposes the foundation of these structures which leads to exposed foundations and finally the structure prone to failure. The flows over and through these structures often occur in the form of jets. Usually, these jets lift the sediment particles and transport them downstream of the affected area, and as a result, a scour hole forms. The area of jet impact is transformed into an energy dissipater with turbulence production. Singh et al. (2017) studied the turbulence characteristics over the degraded channel bed which shows higher turbulence near to degraded bed. In some of the structures like ski-jump, free overfall spillway, jet spillway, the water jet penetrates the sediment bed that reaches its deepest level and is deflected in upward directions resulting in a highly turbulent zone. Investigators are trying to provide a solution to guide and control the scour process so as to lower the risk of failure of hydraulic structures (Pandey et al. 2020; Chaudhuri et al. 2022 and Jain et al. 2021). The scour by water jets is depends on the parameters like jet velocity, jet height, nozzle size, type of structure, and characteristics of the sediment. Different literatures are available related to scour processes due to water jets and first conducted by Rouse (1940). Thereafter, a number of studies conducted to study the response of submerged water jets in various sediment materials, jet velocities, jet heights, and diameter of nozzles. Those are Clarke (1962), Rajaratnam (1982), Uyumaz Ali (1988), Aderibigbe and Rajaratnam (1996), Mazurek et al. (2002), Ansari et al. (2002), Ansari et al. (2003), Rajaratnam and Mazurek (2005), Mazurek et al. (2009), Dehghani et al. (2010), and Chakravarti et al. (2013). They studied scour due to water jet in cohesionless sediment. Dehghani et al. (2010) concluded scour increases with the Froude number in the downstream side of weir based on experimental study, however; studies limited to size, shape, gradation, and hydraulic conditions. Rajaratnam and Mazurek (2005) conducted laboratory study on the perpendicular impingement of circular turbulent jets on rough walls and found that the boundary shear stress increases to a maximum at a radial distance from the jet centerline of about 0.12 of the height of the jet above the boundary and after that decreases further. All the above study on scour jet conducted on cohesionless sediment with limitations of size, shape, gradation, and hydraulics conditions which may be used as research gap for further studies.

6.2 Sediment Characteristics

Sediments are composed mainly of cohesive material in which the clay particles have strong inter particles forces due to their surface ionic attraction between each other. As the clay sediment size reduces, its surface area per unit volume increases and their interparticle forces dominate the behavior of the sediment. There is no clear boundary in between the cohesionless and cohesive materials in this respect (Pu et al. 2021). In general, the finer size of the sediment particles is more cohesive in nature. The sediment size smaller than two microns is normally termed as cohesive sediment. If the sediment size is greater than 0.06 mm, then the sediment normally behaves as cohesionless sediment (Ansari et al. 2003; Shankar et al. 2021; Aamir et al. 2022; Shivashankar et al. 2022). The cohesive sediment consists of organic minerals and inorganic mineral (Hayter 1983). The inorganic minerals mainly consist of Illite, Kaolinite, and Montmorillonite.

6.3 Local Scour Due to Water Jets Around Hydraulic Structures

The local scour process needed to identify in the presence of sand, gravel, and other soil found near the water structures as more scouring damage the stability of water structures like gates, weirs, culverts, spillways, etc. In the case of submerged vertical circular water jet, the main characteristics of flow regions are as follows (Ansari et al. 2002).

1. Potential core flow regions.
2. Free jet flow regions.
3. Impinging jet flow regions.
4. Wall jet flow regions.

The above flow regimes for vertical impinging jet are shown in Fig. 6.1 and discussed below in details:

1. Potential core flow regions—A region where velocity over the jet area is almost uniform is known as potential core region. This region is just below the nozzle exit and along the central portion of the jet. The jet diameter decreases rapidly downstream sides due to shear stress between the jet and the surrounding fluids.
2. Free jet flow regions—The free jet flow region follows the potential core transition and it is characterized by linear increase in width and a Gaussian velocity distribution.
3. Impinging jet flow regions—The impinging jet regions are the region just near the bed surface, an impinging occur in which the water flow is deflected from the axial into the radial motion during the water flow through impinging jets.

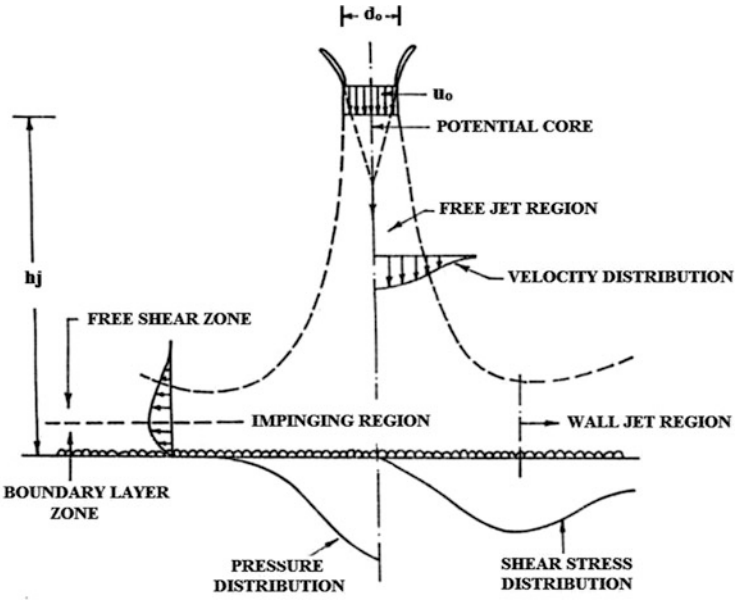

Fig. 6.1 Flow regimes of a vertical impinging jet (Ansari et al. 2002)

4. The wall jet region—The deflected water flow continues as wall jet in the regions containing two types of shear zones—a boundary layer near the wall jet region and a free shear zone. The impinging of a circular vertical submerged water jets on loose bed, i.e. cohesionless sediment beds leads to strong local scouring effects.

Rouse (1940) studied the first systematic research work in local scour by submerged vertical water jet in uniform fine sand by conducting laboratory based experimental study. Rouse found that the scour depth in non-cohesive sediment bed, i.e. sand bed varies linearly with the logarithm of time impingement. He also observed that the jet impingement height from starting bed level is the characteristic length of scoured sand bed profiles. He proposed a functional relationship between two nondimensional parameters like the ratio of depth of scour to jet impingement height, and the ratio of velocity of jet to the fall velocity of sand. Since, a number of investigation have been carried out to investigate the response of channel bed under impinging jet a review of some of the important research contributions are presented herein.

6.4 Local Scour Due to Water Jets Around the Hydraulic Structures in Cohesionless Sediment

Westrich and Kobus (1973) conducted experiment on a uniform sand bed having sediment size, (d_{50}) equal to 1.5 mm with a vertical submerged water jet by taking jet velocity in the range of 0.7–3.7 m/s and nozzle diameter ranging from 20 to 40 mm. The nozzle height was varied from 0 to 0.82 m from the channel bed level. They reported two types of scour holes depending upon the value of K_0 define as:

$$K_0 = (u_m/\omega_f)^2 \tag{6.1}$$

In which, K_0 is the erosion coefficient, u_m is the maximum velocity estimated at the sand bed surface, and ω_f is the fall velocity of the sediment. Also, influence of the jet height on the volume of scour hole was studied. They found that for given jet parameters, the scour hole volume first increases with jet height and then remain constant before decreasing again.

Francis and Mccreath (1979) conducted laboratory study on bed load transport of sediment due to submerged jets. The laboratory work was conducted in Perspex-sided tank having dimension of 10 cm wide and 72 cm deep and 120 cm long. Every end of the working section was fixed to bigger tank in which the weirs were fixed to keep constant water level. Four sizes of sand were taken for the preparation of sediment bed having, d_{50} of 1.08, 0.72, 3.41, and 0.88 mm. The laboratory study was performed under the sediment beds for three different heights of jet, i.e., 50.8, 41.6, and 30 cm. The erosion process has analogy with transport of sediment rates in streams. They found that the transport rate of the sediment is a function of stream power as suggested by Bagnold (1966).

Rajaratnam (1981) conducted laboratory based experimental work on erosion under plane turbulent wall jets. The experiments were performed in three series—in first series scour of non-cohesive materials by plane turbulent air jets was conducted by taking one nozzle having thickness, $d_o = 2.41$ mm. The nozzle jet velocity was measured by a pressure tap attached in the plenum chamber. The cohesionless sediment material, i.e., sand were used having sediment size 1.2 mm and bed thickness 102 mm in a rectangular flume. The flume was 156 mm wide, 330 mm high, and 183 mm long.

In the second series, polystyrene particles under air jets were studied. A total of 7 equilibrium tests were conducted with air jets having thickness of nozzle 5 mm and the size of sand equal to 1.4 mm and the specific gravity of sand equal to 1.04. The laboratory experiments were conducted similar to the experiment performed for sand beds.

In third experimental series, a total of 14 equilibrium laboratory experiments were conducted on erosion of sand beds by submerged water jets in a rectangular test flume have dimension, 5.5 m long, 0.66 m deep, and 0.31 m wide. The flume contained a cohesionless sediment bed having 0.23 m thickness and 0.38 m water depth in the flume was maintained to generate a deeply submerged flow in horizontal

water by a tailgate. They found that the higher scour depth in the form of height of jet is a function of $F_o/\sqrt{h_j/2b_o}$, where F_o is the densimetric Froude number, h_j is the jet height, and b_o is the thickness of the jets. The densimetric Froude number parameter was defined as

$$F_o = \frac{u_o}{\sqrt{gd_{50}\frac{\Delta\rho_s}{\rho_f}}} \tag{6.2}$$

where, $\frac{\Delta\rho_s}{\rho_f}$ is the relative density defined by $\left(\frac{\rho_s-\rho_f}{\rho_f}\right)$, ρ_s is the mass density of bed materials, ρ_f is the mass density of water.

Rajaratnam (1982) carried out experiment on a round jet having nozzle diameter equal to 9.8 mm, impinging on two types of sand beds with sediment size d_{50} equal to 1.2 mm and 2.38 mm, respectively. He proposed the following functional relationship for maximum static scour depth;

$$\frac{d_{sms}}{h_j} = f\left(\frac{F_o}{h_j/d_o}\right) \tag{6.3}$$

where d_{sms} is the maximum static scour depth.

Walter and Kabir (1983) studied impinging of water jets on nonuniform sediment streambed through experimental work and theoretical analysis. The tests were conducted in a 1.2 m wide, 1.5 m deep, and 9 m long flume with white sand (0.3 mm size) and gravel bed. Jet diameters were 0.5 and 25 mm while jet angles were 45°, 60°, and 90°. The jet velocities were 6 m/s and 21 m/s and the heights of jet were varied from 0 to 53 cm from the original bed level. Figure 6.2 indicates the motion of sediment during the impingement of jet. After water jet reaches to its deep rang, it was changed upward near its center line to form vertical circulation taking bed materials. From the center line of the vertical jet, the circulation slowly spreads outward the scour hole of radius.

When the stationary sediment bed was raised, the pressure on the static boundary increased. Finally, about 4 min of jetting, an equilibrium state was attained. The remaining bigger sediment particles left on the minimum circulative motion around the impingement part by virtue of that the dissipation of energy prevented deep penetration of water jet known as armor action. Figure 6.3 shows the change of depth of sediment motion during impingement of jet.

Uyumaz Ali (1988) studied on scour in cohesionless sediment downstream of vertical gate through laboratory experiment. He performed experiment in a flume of 0.60 m wide, 11.5 m long, and 0.85 m deep with a concrete bottom. The vertical gate height was about 0.30 m and the loose gate was placed at the end of the flume. The extent of scour approached asymptotically and after some time the scour reaches in equilibrium condition. It was found that final scour depth was less when there is simultaneous water discharge over and under the gate.

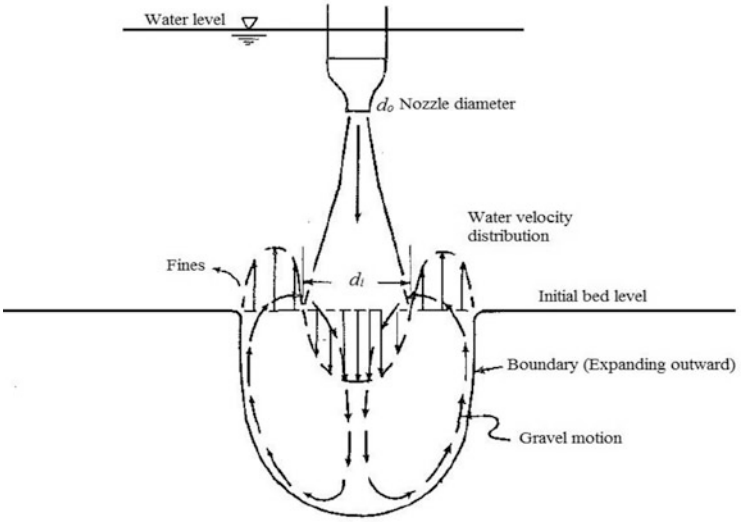

Fig. 6.2 Sediment motion during impingement of jet (Walter and Kabir 1983)

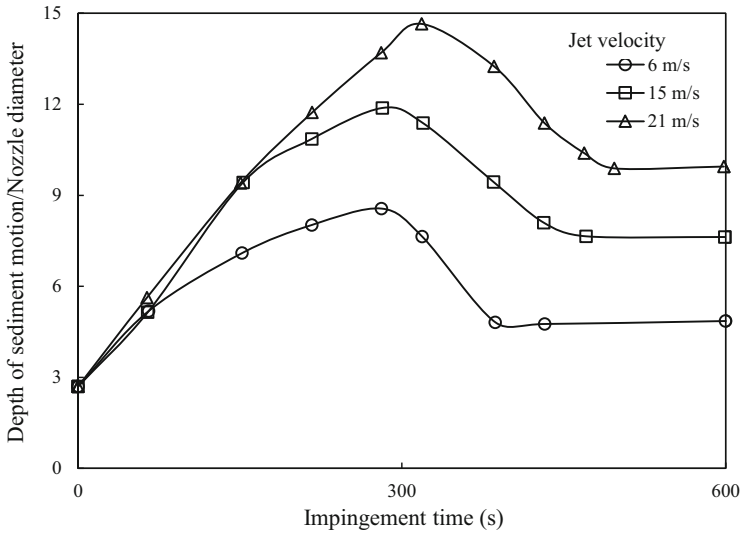

Fig. 6.3 Depth of sediment motion during impingement of jet (Walter and Kabir 1983)

Breusers and Raudkivi (1991) fitted the following equation to the data of Rajaratnam (1982) for the estimation of maximum static scour depth:

$$\frac{d_{sms}}{d_0} = 0.3\frac{u_0}{\sqrt{\Delta\rho_s g d_{50}}} \tag{6.4}$$

Breusers and Raudkivi (1991) re-plotted the original data of Westrich and Kobus (1973), and Rajaratnam (1982) in respect of maximum scour depth and proposed the following equations:

$$\frac{d_{sms}}{d_o} = 0.75\left(\frac{u_o}{u_{*cs}}\right); \quad \text{for} \quad \left(\frac{u_o}{u_{*cs}}\right) < 100 \tag{6.5}$$

$$\frac{d_{sms}}{d_o} = 0.035\left(\frac{u_o}{u_{*cs}}\right); \quad \text{for} \quad \left(\frac{u_o}{u_{*cs}}\right)^{2/3} > 100 \tag{6.6}$$

where u_{*cs} = Critical shear velocity of the cohesionless sediments.

Aderibigbe and Rajaratnam (1996) conducted laboratory experiments on an octagonal plastic box having 0.6 m height and 0.235 m side length. The impinging jet was centrally located and always submerged and fixed to the bottom of a 150 mm diameter. The impinging jet height (h_j) was varied 4–523 mm. The diameter of jet were taken as 4, 8, 12, and 19 mm, particles size of cohesionless materials were taken as 0.88 and 2.42 mm and jet velocities were varied from 2.65 to 4.45 m/s. A total of 67 experimental runs were conducted for the duration of 6–50 hours to reach in the equilibrium state. They examined the asymptotic scoured depths of sand bed for erosion parameter, $E_C < 5$ under above condition and also examined the scoured bed profiles in equilibrium conditions. The erosion parameter was defined as follows:

$$E_c = u_o\left(\frac{d_o}{h_j}\right)/\sqrt{(g d_{50}\Delta p_s/p_f)}; \quad \text{when} \quad \frac{d_o}{h_j} > 8.3 \tag{6.7}$$

They analyzed the following parameters:

1. Effects of impinging jet distance.
   They analyzed the previous studies in respect of effect of impinging jet distance on higher scour depth. Westrich and Kobus (1973) observed two peaks in the changes of the equilibrium scour volume with impinging jet height. The variations of static and dynamic depth of scour with jet height were studied for two sets of experiment and found that there exists a critical impinging jet distance at which static depth of scour is high.
2. Similarity of scoured bed profiles.
   The equilibrium scour profiles for similarity in the maximum static scour depth versus radial distance were analyzed. The value of erosion parameter ranges in between 0.14 and 3.52. The ratio of radius of scour to maximum static depth of scour with erosion parameter is about 1.7 for erosion parameter greater than 0.35 and for erosion parameter less than this value, it rapidly high with decreasing erosion parameter. They concluded the side slope of scour geometry was sensitive to erosion parameter when the latter was less than 0.35.

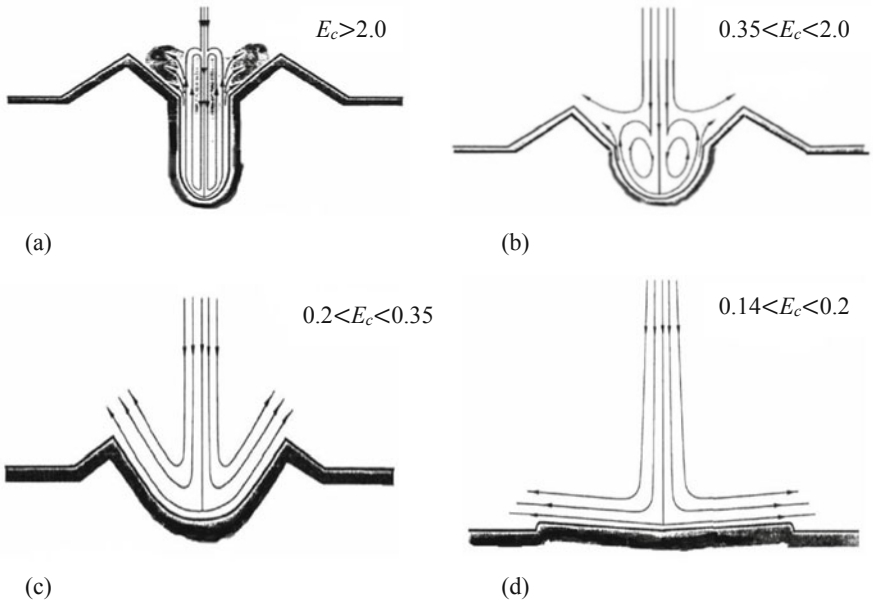

Fig. 6.4 Flow regimes of eroded sand beds (Aderibigbe and Rajaratnam 1996). (**a**) Strongly deflected jet regime I. (**b**) Strongly deflected jet regime II. (**c**) Weakly deflected jet regime I (WDJR I). (**d**) Weakly deflected jet regime II

3. Flow regimes characteristics.

   They classified the regimes of flow as weekly deflected jet regimes (WDJR) and strongly deflected jet regimes (SDJR) in equilibrium condition. These two regimes of flow are associated by narrow transition regimes. The strongly deflected jet regime is divided as SDJR-I and SDJR-II according to the value of erosion parameter E_c. The SDJR flow regimes found at value of erosion parameter E_c greater than 0.35. WDJR is divided into WDJR-I and the WDJR-II. In these flow regimes, the flow occurs at the range of erosion parameter $E_c < 0.35$ and the dynamic and static scour profiles were same. They suggested the following flow patterns and profiles of the eroded sand bed as shown in Fig. 6.4a–d.
4. Equilibrium depth of scour.

   They developed an equation for maximum static scour depth using data from previous studies:

$$\frac{d_{sms}}{h_j} = 1.26E_c^{0.11} - 1 \tag{6.8}$$

Equation (6.9) is valid only for the ratio of impinging jet height to jet diameter greater than 8.3 as noticed by Rajaratnam and Beltaos (1977). They analyzed the

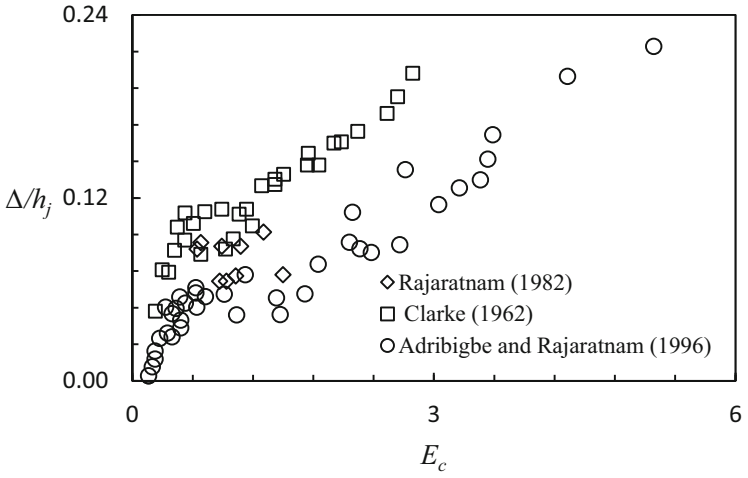

Fig. 6.5 Changes in dune height with erosion parameter (Aderibigbe and Rajaratnam 1996)

data for other length scale parameters of scour bed profile and proposed the following equations to calculate maximum dynamic depth of scour, radius of scour hole, and dune height:

$$\frac{d_{\mathrm{dms}}}{h_{\mathrm{j}}} = 7.32E_{\mathrm{c}}\left(\frac{d_{\mathrm{o}}}{h_{\mathrm{j}}}\right)^{m} - 1 \quad \text{where} \quad m = 1.53E_{\mathrm{c}}^{0.22} - 1 \tag{6.9}$$

$$\frac{r}{h_{\mathrm{j}}} = 0.22 + 0.2E_{\mathrm{c}} \quad \text{for} \quad 0.5 < E_{\mathrm{c}} < 5 \tag{6.10}$$

$$\frac{\Delta}{h_{\mathrm{j}}} = C + 0.044E_{\mathrm{c}} \tag{6.11}$$

where d_{dms} = maximum dynamic depth of scour, m is the exponent, r = radius of scour hole, and Δ is the dune height and C is a coefficient. The value of $C = 0.077$ and -0.02 for higher and minimum rang. The variation of dune height and radius of scour hole with E_{c} are shown in Figs. 6.5 and 6.6, respectively.

Aderibigbe and Rajaratnam (1998) carried out experimental investigation on the effect soil gradation on scour by plane turbulent wall jets. Three different types of cohesionless sediment were used for the study. The cohesionless sediment have $d_{50} = 6.75$, 1.62, and 1.32 mm, while the geometric standard deviations (GSD), $\sigma_{\mathrm{g}} =$ 2.02, 3.13, and 1.32. The reduction in scour profiles in the presence of soil gradation was studied with F_{o}. They found nonuniform soil play an important role on the size of the scour profiles generated by submerged wall jet. Figure 6.7 indicates the changes of equilibrium dynamic deepest scour depth with F_{o}. The variation of relative scour hole length with F_{o} is shown in Fig. 6.8. They observed the scour hole length was effectively smaller on the graded soil. The sediment size for better correlation for the scour depth was found as d_{95} compared to d_{50}.

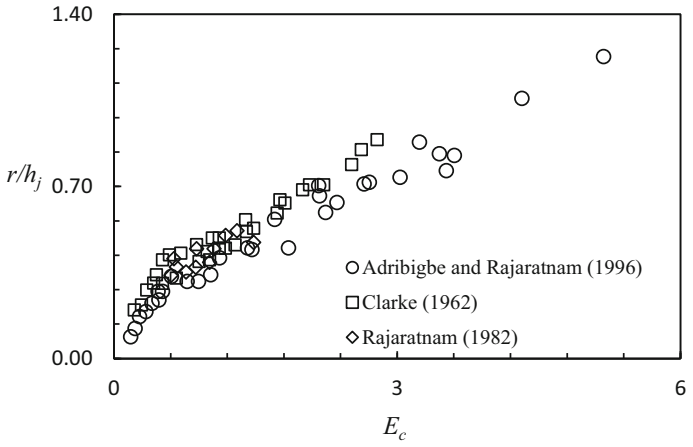

Fig. 6.6 Variation of radius of scour hole with E_c (Aderibigbe and Rajaratnam 1996)

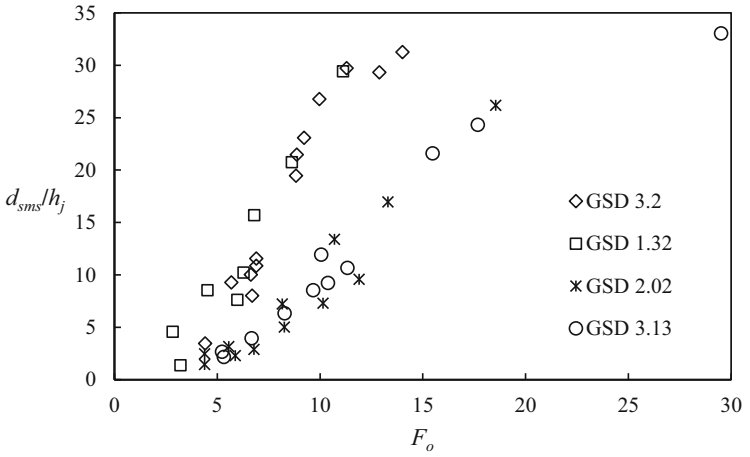

Fig. 6.7 Changes of higher scour depth with F_o (Aderibigbe and Rajaratnam 1998)

Donoghue et al. (2001) performed laboratory study on sand beds under submerged circular vertical water jet. A total of 66 tests were performed using two different types of cohesionless soils having sediment size, d_{50} equal to 0.3 and 0.13 mm. They took four sizes of nozzle having diameter of 13, 30, 40, and 50 mm and the velocity of jet was kept equal to 5.9 m/s. Two jet heights were taken by making the ratio of height of jet to the nozzle diameter ranging between 5 and 13. The erosion parameter was ranging as $1.7 \leq E_c \leq 14.9$ to indicate that all the laboratory work was well for strongly deflected jet regimes. Previous laboratory work indicates a dependence of scour hole on erosion parameter or densimetric Froude number, however, this study indicate a strong dependence on the ratio of

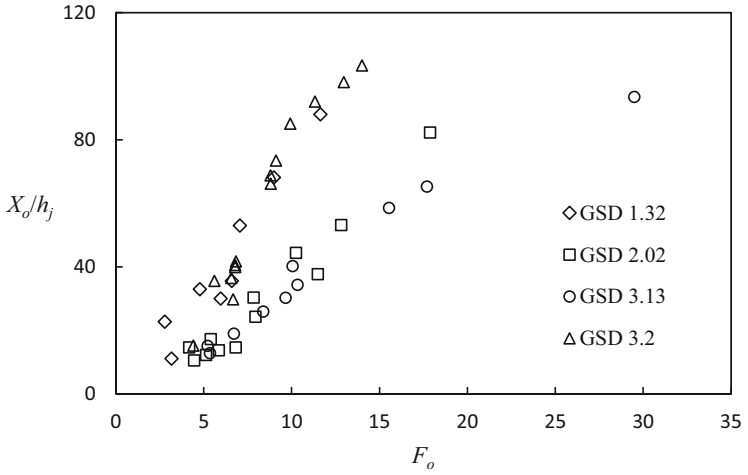

Fig. 6.8 Changes of scour hole length with F_o (Aderibigbe and Rajaratnam 1998)

diameter of jet to size of sediment as well. They proposed empirical equations for the computation of dynamic scour depth and scour hole diameter. These equations were applied for highly scouring jets with the ratio of jet momentum flux to the submerged weight of sediment up to 10^9.

Mazurek et al. (2002) studied the experimental investigation on jet scour under turbulent sand jet in water. They conducted ten experimental runs in a tank having dimension of 1.25 m long, 1.25 m wide, and 1.17 m deep. A flexi glass tank having diameter of 100 mm and 330 mm long added with cone type hopper at the bottom and filled with non-cohesive sediment was used. Four sizes of cohesionless sediment ranging from 0.17 to 1.47 mm and their standard deviation ranging from 1.18 to 1.25 were used. Since, the standard deviation was less than 1.35; therefore it was considered as uniform sediment as suggested by Breusers and Raudkivi (1991). Three types of nozzles having jet diameter 8, 12.7, and 25.4 mm was added at the bottom of hopper. The R of the sand jets varied from 40 to 300. It was investigated that the linear growth rate of scour under sand jets increases with the F_o parameter.

Rajaratnam and Mazurek (2005) conducted experiments on scour in non-cohesive sediment under turbulent water jets having minimum tail water depth. A total of 18 experimental run were conducted for submerged and un-submerged impinging turbulent water jets in an octagonal tank having 0.61 m height and 0.572 m width, using three different types of cohesionless sediment having sizes equal to 1.0, 1.15, and 2.38 mm. Two types of nozzle having nozzle diameter of 9.8 mm and 12.7 mm were used in the experiment. The observation were taken for maximum static and dynamic depth of scour, scour hole radius. They observed that the depth of scour in dynamic condition is three times of scour depth in static state at equilibrium conditions. From the experimental investigation the scour of cohesionless sediment by un-submerged water jets, they concluded that there are two different types of scour, i.e., dynamic and static scour.

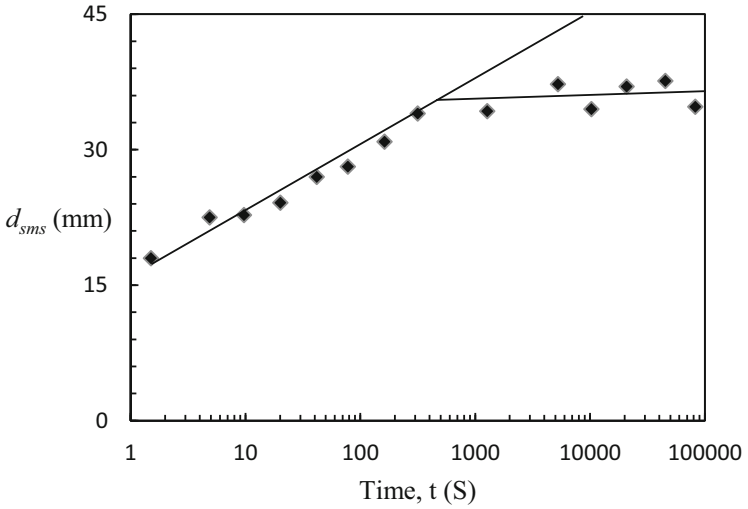

Fig. 6.9 Growth of higher scour depth with time (Rajaratnam and Mazurek 2005)

They found that the higher depth of scour linearly increases with logarithm of time for a major portion of the scour and reaches at equilibrium conditions. Figure 6.9 shows the changes of higher static scour depth with respect to time. The symptomatic range of scour depth and scour hole radius are the functions of densimetric Froude number. The depth of scour in dynamic conditions was observed to be about three times of the static scour at equilibrium state. They also concluded that the higher scour generated due to un-submerged water jet is lower as compared to submerged water jet in case when:

$$F_o/\left(h_j/d_o\right) < 2.1 \tag{6.12}$$

The radius of scour hole for the un-submerged jet is less than that produced by a submerged water jet:

$$\text{where} \quad F_o/\left(h_j/d_o\right) < 1 \tag{6.13}$$

Adduce and Mele (2004) conducted laboratory based experimental study for erosion by turbulent jets to investigate erosion process. A total of nine tests were conducted in tilting flume which has rectangular cross section of 0.8 m wide, 1 m high, and 17 m long. The experimental run were conducted in a 0.8 m wide, 0.3 m high, 3 m length sediment working section fixed at 7 m downstream of the inlet flume and was created raising artificially the flume sediment bed. The uniform sand of size equal to 0.72 mm having density of 2650 kg/m^3 were taken to fill the working section to it mobile bed. The same sediment was also used upstream and downstream of the test section to make sediment bed with homogeneous roughness.

All the experimental runs were performed for clear water condition and the water discharge were regulated constant for total time required for the experiment. Scour hole profile was noted by a camera fixed to a digital videocassette recorder. The temporal variation of scour depth was taken using image analysis techniques. The dimensionless scour hole profiles showed geometrical similarity for all experimental runs if the higher scour depth shall be taken as length scale of the vertical gate and horizontal distances.

Rajaratnam and Mazurek (2005) performed study on a circular air jet impinging on smooth walls having jet nozzle diameter of 6.4 and 12.7 mm and impinging on wall having roughness 15.18, 8.23, and 1.73 mm in a cylindrical plenum, with air regulated by a compressed air arrangement. The nozzle velocity varies 45–90 m/s. Reynolds number $R_e = (u_0\, d_o)/\nu)$ was in the range of 79,000–26,000, height of jet were varied from 310 to 152 mm. The ratio of h_j/d_o was 12–26. The stagnation pressure (p_s) and the maximum shear stress (τ_{om}) can be estimated by the following equations:

$$p_s = C\frac{\rho_s u_o^2/2}{\left(h_j/d_o\right)} \tag{6.14}$$

$$\tau_{om} = 0.16\frac{\rho_s u_o^2}{\left(h_j/d_o\right)} \tag{6.15}$$

where, C = dimensionless coefficient which was 50, 48, and 60.4 by Beltaos and Rajaratnam (1974), respectively.

Yeh et al. (2009) present the experiments on sand beds scour due to moving vertical circular jet to investigate the topographic deformation. Seven experimental run were conducted in which the first two runs have stationary jets. Remaining five experiments were conducted by moving jet by varying carriage speeds. The size of the laboratory tank was 3.66 m wide, 45.72 m long, and 3.05 m deep. The horizontal plate and the jet exit were located at 0.76 m above the sand bed. Sand has $d_{50} = 0.258$ mm and $\sigma_g = 1.71$. The sand bed topography was measured by the use of laser profiler to estimate the changes on the sand bed. Figure 6.10 shows the variation in higher normalized scour depth against jet to ship velocity ratio with $E_c = 5.28$.

The modified Aderibigbe and Rajaratnam (1996) prediction equations for estimation of equilibrium depth of scour (d_{sms}), radius of scour hole (r), and height of dune (Δ) are as follows:

$$\frac{d_{sms}}{h_j} = 0.64E_c^{0.11} - 1 \tag{6.16}$$

$$\frac{r}{h_j} = 0.78\left(1.46E_c^{0.15} - 1\right) \quad \text{For} \quad E_c \le 0.5 \tag{6.17}$$

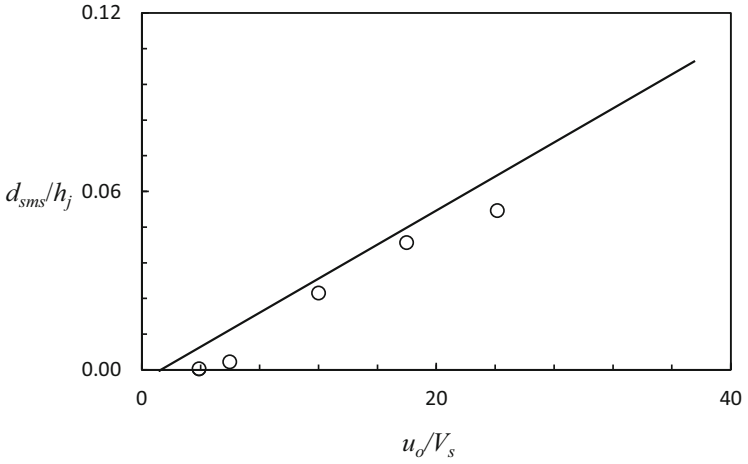

Fig. 6.10 Normalized higher scour depth against jet velocity with $E_c = 5.28$ (Yeh et al. 2009)

$$\frac{r}{h_j} = 0.78(0.22 + 0.20E_c) \quad \text{For} \quad 0.5 < E_c < 5 \tag{6.18}$$

$$\frac{\Delta}{h_j} = 0.52(-0.02 + 0.044E_c) \tag{6.19}$$

These modified equations should take to evaluate the length of scour profile when h_j/d_o is about 6. The formulae were proposed to know the length scales, radius of scour hole, and the dune height. The jet velocity in horizontal direction was varied to know the effect on the scour hole profile geometry. The depth of scour hole in equilibrium condition was estimated.

Mazurek et al. (2009) presented the laboratory study on submergence changes of jet characteristics and scour of plane wall jets in soil. The laboratory works show two different studies on how submergence or tail water depth affects the scour process under plane wall jets in cohesionless material. In case of the first experiment, the effects of submergence on the flow regime, development of temporal scour, and the profile of scour holes at equilibrium condition were determined. In case of second experiment, the characteristics of flow jet in scour holes created by varying submergence condition were studied. The tail water was ranging from 25 to 508 mm for first set of experiment which provided a range of submergence equal to 1 to 20. The velocity of jet at nozzle was varying from 0.26 to1.13 m/s. The Froude numbers at the nozzle was 0.52 to 2.27 and Reynolds numbers at the nozzle varied 6600 to 28,570. The cohesionless sediment as sand was taken sediment size of 2.08 mm and $\sigma_g = 1.33$.

Second stages of experiments were conducted to know the flow in a scour profile at equilibrium condition. Three different types of flow regimes of jet behavior were seen by varying submergence condition. Such profiles were similar to those described by Johnston (1990), i.e., a bed jet regime, a surface jet regime and a bed

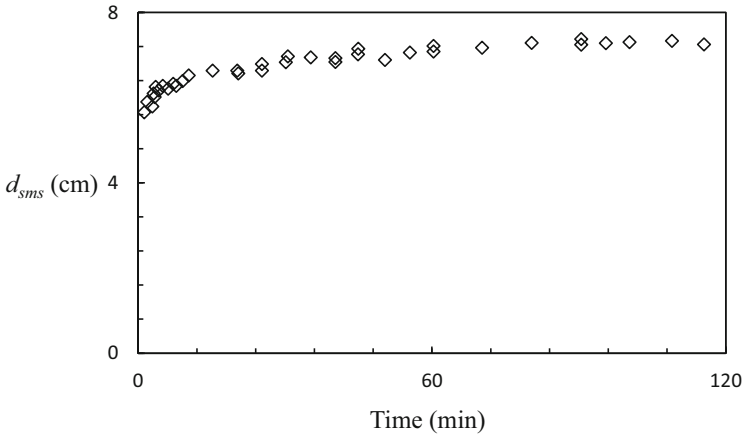

Fig. 6.11 Variation of depth of scour versus time (Dehghani et al. 2010)

surface jet regime. Scour holes created for a jet in the surface jet regime were longer and shallower than those created by the bed jet. It is also seen that the bed jet regime shows a similar behavior to a wall jet on a smooth bed, while the surface jet regime shows a jet behavior similar to a free jump.

Dehghani et al. (2010) conducted experimental investigation on local scour under the jet flow downstream of rectangular sharp crested weirs. The tests were performed on the flume having dimensions of 0.12 m width, 3.7 m long, and 0.17 m depth with bed slope of 0.0001. The sediment bed material was consisted of cohesionless uniform sediment having diameter of sediment 1.5 mm and $\sigma_g = 1.3$. Both the side walls in the working section of the flume were made of glass. A total of 23 experimental runs were performed by taking different discharges and the height of weirs. The cohesionless sediment, i.e., sand was placed on the channel bed in 8 cm thickness. The experiments were performed using clear water condition and were continued until equilibrium condition was reached. All the measurements were taken to observe the scour hole profiles by using a simple point gauge. Figure 6.11 shows the changes of higher scour depth against time. They found higher scour depth reaches in equilibrium condition almost in 60 min from the start of the experiment.

6.5 Conclusion

Based on the comprehensive review of the focused area, it is noted that numerous studies have been carried out on scour in cohesionless sediment under submerged water jets. However, less attention has been focused in case of cohesive sediment. Various equations have been developed using the laboratory and field data for the estimation of various scour parameters like maximum scour depth, scour hole profile, radius of scour hole, dune height, etc. The river bed material generally

consisted of cohesionless and cohesive soils and their mixtures such as clay-gravel mixture, clay-sand-gravel mixture considered as cohesive in behaviour. Little information is available on the process of scour in such bed materials mixture occurring under the submerged jet. Some investigations were studied on jet scour in cohesive sediments. However, these investigations are based on limited amount of data covering a narrow range of variables on jet configurations, physical properties of cohesive sediments, etc. However, a general expression is not available, so far, that can be used for determination of the scour depth its various length scale parameters by water jet. The present survey, therefore, aims at filling the above stated gaps in the knowledge.

References

Aamir M, Ahmad Z, Pandey M, Khan MA, Aldrees A, Mohamed A (2022) The effect of rough rigid apron on scour downstream of sluice gates. Water 14(14):2223. https://doi.org/10.3390/w14142223

Adduce C, Mele P (2004) Local scour by submerged turbulent jets. Adv Hydrosci Eng VI:1–7

Aderibigbe OO, Rajaratnam N (1996) Erosion of loose beds by submerged circular impinging vertical turbulent jets. J Hydraul Res 34(1):19–33

Aderibigbe O, Rajaratnam N (1998) Effects of sediment gradation on erosion by plane turbulent wall jets. J Hydraul Eng, ASCE 124(10):1034–1042

Ahmad Z, Singh UK, Kumar A (2018) Incipient motion for gravel particles in clay-silt-gravel cohesive mixtures. J Soils Sediments 18(10):1–12

Ali U (1988) Scour downstream of vertical gate. J Hydraul Eng ASCE 114(7):811–816

Ansari SA, Kothyari UC, Ranga Raju KG (2002) Influence of cohesion on scour around bridge piers. J Hydraul Res 40(6):717–729

Ansari SA, Kothyari UC, Ranga Raju KG (2003) Influence of cohesion on scour under submerged circular vertical jet. J Hydraul Eng ASCE 129(12):1014–1019

Bagnold RA (1966) An approach to the sediment transport problem from general physics. Physiographic and hydraulic studies of river, geological, survey professional paper 422-I, pp 1–37

Beltaos S, Rajaratnam N (1974) Impinging circular turbulent jets. J Hydraul Div 100(10):1313–1328

Bhave S, Kumar S, Singh UK, Pandey M, Ahmad Z (2020) Experimental investigation of a trench weir with T-shaped bars. J Braz Soc Mech Sci Eng 42(10):1–17

Breusers HNC, Raudkivi AJ (1991) Scouring. In: Hydraulic structure manual, I.A.H.R. Balkema, Rotterdam

Chakravarti A, Jain RK, Kothyari UC (2013) Scour under submerged circular vertical jets in cohesionless sediments. ISH J Hydraul Eng 20(1):32–37

Chaudhuri S, Pandey M, Debnath K, Oliveto G (2022) A comparative study on equilibrium scour volume around circular cylinders in clay-sand mixed cohesive beds, at near threshold velocity of sand–an experimental approach. Water Supply 22:6777. https://doi.org/10.2166/ws.2022.250

Clarke FRW (1962) The action of submerged jets on movable material. Ph.D. thesis. Imperial College, London

Dehghani AA, Bashiri H, Meshkati Shahmirzadi ME (2010) Local scouring due to flow jet at downstream of rectangular sharp-crested weirs. Water and Geoscience conference, Cambridge

Donoghue TO, Trajkovic B, Piggins J (2001) Sand bed response to submerged water jet. Proceedings of the eleventh international offshore and polar engineering conference, Stavanger, Norvey, June 17–22

Francis JRD, Mccreath PS (1979) Bed load transport by submerged jets. Proc Natl Acad Sci U S A 76(9):4159–4161
Hayter EJ (1983) Prediction of cohesive sediment movement in estuarial waters. Ph. D. Thesis, the University of Florida at Gainesville
Jain R, Lodhi AS, Oliveto G, Pandey M (2021) Influence of cohesion on scour at piers founded in clay–sand–gravel mixtures. J Irrig Drain Eng 147(10):04021046
Johnston AJ (1990) Scourhole developments in shallow tailwater. J Hydraul Res 28(3):341–354
Mazurek KA, Christison K, Rajaratnam N (2002) Turbulent sand jets in water. J Hydraul Res 40(4): 527–530
Mazurek KA, Gautam B, Ahsan MR (2009) Submergence effects on jets behavior and scour for plane wall jets in cohesionless materials. 33rd I.A.H.R. congress
Pandey M, Zakwan M, Khan MA, Bhave S (2020) Development of scour around a circular pier and its modelling using genetic algorithm. Water Supply 20(8):3358–3367
Pandey M, Pu JH, Pourshahbaz H, Khan MA (2022a) Reduction of scour around circular piers using collars. J Flood Risk Manag 15:e12812. https://doi.org/10.1111/jfr3.12812
Pandey M, Jamei M, Ahmadianfar I, Karbasi M, Lodhi AS, Chu X (2022b) Assessment of scouring around spur dike in cohesive sediment mixtures: a comparative study on three rigorous machine learning models. J Hydrol 606:127330
Pu JH, Wallwork JT, Khan M, Pandey M, Pourshahbaz H, Satyanaga A, Hanmaiahgari PR, Gough T (2021) Flood suspended sediment transport: combined modelling from dilute to hyper-concentrated flow. Water 13(3):379
Rajaratnam N (1981) Erosion of plane turbulent jets. J Hydraul Res 19(4):339–359
Rajaratnam N (1982) Erosion by submerged circular jets. J Hydraul Div ASCE 108(2):262–267
Rajaratnam N, Beltaos S (1977) Erosion by impinging circular turbulent jets. J Hydraul Div, ASCE 103(10):1191–1205
Rajaratnam N, Mazurek KA (2005) Impingement of circular turbulent jets on rough boundaries. J Hydraul Res 43 (6):688–694
Rouse H (1940) Criteria for similarity in the transportation of sediment. Bulletin 20:33–49
Shankar MS, Pandey M, Shukla AK (2021) Analysis of existing equations for calculating the settling velocity. Water 13(14):1987
Shivashankar M, Pandey M, Zakwan M (2022) Estimation of settling velocity using generalized reduced gradient (GRG) and hybrid generalized reduced gradient–genetic algorithm (hybrid GRG-GA). Acta Geophys 1–11
Singh UK (2018) Influence of cohesion on sediment transport. Ph. D. Thesis, Department of Civil Engineering, Indian Institute of Technology, Roorkee, India
Singh UK, Ahmad Z, Kumar A (2017) Turbulence characteristics of flow over the degraded cohesive bed of clay–silt–sand mixture. ISH J Hydraul Eng 23(3):308–318
Singh UK, Jamei M, Karbasi M, Malik A, Pandey M (2022) Application of a modern multi-level ensemble approach for the estimation of critical shear stress in cohesive sediment mixture. J Hydrol 607:127549
Walter CM, Kabir J (1983) Impingement of water jets on nonuniform streambed. J Hydraul Eng, ASCE 109(4):536–548
Westrich B, Kobus H (1973) Erosion of a uniform sand bed by continuous and pulsating jets. Proceedings of 15th IAHR congress, Istanbul, Turkey, vol 1, pp A13.1–A13.8
Yeh P-H, Chang K-A, Henriksen J, Edge B, Chang P, Silver A, Vargas A (2009) Large-scale laboratory experiment on erosion of sand beds by moving circular vertical jets. Ocean Eng 36:248–255

Chapter 7
Stabilization of Manmade Embankments at Indian Sundarbans Estuary Through Turbulence Control at Flow-Sediment Interface: Field Survey and Flume Experimentation

Vikas Kumar Das, Koustuv Debnath, and Susanta Chaudhuri

Abstract Inhabited Islands of Indian Sundarbans estuaries at the conjunction of Ganga, Padma, Brahmaputra deltaic plane, and Bay of Bengal suffered by the disaster of embankment breaching almost annually, primarily due to enhanced erosion led by high energy tidal flow. Formation of series of basal undercuts at the submerged portion seems to be the initiating factor, finally results in collapse of embankments. Situations became severely devastative when cyclones and oceanic storms hit the estuary. Out of several traditional practices to protect the embankments, emplacement of bamboo fencing at base is the most common one. The present field survey and flume experimentation, intended to evaluate the temporal performance of bamboo fencing to prevent the basal erosion. Comparisons of efficiency between cylindrical wire grids replacing the bamboo fencing to prevent the undercut formation at embankment base were also investigated. A micro-ADV was used to measure the 3-D turbulent velocities at flow-sediment interface to map the flow structure around bamboo ribs and grid-influenced turbulent flow. Outcomes of the study revealed that the emplacement of cylindrical wire-mesh grids at embankment base, modulate the large turbulent scales by breaking into smaller eddies and provides a better sustainable protection towards its stability. Validation of experimental results in natural prototype scale is recommended for better engineering practices and expected that, it will reduce the intensity of disaster caused by embankment breaching, almost in every monsoonal months at Indian Sundarbans.

Keywords Embankment failure · Formation of undercuts · Flow-sediment interface · Flume experimentation · Turbulent scales · Sustainable protection

V. K. Das · K. Debnath
Fluid Mechanics and Hydraulic Laboratory (FMHL), Department of Aerospace Engineering and Applied Mechanics, Indian Institute of Engineering Science and Technology (IIEST), Shibpur, India

S. Chaudhuri (✉)
Department of Geological Sciences, Jadavpur University, Kolkata, India

M. Pandey et al. (eds.), *River Dynamics and Flood Hazards*, Disaster Resilience and Green Growth, https://doi.org/10.1007/978-981-19-7100-6_7

7.1 Introduction

The south-western portion of the lower Ganga–Brahmaputra-Meghna deltaic plane is occupied by the mangrove wetlands known as the Sundarbans estuary expanded in Bangladesh and Eastern India, located at the northern fringe of the Bay of Bengal is the world's largest delta, both in respect to land area (120,000 km^2) and yearly discharge of sediments (Ghosh and Mukhopadhyay 2016; Bandyopadhyay et al. 2019). Marine regression and transgression are locally experienced in its geologic past for the Sundarbans as being prograding delta (Rakshit et al. 2015; Ghosh and Mukhopadhyay 2016). According to Hazra et al. (2002), Ghosh et al. (2003), Ghosh and Mukhopadhyay (2016), the regional tectonic setup of the location further resulted in geomorphological changes those occurred in the millennia scale and is still going on. Dense network of intercalated meandering channels with rapid variation of tidal flow resulted in radical changes and modifications in erosion–transportation–deposition sequences. Steeply meandering river system of Indian Sundarbans estuaries undergo rapid fluvio-morphological dynamicity due to erratic cycle of erosion- deposition make the embankment more vulnerable towards its breaching. Overall, the river system network of river system of the area is being controlled by various interrelated and complex ecological and geophysical processes (ASCE Task Committee 1998).

In the historical past, since the beginning of nineteenth Century, human inhabitation in Sundarbans estuaries adopted a traditional method of constructing embankment along the riverside to restrict the high tide water inflow to the dwelling areas (Hossain et al. 2014; Dhara and Paul 2016; Bhattacharya et al. 2019). This method of flood management amends the natural river hydrodynamic processes and thus the earthen embankments in Sundarbans are exposed to deal with the complex amended hydrodynamics of the natural river systems and breaching of embankments in several areas of Sundarbans is almost an annual event resulting in the submergence of agricultural land that acutely affect the livelihood of the local people (Chowdhury and Maiti 2014; Bandyopadhyay et al. 2019; Chaudhuri et al. 2021; Das et al. 2021a, b). Drastically, during last few decades due to natural and anthropogenic changes this deltaic island system is facing a severe degradation. These areas are prone to vulnerability die to cyclone and storm surges, frequent embankment breaching and failure, beach erosion, and siltation at jetties and navigational channels. In addition, the population growth at an alarming rate had imposed a major threat to its very existence in this ecologically sensitive and fragile niche (Dhara and Paul 2016).

Breaching of manmade embankment is an almost recurring event at Indian Sundarbans, mostly resulted in severe disaster. Rapidness of tide dominated meandering flow leads to erratic fluctuations in erosion-deposition cycles and breaching of embankments is almost an annual event resulting in the submergence of agricultural land that acutely affect the livelihood of the local people. In the recent past, some of the severe cyclonic storm, namely, Aila (2009), Amphan (2020), and Yash (2021) resulted in failure of these embankments to a large extent, as a

consequence of these storm surges huge loss of human settlement, irrigation land and lives were reported.

Contraction of natural river flood plain by the erection of embankment imposed a significant modification of flow and resulted in an increased rate of erosion of the sediment bed (Ravens and Gschwend 1999; Lu and Griffiths 2004; Debnath et al. 2014; Chaudhuri et al. 2014; Karna et al. 2015; Chaudhuri et al. 2018; Das et al. 2020a; John et al. 2021a, b and Chaudhuri et al. 2022). Traditional practices of construction embankments by scooping off river bed sediment alter the natural geotechnical configuration of constituting soil to a considerable extent. The stream flow pattern at the flow-sediment interface is altered at the base of the embankment to a substantial extent due to the construction of these embankments and thereby restricting the river to play in its natural flood plain, which in turn affects the sustainability of erected embankments. Formations of successive undercuts at the base of the flow facing wall are supposed to be the prime initiation factor for its erosion and finally resulted in breaching of embankments. This process closely resemble with the bank failure mechanisms at the lower reach of the River Hooghly (Simon et al. 2000; Das et al. 2019a, b, 2020b; Pandey et al. 2020a, b; Roy et al. 2020; Pu et al. 2021). Progressive development of undercuts at the earthen embankment base by the swirling currents coupled with tidal surges and strong winds resulted in rapid breaching of the relatively weakened soil layer of embankment, prolonged submergence of the embankment base, and, over time resulted its collapse (Manna et al. 2010; Dhara and Paul 2016; Chaudhuri et al. 2021; Das et al. 2021a, b; Shankar et al. 2021; Shivashankar et al. 2022; Singh et al. 2022).

Out of several traditional eco-friendly low-cost preventive measures to restrict and retard the embankment erosion processes, the emplacement of serially arranged fencing of bamboo logs seems to be the most common practice in this area of Sundarbans estuaries. On the contrary intense post-monsoon field survey during October 2018 revealed that in most of the cases for older embankments, basal undercuts behind the emplaced bamboo logs were more severe in the normal situations. Therefore, a question arises on the sustainable efficacy and temporal performance of basal bamboo fencing towards the long-term protection of embankments, from its failure. Das et al. (2021a) concluded that despite retarding the rate of erosion initially, with the propagation of time due to the influence of basal bamboo fencing flow modulation and the related structures enhances its turbulence energy. This increased flow perturbation led to the formation of diminutive pitting and undercuts that radically resulted in the failure of embankment and the bamboo fencing too. From the recent literature survey, it is evident that a good number of investigations were carried out on the adverse impact of embankment failure on relevant environmental issues, sea level ingress, and associated socio-economic ecological aspects (Hazra et al. 2002; Bowen and Riley 2003; Ghosh et al. 2003; Maiti 2008; Payo et al. 2016). Available technical reports (Duncan et al. 2008; Bhattacharya et al. 2019; Chaudhuri et al. 2021) mainly dealt with the protection measures of embankments for better sustainability and are in general concerned with the geotechnical aspects of constituting soil. Except for a few (Manna et al. 2010; Debnath et al. 2014; Dhara and Paul 2016; Das et al. 2019a, b; Barman et al. 2019;

Roy et al. 2019), experimental flume based investigations on bank erosion, with that of natural and artificial sediment mixture are still rare. Flume based experimental to investigate the impact of altered flow filed due to erection of embankments at the peripheral fringe of the floodplains in local scale, relative efficacy of associated preventive mechanisms, in concern with the changed turbulence at flow-sediment interface are still remain almost unexplored. Literature review reveals that practically no experimental study was reported on proposition of sustainable low-cost preventive measure to restrict the manmade embankment failure at Indian Sundarbans, those perform better than bamboo fencing.

In the present experimental study, flume-based investigations were performed to investigate and compare the efficiency of installation of cylindrical wire mesh grids at the base of the erected embankment over the emplacement of bamboo fencing to restrict the entrainment of basal soil to form of series of undercuts. The precise objective of this study aimed to understand and characterize the integrated impact of pulsating turbulent fluctuations at the flow-sediment interface and temporal propagation of basal erosional pattern by emplacing cylindrical wire grid at the embankment base. Finally, a comprehensive comparison was reported to observe how bamboo ribs and cylindrical wire grid modulate scales of turbulence to restrict basal erosion with time to provide a better sustainable option to prevent embankments from breaching.

7.2 Study Area and the Field Survey

Considering the international boundary, the portion of Indian Sundarbans estuaries covering an area of Sundarbans is about 10,000 Km^2. It consits of 102 islands, of different sizes, and out of those 54 islands, human settlements are there (Quartel et al. 2007) with a population of 4.37 million with a density of 957 people/sq.km. Figure 7.1a–d reveals the geographical position of the Sundarbans estuaries in the Indian subcontinent.

In Sundarbans estuaries, construction of embankments has eased the human habitation as it does not allow the salt water to enter the landward region during high tide (Ghosh et al. 2003; Manna et al. 2010; Dhara and Paul 2016), which is exceptionally crucial during monsoonal months. These embankments also served as primary means of communication. At present, inhabited islands of Indian Sundarbans have a total embankment length of nearly 3638 km (World Bank 2014). Eventually, the islands are interconnected by intervening water courses and raised permanently above the high tide water levels.

As reported by Mukhopādhyā⍰a (1981) that retardation in island formation has been observed due to the construction of embankments at comparatively higher speed and has become a widespread practice since the nineteenth century. With time these earthen embankments are progressively weakened by the eddy currents coupled with fluctuating tidal flow and strong winds that result in the undercut development at its toe. Nine (09) out of thirteen (13) subdivisions of Indian

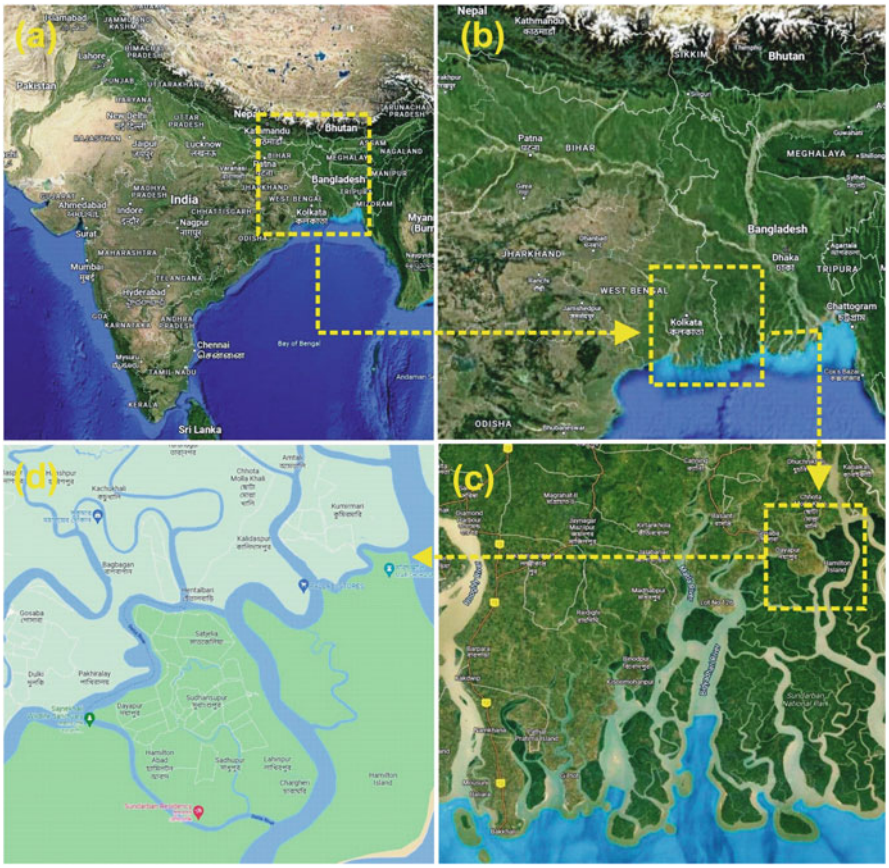

Fig. 7.1 (**a**–**d**) Geospatial position of Indian Sundarbans estuaries in (**a**–**b**) Indian subcontinent and (**c**) field area (**d**) surveyed locations L1—Kumirmari, L2—Chotta mollakhali, L3 Dayapur)

Sundarbans are identified to have potentially feeble embankments, breached recurrently due to natural fluvial and meteorological hazards (Dhara and Paul 2016). Because of repeated breaching, these weak embankments are frequently needed to be reconstructed or renovated almost alternative year. During monsoonal months cyclonic storms resulted in severe disasters and imposed a substantial loss in terms of settlement, cropping area and agricultural yield virtually every year.

In the recent past, severe catastrophic cyclonic storms, namely Aila (May, 2008), Bulbul (November, 2019), Amphun (May, 2020), and Yash (May, 2021), resulted in severe disasters by causing exhaustive destruction of the embankments with prolonged submergence of inhabited islands of Indian Sundarbans. Figure 7.2a, b shows some the photographs of those devastative floods of the cyclonic disasters in the recent past during Amphun (May, 2020) and Yash (May, 2021).

Traditional measures such as bamboo mats and bamboo fencing at the embankment bases are extensively used to decline the soil erosion rate. These are cost-effective and widely available locally. To obtain an overview of the temporal

Fig. 7.2 (**a**–**b**) Devastative floods at Indian Sundarbans caused by massive failure of manmade embankments during severe cyclonic storm disasters during (**a**) Super Cyclone "Amphun," May—2020; (**b**) Cyclone "Yash," May—2021

performance of traditional preventive measures related to restoration processes to protect the embankments from recurring seasonal breaching, a post-monsoon field survey was conducted through the meandering bank of the river Datta and Biyadhari that encompasses most of the significant inhabited areas in Goshaba block of Sundarbans (Fig. 7.1d), namely Kumirmari (L1); Chotta mollakhali (L2); and Dayapur (L3). Samples of soil were collected from the basal part of river-facing wall of erected embankments; those were protected by bamboo fencing at the base. All the samples were collected by standard core cutting method (IS: 2720-29 1975) during low tide from the intervening space between the embankment wall and bamboo ribs. Fig. 7.3a–d presents the photographs of in the embankments the surveyed locations (L1; L2; L3) with protective basal bamboo fencing to restrict basal erosion and the formation of undercuts, which seemed to be the primary reason for its failure (Chaudhuri et al. 2021; Das et al. 2021a). It is pretty clear from the photographs that a few of those (L1 and L3) are almost at the verge of breaching despite having bamboo fencing support at the base. Figure 7.3d reveals the photograph of a portion of the unprotected embankment at location L1 with the formation of basal undercuts, almost at the verge of its failure.

7.3 Materials and Methods

The present investigation intended to draw a comparison of temporal efficiency of traditional embankment protection measures by imposing bamboo fencing at its base with that of emplacement of cylindrical wire mesh rib at the toe region of flow facing wall of embankment. To assess near prototype similitude to the sediment characteristics of an artificially prepared bank in the experimental flume, all the collected soil samples from the embankment bases were tested in the laboratory following standard Geotechnical processes and ranges of major index properties. A total of 9 numbers of soil samples (three from each location) from three surveyed locations (L1; L2; L3) were tested, and values of major in situ geotechnical properties of

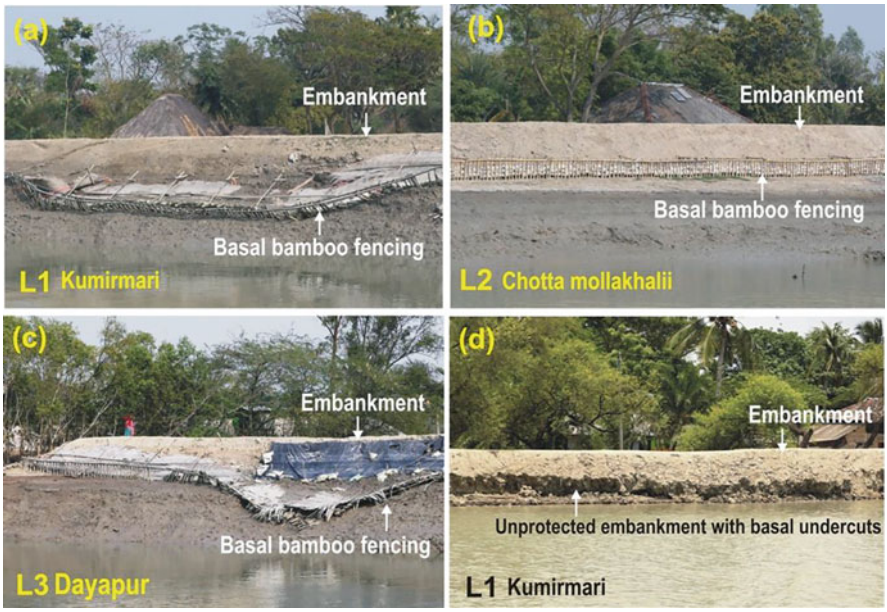

Fig. 7.3 (**a**–**d**) Photographs of the embankments the surveyed locations, with protective basal bamboo fencing (**a**) L1—Kumirmari, (**b**) L2—Chotta Mollakhali; (**c**) L3—Dayapur; (**d**) portion of unprotected embankment with the formation of basal undercuts at location L1

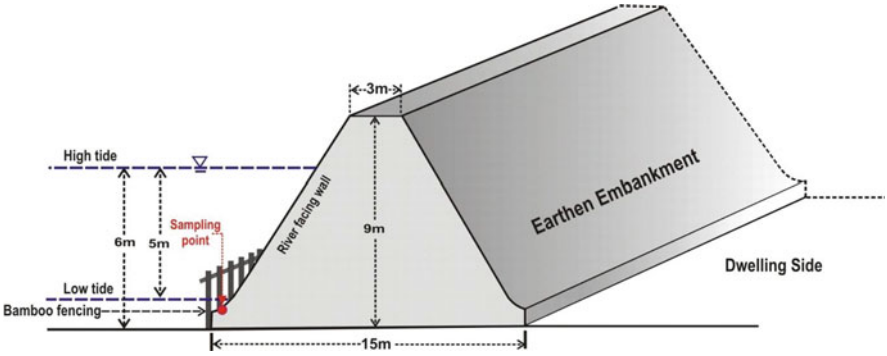

Fig. 7.4 Schematic diagram of the embankment (not to scale) with bamboo ribs at the base and the position of sampling point

constituting soil were estimated. All the soil samples were collected during extreme low tide time from the basal part, from the position in between the bamboo fence and river-facing wall of the embankment. Figure 7.4 represents a generalized schematic diagram of the embankment with bamboo ribs (as surveyed during field) at its base and the position of the sampling point of the surveyed locations.

7.4 Experimental Setup

A sediment bank model of dimensions 3 m long, 0.25 m wide, and 0.4 m high was prepared artificially within the sediment recess section of the flume kept at the Fluid Mechanics and Hydraulics Laboratory of Indian Institute of Engineering Science and Technology, Shibpur. India.

7.5 Characteristics of Embankment Soil and Preparation of Artificial Bank

Table 7.1 represents the estimated primary sediment index properties and ranges of field sediment samples collected from all three locations. This was done to provide prototype similitude to the artificially prepared sediment in the laboratory to carry out flume experiments. In laboratory, artificial river bank sediment material was prepared by mixing kaolinite clay with fine sand by weight fraction ratio of 2:8, respectively, with water. This mixing ratio was finalized with reference to the estimated property of Weight % $D \leq 63$ μm for field samples and microscopic observation of the thin section of the dry soil samples.

Table 7.2 represents the ranges of sediment properties those were estimated for field samples (from embankment) and the artificial sediment mixture prepared for configure the simulated bank at the flume wall.

The thin section of the sediment samples was prepared following the standard procedure of emplacing the dried out grain of the sediment in a thin layer of adhesive (here it was Canada balsam), polishing after that. All the prepared thin sections were studied under a microscope in plane-polarized light at 100× magnification to get an overall understanding of individual grain index properties concern of the sphericity,

Table 7.1 Estimated sediment index properties of field samples

Sample location	Location	ρ_t (gm/cc)	ρ_d (gm/cc)	W_c (%)	D_{50} (μ)	Weight % $D \leq 63$ μm	W_L (%)	P_L (%)
Kumirmari (L1)	L1A	1.42	1.00	42.62	130	32.6	50.34	18.22
	L1B	1.48	1.07	37.77	170	29.8	48.82	22.30
	L1C	1.59	1.19	33.55	140	21.6	45.25	20.16
Chotta Mollakhali (L2)	L2A	1.52	1.01	51.16	180	34.8	55.86	19.84
	L2B	1.71	1.17	46.46	150	32.0	52.30	23.66
	L2C	1.48	1.04	42.23	160	30.7	48.25	20.48
Dayapur (L3)	L3A	1.55	1.11	40.12	110	32.4	46.75	24.42
	L3B	1.47	1.08	36.44	160	33.6	45.67	18.68
	L4C	1.51	1.03	47.18	190	34.1	54.22	19.52
Average		1.53	1.08	41.95	154	31.3	49.72	20.81
Maximum		1.71	1.19	51.16	190	34.8	55.86	24.42
Minimum		1.42	1.00	33.55	110	21.6	45.25	18.22

Table 7.2 Ranges of values of estimated sediment index properties from field and laboratory

Index properties	Embankment sediment (from field)	Prepared sediment (In Lab)
ρ_t (g/cc)	1.42–1.71	1.65
ρ_d (g/cc)	1.00–1.19	
W_c (%)	33.55–51.16	38.62
D_{50} (μ)	110–190	130
Weight % $D \leq 63$ μm	21.6–34.8	32.67
W_L(%)	45.25–55.86	47.22
P_L(%)	18.22–24.42	23.33

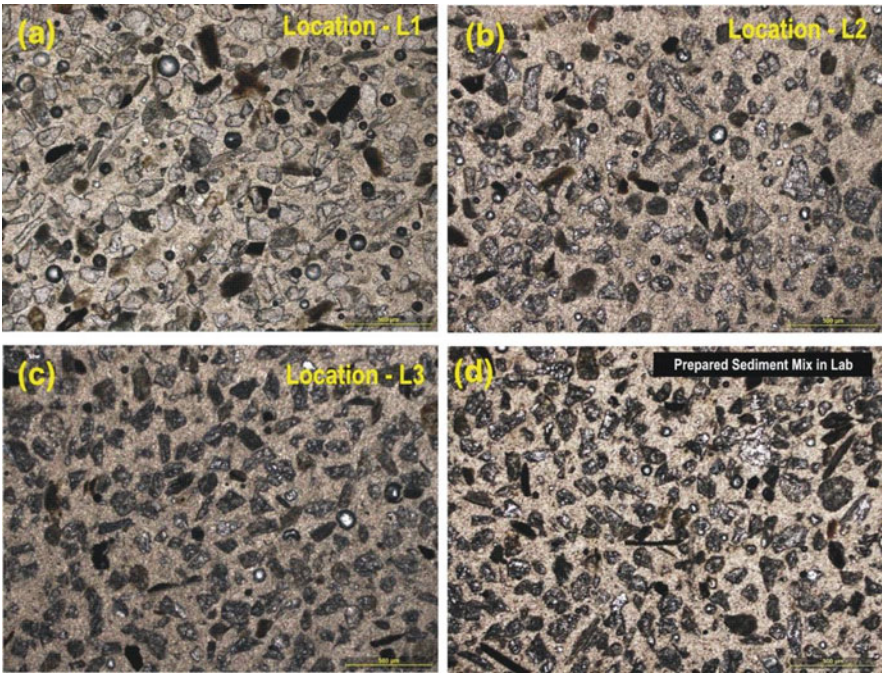

Fig. 7.5 (**a**–**d**) Microscopic images of thin sections of filed soil samples from surveyed locations (**a**) L1; (**b**) L2; (**c**) L3 and (**d**) artificially prepared sediment mixture in the laboratory

roundness and volumetric distribution of different size fractions. For individual locations surveyed (i.e., L1; L2; and L3), all three collected samples (A; B; and C) were then dried completely at 120 °C in a moisture-controlled oven. Dry samples were then lightly hammered (by a rubber hammer) to rupture the bigger lumps and sieved by 250-micron (Sieve No.60) sieve to exclude the organic fraction and larger lumps of the soil samples. All these dried out samples of individual locations mixed up in equal proportion after segregating the larger lumps, following standard geotechnical measures. Figure 7.5a–d presents the observed microscopic images of thin

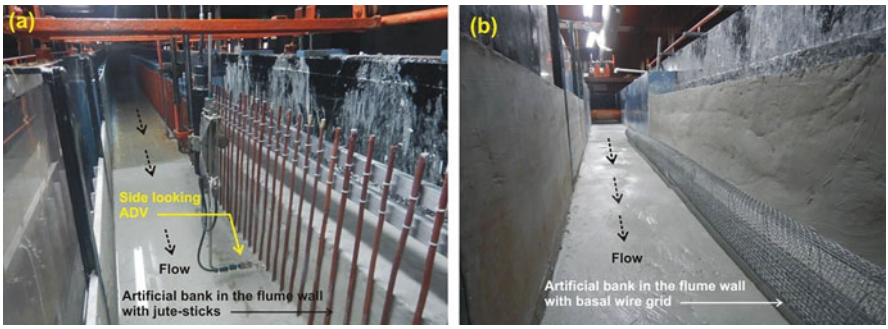

Fig. 7.6 (**a**–**b**) Photographs of experimental set up at the start of experimental runs (**a**) artificially erected bank model with bamboo grid fencing; (**b**) cylindrical wire rib at the base of the bank

sections of filed sediment samples from the three surveyed locations L1; L2; L3 (Fig. 7.5a–c) and artificially prepared sediment mixture in the laboratory (Fig. 7.5d).

Presented images reveal close proximity between the prepared sediment mixture and field soil samples. It is pretty clear that the overall characteristics of the prepared sediment in regard to grain size distributions of different size fractions and proportions are almost near too similar to the prototypes.

Artificial sediment banks were fabricated in-house within the laboratory flume. Figure 7.6a, b shows photographs of an artificially erected bank model. The side facing wall at its base is fenced with model restraining measures of jute sticks (replicate bamboo fencing) and a cylindrical wire mesh grid at the test section of the experimental flume before to start the experimental run. To replicate the bamboo logs, as used in the Sundarbans at the embankment base, jute sticks of diameter 0.015 m were placed vertically touching the side wall of the artificially erected bank in the experimental flume. Centre to centre spacing in between the sticks were maintained at 60 mm to match the dimensional similitude with the prototype. The one-third portion of the jute stick length at its base was inserted into the bed sediment to avoid displacement due to flow. Diameter of jute sticks and the spacing in-between were fixed based on the field study to maintain proximity to dimensional similitude with basal bamboo fencing of prototype embankment. An average of 80 measurements of the dimensions of bamboo logs and their spacing at the field was scaled down at 1:4 for jute sticks used for laboratory experiments (Fig. 7.6a). Furthermore, to test the efficiency of longitudinal cylindrical grids are effective in controlling the development of basal undercuts for both the cases of only-current and wave-current combined flow; a cylindrical wire grid of 10 cm diameter of mesh size 0.5 cm was placed at the base of the prepared bank (Fig. 7.6b).

7.6 Experimental Procedures

The experimental runs were carried out for plane bank (PB), with bamboo rib (BR) and wire grid (WG) influenced cases. These three different cases were conducted at a fixed Reynolds number ($\overline{U}h/\upsilon$) of the current (Re = 73,500), where u = mean velocity, h = water depth, and υ = kinematic viscosity of water. The flow depths during all the experimental runs were maintained at ~21 cm by using a flow control valves.

Son Tek micro-ADV was used to measure the instantaneous random velocity fluctuations and a frequency of 40 Hz (Fig. 7.6a). The instantaneous depth-averaged flow velocity data were recorded for 3 min at individual measurement points, similar to Roy et al. (2019). It was evident from the experimental cases performed here, that the river bank morphology was quasi-static over the ADV sampling period of 3 min and resulted in closely stationary flow velocity signals which, allowed the estimation of turbulence statistics assuming statistical stationery.

The velocity measurements for all the cases were carried out 10 m from the inlet point of the experimental flume within the fully developed flow regime and towards the middle portion of the sediment bank (i.e., at 1.5 m length) and 10 cm from the bed. Furthermore, for the bamboo rib cases the flow velocity measurements were recorded between the middle portion of the two adjacent bamboo ribs, whereas for grid influence cases the measurements were taken within the space between the grid and bank wall by positioning the probe of the micro-ADV at 45 degrees, similar to Das et al. (2021a, b).

7.7 Results and Discussion

Analysis of experimental data & observations revealed that significant controlling functions were flow parameters; temporal propagation of erosion at flow sediment interface for all three experimental conditions (i.e., PB, BR and WG). A relative comparison of the effectiveness of the existing practice of bamboo fencing with the proposed restraining method of emplacement of basal cylindrical wire grid are discussed.

7.8 Statistical Moments

To quantify the velocity (all the three-dimensional components of the instantaneous velocity field), 16-MHz down looking and side facing micro-ADVs were used (Fig. 7.6b). The mean averaged and fluctuating part of the turbulent flow field may be decomposed as (Nezu and Nakagawa 1993):

$$u = \overline{u} + u', \quad v = \overline{v} + v', \quad w = \overline{w} + w' \tag{7.1}$$

where $\overline{u}$,$\overline{v}$,$\overline{w}$ are the time-averaged velocity components (cm.s^{-1}) and u', v', w' are the corresponding velocity fluctuations in *x, y,* and *z* directions, respectively.

The time-averaged velocity (u $\overline{v}$, w), intensity (u^+, v^+, w^+), and Reynold's shear stress component (u, v) are given as:

$$\overline{u} = \frac{1}{n}\sum_{i=1}^{n} u_i; \quad \overline{v} = \frac{1}{n}\sum_{i=1}^{n} v_i; \quad \overline{w} = \frac{1}{n}\sum_{i=1}^{n} w_i \tag{7.2}$$

$$I_u = \sqrt{\overline{u'^2}} = \sqrt{\frac{1}{n}\sum_{i=1}^{n}(u_i - \overline{u})^2}; \quad I_v = \sqrt{\overline{v'^2}} = \sqrt{\frac{1}{n}\sum_{i=1}^{n}(v_i - \overline{v})^2} \tag{7.3}$$

$$\tau_{xy} = -\rho\overline{u'v'} = -\frac{\rho}{n}\sum_{i=1}^{n}(u_i - \overline{u})(v_i - \overline{v}) \tag{7.4}$$

where n is the number of observation and ρ is the density of water.

Note: $\overline{u}$,$\overline{v}$ and $\overline{w}$ are mean velocity (cm.s^{-1}) in the *x*-, *y*-, and *z*-direction, respectively; I_u and I_v are the turbulent intensities in stream wise and lateral direction; τ_{uv} is the shear stress. The estimated three-dimensional mean flow velocity, turbulent intensity, and Reynolds shear stress for plane bank (PB), bamboo rib (BR), and with grid (WG) cases are given in Table 7.2 at the time T1 = 0 h; T2 = 60 h; T3 = 120 h; T4 = 180 h; T5 = 240 h after the commencement of flume experimental run. It is relevant from Table 7.2 that the stream-wise velocity ($\overline{u}$) component is higher for PB case at T1. However, with the progression of the erosion, it is observed that the $\overline{u}$ component increases till T3, and with further progression of erosion, a decrease in $\overline{u}$ component was observed. This shows the presence of Type II erosion process as observed by Das et al. (2019a). The $\overline{u}$ component for BR case was initially small, which increased as the erosion progressed and achieved a maximum value compared to the other cases, (PB and WG) at T5. Moreover, for with grid influence case more or less similar $\overline{u}$ values were observed for the entire time duration.

The vertical flow velocity component ($\overline{w}$) shows a lesser value as compared to the $\overline{u}$. Similar observations are also observed from the velocity fluctuations plotted for plane bank (PB), bamboo rib (BR), and with grid (WG) cases at the different time T1 = 0 h; T2 = 60 h; T3 = 120 h; T4 = 180 h; T5 = 240 h (Fig. 7.7).

The fluctuating velocity for the PB case increases to its maximum until T3 as the erosion progresses. However, with further progression of the erosion process and the growth of undercut depth, the fluctuating velocity for PB case decreases (Fig. 7.2a–e). Whereas the fluctuating velocity for Grid cases shows negligible variations with smaller magnitude (Fig. 7.7k–o), and for the bamboo rib case, the fluctuating velocity was much lower as compared to PB and WG cases till T3 duration. However, as the erosion progressed at T4 and T5, the fluctuating velocity attained a maximum velocity compared to the other cases (Fig. 7.7f–j).

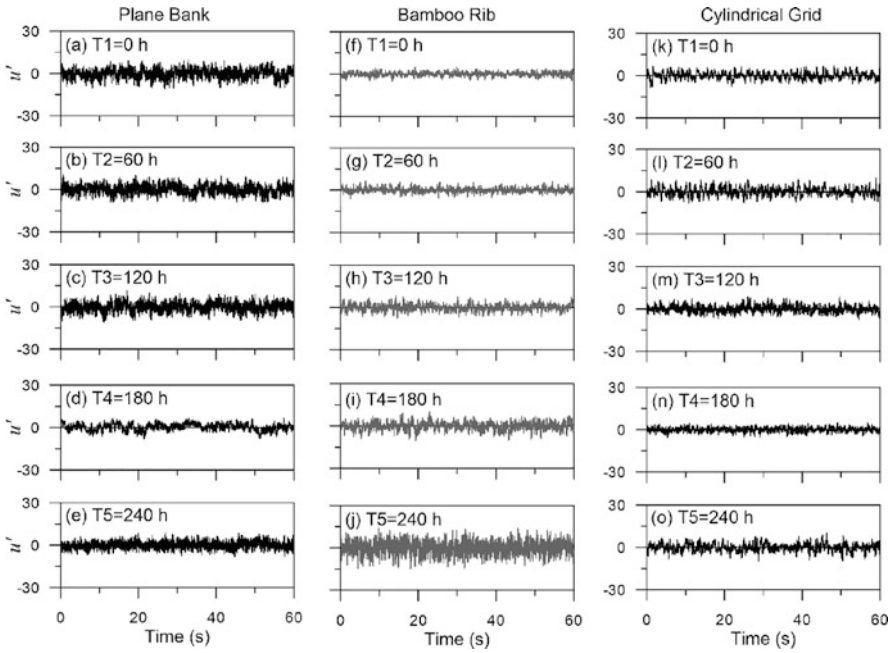

Fig. 7.7 (**a**–**o**) The time series of stream wise, lateral flow velocity, and fluctuations of shear stress for (**a**–**e**) Plane bank; (**f**–**j**) Bamboo ribs; (**k**–**o**) with grid cases for time duration T1 = 0 h; T2 = 60 h; T3 = 120 h; T4 = 180 h; T5 = 240 h

The *v*-component of the flow velocity remains practically almost negligible except a few locations. The negative and significant values of the $\overline{v}$-component occur within the undercuts indicating the flow to be three-dimensional with the formation of smaller vortices and recirculating in nature. The stream-wise turbulent intensities I_u are smaller for the WG case as compared to the other cases (PB and BR). The maximum I_u values were observed for BR cases at T4 and T5 duration and show a similar behaviour as observed for stream-wise velocity. Furthermore, the transverse turbulence intensity I_v was significantly smaller in magnitude as compared to I_u, with near to similar values at different spatial locations. The turbulent intensities indicate the contribution and impact of turbulent kinetic energy to the turbulent transport of momentum. The I_w components were observed to be almost negligible and are not shown here.

It is observed from Table 7.2 that the τ_{uv} value is larger in comparison with the τ_{uw} and τ_{vw}. A substantial modulation in the Reynolds stress value was observed at the boundary of the bank surface under the influence of bamboo rib and with grid cases as compared to plane bank. Reynolds shear stresses provide an insight to the fluxes of momentum, generated by turbulent fluctuations (Engel and Rhoads 2017). Runs with BR case, initially τ_{uv} showed a reduced value of 38% at T1 and 28% at T2 compared to PB case. However, with the progression of erosion, the τ_{uv} value increased for BR cases by 116% at T4 and 285% at T5 compared to the PB case.

Moreover, Reynolds stress (τ_{uw}) for the WG cases was reduced by ~34% at T1 to 28% at T5 compared with the PB cases (Table 7.3).

Figure 7.8a, b reveals the photographs of the basal erosional status at the closure of the experimental runs after siphoning out the water from the sediment recess of the flume. The eddy cascading process is evident from the photographs and obtained findings on flow modification. In the eddy cascading process, the turbulent stresses are modulated as the flow at near grid region are broken into smaller eddies from larger eddies (Zhou et al. 2014). Furthermore, the flow turbulence scales became significantly smaller (smaller eddies) under the influence of the wire-mesh grid and reproduced smaller magnitudes of Reynolds stresses. Figure 7.8b shows that the undercuts formed for the WG experimental cases were relatively smaller in size with less transverse undercut depth than PB cases. Under the influence of the wire-mesh grid at the near bank region, significant modulation of the turbulence characteristics was observed for all the experimental runs.

Furthermore, the impact of unidirectional flow on the initiation of dislodgement of basal soil from the flow facing the bank face was observed to reduce initially under the influence of bamboo ribs fencing. The bamboo ribs primarily acted as a protective measure initially and thereby reduced the rate of erosion process.

It was reported by Roy et al. (2019) that the near bank flow and the associated flow turbulence structures repeatedly modified as the flow facing bank morphology altered with the propagation of erosion. Das et al. (2021a) performed filed and flume based experimentations on natural river bank erosion and reported that scooping out of weak basal sediment at the concave erosive wall of large meandering river bank initiate basal erosion, generate energized flow perturbation. Gradually that intensified lateral flow component enhances the bank erosion by the formation of self similar morphological pattern, resulted finally to its collapse. Chaudhuri et al. 2021 reported that alteration of natural geotechnical configuration of constituting soil during the construction of manmade embankment at Indian Sunderland is one of the major reasons that lead to its breaching. Das et al. (2021b), from their experimental study, concluded that after a certain period of time bamboo fencing at embankment base exaggerates the flow turbulence scale and resulted in sudden collapse of embankment.

Observation and obtained results of the present reveals that dislodgement of the basal sediment particles results in the formation of small elongated pits like depression and formations undercut after that. With time an extended transverse gap was created in between the bamboo ribs and flow facing bank wall because of the size growths of these series of undercuts. This gap allowed the flow to deflect substantially behind the bamboo ribs causing concentration of the flow perturbation around it. This resulted in the considerable rise of the shear stress acting on the bank wall just behind the upstream of the bamboo ribs. As a consequence of this, considerably large volume of sediment aggregates and chunks got dislodged and the dimension of the evolved gap in between expanded largely. Growth of the gap up to a certain magnitude in between the bamboo ribs and the bank sediment face, the turbulence vortex shedding begins followed by the lee-wake erosion. During this span of time, the bed shear stress increases with a greater erosion potential and thereby, the related

Table 7.3 The summary of mean flow velocity and Reynolds stress

	Plane bank					Bamboo rib fencing					With grid				
Flow parameters	T1	T2	T3	T4	T5	T1	T2	T3	T4	T5	T1	T2	T3	T4	T5
$\overline{u}$	4	5.2	6.7	3.9	3.1	1.7	2.6	3.2	5.3	12	2.1	2.3	2.7	2.2	2.0
$\overline{v}$	1.1	1.2	1.5	−1.3	−1.0	0.8	0.9	1.4	−2.1	−3.7	1.0	1.1	1.2	1.0	1.0
$\overline{w}$	0.2	0.3	0.4	0.1	0.1	0.1	0.1	0.2	0.4	0.6	0.2	0.1	0.1	0.2	0.1
I_{u}	3.7	3.9	4.2	3.1	3.0	2.2	2.7	4.7	5.9	7.3	2.2	2.4	2.3	2.2	2.1
I_{v}	1.7	1.8	2.1	1.2	1.0	1.2	1.2	1.9	2.5	2.9	0.9	1.0	1.1	1.0	1.0
τ_{uv}	2.9	3.7	4.2	3.1	2.1	1.8	2.6	4.8	6.7	8.1	1.9	2.1	1.8	1.4	1.5

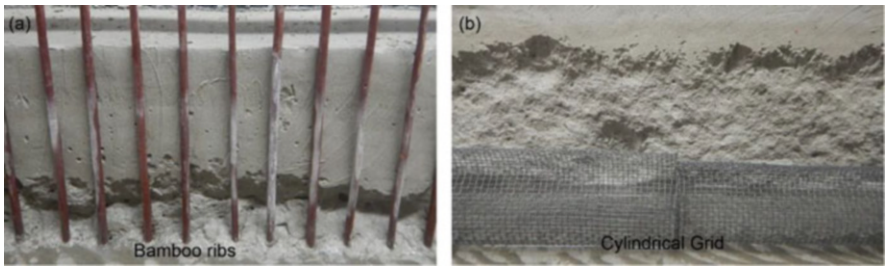

Fig. 7.8 (**a**–**b**) Formation of undercuts after time T5: (**a**) under the influence of Bamboo rib and (**b**) under the influence of grid

erosional processes enhances further. In case of basal bamboo fencing, a strong wake region with increasing turbulence scales was evolved surrounding individual bamboo rib and thereby the turbulence shear stresses were considerably higher than an unprotected bank face (Fig. 7.8a), that accelerated the entire erosion process at embankment base. Thus, it may be concluded the bamboo ribs implemented for bank protection measurement, initially perform well, but finally with time, it led to the enhancement of the erosional process.

7.9 Scales of the Reynolds Shear Stress Fluctuations

Wavelet analyses were performed herein for the characterisation of the Reynolds shear stress fluctuations. The mechanism involves decomposing the flow velocity signals into appropriate-sized time segments in the wavelet scale or pseudo-frequency (f_p). Based on the following equation the central frequency of the wavelet, f_{ct}, is determined as:

$$f_{\mathrm{p}} = {}^{f_{\mathrm{ct}}}\!/_{d.\Delta} \tag{7.5}$$

where f_{p} is the pseudo-frequency correspond to the scale d, in Hz; f_{ct} = centre frequency of a wavelet in Hz; d = scale; Δ = sampling period. Continuous wavelet transforms (CWT) of a signal may be characterized by a family of wavelet functions (e.g., Roy et al. 2019), and can be written as:

$$\varpi(p, w_{\mathrm{s}}) = \frac{1}{\sqrt{w_{\mathrm{s}}}} \int_{-\infty}^{\infty} \tau_{(t)}(t_i)\psi^* \left(\frac{t-r}{w_{\mathrm{s}}}\right) dt \tag{7.6}$$

where ϖ is the wavelet coefficient of fluctuating Reynolds shear stress; p is the position (space or time); w_{s} is the wavelet scale; the * symbol denotes the conjugated value; ψ is the mother wavelet function (Wang et al. 2016).

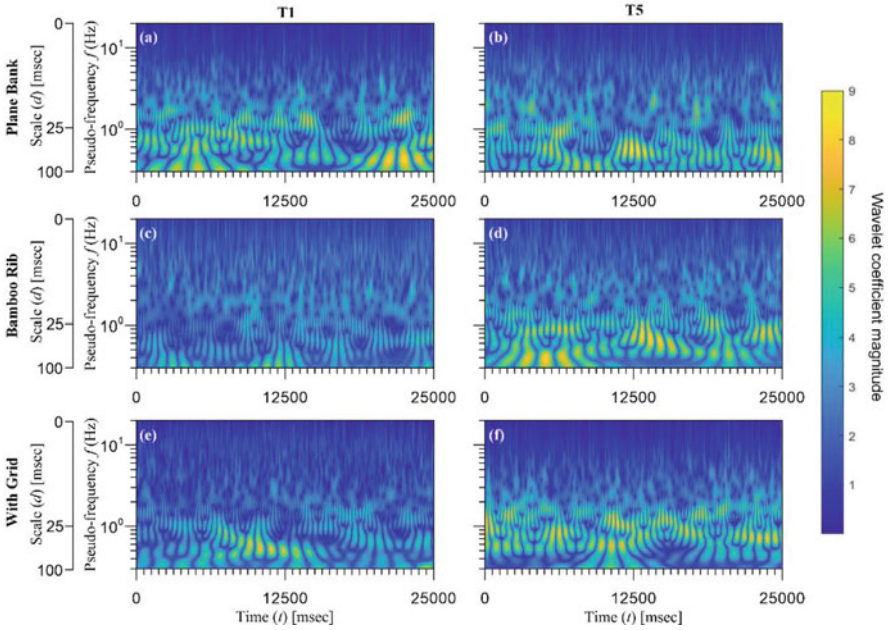

Fig. 7.9 (**a**–**f**) Contours of wavelet coefficient in pseudo-frequency and time domain for fluctuating Reynolds shear stress for (**a**–**b**) Plane bank; (**c**–**d**) Bamboo rib; (**e**–**f**) with grid cases for time duration T1 and T5

The contour plot of wavelet coefficients for Plane bank, Bamboo rib and with grid influence cases for time duration T1 and T5 are shown in Fig. 7.9a–f. It is pertinent from Fig. 7.9a, b that the fluctuating Reynolds shear stress for PB case at time T1 was higher than T5. Furthermore, the fluctuating Reynolds shear stress for BR case at time T1 was much lower as compared to T5 and also when compared to PB case (Figs. 7.4a, f).

Figure 7.9a–f suggests that the value of ϖ for the PB cases is maximum, and the values are reduced for the BR and WG cases. Thus, the higher value of ϖ suggest the occurrence of large scale fluctuating stresses for the PB cases those were responsible for the higher rate of erosion. However, under the effect of bamboo ribs fencing and grid at time T1, smaller values of ϖ are recorded. This indicates a fall or decrease in turbulence scales that result in shear stress reduction, thus entraining comparatively smaller aggregates and thereby retarding the rate of erosion. This retarded erosion rate prevents the initiation of undercuts that finally lead to the formation of an extended cantilever leading to bank mass failure. However, at the experimental condition of T5, the maximum values of ϖ are concentrated for the BR case generated at the lower $f_p = 0.3$–2 Hz s and was observed to be greater than that of the PB and WG cases. However, a smaller scale of the wavelet coefficient for the WG cases as compared to the PB and BR cases resulted to the decay of the erosion mechanisms and thereby undercut formation controlled to a larger extent.

7.10 Conclusions

The present study deploys a conceptually novel method for the stabilization of the river embankments in a conceptually different method. The new method implies modulation of the near bank flow turbulence at the basal region of manmade embankments by placing cylindrical grids. The outcomes of this investigation have a direct application in the Indian Sundarbans region for sustainable stability of the manmade embankments and in favour of better engineering practices. Estimated geotechnical characteristics of comprising soil from the field survey and laboratory flume experimentations reveal that bamboo rib fencing initially act as a protective measure, that retards the erosion the its rate for a certain period of time. However, with temporal progress, the near bank flow modulation and the associated flow turbulence structures under the impact of bamboo ribs led to the formation of smaller pittings and undercuts thereafter. The stream-wise flow velocity was observed to be the maximum with occurrence of negative vertical velocity components. The *v*-component seems to be practically negligible except at few areas, which were extremely closer to the bed sediment face. This indicates that the flow is three-dimensional with the formation of small vortices and recirculating flows.

The formation of these smaller vortices and recirculating flow imposes a sporadic hammering effect behind the bamboo ribs fencing on the bank sediments. This effect resulted in dislodgment of the basal soil particles, formed pits and undercuts. Formation of these undercut, created a gap behind the bamboo ribs, causing the formation of wake vortices, which resulted in substantial rise of the shear stress and thereby increased the rate of erosion. The shear stress in the xy-plane was observed to be more dominant and was the most effective agent for the erosion to take place. Furthermore, due to the influence of bamboo ribs fencing, the Reynolds shear stress showed an increase of 1.7–2.4 times as compared to without bank face bamboo ribs. These undercuts finally grew in size and with time, joined laterally together to form an elongated undercut. The formation of these undercuts results in creation of cantilever, and the overhanging mass collapses after long time duration under the influence of gravity.

Furthermore, the introduction of cylindrical grids at the near bank toe region modulates the turbulence flow structure. It is found to be effective in curbing the turbulent shear stresses and turbulence scales. This modulation in the flow structures results in a delay of the undercut growth and retards the entire erosion process. It is noteworthy to mention that the presence of grid structures reduces the scales of shear stress fluctuations. Thus, this effect results in retardation of the erosion process in the range of 48–64%, prevents the formation of undercuts and provides a longer sustainable stability to the manmade embankments.

Acknowledgments The authors would like to thanks the Department of Science and Technology, Government of India (Contact No. EMR/2015/000266) and RUSA-2.0 (Rashtriya Uchchatar Shiksha Abhiyan), Jadavpur University, Kolkata, India [Ref No. R-11/448/19], for the financial support to carry out this research.

Declaration of Interests The authors are hereby confirming that there are not any known competing financial interests or personal relationships that may have resulted to influence the work reported in this article.

References

ASCE Task Committee on Hydraul., Bank Mech., and Model. of River Width Adjust (1998) River width adjustment. I: processes and mechanisms. J Hydraul Eng 124(9):881–902

Bandyopadhyay D, Singh G, Kulkarni AV (2019) Spatial distribution of decadal ice-thickness change and glacier stored water loss in the upper Ganga basin, India during 2000–2014. Sci Rep 9(1):1–9

Barman K, Roy S, Das VK, Debnath K (2019) Effect of clay fraction on turbulence characteristics of flow near an eroded bank. J Hydrol 571:87–102

Bhattacharya K, Bhandari G, Mukerjee S (2019) Stability analysis of a typical Sunderban embankment during diurnal tidal cycle. In: Soil dynamics and earthquake geotechnical engineering. Springer, Singapore, pp 177–187

Bowen RE, Riley C (2003) Socio-economic indicators and integrated coastal management. Ocean Coastal Manag 46(3–4):299–312

Chaudhuri S, Debnath K, Manik MK (2014) Local scour around abutment in clay-sand mixed cohesive sediment bed. J Hydraul Eng 20(1):46–64. https://doi.org/10.1080/09715010.2013.835103

Chaudhuri S, Singh SK, Debnath K, Manik MK (2018) Pier scour within long contraction in cohesive sediment bed. Environ Fluid Mech 18(2):417–441

Chaudhuri S, Das VK, Debnath K, Hansda S (2021) Embankment breaching at Indian Sundarban–an assessment on altered primary sediment index properties and fluvial flow parameters. ISH J Hydraul Eng 1–12

Chaudhuri S, Pandey M, Debnath K, Oliveto G (2022) A comparative study on equilibrium scour volume around circular cylinders in clay-sand mixed cohesive beds, at near threshold velocity of sand–an experimental approach. Water Supply 22:6777. https://doi.org/10.2166/ws.2022.250

Chowdhury A, Maiti SK (2014) A comparative study of variations in mangrove biodiversity at central and eastern parts of the Sundarban biosphere reserve, India. Am Int J Res Form Appl Nat Sci 5(1):27–31

Das VK, Roy S, Barman K, Debnath K, Chaudhuri S, Mazumder BS (2019a) Investigations on undercutting processes of cohesive river bank. Eng Geol 252:110–124

Das VK, Roy S, Barman K, Chaudhuri S, Debnath K (2019b) Study of clay–sand network structures and its effect on river bank erosion: an experimental approach. Environ Earth Sci 78(20):591

Das VK, Roy S, Barman K, Chaudhuri S, Debnath K (2020a) Cohesive River bank erosion mechanism under wave-current interaction: a flume study. J Earth Syst Sci 129(1):1–20

Das VK, Barman K, Roy S, Chaudhuri S, Debnath K (2020b) Near bank turbulence of a river bend with self-similar morphological structures. Catena 191:104582

Das VK, Hansda S, Debnath K, Chaudhuri S, Mazumder BS (2021a) Assessing the hydraulic performance of bamboo logs in riverbank stabilization: case study of Sundarbans, India. Hydrol Sci J 66(1):134–151

Das VK, Hansda S, Debnath K, Chaudhuri S (2021b) Riverbank stabilization based on the modulation of the near bank turbulence scales. Environment, Development and Sustainability 23:15290–15313

Debnath K, Chaudhuri S, Manik MK (2014) Local scour around abutment in clay/sand-mixed cohesive sediment bed. ISH J Hydraul Eng 20(1):46–64

Dhara S, Paul AK (2016) Embankment breaching and its impact on local community in Indian Sundarban: a case study of some blocks of south west Sundarban. IJISET 3(2):23–32
Duncan FM, Fenster MS, Argow BA, Buynevich IV (2008) Coastal impacts due to sea-level rise. Annu Rev Earth Planet Sci 36:601
Engel FL, Rhoads BL (2017) Velocity profiles and the structure of turbulence at the outer bank of a compound meander bend. Geomorphology 295:191–201
Ghosh A, Mukhopadhyay S (2016) Quantitative study on shoreline changes and Erosion Hazard assessment: case study in Muriganga–Saptamukhi interfluve, Sundarban, India. Model Earth Syst Environ 2(2):75
Ghosh T, Bhandari G, Hazra S (2003) Application of a 'bio-engineering'technique to protect Ghoramara Island (Bay of Bengal) from severe erosion. J Coast Conserv 9(2):171–178
Hazra S, Ghosh T, DasGupta R, Sen G (2002) Sea level and associated changes in the Sundarbans. Sci Cult 68(9/12):309–321
Hossain M, Siddique MRH, Abdullah SR, Saha S, Ghosh DC, Rahman MS, Limon SH (2014) Nutrient dynamics associated with leaching and microbial decomposition of four abundant mangrove species leaf litter of the Sundarbans, Bangladesh. Wetlands 34(3):439–448
John CK, Pu JH, Pandey M, Moruzzi R (2021a) Impacts of sedimentation on rainwater quality: case study at Ikorodu of Lagos, Nigeria. Water Supply 21(7):3356–3369
John CK, Pu JH, Moruzzi R, Pandey M (2021b) Health-risk assessment for roof-harvested rainwater via QMRA in Ikorodu area, Lagos, Nigeria. J Water Climate Change 12(6): 2479–2494
Karna N, Hari Prasad KS, Giri S, Lodhi AS (2015) Effect of fine sediments on river hydraulics–a research review. ISH J Hydraul Eng 21(2):151–161
Lu N, Griffiths DV (2004) Profiles of steady-state suction stress in unsaturated soils. J Geotech Geoenviron 130(10):1063–1076
Maiti R (2008) Land-claim and embankment breaching – a case study along the Raimongal, Sundarban. Conference proceedings DRS PROJECT on "Changing scenario of deltaic environment" Dept. of Geography, University of Calcutta, pp 84–88
Manna S, Chaudhuri K, Bhattacharyya S, Bhattacharyya M (2010) Dynamics of Sundarban estuarine ecosystem: eutrophication induced threat to mangroves. Saline Syst 6(1):1–16
Mukhopādhyā□a Ś (1981) A focus on Sundarban. Editions Indian, Calcutta
Nezu I, Nakagawa H (1993) In: Balkema AA (ed) Turbulence in open-channel flows. CRC Press, Rotterdam
Pandey M, Oliveto G, Pu JH, Sharma PK, Ojha CSP (2020a) Pier scour prediction in non-uniform gravel beds. Water 12(6):1696
Pandey M, Zakwan M, Khan MA, Bhave S (2020b) Development of scour around a circular pier and its modelling using genetic algorithm. Water Supply 20(8):3358–3367
Payo A, Mukhopadhyay A, Hazra S, Ghosh T, Ghosh S, Brown S, Nicholls RJ, Bricheno L, Wolf J, Kay S, Lázár AN (2016) Projected changes in area of the Sundarban mangrove forest in Bangladesh due to SLR by 2100. Clim Chang 139(2):279–291
Pu JH, Wallwork JT, Khan M, Pandey M, Pourshahbaz H, Satyanaga A, Hanmaiahgari PR, Gough T (2021) Flood suspended sediment transport: combined modelling from dilute to hyperconcentrated flow. Water 13(3):379
Quartel S, Kroon A, Augustinus PGEF, Van Santen P, Tri NH (2007) Wave attenuation in coastal mangroves in the red River Delta, Vietnam. J Asian Earth Sci 29(4):576–584
Rakshit D, Sarkar SK, Bhattacharya BD, Jonathan MP, Biswas JK, Mondal P, Mitra S (2015) Human-induced ecological changes in western part of Indian Sundarban megadelta: a threat to ecosystem stability. Mar Pollut Bull 99(1–2):186–194
Ravens TM, Gschwend PM (1999) Flume measurements of sediment erodibility in Boston Harbor. J Hydraul Eng 125(10):998–1005
Roy S, Das VK, Debnath K (2019) Characteristics of intermittent turbulent structures for river bank undercut depth increment. Catena 172:356–368

Roy S, Barman K, Das VK, Debnath K, Mazumder BS (2020) Experimental investigation of undercut mechanisms of river bank erosion based on 3D turbulence characteristics. Environ Processes 7(1):341–366

Shankar MS, Pandey M, Shukla AK (2021) Analysis of existing equations for calculating the settling velocity. Water 13(14):1987

Shivashankar M, Pandey M, Zakwan M (2022) Estimation of settling velocity using generalized reduced gradient (GRG) and hybrid generalized reduced gradient–genetic algorithm (hybrid GRG-GA). Acta Geophys:1–11

Simon A, Curini A, Darby SE, Langendoen EJ (2000) Bank and near-bank processes in an incised channel. Geomorphology 35(3–4):193–217

Singh UK, Jamei M, Karbasi M, Malik A, Pandey M (2022) Application of a modern multi-level ensemble approach for the estimation of critical shear stress in cohesive sediment mixture. J Hydrol 607:127549

Wang H, Lee S, Hassan YA, Ruggles AE (2016) Laser-Doppler measurements of the turbulent mixing of two rectangular water jets impinging on a stationary pool. Int J Heat Mass Transf 92: 206–227

World Bank, 2014. Building resilience for sustainable development of the Sundarbans through estuary management, poverty reduction, and biodiversity conservation. World Bank Report No. 88061-IN, p 273

Zhou Y, Nagata K, Sakai Y, Suzuki H, Ito Y, Terashima O, Hayase T (2014) Development of turbulence behind the single square grid. Phys Fluids 26(4):045102

Chapter 8
A Review of Sedimentation on Different Types of Weirs

Vijay Kaushik, Noopur Awasthi, Shailesh Kumar Gupta, Deepak Singh, and Munendra Kumar

Abstract Almost as much as the volume increases from dams, reservoir storage volume declines owing to sedimentation. To support the river systems, storage capacity must be preserved. For increased storage volume, proper sediment control is preferred. One of the hydraulic structures that are frequently employed for water availability or effective water utilization is the weir. The hydrodynamics of the river interrupts these constructions while also preserving water. Additionally heaped up is the river-borne sediment. The review study of sediment transportation on various weir types in diverse applications is presented in this work. Water is elevated to a level of operation from the standpoint of the hydraulic structure to distinguish the height between upstream and downstream water levels. An initial summary of weirs and their wide varieties were presented. The most popular varieties of weirs, including labyrinth weirs, piano key weirs, submerged weirs, and other weirs, are evaluated in terms of their virtues and shortcomings. The review study suggests that the weir's length and height are essential factors in the transportation of silt. The researchers immediately went over the upstream analysis compared to the downstream. The most common types of technical issues that arise in relation to experimental and numerical models include insufficiency of a forecasting system, a minimal conveyance carrying capacity, unspecified flow rate leads, a lack of knowledge regarding water flooding in the lower region.

Keywords Flow modeling · Hydraulic structures · Sediment Transport · River systems · Weirs

V. Kaushik (✉) · N. Awasthi · S. K. Gupta · D. Singh · M. Kumar
Department of Civil Engineering, Delhi Technological University, Delhi, India
e-mail: vijaykaushik_2k20phdce01@dtu.ac.in; noopurawasthi_2k21phdce502@dtu.ac.in; shaileshkumargupta_2k21phdce14@dtu.ac.in; deepak_phd2k18@dtu.ac.in; munendrakumar@dtu.ac.in

M. Pandey et al. (eds.), *River Dynamics and Flood Hazards*, Disaster Resilience and Green Growth, https://doi.org/10.1007/978-981-19-7100-6_8

8.1 Introduction

Sedimentation impacts many aspects of the environment, such as soil erosion, water quality, water supply, flood control, river regulation, reservoir life span, groundwater table, irrigation, navigation, fishing, tourism, etc. Therefore, it has attracted increasing attention from the public and engineers. For example, in a river basin, soil erosion causes the deterioration of ecology and environment and the degradation of agricultural production. Even more seriously, it makes farmland forever useless by reducing the fertility and productivity of the soil. Furthermore, sediment deposited in river channels raises the water level of floods. Therefore, it brings a series of ecological and environmental problems and aggravates flood disasters, not only by the flood itself but also by the sediment carried by the flood. Several hydraulic engineering operations have modified watercourses throughout the world in recent decades. On the other hand, river restrictions and the installation of transverse structures for riverbed stability have profoundly altered the amount and quality of sediment movement (Gurnell et al. 2012). Both physical and numerical studies are required to better understand the patterns of large-scale hydro-morphological processes in vast model regions with transverse features. Because flow and sediment movement in rivers contain complex three-dimensional characteristics, three-dimensional numerical models offer more accurate findings than two-dimensional techniques (Dallmeier et al. 2020). Rapid hydrological systems advancements have led to improved services in aquatic environments (Bunn and Arthington 2002). There have been numerous changes in barrier construction in the marine ecosystems, such as weirs, culverts, and other artificial infrastructures built for various administrative objectives in the river. The dam is a significant engineering measure that develops a tie-up between water and humans. On the other hand, it assists in administrating ecological coherence.

A reservoir is created upstream of the dam due to the river's damming operation. The water removed from the pool is distributed across the surrounding area, which then becomes flooded. This is the first step in the process of constructing a dam. The dam's construction has influenced the river ecosystem's physical and biological changes. Physical changes include floodplain hydrology, channel structure, and sediment motion. Biological consequences include aquatic and floodplain biota induced by natural association (Aamir et al. 2022). The river ecosystem's controlled water flow and movement of sediment are crucial processes for preserving species diversity and varying the sorts of riverine habitats (Bunn and Arthington 2002; Day et al. 2000). The temporally dynamic condition of the hydrologic system is one of the most significant environmental factors in conserving and supporting the riverine ecosystem (John et al. 2021a, b). For instance, floods affect the distribution of plant seeds into new ecosystems (Gurnell et al. 2012; Bhave et al. 2020) and the reallocation of food resources away from floodplains (Pandey et al. 2022). By modifying the presence of primary consumers (such as algae, cyanobacteria, invertebrates, and small vertebrates) and promoting migratory insect and fish movement, floods also assist in re-establishing the food chain (Chaudhuri et al. 2022).

River ecosystems have been primarily affected and modified by anthropogenic impacts to support the rapid expansion of urban infrastructure, agricultural development of water resources, and protect human properties from natural disasters during modern development periods (Erwin 2009; Everard and Moggridge 2012; Foley et al. 2005; Bunn and Arthington 2002). The likelihood of further flood damage was increased due to intensive land use (such as a residential building) in the vicinity of lower land riverine zones. Because of the high population density in the region around the river, there was a pressing need for expanded risk-reduction infrastructure, which led to rapid changes in the river channel's physical ecosystems (Grill et al. 2019). A fast increase in infrastructures, such as dams, weirs, and levees, has resulted in the loss of different aquatic species (Fang et al. 2006), reducing spatio-temporal linkage across physical ecosystems (Pandey et al. 2021; Singh et al. 2022).

8.1.1 Sediment Transportation

The construction of large reservoir dams to channelize sediments minimized effects such as sediment movement, structure, volume, etc. (Fahmy 2015). The river habitats are being artificially divided due to the development of small-structured reservoirs. As part of the investigation into the weirs and their impacts, the concept of "sediment conveyance" is investigated here. It is defined broadly as structures that do not exceed the elevation of the channel banks, where water discharge typically flows continuously over the dam crest, and where water residence times range from minutes to hours. Generally speaking, this type of dam is considered a gravity dam. The impacts of backwater created by various weirs have decreased the flow velocity, stream energy, and sediment deposition. Weirs have reduced water flow even though they differ in shape, size, and purpose (Bos and Wijbenga 1997). Weir's behavior that affects the sediment dynamics is significant due to the amendments such as supply deficit and regime.

8.1.2 Contribution of the Study

The contributions of this study may be broken down into two categories:

- This paper presents a detailed and broad overview of the numerous forms of weirs used in water engineering sciences.
- The second purpose of this research is to investigate and classify the many cutting-edge weirs used in the sediment control procedure.

This review effort adds to problem-specific guidance for tackling water-related modeling difficulties.

8.2 Theoretical Background

8.2.1 Weirs: An Overview

A weir is a small dam built across a river to control the upstream water level. Weirs have been used for ages to control water flow in streams, rivers, and other water bodies. The term "crest" refers to the edge (or surface) over which water flows, while "nappe," the overflowing sheet of water, is another name for it. The weir permits the unrestricted flow of water. At the same time, the nappe discharges are taken into the air (or) the weir gets submerged if the nappe discharge is partly positioned underneath the weir. The computation of discharge in open channels is a complicated operation that needs a significant amount of time and effort (Arvandi et al. 2013). This is because the channel dimensions do not remain equal throughout the channel, and the water flow varies at different points. The role of weir construction is to organize, channelize, and administer the water flow. It acts as a device to estimate the water flow in an open channel.

8.2.2 Types of Weirs

8.2.2.1 Sharp-Crested Weirs

It is widely used in fields such as hydraulics, irrigation, and environmental research, where it is utilized for flow estimate, diversion, and control of water levels (Guan et al. 2014). It may be combined with geometric forms such as rectangular, triangular, cipolletti, circular, and sutro. The flow direction or direct channel perpendicular to the weir length is not affected by the behavior of these sharp-crested weirs in the same way as it is by the behavior of regular weirs. The conventional construction of a sharp-crested weir can be seen in Fig. 8.1. According to Onen and Agaccioglu

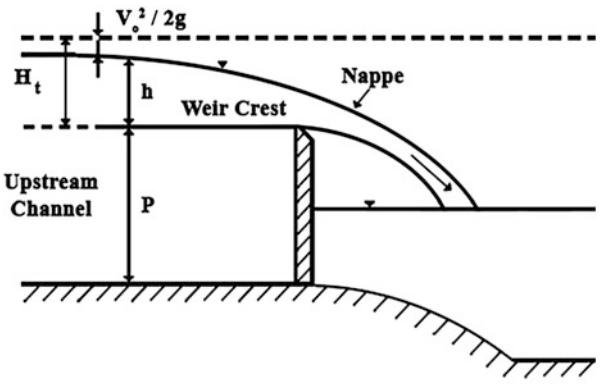

Fig. 8.1 Sharp-crested weir (Kaushik and Kumar 2020)

(2013), sharp-crested weirs may be divided into three distinct varieties, each of which is determined by the channel alignment:

- The axis of the weir is aligned in a perpendicular direction to the channel's axis.
- The axis weir is aligned in a parallel direction to the channel axis.
- The axis of the weir is inclined to the channel axis. This kind of weir is known as a skew weir.

These types have the potential to lengthen the weir, which would result in an increased capacity for discharge flow.

8.2.2.2 Broad-Crested Weirs

The weir depth and flow measurement in a canal system may be controlled using a hydraulic construction known as a broad-crested weir. A flat-crested design is associated with the length of the crest to the depth of flow over the crest (Nguyen et al. 2014). At this point, the peak of the parallel flow grows wider. During this time, the pressure is distributed in a hydrostatic manner. Figure 8.2 illustrates the flow that occurs over the broad-crested weir.

8.2.2.3 Narrow-Crested Weirs

Another kind of weir is known as a narrow-crested weir, and it can be distinguished from other types of weirs by the fact that the height of the water immediately above the weir crest is much higher than the width of the crest of the weir (Bhuiyan et al. 2009). It operates in a manner comparable to a conventional or rectangular weir.

8.3 Non-linear Weirs

This part includes the evaluations of different weirs, from the aspects of merits and demerits.

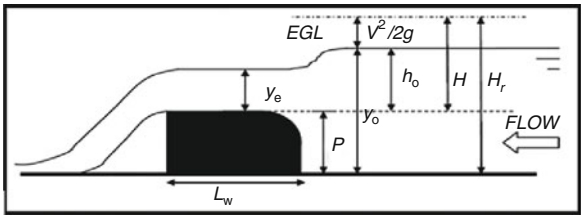

Fig. 8.2 Broad-crested weir (Nguyen et al. 2014)

8.3.1 Labyrinth Weirs

The use of labyrinth weirs to convey sediment has been explored by Herbst (2018). Labyrinth weirs' self-cleaning geometry, discharge, and sedimentation process were all examined in the research. A wide range of scouring circumstances foresaw this possibility. A time-independent scouring procedure investigated four types of sediment: fine quartz sand, fine gravel, medium-grained gravel, and polystyrene granules. Results revealed that sediment mobilization at labyrinth weirs had little effect. Inlet key volume plays a significant role in the sediment process. Researchers used physical models to test two different designs for labyrinth weirs: one rectangular and one trapezoidal. The research was carried out using the Froude number and concluded that threshold settings might forecast the performance of labyrinth weirs.

It was determined whether or not there were any local scour depths in the vicinity of a triangular labyrinth side weir that had been installed in a moveable bed condition (Tunc and Emiroğlu 2018). In the beginning, sediments were laid into the channels to create a movable bed. The parametric research was then conducted for a variety of flow depths, the main channel discharges, volumetric amounts of sediment feed, crest heights, Froude numbers, and flow intensities in both steady and non-steady flow conditions. Flow intensities were also taken into account. It was found that the increases (or reductions) of sediment deposition fluctuate according to the circumstances that are time-variable. A maximum amount of time and scouring pit value were deduced, and both were dependent on the height of the side weir crest. Dizabadi et al. (2020) conducted research on the features of the discharge as well as the flow structure that is seen downstream of labyrinth weirs. The discharge coefficients on weir length and channel width were estimated. Under submerged conditions, the effects of water flow were explored. Then, a contour flow model in 3D velocity components was visualized. The joint probability distribution of different submerged flow conditions has revealed the best solutions for pool-weir fishways (Dizabadi et al. 2020). A triangular labyrinth weir is used in a hydroelectric project, as seen in Fig. 8.3.

8.3.2 Piano Key Weirs

The spillway capacity of dams has expanded, and Piano Key Weirs (PKWs) have increased their scrutiny. PKWs alleviated passage problems during sediment transfer (Seyedjavad et al. 2020). Six discharges, two sediment granulometry, and three PKW configurations were used in an experimental investigation to exacerbate upstream erosion. The passage problem caused by non-cohesive sand was solved entirely by the ramp construction of the PKW weir, in contrast to the labyrinth weirs. It has increased the capacity for self-cleaning.

On the other hand, it did not provide evidence of a widespread sediment bed. PKWs are used to construct most low-head barrages at river power facilities. Even

Fig. 8.3 Triangular Labyrinth Weir (Tunc and Emiroğlu 2018)

though PKWs offer several advantages, including an efficient rating curve and the ability to block driftwood, the mechanical components' examination in various hydraulic situations searches for the best technical protection options for mobile riverbeds. Specifically, an investigation was carried out on the unhindered scour generation and accompanying ridge production brought about by a PKW (Kumar and Ahmad 2021). Alterations were made to the heights of the ridge formation, and several different streamwise orientations were examined. It was discovered that the scour maxima on the outlet and the inlet keys are significant to the process of ridge formation. Researchers looked at the sediment flow on type A PKW inlet keys (Kumar et al. 2021). The amount of upstream bed-shear stress was calculated using an acoustic Doppler velocimeter. Sediment particle motions across the inlet key were studied using a variety of sediment thresholds and regimes. The inclusion of tangential soft beds with particle weight assistance. It was discovered that to increase the effectiveness of sediment movement on the inlet key, shear stress of between 17% and 43% was needed. To support the hydraulically and economically efficient weirs for spillways and rivers, the performance of various shape-based PKWs was examined (Abhash and Pandey 2021). Here, experiments employing discharge and sediment deposit capacity for different geometrical structures were carried out experimentally and numerically. Under free-flow circumstances, rectangular and trapezoidal PKW were modeled, and the vertical components of PKWs have undergone testing. The rectangular PKW was found to be more hydraulically efficient than the trapezoidal PKW.

The pressure and velocity within the channels may guide the turbulence mechanisms. The correlation coefficients of sediment uplift upstream and downstream

Fig. 8.4 Trapezoidal Piano Key Weir (Kumar et al. 2021)

were not discussed at any point in the discussion. The investigation of the flow patterns in trapezoidal piano key side weirs was analyzed by Seyedjavad et al. (2020). PKW is often used to increase the flow discharge capacity that has been researched using weirs having a trapezoidal form. The inflow turbulence was maintained under control by a metal screen that distinguished between the upstream and the downstream. The impacts of hydraulic performance were stabilized based on laboratory standards. The velocity vector was modified by raising the height in the center of the main channel upstream of the weir. However, analysis of the rotational angle and velocity uniformity is required. Singh and Kumar (2022a, b) have provided a concise overview of the hydraulic design and analysis of several PKWs. They have spoken about aeration effectiveness, sediment transportation effectiveness, discharge capacities, and economic factors. Singh and Kumar (2022a, b) conducted an experimental investigation to investigate the energy loss at the base of type-B PKWs in a rectangular channel with free flow. Compared to non-linear or conventional weirs, type-B PKWs have a better energy dissipation efficiency at low heads. Still, this efficiency declines as the discharge or head over the weir grows. The nappe development over the trapezoidal PKW of Terminus Dam is seen in Fig. 8.4.

8.3.3 Submerged Weirs

Wang et al. (2018a) investigated the effects of different upstream circumstances on the local scour that occurs at submerged weirs. A tilting recirculating flume was used for the experimental investigation, which included 24 tests with fine sand and

38 tests with coarse sand. By shortening the weir slope, the upstream weir slope has decreased the scour depth and limited the consequences that have been seen. The study's findings indicated that more robust construction materials are needed for sloping submerged weirs. The research does not, however, focus on the cost of design materials. Local scour at the bridge pier alters the flow pattern and superimposes regions, affecting the downstream of submerged weirs (Wang et al. 2018b). A comparable depth of scouring has mitigated local scour's impacts. Under circumstances of live-bed scour, the submerged weir might, however, dramatically heighten the depth of the pier scour.

The investigation consisted of cutting down on the distance value in the area of upstream scour and increasing the depth of scour at the pier. A significant amount of silt movement is met with the conventional sharp-crested weirs in irrigation canal systems. The water flow upstream has increased the time; thus, it was resolved by half-cosine sharp-crested weirs (Salehi et al. 2019). The experimental examination was done with various weir heights and widths under submerged flow circumstances. Half-cosine weir velocities were measured using an Acoustic Doppler Velocimeter (ADV) probe. Under Fresnel integrals, the velocity variations in half-cosine weirs were modeled. It proved to be effective in removing the sediments than rectangular weirs with lesser sensitivity and higher turbulence capacity.

8.3.4 Numerical Simulations

This part of the paper reviews the work on different weirs using numerical modeling. In order to stop sedimentation from occurring close to the water intake, it is necessary to plan for a time-dependent scouring upstream of a sediment release gate during a flood. Here, a scour volume and depth model based on ordinary differential equations has been investigated (Salehi et al. 2019). Both constant flow circumstances and irregular flow conditions have been tested. The authors have also performed 33 physical scour experiments assessing temporal change of scoured topography, 36 numerical tests using computational fluid dynamics, and 45 scouring inception tests. The sediment supply was observed for various water levels by altering the walls' limits and slits. The ODE-based procedure has outperformed traditional superimposition techniques in 3D numerical simulations. Dallmeier et al. (2020) proposed a 3D modeling morphological structure analysis to quantify the water flow and elevation. Prior 2D modeling was examined to estimate the flow pattern at various morphological modifications with the least amount of computer work. Weirs are included in the hydro-morphological simulations using one of the sediment transport modules called SISYPHE. Upstream and downstream of the conditionalities, the borders were established. It was concluded that the results of the calculations are accurate regardless of the intermediate storage. However, the upstream has a higher bed-load amount than the downstream. The preservation of mass equilibrium is crucial.

8.3.5 Side Weirs

Side weirs are added to establish the flow control pattern in rivers and canals. When the water level increases, the crest is elevated, which leads to improper water flow downstream. It has a significant impact on the side weir's sedimentation process in moveable bed channels (Michelazzo et al. 2016). De Marchi's theory looked into the increased spilled flow during local sediment deposition (Di Bacco and Scorzini 2020). The bed-shear stress and accompanying power were combined to construct Cheezy's law, which described the depth of hydraulic patterns. The design parameters are not investigated, despite the fact that the findings obtained were sufficient for dynamic bed prediction. Weirs with sloped sides were used to study the sediment transfer mechanism (Di Bacco and Scorzini 2020). De Marchi's method identified and modeled the hydraulic and geometric characteristics of inclined side weirs. The sediment capacity may be reduced, and the water loss may impact the deposition on the lateral side. It has been discovered that the weir length was affected by morphological features because of the restricted scour depth downstream.

The removal of the deposited sediments was examined using triangular short-crested weirs. In order to ascertain the degree to which sedimentation influences discharge coefficients, a hydraulics laboratory was outfitted with two unique weir crests and flumes, both of which were tested with and without the presence of horizontal planar sedimentation. The extra velocity profiles have caused errors in synchronization. As a result, the low-head has not produced improved results. To boost the water flow in urban sewage systems, a rectangular side weir is often employed as a flow diversion device (Bhave et al. 2020). With the use of earlier discharge coefficient measurements for the side rectangular sharp-crested weir, a new prediction model was created. The Froude number was regarded as a crucial variable that guaranteed the highest caliber of performance. The discharge coefficient has been impacted by the size and height of the crest in the upstream flow.

8.3.6 Other Weirs

According to Kaushik and Kumar (2020), sediment transport at flow measurement weirs was studied. The discharge coefficients for weirs with 90° triangular, rectangular, and Cipolletti sharp-crested shapes are affected by sediment. According to the investigation, the reduction in discharge coefficient had a favorable impact on sediment movement. Because the flow zone of the rectangular and cipolletti weirs is larger than that of the triangular weir, the fluctuation of the suspended sediment content with the discharge has a bigger influence. Sindelar et al. (2017) conducted a physical model test on run-of-river hydropower facilities to study the impact of weir heights and reservoir expansion during sedimentation. The flushing effectiveness at the reservoir was investigated using weir height as the equilibrium scope. The sediment, geometric, and hydrological characteristics were modeled and analyzed

for the experimental study. The sediment has reduced the effective flow area by 20%. However, the essential factor affecting the flow is the input of sediment.

The river wetlands investigated in four South Korean instances were impacted by the construction of the largest weirs. Two building sites, Nakdong River and Geum River, had their seasonal climates and riverine ecosystems subjected to experimental investigation. The findings showed that the open water surface boosted the sediment and water flow efficiency in the largest weirs built. Because of the permeability and sensitivity of the components, the gabion weir is considered environmentally benign. The majority of flood mitigation systems use it.

The UK's River Nidd's removal of its weir impacts the river systems. Consequently, hydrological characteristics were considered while studying the hydraulics of channels and denitrification (Cisowska and Hutchins 2016). Weirs' existence and absence were investigated in the research. Weir denitrification was first assessed in terms of nutrient flow. Furthermore, confounding variables that deceived weir removal were investigated. This research does not analyze data based on topography. With today's technical advancement, hydrology and hydraulics of surface water are being rethought. Soft computing techniques in river systems are triggered by neurocomputing, a relatively new technology (Zounemat-Kermani et al. 2020). Review studies were undertaken on six water quality problems ranging from surface water bodies to flood risk assessment, sediment transport in river systems to urban water demand forecasting, and hydro-structured flow modeling. The extent of the machine learning and data mining techniques was examined (Zounemat-Kermani et al. 2020). Finally, several suggestions were made in light of the hydraulics soft computing paradigm. Urbanization in Korea has altered the usage of the area, subjected to removing unwanted weirs (Kumar et al. 2021). Simulated physical habitats were investigated for the community of macroinvertebrates. Utilizing River 2D modeling, it was examined. Composite Suitability Index (CSI) was estimated to define the changes happening in the habitat for the target functional habit groups (FHGs).

8.4 Research Gaps

The following are the common technical challenges that have been identified from previous research assessments on a variety of weirs used in a range of applications:

8.4.1 Low Conveyance Carrying Capacity

The river's carrying capacity has been diminished over time due to silt transportation along river channels, which waves and unfinished flood embankments have caused. Numerous applications have investigated various numerical and mathematical flow simulation and sediment movement methods. Some hydraulic systems, such as open

and meandering channels, depending on the stream channel. The weir's depth, breadth, velocity, and suspended load are used to estimate these channel flows. The velocity rises with increases in downstream depth by reducing the weir slope. The ability of the channel's enhanced downstream velocity is delayed by the particle size. It suggests that a more complicated interplay between several elements governs the mean velocity in a particular reach rather than being only determined by the size of the particles that must be delivered.

8.4.2 Uncertain Discharge Leads

Because of the variable flow rate from the dam, the dam authority has trouble performing its numerous maintenance tasks. It is vital to identify areas that are at risk of flooding since these torrential downpours might lead to disastrous floods and waterlogging farther downstream. These include completely or partially submerged weirs located in rivers, coastal regions, and estuaries. These weirs were built to regulate the flow of water, exchange information with one another, and disrupt the water's natural flow. The hydraulic structures may be divided up into the following groups:

- those that hold back water on dams and,
- those that communicate water via channels, spillways, and pipes,
- disrupting water-related systems, including irrigation, fishways, and water intakes.

The procedures for designing, controlling, and restoring hydraulic structures need precise and quick flow modeling. Numerous researchers have started multiple sophisticated computer processes and soft computing techniques. In open channel flow, various input parameters are being used, such as relative roughness, Froude number, and other friction variables. Vent air may also be found in various gate openings for embankment dams. Triangular arced labyrinth weirs have produced the most significant results compared to all other weirs.

8.4.3 Lack of Knowledge on Flooding in the Lower Region

One of the potentially dangerous effects of hurricane activity is flooding along the coast. It is necessary to investigate and produce flood risk elements in order to build coastal flood maps that specify the water level analysis. It is essential to accurately assess the gravity of the water damage caused by the height of the flood. Maximum water elevation (MWE) is a measurement that takes into consideration storm surges, tides, wind waves, river flow, and an estimate of rainfall based on the water levels. Other factors that might affect MWE include wind waves. In addition, the characteristics of peak storm surges include the characteristics of wind speed, storm size,

landfall, geometry, and other topography that is encountered. These qualities are all experienced.

8.4.4 Lack of Forecasting System

Recent research in the fields of surface water hydrology and hydraulics has impressed scientists from all angles. Several topics include river engineering, hydrogeology, hydrometeorology, water resources management, and hydraulics. The primary research studies are:

- Forecasting the water levels in different weirs.
- Modeling, mapping, and risk assessment of various weirs.
- Modeling sediment transport in river systems.
- Forecasting the water demand concerning different weirs.
- Flow modeling through different hydraulic weir structures.

Non-linear processes keep track of the hydrodynamics of weirs, for instance, wetlands, reservoirs, rivers, and seas. It requires forecasting using numerical simulations. The investigation of physical and topographical data and the hydrological conditions for various weirs is fine-tuned regardless of the amount of processing time available. Several different kinds of research have been conducted to monitor, quantify, and control the effects of hydrological factors including climate, evaporation, transportation, and changing water levels on the environment. Underwater quality factors' impact on sediments and sediment drying are unknown. While highlighting the importance of water level evaluations, the best time must be chosen to gather sediment information for all applications. For example, control operations and peak mitigation call for a short-term projection, whereas navigation planning calls for a long-term estimate.

In general, sediments in a fast-moving flow may be exposed to turbulence, which is then carried in suspension. The sink/weir holds the suspended sediments, which gets deposited on the riverbeds and reduces flow. The analysis of suspended sediment concentration (SSC) is related to the dynamics of streamflow. The research of SSC may differ depending on its scope and other elements like hysteresis, seasonality, etc. In a storm, the stream contributes a lot more silt. Furthermore, there is no consideration of the steady-state flow conditions between streamflow and SSC. It will continue to be challenging to forecast.

8.5 Conclusion

A historical data series and high-quality parameters are necessary for hydrodynamics approaches to provide outstanding results. The modeling of sediment flow has only been the focus of a few pieces of study to this point. Experimentally and numerically

based models have been used in many of the research projects that have been carried out to ascertain the capabilities of a wide variety of weirs. To begin, experimental models for hydrological forecasting, namely the prediction of flow through hydraulic infrastructure, are subject to certain limitations. These limitations were established. Second, the majority of the works that have been published have used the conventional style of weir structures for a broad range of applications across their respective bodies of work.

As a consequence, academics still have a considerable amount of area to investigate this specific topic in the framework of numerical modeling and soft computing models. In general, efficient monitoring of the sediment process is necessary in order to give support for applications and to solve concerns that are connected to hydrology and hydraulics. This is because effectively monitoring the sediment process is essential to prevent sediment contamination. The restricted carrying capacity of the conveyance, the unpredictability of the discharge rates, and the absence of information on water encroachment in the lower area, as well as the forecasting system, are all sources of future research.

References

Aamir M, Ahmad Z, Pandey M, Khan MA, Aldrees A, Mohamed A (2022) The effect of rough rigid apron on scour downstream of sluice gates. Water 14(14):2223. https://doi.org/10.3390/w14142223

Abhash A, Pandey KK (2021) Experimental and numerical study of discharge capacity and sediment profile upstream of piano key weirs with different plan geometries. Water Resour Manag 35:1529. https://doi.org/10.1007/s11269-021-02800-y

Arvandi S, Khosrojerdi A, Rostami M, Baser H (2013) Simulation of interaction of side weir overflows with bed-load transport and bed morphology in a channel (SSIIM2.0). Int J Water Resour Environ Eng 5(5):255–261. https://doi.org/10.5897/IJWREE12.124

Bhave S, Kumar S, Singh UK, Pandey M, Ahmad Z (2020) Experimental investigation of a trench weir with T-shaped bars. J Braz Soc Mech Sci Eng 42(10):1–17

Bhuiyan F, Hey RD, Wormleaton PR (2009) Effects of vanes and W-weir on sediment transport in meandering channels. J Hydraul Eng 135(5):339–349. https://doi.org/10.1061/(asce)0733-9429(2009)135:5(339)

Bos MG, Wijbenga JHA (1997) Passage of sediment through flumes and over weirs. Irrig Drain Syst 11(1):29–39. https://doi.org/10.1023/a:1005752711183

Bunn SE, Arthington AH (2002) Basic principles and ecological consequences of altered flow regimes for aquatic biodiversity. Environ Manag 30:492–507. https://doi.org/10.1007/s00267-002-2737-0

Chaudhuri S, Pandey M, Debnath K, Oliveto G (2022) A comparative study on equilibrium scour volume around circular cylinders in clay-sand mixed cohesive beds, at near threshold velocity of sand–an experimental approach. Water Supply 22:6777. https://doi.org/10.2166/ws.2022.250

Cisowska I, Hutchins MG (2016) The effect of weirs on nutrient concentrations. Sci Total Environ 542:997–1003. https://doi.org/10.1016/j.scitotenv.2015.10.064

Dallmeier A, Reisenbüchler M, Bui MD, Rutschmann P (2020) Numerical modelling of sediment transport at weirs. TELEMAC User Conference, pp 9–13. https://hdl.handle.net/20.500.11970/107446

Day JW, Britsch LD, Hawes SR, Shaffer GP, Reed DJ, Cahoon D (2000) Pattern and process of land loss in the Mississippi Delta: a spatial and temporal analysis of wetland habitat change. Estuaries 23:425–438. https://doi.org/10.2307/1353136

Di Bacco M, Scorzini A (2020) Experimental analysis on sediment transport phenomena in channels equipped with inclined side weirs. 8th IAHR international symposium on hydraulic structures ISHS2020. https://doi.org/10.14264/uql.2020.585

Dizabadi S, Hakim SS, Azimi AH (2020) Discharge characteristics and structure of flow in labyrinth weirs with a downstream pool. Flow Meas Instrum 71:101683. https://doi.org/10.1016/j.flowmeasinst.2019.101683

Erwin KL (2009) Wetlands and global climate change: the role of wetland restoration in a changing world. Wetl Ecol Manag 17:71. https://doi.org/10.1007/s11273-008-9119-1

Everard M, Moggridge HL (2012) Rediscovering the value of urban rivers. Urban Ecosyst 15:293–314. https://doi.org/10.1007/s11252-011-0174-7

Fahmy MR (2015) Effect of sediment deposition on the efficiency of Fayoum weir. Flow Meas Instrum 46:133–138. https://doi.org/10.1016/j.flowmeasinst.2015.10.015

Fang J, Wang Z, Zhao S, Li Y, Tang Z, Yu D, Ni L, Liu H, Xie P, Da L, Li Z, Zheng C (2006) Biodiversity changes in the lakes of the Central Yangtze. Front Ecol Environ 4:369–377

Foley JA, DeFries R, Asner GP, Barford C, Bonan G, Carpenter SR, Chapin FS, Coe MT, Daily GC, Gibbs HK, Helkowski JH, Holloway T, Howard EA, Kucharik CJ, Monfreda C, Patz JA, Prentice IC, Ramankutty N, Snyder PK (2005) Global consequences of land use. Science 309:570–574. https://doi.org/10.1126/science.1111772

Grill G, Lehner B, Thieme M, Geenen B, Tickner D, Antonelli F, Babu S, Borrelli P, Cheng L, Crochetiere H, Macedo HE, Filgueiras R, Goichot M, Higgins J, Hogan Z, Lip B, McClain ME, Meng J, Mulligan M, Nilsson C, Olden JD, Opperman JJ, Petry P, Liermann CR, Sáenz L, Salinas-Rodríguez S, Schelle P, Schmitt RJP, Snider J, Tan F, Tockner K, Valdujo PH, van Soesbergen A, Zarfl C (2019) Mapping the world's free-flowing rivers. Nature 569:215–221. https://doi.org/10.1038/s41586-019-1111-9

Guan D, Melville BW, Friedrich H (2014) A preliminary study on scour at submerged weirs in live bed conditions. Taylor & Francis Group, pp 1401–1406

Gurnell AM, Bertoldi W, Corenblit D (2012) Changing river channels: the roles of hydrological processes, plants and pioneer fluvial landforms in humid temperate, mixed load, gravel bed rivers. Earth-Sci Rev 111:129–141. https://doi.org/10.1016/j.earscirev.2011.11.005

Herbst J (2018) Sediment transport over labyrinth weirs. Daniel Bung, Blake Tullis, 7th IAHR international symposium on hydraulic structures, Aachen, Germany, 15–18 May. https://doi.org/10.15142/T3XP91

John CK, Pu JH, Pandey M, Hanmaiahgari PR (2021a) Sediment deposition within rainwater: case study comparison of four different sites in Ikorodu, Nigeria. Fluids 6(3):124

John CK, Pu JH, Moruzzi R, Pandey M (2021b) Health-risk assessment for roof-harvested rainwater via QMRA in Ikorodu area, Lagos, Nigeria. J Water Climate Change 12(6):2479–2494

Kaushik V, Kumar M (2020) Analysis of the sediment laden flows by flow measuring weirs. Int J Adv Sci Technol 29(8):3040–3048

Kumar B, Ahmad Z (2021) Scour downstream of PK weir with and without solid apron. J Irrig Drain Eng 148(1):1–12. https://doi.org/10.1061/(ASCE)IR.1943-4774.0001647

Kumar B, Kadia S, Ahmad Z (2021) Sediment movement over type a piano key weirs. J Irrig Drain Eng 147(6). https://doi.org/10.1061/(ASCE)IR.1943-4774.0001561

Michelazzo G, Minatti L, Paris E, Solari L (2016) Side weir flow on a movable bed. J Hydraul Eng 142(6):04016007. https://doi.org/10.1061/(asce)hy.1943-7900.0001128

Nguyen VT, Moreno CS, Lyu S (2014) Numerical simulation of sediment transport and bedmorphology around Gangjeong weir on Nakdong River. KSCE J Civ Eng 19(7):2291–2297. https://doi.org/10.1007/s12205-014-1255-y

Onen F, Agaccioglu H (2013) Live bed scour at a side-weir intersection located on an Alluvial Channel. Irrig Drain. https://doi.org/10.1002/ird.1749

Pandey M, Jamei M, Karbasi M, Ahmadianfar I, Chu X (2021) Prediction of maximum scour depth near spur dikes in uniform bed sediment using stacked generalization ensemble tree-based frameworks. J Irrig Drain Eng 147(11):04021050

Pandey M, Pu JH, Pourshahbaz H, Khan MA (2022) Reduction of scour around circular piers using collars. J Flood Risk Manag 15:e12812. https://doi.org/10.1111/jfr3.12812

Salehi S, Esmaili K, Azimi AH (2019) Mean velocity and turbulent characteristics of flow over half-cycle cosine sharp-crested weirs. Flow Meas Instrum 66:99–110. https://doi.org/10.1016/j.flowmeasinst.2019.02.002

Seyedjavad M, Naeeni SO, Saneie M (2020) Flow velocity pattern around trapezoidal piano key side weirs. Flow Meas Instrum 76:101847. https://doi.org/10.1016/j.flowmeasinst.2020.101847

Sindelar C, Schobesberger J, Habersack H (2017) Effects of weir height and reservoir widening on sediment continuity at run-of-river hydropower plants in gravel bed rivers. Geomorphology 291:106–115. https://doi.org/10.1016/j.geomorph.2016.07.007

Singh D, Kumar M (2022a) Energy dissipation of flow over the type-B piano key weir. Flow Meas Instrum 83:102109. https://doi.org/10.1016/j.flowmeasinst.2021.102109

Singh D, Kumar M (2022b) Hydraulic design and analysis of piano key weirs: a review. Arab J Sci Eng 47:5093–5107. https://doi.org/10.1007/s13369-021-06370-4

Singh UK, Jamei M, Karbasi M, Malik A, Pandey M (2022) Application of a modern multi-level ensemble approach for the estimation of critical shear stress in cohesive sediment mixture. J Hydrol 607:127549

Tunc M, Emiroğlu ME (2018) Investigation of live-bed scour at labyrinth side weirs. Turk J Sci Technol 13(1):129–136

Wang L, Melville BW, Guan D (2018a) Effects of upstream weir slope on local scour at submerged weirs. J Hydraul Eng 144(3):04018002. https://doi.org/10.1061/(asce)hy.1943-7900.0001431

Wang L, Melville BW, Whittaker CN, Guan D (2018b) Effects of a downstream submerged weir on local scour at bridge piers. J Hydro Environ Res 20:101–109. https://doi.org/10.1016/j.jher.2018.06.001

Zounemat-Kermani M, Matta E, Cominola A, Xia X, Zhang Q, Liang Q, Hinkelmann R (2020) Neurocomputing in surface water hydrology and hydraulics: a review of two decades retrospective, current status and future prospects. J Hydrol 588:125085. https://doi.org/10.1016/j.jhydrol.2020.125085

Chapter 9
A Review on Parametric Studies of Piano Key Weir

Binit Kumar, Eqbal Hassan, and Manish Pandey

Abstract A Piano key weir (PKW) is a modern type of spillway that is used to improve the discharge capacity of dams. The ongoing work on this complex structure is very challenging nowadays for engineers and researchers all over the world. Regardless of this, several prototypes have been successfully installed over the years to enhance the discharge capacity of existing dams. For better understanding the analysis of flow hydraulics and its effects near and over the weir has been studied in this chapter. The present study deals with the effect of different shapes and sizes of PKW on the discharge capacity, variation in scours pattern downstream of the PKW (with or without apron), energy dissipation across the PKW from different techniques, and analyzing it from the channel bed slopes. Numerous numbers of experiments and modeling techniques have been encapsulated in this chapter. This chapter aims to present fundamental outcomes from various experimental studies on different performances carried out on PKW over the years. Here, this chapter discusses some of the analyses from various works that have been done in past either numerically or experimentally so that the reader gets ample knowledge while conducting research in this field. Furthermore, the chapter highlights the significant results and identifies some research gaps that have not been conducted earlier.

Keywords Discharge coefficient · Solid apron · Scour holes · Energy dissipator · Residual energy GEP technique

9.1 Introduction

With the current climate change, the magnitudes of storm events increased which may threaten the safety of existing dams. Many spillways are currently considered undersized and need replacement or proper rehabilitation. Increasing the crest's

B. Kumar (✉) · E. Hassan · M. Pandey
Department of Civil Engineering, National Institute of Technology Warangal, Warangal, Telangana, India
e-mail: ehce21413@student.nitw.ac.in; mpandey@nitw.ac.in

M. Pandey et al. (eds.), *River Dynamics and Flood Hazards*, Disaster Resilience and Green Growth, https://doi.org/10.1007/978-981-19-7100-6_9

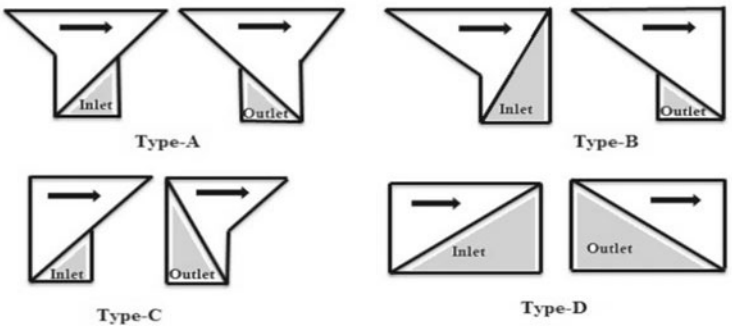

Fig. 9.1 Different types of PKW

Fig. 9.2 3D view of type A PKW model

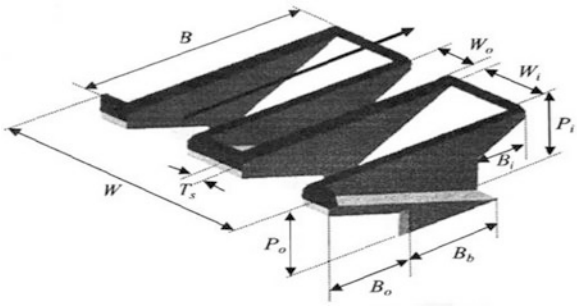

length of a linear weir to increase its discharge capacity is considered an impractical solution due to the limitations of the dam's geometry and other economic reasons. A PKW is a newly designed and one of the types of labyrinth hydraulic structure which is generally placed transverse to rivers. Here the mouth of the weir is alternatively sloped inward and outward of the reservoir and required a small space for its construction. It was first developed by and Ouamane and Lempérière in 2003. A PKW can be classified into four types (Types—A, B, C, and D) as shown in Fig. 9.1, 3D view of type A and plan view and cross-sectional view of PKW are shown in Fig. 9.2, and Fig. 9.3, respectively.

Over the years many studies have been carried out to study the various parameters influencing the performance of PKWs. The main purpose of this chapter is to summarize the information that is available to date. The hydraulic behavior or performance of the PKW depends upon the flow characteristics and its behavior. Many experiments were performed using different inputs to check the coefficient of discharge of the weir. Ghanbari and Heidarnejad (2020) found that the discharge capacity reduced when there was a high hydraulic load upstream of the weir and increasing in the slopes of both inlets and outlets of the weir. However, the discharge capacity increases when the weir length increases and by increasing the (B/w) and lower values of (A/w); Sangsefidi et al. (2021) and conducting different (Wi/Wo) to predict the larger discharge capacity and the greater flow efficiency (Bekheet et al.

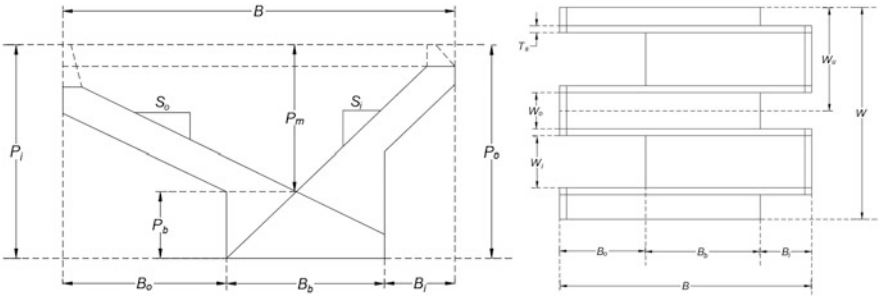

Fig. 9.3 Plan view (left) and cross-sectional view (right) of PKW

2022). Chahartaghi et al. (2019) studied that on increasing the surface of the inlet keys, there is a sudden reduction of velocity inside the keys, and the possibility of the flow being directed into all crest segments.

Scouring downstream of the weir is one of the major issues in the present time. For scouring downstream of the weir, numerous experiments were conducted on scour patterns, and scour holes by different researchers with or without the apron. Kumar and Ahmad (2020) found that there is non-uniformity in the scouring pattern without a solid apron and the scour depth was reduced with proper installation of a solid apron and no scouring effect was observed in high submergence conditions. Moreover, the formation of scour-hole depth depends upon the geometry and type of the weir (Yazdi et al. 2021).

An energy dissipator such as stilling basin, chutes must be installed downstream of the weir to prevent scouring, as it is known that the PKW has a higher discharge capacity, therefore energy dissipation technique is a must, and experiments were conducted with different configurations to opt the most efficient one. To find the energy dissipation, Singh and Kumar (2022a, b, c) conducted a Gene Expression Programming (GEP) technique, which is used to measure the residual energy downstream of the weir and the residual energy highly depends upon the input parameters such as (L/W, B_i/B_o, etc.) and the hydraulic load and inlet-outlet width ratio of the weir (Eslinger and Crookston 2020).

Several attempts were conducted to understand the different performances of the weir, but it can be seen some areas are being left out while conducting the experiments; this includes the shape and sizes of the weir, unique design, aeration, fluid–structure interaction, 3D flow and sediment movement, etc. Hence if these areas will be covered later, it will help to enhance the performance of PKW even better with more accuracy.

9.2 Experimental Setups

The experimental setups carried out by researchers over the past years on basis of their study areas have been displayed in Table 9.1.

9.3 Effect of Flow over PKW

The flow behavior and characteristics in the upstream and downstream of various hydraulic structures facilitate us to design the most economic and efficient structures. Here, PKW is an alternative hydraulic structure with a high discharge capacity that has been discussed in this chapter. It has two important components: inlet key and outlet key (Ouamane and Lempérière 2003; Machiels et al. 2011). Sangsefidi et al. (2021) suggested that the headwater ratio (Ho/P), length magnification ratio (B/w) and apex ratio (A/w) has a significant role in the flow behavior of PKW. The performance of PKW can also be impacted by flow contraction and recirculation zone in the inlet keys and the performance increases with higher values of (H_o/P, B/w, and A/w).

It is found that the discharge capacity of PKW reduces by increasing the upstream hydraulic loads of the weir and the discharge coefficient (C_d) of PKW of triangular type has been found more as compared to PKW of rectangular type (Ghanbari and Heidarnejad 2020). The discharge coefficient can be calculated using the following:

$$Q = \frac{2}{3} C_d \sqrt{2g} L H_t^{\frac{3}{2}} \tag{9.1}$$

And the discharge according to Mehboudi et al. (2016) over the PKW is a function of the following parameters:

$$Q = f\,(W, H, L, B, P, W_i, W_o, B_i, B_o, B_b, T_s, g) \tag{9.2}$$

Again, in some of the research papers, it is found that the width ratio of inlet key (W_i) to outlet key (W_o) gives maximum flow performance of PKW when W_i/W_o is 1.25 as it provides larger discharge which is around 30% more efficient as compared to weir configuration with lower heads (Bekheet et al. 2022). Mero et al. (2022) recommended to avoid using a ratio of Wi/Wo less than 1 and higher than 1.5 in the design of PKW. However, in case of a higher number of PK weir units the W_i/W_o ratio of 1 is the preferable approach for best design as per performance interest (Machiels et al. 2009), but according to Mehboudi et al. (2016), the C_d values were influenced mostly by (L/W). Le et al. (2021) found that the maximum and average discharge efficiencies of PKW as compared to the rectangular weir(RL) is nearly about 6% larger (for $0.3 \leq H/P \leq 0.75$). Moreover, the discharge capacity of the RL

Table 9.1 Details of experimental setups

Author	Flume type and dimension (m^3)	PKW types	Velocity measurement	Results and observations
Tiwari and Sharma (2017)	Tilting flume (open channel) (20 × 2.6 × 1)	Rectangular (type A, type B, type C)	LDV (Laser Doppler velocimeter) Measured at 20 c/s	Type C is more feasible
Bekheet et al. (2022)	Tilting flume(rectangular) (13.5 × 0.3 × 0.5)	Rectangular, trapezoidal, and triangular (Type A, B, C)	MaxiFLo electromagnetic flowmeter	ηtrapezoidal > ηrectangular > ηtriangular ($W_i/W_o = 0.8$) ηtrapezoidal > ηrectangular > ($W_i/W_o = 1.25$), where (W_i/W_o) is the inlet/outlet key width ratio, Type B shows the higher efficiency than Type A
Ghanbari and Heidarnejad (2020)	Rectangular (12.5 × 0.3 × 0.2)	Rectangular and triangular		Flow coefficient(triangular) > flow coefficient (rectangular) with w/p =4.54 flow coefficient of triangular is found 36% greater as compared with rectangular Triangular PKW with 6.7 cm height experience has a maximum flow ratio
Kumar et al. (2021)	Rectangular (15 × 0.39 × 0.5)	Rectangular (1-cycle, 2-cycle, and 3-cycle)	Ultrasonic flowmeter	Max particle velocity (1-cycle>2-cycle>3-cycle), CFD shows a rapid increase in shear stress at the key end
Singh and Kumar (2022a, b, c)	Rectangular (10 × 0.506 × 0.6), testing width = 0.3 m	PKW Type B with 12 parametric configurations	Electromagnetic flowmeter	PKW-B shows higher energy dissipation efficiency at low heads as compared to other weirs, energy dissipation efficiency decreases with an increase in magnification ratio and relative width ratio, and it increases with an increasing number of cycles

(continued)

Table 9.1 (continued)

Author	Flume type and dimension (m^3)	PKW types	Velocity measurement	Results and observations
Kumar and Singh (2022)	Rectangular (10 × 0.506 × 0.6), testing width = 0.3 m	Type A, Type B, Type C	Electromagnetic flowmeter	When $H_t/P < 0.18$, results in a large difference in relative energy dissipation and it decreases with an increase in H_t/P Type A>Type B>Type C (energy dissipation)
Kumar and Ahmad (2020)	Tilting flume rectangular (15 × 0.39 × 0.50)	3-cycle PKW	Ultrasonic flowmeter	Scour depth reduces due to the installation of a solid apron downstream of the weir No scour depth was observed for submerged condition Maximum scour depth was observed at 80% of weir height
Eslinger and Crookston (2020)	Two Rectangular flume (14.63 × 1.23 × 0.91) and (7.32 × 0.93 × 0.61)	Type A with ($W_i/W_o = 1$, 1.25, 1.5, 1.28)	Electromagnetic flowmeter	At a range $0.2 \leq H/P <\leq 0.8$ an effect of energy dissipation was seen but when $H/P \leq 0.2$ and $H/P \geq 0.8$ energy dissipation seems to remain constant

weir (relative to PKW) gets reduced, it is due to the interfering nappes flowing over two adjacent sidewall crests.

9.4 Effect of Sediment and Scouring Downstream of PKW

Scouring is one of the major issues downstream of the PKW. In absence of a downstream solid apron or technical dissipation structure, the occurrence of scour can be observed in loose riverbeds downstream of a PKW. Generally, many investigations were carried out by various researchers on the discharge capacity of the weir based on their different geometries, but sparse literatures are available for scouring patterns downstream of PKW. The scouring pattern differs with or without the installation of a solid apron. It was observed that the scouring pattern downstream the weir without apron was not uniform this is basically due to the complex shape of the weir and maximum scour depth develops generally from the jets emerging out from its inlet and outlet keys and the depth increases for higher discharge as compared to lower discharge and further no scour depth was observed in case of high submerged conditions (Kumar and Ahmad 2020), but when the solid apron was introduced downstream of the weir it was observed that a significant reduction in the scour depth and the average reduction in depth was found in the range of 50–80%. Also, sensitivity analysis suggests that the crest length to width of the weir ratio (L/W) of the PK weir and the tailwater depth to the median size of the sediment ratio (y_t/d_{50}) were the main sensible parameters affecting the maximum scouring depth for both with or without apron (Kumar and Ahmad 2021). And the scour can be lowered downstream by installing a deflector at the end of the outlet keys of the PKW.

Yazdi et al. (2021) studied the scour development downstream of the weir with different types of weir geometry and suggested that the scour hole parameters increase with the increase in discharge rate and weir height of PKW, and according to Jüstrich et al. (2016) the scour depth was found to be more in the rectangular model as compared with the trapezoidal model under same discharge.

9.5 Effect of Energy Dissipation Downstream of PKW

A PKW is an alternative to labyrinth weir and has a large discharge capacity due to which a very high energy dissipation took place downstream of the weir and it is highly notable to avoid scouring and cavitation while designing the structure (energy dissipator) downstream the PKW. Researchers conducted several investigations and experiments with a stepped spillway or stilling basin as an energy dissipator. Eslinger and Crookston (2020) proposed two equations which are a function of headwater ratio (H_t/P) and (W_i/W_o) to predict the relative residual energy downstream of the weir to understand the energy dissipation of type A PKW and

compared it with the existing results and observed that at low flow-head, the energy dissipation is the largest and as the flow increases the energy decreases in a logarithmic-like curve.

For better prediction and good accuracy in the estimation of the residual energy, the Gene Expression Programming (GEP) technique has been used to measure the residual energy downstream of the PK weir. This approach highlights a nonlinear relationship between the input parameters (L/W, W_i/W_o, S_i/S_o, H_t/P, B_i/B_o, and N) with great accuracy and less error for type A PKW (Singh and Kumar 2022a, b, c).

Kumar and Singh (2022) found that as the channel bed slope increases the relative energy dissipation of PKW (type A, B, and C) models increases but decreases with higher discharge over the weirs and vice versa, further it was observed that the overall energy dissipation performance was more in PKW type A than in type B and finally in type C. Thus, it concludes that weir geometry has a significant role and highly influenced energy dissipation.

9.6 Conclusion

This chapter highlights several research studies conducted earlier based on their flow characteristics, scouring, and energy dissipation to analyze the performance of PK weir which can be concluded that the flow discharge coefficient C_d depends upon the Wi/Wo on different ratios and 1.25 is the preferable ratio. Moreover, the effect of (L/W) was found to be the highest in terms of efficiency for a given head, weir discharge increases with higher P values. While the discharge value decreases with the increase in hydraulic loads, for values $H/P < 0.1$, $0.1 < H/P < 0.14$, $0.14 < H/P < 0.18$, $0.18 < H/P < 0.35$, and $H/P > 0.35$, the flow regimes were distinguished as clinging nappe, leaping nappe, springing nappe, transition, and submerged, respectively. For scouring, the scour pattern differs with different values of input conducted, it was found that the scour depth reduces when a solid apron was introduced downstream of the weir while the length and depth of the scour were found to be significant when there is a higher discharge and low tailwater depth and no scour depth was observed at submerged conditions. The maximum scours depth under the inlet keys is found to be less than under outlet keys. Thus, the study is helpful for the installation of a proper foundation of PKW on an erodible bed.

While energy dissipation over the PKW increases when the bed slope increases and vice versa for all models. A minor change in the hydraulic load significantly differs in energy and energy dissipation steadily decreases with an increase in hydraulic load, for a small change in bed slope the energy dissipation is found more in type A than in type B and finally in type C. In addition to these, the W_i/W_o affects the energy dissipation in the range of $0.2 \leq H/P \leq 0.8$ and the dissipation of energy decrease with increase in W_i/W_o (as the hydraulic efficiency of the weir increases). Thus, it will be very helpful for engineers in the design of energy dissipative structures downstream of the weir and thereby reducing the scour, length of the apron for the weir, and length of hydraulic jump (Jüstrich et al. 2016).

Finally, it is seen that several attempts were conducted to understand the different performances of the weir, but some areas are being left out while conducting the experiments, this includes arrangements of different shapes and types of the weir, i.e., some works were done only for type A, while some other conducted with type B only, different dimensions of the weir, discharge rate, shape, and size of sediment, etc. Hence, this chapter discusses some of the analyses from various works that have been done in past either numerically or experimentally so that the reader gets ample knowledge while conducting research in this field.

Notations

B	Length of side weir ($B_i + B_b + B_o$)
B_b	Base length
B_i	Length of overhang portions at the inlet side
B_o	Length of overhang portions at the outlet side
E	Specific energy
ΔE	Relative energy dissipation
g	Acceleration of gravity
H_t	Total energy head
h_t	Piezometric head
L	Total developed crest length
N	Number of cycles P PKW height
Q	Discharge over the PKW
S_i	Inlet key slope of PKW
S_o	Outlet key slope of PKW
W	Channel width of PKW
W_i	Inlet key width of PKW
W_o	Outlet key width of PKW
T_s	Wall thickness of PKW

References

Bekheet AA, AboulAtta NM, Saad NY, El-Molla DA (2022) Effect of the shape and type of piano key weirs on the flow efficiency. Ain Shams Eng J 13(3). https://doi.org/10.1016/j.asej.2021.10.015

Eslinger KR, Crookston BM (2020) Energy dissipation of type a piano key weir. Water 12(5):1253. https://doi.org/10.3390/W12051253

Ghanbari R, Heidarnejad M (2020) Experimental and numerical analysis of flow hydraulics in triangular and rectangular piano key weirs. Water Sci 34(1):32–38. https://doi.org/10.1080/11104929.2020.1724649

Jüstrich S, Pfister M, Schlesis AJ (2016) Mobile riverbed scour downstream of a piano key weir. J Hydraul Eng 142(11):1–12. https://doi.org/10.1061/(ASCE)HY.1943-7900.0001189

Karimi Chahartaghi M, Nazari S, MahmoodianShooshtari M (2019) Experimental and numerical simulation of arced trapezoidal piano key weirs. Flow Meas Instrum 68:101576. https://doi.org/10.1016/j.flowmeasinst.2019.101576

Kumar B, Ahmad Z (2020) Experimental study on scour downstream of a piano key weir with nose. Proceedings of the 8th IAHR international symposium on hydraulic structures, ISHS 2020. https://doi.org/10.14264/uql.2020.595

Kumar B, Ahmad Z (2021) Scour Downstream of a Piano Key Weir with and without a Solid Apron. J Irrig Drain Eng 148(1). https://doi.org/10.1061/(ASCE)IR.1943-4774.0001647

Kumar M, Singh D (2022) Effects of channel bed slope on energy dissipation of different types of Piano Key Weir. Int J Civil Archit Eng 16(5)

Kumar B, Kadia S, Ahmad Z (2021) Sediment movement over type a piano key weirs. J Irrig Drain Eng 147(6). https://doi.org/10.1061/(asce)ir.1943-4774.0001561

Le AT, Hiramatsu K, Nishiyama T (2021) Hydraulic comparison between piano key weir and rectangular labyrinth weir. Int J Geomate 20(82):153–160. https://doi.org/10.21660/2021.82.j2106

Machiels O, Erpicum S, Dewals BJ, Archambeau P, Pirotton M (2011) Experimental observation of flow characteristics over a piano key weir. J Hydraul Res 49(3):359–366. https://doi.org/10.1080/00221686.2011.567761

Mehboudi A, Attari J, Hosseini SA (2016) Experimental study of discharge coefficient for trapezoidal piano key weirs. Flow Meas Instrum 50:65–72. https://doi.org/10.1016/j.flowmeasinst.2016.06.005

Mero SK, Haleem DAJ, Yousif AA (2022) The influence of inlet to outlet width ratio on the hydraulic performance of piano key weir(PKW-type A). Water Pract Technol 17:1273. https://doi.org/10.2166/wpt.2022.055

Ouamane A, Lempérière F (2003) The piano keys weir: a new cost-effective solution for spillways. Int J Hydropower Dams 10

Sangsefidi Y, Tavakol-Davani H, Ghodsian M, Mehraein M, Zarei R (2021) Hydrodynamics and free-flow characteristics of piano key weirs with different plan shapes. Water (Switzerland) 13(15):2108. https://doi.org/10.3390/w13152108

Singh D, Kumar M (2022a) Energy dissipation of flow over the type-B piano key weir. Flow Meas Instrum 83:102109. https://doi.org/10.1016/j.flowmeasinst.2021.102109

Singh D, Kumar M (2022b) Hydraulic design and analysis of piano key weirs: a review. Arabian J Sci Eng 47(4):5093–5107. https://doi.org/10.1007/s13369-021-06370-4

Singh D, Kumar M (2022c) Computation of energy dissipation across the type-A piano key weir by using gene expression programming technique. Water Supply 22:6715. https://doi.org/10.2166/ws.2022.255

Tiwari H, Sharma N (2017) Turbulence study in the vicinity of piano key weir: relevance instrumentation parameters and methods. Appl Water Sci 7(2):525–534. https://doi.org/10.1007/s13201-015-0275-1

Yazdi AM, Abbas Hoseini S, Nazari S, Amanian N (2021) Effects of weir geometry on scour development in the downstream of piano key weirs. Water Sci Technol Water Supply 21(1):289–298. https://doi.org/10.2166/ws.2020.272

Chapter 10
Influence of Boundary Condition on the Modified 2D Shallow Water Model near the Flow–Structure Interaction Zone: A Case Study in Brahmaputra River

Anupal Baruah, Arup Kumar Sarma, and Gilbert Hinge

Abstract This work proposes a modified form of two-dimensional shallow water (2D-SWD) equation with water surface gradient at the source term. This modification was carried out as the conventional 2D-SWD equations often require special treatment when applied to complex braided rivers. The modified model is then applied to two different flow domains of the Brahmaputra river viz. at the braided reach near Umananda Island and reach with a series of spurs dyke near Majuli island. The stability of the model is checked using Courant–Friedrichs–Lewy condition. The maximum flow depth in the braided reach is observed as 15–18 m, and near the spur dykes, it is found as 35–37 m. Model simulated flow depth and velocity are compared with the field measured data. The model's computational accuracy near the flow-hydraulic structure interaction zone is evaluated with two different boundary conditions: no slip condition and reflecting boundary condition. Based on root mean square error (RMSE) and Nash–Sutcliffe Efficiency (NSE), the reflection boundary condition shows superior in simulating the velocity profile (RMSE = 0.11, NSE = 0.60) as compared to no slip condition (RMSE = 0.28, NSE = 0.22). These findings suggested that the water surface gradient in the modified 2D-SWD model gives more flexibility for application in the braided river. It also stresses the importance of considering reflecting boundary conditions while applying the model near the fluid–structure interaction region.

Keywords Shallow water equation · Hydraulic structure · Complex topography · Boundary condition · Explicit scheme

A. Baruah · A. K. Sarma
Department of Civil Engineering, Indian Institute of Technology Guwahati, Guwahati, Assam, India

G. Hinge (✉)
Department of Civil Engineering, National Institute of Technology Durgapur, Durgapur, West Bengal, India

M. Pandey et al. (eds.), *River Dynamics and Flood Hazards*, Disaster Resilience and Green Growth, https://doi.org/10.1007/978-981-19-7100-6_10

10.1 Introduction

Hydrological hazards such as flooding due to dam breaks, excess rainfall, and overflowing of rivers cause loss of life and properties (Baruah et al. 2021; Shivashankar et al. 2022; Shankar et al. 2021; Wallwork et al. 2022). Such hazard causes sedimentation and erosion, which can clog the riverbeds and affect the habitat of aquatic life (Chen et al. 2012; Khan et al. 2021, 2022). In recent years, the occurrence rates and intensities of hydrological hazards have aggravated due to climate change and the increasing anthropogenic disturbance of the natural ecosystem (Dutta et al. 2020). Therefore, modeling and prediction of hydrological hazards is crucial for preventing the losses of life and property.

Shallow water depth models (SWD) have been extensively used to solve various complex hydrological events such as flash floods, dam breaks, sediment transport, and many others (Bi et al. 2014; Chen et al. 2012). Depending upon the purpose, one-dimensional (1-D), two-dimensional (2-D), or three-dimensional (3-D) SWD models are used to compute the flow parameters. 1-D models are commonly applied for short- and long-term simulations of flow and sediment transport processes in rivers, reservoirs, and estuaries (Lauer et al. 2016; Kuiry et al. 2010). Whereas, 2-D and 3-D SWD models are used to predict in more detail the morphological processes under complex flow conditions in curved and braided channels and around river training works, bridge piers, spur-dikes, and water intake structures (Turick et al. 2020; Twigt et al. 2009; Wang et al. 2005). Finite difference, finite element, and finite volume are popular numerical methods for solving two-dimensional, unsteady, free-surface flow problems. HEC-RAS, MIKE21C, and CCHE2D are excellent and user-friendly numerical tools that enable the compute of flow parameters such as water depth, velocity, wetted perimeter, and energy gradient in the stream. To date, multiple works (Yalcin 2020; Lai and Kim 2020; Ayaseh et al. 2019; Chen et al. 2003) have been published based on these numerical schemes and tools to solve hydrodynamic problems in the rivers.

The 2D-SWD models, while applying in complex topographic cross-sections, need special treatment in simulations. For instance, in a braided reach, the bed slope variations are considerably high in longitudinal and transverse directions. The model robustness is affected near those regions where the bed profile abruptly changes from shallower to deeper and vice-versa (Pinos and Timbe 2020). The conventional formulation of the SWD models inbuilt in the above-mentioned numerical tools cannot capture this discontinuity in the domains and often lead to an inferior solution (Qin et al. 2018). Several authors have proposed different 2D SWD models to eliminate this problem (Song et al. 2011; Liang and Marche 2009; Begnudelli and Sanders 2007). Among these, the most popular is the pre-balanced shallow water equation derived by Liang and Borthwick (2009). However, this method often produces negative water depth, particularly at the wet/dry fronts (Bi et al. 2014). The present form of the governing equations used in this study uses the water level gradient as the gravitational force component in the source term. The governing

equations are solved by TVD Mc-Cormack predictor–corrector explicit finite difference scheme. The model is applied in two stretches of the Brahmaputra River.

These models are susceptible to the boundary conditions (BCs) and diverge from the actual results at erroneous BC. The execution of proper boundary at the upstream (u/s) and downstream (d/s) in any hydrodynamic modeling is essential for smooth function and stability. Apart from the u/s and d/s boundary, the fluid–structure interaction conditions also influence the flow characteristics (Koken and Constantinescu 2011). For example, the boundary condition applied around the non-permeable solid groin walls affects the nearby regions' momentum fluxes (Baruah and Sarma 2020). Hence in this study, the influence of boundary conditions at the fluid–structure interaction zone is evaluated by integrating the no slip and reflection condition in the model. Two statistical indexes are used during the study to assess the model performance under these different boundary conditions. The present model can also be applied to the braided and meandering streams to investigate the downstream impact of different river training works.

10.2 Hydrodynamic Model

10.2.1 Derivation of the Modified Governing Equation

Two-dimensional depth-averaged non-viscous shallow water equations in boundary fitted coordinate can be expressed as

$$\frac{\partial}{\partial t}[Js] + \frac{\partial}{\partial \xi}[JhU] + \frac{\partial}{\partial \eta}[JhV] = 0 \tag{10.1}$$

$$\frac{\partial}{\partial t}[Jhu] + \frac{\partial}{\partial \xi}[J\{huU\}] + \frac{\partial}{\partial \eta}[J\{huV\}] = -Jgh\left(\frac{ds}{dx} - sfx\right) \tag{10.2}$$

$$\frac{\partial}{\partial t}[Jhv] + \frac{\partial}{\partial \xi}[J\{hUv\}] + \frac{\partial}{\partial \eta}[J\{hVv\}] = = -Jgh\left(\frac{ds}{dy} - sfy\right) \tag{10.3}$$

where s is the water surface elevation (m), hu and hv are the momentum fluxes, $\frac{ds}{\partial x}$ and $\frac{ds}{\partial y}$ are the water surface gradients, delx and dely represent the grid spacing in x- and y-direction, g is the acceleration due to gravity, delt is the time step, h is the flow depth (m), s_{fx} and s_{fy} are the friction slopes, respectively.

For the solution, the two-dimensional equations are spitted into four one-dimensional equation and each equation are solved successively. The predicted flow depth and velocities from the first cycle are used in the corrector part. The TVD variables are added in the unknown time step to reduce the non-physical oscillations (Kalita 2016).

Predictor-

$$K_{i,j}{}^{p} = K_{i,j}{}^{k} - \frac{\Delta t}{\Delta x}\left(F_{i,j} - F_{i,j-1}\right) - \frac{\Delta t}{\Delta y}\left(G_{i,j} - G_{i-1,j}\right) - \Delta t \times S_{i,j} \tag{10.4}$$

Corrector-

$$K_{i,j}{}^{c} = K_{i,j}{}^{k} - \frac{\Delta t}{\Delta x}\left(F_{i,j+1} - F_{i,j}\right)^{p} - \frac{\Delta t}{\Delta y}\left(G_{i+1,j} - G_{i,j}\right)^{p} - \Delta t * S_{i,j}{}^{p} \tag{10.5}$$

$$K_{i,j}{}^{k+1} = \frac{1}{2}\left(K_{i,j}{}^{p} + K_{i,j}{}^{c}\right) + TVD_{i,j} \tag{10.6}$$

The CFL condition (C_r) is used to check the model stability.

$$C_r = \text{delt} \times \left(\left(\text{squareroot}\left(u^2 + v^2\right)\right) + \text{squareroot}\left(g \times h\right)\right) / \min\ (\text{delx, dely}) \tag{10.7}$$

Where the model is found to be stable and convergent when the courant number is less than 1.

10.2.2 Boundary Condition

Flow rate and the water level used as the upstream and downstream boundary and no slip condition is used at the right and left bank. Two different boundary conditions are employed adjacent to the solid groin walls as presented in Fig. 10.1. In the first case the hydraulic structures in the domain are considered as complete rigid and a no slip condition is employed. The velocity vectors near the flow–structure interaction cell points are assigned a null value. For instance, in Fig. 10.1a the velocity at the grid points (i, j) are considered zero during the computation indicating that no momentum flux exchange is taking place at those points.

$$u(i, j) = 0, v(i, j) = 0.$$

However, in the second case, at the same points the deflected water wave phenomenon modelled by considering the reflecting boundary conditions (Fig. 10.1b. The velocity vectors along the streamflow direction are assigned at cell points (i, j).

$u(i,j) = -u(i,j-1)$, $u(i+1,j) = -u(i+1,j-1)$, and the transverse components are.

$$v(i, j) = 0, v(i+1, j) = 0.$$

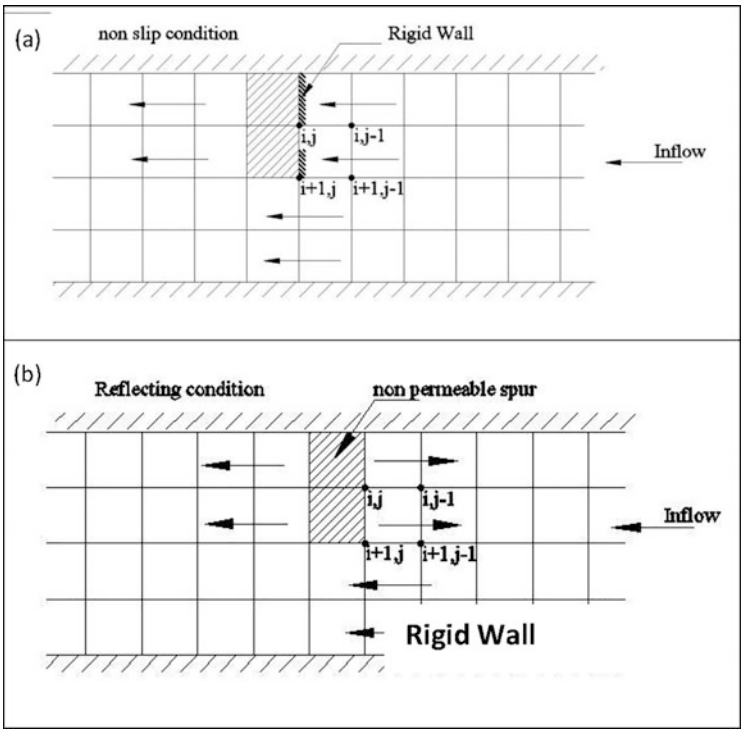

Fig. 10.1 Wall boundary condition near the flow–structure interaction region (**a**) No flow condition (**b**) Reflection boundary condition

10.3 Study Area

10.3.1 Braided Portion in the Brahmaputra River in Guwahati

The hydrodynamic model is calibrated in a 11 km braided portion of Brahmaputra River (Fig. 10.2). The area lies between 91°44′28.51″ E, 26°12′05.91″ N and 91°42′04.45″ E, 26°10′15.64″ N in the Guwahati region. The bed slope in this region is around 0.1 m/km. At the upstream of the flow area, exist a small side channel which is separated from the main channel by a sand-bar (Fig. 10.2a). The bed level and the water surface elevations are measured by an echo sounder and the velocity are measured from a cup type current meter. A discharge of 3000 $\frac{m^3}{s}$ and 20 $\frac{m^3}{s}$ is observed at the main channel and the side channel. The bed level elevation of the domain is presented in Fig. 10.2b.

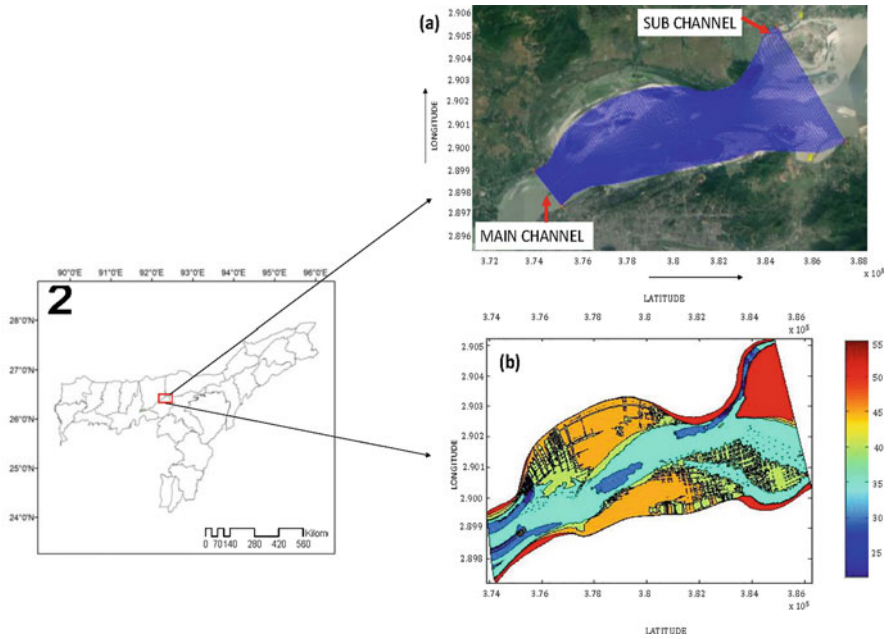

Fig. 10.2 Map of the study area for case 1: (**a**) Generated grid in the computational domain (**b**) bed level elevations(m) in the domain

10.3.2 Domain with a Series of Spurs Dykes near Majuli Island

The model application is further extended to a 3.45 km reach length of Brahmaputra River near Majuli Island, the bed level contours in the flow domain are measured from an echo sounder as shown in Fig. 10.3a, b. The flow velocity is measured using a cup type current meter. Discharge and water level at upstream and downstream are 9847 cumec and 84.14 m.

10.4 Application of the Model

10.4.1 Model Simulation in the Braided Portion near Umananda Island, Guwahati

The hydrodynamic model is calibrated and validated with the observed data collected from different sections. The l time step for each simulation is set as 0.1 s, and the model is run for steady-state condition. A total number of 200 × 400 grid points are generated, as shown in Fig. 10.2a. Initially, upstream discharge of the main and

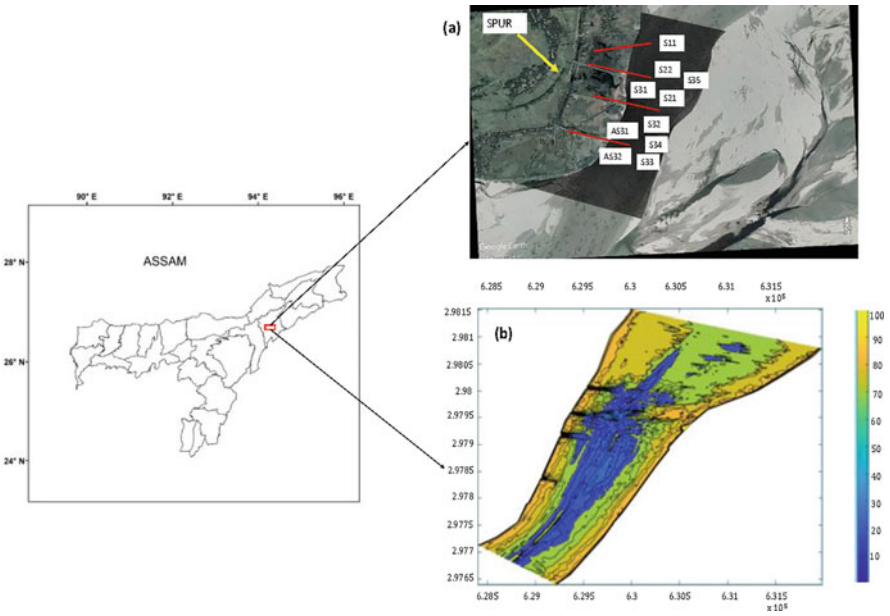

Fig. 10.3 Map of the study area for Case 2: (**a**) Generated grids in the computational domain with the flow measuring points (**b**) Bed level contour

the subchannel is distributed over the discretized domain using a weighing factor method. For instance, in a braided section the bed level undulations prominently affect the discharge distributions and therefore in the numerical model, the uniform distribution of flow discharge at the grid points seems to be erroneous. In order to avoid that, the obtained water stage at the upstream section from the known stage discharge curve is subtracted from the bed profile to calculate the flow depths at the grid points. In general context, more flood water passes through the deeper sections compared to the shallower points in a cross-section. The midchannel points have higher flow depth than the near bank points and depending upon that, the weightage factor is decided for discharge distribution. The unit discharge passes through each cell point is obtained by dividing the weighted discharge with the cell spacing. The sand bars in the braided portions produce negative depth and thus a threshold depth of 0.1 m is considered to classify the dry areas. The grid points with the threshold depth are excluded during the computational run. The CFL criteria are checked at each time step.

10.4.2 Model Simulation around Series of Spurs Dyke in Majuli Island

In the second case, the computational domain has a series of deflecting spurs (S1, S2, S3, and S4) from u/s to d/s located in the Brahmaputra river near Majuli Island. A 60 × 225 number of grid points is generated within the flow area. The time interval for simulation is 0.1 seconds. The computational points with less than 0.1m depth are designated as dry points and excluded from the computations. CFL condition is used to check the model stability. The same methodology is adopted for discharge distribution as mentioned in case 1. The influence of wall boundary conditions near the groins affected regions was assessed using two statistical measurement: Root-mean-square error (RMSE) and Nash–Sutcliffe efficiency (NSE).

1. Root-mean-square error (RMSE)

$$\mathrm{RMSE} = \sqrt{\frac{1}{n}\sum_{i=1}^{n}(p_i - o_i)^2}$$

2. Nash–Sutcliffe efficiency (NSE)

$$\mathrm{NSE} = 1 - \frac{\frac{1}{n}\sum_{i=1}^{n}(p_i - o_i)^2}{\frac{1}{n}\sum_{i=1}^{n}(o_i - \overline{o})^2} \tag{10.8}$$

where o_i is the observed data and p_i is the model predicted data and $\overline{o}$ is the average value of the data series.

10.5 Result and Discussion

10.5.1 Case-1: Model Simulation in the Braided Reach

The computed depth contour is presented in Fig. 10.4a. The Courant number is found to be less than 1 during the simulation. For the given streamflow condition, the maximum flow depth in the main channel is found within 15–18.75 m, and the maximum current speed lies within 2.5–3 m/s. In the subchannel, the maximum flow depth is 12.66 m with a current speed of 0.07–0.1 m/s. At the confluence of the sub and main channel, the flow depth is 0.8–7 m and and the current speed is 0.45–1.2 m/s. Model simulated flow depth and velocity are compared with the field measured data, as shown in Fig. 10.4b, c. A small amount of discrepancy between the computed and observed flow depth is noticed near the deep water regions for the

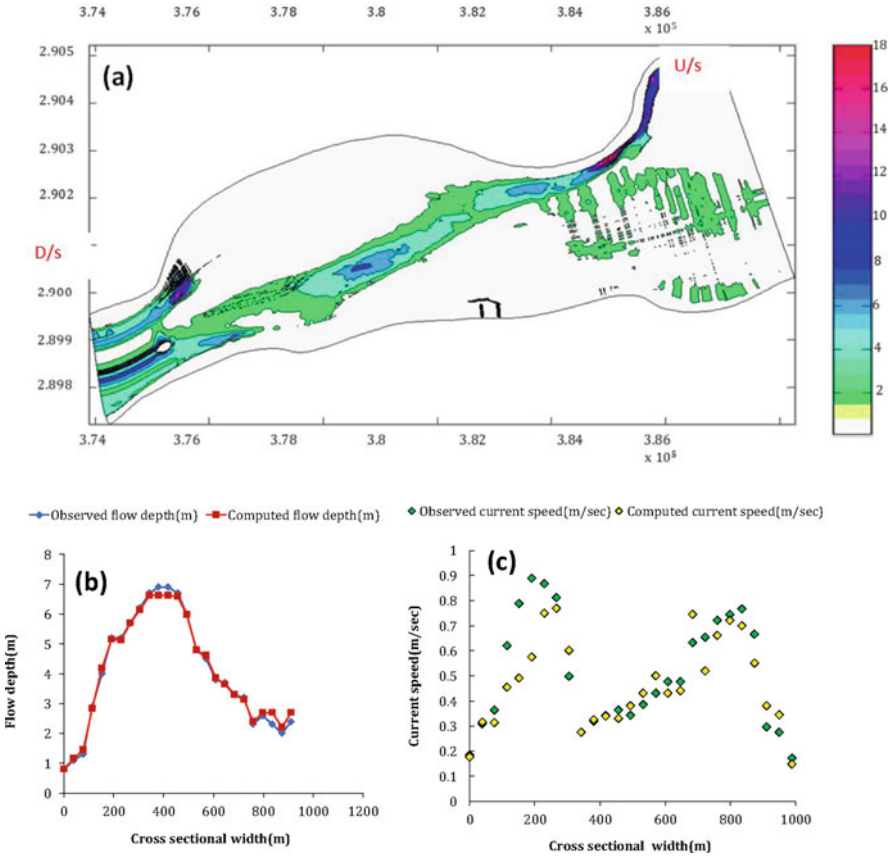

Fig. 10.4 (**a**) Computed flow depth (meter) contour in the braided reach (**b**) Comparison of the computed flow depth with the observed data (**c**) Comparison of the computed current speed with the observed

flow depth. However, a satisfactory agreement is obtained at the rest of the points. While for the velocity profile, the major anomaly between the computed and measured velocity profile (Fig. 10.4c) is found near the maximum observed velocity point. The overall computation error is minimal, which lies within the range of 15–17%. These results suggested the applicability of the modified 2D-SWD in the complex braided reach of the Brahmaputra River.

10.5.2 Case2: Model Simulation around Series of Spurs Dyke in Majuli Island

In the second case, the maximum flow depth is around 30–36 m in the region. The velocity vectors between the spursS2 and S3 are shown in Fig. 10.5b. The numerical model is validated at different flow measurement points in the domain. The results from the simulation and the field observed data are compared in Fig. 10.6a, b. The

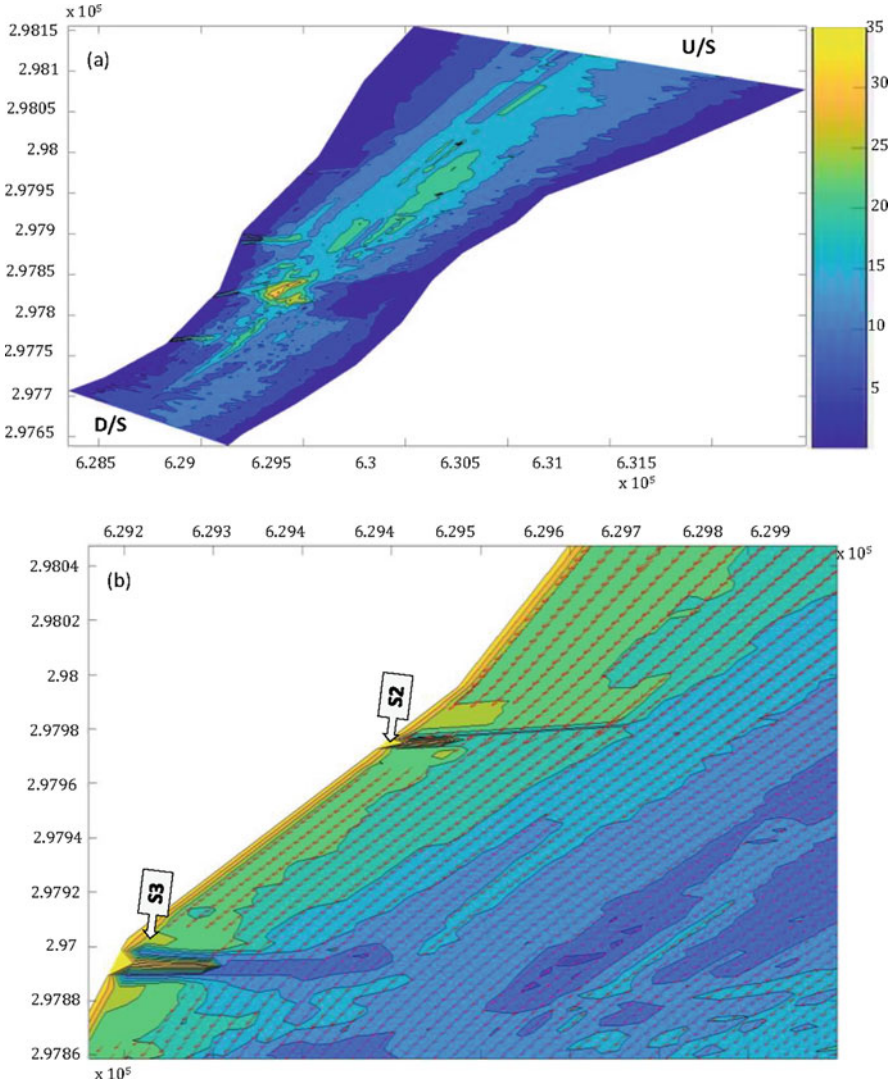

Fig. 10.5 (**a**) Computed flow depth (**b**) Velocity vectors in the flow domain

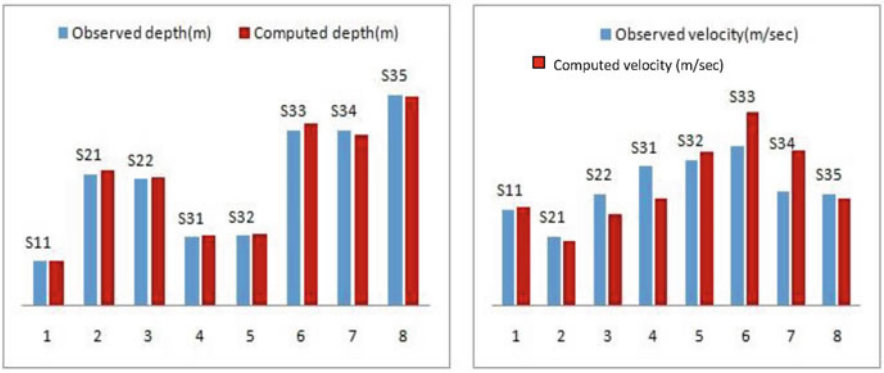

Fig. 10.6 Comparison of the (**a**) computed and observed flow depth (**b**) Comparison of the computed and observed velocity

Table 10.1 Statistical indices for model performance evaluation

Statistical index	Flow depth		Current speed	
	Reflection boundary condition	No slip boundary	Reflection boundary condition	No slip boundary
NSE	0.996	0.991	0.605	0.221
RMSE	0.533	0.825	0.119	0.285

percentage error in velocity computation is found within the range of 8–11%. The influence of wall boundary conditions near the groins affected regions is investigated using two statistical measurements, viz. Nash–Sutcliffe efficiency (NSE) and root-mean-square error (RMSE) (Table 10.1). A very good performance is observed from the model computed flow depth profile (NSE range 0.75–1) with both the boundary conditions. The closer the NSE values to 1, the better are the model performance. On the contrary, a lower RMSE value is found for the computed flow depth profile with the refection boundary condition (RMSE = 0.533) compared to the no slip condition (RMSE = 0.825). Both findings indicate that the variation of the boundary conditions near the fluid–structure interaction zone has less influence on the flow depth profile. However, the current speed in the vicinity of the spur dykes is affected by these boundary conditions. As given in Table 10.1, the reflection boundary condition shows superior in simulating the velocity profile (RMSE = 0.11, NSE = 0.60) compared to the no slip condition (RMSE = 0.28, NSE = 0.22). This is because in a natural flow, the waves got deflected after attacking the spur walls and neighboring regions experience the formation of a mixing layer and a recirculation zone downstream. Incorporating the reflection boundary condition with the numerical models ensures the deflecting wave effects and captures the mixing layer phenomenon near the dyke wall. It is observed that the present model adequately captures the formation of recirculation zone at the d/s of the spur wall due to the wave effect. However, the 2D-SWD models with the no sip condition assume the zero velocity at those points, which is not entirely correct as it contradicts natural flow physics. These

findings suggested the importance of considering the reflecting boundary condition rather than the no slip condition while applying the model near the fluid–structure interaction region.

Another interesting finding from the study is the identification of the zone of influence of the boundary condition near the spur walls. For instance, S34 and S35 points are located at a distance of 155 m from the groin wall (Fig. 10.3a. Being at a farther distance from the spur's nose, the flow parameters near these points are less likely influenced by the changes in boundary conditions. However, S11, S21, and S22 being at a closer distance to the nose of the Spur (S1 = 80 m from spur 1 and S21 and S22 = 50–75 m from spur 2), significant changes in velocity and flow depth under different boundary condition were observed at these points. These results indicated that the boundary condition is effective only when applied near the spur wall. Its influence decrease with an increase in distance from the spur wall.

10.6 Conclusion

The topographical features in natural rivers mainly in large braided streams govern the robustness of SWD models. The presence of wet–dry interface and the large variations in the bed gradients influence the model performance and stability. A modified 2D shallow water model is developed in this study and applied in two different flow domains. The conservativeness of the present model is evaluated by comparing the computed outputs with the field measured results and was founds satisfactory. Two different boundary conditions are used in the hydrodynamic model near the flow–structure interaction region and it is found that the accumulation of computational error in the solution increases with no slip condition near the dyke walls. For the given streamflow event, the zone of influence of the boundary conditions on the flow field is investigated. It is observed that the current speed near the dyke walls is mostly affected and the influence progressively decrease away from the walls. The present model can be further improved by incorporating the sediment transport equations in the hydrodynamic calculations to get a profound understanding of the flow behavior at different boundary conditions. The applicability of the present model can be extended to vegetated channel by incorporating the resistance forces offered by different types of vegetation in the momentum equation.

Declarations *Conflicts of interest*: The authors have no conflicts of interest to declare.

Funding: *The author*(s) received *no* specific *funding for this work.*

Data Availability: *The data that support the finding of the manuscript may be obtain from the corresponding author upon request.*

References

Ayaseh A, Salmasi F, Dalir AH, Arvanaghi H (2019) A performance comparison of CCHE2D model with empirical methods to study sediment and erosion in gravel-bed rivers. Int J Environ Sci Technol 16:7933–7942

Baruah A, Sarma AK (2020) A quasi three dimensional hydrodynamic model for velocity distribution in open channel. ISH J Hydraul Eng 28:186–194

Baruah A, Kumar Sarma A, Hinge G (2021) Hydrological–hydrodynamic nexus for evaluation of fish habitat suitability in the Bhogdoi River, India. J Hydrol Eng 26:4021032

Begnudelli L, Sanders BF (2007) Conservative wetting and drying methodology for quadrilateral grid finite-volume models. J Hydraul Eng 133:312–322

Bi S, Zhou J, Liu Y, Song L (2014) A finite volume method for modeling shallow flows with wet-dry fronts on adaptive Cartesian grids. Math Probl Eng 2014:209562

Chen C, Liu H, Beardsley RC (2003) An unstructured grid, finite-volume, three-dimensional, primitive equations ocean model: application to coastal ocean and estuaries. J Atmos Ocean Technol 20:159–186

Chen Y, Wang Z, Liu Z, Zhu D (2012) 1D–2D coupled numerical model for shallow-water flows. J Hydraul Eng 138:122–132

Dutta P, Hinge G, Marak JDK, Sarma AK (2020) Future climate and its impact on streamflow: a case study of the Brahmaputra river basin. Model Earth Syst Environ 7:2475. https://doi.org/10.1007/s40808-020-01022-2

Kalita HM (2016) A new total variation diminishing predictor corrector approach for two-dimensional shallow water flow. Water Resour Manag 30(4):1481–1497

Khan MA, Sharma N, Pu J, Aamir M, Pandey M (2021) Two-dimensional turbulent burst examination and angle ratio utilization to detect scouring/sedimentation around mid-channel bar. Acta Geophys 69(4):1335–1348

Khan MA, Sharma N, Pu JH, Pandey M, Azamathulla H (2022) Experimental observation of turbulent structure at region surrounding the mid-channel braid bar. Marine Georesour Geotechnol 40(4):448–461

Koken M, Constantinescu G (2011) Flow and turbulence structure around a spur dike in a channel with a large scour hole. Water Resour Res 47

Kuiry SN, Sen D, Bates PD (2010) Coupled 1D–quasi-2D flood inundation model with unstructured grids. J Hydraul Eng 136:493–506

Lai YG, Kim HS (2020) A near-shore linear wave model with the mixed finite volume and finite difference unstructured mesh method. Fluids 5:199

Lauer JW, Viparelli E, Piégay H (2016) Morphodynamics and sediment tracers in 1-D (MAST-1D): 1-D sediment transport that includes exchange with an off-channel sediment reservoir. Adv Water Resour 93:135–149

Liang Q, Borthwick AGL (2009) Adaptive quadtree simulation of shallow flows with wet–dry fronts over complex topography. Comput Fluids 38:221–234

Liang Q, Marche F (2009) Numerical resolution of well-balanced shallow water equations with complex source terms. Adv Water Resour 32:873–884

Pinos J, Timbe L (2020) Mountain riverine floods in Ecuador: issues, challenges, and opportunities. Front Water 2:545880

Qin X, Motley M, LeVeque R, Gonzalez F, Mueller K (2018) A comparison of a two-dimensional depth-averaged flow model and a three-dimensional RANS model for predicting tsunami inundation and fluid forces. Nat Hazards Earth Syst Sci 18(9):2489–2506

Shankar MS, Pandey M, Shukla AK (2021) Analysis of existing equations for calculating the settling velocity. Water 13(14):1987

Shivashankar M, Pandey M, Zakwan M (2022) Estimation of settling velocity using generalized reduced gradient (GRG) and hybrid generalized reduced gradient–genetic algorithm (hybrid GRG-GA). Acta Geophys 1–11

Song L, Zhou J, Guo J, Zou Q, Liu Y (2011) A robust well-balanced finite volume model for shallow water flows with wetting and drying over irregular terrain. Adv Water Resour 34:915–932

Turick V, Voskoboinyk O, Cherny D, Tereshchenko L (2020) Interaction of group of bridge piers on scour. Adv Comput Sci Eng Educ III 1247:3

Twigt DJ, De Goede ED, Zijl F, Schwanenberg D, Chiu AYW (2009) Coupled 1D–3D hydrodynamic modelling, with application to the Pearl River Delta. Ocean Dyn 59:1077

Wallwork JT, Pu JH, Kundu S, Hanmaiahgari PR, Pandey M, Satyanaga A, Pandey M, Satyanaga A, Amir Khan M, Wood A (2022) Review of suspended sediment transport mathematical modelling studies. Fluids 7(1):23

Wang Z, Geng Y, Jin S (2005) Numerical modeling of 2-D shallow water flow with complicated geometry and topography [J]. J Hydraul Eng 4

Yalcin E (2020) Assessing the impact of topography and land cover data resolutions on two-dimensional HEC-RAS hydrodynamic model simulations for urban flood hazard analysis. Nat Hazards 1–23

Chapter 11
A Review on Estimation Methods of Scour Depth Around Bridge Pier

Geeta Devi, Munendra Kumar, and Ajay Bhardwaj

Abstract Sediment scour occurs around the bridge pier by the erosive action of the flowing river. It is also considered as a significant factor in the collapse of bridge structures. These bridge structure failures occur without a prior warning and pose a severe threat to the safety of the environmental ecosystem. Therefore, it becomes crucial to precisely estimate the scour depth with high accuracy, eventually leading to the safe design of bridge piers. A substantial amount of theoretical and experimental study has been undertaken over the years to determine the scour depth around the bridge pier. These works quantize the development of sediment scour depth by focusing on different water flow characteristics, pier shape characteristics, and sediment characteristics. Most of the previous studies proposed empirical formulations for the scour depth estimation using the experimental data. This chapter comprehensively reviews such works and broadly classifies them into two major categories: empirical equations and artificial intelligence (AI) based techniques. It then summarizes the extant work on scour depth estimation methods with an expectation of paving the future roadmap for the researchers.

Keywords Bridge Piers · Bridge Scour · Neural Networks · Regression-based equations · Scour depth estimation

11.1 Introduction

Bridges have historically confronted designers and construction with significant challenges, both during the design stage and for keeping their stability and functionality throughout time. More than 18,000 bridges in the USA have been recognized as scour-critical and in need of repair or replacement by state transportation

G. Devi (✉) · M. Kumar
Delhi Technological University, New Delhi, India
e-mail: geeta_phd2k17@dtu.ac.in

A. Bhardwaj
SRM University, Amaravati, Andhra Pradesh, India

M. Pandey et al. (eds.), *River Dynamics and Flood Hazards*, Disaster Resilience and Green Growth, https://doi.org/10.1007/978-981-19-7100-6_11

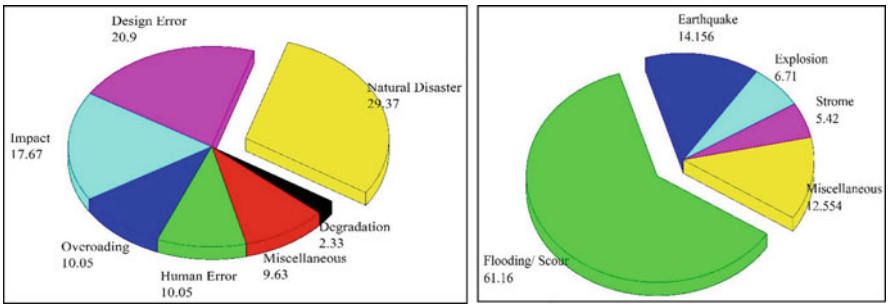

Fig. 11.1 (**a**) Causes of bridge failures (in percentage); (**b**) percentage of natural disasters causing bridge failures

bureaus. Approximately 60% of bridge failures in the previous 30 years have been attributed to foundation scour (Arneson et al. 2012; Jain et al. 2021; Pandey and Md Azamathulla 2021; Chaudhuri et al. 2022). The Federal Highway Administration (FHWA) estimates that scour is responsible for 60% of bridge failures in the USA (Aamir et al. 2022), and that around 50–60 bridges fall each year in the USA. Melville and Coleman (2000) analyzed 500 bridge structure failures in the USA between 1989 and 2000 and discovered that floods, scour, and impacts were the most common causes of bridge failures. The 500 collapsed bridges had an average age of 52.5 years, ranging from 1 year to 157 years. Furthermore, Jain et al. (2021) compiled a comprehensive database of bridge failure from across the world and states that the natural disasters are the leading cause of bridge failures, with floods or scour accounting for around 60% of the failures. According to Pandey et al. (2020a), 132 bridges have fallen since 2000–2019, with 32 of them failing owing to hydraulic failures. Figure 11.1 depicts the percentage of bridge collapses caused by natural disasters, as well as the percentage of bridge failures caused by floods and scouring.

Scour is a result of erosive action due to the hydraulic structure in the waterway, which excavates and transports material around the bridge components (Richardson and Davis 2001; Pandey et al. 2021). In the history of bridge failure, pier and abutment scour is identified as the main cause of failure although there have been significant advances made in this area of research. The formation of scour encircling the bridge pier is a complicated phenomenon, and estimating beforehand is daunting task researchers are facing today. The formation of vortices for scouring hole evolution around the pier is illustrated in Fig. 11.2. To deeply understand the formation of scouring, myriad research on mathematical modelling is present in the literature, such as Devi and Kumar (2022a); Dey et al. (2008); and Pu et al. (2021). Also, several experimental and modelling investigations are carried out to assess the scour depth around the piers. However, many of these estimation formulation cannot precisely determine the scour depth and underestimate or overestimate it.

The structural features of scour investigation aim to reduce the loss of bridges due to local scour. Several approaches have been proposed in the previous literature to

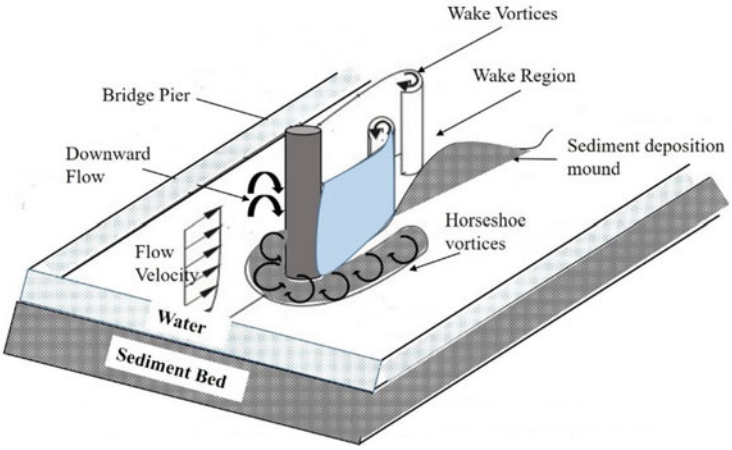

Fig. 11.2 Mechanism of scour development

address this problem. There are mainly three types of approaches. The first is estimations and experiments, extensively employed in the design stage to determine the maximum scour depth. Secondly, countermeasures are proposed during construction to extenuate the local scour. Lastly, installing the scour monitoring instruments on the structures to furnish the safety surveillance in the service stage. The current study focuses on the first stage, which is predication based, so that accurate scour prediction can aid in bridge design and reduce bridge losses.

An accurate assessment and efficient monitoring of scour depth is required because it affects the design of bridge components such as abutments, guide banks, groynes, piers, spurs, and so on. Several equations proposed in the literature for assessing the local scour depth around the bridge piers, are listed in Table 11.1. According to Deng and Cai (2010) most existing equations are conservative and tend to overestimate the scour depth. However, these approaches might lead to unreliable estimations.

With the recent developments in soft-computing techniques, researchers have come up with more accurate scour estimation techniques than the conventional methods. To solve the hydraulics engineering problems, multiple approaches based on artificial intelligence (AI), ANFIS (adaptive neuro-fuzzy inference system), GP (genetic programming), GEP (gene expression programming), and GMDH (group method of data handling) have been proposed by Muzzammil et al. (2015). In addition, a few studies based on Genetic algorithms have been conducted, such as Bateni et al. (2019); Guven and Gunal (2008); Pandey et al. (2020b).

This chapter critically examines various approaches to determine the scour depths lately reported in the literature. These approaches are classified into two parts: (1) based on empirical formulations and (2) based on AI-based techniques.

Table 11.1 List of semi-empirical formulations for scour depth estimation

Equation name	Expression
Inglis (1949) equation	$Y_s = 2.32D\left[\frac{Q^{2/3}}{D}\right]^{0.78} - h$
Ahmad (1951) equation	$Y_s = K_s Q_s^{2/3} - h$
Laursen (1960) equation	$Y_s = 1.11(hD)^{0.5}$
Blench et al. (1962) equation	$Y_s = \left[6.6F_r - 0.51 - 5.49F_r^2\right]h$
Larras (1963) equation	$Y_s = 1.05K_sK_\theta b^{0.75}D$
Neill (1964) equation	$Y_s = 1.5\ D^{0.7}h^{0.3}$
Breusers (1965) equation	$Y_s = 1.4\ b$
Shen et al. (1969) equation	$Y_s = 0.000223\ \left(\frac{Vb}{\nu}\right)^{0.619}$
Hancu (1971) equation	$Y_s = 2.42b\left(\frac{2V}{V_c} - 1\right)\left(\frac{V_c^2}{gb}\right)^{1/3}$
Coleman (1972) equation	$Y_s = 0.54D\left(\frac{h}{D}\right)^{0.19}F_r^{1.19}h^{0.41}$
Neill (1973) equation	$Y_s = K_sD$
Breusers et al. (1977) equation	$Y_s = DK_sK_\alpha\left[2\ \tanh\left(\frac{h}{D}\right)\right]$
Jain and Fischer (1979) equation	$Y_s = 1.86b\left(\frac{h}{b}\right)^{0.5}(F_r - F_{re})^{0.25}$
Jain (1981) equation	$Y_s = 1.84\ b\left(\frac{h}{b}\right)^{0.3}F_{re}^{0.25}$
Chitale (1988) equation	$Y_s = 2.5\ b$
Froehlich (1988) equation	$Y_s = 0.32\ DK_sF_r^{0.2}\left(\frac{D_p}{D}\right)^{0.62}\left(\frac{h}{D}\right)^{0.46}\left(\frac{D}{d_{50}}\right)^{0.08} + 1$
Melville and Sutherland (1988) equation	$Y_s = DK_1K_yK_dK_sK_\theta$
Breusers and Raudkivi (1991) equation	$Y_s = 2.3DK_\sigma K_yK_dK_sK_\theta$
Kothyari et al. (1992) equation	$Y_s = 0.66\ D\ \left(\frac{D}{h}\right)^{-0.25}\left(\frac{h}{D}\right)^{0.16}(F_r)^{0.4}\beta^{-0.3}$
Richardson and Davis (1995) equation	$Y_s = 2D\ K_sK_\theta K_fK_A\left(\frac{h}{b}\right)^{0.35}F_r^{0.43}$
Melville (1997) equation	$Y_s = K_{hb}K_1K_dK_sK_\theta$
Melville and Coleman (2000) equation	$Y_s = K_{yb}K_1K_dK_sK_\theta K_gK_t$
Richardson and Davis (2001) equation	$Y_s = 2.0\ k_1k_2k_3k_w\left(\frac{D}{h_u}\right)^{0.65}F^{0.43}h_u$
Oliveto et al. (2002)	$Y_s = 0.068\sigma^{-1/2}L_RF_d^{1.5}\log T$ $L_R = b^{2/3}y^{1/3}$
IRC (1997,2000) equation	$Y_s = 0.473\ \left(q/f\right)^{1/3}$, when $\frac{L}{B} \geq 1$ $Y_s = 1.34\ \left(\frac{q^2}{f}\right)^{1/3}$, when $\frac{L}{B} \leq 1$
Lança et al. (2013)	$Y_s = \left[1 - \exp\left\{-a_1\left(\frac{vt}{b}\right)^{a_2}\right\}\right]Y_t$ $a_1 = 1.22\left(\frac{b}{d_{50}}\right)^{-0.764}$ and $a_2 = 0.09\left(\frac{b}{d_{50}}\right)^{0.244}$
Sheppard et al. (2014) equation	$\frac{y_s}{D} = 2.5\ f_1f_2f_3$ for $0.4 \leq \frac{V}{V_c} \leq 1.0$ $\frac{y_s}{D} = f_1\left[2.2\left(\frac{\frac{v}{v_c} - 1}{\frac{v_{lp}}{v_c} - 1}\right) + 2.5f_3\left(\frac{\frac{v_{lp}}{v_c} - \frac{v}{v_c}}{\frac{v_{lp}}{v_c} - 1}\right)\right]$ for $1 \leq \frac{V}{V_c} \leq \frac{V_{lp}}{V_c}$ $\frac{Y_s}{D} = 2.2f_1$ for $\frac{V}{V_c} > \frac{V_{lp}}{V_c}$
Modified IRC Equation (Vijayasree and Eldho 2021) equation	$Y_s = 1.34\ C\ \left(\frac{q^2}{f}\right)^{1/3}$

11.2 The Empirical Formulation for Scour Depth Estimation

Over the past decades, based on experimental studies, various empirical methods have been proposed in the literature. Table 11.1 lists the well-known and recent equations for predicting the pier scour, usually applied in practical bridge design. Most of these empirical methods are expressed as mathematical formulations of significant parameters, such as flow characteristics, flow properties, sediment material properties, and bridge geometry. In addition, these methods also have several limitations: (1) these are produced for pier and group of piers foundations with inadequate consideration for scour depth; (2) the experimental study of the river flow for bridge scour frequently achieved using horizontal rectangular flumes; (3) these formulations are carried out for steady-state flow field; and (4) the sediment considered is assumed to be cohesionless. Almost all of the limitations agree well with the data set from which these equations are derived. These limitations lead to an overestimation of the scour depth that may lead to unnecessary, non-economical, deep bridge foundations (Richardson and Davis 2001).

Many mathematical models based on experimental and theoretical studies have been proposed over the last few decades. Sheppard et al. (2014) researched field data and analyzed 23 of the most popular current and widespread equilibrium local scour formulas for non-cohesive sediments. Out of these 23 equations, six were chosen for final evaluation. These six equations, respectively, are Sheppard et al. (2014) equation, modified HEC-18 equation (Arneson et al. 2012), HEC-18 equations (Richardson and Davis 2001), Melville (1997) equation, Froehlich (1988) equation, and Jain and Fischer (1979) equation. To further provide the accurate scour estimation, Hamidifar et al. (2021) in a very recent work compared ten most prominent scour depth assessment equations in conjugation with the eight essential velocity equations and derive their combinational performance. Based on this analysis, three equation models performed better than others; these are (1) Richardson and Davis (2001) equation and Jain and Fischer (1979) equation, (2) Arneson et al. (2012) equation and Jain (1981) equation, and (3) Jain and Fischer (1979) equation. In another recent work, Vijayasree and Eldho (2021) proposed a semi-empirical equation modification of the Indian Road Congress's (IRC) equation. Furthermore, Devi and Kumar (2022b) experimentally validated the four well-known semi-empirical equations, which are (1) Laursen and Toch equation (Laursen and Arthur 1956); (2) Melville and Coleman equation (Melville and Coleman 2000); (3) HEC-18 equation (Arneson et al. 2012); and (4) Sheppard/Melville equation (Sheppard et al. 2014). It has been concluded that the equation provided by Larsen and Toch, and Melville equation is reasonably consistent with the experimental results; however, the HEC-18 and Sheppard/Melville equation overestimates the scour depth.

All the studies mentioned above has been carried out for a single pier using regression-based semi-empirical equations. These equations cannot capture the pro relationship between scour depth and its primary reasons. These equations were

developed decades earlier for complex bridge designs featuring massive piers and multiple footing types and thus may be unable to estimate the scour depth precisely.

Also, the primary reasons for their low performance are (a) scale effect in flume tests cannot be avoided; (b) sediment materials and flow characteristics are excessively simplified; (c) experimental conditions for all the flume tests cannot be kept same as reported in previous works; and (d) data collected is not measured accurately because of complexity in a river or subsea atmosphere or limited availability. When these equations are used, the scour depth is either overestimated or underestimated (Melville and Coleman 2000; Richardson and Davis 2001). Underestimation of scour depth may pose a safety danger, while overestimation may lead to the additional project cost. Various findings can be drawn in this comparative research, although most existing equations are considered conservative.

Jain and Fischer (1979); Laursen and Arthur (1956); Melville and Sutherland (1988) employed a feasible empirical formula considering a single pier and group of piers for local scour depth. Sheppard et al. (2014) conducted comparison experiments to assess the correctness of the already proposed bridge scour equations. Equations that demonstrate more preciseness in scour estimation has been adopted in practice as design approaches and developed by hydraulic organizations in several nations (Melville and Coleman 2000; Richardson and Davis 2001).

Although easy to apply and widely used in engineering practice, empirically derived equations to estimate the scour depth has intrinsic limitations. Moreover, they do not account for the actual, complex, three-dimensional sediment removal process taking place at piers.

11.3 AI-Based Techniques for Scour Depth Estimation

Seeing the limitations of above mentioned empirical equations, these equations have become less acceptable for modern bridge designs. With the recent development of soft computational techniques and their ability to model the scour depth precisely, academia has started using them. Artificial intelligence (AI) based solutions have become an excellent tools for hydrological and environment designers, and eventually, they have come up with a more accurate design. ANNs (artificial neural networks), ANFIS (adaptive network-based fuzzy inference system), GEP (gene expression programming), GMDH (group method of data handling), GA (genetic algorithm), and GP (genetic programming) have considered as AI-based approaches recently developed to solve the hydraulics engineering challenges.

11.3.1 Application of ANN

ANN is a computerised model of the human brain that mimics how the human brain works. It has a collection of adaptive learning approaches for detecting and

extracting patterns and trends, mainly when the input–output correlation has undetermined. In the past, multiple researchers utilize the ANN to assess the scour depth, such as Firat and Gungor (2009). In one of the previous works, Bateni et al. (2019) built and trained an ANN model that helps forecast the scour depth by utilizing the experimental data set. The input parameters for the proposed ANN models: depth of flow, the critical velocity of flow, median particle size, mean velocity, and diameter of the pier. To train the model, back propagation alongside a Bayesian neural network has been utilized. In another work, Firat and Gungor (2009) have also used ANN techniques to assess the scour depth using laboratory results and compare the ANN projected scour outcomes to those estimated by regression analysis and empirical equations. They designed a multi-layer perceptron model with one hidden layer. The work by Guven and Gunal (2008) introduced a linear genetic programming (LGP) model to estimate the scour depth formed because of waves in medium-thick silt and sediment around a cylindrical pier.

From the results of the above-cited works that utilize the ANN modelling, it can be concluded that the ANN-based method has more accuracy in estimating the equilibrium scour.

11.3.2 Application of ANFIS

In the literature, various research works have been reported that utilize the ANFIS to handle scour-related problems and to maintain brevity; few of them has been included in this section, such as Bateni et al. (2019); Choi et al. (2017); Singh et al. 2022.

In recent works, ANFIS has been utilized to predict the equilibrium and temporal scour depth using multiple credible databases. According to the results reported in the above-cited works, the ANFIS-based algorithm estimates the scour depth more precisely than the conventional approaches. Akib et al. (2014) designed an ANFIS model to estimate the scour depth in bridges. They also compared the ANFIS results with the linear regression (LR) based model and concluded that ANFIS-based method has better prediction capability. The impact of the rectangular slot as a protection device around the bridge pier groups and models it using the ANFIS method. From the reported results, it has concluded that ANFIS-based modelling technique has better prediction accuracy, thus making this method an excellent tool to interpret the commonly occurring complexities in any bridge scouring.

In addition, Choi et al. (2017) developed the ANFIS-based approach to estimate the scour depth, and the finding have corroborated using the ANN and empirical formulae. The study indicates that using the ANFIS approach considerably improved the predictions. In another work, to estimate the scour depth in concave and convex arch-shaped round bed sills, Choi et al. (2017) also employ the ANFIS model. To show the efficacy, the model has tested with experimental data. In recent work, Choi et al. (2017) use the experimental data to forecast the scour depth and utilize machine learning techniques. They utilize the particle swarm optimization technique, further

refined by employing the support vector machine. From the results, it has been concluded that for the cylindrical pier, the hybrid-ANFIS model, which uses the Gbell membership function, provides better estimation than the methods solely based on PSO and SVM combination. While for the rectangular and sharp nose pier, the PSO-SVM method provides a better estimate.

11.3.3 Application of GEP

Gene expression programming (GEP) is also a soft-computing technique that provides optimized results in the expression tree. GEP has lately piqued the interest of researchers in estimating hydraulic properties. It acts as a search method for generating computer programs which work on mathematical expressions, utilizes the decision tree formation and polynomial structures, and then makes the logical expressions. It generates the computer programs encoded in terms of linear chromosomes and subsequently translated into expression trees (ETs).

In the literature, very few research works have been reported that utilize the GEP for scour depth estimation around the hydraulic structures, such as Azamathulla and Jarrett (2013); Pandey et al. (2020b). Few recent works reported the GEP application for the scour depth estimation around the bridge piers, such as Devi and Kumar (2022b); Hassan et al. (2022); Mohammed Saleh et al. (2019); Muzzammil et al. (2015); Singh et al. (2022).

Azamathulla and Jarrett (2013) utilizes the GEP to forecast the scour depth around bridge piers and compared their obtained results to those of other regression algorithms. In recent work, Hassan et al. (2022) designed three models to estimate the scour depth around a single pier using ANN, GEP, and NLR approaches. Their results revealed that the ANN-based modelling has more accuracy. Mohammed Saleh et al. (2019) use the GEP-based formulation to forecast the local scour depth for the live bed and clear water flow condition. In another work, Muzzammil et al. (2015) use the laboratory data from the literature to create the GEP modelling for scour in cohesive sediments. In addition, to forecast the scour depth around bridge piers with debris impacts, Singh et al. (2022) employed GEP formulations. Their investigations indicate that the GEP technique outperforms conventional predictors and artificial neural network-based modelling. While the work reported by Devi and Kumar (2022b), experiments have been conducted by utilizing the two piers and forecasting the scour depth surrounding the piers using the GEP technique. The results have been validated with experimental data and other well-known regression-based equations. According to the findings of the study, the GEP model has estimated scour depth precisely.

11.3.4 Performance of the Empirical Formulas and AI-Based Techniques

This part of the study provides the performance comparison of the various methods used, particularly empirical formulation and the AI-based techniques such as GEP, ANN, and MARS (Multivariate Adaptive Regression Splines) to estimate the scour depth around the bridge piers. The performance of these methods has been examined by utilizing the results of Hassan et al. (2022), Pandey et al. (2020b), Bateni et al. (2019), and Mohammed Saleh et al. (2019) against the value of correlation coefficient (R^2). The performance of the empirical formulation and the AI- based techniques has been compared on the bases of the R^2 values as illustrated in Table 11.2. As per the R^2 values indicated in Table 11.2, the AI-based techniques outperforms

Table 11.2 Performance of empirical equations and AI-based techniques

Reference	Models/equation used	Corelation coefficient (R^2)
Hassan et al. (2022)	GEP	0.89
	ANN	0.97
	Non-linear regression (NLR) method	0.86
Pandey et al. (2020b)	Oliveto et al. (2002) equation	0.69
	Kothyari et al. (1992) equation	0.36
	Lança et al. (2013) equation	0.68
	Pandey et al. (2020b) based on MLR (Multiple Linear Regression)	0.88
	Pandey et al. (2020b) based on GA	0.90
Bateni et al. (2019)	MARS	0.90
	GEP	
	Richardson and Davis (2001) equation	0.83
	Behzad and Beheshti (2006) equation	0.73
	Ghaemi et al. (2013) equation	0.75
Mohammed Saleh et al. (2019)	*Live bed*	
	GEP	0.90
	Regression	0.87
	Breusers et al. (1977) equation	0.39
	Melville and Sutherland (1988) equation	0.47
	Richardson and Davis (2001) equation	0.53
	Clear water	
	GEP	0.92
	Regression method	0.90
	Breusers et al. (1977) equation	0.51
	Melville and Sutherland (1988) equation	0.59
	Richardson and Davis (2001) equation	0.56
Azamathulla (2012)	GEP	0.89
	ANN	0.73

the empirical formulation, which means AI-based techniques have better accuracy for the scour estimation.

11.4 Conclusion

This review chapter addressed the complex issue of quantifying the pier scour estimate. The present study organizes the existing scour depth estimation research into two parts: empirical and AI-based techniques. The basic parameters from hydraulic, geotechnical, and structural perspectives and their link with scour outcomes have been evaluated using theoretical and computational approaches. Experimental studies have reported in the literature to determine the complex interplay between different scour parameters; however, experiments under various complex scenarios need to be done to deepen the scour depth understanding.

This chapter comprehensively covers various experimentally determined equations for predicting pier scour. These are simple to implement and are still commonly used in engineering practice. The main problem in employing these equations, they appear to overestimate or underestimate the scour depth while using beyond the limit of application for which they have developed in laboratory studies. Recent works that utilize the new soft-computing approaches, such as ANN, ANFIS, and GEP, have been discussed for scour depth prediction. The estimation ability of these approaches in terms of scour depth has better than the empirical equations. This chapter is intended to be a valuable resource for academicians and technicians dealing with the bridge pier scour problem. There is a scope for further research to analyses the estimation capability of these equations in comparison with each other for the single pier and group of piers.

Conflict of Interest The authors declare no conflict of interest.

List of Symbols

Y_s	Depth of scour (m)
h	Depth of flow (m)
D	Diameter of pier (m)
F	Froude number
g	Acceleration due to gravity
L_R	Reference time
V	Mean velocity of flow (m/s)
Q	Design discharge (m^3/s)
q	Intensity of discharge ($m^3/s/m$)
B	width of channel (m)
V_c	Critical Velocity of flow (m/s)
V_{IP}	Live bed peak velocity of flow (m/s)

References

Aamir M, Ahmad Z, Pandey M, Khan MA, Aldrees A, Mohamed A (2022) The effect of rough rigid apron on scour downstream of sluice gates. Water 14(14):2223. https://doi.org/10.3390/w14142223

Ahmad M (1951) Spacing and protection of spurs for bank protection. Civil Eng Publ Rev 46:3–7

Akib S, Mohammadhassani M, Jahangirzadeh A (2014) Application of ANFIS and LR in prediction of scour depth in bridges. Comput Fluids 91:77–86

Arneson LA, Zevenbergen LW, Lagasse PF, Clopper PE (2012) Evaluating scour at bridges. National Highway Institute (US), (No. FHWA-HIF-12-003). National Highway Institute (US)

Azamathulla HM (2012) Gene-expression programming to predict scour at a bridge abutment. J Hydroinformatics 14(2):324–331

Azamathulla HM, Jarrett RD (2013) Use of gene-expression programming to estimate Manning's roughness coefficient for high gradient streams. Water Resour Manag 27(3):715–729

Bateni SM, Vosoughifar HR, Truce B, Jeng DS (2019) Estimation of clear-water local scour at pile groups using genetic expression programming and multivariate adaptive regression splines. J Waterw Port Coast Ocean Eng 145(1):1–11

Behzad A-A, Beheshti AA (2006) Experimental investigation of clear-water local scour at pile groups. J Hydraul Eng ASCE 132(10)(October):1100–1104

Blench T, Bradley JN, Joglekar DV, Bauer WJ, Tison LJ, Chitale SV, Thomas AR, Ahmad M, Romita PL (1962) Discussion of 'Scour at Bridge Crossings'. Trans Am Soc Civil Eng 127(1):180–207

Breusers HNC (1965) Scouring around drilling platforms. J Hydraul Res 19:276

Breusers HNC, Raudkivi AJ (1991) Scouring. Balkema, Rotterdam

Breusers HNC, Nicollet G, Shen HW (1977) Local scour around cylindrical piers. J Hydraul Res 15(3):211–252

Chaudhuri S, Pandey M, Debnath K, Oliveto G (2022) A comparative study on equilibrium scour volume around circular cylinders in clay-sand mixed cohesive beds, at near threshold velocity of sand–an experimental approach. Water Supply 22:6777. https://doi.org/10.2166/ws.2022.250

Chitale SV (1988) Estimation of scour at bridge piers. Water Energy Int 45(1):57–68

Choi SU, Choi B, Lee S (2017) Prediction of local scour around bridge piers using the ANFIS method. Neural Comput Appl 28:335–344

Coleman NL (1972) Analyzing laboratory measurements of scour at cylindrical piers in sand beds. In: Hydraulic research and its impact on the environment

Deng L, Cai CS (2010) Bridge scour: prediction, modeling, monitoring, and countermeasures—review. Pract Period Struct Des Constr 15(May):125–134

Devi G, Kumar M (2022a) Characteristics assessment of local scour encircling twin bridge piers positioned side by side (SbS). Sādhanā 47(3):109

Devi G, Kumar M (2022b) Estimation of local scour depth around twin piers using gene expression programming (local scour around twin piers). Water Supply 22:5915

Dey S, Chiew Y-M, Kadam MS (2008) Local scour and riprap stability at an abutment in a degrading bed. J Hydraul Eng 134(10):1496–1502

Firat M, Gungor M (2009) Generalized regression neural networks and feed forward neural networks for prediction of scour depth around bridge piers. Adv Eng Softw 40(8):731–737

Froehlich DC (1988) Analysis of onsite measurements of scour at piers. In: Hydraulic engineering: proceedings of the 1988 national conference on hydraulic engineering, pp 534–539

Ghaemi N, Etemad-Shahidi A, Ataie-Ashtiani B (2013) Estimation of current-induced pile groups scour using a rule-based method. J Hydroinf 15(2):516–528

Guven A, Gunal M (2008) Genetic programming approach for prediction of local scour downstream of hydraulic structures. J Irrig Drain Eng 134(2):241–249

Hamidifar H, Zanganeh-Inaloo F, Carnacina I (2021) Hybrid scour depth prediction equations for reliable design of bridge piers. Water 13(15):2019

Hancu S (1971) Computation of local scour in the vicinity of bridge piers. In: Proc., 14th Int. Association of Hydraulic Research (IAHR) Congress, pp 299–305
Hassan WH, Hussein HH, Alshammari MH, Jalal HK, Rasheed SE (2022) Evaluation of gene expression programming and artificial neural networks in PyTorch for the prediction of local scour depth around a bridge pier. Results in Engineering 13:100353
Inglis SC (1949) Maximum depth of scour flatheads of guide bands and groynes, pier noses, and downstream bridges-the behavior and control of rivers and canals. Indian Waterways Experimental Station, Pune, pp 327–348
Jain SC (1981) Maximum clear-water scour around circular piers. J Hydraul Div 107(5):611–626
Jain SC, Fischer EE (1979) Scour around circular bridge piers at high Froude numbers. FHWA-RD-79(April)
Jain R, Lodhi AS, Oliveto G, Pandey M (2021) Influence of cohesion on scour at piers founded in clay–sand–gravel mixtures. J Irrig Drain Eng 147(10):04021046
Kothyari UC, Garde RCJ, Ranga Raju KG (1992) Temporal variation of scour around circular bridge piers. J Hydraul Eng 118(8):1091–1106
Lança RM, Fael CS, Maia RJ, Pêgo JP, Cardoso AH (2013) Clear-water scour at comparatively large cylindrical piers. J Hydraul Eng 139(11):1117–1125
Larras J (1963) Profondeurs Maximales d'Erosion des Fonds Mobiles Autour des Piles en Rivere. Ann Ponts Chaussees 133:411–424
Laursen EM (1960) Scour at bridge crossings. J Hydraul Div 86(2):39–54
Laursen EM, Arthur T (1956) Scour around bridge piers and abutments. Iowa Institute of Hydraulic Research
Melville BW (1997) Pier and abutment scour: integrated approach. J Hydraul Eng 123(2):125–136
Melville BW, Coleman SE (2000) Bridge scour. Water Resources Publication
Melville BW, Sutherland AJ (1988) Design method for local scour at bridge piers. J Hydraul Eng 114(10):1210–1226
Mohammed Saleh LA, Majeed SA A-d, Alnasrawi FA e-k M (2019) Numerical study of the bridge pier scour using gene expression programming. J Appl Water Eng Res 7(4):287–294
Muzzammil M, Alama J, Danish M (2015) Scour prediction at bridge piers in cohesive bed using gene expression programming. Aquatic Procedia 4:789–796
Neill CR (1964) River-bed scour: a review for bridge engineers
Neill CR (1973) Guide to bridge hydraulics: project committee on bridge hydraulics, roads and transportation Association of Canada. University of Toronto Press, Toronto
Oliveto G, Hager WH, Asce F (2002) Temporal evolution of clear-water pier and abutment scour. J Hydraul Eng 128(September):811–820
Pandey M, Md Azamathulla H (2021) Discussion of "gene-expression programming, evolutionary polynomial regression, and model tree to evaluate local scour depth at culvert outlets" by Mohammad Najafzadeh and Ali Reza Kargar. J Pipeline Syst Eng Pract 12(2):07021001
Pandey M, Zakwan M, Khan MA, Bhave S (2020a) Development of scour around a circular pier and its modelling using genetic algorithm. Water Sci Technol Water Supply 20(8):3358–3367
Pandey M, Zakwan M, Sharma PK, Ahmad Z (2020b) Multiple linear regression and genetic algorithm approaches to predict temporal scour depth near circular pier in non-cohesive sediment. ISH J Hydraul Eng 26(1):96–103
Pandey M, Jamei M, Karbasi M, Ahmadianfar I, Chu X (2021) Prediction of maximum scour depth near spur dikes in uniform bed sediment using stacked generalization ensemble tree-based frameworks. J Irrig Drain Eng 147(11):04021050
Pu JH, Wallwork JT, Khan M, Pandey M, Pourshahbaz H, Satyanaga A, Hanmaiahgari PR, Gough T (2021) Flood suspended sediment transport: combined modelling from dilute to hyper-concentrated flow. Water 13(3):379
Richardson EV, Davis SR (1995) Evaluating scour at bridges, Report No. FHWA-IP-90-017, Hydraulic Engineering Circular No. 18 (HEC-18). Office of Technology Applications, HTA-22, Federal Highway Administration
Richardson EV, Davis SR (2001) Evaluating scour at bridges. National Highway Institute (US)

Shen HW, Schneider VR, Karaki S (1969) Local scour around bridge piers. J Hydraul Div 95(6): 1919–1940

Sheppard DM, Melville B, Demir H (2014) Evaluation of existing equations for local scour at bridge piers. J Hydraul Eng 140(1):14–23

Singh UK, Jamei M, Karbasi M, Malik A, Pandey M (2022) Application of a modern multi-level ensemble approach for the estimation of critical shear stress in cohesive sediment mixture. J Hydrol 607:127549

Vijayasree BA, Eldho TI (2021) A modification to the Indian practice of scour depth prediction around bridge piers. Curr Sci 120(12):1875–1881

Chapter 12
Estimation of Shear Force Distribution in Two-Stage Open Channel Using SVM and ANFIS

B. S. Das, J. R. Khuntia, and K. Devi

Abstract The prediction of discharge is a challenging task for compound channel due to exchange of momentum at the junction of main channel and floodplain. From the literature, it has been found that, using apparent shear force (ASF) concept at the interface of floodplain and main channel, the accurate discharge can be predicted. ASF is a function of various non-dimensional parameters such as channel width ratio (α), relative flow depth (β), main channel aspect ratio (δ), relative roughness (γ), bed slope (S_0), Froude number (Fr), and side slope (m). In this paper, an attempt has been made to model ASF by considering the aforementioned non-dimensional parameters. A total of 152 datasets have been collected from various literatures related to ASF. In the recent days, artificial intelligence (AI) and machine learning (ML) techniques are widely used to model hydrological and hydraulic flow problems. In this research work, two soft computing techniques such as support vector machine (SVM) and adaptive neuro fuzzy inference system (ANFIS) have been utilized to model apparent shear force at the two-stage channel. First, SVM has been successfully used in classification and then extended for regression analysis. The SVM classification methods are based on the principle of optimal separation of classes. The computation is critically dependent upon the number of training pattern and selection of hyper-parameters for regression. There are four types of SVM named as cubic SVM, fine Gaussian SVM, medium Gaussian SVM, and coarse Gaussian SVM. In ANFIS modeling, different membership functions have been utilized. All types SVMs modelling and ANFIS modelling are performed using MATLAB tool. Sensitivity analysis has also been performed to check the strength of developed model. The present model is compared with other existing models and

B. S. Das (✉)
Department of Civil Engineering, National Institute of Technology, Patna, Bihar, India

J. R. Khuntia
Department of Civil Engineering, Chaitanya Bharathi Institute of Technology, Hyderabad, Telangana, India

K. Devi
Department of Civil Engineering, Vidya Jyothi Institute of Technology, Hyderabad, Telangana, India

M. Pandey et al. (eds.), *River Dynamics and Flood Hazards*, Disaster Resilience and Green Growth, https://doi.org/10.1007/978-981-19-7100-6_12

found to provide satisfactory results with coefficient of determination (R^2) value greater than 0.93.

Keywords Apparent shear force · Compound channel · SVM, ANFIS · Main channel · Gamma test

12.1 Introduction

Flooding is the most common environmental hazard on the planet. This is due to the vast geographical distribution of river floodplains and low-lying coastal areas. The flood prevention and protection efforts mainly focused on the overtopping of a main channel river to its floodplain during high-flow occurrences. Momentum transfer occurs at the intersection of the main channel and the floodplain as the main channel and floodplain flows decelerate and accelerate, respectively. Therefore, the depth-averaged velocity and boundary shear stress are non-uniform due to the momentum transfer phenomenon. The importance of flow interaction effects between the main channel and floodplains in the prediction of discharge in a compound channel has widely been demonstrated by previous investigators. Understanding the resistance coefficients, erosion, sedimentation, and flood flow requires an understanding of the distribution and properties of boundary shear and depth-averaged velocity in the compound channel (Devi et al. 2016; Das and Khatua 2018a; Khuntia et al. 2018, 2019; Tang 2019; Devi et al. 2021, 2022). Traditional one-dimensional (1-D) channel divisional methods, such as the divided channel method (DCM) and the single channel method (SCM), are still widely used in practice because of their simplicity. However, it is generally recognized that these approaches, particularly for zonal discharge, overestimate or underestimate channel discharge (i.e., discharge in main channel and its floodplain). Furthermore, none of these methods can accurately anticipate discharge for very low floodplain flow depths, which is the most difficult to predict. A model has been built in this research to forecast discharge using a support vector machine and a non-dimensional parameter. Because it is built on a statistical learning framework, support vector machine is one of the most resilient prediction systems. The SVM algorithm creates a model those categories fresh instances. To maximize the width of the separation between the two, SVM map training examples to points in space. Figure 12.1 depicts the cross-sections of

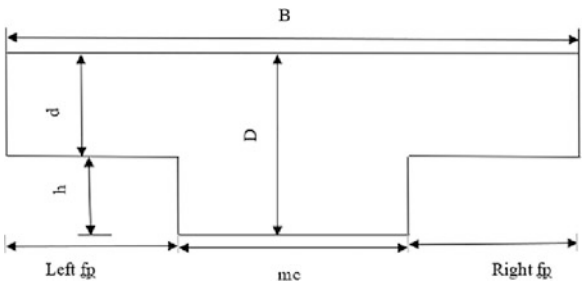

Fig. 12.1 Layout of compound channel

Fig. 12.2 Main channel of river Ganga at NIT Ghat

Fig. 12.3 Floodplain of NIT Ghat during flood period

compound channels, where "D" represents the depth of the main channel, "d" represents the depth of the flood plain, "B" represents the entire width of the channel, "mc" represents the main channel, and "fp" represents the flood plain.

Compound channel—A compound channel consists of a main channel, which carries base flow and frequently occurring runoff up to bank-full flow conditions, and a floodplain on one or both sides that carries overbank flow during times of flooding. The main channel is carrying maximum discharge and thus containing maximum cross-section. Figure 12.2 shows the main channel of river Ganga at NIT Ghat, Patna. A floodplain is a generally flat area of land next to a river or stream. It stretches from the banks of the river to the outer edges of the valley. Figure 12.3 shows the floodplain of river Ganga at NIT Ghat, Patna. Apparent shear force is the internal stress developed at the junction of main channel and floodplains. Its strength depends upon momentum exchange between the main channel and floodplain. Figure 12.4 shows the momentum exchange in channel at the interface.

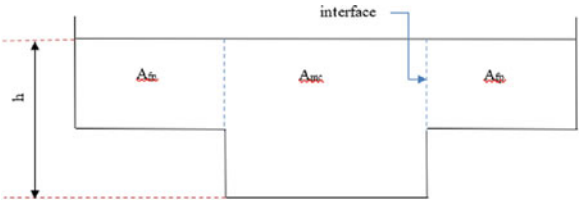

Fig. 12.4 Momentum exchange at the interface of compound channel

Tang (2019) proposed another methodology to work on the forecast of stream in light of clear shear force. In view of their proposed technique, the prescient release shows critical improvement contrasted and the DCM for both homogeneous and heterogeneous compound channels. Mohaghegh and Kouchakzadeh (2008) discovered that momentum transfer has the greatest impact on the horizontal contact between the main channel and the flood plains. The output is compared with divide channel method and it gives more reliable accuracy. Xie et al. (2013) observed the relative flow depths and widths of the floodplain in compound channels have been observed to alter velocity and shear stress distributions. The mean velocity and boundary shear stress distributions, secondary currents, and turbulence statistics predicted by the model can be seen and compared to Tominaga and Nezu's thorough analytical data. The aim of their research is to describe how the LES approach was used in conjunction with a dynamic SGS model to investigate the turbulent structure in compound open-channel flows, including large-scale vortical structures and instantaneous secondary flows, which play a key role in flow resistance and thus in sediment transport fluxes. Chen et al. (2016) demonstrated the assessment with apparent shear force technique which gave great concurrence with trial results. They proposed an improved formula for calculation of apparent shear force with variation of geometrical shape in compound channels and found the improved formula gave comparatively high degree of precision as compared to existing models. Bonakdari et al. (2018) observed that the apparent shear stress at the main channel–floodplain interface is important for the momentum transfer between sub-areas in a compound channel as it facilitates calculating the actual discharge in compound channel. Mohanty and Khatua (2014) proposed that model is capable in predicting both total flow in two-stage meandering compound channels as well as flow distribution. The applicability of their method is then checked by applying it to a number of data series from various small- and large-scale flume experiments. The discharge estimation errors were within acceptable bounds (about 10% for both smooth and rough meandering channels). By using the method to various data series, it is compared to a variety of different methods from the literature. Das et al. (2020) used soft computing technique to determine the discharge in non-prismatic compound channels by considering several non-dimensional input parameters.

Different empirical equations of apparent shear force provided different researchers are given in Eqs. (12.1)–(12.6).

Knight and Demetriou (1983).

$$\%S_{\mathrm{fp}} = 48(\alpha - 0.8)^{0.289}(2\beta)^{m} \tag{12.1}$$

Knight and Hamed (1984).

$$\%S_{\mathrm{fp}} = 48(\alpha - 0.8)^{0.289}(2\beta)^{m}\left\{1 + 1.02\sqrt{\beta}\log\gamma\right\} \tag{12.2}$$

Khatua and Patra (2007).

$$\%S_{\mathrm{fp}} = 1.23(\beta)^{0.1833}(38\ln\alpha + 3.6262) \times \left\{1 + 1.02\sqrt{\beta}\log\gamma\right\} \tag{12.3}$$

Khatua et al. (Prinos and Townsend 1984)

$$\%S_{\mathrm{fp}} = 4.1045\left[\frac{100\beta(\alpha - 1)}{1 + \beta(\alpha - 1)}\right]^{0.6917} \tag{12.4}$$

Mohanty et al. (2014)

$$\%S_{\mathrm{fp}} = 3.3254\left[\frac{100\{\beta\alpha\delta - \beta(\delta + 2s)\}}{\beta\alpha\delta + (1 - \beta)(\delta + s)}\right]^{0.7467} \times \left\{1 + 1.02\sqrt{\beta}\log\gamma\right\} \tag{12.5}$$

Devi et al. (2016)

$$\%S_{\mathrm{fp}} = 3.576\left\{\frac{100\beta\left(\alpha - 1 - \frac{2.5m}{\delta} + \frac{0.5m}{\Psi}\right)}{\left(1 + \frac{m}{\Psi}\right) + \beta\left(\alpha - 1 - \frac{2m}{\delta}\right)}\right\}^{0.717} \tag{12.6}$$

where B/b—width ratio (α), $(H-h)/H$—relative flow depth (β),$n_{\mathrm{f}}/n_{\mathrm{c}}$—relative roughness ($\gamma$), b/h—aspect ratio (δ), b/H—flow aspect ratio.

12.2 Methodology

In this chapter factors that affect the apparent shear force are discussed. The range of datasets is also mentioned. In this paper apparent shear force is calculated using SVM with various input parameters combinations which are selected by Gamma test (GT).

12.2.1 Identification of Influencing Parameters for Apparent Shear Force Modelling

The parameters affecting apparent shear force are geometrical and flow parameters, such as total channel height (H), total bottom width (B), floodplain width (Bf), main channel width (b), bank full flow depth and main channel and floodplain roughness.

Therefore, the apparent shear stress can be written as

$$\tau = f\left[H, h, B, b, n_f, n_c, \mathrm{Fr}, S_0, m\right] \tag{12.7}$$

Buckingham's theorem was adapted to analyze Eq. (3.1), and the dimensionless parameters affecting apparent shear stress can be expressed as

$$\tau = f\left[\frac{B}{b}, \frac{n_f}{n_c}, \frac{(H-h)}{h}, \frac{b}{h}, \frac{b}{H}, \mathrm{Fr}, S_0, m\right] \tag{12.8}$$

In the present study, a total of 152 datasets for percentage shear force have been collected from literatures. Out of which 112 and 40 datasets are chosen for training and testing, respectively. The details of datasets and their ranges have been presented in Table 12.1. It includes the data sets of Knight and Demitriou (1983), Knight and Hamed (1984), Prinos and Townsend (1984), Rezaei (2006), Tang (1999), and Sahoo (2012).

12.2.2 Model Development

The gamma test (GT) was used in this part to recognize the most influencing input parameters to model apparent shear force using SVM and ANFIS models. The GT may be achieved in practice by utilizing the win-Gamma program (Durrant 2001) This technology, according to the authors, is quite successful and might be applied in a variety of hydraulic nonlinear modeling projects. The V-ratio is a metric for determining the predictability of the given yields based on readily available data (Das et al. 2020; Knight and Demetriou 1983). It is found that the input dataset

Table 12.1 Non-dimensional parameters collected from different literatures

S. No.	Author	α	δ	β	γ	Fr
1	K & D (1983)	2.00–4.00	2.00	0.10–0.50	1.00	0.50–1.50
2	K & H (1984)	2.00–4.00	2.00	0.11–0.50	1.1–6.2	0.27–1.21
3	P & T (1984)	3.83–5.25	2.00–3.00	0.09–0.33	1.00–2.00	0.49–0.55
4	Rezaei (2006)	1.50–3.00	8.00	0.05–0.53	1.00	0.08–1.26
5	Tang (1999)	3.04	7.96	0.28–0.75	1.30–2.01	0.92–1.40
6	Sahoo (2012)	15.75	1.50	0.28–0.43	1.00–1.47	0.09–0.74

Table 12.2 Selection of best input combination using Gamma test

S. No.	Combination of input parameters	Γ	Std. error	V-ratio	Mask	Gradient
1	β, α, δ, γ, m	0.000045	0.0068	0.00018	1111010	0.180
2	S_0, β, α, δ, γ, m	0.000318	0.0040	0.00127	1111101	0.171
3	β, α, δ, γ, Fr	0.000360	0.0060	0.00144	1111100	0.128
4	β, α, δ, γ, m	0.000430	0.0038	0.00172	1111010	0.183
5	β, α, γ, Fr, m	0.000771	0.0052	0.00308	1101110	0.085

having the less MSE and less V-ratio values are the most ideal condition for the modeling. In the present paper 50 tests are performed out of which best five is mentioned in Table 12.2.

12.2.3 Support Vector Machine (SVM)

Cortes and Vapnik (1995) proposed a class of nonlinear search algorithms based on the structural risk minimization concept from statistical learning theory. This strategy has been utilized successfully in classification and regression analysis. The classification methods of SVMs are based on the notion of optimal class separation. If the classes are separable, this approach chooses the linear classifier that minimizes the generalization error among an infinite number of options. As a result, the selected hyperplane will leave the biggest margin between the two classes, where the margin is defined as the sum of the hyperplane's distances from the two classes' nearest point. If the two classes cannot be separated, the SVMs seek out the hyperplane that maximizes the margin while minimizing a quantity proportional to the number of misclassification mistakes. The kernel approach allows SVM to do nonlinear regression efficiently. When modelling any time series, the number of training patterns and the selection of hyper-parameters and determining their best values are essential factors. Support vector regression is the name of the SVM method used for regression problems (SVR). SVR aims to create a model that can predict experimental, measured, or observed output datasets, the target vector $T = \{t_1, t_2 \ldots t_n\}$ using input variables $X = \{ \rightarrow_{x_1}, \rightarrow_{x_2}, \ldots., \rightarrow_{x_n}\}$. SVR output vector $Y = \{y_1, y_2 \ldots y_n\}$, Closer values to T indicate better SVR model performance. The linear regression model (Eq. 12.9) establishes a relationship between input and output variables.

$$y_i = w_i^T x_i + b \tag{12.9}$$

where x_i and y_i are the I th input and output samples, and w and b are the considered model's weights and biases, respectively. The loss function L_ε is used to discipline the model in the SVR method. L_ε is defined as follows:

$$L_\varepsilon(t_i, y_i) = \begin{cases} 0 & |t_i - y_i| \le \varepsilon \\ n_i & |t_i - y_i| > \varepsilon \end{cases} \tag{12.10}$$

where n_i is a non-negative slag variable. When the difference between the target and output vectors exceeds a predetermined constant ε, the model is penalized, as shown in Eq. (12.11). As a result, the loss function can be expressed as

$$L_\varepsilon(t_i, y_i) = n_i^- + n_i^+ \tag{12.11}$$

During the training period, SVR tries to minimize L_ε by reducing the function, R_{emp} it is characterized by

$$R_{\text{emp}}[y_i] = \frac{1}{n}\sum\nolimits_{i=1}^{n} L_\varepsilon(t_i, y_i) \tag{12.12}$$

where n is the number of samples. In the procedure of minimizing, R_{emp}, unfavorable model expansion is possible. As a result, the objective function should include a complexity term. R_{reg} (Regularized risk function) is the sum of the R_{emp} (Eq. 12.13) and the standard of the weight matrix w. Therefore, by reducing R_{reg}, the highest accuracy with the smallest model is found. R_{reg} can be found in Eq. (12.13):

$$R_{\text{reg}}(y_i) = R_{\text{emp}}[y_i] + \frac{1}{2} w^T w \tag{12.13}$$

The SVR procedure can make use of a variety of kernel functions. Choosing the right kernel function has a direct impact on SVR regression performance. There are various kernel functions, but this paper adopts the radial basis function, which is the most commonly used kernel function and is the best at modeling nonlinear relations [12.20]. The radial basis function k_{RBF} is defined as

$$k_{\text{RBF}}(x_i, x_j) = \exp\left(-\gamma \left\| x_i - x_j \right\|^2\right) \tag{12.14}$$

where γ = free parameter. Hyperparameter optimization is conducted to find the optimal parameters, γ, C, and ε, via a tenfold cross validation exhaustive grid search. The procedure generates the model based on all possible combinations of γ, C, and ε, where $\gamma \in [2^{-3}; 2^{-1}]$, $C \in [1; 13]$, and $\varepsilon \in [0; 1]$, in order to find the best combination that produces the least model error. All training and testing sets are normalized to the range (0,1) before building the SVR model in order for all variables, regardless of their magnitudes, to be weighted equally (Hsu et al. 2003).

12.2.4 Adaptive Neuro-Fuzzy Inference System (ANFIS)

The adaptive neuro-fuzzy inference system is an artificial intelligence methodology that uses a sequence of artificial neural networks (ANN) and fuzzy systems to build fuzzy IF-THEN rules with suitable membership functions obtained from the training pair, culminating in an inference. Such systems eliminate the requirement for manual fuzzy system parameter optimization and instead rely on ANN to modify the system parameters. Along these lines, combining ANN and FIS improves system operation without requiring administrators to intervene. Figure 12.5 shows the basic structure of ANFIS. The details of grid partitioning technique of ANFIS modelling can be found in Das et al. (2020).

12.2.5 Statistical Indices

To better explain the correlations among the results, five error analyses were considered as provided by Das and Khatua (2018b) Devi et al. (2017), i.e., the mean absolute percentage error (MAPE), mean absolute error (MAE), root mean square error (RMSE), root square (R^2), and Nash–Sutcliffe efficiency (E)

$$\text{MAPE} = \frac{1}{N}\sum_{i=1}^{N}\left(\left|\frac{(\text{Predicted value} - \text{Observed value})}{\text{Observed value}}\right|\right) \times 100 \qquad (12.14)$$

$$\text{MAE} = \frac{1}{N}\sum_{i=1}^{N}|(\text{Predicted value} - \text{Observed value})| \qquad (12.15)$$

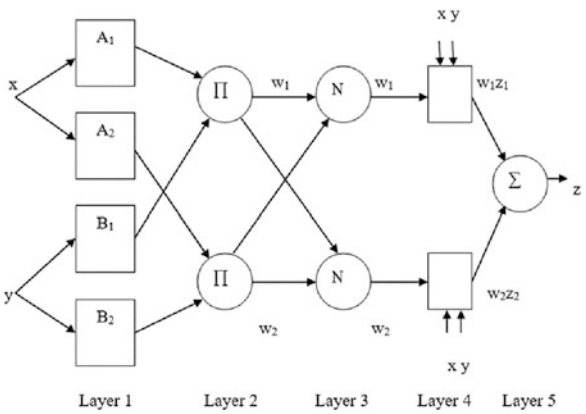

Fig. 12.5 A schematic diagram of ANFIS structure

$$\mathrm{RMSE} = \sqrt{\frac{1}{N}\sum_{i=1}^{N}(\text{Predicted value} - \text{Observed value})^2} \tag{12.16}$$

$$R^2 = 1 - \frac{\sum_1^n(\text{Predicted value} - \text{Observed value})^2}{\sum_1^n\left(\text{Predicted value} - \overline{\text{Observed}}\text{value}\right)^2} \tag{12.17}$$

$$E = 1 - \frac{\sum_{\mathrm{i}}^{n}(\text{Observed} - \text{Predicted})^2}{\sum_{\mathrm{i}}^{n}\left(\text{Observed} - \overline{\text{Observed}}\right)^2} \tag{12.18}$$

12.3 Development of Apparent Shear Force Model Using SVM

In this chapter percentage shear force is calculated using support vector machine (SVM) and by the help of calculated results percentage discharge is obtained. By using Mohanty and Khatua (2014) equation zonal flow rates are calculated and compared with ANFIS model along with other existing models related to percentage discharge calculation by the help of different error analysis method

$$U_{\mathrm{fp}} = \sqrt{\frac{\%S_{\mathrm{fp}}gAS_0}{12.5P_{fp}f_{fp}}} \tag{12.19}$$

$$U_{fp} = \sqrt{\frac{\%S_{\mathrm{mc}}gAS_0}{12.5P_{\mathrm{mc}}f_{\mathrm{mc}}}} \tag{12.20}$$

where U_{mc} and U_{fp}, P_{mc} and P_{fp}, f_{mc} and f_{fp}, $\%S_{\mathrm{mc}}$ and $\%S_{\mathrm{fp}}$ are the mean velocities, wetted perimeters, friction factors, and percentage shear forces in the respective main channel and flood plain. Finally, the expression for $\%Q_{\mathrm{mc}}$ is

$$\%Q_{\mathrm{mc}} = \left(\frac{U_{\mathrm{mc}}A_{\mathrm{mc}}}{(U_{\mathrm{mc}}A_{\mathrm{mc}}) + \left(U_{\mathrm{fp}}A_{\mathrm{fp}}\right)}\right) \times 100 \tag{12.21}$$

where A_{mc} and A_{fp} are area of main channel and floodplain, respectively.

12.3.1 Performance of SVM Model for Percentage Shear Force

After identifying the best input parameter combinations by gamma test, the combinations are further used for modeling in SVM. In SVM, four different kernel functions were introduced like cubic, fine Gaussian, medium Gaussian, and coarse Gaussian. After doing a lot of trials for training and testing, it was found that cubic Gaussian function gave the better result as compared to other functions. From Tables 12.3, 12.4, and 12.5, it is observed that the cubic SVM model is better than other kernel functions in estimating the ASF.

Table 12.3 Error analysis results of four different kernel functions using all seven parameters

Kernel functions	Cubic		Fine Gaussian		Medium Gaussian		Coarse Gaussian	
	TRN	TST	TRN	TST	TRN	TST	TRN	TST
MAE	2.39	**4.40**	4.78	17.29	5.09	6.78	11.13	13.74
MAPE	9.71	**22.41**	22.46	118.4	17.84	28.66	37.44	71.33
E	0.99	**0.99**	0.99	0.89	0.99	0.98	0.98	0.95
RMSE	2.31	**4.04**	4.99	17.96	4.55	6.34	9.91	11.94
R^2	0.99	**0.98**	0.98	0.68	0.97	0.94	0.90	0.85

Table 12.4 Error analysis results of four different kernel functions using five parameters excluding bed slope (S_0) and Froude number (Fr)

Kernel functions	Cubic		Fine Gaussian		Medium Gaussian		Coarse Gaussian	
	TRN	TST	TRN	TST	TRN	TST	TRN	TST
MAE	3.17	**4.61**	5.28	20.16	0.214	7.91	10.92	12.68
MAPE	10.34	**25.07**	24.7	136.3	0.009	32.20	34.29	65.96
E	0.99	**0.99**	0.99	0.86	0.026	0.98	0.98	0.95
RMSE	3.11	**3.11**	5.43	19.97	0.122	7.34	9.65	11.14
R^2	0.98	**0.97**	0.98	0.62	0.924	0.92	0.90	0.88

Table 12.5 Training and testing result for six different kernel function using six parameters excluding Froude No. (Fr)

Kernel functions	Cubic		Fine Gaussian		Medium Gaussian		Coarse Gaussian	
	TRN	TST	TRN	TST	TRN	TST	TRN	TST
MAE	3.25	**4.03**	5.28	19.43	5.40	6.80	10.37	12.75
MAPE	10.3	**16.6**	24.5	130.1	18.61	28.41	34.11	65.48
E	0.99	**0.99**	0.99	0.87	0.99	0.98	0.98	0.95
RMSE	2.99	**2.99**	5.42	19.32	5.10	6.49	9.60	11.23
R^2	0.99	**0.99**	0.98	0.62	0.97	0.94	0.90	0.87

12.3.2 Sensitivity Analysis

Sensitivity analysis is performed to find out efficacy of present model. It is depicted in Table 12.6 in terms of four statistical parameters such as MAPE, E, RMSE and R^2. By the help of sensitivity analyses the variation of %Sfp with different input combinations are performed. From Table 12.6 it is found that $\%S_{fp}$ is sensitive to Fr, m, and γ.

12.3.3 Discharge Calculation Using $\%S_{fp}$ Modelled from SVM

In compound river channel, actual prediction of discharge is rigorous work due to variation of inflow resistance and the difference in geometric and hydraulic characteristics of the subsection. Previously many researchers have formulated for the percentage of flow carried by the main channel ($\%Q_{mc}$) of a compound channel as mentioned below:

Knight and Demetriou (1983).

$$\%Q_{mc} = \left[\frac{100}{\{(\alpha-1)\beta+1\}}\right] + 108\left[\frac{\alpha-1}{\alpha}\right]^{0.25}[3.3\beta]^{\frac{4}{\alpha}}e^{-9.9\beta} \tag{12.22}$$

Khatua and Patra (2007).

$$\%Q_{mc} = 1.2338\left[\frac{100}{\{(\alpha-1)\beta+1\}}\right]^{0.9643} \tag{12.23}$$

Mohanty and Khatua (2014).

Table 12.6 Sensitivity analysis of the present model (Cubic SVM)

Sensitivity analysis	MAPE	E	RMSE	R^2
Model 1: $\%S_{fp} = f(S_o, \beta, \alpha, \delta, \gamma, \text{Fr}, m)$	6.14	0.99	2.21	0.98
Model 2: $\%S_{fp} = f(S_o, \beta, \alpha, \delta, \text{Fr})$	10.95	0.86	4.64	0.83
Model 3: $\%S_{fp} = f(S_o, \beta, \alpha, \delta, \gamma, m)$	6.05	0.91	4.32	0.92
Model 4: $\%S_{fp} = f(S_o, \beta, \alpha, \delta, m)$	9.31	0.84	3.91	0.81
Model 5: $\%S_{fp} = f(S_o, \beta, \alpha, \gamma, \text{Fr}, m)$	7.78	0.82	7.64	0.89
Model 6: $\%S_{fp} = f(S_o, \beta, \delta, \gamma, \text{Fr}, m)$	7.17	0.88	5.45	0.91
Model 7: $\%S_{fp} = f(\beta, \alpha, \delta, \gamma, \text{Fr}, m)$	6.69	0.84	2.8	0.93

$$\%Q_{mc} = \left(\frac{U_{mc}A_{mc}}{(U_{mc}A_{mc}) + (U_{fp}A_{fp})} \right) \times 100 \tag{12.24}$$

Devi et al. (2016)

$$\%Q_{mc} = 1.715 \left\{ \frac{100\Psi(\delta + s + s\beta)}{\Psi(\delta + s) + s\beta(\delta - 2\Psi) + \Psi\delta\beta(\alpha - 1)} \right\}^{0.9} \tag{12.25}$$

In Fig. 12.6a–e scattered plots have been plotted between observed discharge and predicted discharge by present model and various existing models.

12.3.4 Development of Model Using ANFIS

In this section, after the development of percentage shear force by using support vector machine (SVM), now with the help of same non-dimensional input parameters percentage shear force is modelled by ANFIS. With the help of calculated shear force percentage discharge is obtained in floodplains. By selecting input, the 75% training data and 25% of testing data ANFIS modelling is performed for various MF types and with different number of MFs. Error analyses are performed for the outputs obtained by ANFIS Modelling on large scale as mentioned in Table 12.7.

12.3.5 Analyses of Selected Membership Function Type

In Table 12.7 all error analysis is tabulated for various MF types. Among them gbellMF type with number of MF [22223] is better than others MF types with MAPE value 5.02%, RMSE value 1.76, and COD value 0.99. A scattered plot between overserved percentage discharge versus predicted discharge is plotted which are obtained using ANFIS Model is shown in Fig. 12.7.

12.4 Results and Discussions

In the present study percentage shear force in floodplain is calculated by the help of SVM model and ANFIS model. With the help of percentage shear force, percentage discharge is also calculated. Error analyses have been done on the output obtained by the both models.

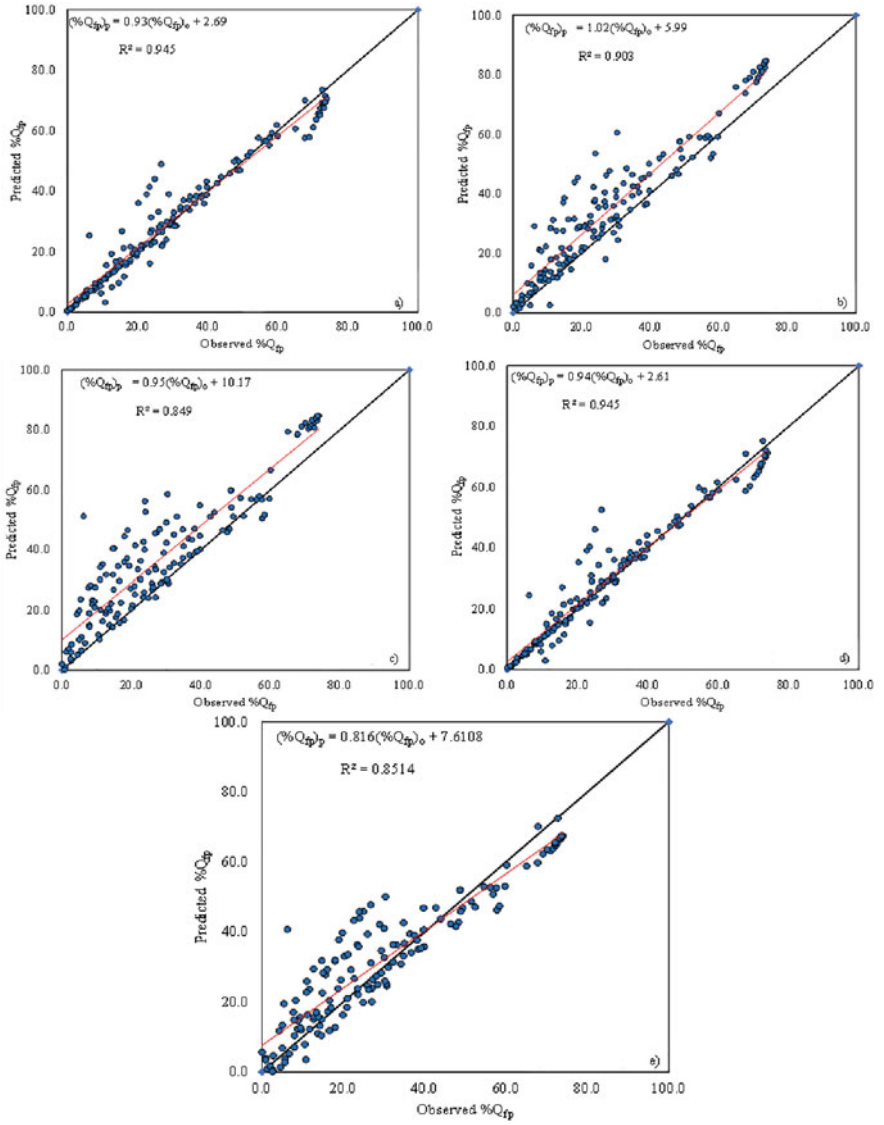

Fig. 12.6 Observed vs. Predicted percentage discharge in floodplain using (**a**) SVM model, (**b**) Knight and Demetriou (1983) (**c**) Khatua and Patra (2007), (**d**) Mohanty and Khatua (2014), and (**e**) Devi et al. (2016)

12.4.1 Comparison Between SVM and ANFIS Model

After performing all six kernels of SVM by using different combination of input dataset it is concluded that cubic SVM is better than other SVMs model. Similarly,

Table 12.7 Different error indices for analyzing the computed shear force

MF TYPE		MAPE		RMSE		R^2		E	
gbellmf	No.of MF	Training	Testing	Training	Testing	Training	Testing	Training	Testing
gbellmf	2 2 2 2 2	1.335	14.428	1.171	3.973	0.997	0.972	0.9995	0.989
gbellmf	2 2 2 2 3	0.377	**5.054**	0.282	**1.766**	1.000	**0.992**	1.0000	0.998
gbellmf	2 2 2 3 2	0.475	32.678	0.378	13.930	1.000	0.535	0.9999	0.870
gbellmf	2 2 3 2 2	0.309	9.612	0.198	7.404	1.000	0.847	1.0000	0.963
gbellmf	2 3 2 2 2	0.867	73.805	0.934	24.691	0.998	0.088	0.9997	**0.593**
gbellmf	3 2 2 2 2	0.458	13.000	0.304	4.418	1.000	0.944	1.0000	0.987
gbellmf	3 3 3 3 3	0.071	13.440	0.049	7.539	1.000	0.856	1.0000	0.962
gbellmf	3 3 3 3 2	0.119	9.001	0.086	8.045	1.000	0.825	1.0000	0.957
gbellmf	3 3 3 2 3	0.086	15.531	0.063	9.156	1.000	0.831	1.0000	0.944
gbellmf	3 3 2 3 3	0.163	15.799	0.126	7.680	1.000	0.850	1.0000	0.961
gbellmf	3 2 3 3 3	0.164	10.338	0.098	6.441	1.000	0.884	1.0000	0.972
gbellmf	2 3 3 3 3	0.081	15.414	0.056	9.251	1.000	0.755	1.0000	0.943
gaussmf	2 2 2 2 2	0.665	12.511	0.436	3.890	1.000	0.960	0.9999	0.990
gaussmf	2 2 2 2 3	0.433	12.131	0.263	3.178	1.000	0.973	1.0000	0.993
gaussmf	2 2 2 3 2	0.506	59.325	0.382	17.317	1.000	0.289	0.9999	0.800
gaussmf	2 2 3 2 2	0.325	10.661	0.204	5.840	1.000	0.899	1.0000	0.977
gaussmf	2 3 2 2 2	0.537	35.328	0.466	10.878	1.000	0.675	0.9999	0.921
gaussmf	3 2 2 2 2	0.490	12.127	0.309	4.395	1.000	0.945	1.0000	0.987
gaussmf	3 3 3 3 3	0.101	16.740	0.067	6.049	1.000	0.909	1.0000	0.976
gaussmf	3 3 3 3 2	0.119	16.498	0.097	4.561	1.000	0.943	1.0000	0.986
gaussmf	3 3 3 2 3	0.107	15.610	0.071	9.068	1.000	0.815	1.0000	0.945
gaussmf	3 3 2 3 3	0.281	72.201	0.310	28.622	1.000	0.079	1.0000	0.453
gaussmf	3 2 3 3 3	0.373	38.403	0.260	12.156	1.000	0.643	1.0000	0.901
gaussmf	2 3 3 3 3	0.061	15.303	0.053	9.516	1.000	0.767	1.0000	0.940

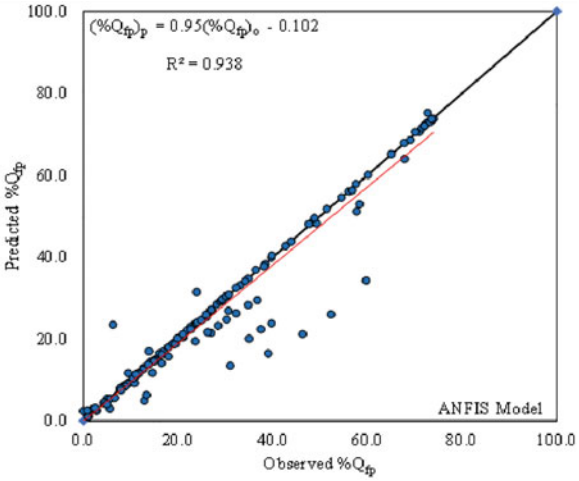

Fig. 12.7 Observed vs. predicted percentage discharge in floodplain using ANFIS

Table 12.8 Error analysis between present model and other existing models in predicting $\%Q$fp

MODELS	MAE	MAPE	E	RMSE	$/R^2$
ANFIS (present model)	3.68	11.48	0.98	5.60	0.93
SVM (present model)	3.57	10.48	0.99	4.84	0.94
K & D (1983)	7.27	12.12	0.93	9.5	0.88
K & H (1984)	9.01	14.36	0.94	11.98	0.84
M & K (2014)	7.89	11.68	0.91	13.84	0.69
Devi et al. (2016)	6.53	10.32	0.96	8.82	0.83

by performing large trial in ANFIS Model, gbellmf type with number of mf (2 2 2 2 3) is found to give better results than other ANFIS model type.

Secondly, percentage discharge is calculated using percentage shear force obtained by both models and error analysis is done which is mentioned in Table 12.8. Scattered plots are drawn between observed percentage discharge and predicted percentage discharged obtained by ANFIS modelling and SVM modelling as shown in Fig. 12.8.

Now percentage discharge calculated by SVM and ANFIS is compared with others existing models as mentioned in Table 12.8. In the present model, the value of MAPE is less than others existing models. Coefficient of determination is greater than 0.9 in present model and other model providing a value less than 0.90. SVM providing MAPE value 10.48% with R^2 value of 0.94, which confirms the better predictability of percentage floodplain discharge in compound channel. Scattered plot between observed percentage discharge versus predicted percentage floodplain discharge by present model and others existing model is shown in Fig. 12.9.

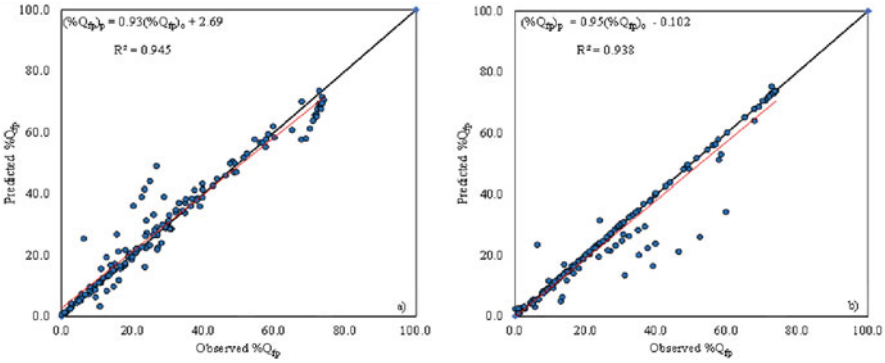

Fig. 12.8 Observed vs. predicted percentage discharge in floodplain using SVM and ANFIS Model

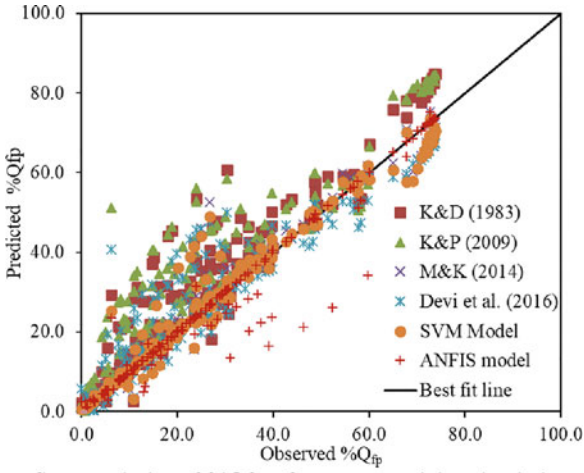

Fig. 12.9 Scattered plot of %Qfp of present model and existing models

12.5 Conclusions

In this paper total number of datasets is 152. Out of which 75% is used for training purpose and 25% is used for testing. SVM and ANFIS models have been developed to calculate percentage shear force by which percentage discharge at floodplain is obtained. Four statistical error analysis (MAPE, E, RMSE, and R^2) have been performed to identify the better SVM model. From the analysis, it is obtained that cubic SVM is better than other SVMs types. Using cubic SVM, percentage shear force of floodplain is calculated. These shear force values are used to estimate the floodplain discharge using empirical relation provided by other researchers. ANFIS modelling for predicting percentage shear force is also performed. It is found that the gbellMF with number of membership function [22223] is found to provide better results among other combination of ANFIS model. Comparison between SVM and

ANFIS model has been performed, SVM model found to provide better results as compared to ANFIS. Furthermore, error analysis is performed for other discharge predicting model along with the present models (SVM and ANFIS). From the analysis, it is found that the MAPE value is less than 11% and coefficient of determination (R^2) is greater than 0.93. It indicates that performance of present model is comparatively better than other existing models. The limitation of the present model is the range of data set used in determining the best predictions. Thus, for the present range of data set, the model can be applied to field conditions.

References

Bonakdari H, Khozani ZS, Zaji AH, Asadpour N (2018) Evaluating the apparent shear stress in prismatic compound channels using the genetic algorithm based on multi-layer perceptron: a comparative study. Appl Math Comput 338:400–411

Chen Z, Chen Q, Jiang L (2016) Determination of apparent shear stress and its application in compound channels. Proc Eng 154:459–466

Cortes C, Vapnik V (1995) Support-vector networks. Mach Learn 20(3):273–297

Das BS, Khatua KK (2018a) Numerical method to compute water surface profile for converging compound channel. Arab J Sci Eng 43(10):5349–5364

Das BS, Khatua KK (2018b) Flow resistance in a compound channel with diverging and converging floodplains. J Hydraul Eng 144(8):04018051

Das BS, Devi K, Khuntia JR, Khatua KK (2020) Discharge estimation in converging and diverging compound open channels by using adaptive neuro-fuzzy inference system. Can J Civ Eng 47(12):1327–1344

Devi K, Khatua KK, Das BS (2016) Apparent shear in an asymmetric compound channel. River Flow 2016:48–56

Devi K, Khatua KK, Das BS, Khuntia JR (2017) Evaluation of interacting length in prediction of over bank flow. ISH J Hydraul Eng 23(2):187–194

Devi K, Das BS, Khuntia JR, Khatua KK (2021) Analytical solution for depth-averaged velocity and boundary shear in a compound channel. Proc Inst Civil Eng Water Manag 174(3):143–158. https://doi.org/10.1680/jwama.18.00062

Devi K, Das BS, Khuntia JR, Khatua KK (2022) Boundary shear stress distributions in compound channels having narrowing and enlarging floodplains. In: Jha R, Singh VP, Singh V, Roy LB, Thendiyath R (eds) River hydraulics. Water Science and Technology Library, vol 110. Springer, Cham. https://doi.org/10.1007/978-3-030-81768-8_11

Durrant PJ (2001) winGamma: a non-linear data analysis and modelling tool with applications to flood prediction. Unpublished PhD thesis, Department of Computer Science, Cardiff University, Wales, UK

Hsu CW, Chang CC, Lin CJ (2003) A practical guide to support vector classification, Tech. rep., Department of Computer Science, National Taiwan University: pp 1396–1400. http://www.datascienceassn.org/sites/default/files/Practical%20Guide%20to%20Support%20Vector%20Classification.pdf

Khatua KK, Patra KC (2007) Boundary shear stress distribution in compound open channel flow. ISH J Hydraul Eng 13(3):39–54

Khuntia JR, Devi K, Khatua KK (2018) Boundary shear stress distribution in straight compound channel flow using artificial neural network. J Hydrol Eng 23(5):04018014

Khuntia JR, Devi K, Khatua KK (2019) Flow distribution in a compound channel using an artificial neural network. Sustain Water Resour Manag 5(4):1847–1858

Knight DW, Demetriou JD (1983) Floodplain and main channel flow interaction. J Hydraul Eng 109(8):1073–1092
Knight DW, Hamed ME (1984) Boundary shear in symmetrical compound channels. J Hydraul Eng 110(10):1412–1430
Mohaghegh A, Kouchakzadeh S (2008) Evaluation of stage-discharge relationship in compound channels. J Hydrodynam B 20(1):81–87
Mohanty PK, Khatua KK (2014) Estimation of discharge and its distribution in compound channels. J Hydrodyn 26(1):144–154
Prinos P, Townsend RD (1984) Comparison of methods for predicting discharge in compound open channels. Adv Water Resour 7(4):180–187
Rezaei B (2006) Overbank flow in compound channels with prismatic and non-prismatic floodplains. Dissertation, University of Birmingham, UK
Sahoo N (2012) Effect of differential roughness on flow characteristics in a compound open channel. Dissertation, NIT Rourkela, India
Tang X (1999) Derivation of the wave speed-discharge relationship from cross section survey for use in approximate flood routing methods. Doctoral dissertation, University of Birmingham
Tang X (2019) A new apparent shear stress-based approach for predicting discharge in uniformly roughened straight compound channels. Flow Meas Instrum 65:280–287
Xie Z, Lin B, Falconer RA (2013) Large-eddy simulation of the turbulent structure in compound open-channel flows. Adv Water Resour 53:66–75

Chapter 13
Sediment Transport Modeling through Machine Learning Methods: Review of Current Challenges and Strategies

Kiyoumars Roushangar, Saman Shahnazi, and Hazi Mohammad Azamathulla

Abstract Sediment transportation in rivers is considered as an important issue for designing and planning the water resources projects and can damage the environment. Therefore, modeling the components of sediment load, including suspended sediment load, bed-load, and total load in rivers is of greatest significance. Effective modeling of sediment load components remains a challenging task since their complicated hydrological procedure. On this account, this chapter aims to appraise the role of machine learning methods in modeling the sediment transport and review the different strategies for increasing the level of modeling accuracy. For this purpose, an overview of machine learning approaches and a discussion of challenges and opportunities of modeling sediment transport which have relatively replaced time-consuming conventional mathematical techniques are provided.

Keywords Sediment transport · Bed-load · Total load · Machine learning

13.1 Introduction

Soil erosion and sediment load in water streams have accelerated by an average of 225 t/km^2/year as a result of anthropogenic proceedings such as deforestation and massive agriculture development (Madani Cherif et al. 2017, Pandey et al. 2019, 2020 and Pu et al. 2021). Massive sediment transport can pose serious hazards to

K. Roushangar
Department of Water Resource Engineering, Faculty of Civil Engineering, University of Tabriz, Tabriz, Iran

Center of Excellence in Hydroinformatics, University of Tabriz, Tabriz, Iran

S. Shahnazi
Department of Water Resource Engineering, Faculty of Civil Engineering, University of Tabriz, Tabriz, Iran

H. M. Azamathulla (✉)
Civil and Environmental Engineering, University of the West indies, Port of Spain, Trinidad

M. Pandey et al. (eds.), *River Dynamics and Flood Hazards*, Disaster Resilience and Green Growth, https://doi.org/10.1007/978-981-19-7100-6_13

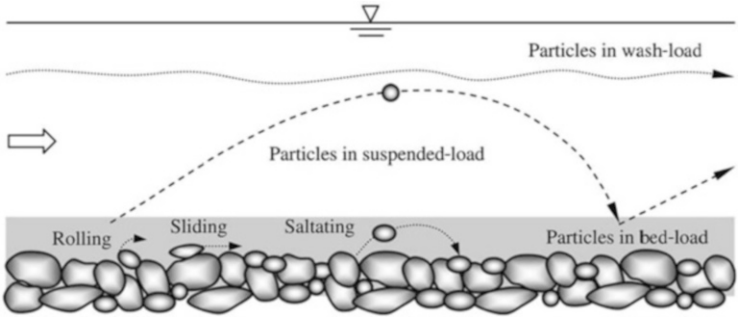

Fig. 13.1 Different forms of sediment transport (Dey 2014)

downvalley settlements and infrastructure. This natural phenomenon decreases the useful volume of dam reservoir and poses a threat to the dam's design life span. In critical conditions the water varieties behind the dam exceeds the crest varieties and water overflows from the crest. High sediment transfer rate can be one of the drivers to increase the flood risk by reducing the cross sections after sedimentation and changing the river pattern (Sinnakaudan et al. 2003; John et al. 2021a, b; Shivashankar et al. 2022). Sediment transport has caused morphodynamic changes due to aggradation and degradation of the rivers bed, which threatens the hydraulic structures. Moreover, it can also lead to environmental issues through the effects on habitats of aquatic biota.

The complicated nature of interaction amongst the turbulent flow and the sediment particles has raised the sediment transport as a highly complicated issue, and thus several influential parameters for instance the basin hydrological regime, the geometry of channel, types of the flow stream, the trend of flow, bed roughness, stream power, gravity, the channel morphology, channel width, channel slope, channel cross-sectional area, and sediment particle sizes distribution of river bed material should be considered in the sediment transportation to and through the river system (Almedeij and Diplas 2003; Pandey and Md Azamathulla 2021; Shankar et al. 2021; Singh et al. 2022). Vanoni (1975) defined the two concepts of bed-load and suspended load as two forms of sediment transport in rivers (Fig. 13.1). In terms of bed-load transport, the movements of individual sediment particles appeared mostly by rolling of the majority of the particles and sliding or hoping of the smallest ones (known as saltation), and rarely by brief sliding of large, angular ones, so they are in frequent contact with the channel bed. On the contrary, in the case of suspended load, the turbulent force of the water supports the weight of particles, and they can move significant distances without contacting the channel bed. Herein, the washed load is ignored, which can be substantial. This can be due to the lack of a reliable parallel record of all three quantities, as well as the greater importance of solid loads in hydraulic projects.

Generally, highly non-linear and interacting procedures raise the complexity of sediment transportation from the beginning of sediment particles detachment during an erosion event to the place of deposition. On the other hand, the direct

measurement of bed-load in rivers is a time-taking and costly procedure, especially during flooding. Therefore, requisite morphological and sediment data are not always available. These reasons encouraged researchers to numerous laborious field works for deeper insight into sediment transport behavior and the estimation of individual components. Having the capability to thoroughly regulate boundary conditions and conduct accurate measurements is one of the reasons for the expansion of laborious field works. However, experimental studies have suffered from some drawbacks: (Ackers and White 1973) they are expensive and time-consuming studies; (Almedeij and Diplas 2003) they are developed under equilibrium sediment transport conditions with the steady and uniform flow for simplification of the natural river; (Azamathulla 2014) experimental studies are scaled forms of a natural system, and hence several issues can be exited in accurately scaling sediment and flow characteristics; and (Azamathulla et al. 2009) the sediment volumes that can be replicated in a laboratory experiment is limited. Therefore, the experimental equations obtained from experimental studies have a high predicting uncertainty degree. The existing sediment transport equations were developed under restricted flow conditions and specific sediment particle features. Thus, their field applicability under varied hydraulic conditions is questionable (Khorram and Ergil 2010a, b). Generally, it is exceedingly problematic for river engineers to choose an appropriate equation for the particular case study. As a consequence, none of these equations has received general adoption for the sediment transport quantification. Moreover, different models of empirical and mathematical, and numerical methods have been extended for modeling the sediment transport that have their own weaknesses. The aforementioned methods are process-based models, and require extensive data for building, calibration, and validation the model. In addition, if the physics is not properly understood, model parameterization and calibration encounter great complexity and difficulty (Hamel et al. 2017). Based on the above-mentioned issues, a versatile and flexible technique with a non-linear modeling structure is needed for the computation of sediment transport rate. In recent years, the emergence of methods of data mining and machine learning are suggesting novel opportunities for modeling complex hydraulic phenomena such as sediment transport. Machine learning approaches can solve non-linear models by deducing the optimum relationship among the inputs (that is important conditioning variables) and the target (that is output variable) and can easily handle a large number of data and complicated models. Over the past years, there has been observed a considerable increase in the number of machine learning techniques used in hydraulic phenomena modeling, especially in predicting the sediment transport rate). Particularly, in the sediment transport prediction area, there are numerous machine learning techniques that have been employed, like artificial neural network (ANN), adaptive network-based fuzzy inference system (ANFIS), support vector machine (SVM), and different algorithms of evolutionary. This can be indicator of a high potential of machine learning based approaches for prediction of localized sediment transport characteristics. As such, the aim of the present chapter is to review how efficiently the employed machine learning techniques have been implemented to model sediment transport rate (bed-load and bed material load), specifically with regard to the machine learning

models structure, different input parameters as well as the machine learning hybrid modeling potency.

13.2 Artificial Neural Network Modeling

Among the numerous machine learning techniques, ANNs can be considered as the most popular and widely used methods in modeling hydrological, hydraulic phenomena, and water resources management. ANNs are one of the powerful modeling methods that are commonly utilized for the recognition of patterns, forecasting, estimation, optimization, and developing relationships between complicated featured parameters. ANN is a massively parallel distributed information processing system that benefits from definite pattern similar to the human brain biological neural networks. ANNs have been developed as computational models inspired by biological neural networks that simulate human brains based on the subsequent instructions described by Govindaraju and Rao (2013): (Ackers and White 1973) Information processing takes place in many individual elements called neurons; (Almedeij and Diplas 2003) connecting links are responsible for passing signals between nodes; (Azamathulla 2014) Each connection link owns a related weight as an indicator of its connection strength; and (Azamathulla et al. 2009) a non-linear transformation known as an activation function is applied to net input of each node for determination of output signal. ANN is capable of learning the exact architecture among the inputs and outputs of the samples without any form of physical intervention or further explanation. ANNs have been effectively employed as a notorious machine learning model for sediment transport prediction. Generally, the performance of employed ANNs models is considerable, and they can accurately predict the sediment transport rates by up to 90%. One of the initial studies in the field of using machine learning in sediment transport modeling is related to Bhattacharya et al. (2007). They prepared a compilation of numerous laboratory and field data sets for modeling sediment transport. The modeling process was established through a minimum set of dimensionless variables; thus, the particle parameter (D_*) and transport stage parameter (T) were considered as input parameters, while the targets were the bed-load and total sediment load. The back-propagation neural network with hyperbolic tangent activation function for hidden layer neurons, and a linear activation function at the output layer neuron was utilized as the training algorithm. The number of hidden layer neurons were determined through a trial and error process. The quantification ability of employed machine learning methods was compared with the empirical equations in which the machine learning methods had better outcomes compared to the empirical methods. In addition, other strategies such as including an additional input variable and dividing the data set into lower and upper regime conditions were used to increase the modeling accuracy, none of which improved the performance of the employed methods.

Doğan et al. (2007) studied the modeling capability of total sediment load concentration with a three-layer feed-forward back-propagation function using the

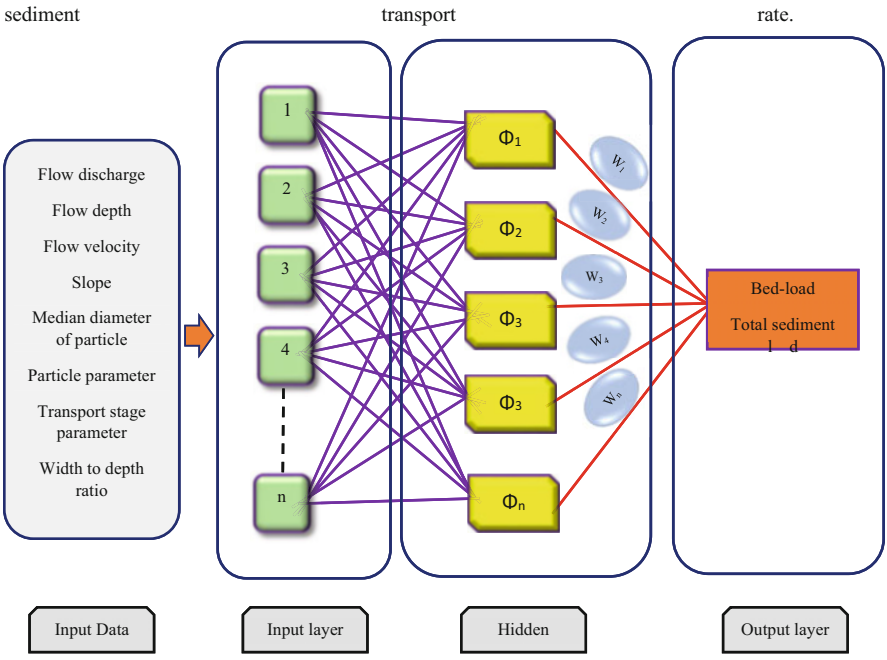

Fig. 13.2 Architecture of ANN sediment transport model

water discharge, channel bed slope, mean sediment diameter, and experimental data. The results obtained from the analysis indicate the occurrence of overfitting with increasing the epoch number. Moreover, based on the performed sensitivity analysis, the water discharge was found to be most effective on modeling the sediment concentration.

Yang et al. (2009) used a three-layered feed-forward net with a back-propagation training algorithm for the prediction of the total sediment load in ten river stations in the USA. Four input variables of average velocity, average depth, water surface slope, and median particle diameter were used where the total sediment load was the target. Comparison between outcomes from the artificial neural network and five well-known formulas in the bed material load estimation of Ackers and White (1973) showed that the neural network provided promising prediction results.

As proposed by Sasal et al. (2009), different combinations of input parameters for bed-load transport was surveyed to acquire precise outcomes. The 592 cross-section averaged bed-load samples from 16 different rivers were used for bed-load estimation. This research demonstrated that a neural network model using two concealed layers and only two inputs (including the particle parameter and transport stage parameter) was found to perform adequately. Figure 13.2 depicts the neural network architecture and the employed input parameters for the prediction of sediment transport rate.

13.3 Adaptive Neuro-Fuzzy Inference System Sediment Model

Jang (1993) proposed the framework and the learning process of the fuzzy inference systems (FISs). An artificial neural network is embedded in this learning method in order to build a series of fuzzy IF-THEN rules with suitable membership functions (MFs) of the input–output model. Three main components, including a fuzzy database, fuzzifier, and defuzzifier, form the structure of the fuzzy system. The key objective of the fuzzifier is to transform the crisp input to fuzzy inputs through MF, which indicates the fuzzy set of input vectors. The Defuzzifier feature, on the other hand, converts the fuzzy output into a crisp output (Fig. 13.3). The fuzzy database comprises two parts, which are the Fuzzy rule base (described through the conditional sentence IF-THEN) and the inference system. Based on the kinds of interface operations within the IF-THEN rule, three kinds of primary fuzzy interface systems, including Kanno's system, Tsukamoto's system, and Mamdani's system can be introduced. Mamdani's system is known as the most widely used fuzzy interface system. On the other hand, Sugeno's system is further compacted and computationally effective; the output is crisp with better processing period as the weighted average substitutes the time-consuming defuzzification operation (Takagi and Sugeno 1985). There are also a number of published studies describing the ANFIS role in modeling sediment transport. The ANFIS initial research in the prediction of rivers bed-load transport was by Azamathulla et al. (2009). They modeled the bed-load transport rate of moderately sized rivers through ANFIS and ANN models. The flow parameter, hydraulic radius, median particle diameter, average velocity, and the specific gravity of sediment were used as observed input parameters of models. A total of 346 sets of bed-load data acquired from four Malaysian rivers were used to assess the performance of employed ANFIS and ANN models. This study showed that the employed ANFIS model is more flexible and time-consuming than the ANN.

Kitsikoudis et al. (2014) predicted the bed-load transport rate of gravel-bed rivers by using ANFIS with the input parameters relying on shear stress and stream power.

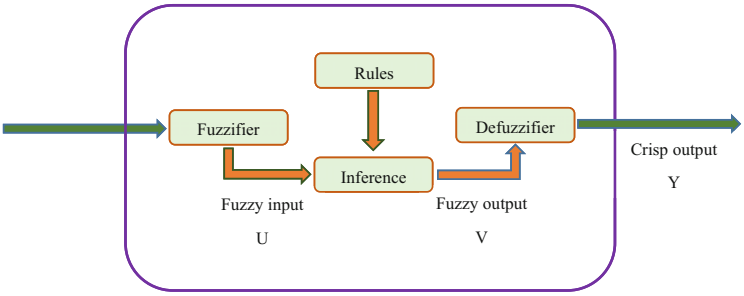

Fig. 13.3 A fuzzy inference system

Both studies stated the similar performance of the models derived from ANNs and ANFIS in predicting bed-load transport rate.

Riahi-Madvar and Seifi (2018) adopted an uncertainty analysis to predict the bed-load transport rate of gravel-bed rivers through ANFIS and ANN models. Twenty-one different combinations of effective parameters, including, median particle diameter, flow depth, surface slope, discharge water shear stress, and hydraulic radius, were used to extent input models for bed-load modeling. This study indicated the worst results of models with one or two input parameters due to the inherent physics of bed-load transport. It was shown that the ANFIS model presented better predictive ability for bed-load transport compared to the ANN outcomes. One of the important challenges in the application of machine learning methods is optimum dividing the data into testing and training subsets, formerly divided randomly through a trial and error process. The training group should include the high and low values of the data in order to enhance the model results validity in unseen data as well as to achieve the superior structure for the records. In order to cover this shortcoming, they combined the subset selection of maximum dissimilarity (SSMD) technique selection with ANN and ANFIS models to optimum select the modeling stages. The satisfactory performance of employed ANFIS and ANN models in the test phases than the training phase, confirmed the proposed SSMD efficiency in the implementations of machine learning models. The findings of this study can help to eliminate the overfitting challenges of machine learning model developments. As described in the introduction section, sediment transport in natural rivers is a very complicated process and produces uncertainty of the prediction. The reasons for uncertainty of ANFIS and ANN for prediction of sediment transport are (Ackers and White 1973) incomplete and noisy training data, (Almedeij and Diplas 2003) model limitations—local minima, suboptimal optimization procedures, and (Azamathulla 2014) unsuitable parameterization technique (network topology) (Talebizadeh et al. 2010; Talebizadeh and Moridnejad 2011). The input and output measuring errors are among the reasons for uncertainty that is unclear. The Monte Carlo simulation was used in the study of Riahi-Madvar and Seifi (2018) to determine the uncertainty analysis of ANN and ANFIS models. The results exhibited relatively large uncertainties of employed models in predicting the bed-load transport rate of gravel-bed rivers and confirmed that practical application of these models requires significant effort in training and developing processes. It was also found that the uncertainty bounds of the ANN model are broader compared with those for the ANFIS model.

13.4 Other Machine Learning Methods

In this section, other machine learning techniques assessment that have been used in sediment transport prediction is introduced. Despite the relative success of neural networks at solving the problem of sediment transport, their implementation as a general-purpose tool is difficult due to some disadvantages. Artificial neural

networks have two major disadvantages. Firstly, their structure should be defined before the training process. Secondly, the regularization methods, in particular, termination and training with noise are somewhat limited. Moreover, ANNs can encounter local minima while training process of the model (Smola 1996). Support Vector Machines (SVM) is based on the structural risk minimization principle, which leads to a good generalization ability. Introduced by Vapnik (1998), SVM is growing in popularity owing to many attractive characteristics and great generalization performance in the water resources field. Moreover, the SVM incorporates the principles of structural risk minimization (SRM) that has been proven to be better than the conventional empirical risk minimization (ERM) used through traditional neural networks. SRM minimizes an upper bound of generalization error versus ERM, which minimizes the error on training data. Thus, while SVM can represent global optimal solutions, other neural network models are prone to fall into a locally optimal solution (Cristianini and Shawe-Taylor 2000). The initial research with the SVM technique in total sediment load prediction was conducted by Azamathulla et al. (2010). The SVM model calibration was carried out in reliance on 214 input-target pairs of the collected data from Malaysian rivers. The outcomes suggested that the employed SVM model is a powerful total load predictor.

Roushangar and Shahnazi (2020a, b) adopted a kernel-based approach represented by the Gaussian process regression (GPR) model to predict the sediment transport rate of 19 gravel-bed rivers in the USA. The radial bases function (RBF) was used as a kernel function to develop the employed models. The modeling outcomes of the GPR model were compared to the commonly used SVM methods, where it was recognized that the GPR has better performance. Performing sensitivity analysis indicated the key role of the ratio of average velocity to shear velocity as the input parameter in the sediment transport rate of gravel-bed rivers. It was also observed that the employed SVM model was more prone to the risk of overfitting than the GPR model. This problem occurs due to the small values of RBF kernel parameters and, consequently, ignoring most of the support vectors, which is considered as one of the major challenges in implementing the kernel-based SVM model.

Similar results were also found by Roushangar and Shahnazi (2020a, b), who applied kernel-based techniques including Kernel-based extreme learning machine (KELM), GPR, and SVM to model the total sediment based on the extensive database collected from mountain rivers. They declared that considering hydraulic characteristics as inputs gives the nearly perfect fit for the observed average total sediment load. RBF kernel parameter represents the optimal width of the kernel function. Higher values of RBF kernel parameter let kernel-based methods have a strong influence over a large area and increase the model complexity. The findings of Roushangar and Shahnazi (2020a, b) demonstrated that utilizing KELM produced more accurate total sediment prediction than GPR and SVM with lower values of RBF kernel parameter (lower complexity) and input parameter.

Machine learning methods can be categorized into computer-aided methods such as ANN, ANFIS, SVM, GPR, and explicit methods such as gene expression programming (GEP). The first group is called black-box techniques, and this

means that they make the connection between inputs and output easily and without understanding the physical information about the process, while the second group is known as white-box techniques, which denotes that they provide explicit expressions. Genetic programming (GP) is one of the evolutionary algorithms that inspired by biological evolution, seeks to find computer programs that conduct user-defined tasks. This technique was developed by Koza (1994) in which various mathematical components such as constants, arithmetic operations, and functions are taken, and equations are developed through merging them into an individual expression. GEP is the extension of the traditional tree-based GP. The primary research employing the evolutionary algorithms in bed material prediction was carried out by Zakaria et al. (2010). They concluded that GEP could effectively model total load transport in a wide fluvial environments diversity, encompassing both gravel and sand rivers.

Chang et al. (2012) examined the potential of GEP in modeling the total sediment load of Malaysian rivers. A GEP model was established to predict the total sediment load using flow discharge, average velocity, river width, flow depth, hydraulic radius, and water surface slope as inputs. The outcomes were compared to the outcomes of ANFIS and ANN models. The outcomes of this study indicated the poor performance of the fuzzy model compared to other employed methods. It was deduced that although GEP requires relatively long training times, it is highly competent and performs well in predicting total bed material load transport. This evolutionary algorithm has the ability to ascertain the inherent non-linearity between hydraulic and sediment parameters of rivers and total bed material load with remarkable accuracy.

Azamathulla (2014) predicted the total bed material load of tropical rivers through three dimensionless parameters, including the width to flow depth ratio, the ratio of hydraulic radius to the median diameter of particle size, and particle densimetric Froude number. A GEP model that was completed with trained values demanding the input of grouped parameters relating to transport, sediment, conveyance shape and mobility was confirmed as a robust sediment load predictor.

Roushangar et al. (2014) predicted the total bed material load by developing the GEP and ANFIS methods with the input parameters derived from the widely-known empirical models. Sediment data from Qotur River (Northwestern Iran) were utilized for evolving and validating of the employed methods. Comparing the effect of various input models on prediction accuracy of employed machine learning methods demonstrated higher reliability of models based on the concept of stream power than models based on shear stress in predicting total bed material load of natural rivers. This study demonstrated that although the ANFIS was relatively superior, but GEP is a robust tool for data analysis and can present a simple and explicit quantitative formula that can be utilized by anyone not specialized with the GEP method. It can be said that GEP gives a practical way for sediment transport prediction and encourages researchers to use GEP as a superior to other proposed machine learning methods.

Despite the high popularity of the genetic algorithm as an evolutionary algorithm with good performance, this algorithm still has some drawbacks. Besides, they could be as slow for real-time application as the extremely complicated nature of some

solutions. In GP, a solution converges randomly, irrespective of the employed fitness function, which is one of the main challenges of using it for even unrealistic applications. The optimization algorithm also involves several parameters that increase the time. Unguided metamorphosis and mutation of GA are considered as the identical rudimentary disadvantage of this evolutionary algorithm. In GA functions, a randomly created number for a parameter of an individual from the population is usually generated through the mutation operator, which results in very slow convergence of the algorithm. Combination of GA with guided search algorithms such as differential evolution can be used to solve this problem. However, this algorithm efficiency is so far to be affirmed with confidence within any sedimentation prediction model.

13.5 Hybrid Machine Learning Methods

Recently, substantial consideration has been provided to the optimization of machine learning hyper-parameters. The quality and performance of machine learning technique depends on optimal hyper-parameters tuning. In machine learning, hyper-parameter refers to the parameters that are fixed before the beginning of the actual learning procedure, which directly cannot be tuned through empirical risk. As the machine learning algorithms are complicated black-box approaches, tuning the related hyper-parameters is challenging. This produces a number of complicated optimization issues, whose objective functions inclined to be unforeseeably varies in computational outlay, non-smooth, discontinuous, and comprise continuous categorical, and/or integer variable. The importance of hyper-parameter optimization is to improve the machine learning model performance. Due to the difficulty and time-consuming process of adjusting each hyper-parameter individually, combining machine learning methods with optimization algorithms has been effective as a successful strategy in improving the prediction process of sediment transport. Significant performance improvement in terms of accuracy is presented with satisfactory additional computational complexity through proper tuning of hyper-parameters. On the other hand, a great diversity of metaheuristic algorithms have been developed and utilized to solve constrained optimization problems. These nature-inspired algorithms are attractive as they do not implement mathematical suppositions in the optimization problems and present better global search capability than conventional optimization algorithms. Combining the merits of different evolutionary algorithms has also been suggested to attain more efficiency from the computational point of view.

One of the first applications of hybrid machine learning techniques in the prediction of sediment transport rate was conducted by Roushangar and Koosheh (2015). They modeled the bed-load in three gravel-bed rivers by a combined genetic algorithm–SVM method. River water discharge, flow depth, median grain size, and the shear stress of river bed were used to develop the input parameters of the model. The genetic algorithm (GA) was employed to find the optimum parameters for the

SVM model. Results showed a satisfactory application of the GA-SVR modeling conception to bed-load transport. Moreover, the results showed that the application of the exponential radial basis function (ERBF) as core tool of the GA-SVM method led to favorable results in all three rivers.

By combining two methods of wavelet Kernel extreme learning machine (WKELM) and PSO algorithm, Roushangar and Shahnazi (2019) predicted the bed-load transport of gravel-bed-rivers. Various independent variables based on hydraulic conditions and sediment characteristic was utilized in various arrangements as input variables. The study showed that the advanced PSO-WKELM model is proficient in predicting bed-load transport with high accuracy. Furthermore, its predicting performance has also improved over the traditional SVM model.

Sahraei et al. (2018) employed a combination of metaheuristic approaches, called particle swarm optimization (PSO) and least square support vector regression (LSSVR) to estimate the bed material load. Model tree (M5P) was also employed for comparative purposes. A combination of experimental and field datasets was considered to feed the employed hybrid models. The dimensionless variables extracted from the Yang (1972) equation were added to the hybrid PSO-LSSVR model, which improved the model training. Converting the data into a logarithmic scale led to a decline in error dispersion and better distribution of errors in the histogram for samples with low concentration.

Zounemat-Kermani et al. (2020) conducted a time series analysis and examined the performance of conventional machine learning models, including ANFIS and SVM, in the sediment load modeling. They utilized two kinds of nature optimization algorithms, i.e., the GA-ANFIS and GA-SVM. As one of the vital hydrological procedures that influence the sediment amount transport, river flow discharge was used as input of both developed GA-ANFIS and GA-SVM to estimate the daily bed-load transport rate. According to the reported results for bed-load estimation, using standalone ANFIS model as well as combining it with GA algorithm provide the best fit between the observed and model outcomes. Despite the considerable performance, employed ANFIS and GA-ANFIS models led to the overestimation of the bed-load for the lower transport values.

Hosseini et al. (2022) introduced a novel block combined neural network (BCNN) to cover the weaknesses of neural networks, including problems related to overfitting, slow training, and convergence to local minimums. They designed a complementary model of GA-BCNN for large-scale bed-load prediction. Eight hundred seventy-nine screened datasets of Snake River catchments of Idaho, USA, were used from 1973 to 2002. Velocity, discharge, median grain size, slope, and water depth were used as input values to the developed GA-BCNN, generalized feed-forward neural network (GFFN), and parallel multilayer perceptrons (MLPs) for bed-load prediction. Obtained results of GA-BCNN, GFFN, and MLPs indicated that the proposed GA-BCNN model might predict the non-linear and nonstationary bed-load transport more precisely than single GFFN or MLPs. The ability to easily expand the BCNN to generate larger-scale network models was introduced as the main advantage of this method over single ANNs.

13.6 Selecting the Best Input Parameters

A literature review showed evident disparities regarding input variables in the sediment transport modeling. Consequently, this section places emphasis on this principal aspect mainly reflected by preceding researches. The appropriate input variables selection in a machine learning model is a fundamental phase during the modeling procedure and entails the domain knowledge integration in the model. This process becomes more challenging as sediment transport is affected by many parameters. It should be noted that there are no specific criteria for proper input parameters selection. However, the use of multivariate data analysis procedures, comprising principal component analysis (PCA), can be effective in evaluating the relationships between numerous variables and feeding machine learning methods with appropriate input variables. PCA is suggested as an advantageous method for extracting the most essential information and optimally compressing the number of parameters. As a technique for identifying groups of variables, PCA simplifies the analysis of the parameters through explaining the maximum amount of common variance in a correlation matrix. Taking advantage of PCA, Tayfur et al. (2013) used a joint PCA-ANN model to model the sediment load for laboratory and field-scales. A genetic algorithm was employed to obtain the best predictive capability of the ANN-based model. The outcomes indicated that the pre-processing of the input parameters through PCA analysis reduces 19 parameters to 6 and 5 parameters in the case of field total sediment and laboratory loads, respectively, as well as increases the efficiency of the coupled GA-ANN.

More recently, Noori et al. (2022) investigated the predictability of total sediment load via a robust methodological approach based on the SVM model modified by the PCA technique. Dimensional analysis was performed to determine the ten influential drivers of total sediment load in rivers. Their study demonstrated the improved performance of the SVM model by eliminating the dependency occurrence among inputs. In order to provide a better view of the variety of input parameters, Table 13.1 provides some details of the aforementioned studies. As can be noticed from Table 13.1, some studies have used dimensionless parameters as input for machine learning methods.

Actually, the use of dimensionless input variables for machine learning methods leads to a predictive model-independent of the change in the system of units. Generally, it can be declared that the type of river (e.g., mountain stream, alluvial stream) and the type of flow regime (ephemeral or perennial) can directly affect the sediment transport mechanism. For this reason, different parameters can affect the sediment transport of rivers with different characteristics and under different hydraulic conditions. Since the mentioned studies investigated different rivers with various field characteristics, thus, various hydraulic variables might be identified as the influential variables in sediment transport for them. As an example, it appears that water surface slope is the critical parameter in the mountain and gravel-bed rivers, which affects shear stress and shear velocity directly. Furthermore, in semi-arid ephemeral river system (where bed-load transport can be initiated by floods), shear

Table 13.1 Different input variables for prediction of sediment transport rate

Author	Input parameter	
	Bed-load	Total load
Bhattacharya et al. (2007)	T,D_*,h,V,d_{50},S, $\frac{h}{d_{50}}$	T, D_*, h, d_{50}, $\theta^{'} - \theta_{cr}$, $\omega - \omega_0$
Doğan et al. (2007)	–	Q, h, S, d_{50}
Yang et al. (2009)	–	V, S, h, d_{50}
Sasal et al. (2009)	T,D_*, $\frac{d_{50}}{h}$, $\frac{B}{h}$, σ_g	–
Azamathulla et al. (2009)	$\frac{(G_s-1)d_{50}}{RS_0}$,R,$d_{50}$,$V$,$G_s$	–
Zakaria et al. (2010)	–	Q, V, B, h, R, S_0, ω_s, d_{50}
Chang et al. (2012)	–	Q, V, B, h, R, S_0
Kitsikoudis et al. (2014)	$\frac{VS}{\sqrt{gd_{50}}}$, Re *,Fr,$\sigma$, Re $_{p50}$,ω^*_{50},θ	–
Azamathulla (2014)	–	F_{rm}, $\frac{R}{d_{50}}$, $\frac{B}{h}$
Roushangar et al. (2014)	–	T,D_*, $\frac{h}{d_{50}}$, Re $_*$, $\frac{\tau}{\tau_c}$
Roushangar and Koosheh (2015)	Q, $\frac{h}{d_{50}}$, $\frac{\tau}{\gamma d_{50}}$	–
Sahraei et al. (2018)	–	Fr, Re ,S_f, $\frac{d_{50}}{h}$, $\frac{B}{h}$, $\frac{\tau-\tau_c}{\gamma_w(G_s-1)d_{50}}$
Riahi-Madvar and Seifi (2018)	Q, h, R, d_{50}, τ, S	–
Roushangar and Shahnazi (2019)	Fr, $\frac{h}{B}$, $\frac{V}{U_*}$,S_0,D_*,T, $\frac{h}{d_{50}}$,θ	–
Roushangar and Shahnazi (2020a, b)	–	Fr, Re , $\frac{h}{B}$, $\frac{V}{U_*}$,S_0,D_*,T, $\frac{R}{d_{50}}$,θ, $\frac{V^3}{ghw_s}$
Zounemat-Kermani et al. (2020)	$Q_{(t)}$, $Q_{(t-1)}$, $Q_{(t-2)}$, $BL_{(t-1)}$	–
Hosseini et al. (2022)	Q, V, h, S, d_{50}	–

Q: flow discharge (m^3/s); $Q_{(t)}$: current discharge (m^3/s); $Q_{(t-1)}$ and $Q_{(t-2)}$: antecedent discharges (m^3/s); $BL_{(t-2)}$: antecedent bed-load (kg/s); h: flow depth (m); V: average flow velocity (m/s); U_*: shear flow velocity; B: channel width (m); R: hydraulic radius (m); S: slope (−); S_0: bed slope of channel (−); G_s: specific gravity of sediment (−); d_{50}: median diameter of sediment particle (mm); T: transport stage parameter (−); D_*: particle parameter (−); $\theta^{'}$: mobility parameter related to grain roughness (−); θ_{cr}: Shields' critical shear stress (−); ω: stream power ($N.m^{-1}.S^{-1}$); ω_0: critical stream power ($N.m^{-1}.S^{-1}$); ω_s: particle fall velocity (m/s); σ_g: sediment gradation factor (−); ψ: flow parameter (−); Fr: Froude number (−); F_{rm}: particle Froude number (−); Re: Reynolds number (−); Re*: Shear Reynolds number (−); Re_{p50}: explicit particle Reynolds number (−); ω^*_{50}: transport parameter (−); σ: the arithmetic standard deviation of the stream bed grain size distribution (−); τ: shear stress of river bed ($N.m^{-2}$); τ_c: critical shear stress ($N.m^{-2}$)

stress is considered as the predominant criterion for incipient motion (Shields parameter). It is clear that the performance of machine learning techniques is affected under various hydraulic conditions. This performance variation is due to the variable sedimentary situations, the inherent bed-load transport rate variants, and various bed-load transport mechanisms under varied flow regimes. In order to investigate this issue in more depth, Roushangar et al. (2022) conducted a comprehensive study to investigate the behavior of machine learning methods in modeling bed-load transport rate under diverse hydraulic conditions. For this purpose, KELM and GPR were used as powerful kernel-based techniques. Moreover, the Grey Wolf

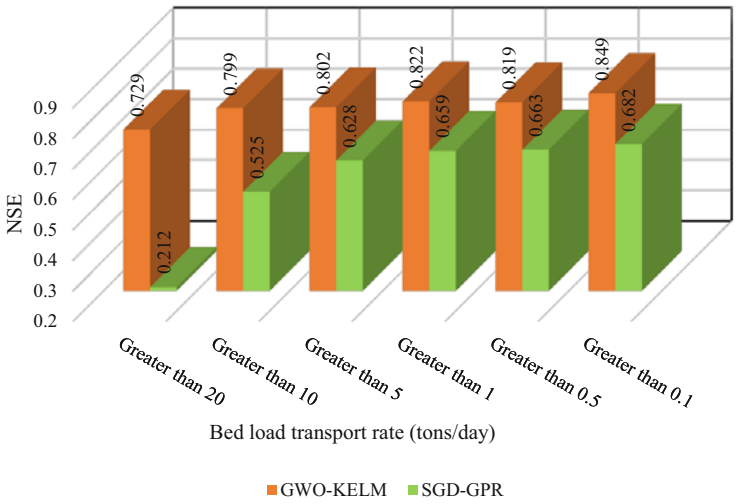

Fig. 13.4 Results of GWO-KELM and SGD-GPR at different intervals of the bed-load transport rates (Roushangar et al. 2022)

Optimization (GWO) and Standard Gradient Descent (SGD) algorithms were coupled with KELM and GPR models, respectively, to search the optimum hyper-parameters and ensure the superlative predictive ability of these machine learning techniques. By choosing the best input combination, the prediction ability of the employed models was evaluated under varied hydraulic regimes. Based on the results, it became apparent that the prediction performance of GWO-KELM and SGD-GPR decreased with increasing flow rates as well as increasing bed-load transport rates (Figs. 13.4 and 13.5). This defect in the implementation of machine learning methods has also been stated in the studies of Talebizadeh et al. (2010), Roushangar and Koosheh (2015), and Riahi-Madvar and Seifi (2018). It can be due to the scarcity of large observed values of data within the training group various active forces of bed-load in low to high flows. Turbulent flow condition occurs at high flow in which velocities fluctuate in space and time. This issue and the particle size randomness, shape, and position, transforms the bed-load transport into a stochastic procedure that varies from low flow (Van Rijn 2007). As indicated by Huisman et al. (2018), storm situations decrease the bed coarsening, and the extent and magnitude of the bed coarsening is strongly associated with the velocity, which leads to reduce the modeling ability of machine learning in high flows compared to low flows. However, Roushangar et al. (2022) suggested the remarkable consistent performance of developed GWO-KELM in high flows. It is obvious that a single machine learning model is unable to simulate high sediment transport rates with the same accuracy as low flows due to different sediment transport mechanisms at low and high flows. Furthermore, due to the different characteristics of sediment in terms of time and space, the exact condition of the river must be determined before any modeling process.

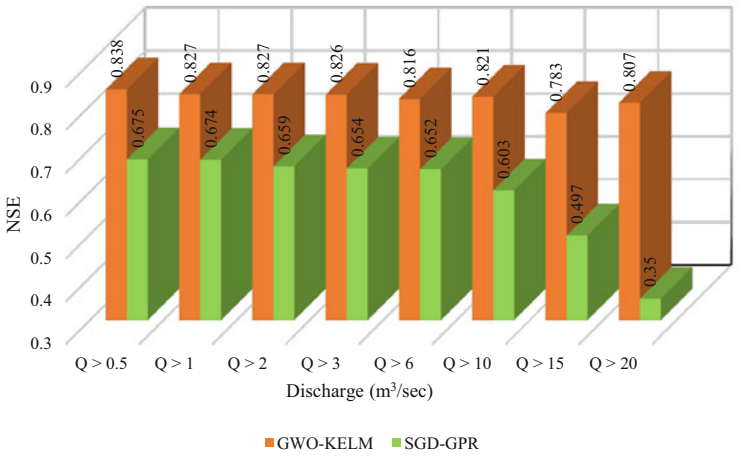

Fig. 13.5 Results of GWO-KELM and SGD-GPR at different intervals of the flow discharge (Roushangar et al. 2022)

13.7 Conclusions

In this chapter, a comprehensive survey of machine learning techniques, specifically employed in the prediction of bed-load and total sediment load, was conducted. Machine learning techniques have proven reliable results in predicting the sediment transport phenomena. The artificial neural network, adaptive neuro-fuzzy inference system, support vector machine, and some evolutionary algorithms are the most effective techniques that have been employed in the area of sediment transport modeling. The continuous progress in machine learning, and its implementation has intensified competition among scientists for building more efficient and accurate predictive models to prevail the complicated, non-stationarity, and dynamism behavior of the sediment transport in rivers. It should be noted that machine learning techniques are data-driven, so further studies should be carried out using a wide range of field data collected from rivers with different hydraulic conditions to confirm the potential of machine learning techniques for modeling sediment transport rate. With a detailed analysis through literature review, it can be seen that the prediction capability of machine learning methods in different hydraulic conditions of river varies due to the non-stationarity and dynamism nature of the sediment transport. Thus, the exact condition of the river must be determined before any modeling process. Moreover, effective parameters in various types of rivers as well as various flow conditions are different and should be determined through sensitivity analysis. For increasing the modeling accuracy, the hybridization of metaheuristics algorithms (i.e., GA, PSO) with machine learning techniques is strongly recommended. Finally, due to different mechanisms of sediment transport in low and high flows and its effect on modeling accuracy, different machine learning methods should be used.

References

Ackers P, White WR (1973) Sediment transport: new approach and analysis. J Hydraul Div 99(11): 2041–2060

Almedeij JH, Diplas P (2003) Bedload transport in gravel-bed streams with unimodal sediment. J Hydraul Eng 129(11):896–904

Azamathulla HM (2014) Development of GEP-based functional relationship for sediment transport in tropical rivers. Neural Comput & Applic 24(2):271–276

Azamathulla HM, Chang CK, Ghani AA, Ariffin J, Zakaria NA, Hasan ZA (2009) An ANFIS-based approach for predicting the bed load for moderately sized rivers. J Hydro Environ Res 3(1):35–44

Azamathulla HM, Ghani AA, Chang CK, Hasan ZA, Zakaria NA (2010) Machine learning approach to predict sediment load–a case study. CLEAN–soil, air. Water 38(10):969–976

Bhattacharya B, Price RK, Solomatine DP (2007) Machine learning approach to modeling sediment transport. J Hydraul Eng 133(4):440–450

Chang CK, Azamathulla H, Zakaria NA, Ghani AA (2012) Appraisal of soft computing techniques in prediction of total bed material load in tropical rivers. J Earth Syst Sci 121(1):125–133

Cristianini N, Shawe-Taylor J (2000) An introduction to support vector machines and other kernel-based learning methods. Cambridge university Press, Cambridge

Dey S (2014) Bed-load transport. In: Fluvial hydrodynamics. Springer, Berlin, pp 261–326

Doğan E, Yüksel İ, Kişi Ö (2007) Estimation of total sediment load concentration obtained by experimental study using artificial neural networks. Environ Fluid Mech 7(4):271–288

Govindaraju RS, Rao AR (eds) (2013) Artificial neural networks in hydrology, vol 36. Springer Science & Business Media, Dordrecht

Hamel P, Falinski K, Sharp R, Auerbach DA, Sánchez-Canales M, Dennedy-Frank PJ (2017) Sediment delivery modeling in practice: comparing the effects of watershed characteristics and data resolution across hydroclimatic regions. Sci Total Environ 580:1381–1388

Hosseini SA, Abbaszadeh Shahri A, Asheghi R (2022) Prediction of bedload transport rate using a block combined network structure. Hydrol Sci J 67:117

Huisman BJA, Ruessink BG, De Schipper MA, Luijendijk AP, Stive MJF (2018) Modelling of bed sediment composition changes at the lower shoreface of the sand motor. Coast Eng 132:33–49

Jang JS (1993) ANFIS: adaptive-network-based fuzzy inference system. IEEE Trans Syst Man Cybern 23(3):665–685

John CK, Pu JH, Pandey M, Hanmaiahgari PR (2021a) Sediment deposition within rainwater: case study comparison of four different sites in Ikorodu, Nigeria. Fluids 6(3):124

John CK, Pu JH, Pandey M, Moruzzi R (2021b) Impacts of sedimentation on rainwater quality: case study at Ikorodu of Lagos, Nigeria. Water Supply 21(7):3356–3369

Khorram S, Ergil M (2010a) A sensitivity analysis of Total-load prediction parameters in standard sediment transport equations 1. JAWRA J Am Water Resour Assoc 46(6):1091–1115

Khorram S, Ergil M (2010b) Most influential parameters for the bed-load sediment flux equations used in alluvial rivers 1. JAWRA J Am Water Resour Assoc 46(6):1065–1090

Kitsikoudis V, Sidiropoulos E, Hrissanthou V (2014) Machine learning utilization for bed load transport in gravel-bed rivers. Water Resour Manag 28(11):3727–3743

Koza JR (1994) Genetic programming as a means for programming computers by natural selection. Stat Comput 4(2):87–112

Madani Cherif H, Khanchoul K, Bouanani A, Terfous A (2017) Prediction of sediment yield at storm period in Northwest Algeria. Arab J Geosci 10(9):1–17

Noori R, Ghiasi B, Salehi S, Esmaeili Bidhendi M, Raeisi A, Partani S, Meysami R, Mahdian M, Hosseinzadeh M, Abolfathi S (2022) An efficient data driven-based model for prediction of the Total sediment load in rivers. Hydrology 9(2):36

Pandey M, Md Azamathulla H (2021) Discussion of "gene-expression programming, evolutionary polynomial regression, and model tree to evaluate local scour depth at culvert outlets" by Mohammad Najafzadeh and Ali Reza Kargar. J Pipeline Syst Eng Prac 12(2):07021001

Pandey M, Chen SC, Sharma PK, Ojha CSP, Kumar V (2019) Local scour of armor layer processes around the circular pier in non-uniform gravel bed. Water 11(7):1421
Pandey M, Oliveto G, Pu JH, Sharma PK, Ojha CSP (2020) Pier scour prediction in non-uniform gravel beds. Water 12(6):1696
Pu JH, Wallwork JT, Khan M, Pandey M, Pourshahbaz H, Satyanaga A, Hanmaiahgari PR, Gough T (2021) Flood suspended sediment transport: combined modelling from dilute to hyper-concentrated flow. Water 13(3):379
Riahi-Madvar H, Seifi A (2018) Uncertainty analysis in bed load transport prediction of gravel bed rivers by ANN and ANFIS. Arab J Geosci 11(21):1–20
Roushangar K, Koosheh A (2015) Evaluation of GA-SVR method for modeling bed load transport in gravel-bed rivers. J Hydrol 527:1142–1152
Roushangar K, Shahnazi S (2019) Bed load prediction in gravel-bed rivers using wavelet kernel extreme learning machine and meta-heuristic methods. Int J Environ Sci Technol 16(12): 8197–8208
Roushangar K, Shahnazi S (2020a) Determination of influential parameters for prediction of total sediment loads in mountain rivers using kernel-based approaches. J Mt Sci 17(2):480–491
Roushangar K, Shahnazi S (2020b) Prediction of sediment transport rates in gravel-bed rivers using Gaussian process regression. J Hydroinf 22(2):249–262
Roushangar K, Mehrabani FV, Shiri J (2014) Modeling river total bed material load discharge using artificial intelligence approaches (based on conceptual inputs). J Hydrol 514:114–122
Roushangar K, Shahnazi S, Azamathulla HM (2022) Partitioning strategy for investigating the prediction capability of bed load transport under varied hydraulic conditions: application of robust GWO-kernel-based ELM approach. Flow Meas Instrum 84:102136
Sahraei S, Alizadeh MR, Talebbeydokhti N, Dehghani M (2018) Bed material load estimation in channels using machine learning and meta-heuristic methods. J Hydroinf 20(1):100–116
Sasal M, Kashyap S, Rennie CD, Nistor I (2009) Artificial neural network for bedload estimation in alluvial rivers. J Hydraul Res 47(2):223–232
Shankar MS, Pandey M, Shukla AK (2021) Analysis of existing equations for calculating the settling velocity. Water 13(14):1987
Shivashankar M, Pandey M, Zakwan M (2022) Estimation of settling velocity using generalized reduced gradient (GRG) and hybrid generalized reduced gradient–genetic algorithm (hybrid GRG-GA). Acta Geophys 1–11
Singh UK, Jamei M, Karbasi M, Malik A, Pandey M (2022) Application of a modern multi-level ensemble approach for the estimation of critical shear stress in cohesive sediment mixture. J Hydrol 607:127549
Sinnakaudan SK, Ab Ghani A, Ahmad MSS, Zakaria NA (2003) Flood risk mapping for Pari River incorporating sediment transport. Environ Model Softw 18(2):119–130
Smola AJ (1996) Regression estimation with support vector learning machines. Doctoral dissertation, Master's thesis, Technische Universität München
Takagi T, Sugeno M (1985) Fuzzy identification of systems and its applications to modeling and control. IEEE Trans Syst Man Cybern 1:116–132
Talebizadeh M, Moridnejad A (2011) Uncertainty analysis for the forecast of lake level fluctuations using ensembles of ANN and ANFIS models. Expert Syst Appl 38(4):4126–4135
Talebizadeh M, Morid S, Ayyoubzadeh SA, Ghasemzadeh M (2010) Uncertainty analysis in sediment load modeling using ANN and SWAT model. Water Resour Manag 24(9):1747–1761
Tayfur G, Karimi Y, Singh VP (2013) Principle component analysis in conjuction with data driven methods for sediment load prediction. Water Resour Manag 27(7):2541–2554
Van Rijn LC (2007) Unified view of sediment transport by currents and waves. I: initiation of motion, bed roughness, and bed-load transport. J Hydraul Eng 133(6):649–667
Vanoni VA (1975) River dynamics. Adv Appl Mech 15:1–87

Yang CT (1972) Unit stream power and sediment transport. J Hydraul Div 98(10):1805–1826
Yang CT, Marsooli R, Aalami MT (2009) Evaluation of total load sediment transport formulas using ANN. Int J Sediment Res 24(3):274–286
Zakaria NA, Azamathulla HM, Chang CK, Ghani AA (2010) Gene expression programming for total bed material load estimation—a case study. Sci Total Environ 408(21):5078–5085
Zounemat-Kermani M, Mahdavi-Meymand A, Alizamir M, Adarsh S, Yaseen ZM (2020) On the complexities of sediment load modeling using integrative machine learning: application of the great river of Loíza in Puerto Rico. J Hydrol 585:124759

Chapter 14
Impact of Anthropocene on the Fluvial Sediment Supply: The Mahanadi River Basin Perspective

Rohan Kar and Arindam Sarkar

Abstract The Mahanadi River basin is the third biggest in central India and the longest in the state of Odisha. The peninsular river basin has a significant history of watershed land use changes and human disturbances in the channel. The Mahanadi Delta, located on India's east coast, is a hybrid delta formed by water, suspended and bed sediments, and minerals from a web of distributaries of the Mahanadi River system. The current state of research on the quantification of river sediment supply and its connection to human catchment disturbances is discussed in this chapter, with an emphasis on the physical characteristics of the river basin. Nonparametric time series assessment methods are used to examine the annual runoff and suspended sediment characteristics of the gauging stations of the basin. The function of various attributes influencing runoff and suspended sediment dynamics of the gauging stations is also investigated. The average correlation between the discharge and suspended sediment load (SSL) is studied using sediment rating curves (SRC). Also, the role of differential supply of sediments from the watershed is characterized using the hysteresis analysis of suspended sediments. The development of the Mahanadi coastline subjected to the regulated sediment supply from the catchment in terms of land loss and gain is evaluated using geospatial data. The statistics of hydrological data reveal a large seasonal variance, with the monsoon being the most dominant. The annual SSL distributions are more irregular and non-normal relative to yearly runoff. The investigation of hysteresis loops revealed that the supply of sediments also significantly affected the transport capacity of all the channels within the basin. A substantial loss in SSL is evident throughout the majority of the stations in comparison to a negligible change in water outflow. Besides, 81% of the stations show a 2-year periodicity in runoff and SSL. Also, the flow of SSL to the ocean has fallen nearly three times more than the annual runoff, which is alarming. It, therefore, shows the strong impact of artificial force relative to natural variations. The statistical estimates for seashore morphological changes on a volumetric basis show that coastal landscapes prone to erosion are susceptible. The rating parameters vary

R. Kar · A. Sarkar (✉)
School of Infrastructure, IIT Bhubaneswar, Khordha, Odisha, India
e-mail: rk49@iitbbs.ac.in; asarkar@iitbbs.ac.in

M. Pandey et al. (eds.), *River Dynamics and Flood Hazards*, Disaster Resilience and Green Growth, https://doi.org/10.1007/978-981-19-7100-6_14

inversely due to intense human-induced activities throughout the catchment. The rise in withdrawal over time for non-monsoon irrigation and hydropower generation is observed from the release of water from the reservoirs. The demand for thermal power stations has increased fourfold in the recent decade, significantly increasing water utilization. Overall, large impoundments, excessive water distribution across multiple business sectors, and varying watershed soil management efforts are highlighted as critical anthropogenic attributes impacting the decline in catchment sediment transport and eventually causing the delta to retreat. Further studies in the basin should focus on the impact of future land use on the sediment budget of the Mahanadi delta. This study aims to shed light on the dynamics of runoff and suspended sediment load over the past five decades and to fill in shortcomings about the evolving nature of rivers in the Mahanadi River basin.

Keywords Mahanadi River basin · Suspended sediment hysteresis · Trend analysis · Human interferences · Runoff · Suspended sediment load

14.1 Introduction

Humans have used river systems for ages without understanding how the river ecology functions and maintains its vitality (Arthington et al. 2010). Rivers convey water and fertile soil from their catchments to the lower reaches, which support agriculture, communities, navigation, and industry. River sediments are also being utilized for various construction purposes. It is important to ensure an effective and consistent supply of sand to support the investment of developing economy in physical infrastructure, utilities, and buildings to raise living standards and social well-being, but it is also important to consider the sustainability of natural fluvial processes. In-stream mining can have substantial environmental damage (Åkesson et al. 2007) and increase the vulnerability of farming, commercial and residential communities, and river ecosystems (Ashraf et al. 2011). Fluvial channels, water, and sediments form a delicately balanced system. Any anthropogenic intervention (dams, bridges, towns, mining, etc.) may produce recognizable changes in the system, including flooding, erosion, and desertification, which may cause loss of essential human resources. Though such generalizations are known, the environmental and geomorphic repercussions are not fully understood due to a lack of data (Kale 2005; Ashraf et al. 2011; Karaki Abou et al. 2016). Dramatic population growth in recent decades, along with large-scale changes in land use and vegetation cover in catchment areas, and widespread development in deltaic regions, have negatively affected the fluvial environment, including runoff, discharge, sedimentation rates, and downstream habitats (Paszkowski et al. 2021). Fluvial systems are delicate and respond quickly and drastically to anthropogenic interference (Petts and Gurnell 2005).

For decades, a primary research focus has been quantifying and comprehending the volume of sediments discharged from a river basin per unit of time and catchment area. It has recently been passionately argued whether humankind has initiated

a new era known as the Anthropocene (Fan 2018; Fan et al. 2019). Over time, it became evident that humans have a significant and quickly expanding impact on catchment sediment yield (Huntington 2006; Borrelli et al. 2017). Various anthropogenic storage intercepts 26% of such sediments worldwide (Syvitski et al. 2005). Quantifying and understanding these effects are a major research priority in hydrology and fluvial landforms (Syvitski et al. 2003; Hoffmann et al. 2010; Tarolli 2016). It is also crucial to properly comprehend anthropogenic influences on carbon flows and the Earth system (Galy et al. 2015). The tropical Indian rivers' flow, sediment conveyance, and channel geometry are primarily influenced by the summer monsoon rainfall, which accounts for almost 80% of yearly precipitation from June to September (Kale 2002). Alterations in meteorological parameters impact runoff in the basin directly and indirectly (Tabatabaei et al. 2020). But on the other side, the impact of man-made changes like urbanization, deforestation, dam construction, and reservoir operation on several components of the water cycle and water resources is frequently underestimated (Sharifi et al. 2021).

Regarding material flow, large river deltas and estuary basins serve as crucial continent-ocean interfaces, having worldwide implications for coastal biogeochemical cycles (Bianchi and Allison 2009; Zhao et al. 2021). Even though deltas and coastline regions only make up a small percentage of the overall land area, they have become essential ecosystems for the world population because of their high biological productivity and ecological importance (Overeem and Syvitski 2009; Zhang and Niu 2021). However, approximately three-fourths of the worldwide sandy coasts retreat at 0.5–1 m yearly (Bird 1985; IPCC 2001). Several of the nation's river deltas have become susceptible to expedited subsidence and erosion in the past few decades (Overeem and Syvitski 2009), including the Nile in Egypt (Fanos 1995; Ali and El-Magd 2016), the Yellow River in China (Xu 2006; Jiang et al. 2017; Sun and Niu 2021), the Mississippi and Colorado Rivers in the USA (Blum and Roberts 2009; Mueller et al. 2017; Maloney et al. 2018), and multiple Indian rivers (Gamage and Smakhtin 2009; Higgins et al. 2018; Hazra et al. 2020). Sediment load, river flow, wave fields, tidal current, sea level rise, and storm surges are all environmental elements that influence morphological alterations. Furthermore, the construction of dams, sand mining, channel scouring, and land reclamation are significant drivers of morphological changes caused by human intervention (Syvitski 2008; Chen et al. 2011; Tang et al. 2016). These reasons have increased worldwide appeal in studying a wide range of delta and estuary environments (Yu et al. 2011; Smajgl et al. 2015; Feng et al. 2020).

The change in catchment sediment supply, typically referred to as hysteresis, affects the efficiency of suspended sediment rating (SRC). A non-distinct connection in SRC develops due to hysteresis, showing varying sediment concentrations for the same discharge. Hysteresis has been addressed in the past through developing seasonal or hydrologically-based SRCs (Harrington and Harrington 2013). Although, such methods did not effectively arrest the hysteresis characteristic of the sediment rating. The study of hysteresis loops in SRC, in particular, helps us evaluate the role of runoff in determining SSC and provides information on the sediment sources of the watershed. SRC hysteresis has been the subject of few recent

studies, with discoveries on the categories of loops, the identification of hydrological impacts throughout specific events, and the time-based uniformity of hysteresis bends (Zuecco et al. 2016; Sadeghi et al. 2019; Malutta et al. 2020). Only a single study has included the SRC hysteresis in predicting sediment concentration for the Mahanadi River basin (Kar and Sarkar 2022). As a result, it is very much needed to characterize the hysteresis in SRC to understand the spatio-temporal variation in sediment supply across the catchment.

In hydro-meteorological data, trend recognition is a must-do operation since it is the foundation for analysing long-term fluctuations in fluvial processes and identifying periodicities and other features. When examining variations in sediment flow series, it is crucial to determine if the increase or decrease in sediment flow is attributable to anthropogenic sources or alterations in climatic conditions. Therefore, research should be conducted accordingly (Walling 1996; Syvitski 2003). The lack of consistent sediment monitoring is a crucial impediment to assessing the effect of climate and anthropogenic factors on the worldwide sediment cycle (Dearing and Jones 2003). In the mid-1980s, India began a sediment monitoring programme with the proper spatial structure of river basins.

On the other hand, certain tropical rivers contain reasonably time series data for a few stations near the mouth of the stream, which have been used for trend research (Gamage and Smakhtin 2009; Panda et al. 2011; Montanher et al. 2018; Das 2021). According to Syvitski et al. (2003), sediment estimations analysis of data of the last monitoring stations would not adequately explain irregular human activities in the watershed. Nonparametric approaches like Mann–Kendall and Sen's slope estimator can identify the trend's amplitude and nature, but not its form. Most hydro-climatic series may have nonlinear rather than linear trends (Sang et al. 2014; Unnikrishnan and Jothiprakash 2015; Hu et al. 2022). Identifying the nonlinear patterns of hydrologic variables is indeed essential for effective modelling. Streamflow reduction, sediment entrapment in reservoirs, land and water conservation, and changing land use reduce sediment load (Adarsh et al. 2016; Kar and Sarkar 2021; Luo et al. 2022). These processes lead to hydrological nonstationarity or shift points (Chen and Wang 2019). Nonstationarity identification enables us to comprehend variable discharge and sediment output (Liu et al. 2015; Conte et al. 2019; Tsyplenkov et al. 2021).

The most frequently mentioned difficulties in deltas are beach erosion and ecological destruction (Li et al. 2018). Tracking coastal change is critical for taking proper action to ensure delta sustainability (Brondizio et al. 2016; Fan et al. 2019). Coastal morphology can be studied using several spatio-temporal approaches. Short-term (minutes to days) morphological changes can be observed explicitly by measuring bed level or implicitly by measuring sediment-dynamic characteristics. Core data and time series analysis of paleo-coastline markers can study decades-to-millennia-long coastal evolution. Intermediate-term morphological modifications can be monitored by comparing satellite or aerial photographs or historical maps and charts (Fan 2012; Xu 2018). Since it is more cost-effective than other databases, various studies have utilized satellite data to detect coastal shifts at more comprehensive spatio-temporal resolutions.

High spatial resolution data from IKONOS, Quick Bird, and GeoEye is increasingly being used with digital elevation models (DEMs) to estimate volumetric changes in coastal landforms (James et al. 2012; Ragia and Krassakis 2019). The global approach to quantifying the vertical transition in deposit load employs the DEMs of difference (DoD) method and cross-shore profile analysis using remote sensing data from multiple periods and is supported by field research and measurements (James et al. 2012; Mohamad et al. 2022). Consequently, it gives a broad overview of erosion and sedimentation mechanisms at different times (Schwendel et al. 2012). DEM data sets such as Shuttle Radar Topography Mission (SRTM) and Advanced Spaceborne Thermal Emission and Reflection Radiometer (ASTER) are used for Geomorphic Change Detection analysis due to their mission-defined precision, i.e., high vertical accuracies across terrain surface and bare soils and medium spatial resolutions (Cuartero et al. 2004). However, to identify actual topographic change from uncertainty and surface error, the mistake caused by DoD must be included (Wheaton et al. 2010; Dewitt et al. 2015). Furthermore, the topographical changes of landforms derived using DEMs show a positive association with field measurements, making them helpful in tracking how landforms vary over time due to coastal sinking or uplift (Smith and Pain 2009; Knight et al. 2011).

Chakrapani and Subramanian (1990) observed that the suspended sediment flow of the Mahanadi watershed to the sea was minimal relative to the Himalayan rivers. The west-moving Narmada River and the east-moving Krishna, Godavari, Kaveri, and Mahanadi River systems (Gupta and Chakrapani 2007; Gamage and Smakhtin 2009; Rao Nageswara et al. 2010; Panda et al. 2011; Das 2021) displayed a diminishing tendency of sediment flow into the ocean. As a result, shoreline degradation increases. The USGS shoreline evaluation system revealed that 65% of the Mahanadi Delta is eroding and will continue to do so in the following decades (Mishra and Panda 2016; Mukhopadhyay et al. 2018). The morphological behaviour of the coastal plain to changes in watershed sediment load is still unknown.

14.2 Rationale of the Study

Recent research on the history of runoff and suspended sediment flow (Bastia and Equeenuddin 2016; Das 2021) of the Mahanadi River basin concentrated on a shorter period. They focus solely on linear trend analysis and consider only a subset of hydrological stations. Nevertheless, no study of the current monitoring sites of the river basin has been conducted throughout the baseline period (1973–2019). Although, several other studies have defined the area of the Mahanadi Delta that is prone to beach attrition (Mishra and Panda 2016; Mukhopadhyay et al. 2018). However, to our knowledge, no previous investigations have studied the nonlinear trend analysis of hydrological variables and the related coastal change. Furthermore, the hysteresis behaviour of the suspended sediment rating curve (SRC) was not explored throughout the baseline period to understand the related sub-watershed

behaviour. As a result, the goals of this paper for the Mahanadi River basin from 1973 to 2019 are as follows:

1. to perform a detailed preliminary investigation of the hydrological variables involved;
2. to quantify the hysteresis of suspended sediment load (SSL) across all major sub-basin outlets to truly comprehend the function of runoff and provide an understanding of the origin of sediments in the watershed;
3. to discover and quantify the presence of linear and nonlinear trends, as well as sudden shifts in recorded annual runoff and SSL, adopting established nonparametric approaches;
4. to identify appropriate particulars that define recorded trends and change points;
5. to numerically investigate the morphological behaviour of the shore towards the changes in catchment SSL; and,
6. to link the change in SSL and delta development from the perspective of anthropogenic stresses throughout the basin.

As a result, the current study will be an essential contribution to the long-term sustainability of the river basin in consideration of diversified anthropic disturbances.

14.3 Limitations of the Study

The limitations of the present study are listed as follows.

1. Trends of the hydrological variables for seasonal or monthly time scales were not considered in the present study.
2. Suspended sediment hysteresis for seasonal, monthly and storm event scales was not carried out.
3. A muti-decadal erosion-accretion map of the Mahanadi delta towards the sediment starvation from the catchment was not prepared.
4. Changes in current and future land use and land cover on the coastal erosion-accretion map were not addressed.

14.4 Materials and Methods

14.4.1 Study Area

The Mahanadi watershed is one of the major tropical river watersheds of peninsular India (Fig. 14.1), with a catchment area of 139681.5 km^2 (CWC 2014). It is India's eighth largest river basin, encompassing 4.3% of the country's land (CWC 2014). At 851 km in length, it is the second-longest east-flowing peninsular river before emptying into the ocean. The catchment territory extends from latitude 19°08'N to

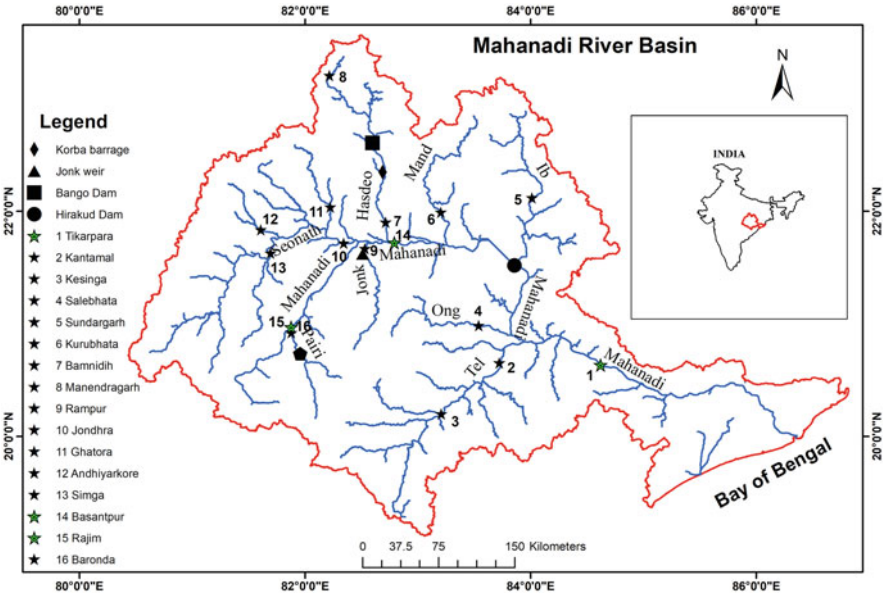

Fig. 14.1 Map of the Mahanadi watershed

longitude 86°43′E. It rises roughly 442 m above sea level out of Sihawa highland in the Dhamtari district of Chhattisgarh. Some 75,136 km^2 of the entire watershed is located in Chhattisgarh; the rest is found in Odisha (65,580 km^2), Bihar (6335 km^2), Maharashtra (235km^2), and other Indian states. The Bango dam on the Hasdeo branch and the Hirakud dam downstream of main Mahanadi are the two most essential dams in the watershed. There are seven major tributaries that meet the Mahanadi in the upper reaches of the basin. With regard to the flow movement, four of them (Seonath, Hasdeo, Mand, and Ib) are on the left bank of the river Mahanadi, while the other three (Pairi, Sukha, and Jonk) meet on the right side of the river. Tel and Ong rivers also join the larger Mahanadi River downstream of the Hirakud Dam. The deltaic part of the basin is bounded northeast by the Brahmani River and southwest by Chilika Lake.

Moreover, 80% of the basin's annual discharge occurs during the monsoon season, when precipitation averages 1350 mm. The catchment discharge is mainly seasonal because the river's primary source is rain. Aside from that, the basin has an average maximum temperature of 39.56 °C. and an average minimum temperature of 20.01 °C. During the eight months of the year, the river follows a narrow and shallow course. However, during the monsoon season, the river rages, causing extensive damage to its banks and floodplains. The basin's average annual discharge is 66.9 BCM (CWC 2014). After splitting into various branches, the river flows into the Bay of Bengal.

A 54.3% of the total surface of the basin is devoted to agriculture, which has a substantial positive impact on India's economy. The remaining 32% is made up of

forests, while 14% is made up of wastelands, aquatic bodies, and populated places. 51.3% of the land is covered by medium-textured soil, with over 42% covered by fine-textured soil (CWC 2014). The Eastern Ghats of the Precambrian period dominate the upstream geology of the catchment. River alluvium is more prevalent in the downstream area. Dolomite, kaolinite, chlorite, and montmorillonite were found in the sediments in suspension and the bed (Chakrapani and Subramanian 1990). Compared to the suspended sediments, bed sediments tend to be coarser in texture (Chakrapani and Subramanian 1990). A silt deposit greater than all other Indian rivers may be seen throughout the river basin.

14.4.2 Data Sources

Suspended sediment load data (metric tonne, *t*) and its accompanying runoff fluctuations (million cubic metres, MCM) were utilized for 16 monitoring sites encompassing the whole watershed during 1973–2019, according to the Central Water Commission (CWC 2019). Figure 14.1 depicts the location of all recording sites and large reservoirs in the basin. Over a decade, CWC constructed 16 hydrological stations across the basin at various times. Thus, the length of the data interval varies depending on the availability of data in specific locations (Table 14.1). For all hydrological analyses in India, the period from the beginning of the monsoon (first June) to its withdrawal on 31st May of the following year is considered a water year.

Table 14.1 Particulars of gauging stations of the Mahanadi watershed

Gauging stations	Latitude (°)	Longitude (°)	Data interval	Altitude (m.a.s.l)	Catchment area (km^2)	Tributary/ sub-tributary
Andhiyarkore	21.83	81.61	1981–2019	252	2210	Seonath
Simga	21.63	81.69	1973–2019	244	30,761	Seonath
Baronda	20.91	81.89	1980–2019	283	3225	Pairi
Rajim	20.97	81.88	1973–2019	275	8760	Mahanadi
Manendragarh	23.20	82.22	1994–2019	411	1100	Hasdeo
Ghatora	22.06	82.22	2001–2019	246	3035	Seonath
Jondhra	21.73	82.35	1981–2019	219	29,645	Seonath
Rampur	21.65	82.52	1977–2019	219	2920	Jonk
Bamnidih	21.90	82.72	1973–2019	223	9730	Hasdeo
Basantpur	21.73	82.79	1973–2019	206	57,780	Mahanadi
Kurubhata	21.99	83.20	1980–2019	215	4625	Mand
Sundargarh	22.12	84.01	1980–2019	214	5870	Ib
Salebhata	20.98	83.54	1973–2019	130	4650	Ong
Kesinga	20.20	83.23	2007–2019	166	11,960	Tel
Kantamal	20.65	83.73	1977–2019	118	19,600	Tel
Tikarpara	22.63	84.62	1973–2019	50	124,450	Mahanadi

Because the rainy season from June to September, when the monsoon rains arrive, carries most of the sediment load, sediment monitoring was done daily during the monsoons and once a week otherwise (October–May). The weighted average discharge for the independent years was used to calculate the sediment content for days when no observations were made (CWC 2019). Sediment content (gm/l) and discharge (m^3/s) were used to calculate the flow-weighted suspended sediment load (t/day) for a recording station. The periodic sediment loads were derived from the ten daily tables describing the sediment loads at each observation point. The Central Water Commission, India, uses the method outlined above. Table 14.1 provides a wealth of information on basin features and hydrological (gauging) stations. Each station's yearly sediment load was calculated as the total monsoon and non-monsoon sediment accumulations.

ASTER digital elevation models (DEMs) (30 m, 2011) and SRTM (90 m, 2000), archived by the United States Geological Survey and the National Aeronautics and Space Administration, were used to detect geomorphological alteration in offshore landforms in this research.

The National Register of Large Dams was used to gather information about the basin's reservoirs (NRLD 2019). For agriculture and hydroelectric production at the Hirakud dam, the data was provided by the Division of Water Resources, state of Odisha (DoWR 2014). The Ministry of Environment and Forests provided the freshwater distributions and constructed thermal energy capacity data for power stations in Chhattisgarh and Odisha (MoEF 2016).

14.4.3 Hysteresis Analysis of Suspended Sediment Rating Curve (SRC)

The hysteresis of the SRC was assessed at all major sub-basin outlet stations for the entire investigation period (1973–2019). The SRC hysteresis evaluation was carried out using Sadeghi et al. (2019) for the selected period. Two parameters, ΔS and ΔAR, were used to describe the hysteresis behaviour of SSC and were evaluated across sub-basins. For example, ΔS and was used to depict changes in SSC, while ΔAR was used to reflect changes in hysteresis. By analysing these factors, information on sediment functioning against variations in runoff was obtained. ΔS and ΔAR are so written as follows:

$$\Delta S\,(\%) = \left(\frac{S_{\mathrm{p}} - S_{\mathrm{b}}}{S_{\max}}\right) \times 100 \tag{14.1}$$

$$\Delta AR\,(\%) = (A_h \times R) \times 100 \tag{14.2}$$

where S_{p} is the SSC at maximum runoff, S_{b} is the SSC at baseflow runoff, $S_{\max}$ is the extreme SSC throughout the time-interval under study, A_{h} is the area of the SRC hysteresis, and R is the rotational form of the hysteresis loops. Runoff and SSC were

normalized to a scale of one by their maximum values before the A_h was computed. A_h value nearer to zero indicates linearity and insignificant change in SSC throughout fluvial conditions; hence A_h is taken to have a value between 0 and 1. Even with similar discharge, A_h values near 1 show large SSC variations. To indicate flushing (dilution), the factor ΔS ranges from −100% to +100%. R can be −1, 1, or 0 for SRC hysteresis loops that are counterclockwise, clockwise, or complex. In counterclockwise loops, the maximum runoff appeared before the maximum SSC, while in the other direction, the reverse is true. Consequently, the value of ΔAR ranges from −100% to +100%. According to the ΔS vs ΔAR representation, the hysteresis structure of SRC was analysed using four dimensions depending on the flushing or diluting condition of suspended sediments. The zone above (below) the *x*-axis denotes flushing (diluting) situations, whereas the zones to the right (left) of the *y*-axis denote clockwise (counterclockwise) loops.

The average hysteresis index (HI_a) is the ratio of the flow-weighted suspended sediment concentration before the runoff peak (S_{brp}) to the concentration after the runoff peak (S_{arp})

$$HI_a = \log_{10}\left(S_{brp}/S_{arp}\right) \tag{14.3}$$

This shows if sediment concentrations are higher between rising and falling stages. Hysteresis indices near zero suggest near-synchronous SSC and runoff hydrographs, with hardly any variation in the SRC between rising and falling stages. Generally, higher levels of HI_a imply more time-varying runoff and SSC behaviour with a bigger hysteresis loop. The HI_a offers visibility into SRC changes during the event. However, to truly comprehend how sediment concentration varies around the runoff peak, mainly when shapes are complex, a non - dimensional indicator of the time difference between the runoff peak (T_{rp}) and SSC peak (T_{sp}), called the peak phase difference (PPD) and described as

$$PPD = \left(\frac{T_{rp} - T_{sp}}{T_f}\right) \tag{14.4}$$

where T_f is the time between the commencement of flood and its end. Close to zero PPD suggest negligible runoff and sediment concentration phase differences. Positive PPD implies clockwise hysteresis under flood peaks, while negative values indicate anticlockwise hysteresis.

14.4.4 Linear and Nonlinear Trend Analysis

There have been numerous statistical methods for spotting patterns in time series data. Parametric and nonparametric approaches can be used to determine whether a hydro-meteorology data series shows a significant trend. Because the

hydro-meteorological data are distinct and not normally distributed, nonparametric tests are more reliable than parametric testing. Techniques for assessing trends in hydro-climatic time series, such as Modified Mann-Kendall and Sen's slope estimators, as well as Pettitt's test, were employed in this study.

14.4.4.1 Modified Mann-Kendall Method

According to Mann-Kendall (MK) trend test (Mann 1945; Kendall 1975), a nonparametric approach to identify trends in hydro-meteorological parameters is extensively utilized. However, serial correlation is not considered by the MK test, making it a noticeable flaw. There is a risk that the MK test may be misinterpreted since a time series with positive autocorrelation reduces the adequate sample size, raising variance and the likelihood of spotting a trend when there is none (Hamed and Ramachandra Rao 1998). Accordingly, the null hypothesis (no significant trends) is more likely to be supported by data with negative autocorrelation than by data with positive autocorrelation. In such cases, a formula can be used to change the variance of test statistics to address this issue. The modified Mann-Kendall (MMK) test statistic is derived as

$$\mathrm{TS} = \sum_{a<b}^{n} \mathrm{sgn}\left(x_b - x_a\right) \tag{14.5}$$

where x_a and x_b are the observations in time series a and b with $a > b$, respectively, sgn denotes the signum function, which is defined as

$$\mathrm{sgn}\left(x_b - x_a\right) = \begin{cases} 1 \text{ if } x_a > x_b \\ 0 \text{ if } x_a = x_b \\ \text{-1 if } x_b > x_a \end{cases} \tag{14.6}$$

The standardized test statistic $\left(Z = {}^{\mathrm{TS}}/_{\sqrt{\mathrm{Var(TS)}}}\right)$ is compared to the standard normal variate (Z_s) to determine the significance of trends at the specified significance level. The variance of the test statistic is calculated using

$$\mathrm{Var(TS)} = \frac{n(n-1)(2n+5)}{18}\left({}^{n}/_{n^*}\right) \tag{14.7}$$

where n defines the real number of data points and n^* is the number of data points needed to account for the autocorrelation factor of the dataset. Here, $\left({}^{n}/_{n^*}\right)$denotes the correction factor involved for the autocorrelated data. Hamed and Ramachandra Rao (1998) deduced the equation of correction factor as

$$(n/n^*) = 1 + \frac{2}{n(n-1)(n-2)} \sum_{j=1}^{n-1} (n-j)(n-j-1)(n-j-2)\rho(j) \tag{14.8}$$

where $\rho(j)$ is the rank autocorrelation function. Stationarity (nonstationarity) and whether the trend is up or down can be determined by the standardized test statistic Z_s. In a two-sided test, the null hypothesis of no trend is rejected at the β level of significance (≈ 0.01 considered in the present study) for the calculated value $|Z_s| > Z_{\beta/2}$. In other words, it means the trend is significant. There are two kinds of Z values: positive values imply rising trends, and negative values indicate falling trends.

14.4.4.2 Sen's Slope Estimator

Using Sen's nonparametric approach (Sen 1968), the actual slope of a data series can be computed. The trend slope (M_i) is calculated for all data pairings as

$$M_i = \left(\frac{x_a - x_b}{a-b}\right), i = 1,2,\ldots,T \tag{14.9}$$

If there are n values in x_a, then $T = \left(n(n-1)/2\right)$. The Sen's slope is given by the median of T values of M_i. The lowest to the highest T values of M_i are ranked, and Sen's estimator is assessed as follows:

$$M = \begin{cases} M_{\frac{T+1}{2}} \text{ if } T \text{ is odd} \\ 0.5\left(M_{\frac{T}{2}} + M_{\frac{T+1}{2}}\right) \text{ if } T \text{ is even} \end{cases} \tag{14.10}$$

where M indicates the data trend and its value, the slope.

14.4.4.3 Empirical Mode Decomposition (EMD)

The EMD methodology detects the periodicity of hydrological variables in the Mahanadi River basin using the wave decomposition method (Huang et al. 1998). Here the initial time series is disintegrated into a sequence of single functions known as intrinsic mode functions (IMFs) without departing from the temporal domain. Through a sifting process, the EMD technique breaks down the signal into its constituent IMFs. All the data between the upper and lower bands of a time series $y(t)$ is covered by the average (a_1) of upper and lower bands. The first IMF1 component is given by

$$s_1 = y(t) - a_1 \tag{14.11}$$

After an initial course of sifting, s_1 was taken as the primary signal. a_2 is the average of the upper and lower bands of a_1. The sifting process is subsequently iterated with

$$s_2 = s_1 - a_2 \tag{14.12}$$

The sifting procedure must be performed m times till s_{i+1} is an IMF.

$$s_i = a_i + 1 = s_{i+1}, i = 1,2,\ldots,m \tag{14.13}$$

The final IMF is the smallest component of the signal, and the initial signal $y(t)$ was described linearly with IMFs and the residue (R_n) and is given by

$$y(t) = \sum_{i=1}^{n} \mathrm{IMF}_i + R_n \tag{14.14}$$

where n is the total amount of IMFs, and i represents the ith IMF. For every IMF (or R_n), the percentage of the entire time sequence variance that each IMF (or residue) contributed was computed.

14.4.5 Change Point Analysis (Pettitt Test)

The nonparametric Pettitt test was used to investigate hydro-climatic series. The complete research interval is separated by abrupt shifts (Pettitt 1979). The technique of the analysis is as follows:

The hydrological temporal data (y_1, y_2, …, y_n) is separated into two samples, namely y_1, y_2,…,y_t and y_{t+1}, y_{t+2},…, y_n. The test method employs a form of the Mann-Whitney statistic ($W_{t,n}$) to confirm if the samples are after the same population or not. The $W_{t,n}$ is computed as

$$W_{t,n} = \sum_{j=1}^{t} \sum_{k=1}^{n} \mathrm{sgn}\,(y_t - y_k), t = 2,3,4,\ldots,n \tag{14.15}$$

The abrupt shift is given where $|W_{t,n}|$meets its maximum value K_n (= max $|W_{t,n}|$). The related significance level is computed using

$$P = \exp\left\{\frac{-6K_n^2}{(n^3 + n^2)}\right\} \tag{14.16}$$

The Pettitt test was used over other change point detection methods because it could be applied to data that is distribution-free and resistant to the presence of outliers. Moreover, the ability of the Pettitt method is higher as the size of the sample increases or the magnitude of the shift is bigger. A study documented that the Pettitt test has zero power in change detection for a sample size of less than or equal to 10 years (Conte et al. 2019). However, the period of data in our study varies from 12 to 46 years.

Further, it was established that the Pettitt test is widely popular worldwide among researchers for the analysis of hydro-climatological shift of a time series (Jiang et al. 2011; Rougé et al. 2013; Suhaila and Yusop 2018; Hu et al. 2022). Also, the Pettitt test is more advantageous because of its ability to identify the point at which the change occurred in the data series without needing prior identification. Besides, according to Xie et al. (2014), using the Pettitt test, the change point at the middle of the series is much easier to be detected; however, the detection ability is distinct for the shift at the first third part and the last third part. As a result, upon considering all the above, the Pettitt is preferred in the current investigation for change point analysis of hydrological variables.

14.4.6 Morphological Change Detection of the Seashore

The DEM data were processed in ArcGIS to analyse the vertical change in beach morphology. The DEM of difference approach was used to analyse DEM datasets for morphological evolution. This approach analysed coastal vertical change by comparing DEMs for 2 years (2000 and 2011). The DEM result shows sediment depth changes due to sediment loss and gain. A shift in sediment depth (in m) equals the difference between two DEMs (2011 and 2000). The details of the DEM used are given in Sect. 4.2. However, the DEM maps offer varying sizes for vertical change assessment.

Applying the cubic convolution resampling technique, SRTM DEM was resized to 30 m extents. Positive and negative output grid amounts imply deposition and attrition. The volumetric shift was calculated by multiplying each pixel's change by its area (≈900 m^2). Merging pixel volumetric change measurements gave the total coastal zone volume change (in m^3). Nevertheless, according to Wood (1996), DEM of difference may produce and amplify errors that must be recognized and addressed. Wheaton et al. (2010) quantified these errors using the following equation:

Error = Reference level ~ Real DEM level (Chen et al. 2011)

where reference level was obtained after the Google Earth image. Google earth's altitudes can be used for basic research and pilot study (El-Ashmawy 2016). Wheaton et al. (2010) mentioned that the error analysis determines the correctness

of the vertical change assessment. Most landform features along the Odisha shoreline are within 0.5 km of the beach (Kankara et al. 2018). As a result, this marginal distance of 0.5 km from the shoreline is regarded a study area for the identification of morphological evolution, as it was expected that coastal response to the variation in catchment sediment yield is not likely to stretch past 0.5 km after the shoreline.

14.5 Results and Discussions

The subsequent sections summarize the findings and explanations of the various analyses done in the current study:

14.5.1 Statistics of the Hydrological Data

The spatial variation of the latest hydrological data employed in the present study during 1973–2019 is given in Table 14.2. The exploratory analysis of the data includes minimum, maximum, mean, coefficient of variation (CV), skewness (skw), and kurtosis (kurt). The CV is the ratio of the standard deviation to the mean, skewness is a divergence from the normal distribution, and kurtosis is a measure of the cumulative weight of tails of a distribution compared to its centre. Variability through many statistical characteristics can shed light on data for future analysis. It is seen that the distributions of the two parameters differ due to variations in the mean values that reflect each variable. Among the two variables, the SSL has the highest CV, skw and kurt across all stations in the main channel and tributaries. It demonstrates that the annual SSL data is more dispersed, extremely irregular, and complicated, with non-normal distributions, than the yearly runoff data. The maximum CV (1.58), skw (3.48), and kurt (12.96) in SSL is observed at Rampur. The skw values in both the variables are only positive (asymmetrically right), while kurt has mixed values (both positive and negative). The extreme positive skw in SSL demonstrates the impact of abnormally high SSL. The extreme kurt values imply that the distribution is more susceptible to outliers than the Gaussian distribution. The high kurt value of SSL revealed a sharply elevated value, reflecting significant variations and non-normal distributions.

The Spearman's rank correlation coefficient (ρ) was used to understand the degree of a nonlinear relation between the variables. The ρ between the annual runoff and SSL across the stations of the MRB is found to be 0.87 (at $p < 0.01$), which indicates a significantly strong nonlinear correlation between them. It also illustrates that runoff has a substantial impact on the SSL of the basin. The range of runoff and SSL is observed maximum at the penultimate monitoring station of the watershed, Tikarpara. In contrast, among the tributaries of the basin, the maximum range of runoff is at Jondhra and second at Kantamal; however, the corresponding maximum range of SSL is at Kantamal. It shows the influence of larger drainage

Table 14.2 Basic description of the hydrological parameters on an annual basis across stations

Stations	Variables	Minimum	Maximum	Mean	CV	Skewness	Kurtosis
Tikarpara	Runoff (km^3/year)	18.66	124.77	47.51	0.40	1.31	4.55
	SSL (Mt/year)	0.04	50.27	15.23	0.80	1.38	1.32
Kantamal	Runoff (km^3/year)	3.36	22.64	11.06	0.48	0.57	−0.56
	SSL (Mt/year)	1.03	22.64	7.75	0.69	1.01	0.59
Kesinga	Runoff (km^3/year)	4.69	12.39	7.95	0.30	0.51	−1.01
	SSL (Mt/year)	0.82	18.35	5.36	1.06	1.60	1.50
Salebhata	Runoff (km^3/year)	0.23	4.95	1.91	0.57	0.80	0.19
	SSL (Mt/year)	0.01	1.91	0.51	0.89	1.23	1.06
Sundargarh	Runoff (km^3/year)	1.79	6.68	3.12	0.33	1.34	2.51
	SSL (Mt/year)	0.65	7.11	2.45	0.60	1.27	1.52
Kurubhata	Runoff (km^3/year)	0.98	5.11	2.32	0.33	1.20	3.04
	SSL (Mt/year)	0.20	5.22	1.99	0.55	0.62	0.84
Bamnidih	Runoff (km^3/year)	1.07	11.84	3.97	0.56	1.23	1.97
	SSL (Mt/year)	0.05	7.25	1.70	1.22	1.37	0.65
Manendragarh	Runoff (km^3/year)	0.10	0.56	0.30	0.40	0.40	−0.61
	SSL (Mt/year)	0.001	0.14	0.04	0.85	1.24	1.14
Rampur	Runoff (km^3/year)	0.17	4.38	1.29	0.65	1.81	4.08
	SSL (Mt/year)	0.01	5.23	0.64	1.58	3.48	12.96
Jondhra	Runoff (km^3/year)	2.03	21.85	8.36	0.54	0.98	1.02
	SSL (Mt/year)	0.55	13.43	3.95	0.71	1.55	2.83
Ghatora	Runoff (km^3/year)	0.22	1.16	0.71	0.38	0.06	−0.97
	SSL (Mt/year)	0.04	0.81	0.16	1.12	2.86	9.21
Andhiyarkore	Runoff (km^3/year)	0.04	0.85	0.31	0.60	1.09	1.18

(continued)

Table 14.2 (continued)

Stations	Variables	Minimum	Maximum	Mean	CV	Skewness	Kurtosis
	SSL (Mt/year)	0.02	1.76	0.36	0.91	2.11	7.33
Simga	Runoff (km^3/year)	1.20	13.23	4.99	0.52	0.83	0.69
	SSL (Mt/year)	0.003	8.63	1.60	0.97	2.59	8.96
Basantpur	Runoff (km^3/year)	6.81	51.36	20.30	0.44	0.90	1.80
	SSL (Mt/year)	0.81	30.76	8.64	0.83	1.34	1.36
Rajim	Runoff (km^3/year)	0.43	6.83	2.82	0.63	0.58	−0.50
	SSL (Mt/year)	0.001	3.67	0.87	1.02	1.39	1.26
Baronda	Runoff (km^3/year)	0.16	2.99	1.30	0.61	0.48	−0.50
	SSL (Mt/year)	0.0007	1.72	0.47	0.88	1.36	2.02

SSL suspended sediment load, *CV* coefficient of variation

areas in spatially controlling the range of the data. The more considerable variation (CV) in the data of runoff and SSL at Rampur may be attributed to the presence of the Jonk diversion weir upstream of Rampur. The CV in SSL, among the tributaries, varies from 0.55 at Kurubhata to 1.58 at Rampur. At the same time, it ranges from 0.8 (Tikarpara) to 1.02 (Rajim) for mainstream stations. The CV of SSL at the tributaries is attributed to the total erosion rates of the basin geology. In this regard, Chakrapani and Subramanian (1990) established that the total erosion rate at Kurubhata is more than double that of Rampur. The same is true for the range of CV in SSL at main stations. The more relief at Rajim and Rampur relative to Tikarpara and Kurubhata, respectively, also defined the more CV in SSL data. The Tel tributary contributes the most average annual SSL to the mainstream amid all sub-basins.

Furthermore, the analysis shows that the sub-basins of the MR having lower catchment areas contribute higher sediment yield relative to the tributaries having larger drainage areas. For example, the Seonath tributary having a basin length of 373 km, conveys a mean suspended sediment yield of 0.00013 Mt/km^2 and a mean runoff yield of 0.00028 km^3/km^2. In contrast, the Ib tributary with a basin length of 197 km discharges a mean suspended sediment yield of 0.00041 Mt/km^2 and a mean runoff yield of 0.00053 km^3/km^2. The annual runoff and SSL to the Bay of Bengal decreased nearly 26% and 71% between 46 years of the data interval. It implies that the SSL has declined almost three times more than the annual runoff and is severely alarming. The data interval across the gauging stations varies from 12 years at Kesinga to 46 years at Simga, Rajim, Bamnidih, Basantpur, Salebhata, and Tikarpara. The standard error of mean in average runoff and SSL at Kesinga is

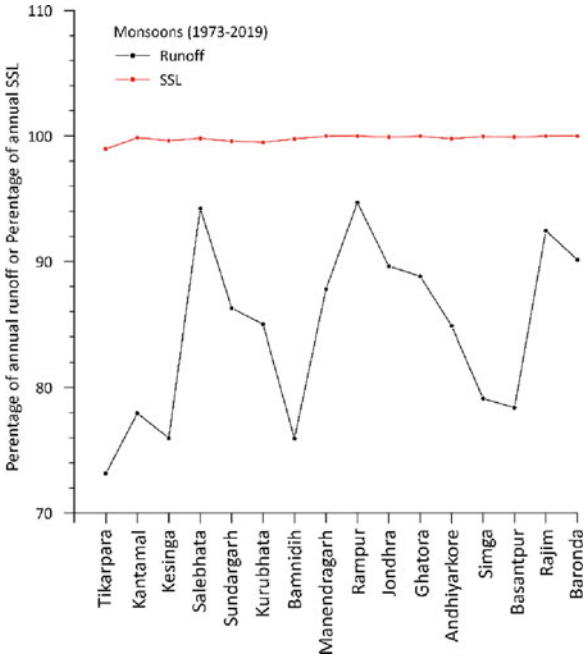

Fig. 14.2 Spatial variation of the monsoon runoff and suspended sediment load (SSL)

higher by 141% and 768%, respectively, than at other tributary sites with data spanning 46 years. It demonstrates that the greater the number of observations in the analysis, the lower the standard error of the mean. Figure 14.2 depicts the variation in the proportion of yearly runoff and SSL transported during monsoons across the basin. 73–95% of the annual runoff flows during monsoons, with wide spatial variations. This fraction increases further upstream in the basin. However, during the monsoons, the fraction of SSL is about 100%, spatially almost constant. This observation demonstrates that rivers in the MRB are majorly rain-fed and carry much runoff and sediment during the monsoons compared to the rest of the year. The data also reveals the substantial seasonality of these parameters. The monsoon runoff is relatively low at Tikarpara, Bamnidih, and Basantpur, owing to dams upstream of these locations.

14.5.2 Analysis of SSL Hysteresis for the Entire Study Period

The loop of the SSL hysteresis for all the major sub-basin stations of the MR is presented in Table 14.3. The properties of the sediment hysteresis were analysed using ΔS and ΔAR. Also, the average hysteresis index (HI_a) and peak phase difference were evaluated. The difference in hysteresis pattern among the nine sub-basins reflects diversity in probable sediment sources at various distances from the gauging stations. The hysteresis and sediment behaviour patterns

Table 14.3 Hysteresis parameters and their characteristics for all the major sub-basins during 1973–2019

Stations	Sub-basins	ΔS (%)	ΔAR (%)	Sediment behaviour	Hysteresis pattern	HI_a	PPD
Tikarpara	Mahanadi	79.42	0	Flushing	Complex	0.41	0
Kantamal	Tel	72.38	−10.01	Flushing	Counterclockwise	0.11	−0.27
Salebhata	Ong	78.22	18.58	Flushing	Clockwise	0.21	0.50
Sundargarh	Ib	79.60	0	Flushing	Complex	0.20	0
Kurubhata	Mand	96.23	0	Flushing	Complex	0.19	0
Bamnidih	Hasdeo	98.60	0	Flushing	Complex	0.84	0
Rampur	Pairi	81.08	−11.09	Flushing	Counterclockwise	−0.14	−0.12
Jondhra	Seonath	91.29	0	Flushing	Complex	0.11	0
Baronda	Pairi	94.98	0	Flushing	Complex	0.16	0

ΔS and ΔAR are the parameters of hysteresis, HI_a: Average Hysteresis index, PPD: Peak phase difference

demonstrate that all stations, except for Kantamal, Salebhata, and Rampur, exhibit a complex or ambiguous pattern impacted by a range of attributes linked to sediment supply in the sub-basins with a flushing nature. It illustrates the impact of human interventions, which resulted in a complex hysteresis with flushing behaviour (Sadeghi et al. 2019). It also represents the periodic fluctuations in SSL for these stations due to multiple anthropogenic events. As perceived from the ΔS values, the changes in SSL are significant (>90%) for the data of Kurubhata, Bamnidih, Jondhra and Baronda. However, the SSL hysteresis has a flushing nature with a counter-clockwise loop at Kantamal and Rampur. Due to sediment reduction in the channel bed near these stations, the sediment supply seems to be primarily situated in the upstream basin/channel compared to the riverbed itself, i.e., near the gauging station. The only station where the clockwise pattern of SSL hysteresis with flushing sediments is at Salebhata. It demonstrates that throughout 1973–2019, SSL was high for the ascending limb of the hydrograph, indicating sediment accessibility in the sub-basins from various sources. Origin of sediments, precipitation characteristics, and the impact of water-sediment interactions are some attributes resulting in a distinct nature of SSL hysteresis (Keesstra et al. 2019). The hysteresis loops for a given timescale show hydro-sedimentary processes that contribute to varying hysteresis loops due to sediment transport mechanisms. However, SSL hysteresis investigation depends on the study timescale as the hysteresis outcomes are non-stationary (Sadeghi et al. 2019).

The HI_a was used to compare the fluctuations of sediment concentration at the rising and falling limbs of the hydrograph in all the considered sub-basins (Table 14.3). This measure is chiefly used to determine if a river becomes cleaner or cloudier after the downturn of an event. The HI_a varies from −0.14 at Rampur to 0.84 at Bamnidih. However, Kantamal and Jondhra have HI_a values nearer to zero ($HI_a = 0.11$), implying a somewhat fairer balance of SSC among rising and falling

stages. The only negative HI_a at Rampur (−0.14) is likely by virtue of its significant forest plantation (CWC 2014). Additionally, it suggests often cloudier falling stages. The other catchments with significant forest plantations include Baronda, Bamnidih and Kurubhata (CWC 2014). In this regard, a Pearson correlation (r) of 0.96 (at $p < 0.05$) indicates a strong linear relationship between HI_a and sub-basin area for forested catchments (Fig. 14.3). This suggests that as sub-basin area reduces, falling limbs likely to be muddier than rising ones, particularly in sub-basins controlled by forests. Haddadchi and Hicks (2021) also observed a similar finding for various catchments in New Zealand. In addition, most sub-basins have no latency between the flow and SSC peak. It excludes sub-basins as Salebhata, Kanatamal, and Rampur. The peak flow delays the SSC peak by 21% of the typical flood duration at Salebhata, with a sub-basin dominated by cropland. In contrast, the flow peak leads the SSC peak by 27% and 12% of the flood duration for the remaining two stations with mixed and forest-dominated sub-basins, respectively. A model that produces SSC as a discharge function can exploit this HI_a dependency on land cover to incorporate hysteresis. In addition, the HI_a could be used to monitor the effectiveness of sediment routing models capable of developing hysteresis in sediment transport (Zhong 2013). This can be accomplished by comparing measured HI_a to HI_a calculated from predicted SSC and runoff data.

14.5.3 Trend Analysis and Detection of Periodicity in Hydrological Variables

The annual runoff and suspended sediment load trends were evaluated using the Mann-Kendall/ Modified Mann-Kendall nonparametric method for different station data periods. Also, the direction of the trend was established using Sen's slope estimator. Table 14.4 summarizes the results of the MMK and Sen's slope estimator. Furthermore, the spatial variation of the trend for runoff and SSL are represented in Fig. 14.4 and Fig. 14.5, respectively. All the present analyses are conducted at a 99% significance level, where the bold values in Table 14.4 represent the significant ones. No significant trend is observed in the annual runoff across stations except at Bamnidih. The only station in the Hasdeo tributary showing a significant declining trend is explained by the retention of the bulk volume of water in the reservoir and barrage present upstream of Bamnidih. The observed declining trend has a magnitude of 0.07 km^3/year. A non-significant trend in annual runoff detected at 94% of the studied stations shows that the anthropogenic factors have the most negligible influence on the annual runoff of the MRB, which possibly maintains an adequate flow spatially for meeting various competing demands. Furthermore, the non-significant trend in annual runoff is also due to the contrasting streamflow trends between seasons and the non-significant trend in annual precipitation (Panda et al. 2013).

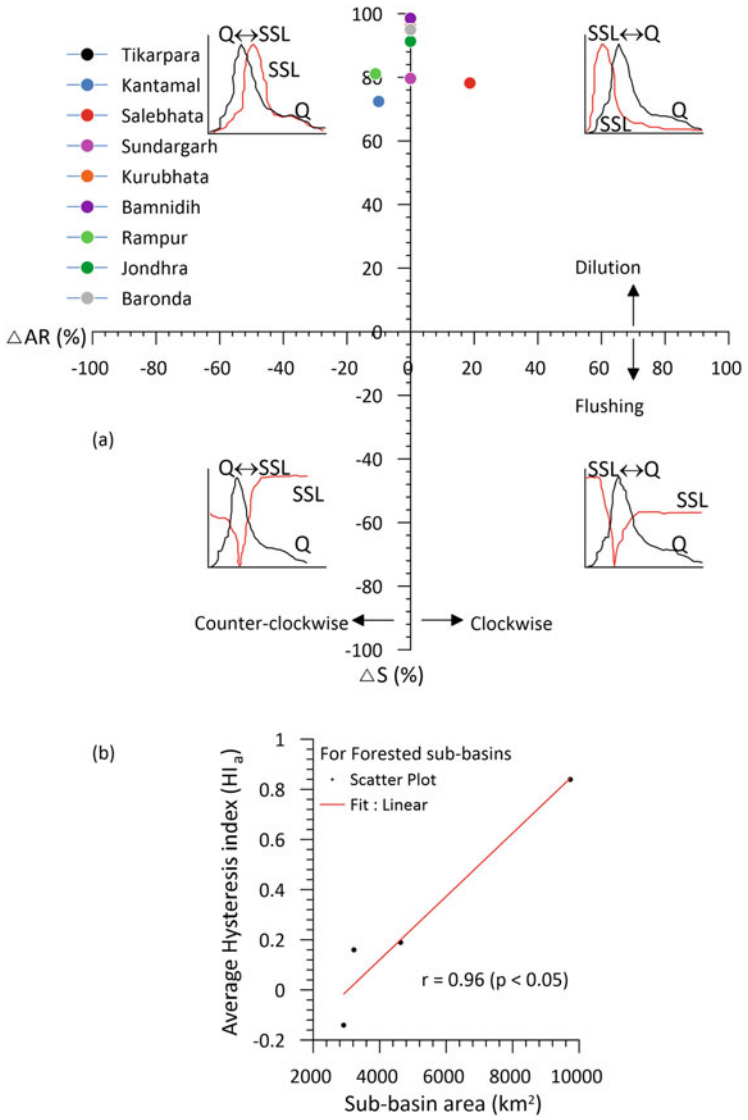

Fig. 14.3 Plot showing (**a**) Variation of hysteresis parameters for the entire study period across major sub-basins and (**b**) Correlation between sub-basin area and hysteresis index across forest-dominated sub-basins

In contrast, the annual SSL shows a significant decline at 11 out of 16 stations at a 99% significance level. The stations which offer no trend include Kantamal, Kesinga, Rampur, Jondhra, and Ghatora. The steepest considerable decline in annual SSL at 0.47 Mt/year is observed at the last gauging station of main Mahanadi compared to 0.02 Mt/year at most upstream Rajim. In contrast, among the

Table 14.4 Result summary of spatio-temporal trend analysis in annual runoff and SSL

Stations	Annual runoff		Annual SSL	
	MK/MMK test statistic	Sen's slope	MK/MMK test statistic	Sen's slope
Tikarpara	−0.62	−0.13	**−4.60**	**−0.47**
Kantamal	0.97	0.06	−1.04	−0.06
Kesinga	−0.75	−0.19	0	−0.03
Salebhata	−0.35	−0.006	**−2.74**	**−0.01**
Sundargarh	−1.64	−0.01	**−3.16**	**−0.04**
Kurubhata	−1.5	−0.01	**−3.19**	**−0.04**
Bamnidih	**−3.51**	**−0.07**	**−4.73**	**−0.06**
Manendragrah	−2.35	−0.009	**−4.22**	**−0.003**
Rampur	−1.15	−0.009	−2.19	−0.009
Jondhra	−0.37	−0.02	−1.1	−0.03
Ghatora	−0.45	−0.01	−0.53	−0.003
Andhiyarkore	−1.15	−0.003	**−3.44**	**−0.01**
Simga	−0.60	−0.02	**−3.65**	**−0.04**
Basantpur	−1.24	−0.14	**−4.35**	**−0.28**
Rajim	−0.07	−0.003	**−2.67**	**−0.01**
Baronda	−0.47	−0.005	**−2.34**	**−0.01**

SSL suspended sediment load, *MK/MMK* Mann-Kendall/modified Mann-Kendall method, Bold values indicates the significant ones at a 99% significance level

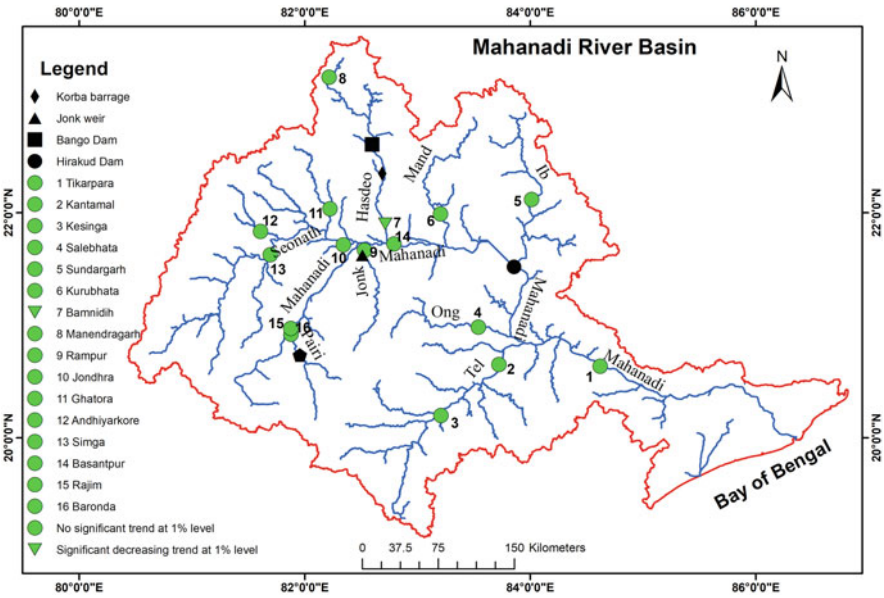

Fig. 14.4 Spatial representation of annual runoff trend

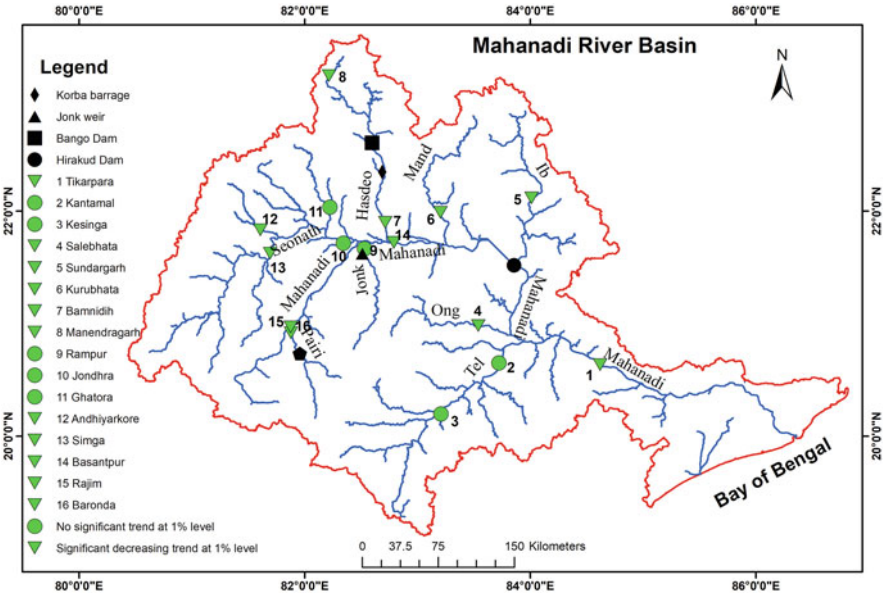

Fig. 14.5 Spatial representation of annual suspended sediment load trend

tributaries, the significant reduction of the least (0.003 Mt/year) and maximum (0.06 Mt/year) are at Manendragarh and Bamnidih of the Hasdeo sub-basin, respectively. The reduction in annual SSL is more prominent spatially along the main channel relative to the tributaries involved. The Minimato Bango reservoir and Bango barrage simultaneously affect the substantial annual runoff and SSL reduction at Bamnidih. Conversely to the non-significant trend of annual runoff, the drop in annual SSL reaching the shore is notable. Furthermore, this demonstrates that the normal change process in rainfall may not be the primary driver of the severe decline in SSL reported.

The linear (by Sen's slope) and nonlinear trends (captured by the EMD method) in the hydrological variables are represented in Fig. 14.5. The nonlinear trend in hydrological variables follows a similar direction to the linear trend. The temporal trend of annual runoff and SSL was decomposed into four sub-series and another residual term for all the hydrological stations of the basin using the EMD method. The plot of the trend adopting the EMD method is shown in Fig. 14.6. The runoff trends exhibit continuous periodicities of 2.12, 4.32, 9.1, and 30.8 years in the ultimate monitoring station of the watershed.

In contrast, the SSL series display continuous periodicities of 2.07, 5.82, 9.1, and 12.8 years. These periodicities equate to IMF-1, IMF-2, IMF-3, and IMF-4. Table 14.5 shows an overview of the periodicities and an associated impact rate of variation for yearly runoff and SSL at various locations. The aggregate variance contribution of the four IMFs to the overall variation for yearly SSL is greatest in Rampur, contributing 67.1%, and lowest at Kurubhata, accounting for 16.81%. For

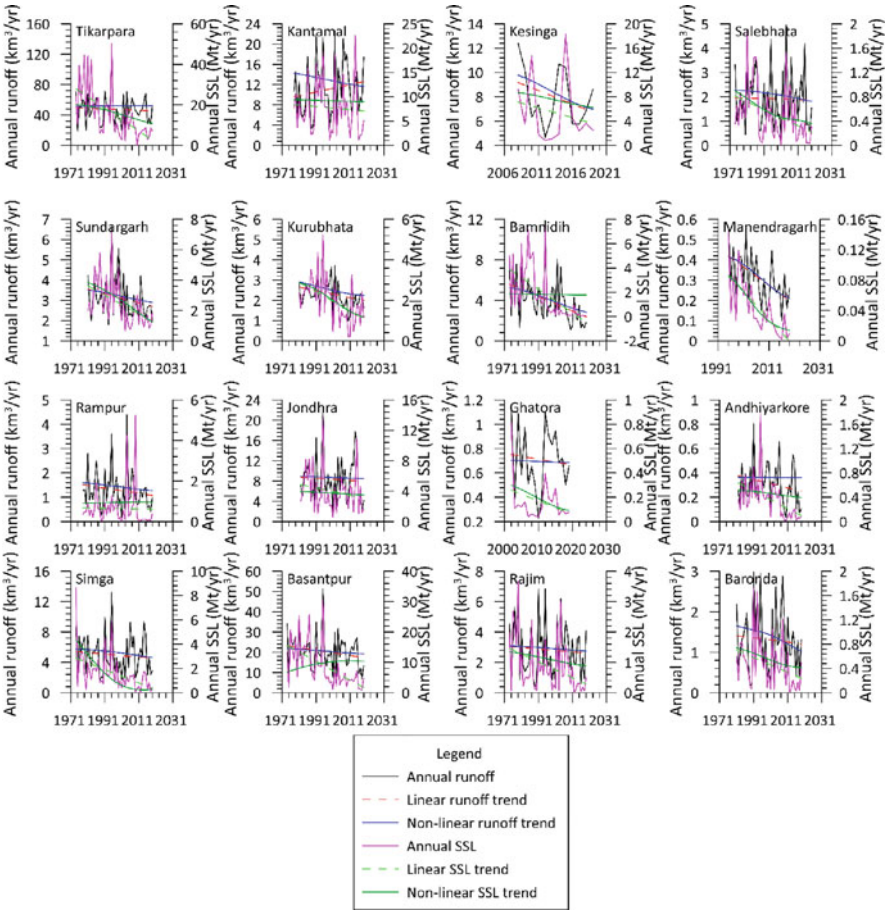

Fig. 14.6 Plots of linear and nonlinear trend assessment of annual runoff and suspended sediment load (SSL) for all monitoring stations

runoff statistics, it is observed to be maximum at Baronda (27.95%) and lowest at Kesinga (7.39%). Except for Bamnidih, Ghatora, and Basantpur, the first IMF for yearly SSL has the maximum contribution rate for all stations. However, the first IMF has the highest contribution rate for runoff series for all stations. As a result, all 13 stations had a 2-year periodicity in runoff and SSL. This periodicity can be ascribed to changes in climate trends, which eventually affect the runoff and SSL of a river basin.

The authors would like to point out that according to some previous studies (Fu et al. 2012; Zhao et al. 2014; Tamaddun et al. 2019), it was established that the periodicities are likely related to various climatic patterns like the El Niño/La Niña-Southern Oscillation (ENSO). Studies have also suggested that other factors complementary to ENSO may affect the Indian Summer Monsoon (ISM), e.g., the Indian

Table 14.5 Periodicity and a variation impact rate of annual runoff and SSL at each station

Stations	EMD parameters	Annual runoff					Annual SSL				
		IMF-1	IMF-2	IMF-3	IMF-4	Residual term	IMF-1	IMF-2	IMF-3	IMF-4	Residual term
Tikarpara	P	2.12	4.32	9.1	30.8	–	2.07	5.82	9.2	12.8	–
	VIR	9.43	2.67	0.87	0.39	86.64	16.52	8.49	2.07	5.42	67.51
Kantamal	P	2.02	4.89	11.4	20	–	2.09	4.26	11.5	7.2	–
	VIR	9.62	6.35	1.65	0.31	82.07	21.32	4.65	1.83	0.72	71.48
Kesinga	P	2.14	3.6	6.41	–	–	2.24	5.73	–	–	–
	VIR	4.10	2.93	0.36	–	92.62	38.06	8.37	–	–	53.57
Salebhata	P	2.07	4.35	7.12	13.4	–	2.03	4.37	12.4	–	–
	VIR	15.55	4.56	1.84	0.45	77.61	12.97	9.13	12.42	–	65.47
Sundargarh	P	2.1	4.19	11.2	26.5	–	2.15	4.82	4.99	–	–
	VIR	6.37	0.62	1.43	0.78	90.79	11.19	4.47	2.76	–	81.57
Kurubhata	P	2.09	5.3	9.13	12	–	2.1	4.23	5.47	–	–
	VIR	6.11	2.96	0.04	0.86	90.02	12.88	1.16	2.77	–	83.19
Bamnidih	P	2.1	5	7.38	18.8	–	2.1	6.14	13.2	8.31	–
	VIR	15.57	4.14	0.27	1.53	78.49	19.52	11.11	5.75	22.85	40.76
Manendragrah	P	2.17	3.99	7.38	–	–	2.18	2.47	10.1	–	–
	VIR	7.76	1.42	0.12	–	90.69	14.11	2.73	1.52	–	81.64
Rampur	P	2.06	4.38	12	28.1	–	2.18	7.89	12.4	28.2	–
	VIR	18.34	8.85	0.23	1.70	70.88	44.78	12.81	8.45	1.06	32.9
Jondhra	P	2.08	5.83	15.3	25.4	–	2.02	5.59	15.2	17.2	–
	VIR	13.28	8.72	1.23	0.07	76.70	21.92	14.07	3.98	0.15	59.88
Ghatora	P	2.04	6.46	12.3	–	–	2.07	2.31	10.2	9.1	–
	VIR	7.86	4.66	0.58	–	86.90	10.52	13.46	17.03	0.55	58.45
Andhiyarkore	P	2.1	6.99	19.4	–	–	2.1	5.09	17.1	–	–
	VIR	14.41	4.85	8.04	–	72.69	17.63	7.45	15.34	–	59.57

(continued)

Table 14.5 (continued)

Stations	EMD parameters	Annual runoff					Annual SSL				
		IMF-1	IMF-2	IMF-3	IMF-4	Residual term	IMF-1	IMF-2	IMF-3	IMF-4	Residual term
Simga	P	2.08	6.25	11.4	30.9	–	2.14	4.24	8.39	16.9	–
	VIR	14.74	9.7	0.2	0.3	75.05	20.17	8.08	1.37	11.62	58.74
Basantpur	P	2.09	5.41	8.92	30.4	–	2.2	5.51	7.34	25.7	–
	VIR	10.24	5.10	0.71	0.77	83.17	15.11	5.87	0.44	18.7	59.87
Rajim	P	2.05	4.46	12.8	23.6	–	2.08	6.78	13.4	28.9	–
	VIR	20.43	4	2.97	0.16	72.44	22.17	16.77	0.26	1.74	59.05
Baronda	P	2.13	5.71	8.35	–	–	2.11	5.2	9.01	–	–
	VIR	20.11	4.8	3.04	–	72.05	23	12.49	3.36	–	61.15

P periodicity in years, *VIR* variation impact rate in %

Ocean dipole (IOD), complex coupling and dynamics of multiple variables, and variations in heat flux over different land masses (Ashok et al. 2001; Wang et al. 2005). These climatic patterns significantly impact the variability of ISM, as studied by Indian Meteorological Department (IMD) (Ju and Slingo 1995; Kumar et al. 1999). ENSO is a natural cycle caused by the sea surface temperature fluctuations originating from the strengthening and weakening of the trade winds. It is observed in the tropical Pacific and affects the surrounding oceanic-atmospheric systems, which occurs over 2–7 years. The tropical Indian Ocean experiences a basin-wide change after an ENSO event. Also, previous studies suggest notable relationships exist between ENSO and hydro-climatic variables (Chiew and McMahon 2002) as ENSO events can impact regional runoff and subsequent sediment load by changing the rainfall patterns (Wang et al. 2006). However, in the current study, our main focus is to analyse the contribution of anthropogenic stresses on SSL, and as such climatic influence on SSL is not included.

14.5.4 Change Point Analysis

The nonparametric Pettit test was employed to detect the shift in the trend of annual runoff and SSL across the gauging stations of the basin. Figure 14.7 depicts the extent of change in annual runoff and SSL for all stations at a significance level of

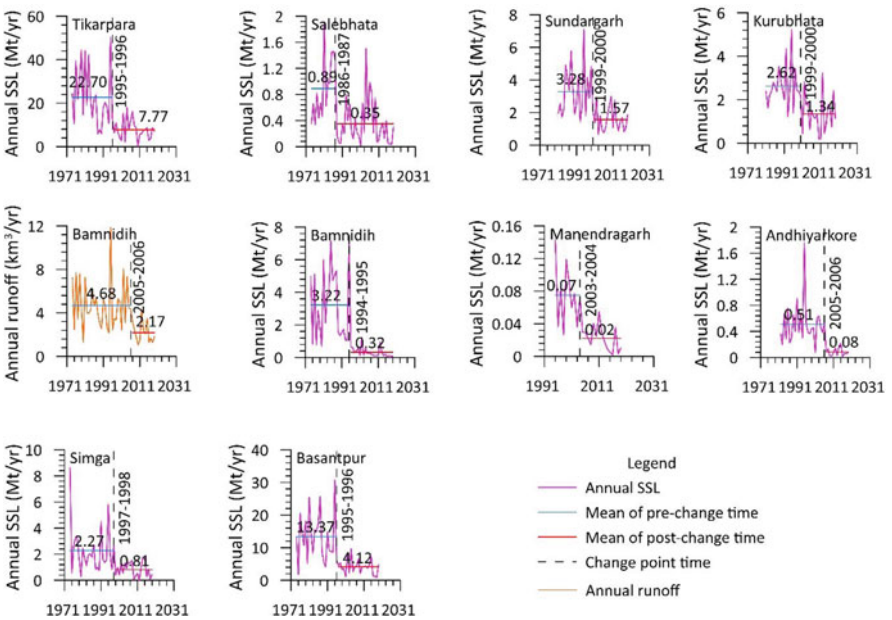

Fig. 14.7 Abrupt change point time of annual runoff and suspended sediment load (SSL) across identified stations of the basin at 99% significance level

Table 14.6 Result summary of Spatio-temporal change point assessment in annual runoff and SSL

Locations	Annual runoff	Annual SSL
Tikarpara	NCP	1995–1996
Kantamal	NCP	NCP
Kesinga	NCP	NCP
Salebhata	NCP	1986–1987
Sundargarh	NCP	1999–2000
Kurubhata	NCP	1999–2000
Bamnidih	2005–2006	1994–1995
Manendragrah	NCP	2003–2004
Rampur	NCP	NCP
Jondhra	NCP	NCP
Ghatora	NCP	NCP
Andhiyarkore	NCP	2005–2006
Simga	NCP	1997–1998
Basantpur	NCP	1995–1996
Rajim	NCP	NCP
Baronda	NCP	NCP

SSL suspended sediment load, *NCP* no change point identified at 99% significance level

1%. In this regard, Table 14.6 summarizes the results of the Pettitt test. Except for Bamnidih at the Hasdeo tributary, no substantial step shift in annual runoff is recognized. It showed a considerable change in 2005–2006. The most significant change in mean runoff occurs during 2005–2006, when it falls from 4.68 km^3/year to 2.17 km^3/year, contributing to a decrease of about 54% over the step. This is related to a 48% decline in dependable flow (at 75% likelihood) at the Bango barrage between 1999 and 2015. The abrupt changes in annual SSL at two stations (Andhiyarkore and Manendragarh) occurred post-2000s, while for the remaining stations, it mainly was pre-2000 at the 99% confidence level. Compared to mainstream stations, the transition time in the step of annual SSL varies across tributary stations. Different shift durations at tributaries are caused by a wide range of runoff and anthropogenic disturbances.

Likewise, the time series is segmented between a pre-change phase with comparatively restricted anthropogenic activities and a post-change period characterized by dense human activities that influence river SSL. Sundargarh and Kurubhata have the same shift period among the tributaries due to the same basin geology of limestone, sandstone, and shales and similar total erosion rates, as stated by Chakrapani and Subramanian (1990). The shift in annual SSL in Bamnidih (1994–1995) and Basantpur (1995–1996) results from the Bango reservoir's operation, which commenced in 1990; nevertheless, the reservoir was filled in 1994–1995 (Dsouza et al. 2017). As the change point analysis perceives, the reservoir results in significant sequestration of sediments by 90% before Bamnidih and 69% before Basantpur. However, most upstream stations Rajim and Baronda have shown no significant change in annual SSL. This regularity in annual SSL at

these stations may result from its presence in the headwater streams from whence the primary Mahanadi emerges. According to a change point study at Tikarpara, the accumulation of sediments in the basin accounts for approximately 66% between 1995 and 2019. This would significantly impact the coastal delta due to the sediment starvation from the catchment. Human impacts and climate variability have affected the flow and sediment load of the world's largest rivers (Maloney et al. 2018; Das 2021; Hu et al. 2022). Recently, sediment conveyance to the sea has decreased significantly due to the rise in the construction of dams and barrages for water supply, hydropower, and flood mitigation.

14.5.5 Geomorphic Change Analysis of the Coastal Stretch

To better comprehend the implications, an effort was made to estimate the impact of the large drop in annual SSL on the coastal shore from 2000 till 2011. The morphological change assessment of the coastal stretch was determined using the DEM of difference approach over a coastal land of 114.83 km^2 starting from Mahanadi River meeting the Bay of Bengal (BoB) to the end of the Chilika lake, stretching up to the mouth of Rushikulya stream joining BoB. The aggregate amount of erosion and sedimentation was found to be at 18% and 76%, respectively, with no changing area of around 6%. It is reasonable to state that no change region has preserved the natural sediment balance. Additionally, the similar volumetric characteristic of the stretch provides the overall volume of erosion and sedimentation of 0.06 km^3 and 0.46 km^3, respectively. As a result, the vertically mean annual erosion and accumulation are 0.29 m and 0.48 m, respectively. These numerical estimates of morphological variations over the investigation show that sensitive coastal features are susceptible. It is demonstrated by only 0.65 times increase in the proportion of vertical deposition against vertical loss when the comparable areal deposition is raised by 3.3 times against areal loss. In this regard, mean erosion and deposition of 0.2 m and 0.4 m vertically were observed on one of the southeast Asian coasts (Le Nguyen and Vo Luong 2019). Such substantial coastline loss is ascribed to torrential precipitation generating severe flooding in 2011 due to the sudden opening of the floodgates of the Hirakud dam, resulting in significant economic and environmental destruction to the coastline regions (Panda et al. 2013).

Furthermore, these considerable volumetric fluctuations are linked to regional variances in sediment load caused by diverse coastal and fluvial processes and anthropogenic activities throughout the basin. Typically, the areal deposition length is greater than erosion; nonetheless, important cities and tourist destinations are prone to severe coastal erosion. Consequently, this is a cause for concern because this is one of the largest inhabited coastal zones of the nation (Census 2011). As a result, the research depicts the severe influence of watershed sediment shortage, which results in rapid coastal erosion in several areas along the coast of the Mahanadi delta. The morphological change assessment result is established using ground coordinate points taken as a benchmark from Google Earth. These coordinate

point elevation data were obtained from SRTM and ASTER digital elevation models. The mean discrepancy between the benchmark and the DEM observation points was 2.0 m. As a result, the uncertainty appears to be the rationale for estimating the vertical variation of the coast.

14.5.6 Impact of Anthropogenic Disturbances on the Sediment Delivery from the Catchment

14.5.6.1 Impact of Large Hydraulic Structures

The impact of constructing large reservoirs in the Mahanadi River basin is researched from 1977 to 2019 to assess the influence of significant human forces in the watershed on the degree of sediment supply to the coast. In this regard, the annual fluctuation of sediment is a helpful indicator for determining the effects of human activities on the river basin (Wang et al. 2007). Figure 14.8 shows the simultaneous variation of annual SSL at the final monitoring station of the watershed and the construction of large reservoirs over 42 years. There is a strong inverse connection between the increase in the construction of large reservoirs in the catchment throughout the previous four decades and the annual SSL reported at

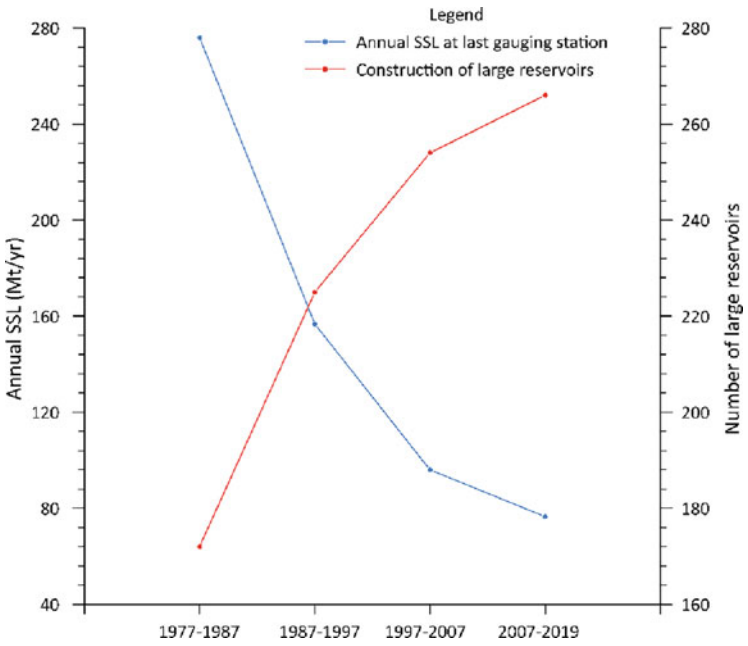

Fig. 14.8 Simultaneous variation of annual suspended sediment load (SSL) from the catchment and the construction of large reservoirs from 1977–2019

the Tikarpara. It shows how installing large reservoirs affects the decadal behaviour of the basin's sediment load. For example, suppose we look into the storage capacities of the two major reservoirs in the river basin, i.e., The Bango dam and the Hirakud dam; these structures severely impact the yearly SSL after the impoundment. The average annual SSL before the construction of the Bango dam in 1990 was 3.42 Mt/year, which has reduced to 0.70 Mt/year after 1990, accounting for a reduction of nearly 80% after the impoundment. Likewise, it is observed that the dead storage capacity of the Hirakud reservoir decreased from 2262 MCM (in 1957) to 1073 MCM (in 2000). It shows a capacity reduction (or sedimentation increase) of up to approximately 53% after the impoundment in 1957 (WRIS 2022). Large dams hold a lot of sediments, but they often provide water and electricity for agricultural, residential, and industrial purposes.

14.5.6.2 Impact on Suspended Sediment Rating Parameters

Runoff and suspended sediment load (SSL) have a power-law relationship ($SSL = aR^b$, where a and b are the rating parameters) for a significantly larger dataset, and the suspended sediment rating curve (SRC) explains this relationship for a specific measuring station (Asselman 2000). The same power form of the relationship between the variables was investigated in the present study across the three mainstream gauging stations. The purpose of choosing the three mainstream stations: Rajim, Basantpur, and Tikarpara, is that these stations, respectively, cover the upper, mid, and lower Mahanadi River basin as a whole. The SRC of these stations is plotted in Fig. 14.9, considering the entire data length for the last 46 years on an annual basis. The Rajim has the greatest R^2 of 0.65, followed by Basantpur ($R^2 = 0.52$) and Tikarpara ($R^2 = 0.40$). Positive correlations are seen at all sites, with the most upstream station showing the strongest link between annual runoff and SSL and decreasing as one moves downstream in the basin. This is due to a large amount of anthropogenic stress across the entire basin.

Wang et al. (2008) established that human impacts such as dam construction and land conservation efforts in a basin reduce the natural availability of sediments, i.e.,

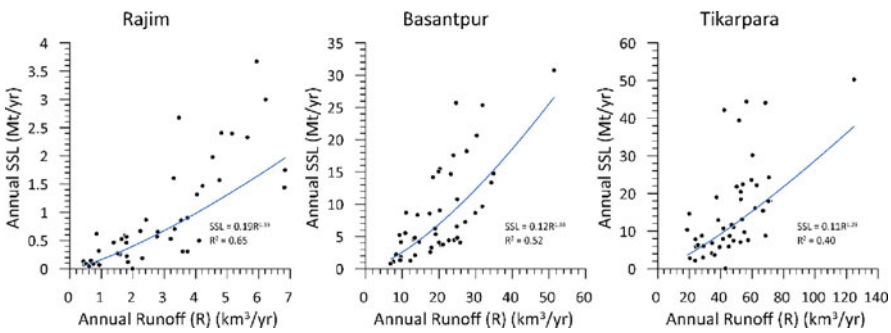

Fig. 14.9 Plot of suspended sediment rating across the mainstream stations

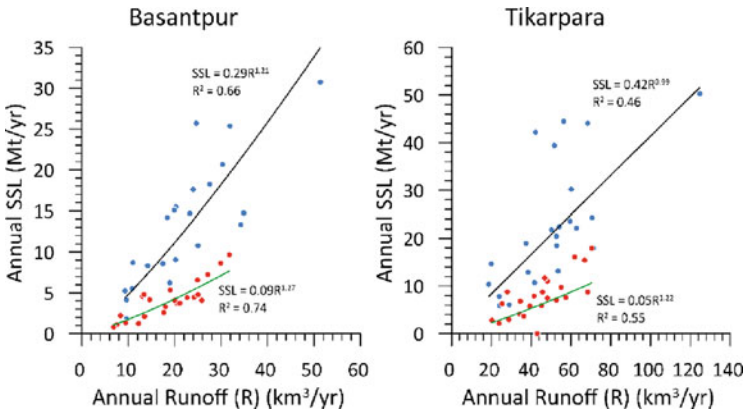

Fig. 14.10 Variation of rating parameters across the abrupt change point at Basantpur and Tikarpara

rating parameter *a*, while enhancing a stream's erosive capability, i.e., rating parameter *b*. The same observation is depicted in Fig. 14.10. From the previous change point analysis, it was reported that Rajim has no significant breakpoint in annual SSL; however, both Basantpur and Tikarpara have an abrupt shift in annual SSL during 1995–1996 at a 99% level of significance. Therefore, the rating parameters (a and b) variation is further analysed before and after the abrupt change point only at Basantpur and Tikarpara. The parameter *a* at Basantpur reduces drastically from 0.29 to 0.09, whereas *b* increases marginally from 1.21 to 1.27 pre-and post-1996. Similarly, the rating coefficient *a* decreases immensely from 0.42 to 0.05 and coefficient *b* increases from 0.99 to 1.22 pre-and-post the same change point in time at Tikarpara. The commissioning and inundation of the Bango dam in the Hasdeo tributary caused a sudden shift in the rating parameters at Basantpur between 1995 and 1996. The dam was operational in 1990, although the reservoir was not filled until 1995 (Dsouza et al. 2017). On the other hand, the difference in rating parameters in Tikarpara is related to the long-term impact of significant soil conservation efforts in the Hirakud watershed (Kumar 1989) as well as the operation of the Bango dam. This extensive evidence supports the notion that anthropic intervention has an extending impact on the geomorphological variation of a watershed.

14.5.6.3 Impact of Reservoir Storage Water Supply and Its Associated Utilization across Sectors

The 5-year moving average of the water release from the final monitoring station of the watershed during monsoon and non-monsoon seasons is depicted in Fig. 14.11. The monsoon water release shows a significant falling trend (at $p < 0.01$), but the non-monsoon season shows a definite growing trend (at $p < 0.01$) for more than the last four decades. As a result, it demonstrates the extended impact of the man-made

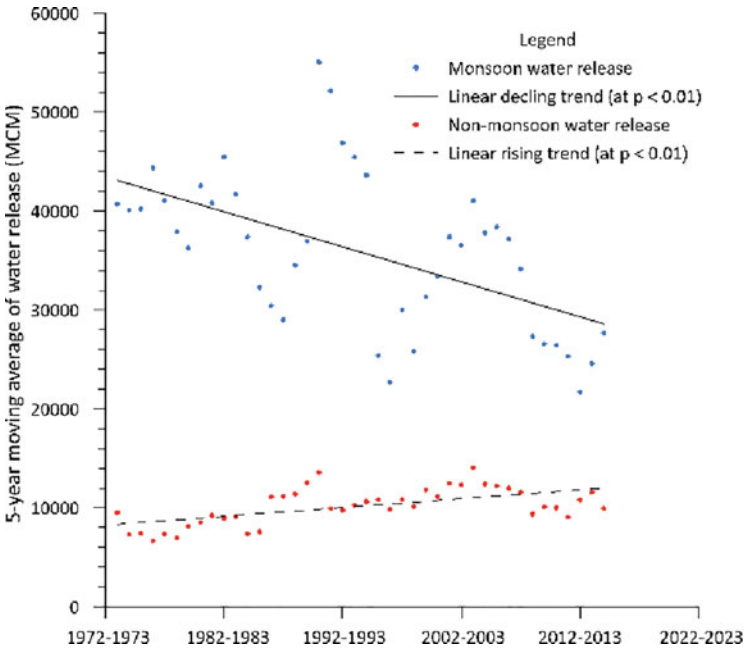

Fig. 14.11 Trend of the 5-year moving average of seasonal water release from the basin

intervention on the seasonal trend of annual water release from the complete watershed. It also indicates that more water is held in reservoirs during the monsoon season, which is then discharged during the dry season.

The utilization of reservoir water storage across various sectors of the river basin was investigated. The major sectors where river water exploitation occurs involve agriculture, hydroelectricity and thermal power stations. The seasonal water utilization trend for the agricultural industry and hydroelectricity generation from one of the longest dams of the river basin, the Hirakud, is shown as a 5-year moving average in Fig. 14.12. This trend analysis also shows the progress in human freshwater use from reservoirs over the decades. Monsoon and non-monsoon seasons have exhibited an inclining trend in agricultural intake; however, the non-monsoon season has a higher rising trend than the monsoon season. Likewise, during monsoons, utilization in the energy generation using reservoir water shows a significant increase; nevertheless, non-monsoon power usage is essentially non-existent, with no trend noted. All the above trends were calculated at a 99% significance level. The water distribution pattern of the basin for the thermal energy industry is classified under the two central states (Chhattisgarh and Odisha) that cover the river basin, as illustrated in Fig. 14.13. The distribution of reservoir storage in Chhattisgarh has been expanding in tandem with the demand for thermal sectors since 2000. However, the scenario flips with the requirement for a thermal industry, which has dramatically surpassed water delivery since 2000.

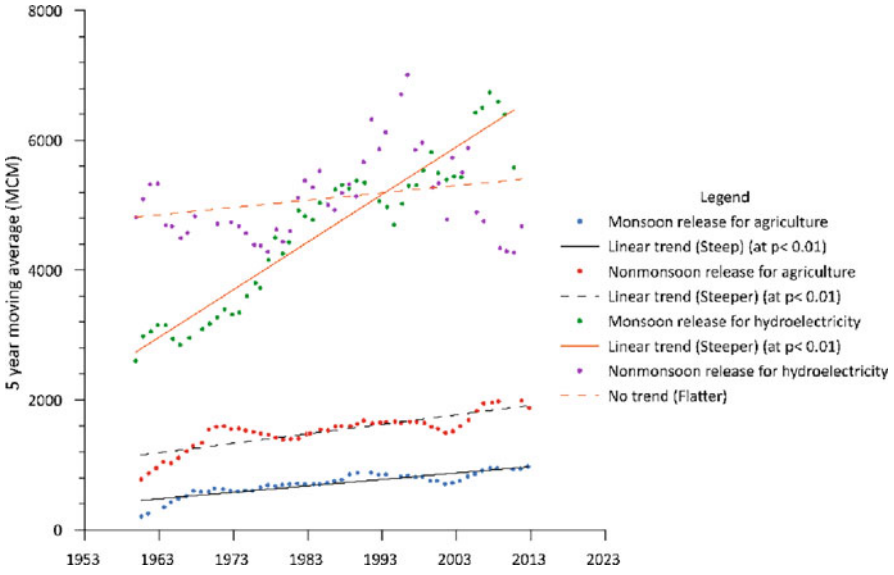

Fig. 14.12 Trend of the 5-year moving average of seasonal water release from the Hirakud dam

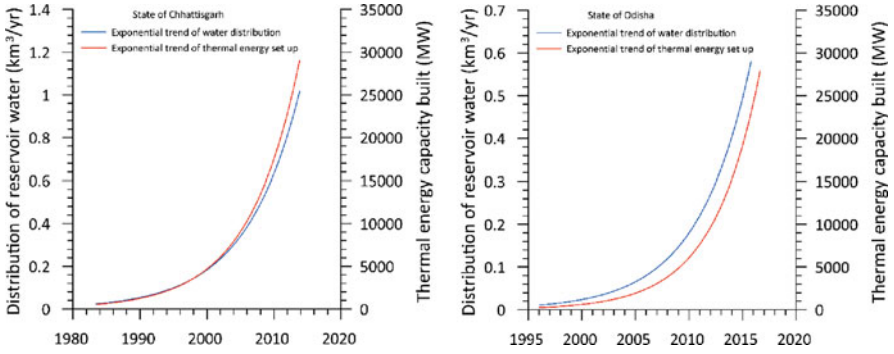

Fig. 14.13 Trend of the distribution of reservoir water and a corresponding set-up of thermal energy across the states covering the Mahanadi River basin

In contrast, the trend of water distribution in Odisha is larger than that of thermal demand. The supply-demand gap is smaller in the early years but grows dramatically after 2005. However, the river basin has seen a surge in demand for the industrial sector for many decades. It causes considerable water diversions from principal storage systems of the river basin. It demonstrates the increasing degree of human intervention in the basin, affecting the suspended sediment flow released into the estuary.

14.6 Recommendations

Current research highlights linear and nonlinear trends and sharp variations in the annual runoff and suspended sediment load (SSL) of the Mahanadi River watershed using nonparametric statistical techniques. The yearly SSL hysteresis pattern was eventually characterized to analyse the source of sediment supply for the sub-catchments. Also, a decadal implication of the coastal shore to the change in watershed sediment output was investigated, and the associated anthropic influences were identified. The following are the recommendations listed based on the findings of the present study.

1. Similar statistical approaches may also be implemented to analyse the measured hydrological data from various stations at seasonal, monthly, and daily time scales.
2. Analysis of suspended sediment hysteresis at a higher temporal resolution may be carried out to plan for effective watershed management.
3. The volumetric changes of the coastal delta of Odisha on a multi-decadal basis in response to variations in basin sediment load may be explored to build an erosion-accretion map of the coastal belt.
4. The influence of changes in current and future land use and land cover on the status of the erosion-accretion map of the coastal belt may also be analysed.

14.7 Conclusions

The current research has demonstrated the determination of linear and nonlinear trends and abrupt changes in the latest recorded annual runoff and suspended sediment load of the Mahanadi River basin. The preliminary spatio-temporal investigations of hydrological variables in the Mahanadi River basin indicate that annual suspended sediment load (SSL) data is more distributed, exceedingly irregular, and convoluted, with non-normal distributions than annual runoff data. This insight would be helpful in further modelling of SSL for the entire basin. It is noticed that SSL to the sea has declined almost three times more than the annual runoff and is therefore severely distressing. The basin discharges its entire suspended sediment load during the monsoon season, confirming its high dominating seasonality.

Different hysteresis patterns among the nine sub-basins reflect sediment sources at varying distances from gauging stations. As the sub-basin area decreases, falling limbs are likely to be muddier than rising limbs, especially in sub-basins governed by forests, according to a correlation between the hysteresis index and sub-basin area. The suspended sediment load from the Mahanadi River basin has decreased significantly over the past 46 years, although the annual flow pattern has not changed considerably. A nonlinear trend follows the linear trend in hydrological variables. However, 81% of the considered stations show a 2-year periodicity in runoff and suspended sediment load. Various runoff and anthropogenic disturbances induce

different shift durations at tributaries compared to mainstream stations. The numerical estimations of morphological modifications of the coast during the study reveal that sensitive coastal features are vulnerable. Large dam operations, increased water distribution priorities for many sectors, and extensive catchment soil conservation efforts reduce sediment transport to the sea. Variation in sediment rating characteristics from anthropogenic disturbances was also shown. The increased monsoon storage and subsequent non-monsoon release indicate the increase in non-monsoon agriculture and hydroelectricity output. The rapid development of new reservoirs in the basin over more than four decades has led to a significant decline in suspended sediment outflow into the ocean. The analysis warns policymakers that the current and future reservoir projects in the watershed will generate an unsustainable imbalance in the shoreline sediment budget.

References

Adarsh S, VishnuPriya MS, Narayanan S, Smruthi MS, George P, Benjie NM (2016) Trend analysis of sediment flux time series from tropical river basins in India using nonparametric tests and multiscale decomposition. Model Earth Syst Environ 2(4):1–16. https://doi.org/10.1007/s40808-016-0245-0

Åkesson U, Stigh J, Lindqvist JE, Göransson M, Shah MT, Shervais JW et al (2007) A general overview of the technology of in-stream mining of sand and gravel resources, associated potential environmental impacts, and methods to control potential impacts. Constr Build Mater 20(1):1–196

Ali EM, El-Magd IA (2016) Impact of human interventions and coastal processes along the Nile Delta coast, Egypt during the past twenty-five years. Egypt J Aquat Res 42(1):1–10. https://doi.org/10.1016/j.ejar.2016.01.002

Arthington AH, Naiman RJ, McClain ME, Nilsson C (2010) Preserving the biodiversity and ecological services of rivers: new challenges and research opportunities. Freshw Biol 55(1):1–16. https://doi.org/10.1111/J.1365-2427.2009.02340.X

Ashok K, Guan Z, Yamagata T (2001) Impact of the Indian Ocean dipole on the relationship between the Indian monsoon rainfall and ENSO. Geophys Res Lett 28(23):4499–4502. https://doi.org/10.1029/2001GL013294

Ashraf MA, Maah MJ, Yusoff I, Wajid A, Mahmood K (2011) Sand mining effects, causes and concerns: a case study from bestari jaya, Selangor, Peninsular Malaysia. Sci Res Essays 6(6):1216–1231. https://doi.org/10.5897/SRE10.690

Asselman NEM (2000) Fitting and interpretation of sediment rating curves. J Hydrol 234(3–4):228–248. https://doi.org/10.1016/S0022-1694(00)00253-5

Bastia F, Equeenuddin SM (2016) Spatio-temporal variation of water flow and sediment discharge in the Mahanadi River, India. Glob Planet Chang 144:51–66. https://doi.org/10.1016/j.gloplacha.2016.07.004

Bianchi TS, Allison MA (2009) Large-river delta-front estuaries as natural "recorders" of global environmental change. Proc Natl Acad Sci U S A 106(20):8085–8092. https://doi.org/10.1073/pnas.0812878106

Bird ECF (1985) Coastline changes: a global review. Wiley, Chichester (West Sussex)

Blum MD, Roberts HH (2009) Drowning of the Mississippi Delta due to insufficient sediment supply and global sea-levelrise. Nat Geosci 2(7):488–491. https://doi.org/10.1038/ngeo553

Borrelli P, Robinson DA, Fleischer LR, Lugato E, Ballabio C, Alewell C et al (2017) An assessment of the global impact of 21st century land use change on soil erosion. Nat Commun 8(1):1–13. https://doi.org/10.1038/s41467-017-02142-7

Brondizio ES, Foufoula-Georgiou E, Szabo S, Vogt N, Sebesvari Z, Renaud FG et al (2016) Catalyzing action towards the sustainability of deltas. Curr Opin Environ Sustain 19:182–194. https://doi.org/10.1016/j.cosust.2016.05.001

Census (2011) Primary Census Abstracts, Registrar General of India. Ministry of Home Affairs, Government of India

Chakrapani GJ, Subramanian V (1990) Preliminary studies on the geochemistry of the Mahanadi River basin, India. Chem Geol 81(3):241–253. https://doi.org/10.1016/0009-2541(90)90118-Q

Chen Y, Wang Y-G (2019) Variations in basin sediment yield and channel sediment transport in the upper Yangtze River and influencing factors. J Hydrol Eng 24(7):05019016. https://doi.org/10.1061/(asce)he.1943-5584.0001783

Chen XW, Liu X, Zhang W (2011) Shore reclamation in Pearl River esturay and its impact analysis. J Hohai Univ Nat Sci 39(1):39–43

Chiew FHS, McMahon TA (2002) Global ENSO-streamflow teleconnection, streamflow forecasting and interannual variability. Hydrol Sci J 47(3):505–522. https://doi.org/10.1080/02626660209492950

Conte LC, Bayer DM, Bayer FM (2019) Bootstrap Pettitt test for detecting change points in hydroclimatological data: case study of Itaipu hydroelectric plant, Brazil. Hydrolog Sci J 64(11):1312–1326. https://doi.org/10.1080/02626667.2019.1632461

Cuartero A, Felicísimo AM, Ariza FJ (2004) Accuracy of DEM genaration from TERRA-ASTER stereo data. International Archives of the Photogrammetry, Remote Sensing and Spatial Information Sciences - ISPRS Archives, p 35

CWC (2014) Mahanadi basin. Ministry of Water Resources, Govt. of India, New Delhi

CWC (2019) Water year book (June 2018 – May 2019), Hydrological observation circle Bhubaneswar, vol 1. Ministry of Water Resources, Govt. of India, New Delhi

Das S (2021) Dynamics of streamflow and sediment load in Peninsular Indian rivers (1965–2015). Sci Total Environ 799:149372. https://doi.org/10.1016/j.scitotenv.2021.149372

Dearing JA, Jones RT (2003) Coupling temporal and spatial dimensions of global sediment flux through lake and marine sediment records. Glob Planet Chang 39(1–2):147–168. https://doi.org/10.1016/S0921-8181(03)00022-5

Dewitt JD, Warner TA, Conley JF (2015) Comparison of DEMS derived from USGS DLG, SRTM, a statewide photogrammetry program, ASTER GDEM and LiDAR: implications for change detection. GIScience Remote Sens 52(2):179–197. https://doi.org/10.1080/15481603.2015.1019708

DoWR, Government of Orissa (2014) Flood report of the Hirakud dam. Superintending Engineer, Hirakud Dam Circle. Government of Odisha, Burla

Dsouza C et al (2017) Water allocations and use in the Mahanadi River basin. Forum for Policy Dialogue on Water Conflicts in India, Pune

El-Ashmawy KLA (2016) Investigation of the accuracy of Google earth elevation data. Artif Satellites 51(3):89–97. https://doi.org/10.1515/arsa-2016-0008

Fan D (2012) Open-coast tidal flats. In: Davis RA Jr, Dalrymple RW (eds) Principles of tidal sedimentology. Springer, New York, NY, pp 187–229

Fan D (2018) Has anthropogenic agent already created a new epoch of Anthropocene? In: Zhao X (ed) 10000 selected problems in sciences: ocean science. Science China Press, Beijing, pp 509–513

Fan D, Nguyen DV, Su J, Van Bui V, Tran DL (2019) Coastal morphological changes in the red river delta under increasing natural and anthropic stresses. Anthropocene Coasts 2(1):51–71. https://doi.org/10.1139/anc-2018-0022

Fanos AM (1995) The impact of human activities on the erosion and accretion of the Nile Delta coast. J Coast Res. https://www.jstor.org/stable/4298383. Accessed 11 June 2022

Feng H, Tang L, Wang Y, Guo C, Liu D, Zhao H et al (2020) Effects of recent morphological change on the redistribution of flow discharge in the Yangtze River Delta. Cont Shelf Res 208: 104218. https://doi.org/10.1016/j.csr.2020.104218

Fu C, James AL, Wachowiak MP (2012) Analyzing the combined influence of solar activity and El Niño on streamflow across southern Canada. Water Resour Res 48(5). https://doi.org/10.1029/2011WR011507

Galy V, Peucker-Ehrenbrink B, Eglinton T (2015) Global carbon export from the terrestrial biosphere controlled by erosion. Nature 521(7551):204–207. https://doi.org/10.1038/nature14400

Gamage N, Smakhtin V (2009) Do river deltas in east India retreat? A case of the Krishna Delta. Geomorphology 103(4):533–540. https://doi.org/10.1016/j.geomorph.2008.07.022

Gupta H, Chakrapani GJ (2007) Temporal and spatial variations in water flow and sediment load in the Narmada river. Curr Sci 92(5):679–684. https://doi.org/10.1007/S00254-005-1314-2/FIGURES/11

Haddadchi A, Hicks M (2021) Interpreting event-based suspended sediment concentration and flow hysteresis patterns. J Soils Sediments 21(1):592–612. https://doi.org/10.1007/s11368-020-02777-y

Hamed KH, Ramachandra Rao A (1998) A modified Mann-Kendall trend test for autocorrelated data. J Hydrol 204(1–4):182–196. https://doi.org/10.1016/S0022-1694(97)00125-X

Harrington ST, Harrington JR (2013) An assessment of the suspended sediment rating curve approach for load estimation on the Rivers Bandon and Owenabue, Ireland. Geomorphology 185:27–38. https://doi.org/10.1016/j.geomorph.2012.12.002

Hazra S, Das S, Ghosh A, Raju PV, Patel A (2020) The Mahanadi Delta: a rapidly developing Delta in India. Deltas in the Anthropocene. Palgrave Macmillan, Cham, pp 53–77. https://doi.org/10.1007/978-3-030-23517-8_3

Higgins SA, Overeem I, Rogers KG, Kalina EA (2018) River linking in India: downstream impacts on water discharge and suspended sediment transport to deltas. Elementa 6. https://doi.org/10.1525/elementa.269

Hoffmann T, Thorndycraft VR, Brown AG, Coulthard TJ, Damnati B, Kale VS et al (2010) Human impact on fluvial regimes and sediment flux during the Holocene: review and future research agenda. Glob Planet Chang 72(3):87–98. https://doi.org/10.1016/j.gloplacha.2010.04.008

Hu J, Li P, Zhao G, Mu X, Hörmann G, Gao P et al (2022) Effects of climate variability and anthropogenic factors on sediment load reduction in the Weihe River basin, China. Hydrolog Process 36(4):e14562. https://doi.org/10.1002/hyp.14562

Huang NE, Shen Z, Long SR, Wu MC, Snin HH, Zheng Q et al (1998) The empirical mode decomposition and the Hubert spectrum for nonlinear and non-stationary time series analysis. Proc R Soc A Math Phys Eng Sci 454(1971):903–995. https://doi.org/10.1098/rspa.1998.0193

Huntington TG (2006) Evidence for intensification of the global water cycle: review and synthesis. J Hydrol 319(1–4):83–95. https://doi.org/10.1016/J.JHYDROL.2005.07.003

IPCC (2001) Contribution of working Group I to the third assessment report of the intergovernmental panel on climate change. In: Houghton JE (ed) Climate change 2001: the scientific basis. Cambridge University Press, New York

James LA, Hodgson ME, Ghoshal S, Latiolais MM (2012) Geomorphic change detection using historic maps and DEM differencing: the temporal dimension of geospatial analysis. Geomorphology 137(1):181–198. https://doi.org/10.1016/j.geomorph.2010.10.039

Jiang S, Ren L, Yong B, Singh VP, Yang X, Yuan F (2011) Quantifying the effects of climate variability and human activities on runoff from the Laohahe basin in northern China using three different methods. Hydrol Process 25(16):2492–2505. https://doi.org/10.1002/hyp.8002

Jiang C, Pan S, Chen S (2017) Recent morphological changes of the Yellow River (Huanghe) submerged delta: causes and environmental implications. Geomorphology 293:93–107. https://doi.org/10.1016/j.geomorph.2017.04.036

Ju J, Slingo J (1995) The Asian summer monsoon and ENSO. Q J R Meteorol Soc 121(525): 1133–1168. https://doi.org/10.1002/qj.49712152509

Kale VS (2002) Fluvial geomorphology of Indian rivers: an overview. Prog Phys Geogr 26(3): 400–433. https://doi.org/10.1191/0309133302pp343ra

Kale VS (2005) Fluvial hydrology and geomorphology of monsoon-dominated Indian rivers. Revista Brasileira de Geomorfologia 6(1). https://doi.org/10.20502/rbg.v6i1.39

Kankara RS, Ramana Murthy MV, Rajeevan M (2018) National assessment of shoreline changes along Indian coast- a status report of 26 years 1990–2016. NCCR Publication

Kar R, Sarkar A (2021) Anthropogenic influences on the variation of runoff and sediment load of the Mahanadi River basin. Hydrol Sci J 66(12):1820–1844. https://doi.org/10.1080/02626667.2021.1967957

Kar R, Sarkar A (2022) Potential predictability of suspended sediment concentration in the data constrained regions of the Mahanadi River basin, Eastern India. Int J River Basin Manag. https://doi.org/10.1080/15715124.2021.2016782

Karaki Abou N, Fiaschi S, Closson D (2016) Sustainable development and anthropogenic induced geomorphic hazards in subsiding areas. Earth Surf Process Landf 41(15):2282–2295. https://doi.org/10.1002/esp.4047

Keesstra SD, Davis J, Masselink RH, Casalí J, Peeters ETHM, Dijksma R (2019) Coupling hysteresis analysis with sediment and hydrological connectivity in three agricultural catchments in Navarre, Spain. J Soils Sediments 19(3):1598–1612. https://doi.org/10.1007/s11368-018-02223-0

Kendall MG (1975) Rank correlation methods. Griffin, London

Knight J, Mitchell W, Rose J (2011) Geomorphological field mapping. In: Smith MJ, Paron P, Griffiths J (eds) Geomorphological mapping: methods and applications. Elsevier, London, pp 151–188

Kumar K (1989) Management of water in Hirakud Dam project. Technical report, Ministry of Environment and Forests, Government of India

Kumar KK, Rajagopalan B, Cane MA (1999) On the weakening relationship between the indian monsoon and ENSO. Science 284(5423):2156–2159. https://doi.org/10.1126/science.284.5423.2156

Le Nguyen HT, Vo Luong HP (2019) Erosion and deposition processes from field experiments of hydrodynamics in the coastal mangrove area of Can Gio, Vietnam. Oceanologia 61(2):252–264. https://doi.org/10.1016/j.oceano.2018.11.004

Li X, Bellerby R, Craft C, Widney SE (2018) Coastal wetland loss, consequences, and challenges for restoration. Anthropocene Coasts 1(1):1–15. https://doi.org/10.1139/anc-2017-0001

Liu T, Huang HQ, Shao M, Yao W, Gu J, Yu G (2015) Responses of streamflow and sediment load to climate change and human activity in the upper Yellow River, China: a case of the ten great gullies basin. Water Sci Technol 71(12):1893–1900. https://doi.org/10.2166/wst.2015.167

Luo W, Shen F, He Q, Cao F, Zhao H, Li M (2022) Changes in suspended sediments in the Yangtze River Estuary from 1984 to 2020: responses to basin and estuarine engineering constructions. Sci Total Environ 805:150381. https://doi.org/10.1016/j.scitotenv.2021.150381

Maloney JM, Bentley SJ, Xu K, Obelcz J, Georgiou IY, Miner MD (2018) Mississippi River subaqueous delta is entering a stage of retrogradation. Mar Geol 400:12–23. https://doi.org/10.1016/j.margeo.2018.03.001

Malutta S, Kobiyama M, Chaffe PLB, Bonumá NB (2020) Hysteresis analysis to quantify and qualify the sediment dynamics: state of the art. Water Sci Technol 81(12):2471–2487. https://doi.org/10.2166/wst.2020.279

Mann HB (1945) Nonparametric tests against trend. Econometrica 13(3):245. https://doi.org/10.2307/1907187

Mishra M, Panda GK (2016) Studies on shoreline changes using space born data along the part of Mahanadi delta, East Coast of India. J Coastal Sci 3(2):18–25

MoEF (2016) Environmental clearance reports of industries in the Mahanadi basin. MoEF, Government of India

Mohamad N, Ahmad A, Khanan MFA, Din AHM (2022) Surface elevation changes estimation underneath mangrove canopy using SNERL filtering algorithm and DoD technique on UAV-derived DSM data. ISPRS Int J Geo Inf 11(1):32. https://doi.org/10.3390/ijgi11010032

Montanher OC, de Morais Novo EML, de Souza Filho EE (2018) Temporal trend of the suspended sediment transport of the Amazon River (1984–2016). Hydrol Sci J 63(13–14):1901–1912. https://doi.org/10.1080/02626667.2018.1546387

Mueller ER, Schmidt JC, Topping DJ, Shafroth PB, Rodríguez-Burgueño JE, Ramírez-Hernández J, Grams PE (2017) Geomorphic change and sediment transport during a small artificial flood in a transformed post-dam delta: the Colorado River delta, United States and Mexico. Ecol Eng 106:757–775. https://doi.org/10.1016/j.ecoleng.2016.08.009

Mukhopadhyay A, Ghosh P, Chanda A, Ghosh A, Ghosh S, Das S et al (2018) Threats to coastal communities of Mahanadi delta due to imminent consequences of erosion – present and near future. Sci Total Environ 637–638:717–729. https://doi.org/10.1016/j.scitotenv.2018.05.076

NRLD (2019) National register of large dams. Government of India, New Delhi

Overeem I, Syvitski JPM (2009) Dynamics and vulnerability of Delta systems LAND-OCEAN INTERACTIONS IN THE COASTAL ZONE (LOICZ) Core Project of the International Geosphere-Biosphere Programme (IGBP) and the International Human Dimensions Programme on Global Environmental Change (IHDP)

Panda DK, Kumar A, Mohanty S (2011) Recent trends in sediment load of the tropical (Peninsular) river basins of India. Glob Planet Chang 75(3–4):108–118. https://doi.org/10.1016/j.gloplacha.2010.10.012

Panda DK, Kumar A, Ghosh S, Mohanty RK (2013) Streamflow trends in the mahanadi river basin (India): linkages to tropical climate variability. J Hydrol 495:135–149. https://doi.org/10.1016/j.jhydrol.2013.04.054

Paszkowski A, Goodbred S, Borgomeo E, Khan MSA, Hall JW (2021) Geomorphic change in the Ganges–Brahmaputra–Meghna delta. Nat Rev Earth Environ 2(11):763–780. https://doi.org/10.1038/s43017-021-00213-4

Pettitt AN (1979) A nonparametric approach to the change-point problem. Appl Stat 28(2):126. https://doi.org/10.2307/2346729

Petts GE, Gurnell AM (2005) Dams and geomorphology: research progress and future directions. Geomorphology 71(1–2):27–47. https://doi.org/10.1016/j.geomorph.2004.02.015

Ragia L, Krassakis P (2019) Monitoring the changes of the coastal areas using remote sensing data and geographic information systems. Proc. SPIE 11174:48. https://doi.org/10.1117/12.2533659

Rao Nageswara K, Subraelu P, Naga Kumar KCV, Demudu G, Hema Malini B, Rajawat AS, Ajai. (2010) Impacts of sediment retention by dams on delta shoreline recession: evidences from the Krishna and Godavari deltas, India. Earth Surface Process Landforms 35(7):817–827. https://doi.org/10.1002/esp.1977

Rougé C, Ge Y, Cai X (2013) Detecting gradual and abrupt changes in hydrological records. Adv Water Resour 53:33–44. https://doi.org/10.1016/j.advwatres.2012.09.008

Sadeghi SHR, Saeidi P, Singh VP, Telvari AR (2019) How persistent are hysteresis patterns between suspended sediment concentration and discharge at different timescales? Hydrol Sci J 64(15):1909–1917. https://doi.org/10.1080/02626667.2019.1676895

Sang YF, Wang Z, Liu C (2014) Comparison of the MK test and EMD method for trend identification in hydrological time series. J Hydrol 510:293–298. https://doi.org/10.1016/j.jhydrol.2013.12.039

Schwendel AC, Fuller IC, Death RG (2012) Assessing DEM interpolation methods for effective representation of upland stream morphology for rapid appraisal of bed stability. River Res Appl 28(5):567–584. https://doi.org/10.1002/rra.1475

Sen PK (1968) Estimates of the regression coefficient based on Kendall's Tau. J Am Stat Assoc 63(324):1379–1389. https://doi.org/10.1080/01621459.1968.10480934

Sharifi A, Mirchi A, Pirmoradian R, Mirabbasi R, Tourian MJ, Haghighi AT, Madani K (2021) Battling water limits to growth: lessons from water trends in the central plateau of Iran. Environ Manag 68(1):53–64. https://doi.org/10.1007/s00267-021-01447-0

Smajgl A, Toan TQ, Nhan DK, Ward J, Trung NH, Tri LQ et al (2015) Responding to rising sea levels in the Mekong Delta. Nat Clim Chang 5(2):167–174. https://doi.org/10.1038/nclimate2469

Smith MJ, Pain CF (2009) Applications of remote sensing in geomorphology. Prog Phys Geogr 33(4):568–582. https://doi.org/10.1177/0309133309346648

Suhaila J, Yusop Z (2018) Trend analysis and change point detection of annual and seasonal temperature series in Peninsular Malaysia. Meteorog Atmos Phys 130(5):565–581. https://doi.org/10.1007/s00703-017-0537-6

Sun Z, Niu X (2021) Variation tendency of coastline under natural and anthropogenic disturbance around the abandoned yellow river delta in 1984–2019. Remote Sens 13(17):3391. https://doi.org/10.3390/rs13173391

Syvitski JPM (2003) Supply and flux of sediment along hydrological pathways: research for the 21st century. Glob Planet Chang 39(1–2):1–11. https://doi.org/10.1016/S0921-8181(03)00008-0

Syvitski JPM (2008) Deltas at risk. Sustain Sci 3(1):23–32. https://doi.org/10.1007/s11625-008-0043-3

Syvitski JPM, Peckham SD, Hilberman R, Mulder T (2003) Predicting the terrestrial flux of sediment to the global ocean: a planetary perspective. Sediment Geol 162(1–2):5–24. https://doi.org/10.1016/S0037-0738(03)00232-X

Syvitski JPM, Vörösmarty CJ, Kettner AJ, Green P (2005) Impact of humans on the flux of terrestrial sediment to the global coastal ocean. Science 308(5720):376–380. https://doi.org/10.1126/science.1109454

Tabatabaei SH, Nourmahnad N, Kermani SG, Tabatabaei SA, Najafi P, Heidarpour M (2020) Urban wastewater reuse in agriculture for irrigation in arid and semi-arid regions - a review. Int J Recycling Organic Waste Agric 9(2):193–220. https://doi.org/10.30486/ijrowa.2020.671672

Tamaddun KA, Kalra A, Bernardez M, Ahmad S (2019) Effects of ENSO on temperature, precipitation, and potential evapotranspiration of North India's monsoon: an analysis of trend and entropy. Water 11(2):189. https://doi.org/10.3390/w11020189

Tang Q, Bao Y, He X, Fu B, Collins AL, Zhang X (2016) Flow regulation manipulates contemporary seasonal sedimentary dynamics in the reservoir fluctuation zone of the three gorges reservoir, China. Sci Total Environ 548–549:410–420. https://doi.org/10.1016/j.scitotenv.2015.12.158

Tarolli P (2016) Humans and the Earth's surface. Earth Surf Process Landf 41(15):2301–2304. https://doi.org/10.1002/esp.4059

Tsyplenkov A, Golosov V, Belyakova P (2021) How did the suspended sediment load change in the North Caucasus during the Anthropocene? Hydrol Process 35(10):e14403. https://doi.org/10.1002/hyp.14403

Unnikrishnan P, Jothiprakash V (2015) Extraction of nonlinear rainfall trends using singular spectrum analysis. J Hydrol Eng 20(12):05015007. https://doi.org/10.1061/(asce)he.1943-5584.0001237

Walling DE (1996) Erosion and sediment yield in a changing environment. Geol Soc Lond, Spec Publ 115(1):43–56. https://doi.org/10.1144/GSL.SP.1996.115.01.05

Wang P, Clemens S, Beaufort L, Braconnot P, Ganssen G, Jian Z et al (2005) Evolution and variability of the Asian monsoon system: state of the art and outstanding issues. Quat Sci Rev 24(5–6):595–629. https://doi.org/10.1016/J.QUASCIREV.2004.10.002

Wang H, Yang Z, Saito Y, Liu JP, Sun X (2006) Interannual and seasonal variation of the Huanghe (Yellow River) water discharge over the past 50 years: connections to impacts from ENSO events and dams. Glob Planet Chang 50(3–4):212–225. https://doi.org/10.1016/j.gloplacha.2006.01.005

Wang H, Yang Z, Saito Y, Liu JP, Sun X, Wang Y (2007) Stepwise decreases of the Huanghe (Yellow River) sediment load (1950-2005): impacts of climate change and human activities. Glob Planet Chang 57(3–4):331–354. https://doi.org/10.1016/j.gloplacha.2007.01.003

Wang H, Yang Z, Wang Y, Saito Y, Liu JP (2008) Reconstruction of sediment flux from the Changjiang (Yangtze River) to the sea since the 1860s. J Hydrol 349(3–4):318–332. https://doi.org/10.1016/j.jhydrol.2007.11.005

Wheaton JM, Brasington J, Darby SE, Sear DA (2010) Accounting for uncertainty in DEMs from repeat topographic surveys: improved sediment budgets. Earth Surf Process Landf 35(2): 136–156. https://doi.org/10.1002/esp.1886

Wood J (1996) The geomorphological characterization of digital elevation models. Thesis (PhD). Leicester, UK: Department of Geography, University of Leicester, pp 60–72

WRIS (2022). https://indiawris.gov.in/wris/#/Reservoirs. Accessed 16 July 2022

Xie H, Li D, Xiong L (2014) Exploring the ability of the Pettitt method for detecting change point by Monte Carlo simulation. Stoch Env Res Risk A 28(7):1643–1655. https://doi.org/10.1007/s00477-013-0814-y

Xu J (2006) Land accretion of the Yellow River Delta as influenced by drainage basin factors. Geogr Ann Ser B 88(1):31–41. https://doi.org/10.1111/j.0435-3676.2006.00281.x

Xu N (2018) Detecting coastline change with all available landsat data over 1986-2015: a case study for the state of Texas, USA. Atmos 9(3):107. https://doi.org/10.3390/atmos9030107

Yu J, Fu Y, Li Y, Han G, Wang Y, Zhou D et al (2011) Effects of water discharge and sediment load on evolution of modern Yellow River Delta, China, over the period from 1976 to 2009. Biogeosciences 8(9):2427–2435. https://doi.org/10.5194/bg-8-2427-2011

Zhang T, Niu X (2021) Analysis on the utilization and carrying capacity of coastal tidal flat in bays around the Bohai Sea. Ocean Coast Manag 203:105449. https://doi.org/10.1016/j.ocecoaman.2020.105449

Zhao G, Tian P, Mu X, Jiao J, Wang F, Gao P (2014) Quantifying the impact of climate variability and human activities on streamflow in the middle reaches of the Yellow River basin, China. J Hydrol 519(PA):387–398. https://doi.org/10.1016/j.jhydrol.2014.07.014

Zhao Y, Zou X, Liu Q, Xu M, Yao Y (2021) Recent morphological changes of the Changjiang (Yangtze River) mega-delta in the Anthropocene, China: impact from natural and anthropogenic changes. The Holocene 31(5):791–801. https://doi.org/10.1177/0959683620988042

Zhong Y (2013) Modelling sediment transportation and overland flow. University of Oxford, Oxford

Zuecco G, Penna D, Borga M, van Meerveld HJ (2016) A versatile index to characterize hysteresis between hydrological variables at the runoff event timescale. Hydrol Process 30(9):1449–1466. https://doi.org/10.1002/hyp.10681

Chapter 15
Assessment of Sediment Hazards by Bed Level Variations Around the Bridge Pier

Laxmi Narayana Pasupuleti, Prafulkumar Vasharambhai Timbadiya, and Prem Lal Patel

Abstract Local scour around the hydraulic structure is one of the prime responsibilities for the sediment hazards. The present study investigated the bed level variations around the bridge pier on uniform sediments under varied flow intensities ($U/U_c = 0.66$, 0.82, and 0.98) to assess the sediment hazard around the hydraulic structures, viz., bridge pier. A single pier of diameter ($d = 8.8$ cm) was positioned on a sediment bed of 15 cm thick, having mean sediment size, $d_{50} = 0.75$ mm, standard deviation, $\sigma_g = 1.29$, specific gravity of 2.65 were used during the experimentation. The SeaTek 5 MHz Ultrasonic Ranging System (URS) has been used to measure the instantaneous bed levels at different grid points around the pier during the experiments. The scour hole structure was quantified during its evolution, i.e., at 25%, 50%, 75%, and 100% scour depth. The quantities of scour hole in terms of areal and volume studies, temporal variations at different time intervals, three-dimensional scour depths are computed from measured bed levels. From the analysis, the scour depths are observed 20% more at vicinity of bridge pier at $U/U_c = 0.98$, vis-à-vis $U/U_c = 0.66$. The present study suggested that the volume and areal extent of local scour, though challenging, is also essential along with scour depth computations to assess sediment hazards around the bridge piers.

Keywords Sediment hazard · Risk assessment · Local scour · Volume studies · Ultrasonic ranging system

L. N. Pasupuleti (✉)
Department of Civil Engineering, Aditya Engineering College, Surampalem, India

P. V. Timbadiya · P. L. Patel
Department of Civil Engineering, Sardar Vallabhbhai National Institute of Technology, Surat, India
e-mail: pvtimbadiya@ced.svnit.ac.in; plpatel@ced.svnit.ac.in

M. Pandey et al. (eds.), *River Dynamics and Flood Hazards*, Disaster Resilience and Green Growth, https://doi.org/10.1007/978-981-19-7100-6_15

15.1 Introduction

The current study presents an assessment of sediment hazards by studying the local scour around the hydraulic structure. The rapid urbanization increased the construction of additional bridges either of sides with reference to existing bridge. Hence, the safety of such bridge piers is essential for smooth operative of traffic. Local scour around the hydraulic structure is one of the prime responsible for the sediment hazards (Kothyari et al. 1992; Aamir et al. 2022). Due to severe periodic sedimentation and flooding hazards the progression of alluvial fans may be at risk (Jain et al. 2021; Chaudhuri et al. 2022). Since, in 1983, extensive flooding and mudflows caused an estimated $250 million in damages to Davis County communities located on numerous alluvial fans along the base of the Wasatch Mountains in Utah (MacArthur 1988). Clear water flood condition and steady-state condition were used to delineate potential flood hazard zones. However, these studies did not account for the severe sedimentation processes associated with the events. The City of Rancho Mirage, located in Coachella Valley, California, experienced similar sedimentation hazards, and debris-flow flood events on the Magnesia Spring Creek alluvial fan in 1976 and 1979. The occurrences of these destructive, high-velocity sedimentation-associated flood events led to the design and construction of a flood-control project and debris-control facilities subject to such episodic, high-energy flood hazards (Garcìa et al. 2008; Shankar et al. 2021).

The fluvial hydraulics states that the combination of the primary vortex and secondary vortex created the three-dimensional flow structure at the foot of the pier, leading to erosion at upstream and transporting the sediments to downstream, resulting in the formation of scour hole (Graf and Yulistiyanto 1998; Euler and Herget 2012; Dey and Raikar 2007; Pasupuleti et al. 2021a, b; Singh et al. 2022; Wallwork et al. 2022). Several experimentations on local scour were conducted extensively around single bridge pier (Breusers et al. 1977; Baker 1980; Raudkivi and Ettema 1983; Dargahi 1989; Dey et al. 1995; Chiew and Melville 1987; Melville and Chiew 1999; Graf and Istiarto 2002; Pandey et al. 2020; Yang et al. 2020). Among the studies, Yang et al. (2020) identified four stages for the development of scour around the piers, i.e., initiation, stagnation, developing, and equilibrium stages in which the scour process is very rapid in the initiation stage whereas the scouring process is significantly reduced in the stagnation stage. In the developing stage, the scour process is accelerated once again and lasts for a long time. The rate of scour depth is negligible in the equilibrium stage, i.e. the maximum scour depth is reached. Sarkar et al. (2015) investigated the temporal variations of bed forms around isolated submerged piers of four different shapes (circle, square, triangle, and elliptical). The study found that scour depth was maximum in circular pier while elliptical shape had shown the minimum scour depth. Vijayasree et al. (2017) experimentally investigated influence of pier shape (including, rectangular, trapezoidal, triangular, oblong, and lenticular shapes) on flow field and scour geometry on the sediment bed. The study found maximum scour depth occurred at rectangular and minimum scour depth occurred at lenticular shape. Few studies (Kothyari et al. 1992; Baker 1980;

Chiew and Melville 1989; Sheppard et al. 2014; Pournazeri et al. 2014; Pandey et al. 2017; Gazi and Afzal 2020) developed mathematical models to predict the scour depth around the single circular pier. Through experiments, the researchers (Zarrati et al. 2006; Selamoglu et al. 2014; Wang et al. 2016; Khaple et al. 2017; Keshavarzi et al. 2018; Memar et al. 2020; Chavan et al. 2020) focused on scour depth around tandem piers. In recent studies, Chavan et al. (2020) investigated the effect of seepage, i.e., no seepages, 10% seepage, and 15% seepage, on scour depth by placing piers of two different diameters, one at upstream and other at downstream. The study found minimum scour depth at upstream piers under 15% seepage. On other hand, maximum scour was found under no seepage condition.

The quantities of scour holes in terms of areal and volume studies, temporal variations at different time intervals, three-dimensional scour depths from instantaneous bed levels are scarce in the literature. Due to marginal availability on sediment hazard assessment, the present study focused on quantification of scour hole around pier at different flow intensities, the three-dimensional behavior of scour hole during its evolution, volume, and areal extents during the evolution of scour hole, i.e., scour hole at 25%, 50%, 75%, and 100% of equilibrium scour depth around the pier under varied flow conditions.

15.2 Experimentation

A series of experiments were performed in a re-circulating sediment transport flume which situated in the Advanced Hydraulics laboratory at the Sardar Vallabhbhai National Institute of Technology, Surat, Gujarat, and India. The channel having dimensions, 15 m long, 0.89 m wide, and 0.6 m deep, see Fig. 15.1 (Pasupuleti et al. 2020). At 5.0 m downstream from inlet, a 6.0 m long working section was located with sides having perspex glass to have clear view of the flow. A couple of honeycomb cages were positioned with 0.5 m gap at the inlet to allow smooth flows over the working section. A tail gate was placed at the end of the channel to maintain the uniform flow over the working section. A digital flow meter was fixed at the inlet pipe to measure the discharges released from the overhead tank through supervisory control data acquisition (SCADA) system.

The alluvial channel consists of a 15 cm thick sediment bed with the median size $d_{50} = 0.75$ mm, geometric standard deviation σ_g $(d_{84}/d_{16})^{0.5} = 1.29$, and angle of repose, $\phi = 31.5°$, in the entire working section of 6.0 m long and 0.89 width. The cylindrical pier having diameter ($d = 8.8$ cm) was placed 8.0 m downstream from inlet, to ensure fully developed flow (Pasupuleti et al. 2020). Total three experiments were carried around the pier, see Table 15.1. The flow intensity, $U/U_c = 0.64$–0.98, was gradually maintain to avoid sudden deformations around the piers. The Reynolds number ($R_e = UZ_0/\nu$) of the approaching flow are tabulated in Table 15.1. The instantaneous bed levels were recorded around the single by ultrasonic ranging system (URS) composed of 32 transducers (Tr.) developed by the SeaTek. The

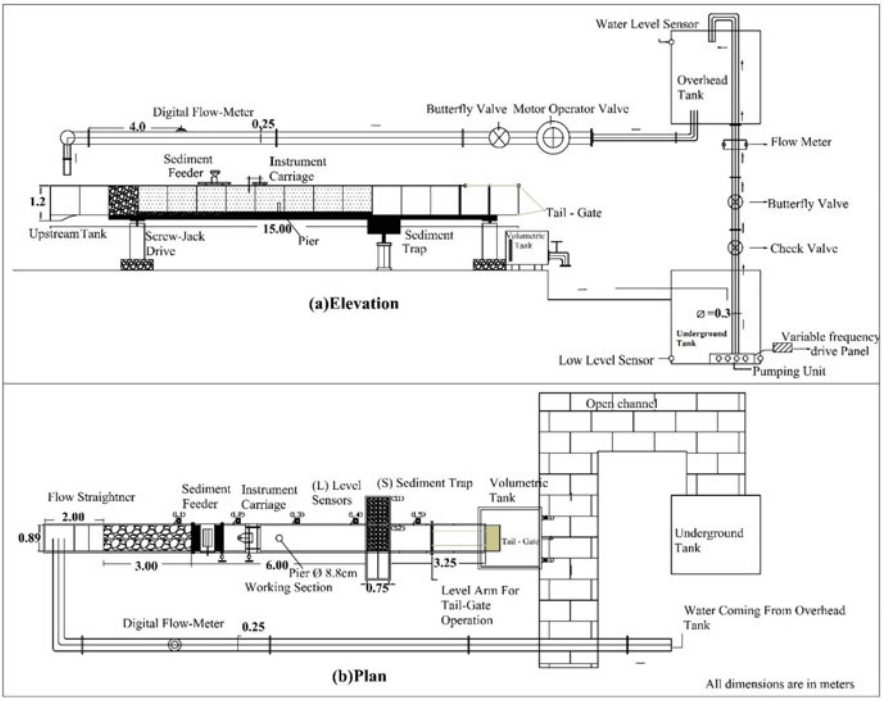

Fig. 15.1 Schematic of the experimental set-up

Table 15.1 Flow conditions used in the current study

Run	Discharge (m^3/s)	Flow depth (m)	Diameter of pier (m)	Approaching mean flow velocity (U) (m/s)	Flow intensity (U/U_c)	Pier Reynolds number (R_e)
1	0.020	0.105	0.088	0.214	0.66	2.2×10^4
2	0.025	0.105	0.088	0.267	0.82	2.8×10^4
3	0.030	0.105	0.088	0.320	0.98	3.36×10^4

plan of transducers locations for data collection over both the pier arrangements along with flow directions are shown in Fig. 15.2.

15.3 Results and Discussion

Areal and volume extents of scour hole, the temporal variation of scour depth during its evolution, scale measurements, and three-dimensional scour structures during the 25% to 100% of scour hole formations are described in the following paragraphs:

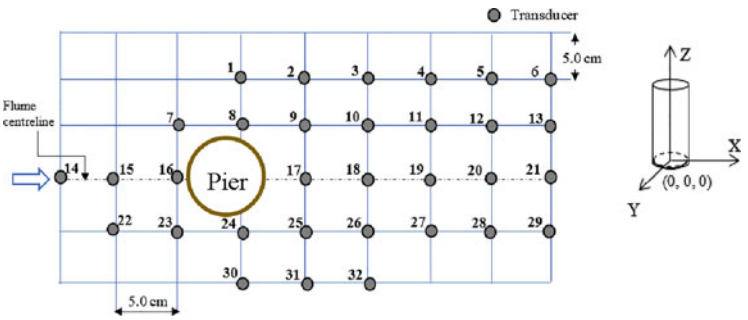

Fig. 15.2 Placement of URS transducers in plan around pier

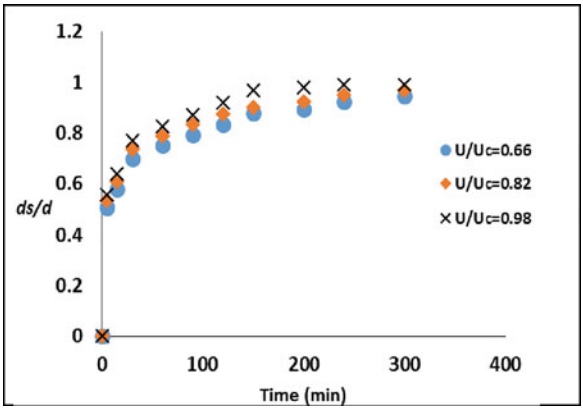

Fig. 15.3 Equilibrium scour depth around the pier at different flow intensity

15.3.1 Areal and Volumes of Scour Hole

The bed elevations were continuously recorded over the period of 300 min around the pier using URS transducers at different grids (see Fig. 15.2). Thereafter, the scour depths are recorded as ±1 mm. The dimensionless equilibrium scour depth (d_s/d) is shown in Fig. 15.3 for all the three flow intensities. Here, d_s is the scour depth at time t and d is the pier diameter. From Fig. 15.3, at higher flow intensity, $U/U_c = 0.98$, the scour depths reach stable condition compared to $U/U_c = 0.66$. The threshold condition prevails more accurate at higher flow intensity. The scale measurements were collected on stabled bed condition after end of each run, it is observed that the radius of scour hole for $U/U_c = 0.66$ is 18 cm, while, for $U/U_c = 0.82$ and 0.98 are 20 and 22, respectively, i.e., with increase in flow discharge of 5 L/s, the radius of scour hole was increased by 11% (Table 15.2). Furthermore, the volume of sediments eroded from the scour hole and deposited in the downstream of pier were computed using ArcMap 10 based on the procedure adopted in the previous studies (Pasupuleti et al. 2020). It can be seen that, at equilibrium state, i.e., evolution of scour hole at 100%, the volume of sediment eroded and volume of sediment

Table 15.2 Areal measurements of scour holes around the piers

Scour radii (distance from pier center) (cm)						
	Longitudinal direction			Transverse direction		
Flow intensity (U/U_c)	0.66	0.82	0.98	0.66	0.82	0.98
Radial distance	18	20	22	18	20	22
Affected deformed zone (cm)						
Flow intensity (U/U_c)	0.66		0.82		0.98	
Flow direction	40		50		75	

Table 15.3 Total quantities of scour hole

Flow intensity (U/U_c)	Pier diameter (cm)	Scour hole (%)	Single pier	Single pier	
			Dimensionless scour depth (d_s/d)	Volume eroded (cm^3)	Volume deposited (cm^3)
0.66	8.8	25	0.30	210	100
0.66	8.8	50	0.45	375	160
0.66	8.8	75	0.72	522	280
0.66	8.8	100	0.94	756	350
0.82	8.8	25	0.38	230	110
0.82	8.8	50	0.48	410	178
0.82	8.8	75	0.75	578	305
0.82	8.8	100	0.97	822	398
0.98	8.8	25	0.40	260	130
0.98	8.8	50	0.50	450	195
0.98	8.8	75	0.80	650	350
0.98	8.8	100	0.99	900	450

deposited are significantly increased vis-à-vis scour hole at 25%. It is observed that both the volumes are increased by 3.5 times at equilibrium condition for all the three flow intensities (see Table 15.3).

15.3.2 Temporal Variations in Bed Levels

Temporal variations of bed elevations around the pier during the evolution of scour hole are shown in Figs. 15.4, 15.5, and 15.6. Here, Fig. 15.4a–d represents the space-time dynamics of bed at 25%, 50%, 75%, and 100%, respectively, for flow intensity, U/U_c= 0.66. Similarly, Figs. 15.5a–d and 15.6a–d are for U/U_c = 0.82 and 0.98, respectively. From Figs. 15.4, 15.5, and 15.6, it can be observed that 20% more elevations were observed for U/U_c = 0.98 in comparison to U/U_c = 0.66 under the identical conditions. Furthermore, maximum depositions are occurred in U/U_c = 0.98 vis-à-vis U/U_c = 0.66.

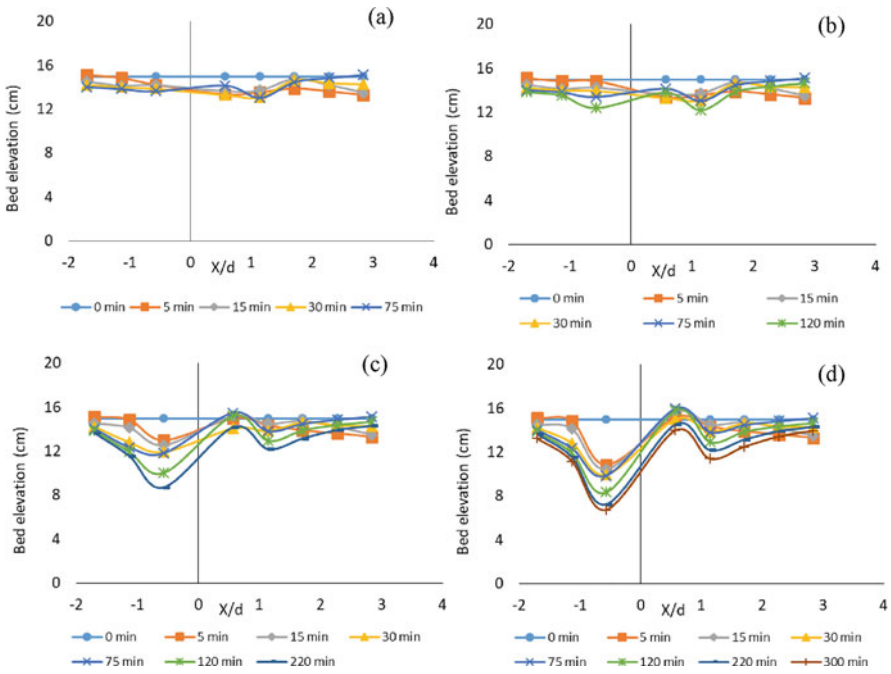

Fig. 15.4 Temporal variations at some time intervals around the pier at $U/U_c = 0.66$ during formation of scour hole at (**a**) 25% (75 min), (**b**) 50% (150 min), (**c**) 75% (220 min), and (**d**) 100% (300 min)

To escalate scour around the pier, three-dimensional surface contours are derived from bed elevation data with the help of Surf packages available in MATLAB 2014 (Sarkar et al. 2016). The Surf creates a three-dimensional surface for a given spatial coordinates (X and Y) and elevation data (Z) (Pasupuleti et al. 2021a, b). The current study collected the bed elevations at a grid size of 5 × 5 cm. To create the finer mesh, the elevations were cubically interpolated. In the Surf plots, the values in matrix Z as heights above a bed in the x–y plane defined by X and Y are shown in Figs. 15.7 and 15.8. Here, Fig. 15.7a–d represents 3D surface contour of bed at 25%, 50%, 75%, and 100%, respectively, for flow intensity, $U/U_c = 0.66$. Similarly, Fig. 15.8a–d for $U/U_c = 0.98$. From Figs. 15.7 and 15.8, it can be observed that the scour depths are seen 20% more at $U/U_c = 0.98$ as compared to $U/U_c = 0.66$.

15.4 Conclusions

Space-time dynamics during the evolution of scour hole around the pier are studied in the current study. The experiments were carried under clear water condition at different flow intensities, viz., $U/U_c = 0.66$, 0.82, and 0.98 using the ultrasonic

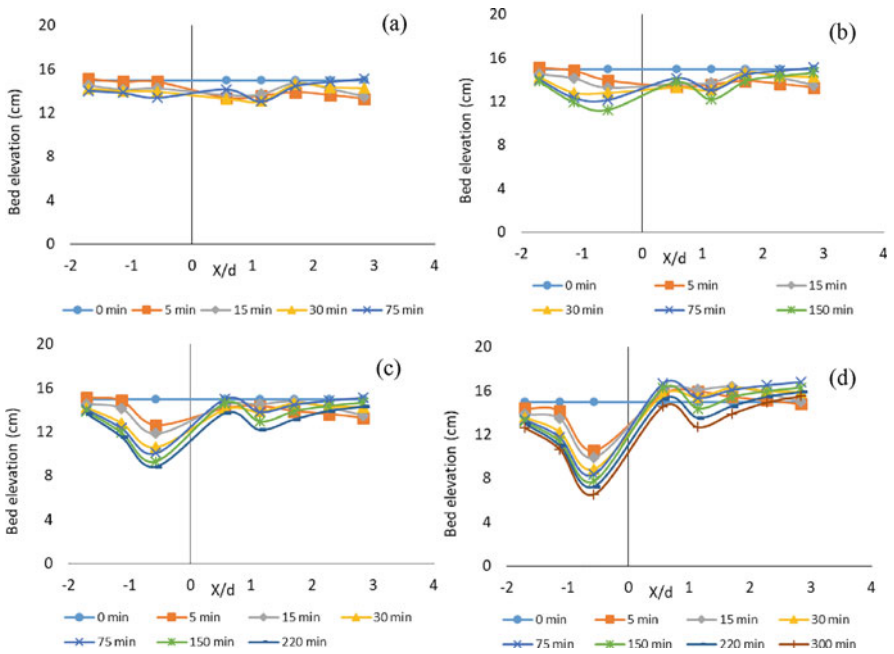

Fig. 15.5 Temporal variations at some time intervals around the pier at $U/U_c = 0.82$ during formation of scour hole at (**a**) 25% (75 min), (**b**) 50% (150 min), (**c**) 75% (220 min), and (**d**) 100% (300 min)

ranging system having 32 transducers. The measured instantaneous bed elevations are used to compute areal and volume extents of scour hole during evolution of scour hole, temporal variations at some time intervals around the said pier and, the three-dimensional surface contours are presented. From the ongoing study, the following key conclusions are drawn.

1. Areal and volume quantities of scour hole were observed 3.5 times more for flow intensity, $U/U_c = 0.98$ vis-à-vis $U/U_c = 0.66$.
2. Maximum erosions and maximum depositions are seen at $U/U_c = 0.98$ in comparison with $U/U_c = 0.66$. Furthermore, temporal variations of bed elevations are increased by 20% for higher flow intensity in comparison to lower one, under the identical conditions.
3. The evolution of bed topography around the pier are studied using the 3D surface contours developed with surf packages available in MATLAB R2014b. The scour depths are seen 20% more at $U/U_c = 0.98$ vis-à-vis $U/U_c = 0.66$.
4. The assessment of sediment hazard around the bridge pier was observed by studying local scour around there, it is observed that 20% more at vicinity of bridge pier at $U/U_c = 0.98$, vis-à-vis $U/U_c = 0.66$. The present study suggested that the volume and areal extent of local scour, though challenging, is also essential along with scour depth computations.

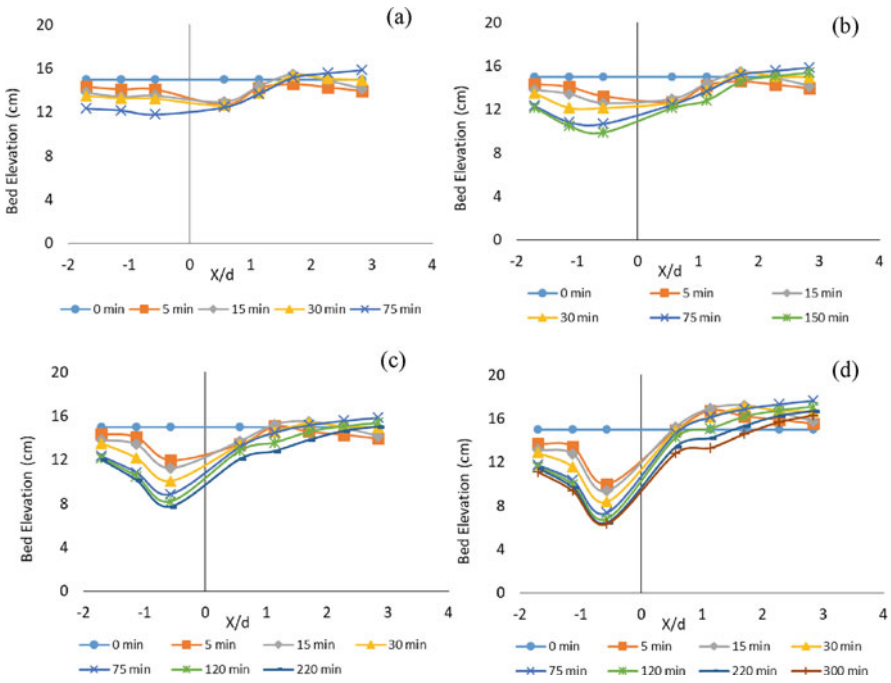

Fig. 15.6 Temporal variations at some time intervals around the pier at $U/U_c = 0.98$ during formation of scour hole at (**a**) 25% (75 min), (**b**) 50% (150 min), (**c**) 75% (220 min), and (**d**) 100% (300 min)

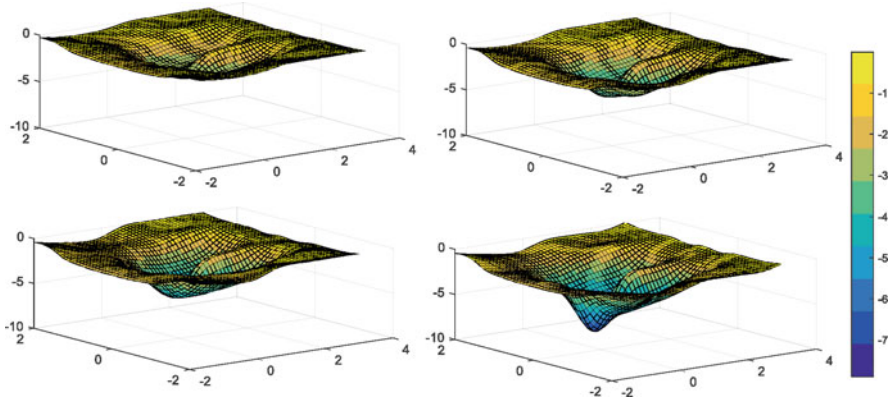

Fig. 15.7 Three-dimensional surface contours pier for $U/U_c = 0.66$ during formation of scour hole at (**a**) 25% (75 min), (**b**) 50% (150 min), (**c**) 75% (220 min), and (**d**) 100% (300 min)

The current study may be used to assess the risk on sediment hazard around hydraulic structure and will be used to predict the periodic sedimentation and flooding hazards on progression of alluvial fans. The current study associated to

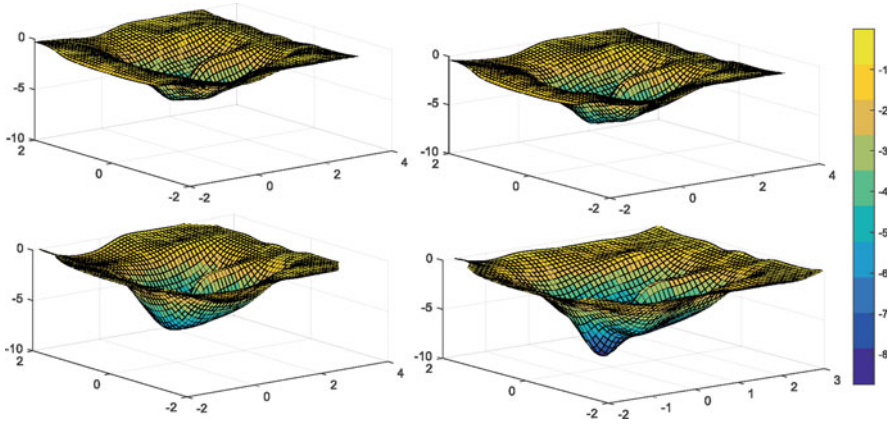

Fig. 15.8 Three-dimensional surface contours pier for $U/U_c = 0.98$ during formation of scour hole at (**a**) 25% (75 min), (**b**) 50% (150 min), (**c**) 75% (220 min), and (**d**) 100% (300 min)

temporal variations of bed level variations around the bridge pier for uniform and clear water conditions in the channel. The following are key limitations of the current study.

1. The flow depth, discharge, diameter of pier were kept constant in current study. More experimental runs by varying these variables can be useful to risk assessment around sediment hazardous around hydraulic structures.
2. The current study is based on clear water condition in the flume. Similar investigation can be performed with live bed conditions in the channel which is close to actual field condition in alluvial rivers.

Acknowledgments Authors are thankful to the Centre of Excellence (CoE) on "Water Resources and Flood Management" at Sardar Vallabhbhai National Institute of Technology (SVNIT)-Surat, Gujarat, India funded by TEQIP-II, Ministry of Education (MoE), Government of India. The experimental facility utilized in the current work was developed through the Department of Science and Technology (DST), Government of India funded research project on "Erosion of non-uniform unimodal and bimodal sediments" which authors duly acknowledged.

References

Aamir M, Ahmad Z, Pandey M, Khan MA, Aldrees A, Mohamed A (2022) The effect of rough rigid apron on scour downstream of sluice gates. Watermark 14(14):2223. https://doi.org/10.3390/w14142223

Baker CJ (1980) The turbulent horseshoe vortex. J Wind Eng Ind Aerodyn 6(1-2):9–23

Breusers HNC, Nicollet G, Shen HW (1977) Local scour around cylindrical piers. J Hydraul Res 15(3):211–252

Chaudhuri S, Pandey M, Debnath K, Oliveto G (2022) A comparative study on equilibrium scour volume around circular cylinders in clay-sand mixed cohesive beds, at near threshold velocity of sand–an experimental approach. Water Supply. https://doi.org/10.2166/ws.2022.250

Chavan R, Huai W, Kumar B (2020) Alluvial channel hydrodynamics around tandem piers with downward seepage. Front Struct Civ Eng 14(6):1445–1461
Chiew YM, Melville BW (1987) Local scour around bridge piers. J Hydraul Res 25(1):15–26
Chiew YM, Melville BW (1989) Local scour at bridge piers with non-uniform sediments. Proc Inst Civ Eng 87(2):215–224
Dargahi B (1989) The turbulent flow field around a circular cylinder. Exp Fluids 8:1–12
Dey S, Raikar RV (2007) Characteristics of horseshoe vortex in developing scour holes at piers. J Hydraul Eng 133(4):399–413
Dey S, Bose SK, Sastry GL (1995) Clear water scour at circular piers: a model. J Hydraul Eng 121(12):869–876
Euler T, Herget J (2012) Controls on local scour and deposition induced by obstacles in fluvial environments. Catena 91:35–46
Garcìa M, MacArthur R, French R, Miller J, Bradley J, Grindeland T, Hadley H (2008) Sedimentation hazards. In: Sedimentation engineering process measurements, modeling and practices. ASCE, Reston, pp 885–936
Gazi AH, Afzal MS (2020) A new mathematical model to calculate the equilibrium scour depth around a pier. Acta Geophys 68(1):181–187
Graf WH, Istiarto I (2002) Flow pattern in the scour hole around a cylinder. J Hydraul Res 40:13–20
Graf WH, Yulistiyanto B (1998) Experiments on flow around a cylinder: the velocity and vorticity fields. J Hydraul Res 36(4):637–653
Jain R, Lodhi AS, Oliveto G, Pandey M (2021) Influence of cohesion on scour at piers founded in clay–sand–gravel mixtures. J Irrig Drain Eng 147(10):04021046
Keshavarzi A, Shrestha CK, Melville B, Khabaz H, Ranjbar-Zahedani M, Ball J (2018) Estimation of maximum scour depths at upstream of front and rear piers for two in-line circular columns. Environ Fluid Mech 18:537–550
Khaple S, Hanmaiahgari PR, Gaudio R, Dey S (2017) Interference of an front pier on local scour at rear piers. Acta Geophys 65(1):29–46
Kothyari UC, Garde RCJ, Ranga Raju KG (1992) Temporal variation of scour around circular bridge piers. J Hydraul Eng 118(8):1091–1106
MacArthur RC (1988) Review of the US Army Corps of Engineers Involvement with Alluvial Fan Flooding Problems (No. 124), US Army Corps of Engineers
Melville BW, Chiew YM (1999) Time scale for local scour at bridge piers. J Hydraul Eng 125(1): 59–65
Memar S, Zounemat-Kermani M, Beheshti A, Rahimpour M, De Cesare G, Schleiss AJ (2020) The performance of collars on scour reduction at tandem piers aligned with different skew angles. Mar Georesour Geotechnol 38(8):911–922
Pandey M, Sharma PK, Ahmad Z, Singh UK (2017) Evaluation of existing equations for temporal scour depth around circular bridge piers. Environ Fluid Mech 17(5):981–995
Pandey M, Zakwan M, Khan MA, Bhave S (2020) Development of scour around a circular pier and its modelling using genetic algorithm. Water Supply 20(8):3358–3367
Pasupuleti LN, Timbadiya PV, Patel PL (2020) Bed level variations around the submerged tandem piers in sand beds. ISH J Hydraul Eng 28(1):149–157
Pasupuleti LN, Timbadiya PV, Patel PL (2021a) Vorticity fields around a pier on rigid and mobile bed channels. ISH J Hydraul Eng 2021:1–10
Pasupuleti LN, Timbadiya PV, Patel PL (2021b) Experimental investigation on evolution of scour hole around tandem piers in an alluvial channel. J Indian Natl Group Int Assoc Bridge Struct Eng 51(1):51–63
Pournazeri S, Li SS, Haghighat F (2014) A bridge pier scour model with non-uniform sediments. Water Manage 167(9):499–511
Raudkivi AJ, Ettema R (1983) Clear-water scour at cylindrical piers. J Hydraul Eng 109(3): 338–350
Sarkar K, Chakraborty C, Mazumder BS (2015) Space-time dynamics of bed forms due to turbulence around submerged bridge piers. Stoch Env Res Risk A 29(3):995–1017

Sarkar K, Chakraborty C, Mazumder BS (2016) Variations of bed elevations due to turbulence around submerged cylinder in sand beds. Environ Fluid Mech 16(3):659–693

Selamoglu M, Yanmaz AM, Koken M (2014) Temporal variation of scouring topography around dual bridge piers. In: Proceedings of the seventh International Conference on scour and Erosion, Perth, Western Australia, pp 495–500

Shankar MS, Pandey M, Shukla AK (2021) Analysis of existing equations for calculating the settling velocity. Watermark 13(14):1987

Sheppard DM, Melville BW, Demir H (2014) Evaluation of existing equations for local scour at bridge piers. J Hydraul Eng 140(1):14–23

Singh UK, Jamei M, Karbasi M, Malik A, Pandey M (2022) Application of a modern multi-level ensemble approach for the estimation of critical shear stress in cohesive sediment mixture. J Hydrol 607:127549

Vijayasree BA, Eldho TI, Mazumder BS, Ahmad N (2017) Influence of bridge pier shape on flow field and scour geometry. Int J River Basin Manage 17(1):109–129

Wallwork JT, Pu JH, Kundu S, Hanmaiahgari PR, Pandey M, Satyanaga A, Pandey M, Satyanaga A, Amir Khan M, Wood A (2022) Review of suspended sediment transport mathematical modelling studies. Fluids 7(1):23

Wang H, Tang H, Liu Q, Wang Y (2016) Local scouring around twin bridge piers in open-channel flows. J Hydraul Eng 142(9):06016008

Yang Y, Melville BW, Macky GH, Shamseldin AY (2020) Temporal evolution of clear-water local scour at aligned and skewed complex bridge piers. J Hydraul Eng 146(4):04020026

Zarrati AR, Nazariha M, Mashahir MB (2006) Reduction of local scour in the vicinity of bridge pier groups using collars and riprap. J Hydraul Eng 132(2):154–162

Chapter 16
Equation Development for Equilibrium Bed Load

Umesh K. Singh, Sanjeet Kumar, Z. Ahmad, Ankit Chakravarti, Swati Bhave, and Manish Pandey

Abstract Equilibrium condition is one of the important aspects in sediment transport hydraulics. The cohesive sediment mixture differently behaves in respect of cohesionless mixture in obtaining equilibrium condition of the stream in respect of sediment discharge. Present experimental study leads to the computation of cumulative bed load eroded from the channel bed till stable bed condition, i.e. equilibrium condition reached for the of clay-silt-sand mixture. The proportion of clay varied up to 50% on dry weight basis in the present study. The sediment transported from the channel bed due to excessive shear stress developed by the incoming clear water flow on the channel bed. Bed load collected using rectangular trap in the present study. It is found that clay content has reciprocal effect on the cumulative bed load as clay content increases then cumulative bed load increases. A formulation proposed to compute dimensionless cumulative bed load eroded from the channel bed till equilibrium condition reached for clay-silt-sand mixture. The correlation and regression analysis results found in-line with the proposed formulation.

Keywords Cohesive sediment · Cumulative bed load · Sediment load · Equilibrium condition · Hydraulics

U. K. Singh (✉) · S. Kumar
Department of Civil Engineering, Koneru Lakshmaiah Education Foundation, Guntur, Andhra Pradesh, India

Z. Ahmad
Department of Civil Engineering, Indian Institute of Technology Roorkee, Roorkee, Uttarakhand, India

A. Chakravarti
School of Civil and Environmental Engineering, Ambo University, Ambo, Ethiopia

S. Bhave
Department of Civil Engineering, Visvesvaraya NIT Nagpur, Nagpur, Maharashtra, India

M. Pandey
Department of Civil Engineering, National Institute of Technology Warangal, Warangal, Telangana, India

M. Pandey et al. (eds.), *River Dynamics and Flood Hazards*, Disaster Resilience and Green Growth, https://doi.org/10.1007/978-981-19-7100-6_16

16.1 Introduction

The transport and deposition of coarser bed load materials in the channel may reduce the expected design life of hydraulic structures. Deposition of sediment may block the navigation channel which may result in flooding. Degradation of channel may result in widening (sediment loss from banks of the channel) if less sediment available for degradation from channel bed which may ultimately leads to the river-bank collapse. Garde and Ranga Raju (2000) cited the failure of Islam weir on the Sutlej River due to degradation. Generally, most of the sediment is retained by the reservoir and degradation occurs due to enhancing transport capacity of clear water below the dam which may lead to failure of dam. Kothyari (1996) reported aggradation leads to reduction in clearance up to 12.2 m in 1941 for a bridge constructed in 1919 over a torrent crossing the Dehradun-Mussoorie road. Analyzing the problem of erosion and transport of sediment on laboratory scale may enhance the understanding of sediment transport problems which may contribute in the upgradation of existing knowledge on sediment transport. Mitchener and Torfs (1996) reported the presence of mud in the range of 3–15% leads to change in the erosion mode from cohesionless to cohesive behavior. Here in the present study the focus is given on the transport of cohesive sediment mixture. Equilibrium of the stream may define as "a stream in equilibrium is one whose channel dimensions and slope have been altered over time to carry incoming sediment load and water without causing significant erosion or deposition" (Mackin 1948). Garde and Ranga Raju (2000) defined equilibrium stream as "a specific length of an alluvial stream is considered to be in equilibrium if the amount of sediment arriving into this reach is equal to the amount of sediment leaving the same reach." A deviation from equilibrium conditions allows the alluvial river system for changing the channel geometry which may causes the lowering of channel bed, i.e. occurring of degradation and it may continue till the equilibrium condition of flow reached so that it restores the balance between inflowing and outflowing water and sediment discharges. Most of the studies conducted on transport rate of sediment from the reach in a channel. Empirical formulations have been derived for the computation of erosion rate of cohesionless as well as cohesive sediment by various researchers (Meyer-Peter and Müller 1948; Einstein 1950; Partheniades 1965; Ashida and Michiue 1972; Parker 1990; Mitchener and Torfs 1996; Jepsen et al. 1997; Sanford and Maa 2001; Aberle et al. 2004; Wong and Parker 2006; Jain and Kothyari 2009; Van Prooijen and Winterwerp 2010; Winterwerp et al. 2012; Xu et al. 2014; Singh and Ahmad 2019). Misri et al. (1984) given formulation for bed load transport rate based on experimental study. They used four coarse (gravel) uniform materials and nine different proportion of gravel-sand mixture as bed material. They maintained the equilibrium condition by collecting the sediment at downstream (d/s) end and feeding it back at the upstream (u/s) with a constant rate. Jain and Kothyari (2009) conducted the experiment on the transport of cohesive sediment mixture and proposed the transport rate for bed load with no sediment feeding in channel. When the incoming flow in the channel is clear water (i.e., no feeding of sediment in the

channel) then degradation occurs due to high shear stress developed on the channel bed and it continues till a stable bed condition reached (in case of sufficient bed depth) further which there is no transport of sediment due to development of an armor layer and this armor layer is representative of stable bed conditions (Julien 2002) and this stable condition is treated as equilibrium condition as there is no incoming sediment and no outgoing sediment. In the present study, the stable condition reached after sediment eroded from the channel bed and in this process the total bed load obtained called as cumulative bed load. The cumulative bed load determination for clay-silt-sand mixture has not been reported earlier as per the best of knowledge of authors. Hence, presents study leads to the formulation of the cumulative bed load eroded from the channel bed till the stable bed condition reached for clay-silt-sand mixture.

16.2 Visual Inspection

The experiment was carried out in the Hydraulic Engineering Laboratory, Civil Engineering Department, Indian Institute of Technology Roorkee, Roorkee, India, utilizing clay, silt, and sand sediments on a tilting flume with a length of 16 m, a width of 0.75 m, and a depth of 0.50 m (Singh and Ahmad 2019). The size distribution of sediment used in the present study shown in Fig. 16.1. Before saturating the prepared channel bed the flume was set at desired slope by electrical operating switch as the flume is tilting in nature. Channel bed was saturated before

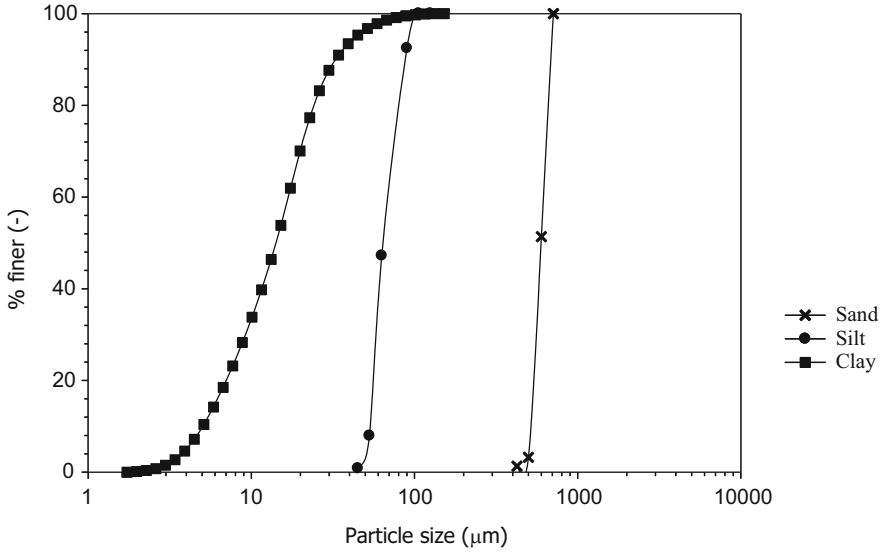

Fig. 16.1 Sediment size distribution for the present study

starting the experimental run. Experiments started with the low discharge in the flume so that no sediment detachment occurs then increment in the flow done slowly using valve inserted in the pipe and at the same time uniform flow maintained using tail gate located at the end of the flume. Finally, desired flow discharge obtained in the channel. After the tailgate, a volumetric tank was used to quantify the discharge. The shear stress accumulated at the bottom of the channel corresponding to incoming flow discharge is high enough to detach the sediments from the channel bed. The transported sediment as bed load from the test section of channel bed collected using the rectangular trap installed at the end of the flume just after the tail gate. Bed load collected at regular time interval. Initially, it was collected at an interval of around 15 min as the more transportation of sediment was observed which may be in response of higher erosion rate than later on the time interval was increased as the erosion rate comes down with the time passes. Measurements of bed surface profile, water surface profile, and suspended load was taken simultaneously with the bed load. Bed surface profile was measured using 2D bed profiler installed over the flume along with the water surface profile. The water and bed profiles measured at the center line of the flume in the direction of flow spatially at an interval of 50 cm. It was observed that collected bed load decreases with the time passes and the run was continued till the low amount of bed load collected for a long duration and simultaneously bed surface profile and water surface profile comes into nearly stable state. This condition is here treated as equilibrium condition as there is no feeding of sediment in the channel and test section also tends to in stable condition with nearly no outflow of sediment. The similar run was conducted for each sediment mixture in which clay percentage varied up to 50%. In interval of 10% clay content, the run was conducted corresponding to two discharges and two channel bed slopes for each clay percentage, i.e. four runs were conducted for each clay percentage. It was observed that the duration of total time for conducting each run (termed as equilibrium time) varied with the clay content present in the mixture.

The top surface of channel bed is visualized after the equilibrium condition reached. In clay-silt-sand mixture, a thin layer of sand particles observed on the top surface of the test section. This seems because of the stronger bond between the clay and sand particles. The size of silt particles may not large enough to resist the flow and hence, the appearance of the top bed layer seems to have clay-sandy bed. The appearance of clayey bed was observed to be more prominent in case of 40–50% of clay content; however, the behavior of appearance of bed on test section seems to be changing at 30% of clay content more degradation appeared towards the u/s test section compared to d/s test section while the mass erosion observed more prominent in the central part of the flume for the case of 40% to 50% clay content as shown in Fig. 16.2.

Fig. 16.2 Visual observations before and after experimental run

16.3 Results and Discussions

There are several parameters which affect the cumulative bed load collected (till the equilibrium condition reached) for the cohesive sediment mixture. Here, several parameters have been considered to formulate the expression to computation cumulative bed load till equilibrium condition of the flow reached, however, only the parameters which shows good results for the formulation were considered and represented in the analysis as follows:

$$M_{BL,e}^{c} = f(P_c, \tau, \tau_{cc}, q, \rho, \rho_s, d_a, b, l, g) \tag{16.1}$$

Here, $M_{BL,e}^{c}$ is the cumulative bed load (Kg) collected till the equilibrium condition reached; P_c is the fraction clay content; τ is the shear stress (N/m^2) developed on the test section of the channel bed due to the incoming flow; τ_{cc} is the critical shear stress (N/m^2) for cohesive mixture; q is the unit discharge (m^2/s), i.e. discharge per unit width of the channel; ρ_s and ρ are particle and fluid densities (kg/m^3) respectively; d_a is the arithmetic mean size (m) of the cohesive sediment mixture; b is the width (m) of the test section; l is the length (m) of the test section; and g is the gravitational acceleration (m/s^2).

Dimensionless representation of Eq. (16.1) using dimensional analysis:

$$M_{BL,e}^{c*} = f\left(P_c, \tau_e^*, h^*\right) \tag{16.2}$$

Here, $M_{BL,e}^{c*}$ is the dimensionless cumulative bed load till equilibrium condition of flow reached which can be computed as

$$M_{BL,e}^{c*} = \frac{\left(M_{BL,e}^{c} g/bl\right)}{\left(\rho_s - \rho\right) g d_a} \tag{16.3}$$

where τ_e^* is the dimensionless excess shear stress on the test section of channel bed and computed as

$$\tau_e^* = \frac{\tau - \tau_{cc}}{(\rho_s - \rho) g d_a} \tag{16.4}$$

where h^* is the dimensionless form of flow depth in terms of unit discharge and computed as

$$h^* = \frac{\left(q^2/g\right)^{1/3}}{d_a} \tag{16.5}$$

Here,

$$d_a = \frac{\sum (d_{50} P)}{P} \tag{16.6}$$

P is the percentage of the individual sediment in the sediment mixture.

Equation (16.2) represents the functional relationship for the dimensionless cumulative bed load, i.e., $M_{BL,e}^{c*}$ with the dimensionless parameterP_c, τ_e^*, and h^*. The change of clay percentage in the cohesive bed influences the bed load transport; hence, to account the influence of cohesion P_c has been considered in the present study.

Transport of sediment occurs when shear stress developed on the channel bed exceeds in fair amount from the critical shear stress, so the parameter τ_e^* has been taken into consideration to account for phenomena of sediment transport for the formulation development. Excess shear stress developed due to discharge is responsible for the sediment transport; however, it is found not enough to represent the phenomena and hence an additional parameter in terms of discharge included to support sediment transport phenomena. For this, the third parameter h^* has been considered in the formulation which represents the dimensionless depth of flow in terms of unit discharge, and it acts as a catalyst which enhances the accuracy in the computation towards the observed data.

Various parameters have been considered.

Based on the selected parameters, the relationship proposed to compute dimensionless cumulative bed load $M_{BL,e}^{c*}$ for the clay-silt-sand mixture:

$$M_{BL,e}^{c*} = 0.211(1 + P_c)^{-2.447} \left(\tau_e^*\right)^{0.327} (h^*)^{1.134} \tag{16.7}$$

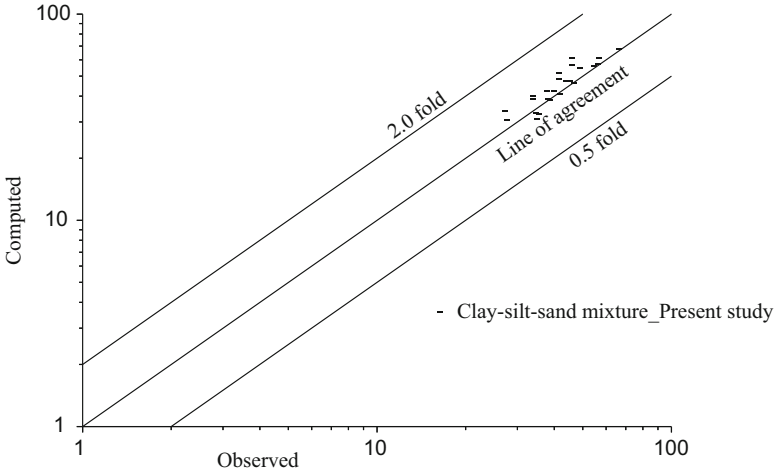

Fig. 16.3 Line of agreement between observed and computed $M_{BT,e}^{c*}$ using Eq. (16.7)

Equation (16.7) is proposed for the computation of $M_{BL,e}^{c*}$ for clay-silt-sand mixture. The computed value of $M_{BL,e}^{c*}$ were plotted against the observed ones for the computation of regression coefficient.

Only regression coefficient may not enough for knowing the how well computed values supported by observed ones, hence, test for goodness of fit analyzed between observed and computed value for the proposed equation in the present study which shows how much percentage of data lies between the error lines and around the line of agreement. The line of agreement plotted which tells about the deviation of data from the line of agreement. The mean discrepancy ratio, standard deviation, and percentage of data within the error line of 0.5-fold and 2.0-fold were computed for all the equations in the present study to test the goodness of fit as per Yang et al. (1996).

Discrepancy ratio, $R_i = \frac{\left(M_{BL,e}^{c*}\right)_{c,i}}{\left(M_{BL,e}^{c*}\right)_{o,i}}$

Here, $\left(M_{BL,e}^{c*}\right)_{c,i}$ represents the computed value and $\left(M_{BL,e}^{c*}\right)_{o,i}$ observed ones for $\left(M_{BL,e}^{c*}\right)$, respectively.

Mean discrepancy ratio, $\overline{R} = \frac{\sum_{i}^{N} R_i}{N}$

Here, N is the total number of observations.

Standard deviation, $\sigma_{oc} = \sqrt{\frac{\sum_{i}^{N} \left(R_i - \overline{R}\right)^2}{N-1}}$

Here, σ_{oc} is the standard deviation for the discrepancy ratio.

Figure 16.3 shows the plot of computed value of $M_{BL,e}^{c*}$ using proposed Eq. (16.7) against the observed ones for present study data.

Table 16.1 shows a good value of regression coefficient ($R^2 = 0.78$) for the cohesive sediment mixture of clay-silt-sand in which clay content varied from 10%

Table 16.1 Discrepancy ratio and regression coefficient for $M_{BL,e}^{c*}$

Equation	Data	Cohesive sediment mixture	Clay (%)	N	Discrepancy ratio					R^2
						% of data in range				
					$\overline{R}$	0.75–1.25	0.75–1.50	0.50–2.00	σ_{oc}	
Proposed Eq. (16.7)	Present study	Clay-silt-sand	10–50	20	1.119	80.00	100.00	100.00	0.121	0.78

to 50%. It also shows that 80%, 100%, and 100% data lies in the range for discrepancy ratio of 0.75–1.25, 0.75–1.50, and 0.50–2.0, respectively, for the clay-silt-sand mixture. The data also lies around the line of agreement as illustrated in Fig. 16.3. Hence, the proposed Eq. (16.7) well supports the observed values for $M^{c*}_{BL,e}$ for clay-silt-sand mixture in the present study.

16.4 Conclusions

The experimental study has been conducted to compute cumulative bed load that transported after the erosion from the channel bed. The cumulative bed load is the total bed load collected till the flow attained the equilibrium condition, i.e. no transport of sediment with the flow as there is no feeding of sediment in the u/s of the channel bed. The channel degradation occurs due to the excess shear stress developed on the test section of the channel bed by the incoming clear water flow. The visual observations indicates that the physical appearance changes with the change of clay percentage. More degradation observed towards the u/s of test section compared to d/s section for clay content up to 30% and dominancy of mass erosion found in the central part of test section along the flow for 40–50% of clay content. A formulation in the form of Eq. (16.7) proposed for the cumulative bed load against equilibrium condition for clay-silt-sand mixture in the present study. The goodness of fit test (Yang et al. 1996) as well as regression analysis analyzed which shows the computations for $M^{c*}_{BL,e}$ well supported by the observed data.

Notations

b is the width (m) of the test section

d_a is the arithmetic mean size (m) of the cohesive sediment mixture

g is the gravitational acceleration (m/s^2)

h^* is the dimensionless form of flow depth in terms of unit discharge (–)

l is the length (m) of the test section

$M^{c}_{BL,e}$ is the cumulative bed load (kg) collected till the equilibrium condition reached

$M^{c*}_{BL,e}$ is the dimensionless cumulative bed load till equilibrium condition of flow reached (–)

$\left(M^{c*}_{BL,e}\right)_{c,i}$ represents the computed value for dimensionless cumulative bed load (–)

$\left(M^{c*}_{BL,e}\right)_{o,i}$ observed value for dimensionless cumulative bed load (–)

N is the total number of observations (–)

P is the percentage of the individual sediment in the sediment mixture (%)

P_c is the fraction clay content (–)

q is the unit discharge (m^2/s), i.e., discharge per unit width of the channel

$\overline{R}$ is the discrepancy ratio (–)

τ is the shear stress (N/m^2)

τ_{cc} is the critical shear stress (N/m^2) for cohesive mixture
τ_e^* is the dimensionless excess shear stress on the test section of channel bed (–)
ρ_s is the particle densities (kg/m^3)
ρ_s is the fluid densities (kg/m^3)
σ_{oc} is the standard deviation for the discrepancy ratio (–)

References

Aberle J, Nikora V, Walters R (2004) Effects of bed material properties on cohesive sediment erosion. Mar Geol 207:83–93

Ashida K, Michiue M (1972) Study on hydraulic resistance and bedload transport raten alluvial streams. Trans Jpn Soc Civ Eng 206:59–69

Einstein HA (1950) The bed-load function for sediment transportation in open channel flows. Technical Bulletin 1026, U.S. Dept. of the Army, Soil Conservation Service

Garde RJ, Ranga Raju KG (2000) Mechanics of sediment transport and alluvial stream problems, 3rd edn. New Age International Publisher, New Delhi

Jain RK, Kothyari UC (2009) Cohesion influences on erosion and bed load transport. Water Resour Res 45:W06410

Jepsen R, Roberts J, Lick W (1997) Effects of sediment bulk density on sediment erosion rates. Water Air Soil Pollut 99:21–37

Julien PY (2002) River mechanics. Cambridge University Press, Cambridge

Kothyari UC (1996) Erosion and sedimentation problems in India. Erosion and sediment yield: global and regional perspectives. Proceedings of the Exeter Symposium. IAHS Publ. no. 236, pp 531–540

Mackin JH (1948) Concept of the graded river. Bull Geol Soc Am 59:463–512

Meyer-Peter E, Müller R (1948) Formulas for bed-load transport. In: Proceedings, 2nd congress. International Association of Hydraulic Research, Stockholm, pp 39–64

Misri RL, RangaRaju KG, Garde RJ (1984) Bed load transport of coarse nonuniform sediment. J Hydraul Eng 110(3):312–328

Mitchener H, Torfs H (1996) Erosion of mud-sand mixtures. J Coastal Eng 29:1–25

Parker G (1990) Surface based bed load transport relation for gravel rivers. J Hydraul Res 28(4): 417–436

Partheniades E (1965) Erosion and deposition of cohesive soils. J Hydraul Div Am Soc Civ Eng 91(1):105–139

Sanford L, Maa JP-Y (2001) A unified erosion formulation for fine sediments. Mar Geol 179:9–23

Singh UK, Ahmad Z (2019) Transport rate and bed profile computations for clay–silt–gravel mixture. Environ Earth Sci 78:432

Van Prooijen BC, Winterwerp JC (2010) A stochastic formulation for erosion of cohesive sediments. J Geophys Res 115:C01005

Winterwerp JC, Van Kesteren WGM, Van Prooijen B, Jacobs W (2012) A conceptual framework for shear flow–induced erosion of soft cohesive sediment beds. J Geophys Res 117:C10020

Wong M, Parker G (2006) Reanalysis and correction of bed-load relation of Meyer-Peter and Müller using their own database. J Hydraul Eng 132:1159–1168

Xu YF, Jiang H, Chu FF, Liu CX (2014) Fractal model for surface erosion of cohesive sediments. Fractals 22(3):1440006

Yang CT, Molinas A, Wu B (1996) Sediment transport in the Yellow River. J Hydraul Eng 122(5): 237–244

Part III
Hydrological Hazards and Ecological Restoration

Chapter 17
Flood Mitigation with River Restoration Using Porcupine Systems

Mohammad Aamir, Nayan Sharma, and Mohammad Amir Khan

Abstract Erosion of bed and banks of rivers is a problem of great concern in India and abroad. A meandering river generally erodes the outer bank and deposits the sediments on the inner bank. Protection of riverbank, also termed as river restoration, thus becomes a necessity in such reaches of a river where scouring of banks and bed material leads to change of course of the river, thereby causing loss not only to land and property, but also to flora and fauna of the region. Porcupine systems have been found to be successful in big Indian rivers such as Ganga, Brahmaputra and Kosi as a cost-effective measure for river restoration. In this chapter, sediment trap efficiency of porcupine systems has been studied with laboratory experiments. Sediment trap efficiency of porcupines is found to be higher for low submergence and high sediment concentration. A comparison has been made in between the conventional triangular/tetrahedral porcupines and a relatively new prismatic design. Various configurations of layout of porcupines have been investigated to gain an insight into the sediment deposition pattern for a particular discharge, water depth and sediment concentration of the river. Performance of prismatic porcupines is found to be almost similar to that of conventional porcupines, although they comprise nine members in contrast with the triangular porcupines, which consist of six members only. Trap efficiency of conventional porcupines in capturing sediment is found to be as much as 82%, whereas in case of prismatic porcupines, maximum trap efficiency is found to be 74.26%, other parameters being the same. Therefore, the use of prismatic porcupines is rather not advantageous for erosion control or reclamation. Also, they are economically more expensive since they require nine

M. Aamir (✉)
Department of Civil Engineering, Imam Mohammad Ibn Saud Islamic University, Riyadh, Saudi Arabia

N. Sharma
Center for Environmental Sciences and Engineering, Shiv Nadar University, Noida, India
e-mail: nayanfwt@iitr.ac.in

M. A. Khan
Department of Civil Engineering, Galgotias College of Engineering and Technology, Greater Noida, India

M. Pandey et al. (eds.), *River Dynamics and Flood Hazards*, Disaster Resilience and Green Growth, https://doi.org/10.1007/978-981-19-7100-6_17

members instead of six. However, they can prove to be safer and better at trimmed bank slopes of rivers.

Keywords Porcupine systems · River training · Environment · River restoration · Riverbank protection

17.1 Introduction

The major rivers with meandering nature have severe erosion tendency. In case timely action is not taken, it leads to a serious, non-repairable and uncontrollable situation, even leading to disruption of traffic. Continued erosion from the inner bank and simultaneous deposition on the outer bank is extremely hazardous for the river, since it may lead to the formation of oxbow lakes if meander cut-offs are not checked (John et al. 2021a, b; Pu et al. 2021; Khan et al. 2022; Wallwork et al. 2022). When river starts eroding fast, generally during monsoon, other problems start simultaneously, i.e. for protection work man and materials are not easily available, site becomes inaccessible and difficult for execution and time to act remains very short. The only solution is to take preventive steps in advance, by studying river pattern and initiating timely river training action. Training of rivers is required in those extents of the river where it confronts excessive erosion of banks or bed. Meandering, braiding, breaching of embankments, damages of hydraulic structures, roads and railways, etc. are some of the major consequences of an untrained river. Successful approaches for preventing scour are generally intended to reduce flow velocity through re-vegetation and, in some cases, through designed bank or channel works. River training structures are essential to steady the river channel along a definite alignment and with a particular cross section to train it for protection of its banks, in order to avoid excessive meandering, avert shifting of its course and retain navigability.

Protection of banks of the river is usually achieved by a range of river training works, including levees or marginal embankment, guide bunds, guide banks, spurs or groynes, cut-offs, submerged vanes, pitched islands, pitching of banks, closing dykes, sills and longitudinal dykes (Pandey et al. 2019; Aamir and Sharma 2015a, b; Chaudhuri et al. 2022). Some of these structures are less expensive than others. Besides effectiveness, other considerations in their use include cost of construction, environmental impact and aesthetics. Permeable river training structures are the least expensive to construct. The increasing demand of bank protection work in many reaches of rivers has engrossed attention on an essential requirement to develop and adopt cost-effective river training measures. Therefore, application of framed structures has gained importance as a cost-effective measure for river management. Board fencing, bandalling, tetrahedral frames and jack jetty systems are some of the cost-effective methods used for training of rivers (Rahman et al. 2003, 2011; Zhang et al. 2010; Nakagawa et al. 2011; Pandey et al. 2021). Porcupines have also been used in huge Indian rivers like Ganga and Brahmaputra, and have produced rather good results. Following frequent failure of earthen spurs both downstream and upstream

of the Farakka barrage on River Ganga, the Central Water Commission of India used RCC porcupines to prevent erosion of the left bank. It is testified that the porcupines were extremely efficient and facilitated the siltation of the bank. RCC porcupines were also installed at the Majuli Island in Assam, India and they were observed to be very effective in diminishing the scouring capacity of river Brahmaputra (Kharya and Kumar 2012). Aamir and Sharma (2015a, b, 2016) proposed a novel rational design methodology for the protection of riverbank with RCC porcupines.

The elementary principle of riverbank protection using porcupines is the impeding effect of its member bars (Yu et al. 2011), which induce obstruction to flow and hence cause reduction in flow velocity. Lu et al. (2011) studied the turbulence characteristics of the flow passing through a porcupine and inferred that it decreases the capacity of sediment entrainment of the flow by impeding the flow and diminishing the boundary shear stress. Furthermore, it also induces sediment accumulation in a sediment laden flow by altering the direction of flow and increasing the energy dissipation. Gao et al. (2009, 2011) performed investigation on 3D hydrodynamic numerical models of porcupines using CFD. In addition to offering protection to riverbank, porcupines can as well be used for safety of bridge piers against scouring and preventing root-stones loss (Shi et al. 2011)

Though there is some research done on Porcupines which brings forth their application as cost-effective river training structures, there is a lack of knowledge about the physics of flow around such structures, and also about their effectiveness in capturing sediment for river restoration. This study aims to address this issue with an experimental analysis.

17.2 Porcupine Systems

Figure 17.1 shows the three-dimensional sketch of triangular (or tetrahedral) and prismatic porcupines. A triangular porcupine unit consists of six members of RCC having equal lengths (2–3 m, depending upon the field requirements), joined together with nuts and bolts to form a tetrahedron. A prismatic porcupine unit, on the other hand, comprises nine RCC members, six of which have length equal to that of the triangular one, while other three members are 2–3 times longer than the triangular members. Prismatic porcupines are so placed in the field that the triangular faces are aligned along the direction of flow. Generally, RCC poles of cross section 15 × 15 cm are used as member bars (Kakran and Keshri 2012). Reinforcement is provided with four number of mild steel bars having a diameter of 6 mm, along with stirrups at a spacing of 15 cm centre to centre.

An arrangement of porcupines is placed both lengthwise and transverse to the flow to create a porcupine field, as shown in Fig. 17.2. Diversion line is formed by placing the porcupines along the flow, while transverse arrays of porcupines at regular intervals are known as Retards. In the figure, L_r denotes the length of one retard and L_s denotes the spacing between two retards. The idea of providing a

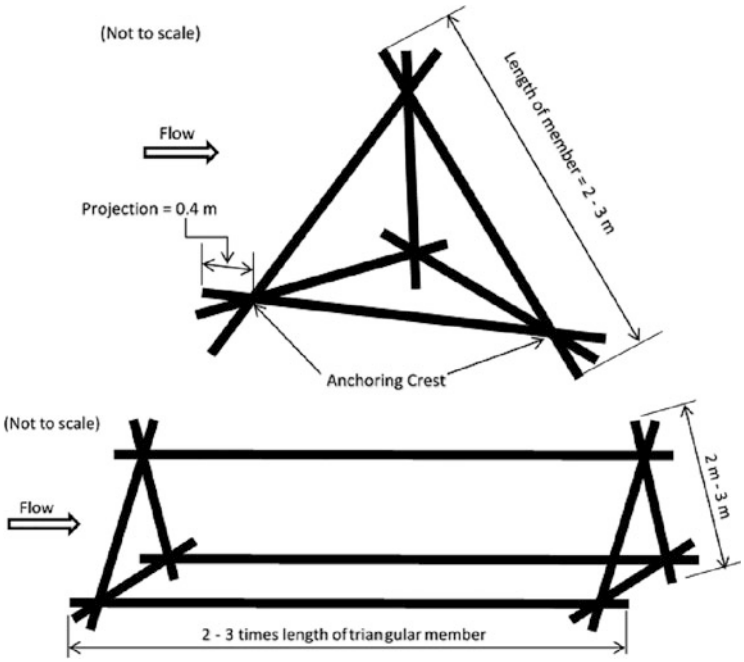

Fig. 17.1 Three-dimensional sketch of (**a**) triangular and (**b**) prismatic porcupine unit

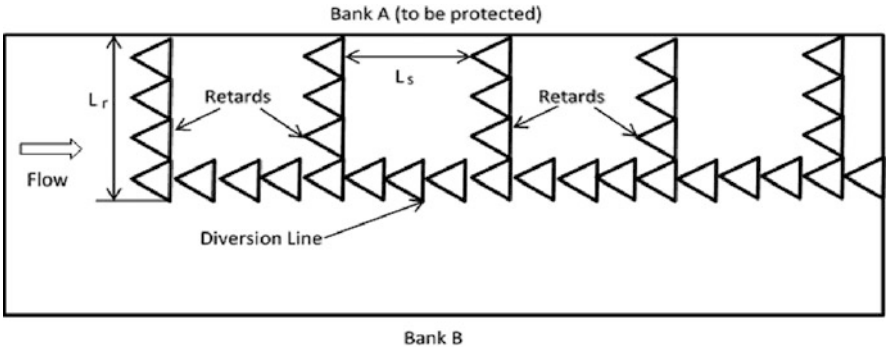

Fig. 17.2 Layout plan of a typical porcupine field

diversion line along with a number of retards has been taken from the design of jack jetty developed by Nayak (2012).

17.3 Experimental Procedure

The experiments were performed in the River Engineering Field Laboratory of the Department of Water Resources Development and Management, Indian Institute of Technology Roorkee. Recirculating experimental flume of 6 m length, 0.86 m width and 0.54 m depth was used, with a sediment recess of 0.15 m thickness. Figure 17.3 shows the experimental flume with both triangular and prismatic porcupine field after an experimental run. Porcupine models were fabricated using 4 mm diameter mild steel rods in the workshop. Six pieces of 0.10 m long rods were welded together to fabricate the triangular (also known as tetrahedral) shape, while additional three pieces of 0.30 m length were used to fabricate the prismatic variant. The effective height of both the models when placed in the flume was 0.09 m.

Controlled flow rate was allowed to pass into the flume from an overhead tank with an outlet valve. To measure the flow rate, a 90° V-notch was used which was installed at the outlet of the overhead tank. The flow rate passing over the V-notch was calculated using Eq. (17.1). The value of C_d for the V-notch was calibrated to be 0.622.

$$Q = \frac{8}{15} C_d \sqrt{2g} \tan \frac{\theta}{2} h^{5/2} \tag{17.1}$$

where Q = rate of discharge; C_d = coefficient of discharge; θ = V − notch angle; g = gravitational acceleration; and hh = head over V-notch. To allow steady flow to enter into the flume, flow over the V-notch was allowed to pass into another tank having perforated walls on the upstream of the flume. Tailwater level was maintained by a tail gate fixed at the downstream end of the flume.

Fig. 17.3 Experimental flume with triangular and prismatic porcupine fields

Experiments were carried out with different arrangements of length and number of retards. The effect of different arrangements of porcupines on the sediment laden flow was investigated. The optimal layout of the porcupine field was achieved to meet with the proposed objective of erosion control, moderate reclaim or high reclaim. Before the commencement of experiments, uniform flow condition in the flume was ensured with the help of boundary layer development. Incipient motion condition was maintained by keeping the average bed shear stress less than the critical shear stress, by fixing the Shields' parameter (Shields 1936) to 0.045 as per Yalin and Karahan (Yalin and Karahan 1979). This facilitated clear water condition in order to avoid movement of sediment. Average bed shear stress (τ_o) and critical shear stress (τ_c) were calculated by Eqs. (17.2) and (17.3), respectively,

$$\tau_o = \gamma_f RS \tag{17.2}$$

$$\tau_c = \tau_{ci} \times \left(\gamma_s - \gamma_f\right) d \tag{17.3}$$

where τ_{ci} = dimensionless critical shear stress, also known as the Shields' parameter (which is a function of corresponding shear Reynolds number $\mathrm{Re}^* = u^* d/\nu$ for a given sediment size, where u^* = shear velocity; ν = kinematic viscosity); γ_s = weight density of sediment; γ_f = weight density of water; R = hydraulic mean depth; S = slope of water surface; and d = median particle diameter of sediment. Incipient motion condition was achieved by maintaining the bed slope such that the average bed shear stress remains less than the critical shear stress (Aamir and Sharma 2014, 2015b).

Prior to placing porcupine field layout configuration, sediment bed of the flume was levelled properly using pointer gauge, maintaining the desired slope. Initially, a small discharge was introduced into the flume keeping the tail gate closed, so as not to disturb the sediment bed. Once the desired flow was achieved, the tailgate was opened slowly and uniform flow condition was maintained. The flow was continued for an hour. Water was then discharged gradually such that the sediment bed is not disturbed. Bed levels were recorded with a pointer gauge.

The experimental run was repeated with the same discharge. Desired concentration of sediment was injected into the flume at a section 0.5 m upstream of the porcupine field. Once the required amount of sediment is introduced into the flume, the experimental run is continued for another 2 h. Bed level measurement was then recorded again with a pointer gauge.

All the experiments were performed with sediment having median diameter of 0.23 mm and specific gravity of 2.65. Tables 17.1 and 17.2 show the range of parameters used in the experiments.

Table 17.1 Range of parameters for triangular porcupines

Experiment No.	Sediment concentration q_s (ppm)	L_r/L_s	Discharge (m^3/s)	Water depth (m)	Submergence ratio
1	500	1.0	0.030	0.24	0.625
2	500	1.5	0.030	0.24	0.625
3	500	2.0	0.030	0.24	0.625
4	500	1.0	0.025	0.20	0.550
5	500	1.5	0.025	0.20	0.550
6	500	2.0	0.025	0.20	0.550
7	500	1.0	0.017	0.15	0.400
8	500	1.5	0.017	0.15	0.400
9	500	2.0	0.017	0.15	0.400
10	750	1.0	0.017	0.15	0.400
11	750	1.5	0.017	0.15	0.400
12	750	2.0	0.017	0.15	0.400
13	1000	1.0	0.017	0.15	0.400
14	1000	1.5	0.017	0.15	0.400
15	1000	2.0	0.017	0.15	0.400

Table 17.2 Range of parameters for prismatic porcupines

Experiment No.	Sediment concentration q_s (ppm)	L_r/L_s	Discharge (m^3/s)	Water depth (m)	Submergence ratio
1	500	1.0	0.017	0.15	0.400
2	500	1.5	0.017	0.15	0.400
3	500	2.0	0.017	0.15	0.400
4	1000	1.0	0.017	0.15	0.400
5	1000	1.5	0.017	0.15	0.400
6	1000	2.0	0.017	0.15	0.400

17.4 Results and Discussion

Measurement of bed profile was taken after each experimental run in the form of grids of 10 × 10 cm with a pointer gauge. In order to quantify the change in the bed profile of the porcupine field, three indices, viz. PFDI (porcupine field density index), PFSI (porcupine field submergence index) and PFLF (porcupine field length factor) were developed for layout of porcupines (Fig. 17.4):

$$\text{PFDI} = L_r/L_s$$

$$\text{PFSI} = (H - h)/H$$

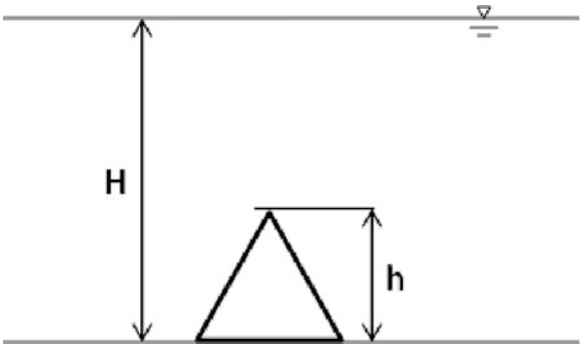

Fig. 17.4 Schematic of a submerged porcupine model

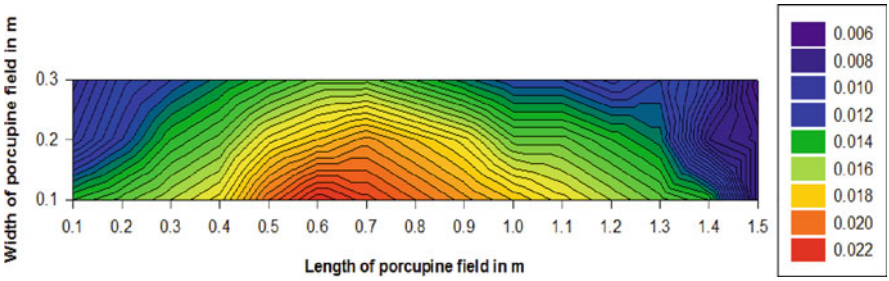

Fig. 17.5 Sediment deposition in triangular porcupine field for PFDI = 1.0, PFSI = 0.400 and q_s = 500 ppm

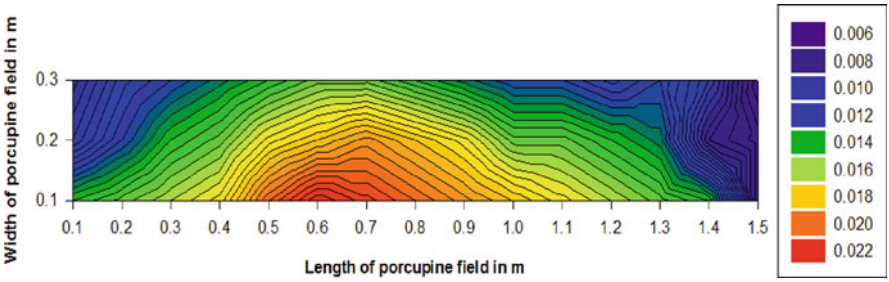

Fig. 17.6 Sediment deposition in prismatic porcupine field for PFDI = 1.0, PFSI = 0.400 and q_s = 500 ppm

PFLF
= Length of one compartment of porcupine field/Total length of the compartments.

Length of one compartment is taken as 0.1 m, staring from the first row of retards. Total length of the compartments is 1.5 m.

Figures 17.5 and 17.6 show contours for sediment deposition in triangular porcupine field with PFDI = 1.0, PFSI = 0.400 and q_s = 500 ppm, and prismatic porcupine field with PFDI = 1.0, PFSI = 0.400 and q_s = 500 ppm, respectively.

Length of the porcupine field is taken from the upstream end of flume and width is taken from the side wall of the flume. The colour legend shows sediment deposition in m. Significant amount of sediment deposition is clearly observed around both the porcupine fields. The deposition is more near the upstream end, which goes on decreasing towards the downstream. The reason for this may be because a large amount of sediment is captured by the first screen itself, and as there is lesser sediment available for the subsequent screens, hence the deposition also gets reduced. Furthermore, the maximum deposition is observed near the side wall of the flume, which decreases as we move further away from the wall.

17.4.1 Calculation of Trap Efficiency

Table 17.3 presents the calculation of trap efficiency for a particular set of experimental run with PFDI = 1.0, PFSI = 0.625 and q_s = 500 ppm. First column is the distance along the length of the channel; second to forth columns present the sand deposition height at each cross section along the three longitudinal sections. The sections 'A', 'B' and 'C' are the sections along the length of flume at 0.10 m, 0.20 m and 0.30 m, respectively from the wall. Fifth column calculates the radius of the sand deposition taking into consideration the angle of repose of soil as 32° for wet sand and the depth of deposition. Sixth column calculates the volume of sand deposited

Table 17.3 Estimation of sand deposition in the porcupine field

Distance along the length of flume (m)	Berm height with sediment laden water (cm)			Radius of cone	Total volume of sand (m3) ($\times 10^{-5}$)	Volume of sand taking porosity into consideration (m3) ($\times 10^{-6}$)	Weight of sand (kg)
	at C	at B	at A	at C			
(1)	(2)	(3)	(4)	(5)	(6)	(7)	(8)
0.1	0.8	1.0	1.3	0.0121	0.1	0.8	0.002
0.2	1.0	1.3	1.5	0.0151	0.2	1.6	0.004
0.3	1.3	1.5	1.6	0.0197	0.5	3.4	0.009
0.4	1.5	1.6	1.7	0.0227	0.8	5.3	0.014
0.5	1.7	2.1	2.3	0.0257	1.2	7.7	0.020
0.6	1.6	1.9	2.1	0.0242	1.0	6.4	0.017
0.7	1.5	1.8	2.0	0.0227	0.8	5.3	0.014
0.8	1.3	1.6	1.9	0.0197	0.5	3.4	0.009
0.9	1.3	1.5	1.7	0.0197	0.5	3.4	0.009
1.0	1.2	1.4	1.6	0.0182	0.4	2.7	0.007
1.1	1.1	1.2	1.4	0.0166	0.3	2.1	0.005
1.2	0.9	1.3	1.5	0.0136	0.2	1.1	0.003
1.3	1.1	1.3	1.4	0.0166	0.3	2.1	0.005
1.4	0.9	1.1	1.3	0.0136	0.2	1.1	0.003
1.5	0.7	1.1	1.2	0.0106	0.1	0.5	0.001
						Total weight=	0.124

Table 17.4 Trap efficiency calculation for triangular porcupines

L_r/L_s	Discharge (l/s)	Water depth (cm)	q_s (ppm)	Weight of sand deposited (kg)	Weight of sand injected (kg)	Trap efficiency (%)
(1)	(2)	(3)	(4)	(5)	(6)	(7)
1.0	30	24	500	0.637	5.0	12.74
1.5	30	24	500	0.986	5.0	19.72
2.0	30	24	500	1.763	5.0	35.26
1.0	25	20	500	0.804	5.0	16.08
1.5	25	20	500	1.115	5.0	22.30
2.0	25	20	500	2.869	5.0	57.38
1.0	17	15	500	0.704	5.0	14.08
1.5	17	15	500	1.336	5.0	26.72
2.0	17	15	500	3.473	5.0	69.46
1.0	17	15	750	1.859	5.0	37.18
1.5	17	15	750	2.123	5.0	42.46
2.0	17	15	750	3.602	5.0	72.04
1.0	17	15	1000	2.695	5.0	53.90
1.5	17	15	1000	3.713	5.0	74.26
2.0	17	15	1000	4.100	5.0	82.00

Table 17.5 Trap efficiency calculation for prismatic porcupines

L_r/L_s	Discharge (l/s)	Water depth (cm)	q_s (ppm)	Weight of sand deposited (kg)	Weight of sand injected (kg)	Trap efficiency (%)
(1)	(2)	(3)	(4)	(5)	(6)	(7)
1.0	17	15	500	0.649	5.0	12.98
1.5	17	15	500	1.218	5.0	24.36
2.0	17	15	500	3.138	5.0	62.76
1.0	17	15	1000	2.414	5.0	48.28
1.5	17	15	1000	2.884	5.0	57.68
2.0	17	15	1000	3.713	5.0	74.26

and seventh column is the volume of sand after consideration of porosity which is taken as 35% for lightly compacted sand. Eighth column presents the weight of sand deposited taking into account the unit weight of sand which is 2650 kg/m^3. Fifth to eighth columns show the calculation of sand deposited along the diversion line of the porcupine field at 0.30 m from flume side wall. Similar procedure has been adopted for the evaluation of sand deposition along the other two longitudinal sections inside the porcupine field.

Tables 17.4 and 17.5 are a compilation of mass balance for all the sets of experimental runs. These tables give an account of the trap efficiency of the porcupine field. First to fourth columns are the various combinations of parameters for the runs. Fifth column is weight of the sand deposited in the porcupine field and

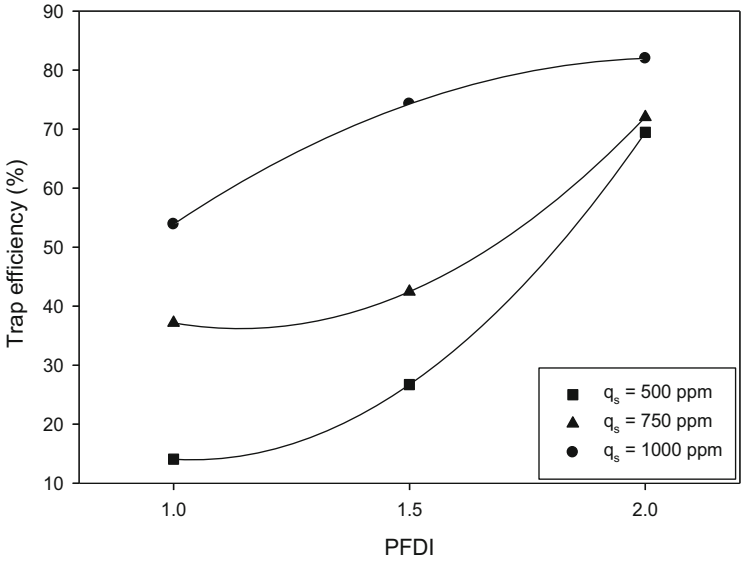

Fig. 17.7 Trap efficiency vs. PFDI for triangular porcupines

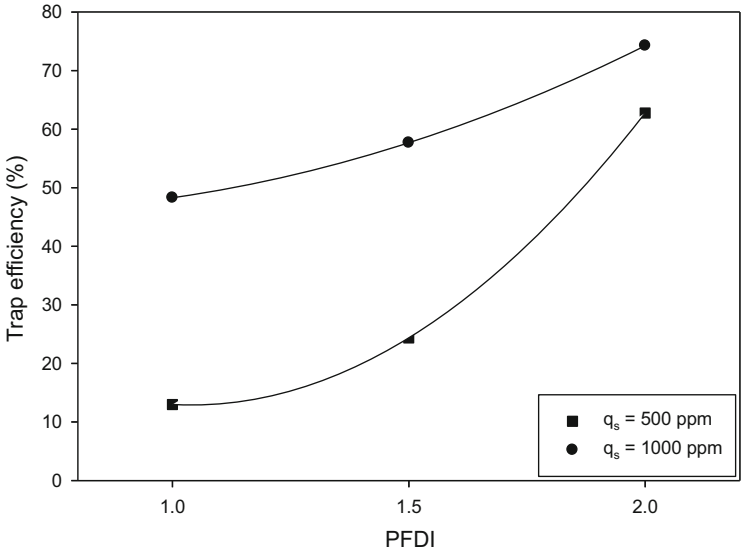

Fig. 17.8 Trap efficiency vs. PFDI for prismatic porcupines

sixth column is the quantity of sand injected in the flow. Seventh column calculates the trap efficiency of the porcupine field.

Figures 17.7, 17.8, and 17.9 show the plots of trap efficiency vs. PFDI. Figure 17.7 shows the variation of trap efficiency with PFDI for triangular porcupines

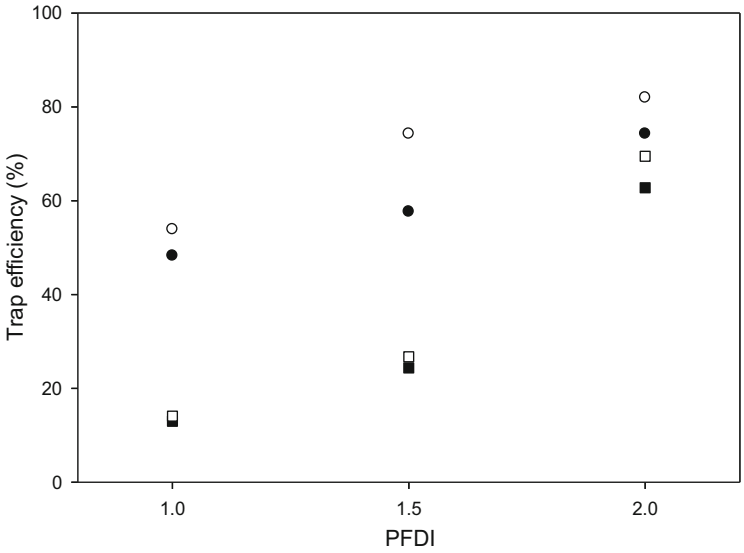

Fig. 17.9 Comparison of trap efficiency for triangular and prismatic porcupines

for different values of sediment concentration and fixed value of PFSI = 0.400. It is seen that there is more sediment deposition for higher sediment concentration and vice versa. This means that trap efficiency increases with increasing sediment concentration, i.e. trap efficiency is directly proportional to sediment concentration. The reason for this may be attributed to the availability of more sediment for the screens to capture.

Figure 17.8 shows the variation of trap efficiency with PFDI for prismatic porcupines for different values of sediment concentration and PFSI = 0.400. Similar trend is observed in this case also. However, a comparison of trap efficiency for triangular and prismatic porcupines shows that the performance of triangular porcupines in capturing sediment is better than the prismatic porcupines. This comparison is shown in Fig. 17.9. For the same value of sediment concentration, trap efficiency of triangular porcupines is more than that of prismatic porcupines.

17.5 Conclusions

The following conclusions are drawn from this study:

- The use of porcupine systems is an effective and economic method for river training purpose. It is effective because it causes substantial reduction in velocity of flow, which in turn reduces the intensity of flow and hence, facilitates deposition of sediments. Therefore, they can be installed in scour-prone areas of the

river, which would serve the purpose of not only checking the scour, but also causing deposition of sediments to a considerable amount.

- Sediment trap efficiency of porcupines has been found to be very good for low submergence and high sediment concentration. Moreover, the construction of these framed structures is very easy and simple and the materials required are concrete and steel rods, with a few numbers of nuts and bolts only. This makes them one of the most cost-effective structures, as compared to steel jack jetties. The method of installation needs no skilled labour as they can be installed by just placing them in position one after the other and connecting them together with wire rope.
- Densely configured porcupine field is able to entrain more sediment than a sparse field. Sediment entraining capacity also increases with an increase in sediment concentration of the flow.
- Performance of triangular porcupines in capturing sediment is better than the prismatic porcupines.
- Although, use of prismatic porcupines is economically not advantageous since they require nine members instead of six, but they can prove to be safer and better at trimmed bank slopes of rivers.

Hence, it is established that porcupine systems can be used for the purpose of river restoration, which in turn manages the natural flow of the river and deters any form of infiltration in the ecosystem, thereby saving the flora and fauna of the region. However, there is an imperative need in future to carry out exclusive investigation to gain an insight into the hydraulics of complex flow mechanism before and after the porcupine including dampening of turbulent fluctuation.

This study is limited to response of sediment laden flow on various combinations of porcupine fields in terms of number of retards and centre to centre spacing of retards. Diversion line in a braided stream will entail very elaborate experimentation and field study by varying the angle of approach and configuration of alternate diversion lines which needs further research. Furthermore, the present study has been done with clear water condition which can be extended with mobile bed condition.

References

Aamir M, Sharma N (2014) Sediment trap efficiency of Porcupine systems for riverbank protection. HYDRO 2014 International, 19th International Conference on Hydraulics, Water Resources, Coastal and Environmental Engineering, MANIT, Bhopal, India, December 18–20

Aamir M, Sharma N (2015a) Riverbank protection with porcupine systems: development of rational design methodology. ISH J Hydraul Eng 21(3):317–332

Aamir M, Sharma N (2015b) Efficiency of triangular and prismatic Porcupines in capturing sediment for river training. HYDRO 2015 International, 20th international conference on hydraulics, water resources and river engineering, IIT Roorkee, India, December 17–19

Aamir M, Sharma N (2016) Reply to the 'Discussion by SK Mazumder on "Riverbank protection with Porcupine systems: development of rational design methodology" by M. Aamir and N. Sharma (2015)'. ISH J Hydraul Eng 22(3):272–273

Chaudhuri S, Pandey M, Debnath K, Oliveto G (2022) A comparative study on equilibrium scour volume around circular cylinders in clay-sand mixed cohesive beds, at near threshold velocity of sand–an experimental approach. Water Supply. https://doi.org/10.2166/ws.2022.250

Gao Z, Li X, Tang HW, Gu ZH (2009) Three-dimensional hydrodynamic model of concrete tetrahedral frame revetments. J Mar Sci Appl 8(4):338–342

Gao Z, Huichao D, Tang H, Hong C, Gu Z (2011) A drag estimation method of single tetrahedral frame in multi-direction flow. In: 2011 international symposium on water resource and environmental protection, vol 1. IEEE, Piscataway, pp 654–657

John CK, Pu JH, Pandey M, Hanmaiahgari PR (2021a) Sediment deposition within rainwater: case study comparison of four different sites in Ikorodu, Nigeria. Fluids 6(3):124

John CK, Pu JH, Pandey M, Moruzzi R (2021b) Impacts of sedimentation on rainwater quality: case study at Ikorodu of Lagos, Nigeria. Water Supply 21(7):3356–3369

Kakran SP, Keshri KN (2012) Handbook for flood protection. Anti erosion and river training work. Flood Management Organization, New Delhi

Khan MA, Sharma N, Pu JH, Pandey M, Azamathulla H (2022) Experimental observation of turbulent structure at region surrounding the mid-channel braid bar. Mar Georesour Geotechnol 40(4):448–461

Kharya A, Kumar P (2012) RCC porcupines: an effective river bank protection measure–a case study of protection of Majuli Island. India water week: water, energy and food security: call for solutions, pp 10–14

Lu JY, Chang TF, Chiew YM, Hung SP, Hong JH (2011) Turbulence characteristics of flows passing through a tetrahedron frame in a smooth open-channel. Adv Water Resour 34(6): 718–730

Nakagawa H, Teraguchi H, Kawaike K, Baba Y, Zhang H (2011) Analysis of bed variation around bandal-like structures. Annu Disaster Prev Res Inst 54(B):497–510

Nayak A (2012) Experimental study of RCC jack jetty systems for river training. Doctoral dissertation, Ph.D. Thesis, Indian Institute of Technology Roorkee, Roorkee, India

Pandey M, Chen SC, Sharma PK, Ojha CSP, Kumar V (2019) Local scour of armor layer processes around the circular pier in non-uniform gravel bed. Watermark 11(7):1421

Pandey M, Jamei M, Karbasi M, Ahmadianfar I, Chu X (2021) Prediction of maximum scour depth near spur dikes in uniform bed sediment using stacked generalization ensemble tree-based frameworks. J Irrig Drain Eng 147(11):04021050

Pu JH, Wallwork JT, Khan M, Pandey M, Pourshahbaz H, Satyanaga A, Hanmaiahgari PR, Gough T (2021) Flood suspended sediment transport: combined modelling from dilute to hyper-concentrated flow. Watermark 13(3):379

Rahman M, Nakagawa H, Ishigaki T, Khaleduzzaman ATM (2003) Channel stabilization using bandalling. Annu Disaster Prev Res Inst 46(B):613–618

Rahman ML, Basak BC, Osman MS (2011) Velocity distribution around bandalling for navigation channel development. In: Int. Conf. Mechanical Engineering, Dhaka

Shi J, Zhang XL, Huang ZX (2011) Experimental research on preventing root-stones loss with tetrahedron-like concrete penetrating frames. In: Advanced materials research, vol 233. Trans Tech Publications Ltd., Zurich, pp 1930–1934

Shields A (1936) Application of similarity principles and turbulence research to bed-load movement. Calif Inst Technol 167:43

Wallwork JT, Pu JH, Kundu S, Hanmaiahgari PR, Pandey M, Satyanaga A, Pandey M, Satyanaga A, Amir Khan M, Wood A (2022) Review of suspended sediment transport mathematical modelling studies. Fluids 7(1):23

Yalin MS, Karahan E (1979) Inception of sediment transport. J Hydraul Div 105(11):1433–1443

Yu T, Wang PY, Liu QY, Zheng JT (2011) Study on the beach protection with the tetrahedron like penetrating frame groups. In: Applied mechanics and materials, vol 90. Trans Tech Publications Ltd., Zurich, pp 2533–2536

Zhang H, Nakagawa H, Baba Y, Kawaike K, Teraguchi H (2010) Three-dimensional flow around bandal-like structures. Ann J Hydraul Eng 54:175–180

Chapter 18
Flood Prioritization of Basins Based on Geomorphometric Properties Using Morphometric Analysis and Principal Component Analysis: A Case Study of the Maner River Basin

Aneesh Mathew and Padala Raja Shekar

Abstract Watershed characterization and its prioritization could help identify crucial sub-watersheds for conservation and mitigation efforts. Traditional methods for determining morphometric characteristics are time-consuming, costly, and labor-intensive. However, as remote sensing (RS) and geographic information system (GIS) technology have advanced, the process has become simpler, less expensive, and faster. The present chapter study prioritizes sub-watersheds based on morphometry using RS and GIS in the Maner watershed, Maharashtra state. The shuttle radar topography mission (SRTM) digital elevation model (DEM) with a resolution of 30 m was utilized to design drainage networks and identify sub-watersheds. The watershed was divided into nine sub-watersheds (SWs) (SW1–SW9), and the sub-watersheds were prioritized depending on morphometric data. Sub-watersheds were prioritized depending on morphometric analysis and principal component analysis (PCA). Several morphometric features such as linear, shape, and relief features were determined for each sub-watershed to prioritize ranking depending on morphometric analysis. Depending on morphometric analysis, four parameters were used in the PCA to rank and prioritize sub-watersheds. The sub-watersheds were divided into low, medium, and high priority depending on morphometric and PCA. SW9 and SW2 were given high priorities depending on morphometric and PCA. For morphometric analysis, high priority has been given to SW2 and SW9, while for PCA, high priority has been given to SW4 and SW7. SW6 is the most common sub-watershed to come under each priority. The high priority indicates that the sub-watershed is most vulnerable to flooding and soil erosion. Statistical research shows that stream order and stream number, as well as stream order and stream length, have a significant association. The results of this chapter may be applicable to

A. Mathew (✉) · P. R. Shekar
Civil Engineering Department, National Institute of Technology, Tiruchirappalli, Tamil Nadu, India
e-mail: aneesh@nitt.edu

M. Pandey et al. (eds.), *River Dynamics and Flood Hazards*, Disaster Resilience and Green Growth, https://doi.org/10.1007/978-981-19-7100-6_18

many stakeholders involved in managing water and soil conservation and developing watersheds.

Keywords Prioritization · Sub-watersheds · Flooding · GIS

18.1 Introduction

The entire watershed may not be able to be treated with land treatment techniques as part of a watershed management program, especially in the case of huge watersheds. For development planning and conservation activity implementation according to level of need and condition of degradation, it is necessary to identify and pick a small number of locations or sub-watersheds having comparatively greater degradation problems (Bajirao et al. 2019; Aamir et al. 2022; Chaudhuri et al. 2022). The priority watersheds are a small number of carefully chosen sub-watersheds within a larger watershed. After properly prioritizing watersheds (sub-watersheds), a sub-watershed management plan is created for each priority sub-watershed to reduce natural and human-induced hazards and safeguard precious resources (soil and water). Utilizing natural resources sustainably is the goal of watershed management in order to maximize output with little to no environmental hazard (Nigam et al. 2017; John et al. 2021a, b). Poor watershed circumstances containing surface runoff, poor infiltration, increased soil erosion, and low yield, as well as natural hazards such as floods and drought, can be overcome by a well-planned watershed management technique (Choudhari et al. 2018). Decision-makers must therefore be knowledgeable of the watershed's characteristics and the hydrological processes that take place there. The watershed characteristics, which may be properly investigated by morphometric analysis, have an impact on the hydrological processes inside a watershed (Kushwaha et al. 2022).

The watershed's morphology is a quantitative illustration of the watershed. In fact, morphology includes a quantitative research approach of the area, height, volume, gradient, land profile, and drainage watershed features of the area concerned (Singh 1972; Shankar et al. 2021; Shivashankar et al. 2022). A morphological analysis of a watershed gives data about the river system's features, the topographic arrangement of the earth's surface, and the structure and dimensions of its landforms (Agarwal 1998; Obi et al. 2002; Clarke 1996). It is also an essential method of evaluating and comprehending the role of river system dynamics (Singh et al. 2018a, b; Prakash et al. 2016; Withanage et al. 2014). With the degree of lithological and structural controls, the morphometric analysis reinforces the basic value of the fluvial landscape's dimensional individuality (Pophare and Balpande 2014).

The morphometric characteristics of any watershed represent the incorporation of a collection of upriver control systems, most noticeably climatological, and geographical features, which decide the hydrologic system (Prakash et al. 2016; Singh et al. 2013; Yadav 2014). The morphometric analysis is completed effectively by measuring the watershed's features, and contributing ground slope (Rai et al. 2017; Javed et al. 2009; Nookaratnam et al. 2005). Within the watershed, geomorphic and

hydrologic processes occur, and morphometric description at the watershed level shows data about the configuration and growth of land surface procedures (Dar et al. 2013). The river system's surface runoff and flow intensity can be calculated by utilizing geomorphological aspects connected with morphometry (Ozdemir and Bird 2009; Patel and Srivastava 2013). Various hydrological phenomena can be connected to the physiographic features of a river watershed, like its size, structure, gradient, and so on (Rai et al. 2017).

Furthermore, morphometric analysis is necessary for detecting and assessing seasonal changes in watershed features, understanding groundwater potentialities, and addressing flood proneness issues during higher flows (Choudhari et al. 2018; Mangan et al. 2019). Moreover, different studies have utilized morphometry to prioritize and compare sub-watersheds (Sharma et al. 2010; Thapliyal et al. 2017; Kumar et al. 2015; Kumar and Lal 2017). Watershed prioritization refers to the order in which various sub-watersheds of a watershed must get hold of water and soil protection (Iqbal and Sajjad 2014). In addition, comprehensive watershed management planning was required. In general, watershed morphometric studies are critical for giving effective data about the river system and hydro-geomorphometric features, of the watershed for sustainable natural resource control as well as planning (Mfwango et al. 2022; Gunjan et al. 2019; Karabulut and Özdemir 2019; Redvan and Mustafa 2021; Nitheshnirmal et al. 2019; Singh et al. 2021).

Traditional watershed prioritization procedures include digitizing contours in a topographic map as well as conducting a thorough field research, digitizing river systems, river categorization to completely distinct stream orders, and conventional measurement techniques of stream length, that include streams, and estimating watershed perimeter, area, and other dependent factors to quantify morphometric features (Shekar and Mathew 2022b). As a result, this conventional approach requires a significant amount of time, money, and labor. The use of a GIS and RS technique to evaluate watershed priorities and morphometric features saves money, time, and labor (Grohmann et al. 2007; Sarangi et al. 2003). Many investigators have utilized RS and GIS approaches to study as well as calculate watershed morphometry (Magesh and Chandrasekar 2012; Chopra et al. 2005). The primary benefits of GIS approaches for river analysis over conventional techniques of analysis are that the RS and GIS are proficient at controlling and processing huge amounts of data effectively as well as accurately. Management tools are frequently regarded as critical components of management, allowing decision-makers to make more efficient and beneficial choices (Burrough and McDonnell 1998). Previous research has mainly used a standard compound value for the analysis method of prioritizing, which is calculated by averaging the starting ranks of importance for all parameters (Aher et al. 2014; Rahman et al. 2022). However, PCA has been utilized to inform a few investigations (Farhan et al. 2017; Meshram and Sharma 2018). The authors (Sharm et al. 2015; Arefn et al. 2020) proposed reducing the dimension of morphometric parameters based on the PCA and finding variables that largely account for the variance exhibited in a variety of metrics. The regionalization of the hydrologic models is made easier by recent geomorphologic research. The study of the geomorphologic properties of such catchments becomes significantly more relevant

because the majority of catchments are either ungauged or lack appropriate data (Sharma et al. 2009).

The objectives of this chapter are to both prioritize sub-watersheds based on morphometric parameters including linear, areal or shape, and relief parameters of each sub-watershed and to prioritize sub-watersheds using PCA of each sub-watershed based on morphometric parameters. Furthermore, the study uses PCA and morphometric analysis to find the most common sub-watersheds that belong to the same priority.

18.2 Study Area

The location of the Maner watershed is depicted in Fig. 18.1. The Maner watershed area is defined by longitudes 76°30′0′′ and 77°45′0′′ East, and latitudes 17°45′0′′ and 19°00′0′′ North. The Maner River's outlet can be found at longitudes of 77° 32′ 42′′ East and latitudes of 18° 42′ 18′′ North. The watershed area covers 2056 km^2 in total. Soil classification as per FAO (1988): the area's principal soil units are vertic cambisols and chromic vertisols. The slope varies from 0 to 29.15°. According to the SRTM-DEM, the height of the Maner River basin spans from 352 m to 706 m above sea level. The study region features significant rock, according to the United States Geological Survey's (USGS) World Geologic Maps. The types of rock that were seen in the study region were paleocene cretaceous extrusive rocks.

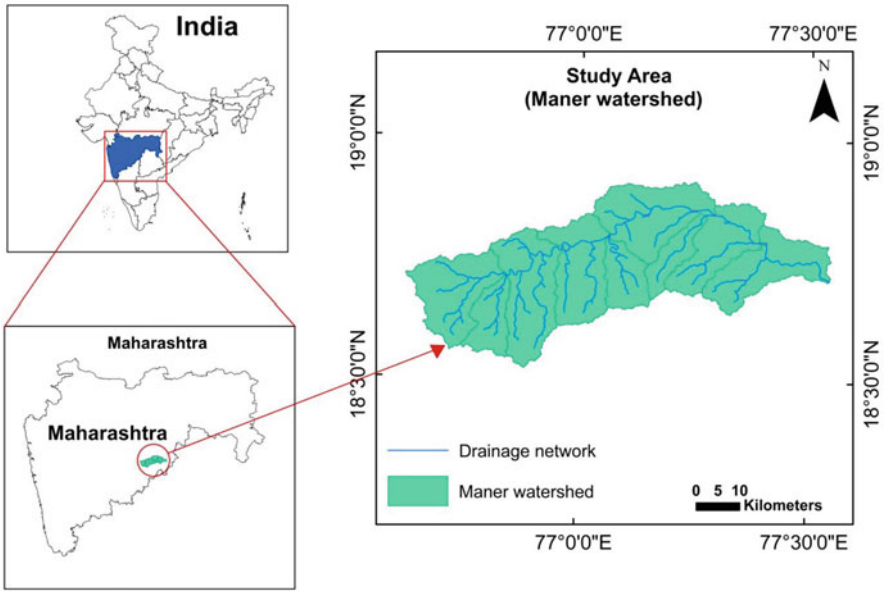

Fig. 18.1 Study area of Maner watershed

18.3 Methodology

18.3.1 Morphometric Analysis

In this present chapter study, the watershed was delineated by utilizing SRTM-DEM. It was obtained from the USGS Earth Explorer website. The resolution of the digital elevation model is 30 m. The Maner watershed's nine sub-watersheds were investigated utilizing quantifiable morphometric aspects. Figure 18.2 shows the processing of DEM, including fill, flow direction, flow accumulation, stream definition, stream to features, etc. Sub-watersheds (SW1–SW9) are classified utilizing ArcGIS 10.4.1 software depending on three types of morphometric features such as shape, relief, and linear features. These features are calculated by utilizing different empirical approaches as given in Table 18.1. Table 18.2 illustrates the measured linear aspects of the Maner watershed (SW1–SW9). The rank of each feature in each sub-watershed was calculated. The compound parameter (C_p) value for each individual sub-watershed is then determined. On the source of the C_p results, the sub-watersheds were grouped into three: high, medium, and low.

18.3.2 Principal Component Analysis (PCA)

PCA was utilized to identify the significant morphometric features, which were then used to prioritize catchments based on features that are significantly associated with components. The statistical program for the social sciences (SPSS) version 22.0 software was used to reduce the 19 morphometric features into four features for the current investigation. The rotated component matrix considers one highly significant feature for each component. Once four parameters have been obtained using the PCA technique, each sub-watershed characteristic is ranked. The Cp value calculation comes after that. The sub-watersheds were split into three categories based on their Cp values: high, medium, and low.

18.4 Results and Discussion

The present chapter emphasizes the use of RS and GIS for morphometric analysis, specifically linear, shape, and relief features, with the results discussed below.

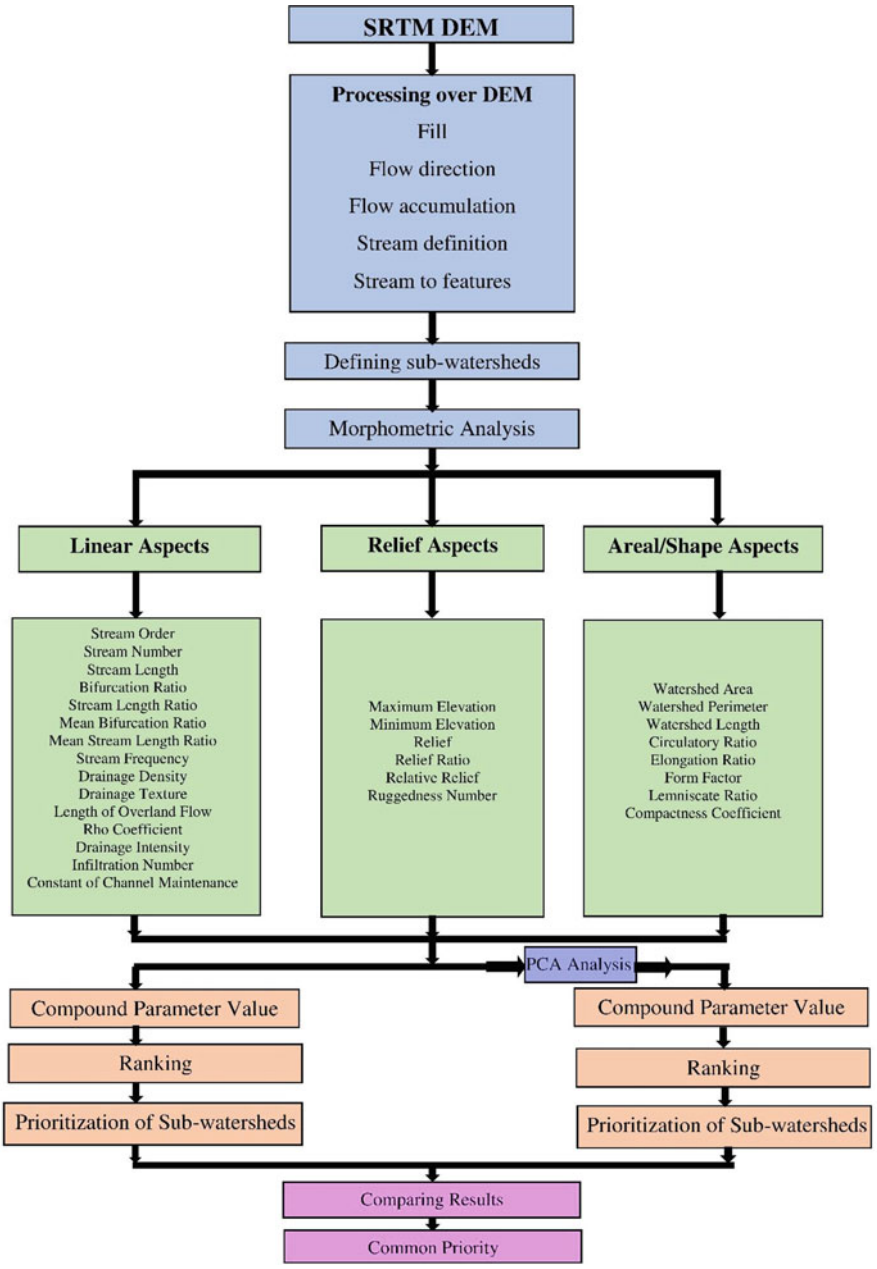

Fig. 18.2 Flowchart of methodology

Table 18.1 Maner watershed (formulae)

Parameters or features	Formulae	References
Stream order (U)	Hierarchical rank	Strahler (1964)
Mean bifurcation ratio (R_{bm})	Average of bifurcation ratio of all orders	Strahler (1957)
Infiltration number (I_f)	$I_f = F_s \times D_d$	Faniran (1968)
Bifurcation ratio (R_b)	$R_b = (N_u/N_u + 1)$	Strahler (1964)
Drainage density (D_d)	$D_d = (\sum L_u)/\mathrm{A}$	Schumm (1956)
Stream number (N_u)	$N_u = N_{u1} + N_{u2} + \ldots + N_{un}$	Horton (1945)
Drainage texture (D_t)	$D_t = (\sum N_u)/P$	Schumm (1956)
Stream length (L_u)	$L_u = L_{u1} + L_{u2} + \ldots + L_{un}$	Horton (1945)
Mean stream length ratio (R_{lm})	The average of the steam length ratio of all orders	Strahler (1964)
Drainage intensity (D_i)	$D_i = F_s/D_d$	Faniran (1968)
Constant of channel maintenance (C_{cm})	$C = 1/D_d$	Schumm (1956)
Length of overland flow (L_o)	$L_o = (1/(2D_d))$	Horton (1945)
Stream length ratio (R_l)	$R_l = L_u/L_u - 1$	Horton (1945)
Minimum elevation (h)	GIS software	
Ruggedness number (R_n)	$R_n = (B_h \times D_d)$	Strahler (1952)
Maximum elevation (H)	GIS software	
RHO coefficient (ρ)	R_{lm}/R_{bm}	Horton (1945)
Relative relief (R_{hp})	$R_{hp} = \mathrm{H} \times 100/P$	Melton (1957)
Stream frequency (F_s)	$F_s = (\sum N_u)/A$	Schumm (1956)
Relief ratio (R_h)	$R_h = B_h/L_b$	Schumm (1956)
Relief (B_h)	$B_h = H - h$	Strahler (1952)
Area of the watershed (A)	GIS software	
Watershed length (L_b)	$L_b = 1.312 \times A^{0.568}$	Nookaratnam et al. (2005)
Perimeter of the watershed (P)	GIS software	
Circulatory ratio (R_c)	$R_c = 4\pi\mathrm{A}/\mathrm{P}^2$	Miller (1953)
Compactness coefficient (C_c)	$C_c = (\mathrm{P}/2(\pi\mathrm{A})^{0.5})$; where $\pi = 3.14$	Horton (1945)
Elongation ratio (R_e)	$R_e = (2*(A/\pi)^{0.5})/(L_b)$	Schumm (1956)
Lemniscate ratio (K)	$K = (L_b^2/4A)$	Chorley et al. (1957)
Form factor (F_f)	$F_f = (A/L_b^2)$	Horton (1932)

18.4.1 Linear Parameters

18.4.1.1 Stream Order (U)

Strahler's (1964) classification was used to rank the streams in the study area. Streams without any tributaries are classified as the first order of the streams; then the two first order streams join together to form the second order of the stream, and so on. SW8 is in the fifth order, while SW1, SW4, SW5, SW7, SW3, SW6, and SW9

Table 18.2 Maner watershed (linear features)

SW	Stream order (U)	Stream number (N_u)	$\log_{10}$ (N_u)	Stream length (L_u)	$\log_{10}$ (L_u)	Bifurcation ratio (R_b)	Stream length ratio (R_l)
SW 1	1	87	1.94	99	2.00	No	No
	2	18	1.26	63	1.80	4.83	0.64
	3	6	0.78	31	1.49	3.00	0.49
	4	1	0.00	22	1.34	6.00	0.71
		$\sum N_u = 112$		$\sum L_u = 215$		$\sum R_b = 13.83$	$\sum \mathrm{R_l} = 1.84$
						$\sum \mathrm{R_{bm}} = 4.61$	$\sum R_{\mathrm{lm}} = 0.61$
SW 2	1	65	1.81	49	1.69	No	No
	2	12	1.08	22	1.34	5.42	0.45
	3	1	0.00	19	1.28	12.00	0.86
		$\sum N_u = 78$		$\sum L_u = 90$		$\sum R_b = 17.42$	$\sum R_l = 1.31$
						$\sum R_{\mathrm{bm}} = 8.71$	$\sum R_{\mathrm{lm}} = 0.66$
SW3	1	95	1.98	108	2.03	No	No
	2	18	1.26	42	1.62	5.28	0.39
	3	3	0.48	40	1.60	6.00	0.95
	4	1	0.00	4	0.60	3.00	0.10
		$\sum N_u = 117$		$\sum L_u = 194$		$\sum R_b = 14.28$	$\sum R_l = 1.44$
						$\sum R_{\mathrm{bm}} = 4.76$	$\sum R_{\mathrm{lm}} = 0.48$
SW4	1	98	1.99	100	2	No	No
	2	17	1.23	52	1.72	5.76	0.52
	3	3	0.48	19	1.28	5.67	0.37
	4	1	0.00	17	1.23	3.00	0.89
		$\sum N_u = 119$		$\sum L_u = 188$		$\sum R_b = 14.43$	$\sum R_l = 1.78$
						$\sum R_{\mathrm{bm}} = 4.81$	$\sum R_{\mathrm{lm}} = 0.59$
SW5	1	57	1.76	52	1.72	No	No
	2	13	1.11	30	1.48	4.38	0.58
	3	4	0.60	12	1.08	3.25	0.40
	4	1	0	15	1.18	4.00	1.25
		$\sum N_u = 75$		$\sum L_u = 109$		$\sum R_b = 11.63$	$\sum R_l = 2.23$
						$\sum R_{\mathrm{bm}} = 3.88$	$\sum R_{\mathrm{lm}} = 0.74$
SW6	1	95	1.98	112	2.05	No	No
	2	14	1.15	41	1.61	6.79	0.37
	3	4	0.60	51	1.71	3.50	1.24
	4	1	0	24	1.38	4.00	0.47
		$\sum N_u = 114$		$\sum L_u = 228$	4	$\sum R_b = 14.29$	$\sum R_l = 2.08$
						$\sum R_{\mathrm{bm}} = 4.76$	$\sum R_{\mathrm{lm}} = 0.69$
SW7	1	86	1.93	141	2.15	No	No

(continued)

Table 18.2 (continued)

SW	Stream order (U)	Stream number (N_u)	$\log_{10}$ (N_u)	Stream length (L_u)	$\log_{10}$ (L_u)	Bifurcation ratio (R_b)	Stream length ratio (R_l)
	2	33	1.52	81	1.91	2.61	0.57
	3	9	0.95	23	1.36	3.67	0.28
	4	1	0	32	1.51	9.00	1.39
		$\sum N_u = 129$		$\sum L_u = 277$		$\sum R_b = 15.27$	$\sum R_l = 2.25$
						$\sum R_{bm} = 5.09$	$\sum R_{lm} = 0.75$
SW8	1	77	1.89	108	2.03	No	No
	2	17	1.23	50	1.70	4.53	0.46
	3	5	0.70	32	1.51	3.40	0.64
	4	2	0.30	12	1.08	2.50	0.38
	5	1	0.00	6	0.78	2.00	0.50
		$\sum N_u = 102$		$\sum L_u = 208$		$\sum R_b = 12.43$	$\sum R_l = 1.98$
						$\sum R_{bm} = 3.11$	$\sum R_{lm} = 0.49$
SW9	1	78	1.89	61	1.79	No	No
	2	12	1.08	31	1.49	6.50	0.51
	3	3	0.48	10	1.00	4.00	0.32
	4	1	0.00	17	1.23	3.00	1.70
		$\sum N_u = 94$		$\sum L_u = 119$		$\sum R_b = 13.50$	$\sum R_l = 2.53$
						$\sum R_{bm} = 4.50$	$\sum R_{lm} = 0.84$

are in the fourth order, and SW2 is in the third order in the Maner watershed, as shown in Fig. 18.3.

18.4.1.2 Stream Number (N_u)

It is the overall number of stream segments ordered in the ascending order (Horton 1945). SW7 and SW5 have the maximum and minimum stream numbers in this present chapter, respectively.

18.4.1.3 Stream Length (L_u)

It is the overall length of streams in a particular order. The length of the stream was calculated by utilizing Horton (1945) law. The overall length of stream segments is greatest in first-order streams and decreases as stream order increases. SW7 and SW2 are the lengths of the high and low streams in this study.

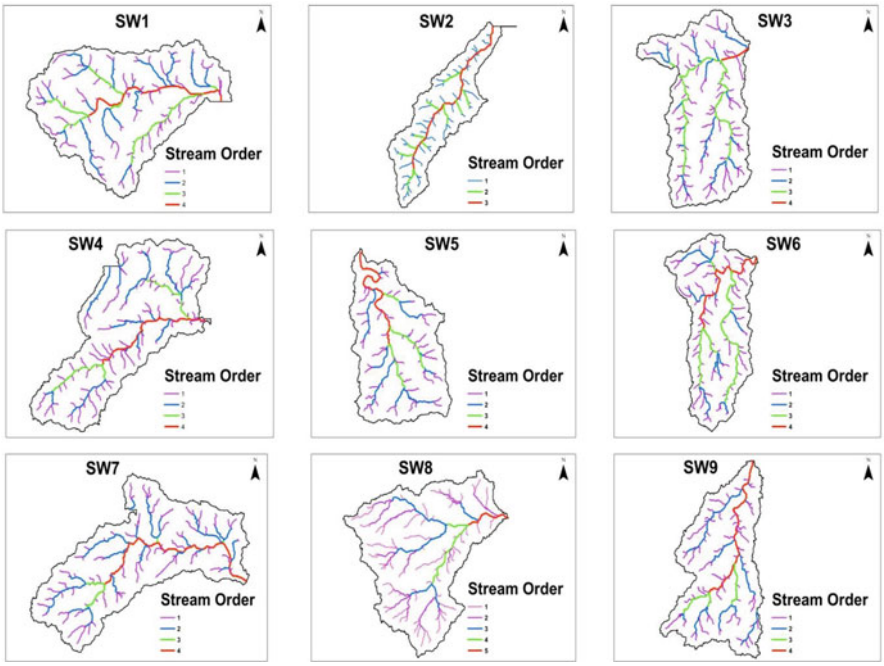

Fig. 18.3 Sub-watersheds and drainage networks

18.4.1.4 Bifurcation Ratio (R_b)

According to Schumm (1956), it is the ratio of the number of stream segments of a given order to the number of stream segments of the next higher orders. In this study, SW2 and SW5 have the highest bifurcation ratios, while SW4 has the lowest.

18.4.1.5 Stream Length Ratio (R_l)

It is the ratio of the mean length of one order of stream segments to the next lower order of stream segments (Horton 1945). In this present chapter study, SW9 has the maximum stream length ratio, while SW3 has the minimum.

There are two basic laws which link the stream number with the stream length of unique orders in a river watershed (Horton 1945). The first is the law of N_u, which explains the relationship among the N_u of a provided order and its "U" utilizing an inverted geometric series is used to express this rule with the R_b as the base. A good relationship among U and N_u, with coefficients of determination varying from SW7 (0.964) to SW5 (0.998), as shown in Fig. 18.4.

The second law of L_u is the average length of first-order streams, R_l, and the mean length of a provided order when it comes to the order of stream. A direct geometric series is used to express this rule. Figure 18.5 depicts a strong relationship among

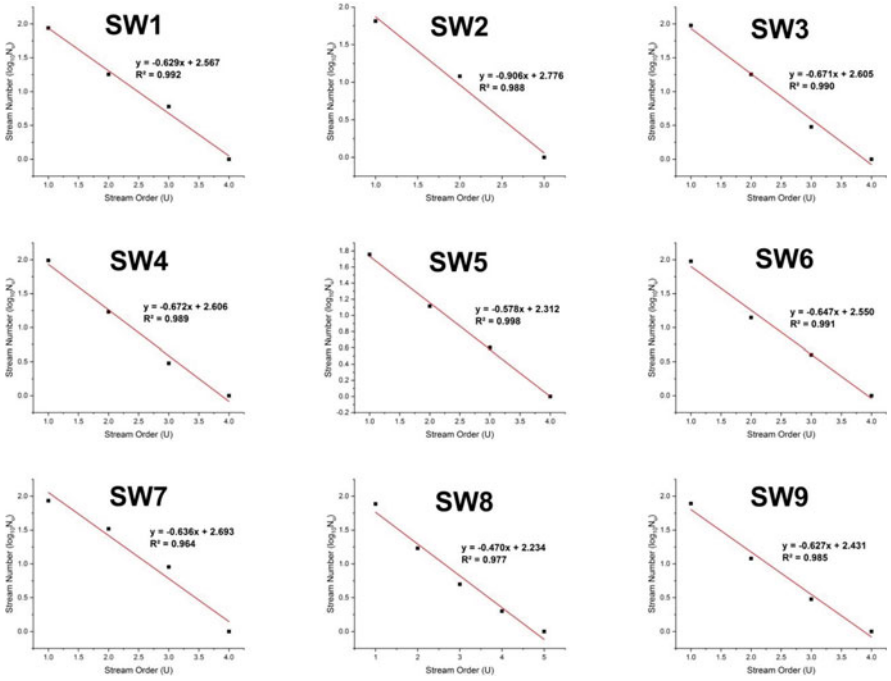

Fig. 18.4 Stream number and stream order

U and L_u, with coefficients of determination varying from SW9 (0.676) to SW8 (0.990).

18.4.1.6 Stream Frequency (F_s)

It is the whole stream number ($\sum N_u$) segments of all orders per unit region (A) (Horton 1945), and it is affected by the watershed's lithology and reflects the texture of the river system. SW2 has the highest value in this study, while SW6 has the lowest.

18.4.1.7 Drainage Density (D_d)

It is the whole stream length ($\sum L_u$) per unit region (A) (Horton 1945). It represents the development of channels and their proximity in the watershed. SW7 has the highest value in this study, while SW1 has the lowest.

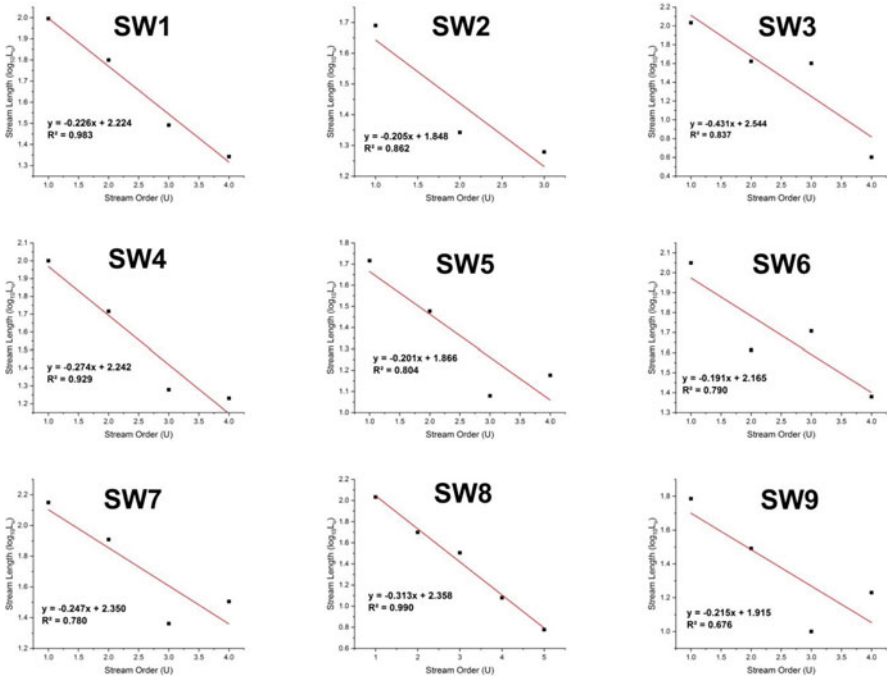

Fig. 18.5 Stream length and stream order

18.4.1.8 Drainage Texture (D_t)

It is the whole stream number ($\sum N_u$) segments of all orders per perimeter (P) (Horton 1945). Lithology, vegetation, rainfall, soil type, infiltration capacity, relief, and stage of growth all have an impact on D_t (Smith 1950). In this study, SW9 has the highest value, while SW8 has the lowest.

18.4.1.9 Length of the Overland Flow (L_o)

It is approximately half the reciprocal of D_d (Horton 1945). SW1 has the maximum value in this study, while SW7 has the minimum.

18.4.1.10 Drainage Intensity (D_i)

According to Faniran (1968), it is the ratio of F_s to D_d. In this present chapter investigation, the D_i is high at SW2 and low at SW5.

18.4.1.11 Rho Coefficient (ρ)

It is the ratio of R_{lm} to R_{bm}. It is an essential feature for relating D_d to physiographic growth, which calculates the drainage network's storage capacity and the ultimate degree of drainage growth (Horton 1945). In this study, the ρ is maximum at SW2 and minimum at SW5.

18.4.1.12 Infiltration Number (I_f)

It is the product of D_d and F_s, and it gives data about the watershed's infiltration characteristics. Higher infiltration numbers result in lower infiltration rates and higher surface overflow (Faniran 1968). In this study, the infiltration number is highest at SW2 and lowest at SW1.

18.4.1.13 Constant of Channel Maintenance (C_{cm})

According to Schumm (1956), it is the inverse of D_d. The channel maintenance constant is maximum and minimum in this study at SW1 and SW7, respectively.

18.4.2 Relief Parameters

18.4.2.1 Relief (B_h)

The variation in elevation among the watershed's highest and lowest points is referred to as its relief. SW6 provides the most relief in this study, while SW5 provides the least.

18.4.2.2 Relief Ratio (R_h)

The overall relief of a river system is the variation in elevation among both the maximum location of a watershed and the minimum location on the valley floor. SW9 has a higher value in this study than SW1, which has a lower value.

18.4.2.3 Relative Relief (R_{hp})

It has been calculated using the perimeter and watershed relief (Melton 1957). SW9 has a higher value in this study than SW7, which has a lower value.

18.4.2.4 Ruggedness number (R_n)

It is the product of B_h and D_d (Strahler 1964). This investigation discovered the greater and lower values at SW9 and SW1, respectively.

18.4.3 Areal Parameters

18.4.3.1 Area of Watershed (*A*)

It is one of the essential watershed features for hydrologic design because it represents the volume of water that is able to be produced from precipitation. The watershed encompasses an area of 2056 km^2. The largest and smallest sub-watershed regions in the present chapter study are SW6 and SW2, respectively, as shown in Fig. 18.6.

18.4.3.2 The Perimeter of a Watershed (*P*)

The perimeter of a watershed is the outside boundary of the watershed that encompasses its region. It is calculated along a watershed separates and can be utilized to estimate watershed size and structure. As shown in Fig. 18.7, the maximum and minimum sub-watershed perimeters of the nine Maner basins are SW6 and SW2, respectively.

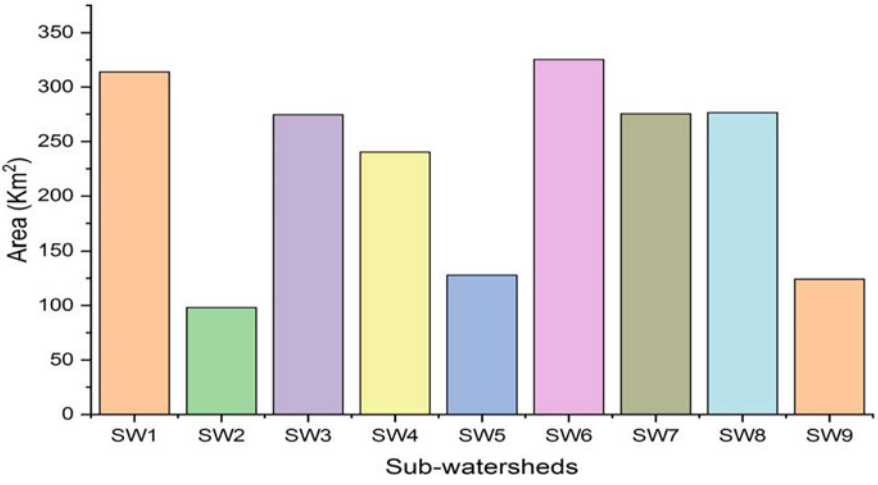

Fig. 18.6 Areas of sub-watersheds

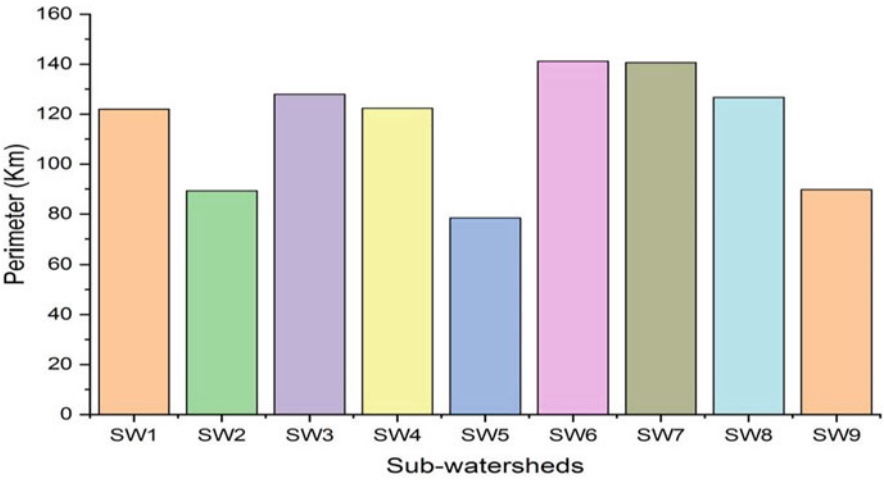

Fig. 18.7 Perimeter of sub-watersheds

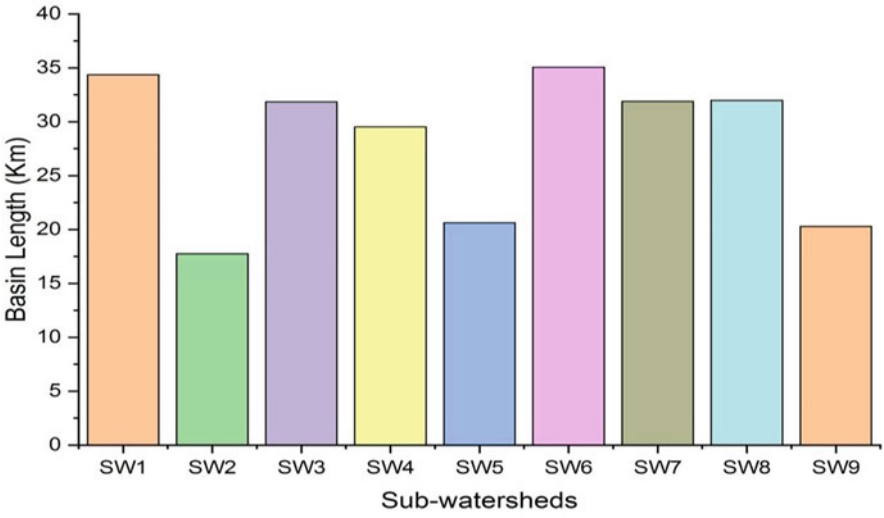

Fig. 18.8 Watershed length of sub-watersheds

18.4.3.3 Watershed Length (L_b)

The distance calculated along the main channel from the watershed outlet to the watershed separate is commonly used to define watershed length. The basic input feature for counting the major shape features is watershed length. SW6 has the longest sub-watershed length in the present chapter study, while SW2 has the shortest, as shown in Fig. 18.8.

18.4.3.4 Circulatory Ratio (R_c)

It is the ratio of the watershed region to the region of a circle with the same circumference as the watershed's perimeter (Miller 1953). In this study, SW1 had a higher circulatory ratio than SW2, which had a lower circulatory ratio.

18.4.3.5 Elongation Ratio (R_e)

The ratio of the diameter of a circle with the same region as the river watershed to the longest length of the watershed, according to Schumm (1956), is what defines it. In this study, SW2 had a higher elongation ratio than SW1, which had a lower elongation ratio.

18.4.3.6 Form Factor (F_f)

It is the ratio of watershed region to watershed length squared. The longer the watershed, the lower the form factor value (Strahler 1964). In this study, SW2 has a maximum F_f than SW1, which has a lower minimum F_f.

18.4.3.7 Lemniscate's Ratio (K)

It is utilized to calculate the gradient of the river watershed (Chorley et al. 1957). In this present chapter, SW1 has a maximum Lemniscate's ratio, whereas SW2 has a minimum form factor, as given in Table 18.3.

18.4.3.8 Compactness Coefficient (C_c)

It is the ratio of the watershed region to the watershed perimeter. It is slope-dependent and size-independent. Lower values of this parameter indicate less erosion and greater watershed elongation (Horton 1945). In this study, SW2 has a maximum C_c, whereas SW1 has a minimum C_c, as shown in Fig. 18.9.

18.5 Sub-watershed Prioritization Based on Morphometric Analysis

Morphometric characteristics are classified into three types: shape, relief, and linear aspects. These three types were used to prioritize more vulnerable sub-watersheds due to their direct or inverse association with flood and soil erosion risk

Table 18.3 Maner watershed (morphometric results)

Sl. No	Features	SW 1	SW2	SW 3	SW 4	SW 5	SW 6	SW 7	SW 8	SW 9
1	Stream order	4	3	4	4	4	4	4	5	4
2	Stream number	112	78	117	119	75	114	129	102	94
3	Stream length	215	90	194	188	109	228	277	208	119
4	Bifurcation ratio	13.83	17.42	14.28	14.43	11.63	14.29	15.27	12.43	13.50
5	Stream length ratio	1.84	1.31	1.44	1.78	2.23	2.08	2.25	1.98	2.53
6	Mean bifurcation ratio	4.61	8.71	4.76	4.81	3.88	4.76	5.09	3.11	4.5
7	Mean stream length ratio	0.61	0.66	0.48	0.59	0.74	0.69	0.75	0.49	0.84
8	Stream frequency	0.36	0.80	0.43	0.50	0.59	0.35	0.47	0.37	0.76
9	Drainage density	0.69	0.92	0.71	0.78	0.85	0.70	1.01	0.75	0.96
10	Drainage texture	0.92	0.87	0.91	0.97	0.96	0.81	0.92	0.81	1.05
11	Length of overland flow	0.73	0.54	0.71	0.64	0.59	0.71	0.50	0.66	0.52
12	Rho coefficient	7.53	13.27	9.91	8.11	5.22	6.87	6.79	6.28	5.33
13	Drainage intensity	0.52	0.87	0.60	0.63	0.69	0.50	0.47	0.49	0.79
14	Infiltration number	0.24	0.73	0.30	0.39	0.50	0.25	0.47	0.28	0.73
15	Constant of channel maintenance	1.46	1.09	1.42	1.28	1.17	1.43	0.99	1.33	1.04
16	Maximum elevation	543	562	590	551	563	665	527	666	706
17	Minimum elevation	373	388	416	366	419	445	352	491	492
18	Relief	0.17	0.17	0.17	0.19	0.14	0.22	0.18	0.18	0.21
19	Relief ratio	0.0049	0.0098	0.0055	0.0063	0.0070	0.0063	0.0055	0.0055	0.0105
20	Relative relief	0.45	0.63	0.46	0.45	0.72	0.47	0.37	0.53	0.79
21	Ruggedness number	0.12	0.16	0.12	0.14	0.12	0.15	0.18	0.13	0.21
22	Watershed area	313.80	98.06	274.67	240.33	127.91	325.37	275.38	276.56	124.14
23	Watershed perimeter	122.00	89.31	127.97	122.37	78.41	141.18	140.57	126.69	89.74
24	Basin length	34.36	17.75	31.86	29.53	20.64	35.07	31.90	31.98	20.29
25	Circulatory ratio	0.26	0.15	0.21	0.20	0.26	0.17	0.18	0.22	0.19

(continued)

Table 18.3 (continued)

Sl. No	Features	SW 1	SW2	SW 3	SW 4	SW 5	SW 6	SW 7	SW 8	SW 9
26	Elongation ratio	0.58	0.63	0.59	0.59	0.62	0.63	0.59	0.59	0.62
27	Form factor	0.27	0.31	0.27	0.28	0.30	0.31	0.27	0.27	0.30
28	Lemniscate ratio	0.94	0.80	0.92	0.91	0.83	0.81	0.92	0.92	0.83
29	Compactness coefficient	1.94	2.54	2.18	2.23	1.96	2.43	2.39	2.15	2.27

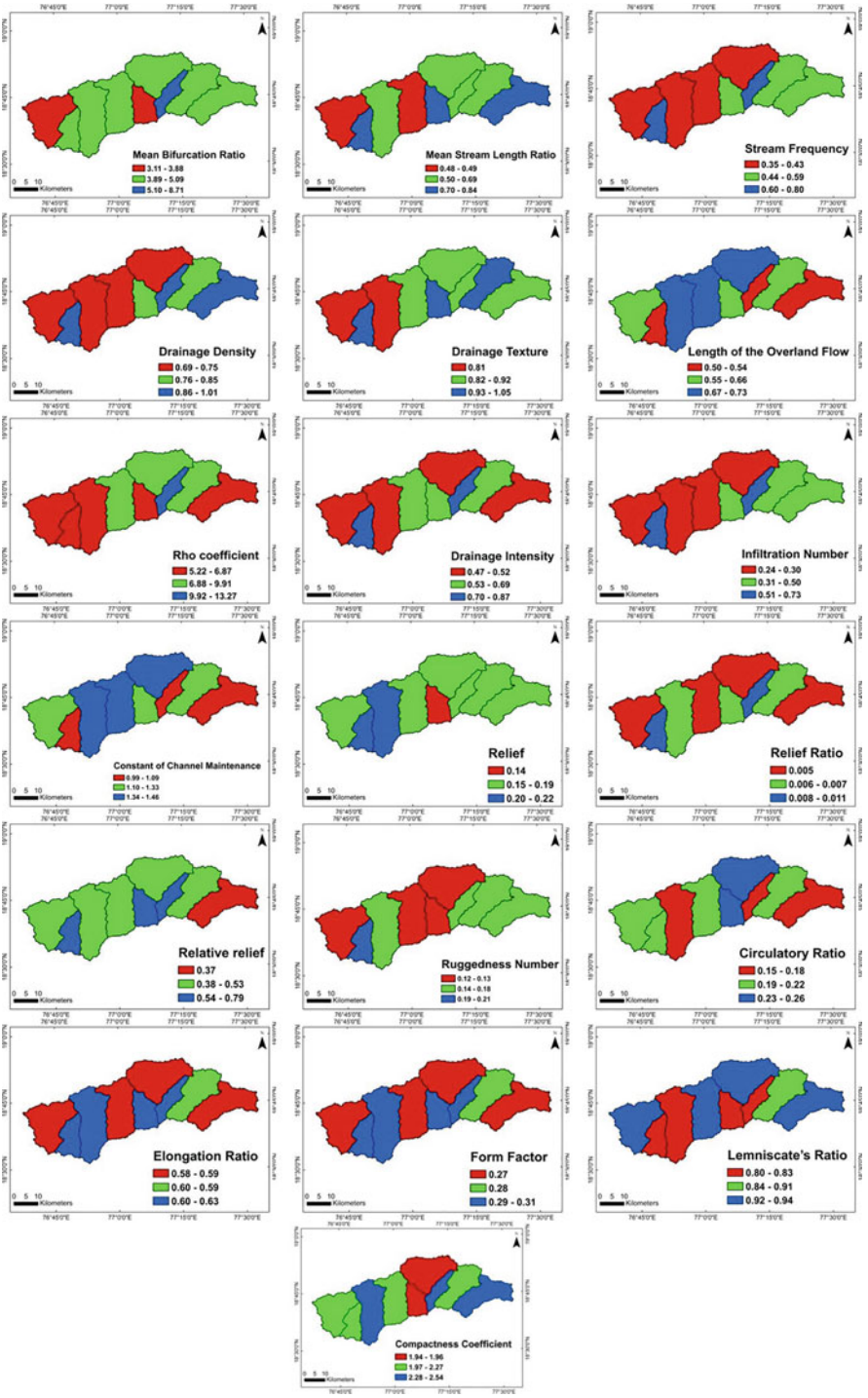

Fig. 18.9 Morphometric analysis of nine sub-watersheds

(Nookaratnam et al. 2005; Shekar and Mathew 2022a). The linear and relief features are directly related to the erosion of soil. The sub-watershed with the highest value is ranked first, followed by the second highest value, the third highest value, and so on. The shape feature, on the other hand, has an indirect association with soil erosion. The sub-watershed with the lower shape feature value will therefore be ranked first, and then the sub-watershed with the second lowest value will be ranked 2, and so on.

Following the assignment of a rank depending on individual features, the rank results for all nine sub-watersheds were averaged to get a C_p value, as given in Table 18.4. SW1 has a C_p value of 5.45 when all of its ranks are added together and divisible by its 19 features. The process was repeated for the remaining eight sub-watersheds.

The sub-watersheds were grouped into 3: low ($\geq$4.98 to $<$5.65), medium ($\geq$4.31 to $<$4.98), and high ($\geq$3.65 to $<$4.31) depending on C_p value. Among nine sub-watersheds, SW9 and SW2 were high priority, SW7, SW4, SW6, and SW5 were medium priority, and SW1, SW8, and SW3 were low priority. This implies that the sub-watersheds with the highest priority are most vulnerable to runoff and erosion of soil (Javed et al. 2009; Nookaratnam et al. 2005). The final priority of the sub-watersheds in the Maner watershed is shown in Fig. 18.10.

18.6 Sub-watershed Prioritization Based on PCA

PCA is a statistical tool for identifying hidden features that simplify the pattern of correlations inside a set of observable features or variables while maintaining true initial data. The component loading matrix is given in Table 18.5. The top four components, which all have eigenvalues greater than one, account for 92.103% of the total variance in the actual data and are clearly significant. Component 1 is substantially connected with drainage density, component 2 is highly correlated with form factor, component 3 is highly correlated with the RHO coefficient, and component 4 is highly correlated with relief, according to the rotated component matrix (Table 18.6) (Meshram and Sharma 2017). Drainage density, form factor, RHO coefficient, and relief are the essential morphometric characteristics derived from PCA. As a result, these factors are used to prioritize the Maner catchment's nine sub-watersheds.

The C_p value would be 5.5 if all the ranks in sub-watershed 1 (SW1) were totaled up and divided by the four features. Other sub-watersheds have undergone the same process. Table 18.7 shows the final priority ranks and Cp values based on the four morphometric features calculated using the PCA approach. On the source of C_p results, sub-watersheds were grouped into high ($\geq$3.5 to $<$4.67), medium ($\geq$4.67 to $<$5.83), and low ($\geq$5.83 to $<$7). Among nine sub-watersheds, SW4 and SW7 fall inside a high priority. The Maner sub-watersheds' final PCA priority map is shown in Fig. 18.11.

Table 18.4 Ranking of Maner watershed

Parameters	SW 1	SW2	SW 3	SW 4	SW 5	SW 6	SW 7	SW 8	SW 9
Mean bifurcation ratio	6	1	5	3	8	4	2	9	7
Mean steam length ratio	6	5	9	7	3	4	2	8	1
Stream frequency	8	1	6	4	3	9	5	7	2
Drainage density	9	3	7	5	4	8	1	6	2
Drainage texture	4	7	6	2	3	8	5	9	1
Length of overland flow	1	7	3	5	6	2	9	4	8
Rho coefficient	4	1	2	3	9	5	6	7	8
Drainage intensity	6	1	5	4	3	7	9	8	2
Infiltration number	9	1	6	5	3	8	4	7	2
Constant of channel maintenance	1	7	3	5	6	2	9	4	8
Relief	8	6	7	3	9	1	4	5	2
Relief ratio	9	2	8	5	3	4	6	7	1
Relative ratio	8	3	6	7	2	5	9	4	1
Ruggedness number	9	3	7	5	8	4	2	6	1
Circulatory ratio	9	1	6	5	8	2	3	7	4
Elongation ratio	1	9	4	5	6	8	3	2	7
Form factor	1	9	4	5	6	8	3	2	7
Lemniscate ratio	9	1	6	5	4	2	7	8	3
Compactness coefficient	1	9	4	5	2	8	7	3	6
Sum of rankings (X)	109	77	104	88	96	99	96	113	73
Total number of parameters (Y)	19	19	19	19	19	19	19	19	19
Compound parameter (X/Y)	5.45	3.85	5.2	4.4	4.8	4.95	4.8	5.65	3.65
Ranking	8	2	7	3	4	6	5	9	1
Final priority	Low	High	Low	Medium	Medium	Medium	Medium	Low	High

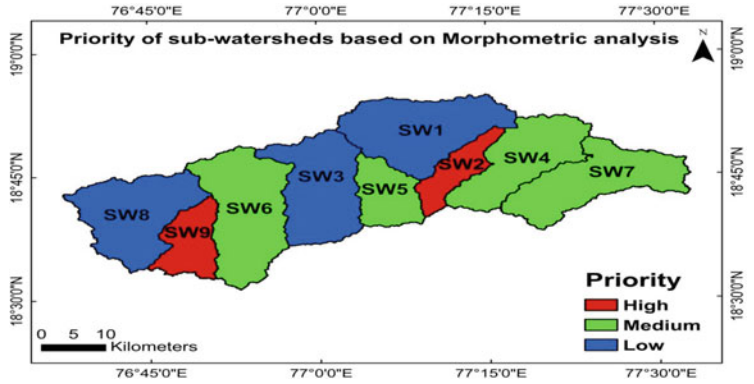

Fig. 18.10 Priority of Maner watershed based on morphometric analysis

18.7 Common Sub-watersheds

To determine the common sub-watersheds falling under each priority, the results of morphometric analysis, and PCA have been compared. Two methods identify one sub-watershed has common sub-watersheds with a medium priority: SW6. The other eight sub-watersheds exhibit a slight difference in their priority under the two methods. Table 18.8 shows the common priority among the three methods.

18.8 Conclusion

Morphometric analysis and PCA, which were carried out using RS and GIS tools, are useful approaches for hydrological analysis of river systems and watershed extraction. The Maner watershed underwent morphometric analysis and PCA. To prioritize ranking, morphometric features such as linear, relief, and shape features were evaluated for each sub-watershed. In this present chapter study, 19 morphometric parameters were calculated and scientifically analyzed. Depending on morphometric analysis, four parameters were used in the PCA to rank and prioritize sub-watersheds. Depending on morphometric and PCA, the sub-watersheds were grouped as low, medium, and high priority. For morphometric analysis, high priority has been given to SW2 and SW9, while for PCA, high priority has been given to SW4 and SW7. SW6 is the most common sub-watershed to fall under each priority. The sub-watershed has a high hazard of flooding and soil erosion, as shown by the high priority. The results of this study point to a useful tool for identifying regions that should receive top priority when formulating plans for measures to stop soil erosion and encourage soil conservation. This may require both biological and physical solutions, such as erecting bunds, farm ponds, check dams, providing vegetation and stone barriers, and planting multipurpose tree species, depending

Table 18.5 Overall variance explained of the morphometric indices

	Initial eigenvalues			Extraction sums of squared loadings			Rotation sums of squared loadings		
Component	Total	% of variance	Cumulative (%)	Total	% of variance	Cumulative (%)	Total	% of variance	Cumulative (%)
1	9.697	51.039	51.039	9.697	51.039	51.039	6.164	32.442	32.442
2	3.253	17.119	68.158	3.253	17.119	68.158	5.352	28.170	60.612
3	2.428	12.777	80.935	2.428	12.777	80.935	3.100	16.317	76.929
4	2.122	11.169	92.103	2.122	11.169	92.103	2.883	15.174	92.103
5	0.903	4.751	96.854						
6	0.434	2.283	99.137						
7	0.134	0.703	99.840						
8	0.030	0.160	100.000						
9	1.026×10^{-15}	5.398×10^{-15}	100.000						
10	3.845×10^{-16}	2.024×10^{-15}	100.000						
11	3.419×10^{-16}	1.800×10^{-15}	100.000						
12	2.993×10^{-16}	1.575×10^{-15}	100.000						
13	1.483×10^{-16}	7.803×10^{-16}	100.000						
14	1.212×10^{-16}	6.380×10^{-16}	100.000						
15	-3.269×10^{-17}	-1.721×10^{-16}	100.000						
16	-6.049×10^{-17}	-3.184×10^{-16}	100.000						
17	-3.843×10^{-16}	-2.023×10^{-15}	100.000						
18	-6.688×10^{-16}	-3.520×10^{-15}	100.000						
19	-9.655×10^{-16}	-5.081×10^{-15}	100.000						

Table 18.6 Rotated component matrix

Parameters	1	2	3	4
Mean bifurcation ratio	0.225	0.287	0.870	0.141
Mean stream length ratio	0.670	0.458	–0.330	0.244
Stream frequency	0.698	0.597	0.346	–0.135
Drainage density	**0.952**	0.095	0.114	0.143
Drainage texture	0.675	0.123	–0.302	–0.349
Length of overland flow	–0.937	–0.159	–0.127	–0.120
RHO coefficient	–0.113	0.048	**0.979**	–0.024
Drainage intensity	0.446	0.701	0.414	–0.267
Infiltration number	0.803	0.516	0.285	–0.031
Constant of channel maintenance	–0.944	–0.144	–0.108	–0.100
Relief	–0.043	0.119	–0.211	**0.854**
Relief ratio	0.560	0.745	0.212	0.090
Relative ratio	0.385	0.802	–0.178	–0.302
Ruggedness number	0.757	0.202	–0.063	0.566
Circulatory ratio	–0.250	–0.181	–0.541	–0.766
Elongation ratio	0.108	0.911	0.117	0.296
Form factor	0.071	**0.932**	0.117	0.263
Lemniscate ratio	–0.132	–0.927	–0.132	–0.254
Compactness coefficient	0.239	0.177	0.556	0.767

Bold values specify parameters for that specific component, which are further demonstrated in Table 18.7

on the right site (high priority) and design criteria. The results of this chapter may be applicable to many stakeholders involved in managing water and soil conservation and developing watersheds.

Acknowledgments The authors appreciate the insightful comments provided by the anonymous reviewers, which helped to make this paper better. The US Geological Survey (USGS) is also acknowledged by the authors for providing the satellite data.

Table 18.7 Prioritization and ranking

Parameters	SW 1	SW2	SW 3	SW 4	SW 5	SW 6	SW 7	SW 8	SW 9
Drainage density (component 1)	9	3	7	5	4	8	1	6	2
Form factor (component 2)	1	9	4	5	6	8	3	2	7
Rho coefficient (component 3)	4	1	2	3	9	5	6	7	8
Relief (component 4)	8	6	7	3	9	1	4	5	2
Sum of rankings (x)	22	19	20	16	28	22	14	20	19
Total number of features (y)	04	04	04	04	04	04	04	04	04
C_p (x/y)	5.5	4.75	5	4	7	5.5	3.5	5	4.75
Ranking	7	3	5	2	9	8	1	6	4
Final priority	Medium	Medium	Medium	High	Low	Medium	High	Medium	Medium

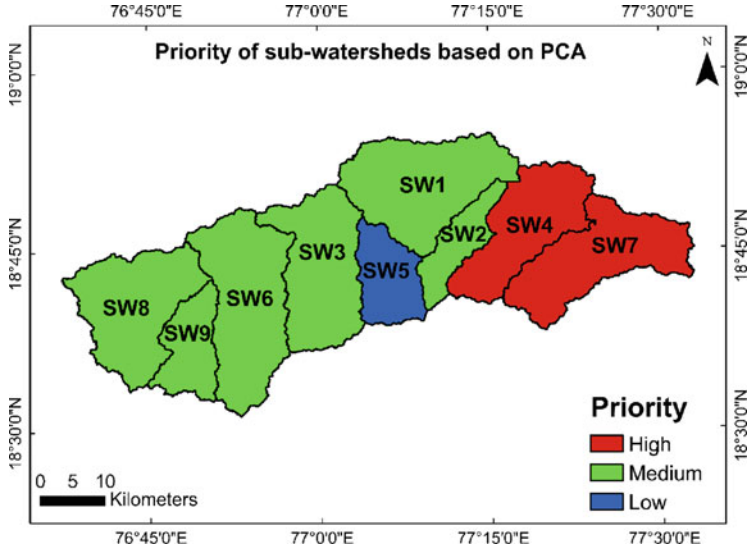

Fig. 18.11 Sub-watersheds' priority using PCA

Table 18.8 Common priority ranking

Parameters	SW 1	SW2	SW 3	SW 4	SW 5	SW 6	SW 7	SW 8	SW 9
Morphometric analysis	Low	High	Low	Medium	Medium	Medium	Medium	Low	High
PCA	Medium	Medium	Medium	High	Low	Medium	High	Medium	Medium
Common priority	–	–	–	–	–	Medium	–	–	–

Data Availability Statement The corresponding author will provide the data created throughout and/or analyzed during the current chapter study upon reasonable request.

Declaration of Interests The authors confirm that they have no known financial or interpersonal conflicts that might have appeared to have an impact on the work described in this chapter.

References

Aamir M, Ahmad Z, Pandey M, Khan MA, Aldrees A, Mohamed A (2022) The effect of rough rigid apron on scour downstream of sluice gates. Watermark 14(14):2223. https://doi.org/10.3390/w14142223

Agarwal CS (1998) Study of drainage pattern through aerial data in Naugarh area of Varanasi district, UP. J Indian Soc Remote Sens 26:169–175

Aher PD, Adinarayana J, Gorantiwar SD (2014) Quantification of morphometric characterization and prioritization for management planning in semi-arid tropics of India: a remote sensing and GIS approach. J Hydrol 511:850–860. https://doi.org/10.1016/j.jhydrol.2014.02.028

Arefn R, Mohir MMI, Alam J (2020) Watershed prioritization for soil and water conservation aspect using GIS and remote sensing: PCA-based approach at northern elevated tract Bangladesh. Appl Water Sci 10:91. https://doi.org/10.1007/s13201-020-1176-5

Bajirao TS, Kumar P, Kumar A (2019) Application of remote sensing and GIS for morphometric analysis of watershed: a review. Int J Chem Stud 7(2):709–713

Burrough PA, McDonnell RA (1998) Principles of geographical information systems. Oxford University Press, Oxford, p 333

Chaudhuri S, Pandey M, Debnath K, Oliveto G (2022) A comparative study on equilibrium scour volume around circular cylinders in clay-sand mixed cohesive beds, at near threshold velocity of sand–an experimental approach. Water Supply. https://doi.org/10.2166/ws.2022.250

Chopra R, Dhiman RD, Sharma PK (2005) Morphometric analysis of sub-watersheds in Gurdaspur district, Punjab using remote sensing and GIS techniques. J Indian Soc Remote Sens 33(4):531–539

Chorley RJ, Malm DEG, Pogorzelski HA (1957) A new standard for estimating drainage basin shape. Am J Sci 225:138–141

Choudhari PP, Nigam GK, Singh SK, Thakur S (2018) Morphometric based prioritization of watershed for groundwater potential of Mula river basin, Maharashtra, India. Geol Ecol Landsc 2(4):256–267. https://doi.org/10.1080/24749508.2018.1452482

Clarke JI (1996) Morphometry from maps. Essays in geomorphology. Elsevier, New York, pp 235–274

Dar RA, Chandra R, Romshoo SA (2013) Morphotectonic and lithostratigraphic analysis of intermontane Karewa basin of Kashmir Himalayas. J Mt Sci 10(1):731–741

Faniran A (1968) The index of drainage intensity: a provisional new drainage factor. Aust J Sci 31(9):326–330

FAO (1988a) FAO Soil Map of the world, Revised Legend With Corrections and Updates World Soil Resource Food and agricultural organization. FAO, Rome, Italy, Report 60

Farhan Y, Anbar A, Al-Shaikh N, Mousa R (2017) Prioritization of semi-arid agricultural watershed using morphometric and principal component analysis, remote sensing, and GIS techniques, the Zerqa River Watershed, Northern Jordan. Agric Sci 8(1):113–148. https://doi.org/10.4236/as.2017.81009

Grohmann CH, Riccomini C, Alves FM (2007) SRTM-based morphotectonic analysis of the Pocos de Caldas alkaline Massif, southeastern Brazil. Comput Geosci 33:10–19

Gunjan P, Mishra SK, Lohani AK, Chandniha SK (2019) The study of morphological characteristics for best management practices over the Rampur watershed of Mahanadi River Basin using prioritization. J Indian Soc Remote Sens. https://doi.org/10.1007/s12524-019-01061-y

Horton RE (1932) Drainage basin characteristics. Trans Am Geophys Union 13:350–361

Horton RE (1945) Erosional development of streams and their drainage basins; hydro physical approach to quantitative morphology. Bull Geol Soc Am 56:275–370

Iqbal M, Sajjad H (2014) Watershed prioritization using morphometric and land use/land cover parameters of Dudhganga Watershed Kashmir Valley India using spatial technology. J Geophys Remote Sens 3:115

Javed A, Khanday MY, Ahmed R (2009) Prioritization of subwatersheds based on morphometric and land use analysis using remote sensing and GIS techniques. J Indian Soc Remote Sens 37: 261–274

John CK, Pu JH, Pandey M, Hanmaiahgari PR (2021a) Sediment deposition within rainwater: case study comparison of four different sites in Ikorodu, Nigeria. Fluids 6(3):124

John CK, Pu JH, Moruzzi R, Pandey M (2021b) Health-risk assessment for roof-harvested rainwater via QMRA in Ikorodu area, Lagos, Nigeria. J Water Clim Change 12(6):2479–2494

Karabulut MS, Özdemir H (2019) Comparison of basin morphometry analyses derived from different DEMs on two drainage basins in Turkey. Environ Earth Sci. https://doi.org/10.1007/s12665-019-8585-5

Kumar SCH, Lal MK (2017) Prioritization of sub-watersheds based on morphometric analysis using geospatial technique in Piperiya watershed, India. Appl Water Sci 7:329–338

Kumar SD, Sharma D, Mundetia N (2015) Morphometric analysis of the Banas River Basin using the geographical information system, Rajasthan, India. J Hydrol 3(5):47–54

Kushwaha N, Elbeltagi A, Mehan S, Malik A, Yousuf A (2022) Comparative study on morphometric analysis and RUSLE-based approaches for micro-watershed prioritization using remote sensing and GIS. Arab J Geosci 15:564. https://doi.org/10.1007/s12517-022-09837-2

Magesh NS, Chandrasekar N (2012) GIS model-based morphometric evaluation of Tamiraparani subbasin, Tirunelveli district, Tamil Nadu, India. Arab J Geosci. https://doi.org/10.1007/s12517-012-0742-z

Mangan P, Haq MA, Baral P (2019) Morphometric analysis of watershed using remote sensing and GIS—a case study of Nanganji River Basin in Tamil Nadu, India. Arab J Geosci 12:202. https://doi.org/10.1007/s12517-019-4382-4

Melton M (1957) An analysis of the relations among elements of climate, surface properties and geomorphology. Project NR 389-042, technical report 11, Columbia University, Technical Report, 11, Project NR 389-042

Meshram SG, Sharma SK (2017) Prioritization of watershed through morphometric parameters: a PCA-based approach. Appl Water Sci 7(3):1505–1519. https://doi.org/10.1007/s13201-015-0332-9

Meshram SG, Sharma SK (2018) Application of principal component analysis for grouping of morphometric parameters and prioritization of watershed. Hydrol Model 2018:447–458. https://doi.org/10.1007/978-981-10-5801-1_31

Mfwango LH, Kisiki CP, Ayenew T, Mahoo HF (2022) The impact of land use/cover change on surface runoff at Kibungo sub-watershed of Upper Ruvu watershed in Tanzania. Environ Challenges 7:100466

Miller VC (1953) A quantitative geomorphologic study of drainage basin characteristics in the Clinch mountain area, Virginia and Tennessee. Technical report 3. Columbia University, New York, pp 389–402

Nigam GK, Tripathi MP, Ambast SK, Kumar L, Khalkho D (2017) Morphometric analysis of drainage basin using aerial photographs: a case of Karun Watershed of Seonath Subbasin of Chhattisgarh. Int J Adv Biol Res 7(3):623–629

Nitheshnirmal S, Bhardwaj A, Dineshkumar C, Rahaman SA (2019) Prioritization of erosion prone micro-watersheds using morphometric analysis coupled with multi-criteria decision making. PRO 24(1):11

Nookaratnam K, Srivastava YK, Venkateswarao V, Amminedu E, Murthy KSR (2005) Check dam positioning by prioritization of micro-watersheds using SYI model and morphometric analysis remote sensing and GIS perspective. J Indian Soc Remote Sens 33(1):25–38

Obi RGE, Maji AK, Gajbhiye KS (2002) GIS for morphometric analysis of drainage basins. GIS India 4(11):9–14

Ozdemir H, Bird D (2009) Evaluation of morphometric parameters of drainage networks derived from topographic maps and DEM in point floods. Environ Geol 56:1405–1415

Patel D, Srivastava PK (2013) Flood hazards mitigation analysis using remote sensing and GIS correspondence with town planning scheme. Water Resour Manag 27:2353–2368

Pophare AM, Balpande US (2014) Morphometric analysis of Suketi river basin, Himachal Himalaya, India. J Earth Syst Sci 123:1501–1515

Prakash K, Mohanty T, Singh S, Chaubey K, Prakash P (2016) Drainage morphometry of the Dhasan river basin, Bundelkhand craton, Central India using remote sensing and GIS techniques. J Geom 10:121–132

Rahman MM, Zaman MN, Biswas PK (2022) Optimization of significant morphometric parameters and sub-watershed prioritization using PCA and PCA-WSM for soil conservation: a case study in Dharla River watershed, Bangladesh. Model Earth Syst Environ 8:2661–2674. https://doi.org/10.1007/s40808-021-01255-9

Rai PK, Mishra VN, Mohan K (2017) A study of morphometric evaluation of the Son Basin, India using geospatial approach. Remote Sens Appl Soc Environ 7:9–20

Redvan G, Mustafa U (2021) Flood prioritization of basin based on geomorphometric properties using principal component analysis, morphometric analysis and redvan's priority methods: a case study of harshit river basin. J Hydrol. https://doi.org/10.1016/j.jhydrol.2021.127061

Sarangi A, Madramootoo CA, Enright P (2003) Development of user interface in ArcGIS for estimation of watershed geomorphology. CSAE/SCGR 2003 meeting, paper No. 03. pp 120–130

Schumm SA (1956) Evaluation of drainage system and slopes in badlands at Perth Amboy, New Jersey. Geol Soc Am Bull 67(5):597–646

Shankar MS, Pandey M, Shukla AK (2021) Analysis of existing equations for calculating the settling velocity. Watermark 13(14):1987

Sharm SK, Gajbhiye S, Tignath S (2015) Application of principal component analysis in grouping geomorphic parameters of a watershed for hydrological modelling. Appl Water Sci 5:89–96. https://doi.org/10.1007/s13201-014-0170-1

Sharma SK, Gajbhiye S, Prasad T (2009) Identification of influential geomorphological parameters for hydrologic modeling. Science 3:9–16

Sharma SK, Rajput GS, Tignath S, Pandey RP (2010) Morphometric analysis and prioritization of a watershed using GIS. J Ind Water Res Soc 30(2):33–39

Shekar PR, Mathew A (2022a) Morphometric analysis for prioritizing sub-watersheds of Murredu River basin, Telangana State, India, using a geographical information system. J Eng Appl Sci 69:44. https://doi.org/10.1186/s44147-022-00094-4

Shekar PR, Mathew A (2022b) Evaluation of morphometric and hypsometric analysis of the Bagh river basin using remote sensing and geographic information system techniques. Energy Nexus 7:100104

Shivashankar M, Pandey M, Zakwan M (2022) Estimation of settling velocity using generalized reduced gradient (GRG) and hybrid generalized reduced gradient–genetic algorithm (hybrid GRG-GA). Acta Geophys 2022:1–11

Singh S (1972) Altimetric analysis - a morphometric technique of landform study. Natl Geogr 7:59–68

Singh P, Thakur J, Singh UC (2013) Morphometric analysis of morar river basin, madhya pradesh, India, using remote sensing and GIS techniques. Environ Earth Sci 68:1967–1977

Singh S, Kanhaiya S, Singh A, Chaubey K (2018a) Drainage network characteristics of the Ghaghghar River Basin (GRB), Son Valley, India. Geol Ecol Landsc. https://doi.org/10.1080/24749508.2018.1525670

Singh S, Kumar S, Mittal P, Kanhaiya S, Prakash P, Kumar R (2018b) Drainage basin parameters of Bagh river, a sub-basin of Narmada river, Central India: analysis and implications. J Appl Geochem 20(1):91–102

Singh WR, Barman S, Trikey G (2021) Morphometric analysis and watershed prioritization in relation to soil erosion in Dudhnai watershed. Appl Water Sci. https://doi.org/10.1007/s13201-021-01483-5

Smith KG (1950) Standards for grading texture of erosional topography. Am J Sci 248:655–668. https://doi.org/10.2475/ajs.248.9.655

Strahler AN (1952) Hypsometric analysis of erosional topography. Geol Soc Am Bull 63:1117–1142

Strahler AN (1957) Quantitative analysis of watershed geomorphology in drainage basin morphometry. Trans Am Geophys Union 38(6):913–920

Strahler AN (1964) Quantitative geomorphology of drainage basins and channel networks. In: Chow V (ed) Handbook of applied hydrology. McGraw Hill, New York, pp 439–476

Thapliyal A, Panwar A, Kimothi S (2017) Prioritization based on morphometric analysis in Alaknanda Basin. Glob J Sci Front Res H Environ Earth Sci 17(3):29–34

Withanage W, Dayawansa NDK, De Silva RP (2014) Morphometric analysis of the Gal Oya river basin using spatial data derived from GIS. Trop Agric Res 26:175–188

Yadav SK (2014) Morphometric analysis of Upper Tons basin from Northern Foreland of Peninsular India using CARTOSAT satellite and GIS. Geocarto Int 29(8):895–914. https://doi.org/10.1080/10106049.2013.868049

Chapter 19
Flood Modelling of Krishna River at Sangli Using HEC-RAS

Girish Biradar and Swati Bhave

Abstract A flood occurs when water overflows and submerges ordinarily dry terrain. When the flow rate of a river exceeds the capacity of the river channel, particularly near bends or meanders, flooding can occur. As a result, settlements are destroyed, human lives are harmed, and infrastructure and public services are lost. It is necessary to model flood plains in order to determine the flood plain and its extent in advance of taking adequate flood mitigation measures. Decision makers can make better decisions about how to effectively deploy resources to prepare for catastrophes and improve the quality of life by assessing the degree of floods and floodwater inundation. The software created models from the HEC-RAS simulations are extremely useful in a variety of ways, including determining the extent of floods, associating high flood levels with the design and planning of hydraulic structures, and generating flood plain maps that can be used in town planning or estimating the approximate amount of damages. The objective of this study was to map flood inundation areas along the Krishna River. Using the HEC-RAS model, ArcGIS for spatial data processing, and Ras mapper for creating geometry, the flooded areas along the Krishna River were mapped based on peak flows for different return periods. The lands around the Krishna River were simulated to be inundated and results from modelling showed that 7.1 km^2, 8.22 km^2, 9.2 km^2 area is inundated for return period of 25-, 50-, 100-year, respectively. Proper land use management and tree plantations are crucial in reducing the negative effects of floods, especially in low-lying flood-prone areas. The findings of this study will assist the responsible agencies in developing plans based on flood plain mapping and hazard levels in the area.

Keywords Hydrological hazards · Flood modeling · HEC-RAS

G. Biradar (✉) · S. Bhave
Visvesvaraya National Institute of Technology, Nagpur, India

M. Pandey et al. (eds.), *River Dynamics and Flood Hazards*, Disaster Resilience and Green Growth, https://doi.org/10.1007/978-981-19-7100-6_19

19.1 Introduction

Different forms of hydrological hazards globally create a wide range of scientific and governmental challenges. Hydrological hazards are defined as extreme phenomena linked to the occurrence, transport, and distribution of water (John et al. 2021a, b). Given the complexity of nonlinear hydrometeorological and hydroclimatological processes, it is essential to use modern scientific research and technical advancements to increase our understanding of hydrological hazards and our capacity to respond to droughts and floods (Pu et al. 2021; Wallwork et al. 2022).

A flood is an abnormally high level of flow of water caused by run-off, which is usually caused by excessive rainfall. The overflowing river exceeds its banks, flooding the surrounding region (Shankar et al. 2021; Shivashankar et al. 2022). Floods cause substantial harm every year, ranging from property damage to economic disruption to loss of life. Floods are a major threat in India. More than 40 million hectares of the whole geographical area of 329 million hectares is flood-prone. Floods are a common occurrence that results in a significant loss of life and damage to property, infrastructure, and public services each year. One-dimensional steady flow analysis will be used in this work to determine the behaviour and significant information of river flood profiles. The RAS Mapper is a HEC-RAS tool which has the ability to create geometry file without using any extension like HEC-GeoRAS. With the help of RAS Mapper, stream centre line, bank lines. Flow path lines, and cross-section cut lines can be digitized on a particular river, which is useful to get the necessary information to perform 1D steady flow analysis. It is useful for floodplain mapping. Inundation depth and flood inundation boundary can be created in RAS Mapper. Also, flood inundation length and area can be known using RAS Mapper.

The aim of the study is to evaluate the flood risk in Upper Krishna basin especially near sangli region and develop floodplain map to further assist responsible authority in flood management efforts. The objectives of the research have been formulated as follows:

- Flood inundation maps are generated using a mix of hydrodynamic modelling and spatial analysis tools accessible in geographical information systems.
- Calculation of discharge for future floods of time period 25-, 50-, 100 years using flood frequency analysis.
- To suggest the appropriate safety measure to counter the floods.

19.2 Study Area

The Krishna basin (Fig. 19.1) includes the Upper Krishna basin, which has an aerial size of 55,537.60 km^2. Within the states of Maharashtra and Karnataka, the basin is located between 15°3′20″ and 18° 6′20″ north latitudes and 73°39′30″ and 77°23′10″ east longitudes. The basin region is made up of 12 districts from both states, with

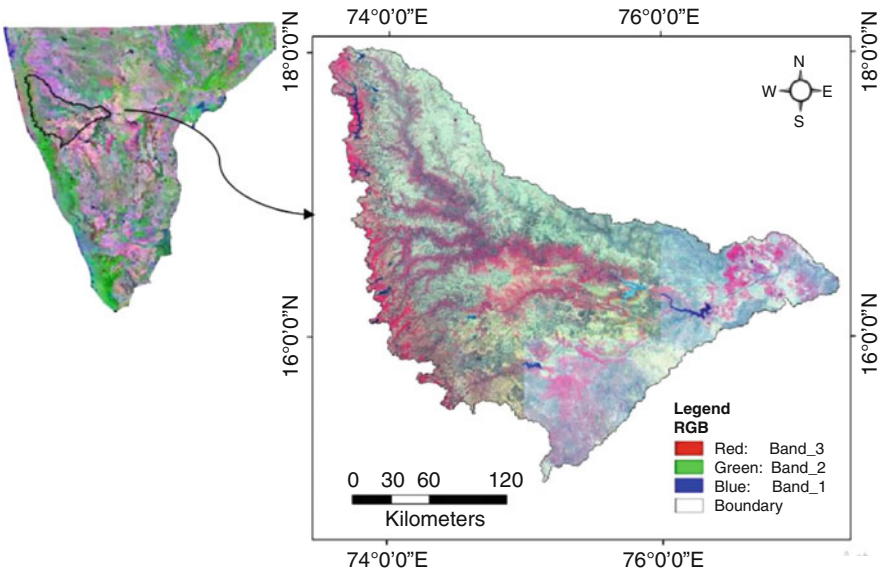

Fig. 19.1 Location of upper Krishna basin

nine districts in Karnataka (Bagalkot, Belgaum, Bijapur, Dharwad, Gadag, Gulbarga, Haveri, Koppal, and Raichur) and three districts in Maharashtra (Kolhapur, Sangli, and Satara). The basin is generally triangular in shape, with the Western Ghats forming its western boundary, the ridges parted by the Bhima basin forming its northern boundary, and the Tungabhadra basin forming its southern boundary. The main Krishna River begins near Mahabaleshwar in Maharashtra's Western Ghats at an elevation of 1360 m above sea level and flows for 642.22 km until joining the Bhima River at Sangam village in Gulbarga district.

Due to significant rainfall, the upper Krishna basin area near Sangli was flooded during the high flood period of 2019. As a result, a 15-kilometre stretch of the Krishna River was chosen for the research in order to define the floodplain border and generate a flood risk map.

19.3 Methodology

The idea of flood analysis includes determining a risky place, simulating a flood occurrence, identifying the nature of the hazard, and providing a corrective remedy. The following methods should be followed to achieve the flood analysis' goals (Fig. 19.2).

Sources from which data was obtained and software used with their purpose are mentioned in Table 19.1.

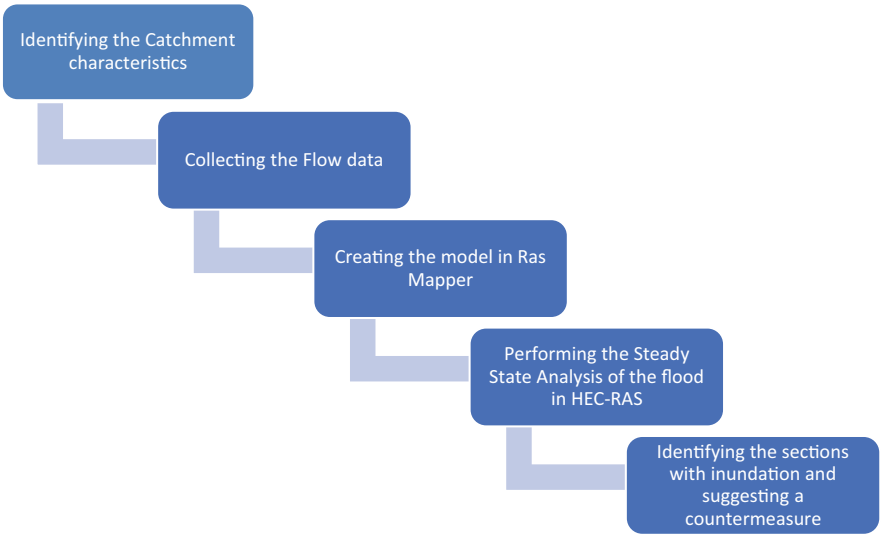

Fig. 19.2 Methodology to be followed to perform flood analysis

Steps involved in performing steady flow analysis and floodplain mapping using HEC-RAS and Ras Mapper. The approach to floodplain mapping is followed by two stages.

Stage 1: Creating the Geometry

Step 1: Set projection.

Add the projection file from the spatial reference organization's website as the initial step. Set the units to SI.

Step 2: Create new terrain.

By incorporating DEM into this stage, a new terrain has been generated. Web imagery layers may be readily added to RAS Mapper to check whether the terrain is in the correct projection. It may be observed by adjusting the layer's transparency.

Step 3: Add new geometry

Define the river's centreline, bank lines, flow path lines, and cross-section cut lines in this stage. The main river, which is 11.2 km long, and a branch, which is 3.8 km long, have both been digitized. On the main and branch rivers, a total of 32 cross-section cut lines have been digitized, with ten cross-section cut lines on the branch and 22 cross-section cut lines on the main river.

Stage 2: HEC-RAS Model Execution

In stage 2 open the geometry data in the geometric data editor window.

Step 1: Manning's *n* value

Add manning's *n* value. The manning's roughness coefficient for banks has been set at 0.05 and for channels at 0.025, based on a prior research in the same location.

Step 2: Bridge creation

Table 19.1 Data collection and software used

Sr. No.	Data	Purpose	Source
1	30 m resolution DEM	To extract elevation data of the study area	bhuvan.nrsc.gov.in
2	Projection file	To give downloaded DEM projection	Spatialreference.org
3	Flow data	To perform 1-D steady state analysis	CWC.gov.in
4	Manning's Roughness coefficient	To create similar condition as of present in actual river bed	Literature review
	Software used	Purpose	Source
5	HEC-RAS (6.1)	Flow Analysis	US Army Corps of Engineers
6	Ras Mapper	Floodplain mapping	US Army Corps of Engineers

Using the bridge culvert data editor window, a bridge has been added over the river at its corresponding positions. Using the deck/roadway data editor, the openings were roughly built. Due to the lack of bridge information, piers have been created roughly using the bridge design editor.

Step 3: Enter maximum discharge data

In the steady flow data editor window, maximum discharge data has been provided. For 25-, 50-, and 100-year return periods, the maximum value of discharge measured at the Karad discharge gauging station and the Samdoli discharge gauging station has been entered as input. At the river's downstream end, normal depth has been defined as a border requirement. Also, the downstream slope has been set at 0.002. It should be less than 0.1 for 1-D analysis. Because the flow is somewhat flat, the flow regime has been considered to be subcritical.

Step 4: Run steady flow simulation

The steady flow simulation was then carried out, while floodplain mapping was also carried out.

Step 5: Viewing the results

Tables and charts have been used to clarify the results of the 1-D steady flow study. Floodplain maps may be made with the use of RAS Mapper. The attribute tables can be used to determine the length and size of the flood inundation border.

Calculation of Maximum Discharge Data

From the available maximum discharge data for each year, maximum discharge data for 25-, 50-, and 100-year return period is calculated using flood frequency analysis.

Step 1: Obtain maximum discharge data for sufficient amount of years (N) (40–50 years).

Step 2: Arrange the obtained discharge in the descending order and give them rank number (M).

Step 3: Calculate exceedance probability (P) for each ranked annual peak discharge, by using the following formula

$$P = \frac{m}{N+1} \tag{19.1}$$

Step 4: Calculate return period (T) for each ranked annual peak discharge, which is basically reciprocal of exceedance probability (P).

$$T = \frac{1}{P} \tag{19.2}$$

Step 5: Now plot the graph such that discharges Q (m^3/s) on X-axis against return period (T) on Y-axis in Microsoft excel. Try to find a curve fitting maximum points in the graph. Now by using equation of this curve you can calculate discharges for required time period.

19.4 Results and Discussion

The result of the 1-D steady flow analysis includes floodplain maps for different return periods calculated using flood frequency analysis. Table 19.2 contains information about how much area is inundated for 25-, 30-, and 100-year return period.

Table 19.2 Inundation area and length for corresponding return period

Return period	Inundation area	Inundation length
25-year return period	7.1 km^2	95 km
50-year return period	8.22 km^2	107 km
100-year return period	9.2 km^2	108 km

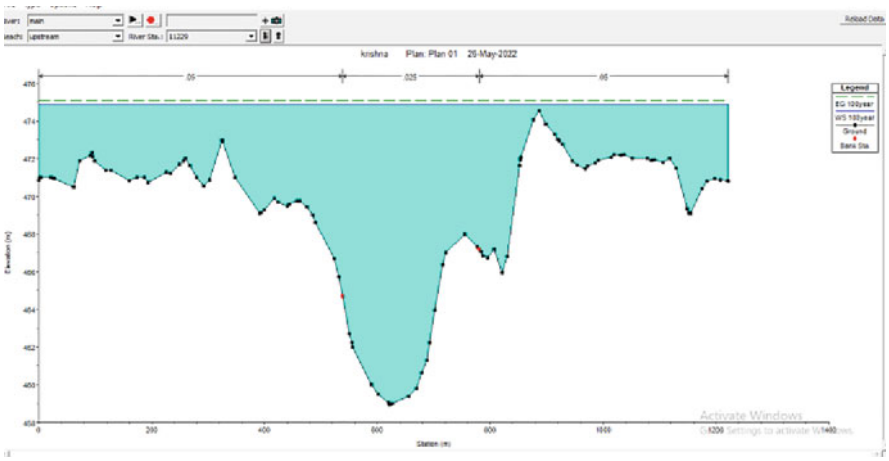

Fig. 19.3 Water profile of cross-section at station number 11229

HEC-RAS also gives output in the form of graph. This graph contains cross-section and water elevation in that cross-section for different time period. Some of the cross-sections are given below which are in urgent need of repair because of over toppling of water from banks.

Figure 19.3 is a graphical representation that shows water profile of cross-section on Krishna River. The station number of cross-section is 11229 that mean it is situated at upstream. In this cross-section water profile is created by a flood of 100-year return period. From the figure it is observed that the banks are overtopped. The maximum water surface elevation is found to be 474.91 m.

Similarly cross-sections at station number 10862, 10496, and 10157 were also showing inadequacy to contain the 100-year flood, so these cross-sections also need repair immediately.

19.5 Conclusion

- The flood frequency study yielded 6280, 7410, and 8530 cumec for the Main River, i.e. Krishna, for the 25-, 50-, and 100-year return periods, respectively. Flood frequency study yielded 2700, 3100, and 3480 cumec for a branch of the Main River, the Warna tributary, for 25-, 50-, and 100-year return periods, respectively.
- For the aforementioned 25-, 50-, and 100-year return period floods, the flooded areas estimated using HEC-RAS were of the order of 7.1, 8.22, and 9.2 km^2, respectively.
- The water surface elevation upstream has been found higher than downstream.
- Following an examination of floodplain maps and cross-section graphs, it was discovered that cross-sections on the upstream side were unable to absorb flood, resulting in a greater likelihood of water overtopping. The river stretch near Krishna Nagar in Sangli needs to be repaired immediately. It can be accomplished by reducing encroachment on the river's floodplain or by constructing a levee along the river's bank.
- It can be observed that left bank of river is capable of handling the increased discharge but right bank is in need of repair.
- The upper Krishna basin requires river channelization. It improves river channel capacity by deepening and expanding the channel, lowering floodwater levels. Straightening the river channel will help eliminating the rivers' severe meandering issues and boost flow velocity.
- The floodplain maps were made without the need of the pricey ARC-GIS and HEC-GeoRAS extension, demonstrating the usability of the RAS Mapper tool. In addition, the flood inundation area and length of the inundation border may be easily determined.

References

John CK, Pu JH, Moruzzi R, Pandey M (2021a) Health-risk assessment for roof-harvested rainwater via QMRA in Ikorodu area, Lagos, Nigeria. J Water Clim Change 12(6):2479–2494

John CK, Pu JH, Pandey M, Hanmaiahgari PR (2021b) Sediment deposition within rainwater: case study comparison of four different sites in Ikorodu, Nigeria. Fluids 6(3):124

Pu JH, Wallwork JT, Khan M, Pandey M, Pourshahbaz H, Satyanaga A, Hanmaiahgari PR, Gough T (2021) Flood suspended sediment transport: combined modelling from dilute to hyper-concentrated flow. Watermark 13(3):379

Shankar MS, Pandey M, Shukla AK (2021) Analysis of existing equations for calculating the settling velocity. Watermark 13(14):1987

Shivashankar M, Pandey M, Zakwan M (2022) Estimation of settling velocity using generalized reduced gradient (GRG) and hybrid generalized reduced gradient–genetic algorithm (hybrid GRG-GA). Acta Geophys. https://doi.org/10.1007/s11600-021-00706-2

Wallwork JT, Pu JH, Kundu S, Hanmaiahgari PR, Pandey M, Satyanaga A, Pandey M, Satyanaga A, Amir Khan M, Wood A (2022) Review of suspended sediment transport mathematical modelling studies. Fluids 7(1):23

Chapter 20
Development of Machine Learning Based Flood Prediction Model for Godavari River Basin

V. Manohar Reddy and Litan Kumar Ray

Abstract Floods are the most prominent and lethal event of this century. Unfortunately, the lack of a robust flood prediction framework has led to the loss of human life and infrastructures. Flood prediction models are very important for assessing and managing extreme flood events. They provide robust and accurate predictions that can be utilized for policy analysis and evacuation planning. Due to the limitations of long-term observed rainfall and runoff dataset, which are the necessity of the traditional statistical and physical models, the use of data-driven models has increased. Modern data-driven models, such as those developed by machine learning, are more advantageous due to their ability to develop models with minimal inputs. They can also numerically formulate flood nonlinearity using historical data. Therefore, a support vector machine (SVM) algorithm was used to develop the flood prediction model in this study. The developed flood prediction model was then used to simulate the flood at three gauging stations namely, Purna, GR Bridge and Yelli of the Godavari river basin. The model was calibrated with four historical flood events and validated with two flood events. Historical gridded rainfall data from IMD is given as input to the model for the simulation of floods. The performance evolution of the developed SVM model was done with the NSE, Error in Peak and Error in time to Peak. In calibration, the average NSE was obtained as 0.96, 0.97 and 0.96 at the G.R. Bridge, Purna and Yelli, respectively, and in validation, it was found to be 0.93, 0.95 and 0.87 respectively. The error in time to peak was found to be zero except for one event at Yelli. The error in magnitude of peak flow at each gauging location was less than 10% in both calibration and validation, which shows that the developed SVM models were good enough to predict future flood events at respective gauging locations. The bias corrected rainfall of best performing GCM and multimodel ensemble (MME) mean of CMIP6 GCM rainfall were used to generate future flood events in the Godavari river basin. A considerable flood peak reduction around 10%–37% was observed for the future flood events under both the scenarios for the MME mean rainfall and best performing GCMs rainfall in comparison to

V. Manohar Reddy · L. K. Ray (✉)
Department of Civil Engineering, National Institute of Technology Warangal, Warangal, India
e-mail: vm721007@student.nitw.ac.in; litan@nitw.ac.in

M. Pandey et al. (eds.), *River Dynamics and Flood Hazards*, Disaster Resilience and Green Growth, https://doi.org/10.1007/978-981-19-7100-6_20

historical floods. Future bias corrected MME mean was on low side compared to the historical rainfall and this results the reduction of future flood peaks in the study area.

The HEC-RAS model was also used to prepare the flood inundation maps from the output of the SVM model. Future flood inundation maps were generated for the simulated flood events from MME mean over the period 2070–2100. The future flood inundation maps showed that the river reach from GR Bridge to Yelli is vulnerable to floods. The extent of flood maps is more for the SSP585 than SSP245 for the period of 2070–2100. Nanded town, on the bank of river Godavari is going to inundate for the above-mentioned period under high emission scenario (SSP585). The results of this study may help the local stakeholders and organizations to better understand the flood behaviour in the Godavari river basin and are useful to form mitigation strategies for the future.

Keywords Flood prediction model · Godavari basin · Support vector machine (SVM) algorithm

20.1 Introduction

Floods are the most common and destructive natural hazard of this century. The analysis and prediction of floods are two key factors to implement the mitigation measures of flood hazard. Unfortunately, the lack of a robust flood prediction framework has led to the loss of human life and infrastructures. In this regard, the flood hazard and flood risk maps are key elements for flood risk management around the world. These maps are used to identify the areas of potential damage and minimize the impact of floods (Pourghasemi et al. 2017). Management and assessment of flood risks are the most important two steps to improve the efficiency of any flood operation. Understanding the flood and its effects are crucial factors that are considered when it comes to formulating flood prevention measures (Xie et al. 2017; John et al. 2021a, b; Pu et al. 2021; Wallwork et al. 2022). It is also important to predict the exact time to reach the floods to its peak to improve the management of flood related hazards. Flood prediction models are widely used in assessing the likelihood of a disaster and developing effective evacuation strategies. They can also contribute to the formulation of policies and procedures related to water management. These models are able to mimic the complex mathematical representations of basin behaviour and physical processes.

Despite the capabilities of physical models to predict various types of flooding scenarios, they are typically not capable of providing a short-term prediction due to the complexity of their computation (Kim et al. 2015). This is because they often require the use of various hydro-geological monitoring datasets. In addition, developing physical models require high expertise and computation time (Nayak et al. 2005). The drawbacks of these physical models encourage the use of data-driven models, such as machine learning models (Mekanik et al. 2013). These models can perform variety aspects of floods, such as calculating the flood peak, volume and nonlinearity.

Support vector machine (SVM) is one of the popular machine algorithms, which is widely used for flood modelling studies (Mosavi et al. 2018). It is a supervised machine learning algorithm, which works based on the statistical learning theory and the structural risk minimization (Vapnik 1999). SVM trains models with non-probabilistic linear techniques to minimize the errors and maximize the geometric margin. SVM is used to develop the flood prediction model with historical precipitation data. The developed flood prediction model was further used for predicting the future flood events. The main aim of this study is to prepare a machine learning based flood prediction model which can be useful for future flood generation. The same model results can be used to generate the future flood hazard maps for the study area.

In the present study, the Coupled Model Intercomparison Project phase 6 (CMIP6) precipitation data were used for predicting the future flood events. Due to the exiting bias in GCMs data, empirical quantile mapping was used for bias correction. In order to find the risk of future flood events in terms of return period, at-site flood frequency analysis was performed in the study area. Kolmogorov–Smirnov goodness of fit test was used for finding the best distribution among the candidate distributions. The hazard map of the future flood events was generated by using an open-source software Hydrologic Engineering Center- River Analysis System (HEC-RAS). It is a hydro-dynamic model which works in 1D and 2D modelling with better prediction skills of flood event characteristics (Quirogaa et al. 2016).

20.2 Study Area

The Godavari River, which originates in Nasik, is one of the major rivers in southern peninsular India. The study area lies in between the latitudes 18.70° N and 20.50° N and longitudes 73.48° E and 77.62° E (Fig. 20.1). The average annual precipitation is ranging from 1000 mm to 1300 mm. The Indian summer monsoon contributes major percentage of rainfall over the basin. A change in the Indian summer monsoon rainfall due to climate change may create hydrological and environmental problems in the basin. During the monsoon, the river overflows its banks for some parts in upper and middle parts of the basin. To address the future flood problems in the basin, the flood prediction models were developed in the upper and middle Godavari river basins.

20.3 Data Used

The daily precipitation data were collected for the period of 1951–2020 from Indian Meteorological Department (IMD) (Pai et al. 2014). The future precipitation data was collected from CMIP6 GCMs (https://esgf-node.llnl.gov/projects/cmip6/) for

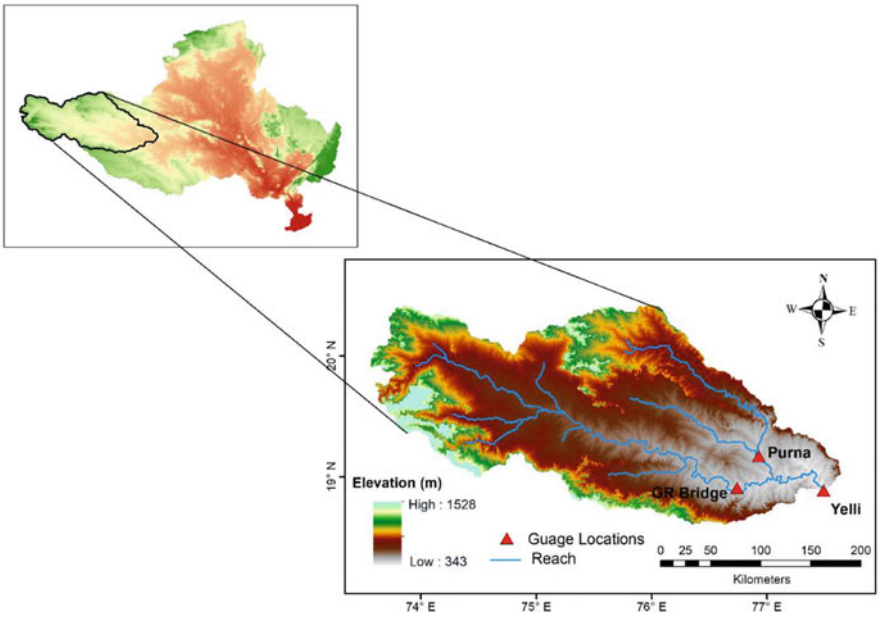

Fig. 20.1 Study area map

Table 20.1 List of CMIP6 GCMs used in the present study

S No	Model Id	Atmospheric resolution (lat × long)	Name of originating institute	
1	CMCC-CM2-SR5	0.90° × 1.25°	Fondazione Centro Euro-Mediterraneo sui Cambiamenti Climatici, Italy	Lovato and Peano (2020)
2	EC-EARTH3	0.70° × 0.70°	EC-EARTH consortium published at Irish Centre for High-end Computing, Netherlands/Ireland	EC-Earth Consortium (EC-Earth) (2019a)
3	EC-EARTH3-VEG	0.70° × 0.70°	EC-EARTH consortium published at Irish Centre for High-end Computing, Netherlands/Ireland	EC-Earth Consortium (EC-Earth) (2019b)
4	MPI-ESM 1-2 HR	0.94° × 0.94°	Max Planck Institute for Meteorology, Germany	Schupfner et al. (2019)
5	MRI-ESM 2-0	1.12° × 1.13°	Meteorological Research Institute, Japan	Yukimoto et al. (2019)

historical period of 1951–2014 and for the future period of 2015–2100. In the present analysis, five low resolution GCMs were considered for the analysis, and the list of GCMs was given in Table 20.1. The daily stream flow data at G R Bridge, Purna and Yelli of Godavari river basin was obtained from India-Water resources

Information System (WRIS). Shuttle Radar Topography Mission (SRTM) 90 × 90 m resolution digital elevation map was collected from https://srtm.csi.cgiar.org/portal.

20.4 Methodology

In the present study, a machine learning model was developed between precipitation and flood events in the basin. Support vector machine (SVM) framework was used for the model setup. The SVM model was first calibrated with four flood events and validated with two more flood events. Three different SVM models were developed at the three gauging locations. The developed SVM model was used to generate the future flood events by taking the future bias corrected precipitation over the basin. The generated future flood events were further used to generate the flood inundation maps over the study area. HEC-RAS software was used for the generation of flood inundation maps.

20.5 SVM Model Setup

Vapnik has first developed the SVM model and it gains popularity in mid-1990s (Vapnik 1999). SVM model is better in reducing the overfitting and enables better simulations by using the structural risk minimization principle (Vapnik 1999). It predicts the nonlinearity of the observed data by using an alternative loss function in a high dimensional feature space. SVM operates with the help of kernels. The radial basis function (RBF) has proved to be the best kernel function for regression problems. SVM has been further explored in hydrology applications like flood forecasting (Li et al. 2016), flood prediction (Mosavi et al. 2018), groundwater level forecasting (Liu et al. 2021), etc. For more details about SVM, readers can refer to (Anandhi et al. 2009; Ghosh 2010). In the present analysis, Nash–Sutcliffe efficiency (NSE), peak flow error and time to peak error were used for the performance evolution of the developed SVM model. The performance indicators were given in Table 20.2.

20.6 Bias Correction

CMIP6 GCMs future precipitation simulations have some bias due to the model structure and resolution (Raju and Kumar 2020). To remove this bias Empirical quantile mapping method was used in the present study. EQM generally reduce the discrepancies between the observed and GCM simulations by matching the CDF of each other (Piani et al. 2010).

Bias corrected data will be computed by Eq. (20.1).

Table 20.2 Performance evaluation metrics considered for the analysis

Performance indicators	Formula
Nash–Sutcliffe efficiency	$\mathrm{NSE} = 1 - \frac{\sum_{i=1}^{n} \left(Q_i^{\mathrm{sim}} - Q_i^{\mathrm{obs}}\right)^2}{\sum_{i=1}^{n} \left(Q_i^{\mathrm{obs}} - \left(Q_i^{\mathrm{obs}}\right)_{\mathrm{avg}}\right)}$
Peak flow error	$\Delta Q_p = \left(\frac{Q_p^{\mathrm{sim}} - Q_p^{\mathrm{obs}}}{Q_p^{\mathrm{obs}}}\right) \times 100$
Time to peak error	$\Delta t_p = \left(\frac{t\left(Q_p^{\mathrm{sim}}\right) - t\left(Q_p^{\mathrm{obs}}\right)}{t\left(Q_p^{\mathrm{obs}}\right)}\right) \times 100$

where Q_i^{obs} = Observed flow value, Q_i^{obs} = Simulated flow value, Q_p^{sim} = Simulated flood peak value, Q_p^{obs} = Observed flood peak value

$$x_m^*(t) = F_o^{-1}\{F_m\,[x_m(t)]\} \tag{20.1}$$

where $x_m^*(t)$ = bias corrected model output, $x_m(t)$ = raw model output, F_m and F_0 are the cumulative distribution functions (CDFs) of $x_m(t)$ and $x_o(t)$, respectively.

20.7 Ranking of GCMs

The bias corrected precipitations were not same for different GCMs in general. To reduce the uncertainties from bias corrected rainfall ranking of GCMs were employed. In the present study Technique for Order Preference by Similarity to an Ideal Solution (TOPSIS) was used for the ranking of GCMs. It is based on the principle that the chosen alternative should have the shortest distance from the ideal solution and furthest distance from the anti-ideal solution (Kishore et al. 2016). Nash–Sutcliffe efficiency and NRMSE are used for the performance evolution of bias corrected precipitation data. A payoff matrix (19 × 3) formed between the performance indicators and corresponding GCMs. TOPSIS computes the positive separation measure (D_a^+) (Eq. (20.2)) from the positive ideal solution, the negative separation measure (Eq. (20.3)) (D_a^-) from the negative ideal solution and the closeness index (Eq. (20.4)) C_a. The higher the C_a value, the better the GCM.

The methodology of TOPSIS consists of the following.

1. Compute the Euclidean distance of each alternative from its ideal value (D_a^+)

$$D_a^+ = \sqrt{\sum_{j=1}^{J} \left(w_j f_j(a) - w_j f_j^*\right)^2} \tag{20.2}$$

where $j = 1,2\ldots j$; $f_j(a)$ = normalized value of criterion j for alternative a, f_j^* = Normalized ideal value of criterionj, w_j = weight assigned to the criterion j.

2. Compute the Euclidean distance of each alternative from anti-ideal value (D_a^-)

$$D_a^- = \sqrt{\sum_{j=1}^{J} \left(w_j f_j(a) - w_j f_j^{**} \right)^2} \tag{20.3}$$

where f_j^{**} = normalized anti-ideal value of criterion j.

3. Compute the relative closeness of each alternative is C_a

$$C_a = \frac{D_a^-}{\left(D_a^- + D_a^+ \right)} \tag{20.4}$$

Higher C_a indicates best GCM for the region.

20.8 Multimodel Ensemble (MME) Mean

Bias corrected precipitation from the GCMs are variable with each other due to the complex nature of atmospheric circulation. Raju and Kumar (2020) suggests that multimodel ensemble mean projections reduce the uncertainty regarding the future precipitation. Therefore, in the present analysis multimodel ensemble mean of bias corrected precipitation was used for generation of future flood events. MME mean was calculated by the following equation:

$$r_{\text{MME}} = \frac{1}{n} \sum_{i=1}^{n} r_i \tag{20.5}$$

where r_{MME} = Multimodel ensemble mean, r_i = rainfall of individual GCM, n = Number of GCMs.

20.9 Flood Frequency Analysis

The flood frequency analysis was performed at gauging locations in the study area. Annual maximum series at each location was used for the flood frequency analysis. The extraction of annual maxima is relatively straightforward in regard to independence. Finding the best distribution is vital for frequency analysis. For finding the best fit distribution, nine distributions were considered in the study, namely normal, lognormal, Generalized Extreme Value, Generalized Pareto, Gumbel, Cauchy, logistic, uniform and Pierson type 3 distributions. These distributions were

commonly used distributions and are applicable for at-site and regional flood frequency analysis.

In order to evaluate the adequacy of the selected distribution functions, the goodness of fit was tested using the Kolmogorov–Smirnov test (KS) at 5% significance level (Melo et al. 2009; Wang and Wang 2010). In the KS test, the largest discrepancy between the theoretical ($F_D(Q_i)$) and empirical ($F_e(Q_i)$) cumulative distribution functions of the data set was calculated by using the following equation:

$$D_{\max} = \mathrm{Max}_{i=1}^{n}(F_e(Q_i) - F_D(Q_i)) \tag{20.6}$$

If $D_{\max} < D_\alpha$, the distribution is accepted, where D_α is at significance level for a sample size.

20.10 HEC-RAS 2D Modelling

The Hydrologic Engineering Center's River Analysis System, known as the HEC-RAS, was used for this study. This is used for performing various calculations related to the flow of water. It can be used for performing 1D and 2D unsteady flow calculations, as well as sediment transport modelling and water quality analysis (Costabile et al. 2020). In the present study, 2D unsteady flow modelling was used for the generation of flood hazard maps. It uses shallow water equations to describe the movement of water in response to the forces of friction and gravity (Eqs. (7), (8), and (9)) (Rodi 2017). They are used to represent the conservation of momentum and mass in a plane (Sharma and Regonda 2021).

$$\frac{\partial H}{\partial t} + \frac{\partial p}{\partial x} + \frac{\partial q}{\partial y} = r \tag{20.7}$$

$$\frac{\partial p}{\partial t} + \frac{\partial}{\partial x}\left(\frac{p^2}{h}\right) + \frac{\partial}{\partial y}\left(\frac{pq}{h}\right) = \frac{n^2 pg\sqrt{p^2+q^2}}{h^2} - gh\frac{\partial H}{\partial x} + pf + \frac{\partial}{\rho\partial x}(h\tau_{xx}) + \frac{\partial}{\rho\partial y}(h\tau_{xy}) \tag{20.8}$$

$$\frac{\partial p}{\partial t} + \frac{\partial}{\partial x}\left(\frac{\mathrm{pq}}{h}\right) + \frac{\partial}{\partial y}\left(\frac{q^2}{h}\right) = \frac{n^2 qg\sqrt{p^2+q^2}}{h^2} - gh\frac{\partial H}{\partial y} + qf + \frac{\partial}{\rho\partial x}(h\tau_{xy}) + \frac{\partial}{\rho\partial y}(h\tau_{yy}) \tag{20.9}$$

where H = surface elevation (m), h = water depth (m), p=specific flow in x-direction (m^2/s), q=specific flow in y-direction (m^2/s), r = net rain (m), g = acceleration due to the gravity (m/s^2), n = Manning's roughness coefficient ($s/m^{1/3}$),

ρ = water density (kg/m^3), f = Coriolis parameter (s^{-1}) and τ_{xx}, τ_{yy} and τ_{xy} are the components of the stress tensor.

20.11 HEC-RAS Model Setup

2D modelling performs along and across the river flow. It requires mesh (2D flow area), which discretized the study area into small grid boxes. In the present study, mesh created by 90 × 90 m grid boxes. In the present study two types of boundary conditions were used. Future flood hydrographs were used as upstream boundary conditions at GR Bridge and Purna. Normal depth was used as downstream boundary conditions at Yelli. The present HEC-RAS model computes the flood hazard and vulnerable areas between the area of upstream and downstream locations.

20.12 Results and Discussion

20.12.1 SVM Model Setup and Performance

SVM model was developed at each of the three gauging locations in the study area for discrete flood event prediction. SVM model was calibrated with the four discrete flood events and validated with two more flood events. Tenfold cross validation technique was used for the parameter fitting in the SVM model. SVM model parameters cost, gamma and epsilon were tuned with tenfold cross validation technique, to each of the flood event in calibration. The averaged parameters from the four calibrated events were further used to develop the SVM model at gauging locations. The best model parameters at each gauging location were tabulated in Table 20.3.

Three performance indicators Nash–Sutcliffe efficiency (NSE), peak flow error and time to peak error were used for the developed SVM model performance. The values of performance indicators for calibration and validation were given in Table 20.4, for each flood event at the three gauging locations.

From Table 20.4, it was found that the developed SVM models simulated the flood events satisfactorily at each gauging location. In calibration, the average NSE was obtained as 0.96, 0.97 and 0.96 at the G.R. Bridge, Purna and Yelli, respectively, and in validation, it was found to be 0.93, 0.95 and 0.87, respectively. The peak flow error shows the deviation of the simulated flood peak compared to the

Table 20.3 Best SVM model Parameters at gauging locations

Gauging location	Cost	Gamma	Epsilon
GR Bridge	64	0.1	0.0001
Purna	16	0.01	0.0001
Yelli	8	0.01	0.0001

Table 20.4 Performance results of SVM models at gauging locations (negative sign shows the decrease in percentage.)

Gauging location	Flood event	Calibration			Validation		
		NSE	Error in peak (%)	Error in time to peak	NSE	Error in peak	Error in time to peak
GR bridge	Event 1	0.91	–5.32	0			
	Event 2	0.99	0.01	0			
	Event 3	0.97	0	0			
	Event 4	1	0	0			
	Event 5				0.95	0.72	0
	Event 6				0.92	15.40	0
Purna	Event 1	0.97	–0.02	0			
	Event 2	0.97	0.01	0			
	Event 3	1	0	0			
	Event 4	0.96	2.70	0			
	Event 5				0.95	2.02	0
	Event 6				0.95	–3.48	0.14
Yelli	Event 1	0.93	0	0			
	Event 2	0.99	–12.88	0			
	Event 3	0.95	–0.01	0			
	Event 4	0.99	0.01	0			
	Event 5				0.86	1.64	0
	Event 6				0.82	12.29	0

observed flood peak. The error in time to peak indicator shows the deviation in flood peak date compared to the observed flood peaks. Among the considered flood events at each gauging location, only three flood events had more than a 10% error in peak prediction, and the remaining events showed less than a 10% error in peak prediction. The error in time to peak was observed only in one flood event. The results indicated that the fitted model suitably simulates the flood magnitudes and time to peak. The calibrated and validated events plotted against observed flood events were given in Figs. 20.2, 20.3, and 20.4 at each gauging location. Therefore, the best model parameters were further used to find the future flood events at the gauging locations.

Future flood events were simulated from individual SVM model at the gauging locations. Maximum consecutive 12 days precipitation was extracted from 2070 to 2100, and used for simulation of flood events under SSP245 and SSP585 scenarios. It was observed that maximum flood volumes were observed under SSP585 at all the gauging locations. Flood events were also calculated for the best performing GCM (EC-Earth3-Veg) in future under SSP245 and SSP585 scenarios. The obtained future flood events were given in Figs. 20.5 and 20.6 for SSP245 and SSP585 scenarios, respectively, from the best performing GCM EC-Earth3-VEG and MME mean. From Figs. 20.5 and 20.6, it was found that flood peak is more for the flood events simulated form EC-Earth3-VEG and flood magnitude is more for the flood events

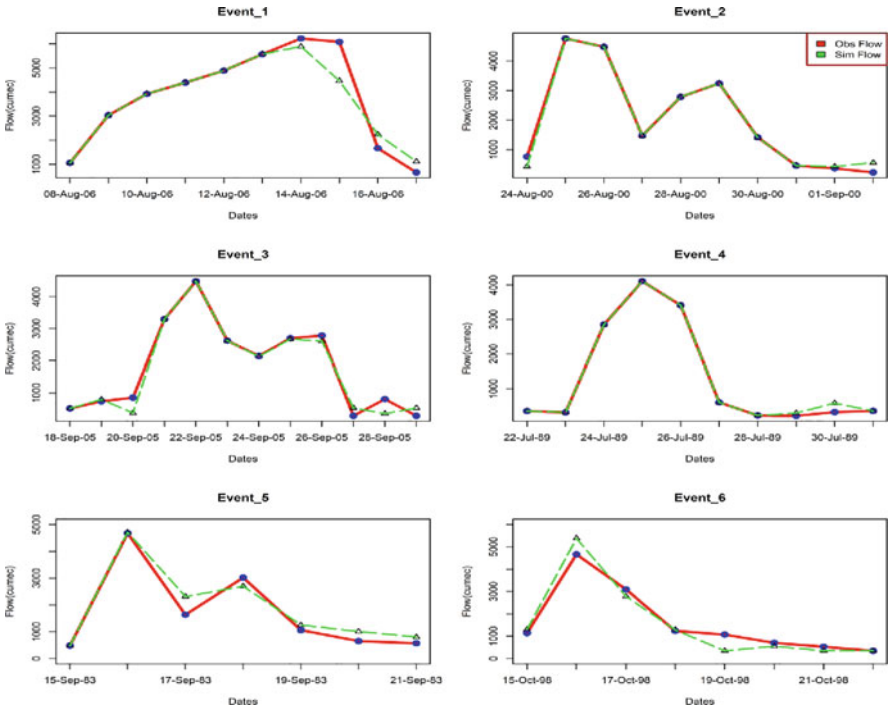

Fig. 20.2 Calibrated (1st and 2nd rows) and validated (3rd row) flood events at G.R. Bridge

corresponding to MME mean. The percentage of increment/decrement in the future flood peaks compared to historical maximum flood events were given in Table 20.5. From Table 20.5, it was found that the percentage change in flood peaks from the EC-Earth3-Veg rainfall were decreasing at Purna and Yelli, and increasing at GR Bridge. The percentage change was comparatively low in the case of EC-Earth3-Veg rainfall compared to MME mean rainfall.

A considerable flood peak reduction around 10–37% was observed for the future flood events under both the scenarios in the two cases of rainfall. Traditionally, the considered study area is semi-arid nature and rainfall was considerably low in this area compared to the remaining Godavari river basin. The intensity of the future MME mean was low compared to the observed precipitation over the study region. Earlier, Das and Umamahesh (2016) predicted the future rainfall over the Godavari river basin and predicted the rainfall intensity over the study region was low under future scenarios for the period 2070–2100. The results of the future bias corrected rainfall of the present study are in line with the Das and Umamahesh (2016). The low intensity future rainfall might be the reason for the low flood peaks in future.

At-site flood frequency analysis was done at the gauging locations to quantify the future flood risk in the terms of the return period. KS test was used to find the best distribution among the nine distributions. The KS statistic values at gauging locations were given in Table 20.6. From KS test D_α vales at 5% significance level at GR

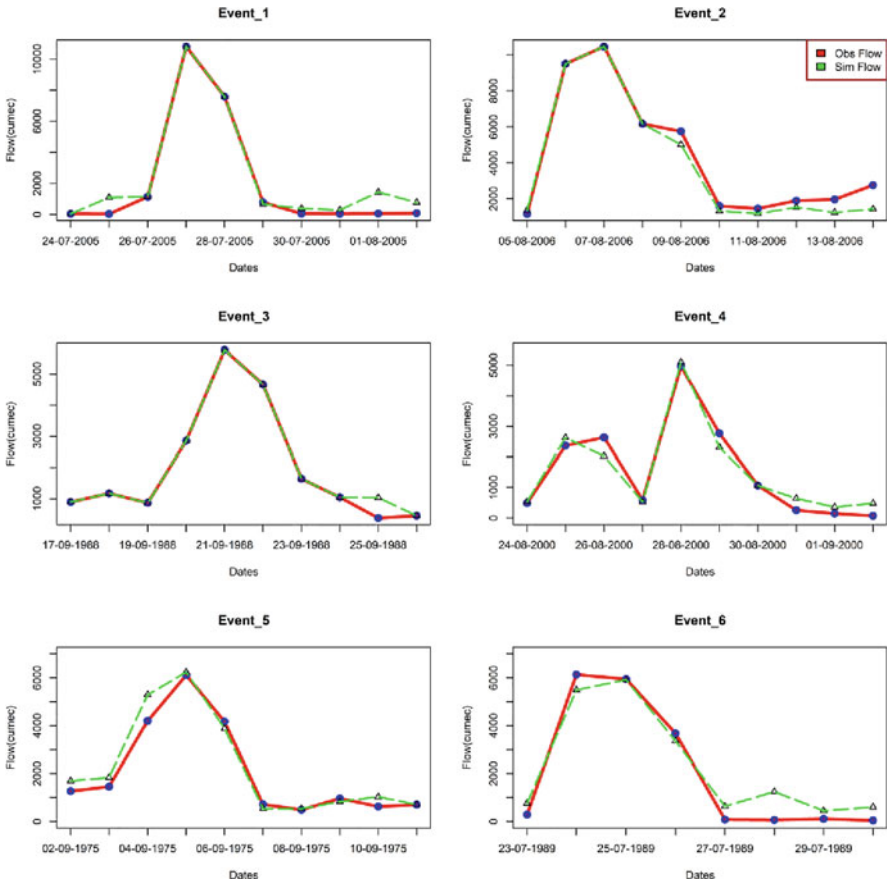

Fig. 20.3 Calibrated (1st and 2nd rows) and validated (3rd row) flood events at Purna

Bridge, Purna and Yelli were 0.21, 0.20 and 0.22, respectively. As per Table 20.6, D_{max} values were low for lognormal distribution, which means lognormal distribution was best fitted for the annual maximum series at the gauging locations. Flow values were obtained from the lognormal distribution corresponding to 2-, 5-, 10-, 20-, 50-, 100-, 200- and 500-year return periods. The flood frequency analysis graph at the gauging locations was shown in Fig. 20.7.

As per Fig. 20.7, it was found that the simulated future flood peaks in the basin were in between 10- and 20-year return period flows. The magnitude of flood in the future were increasing the flood risk in the study area. Therefore, it is necessary to find the flood hazard areas for future flood events.

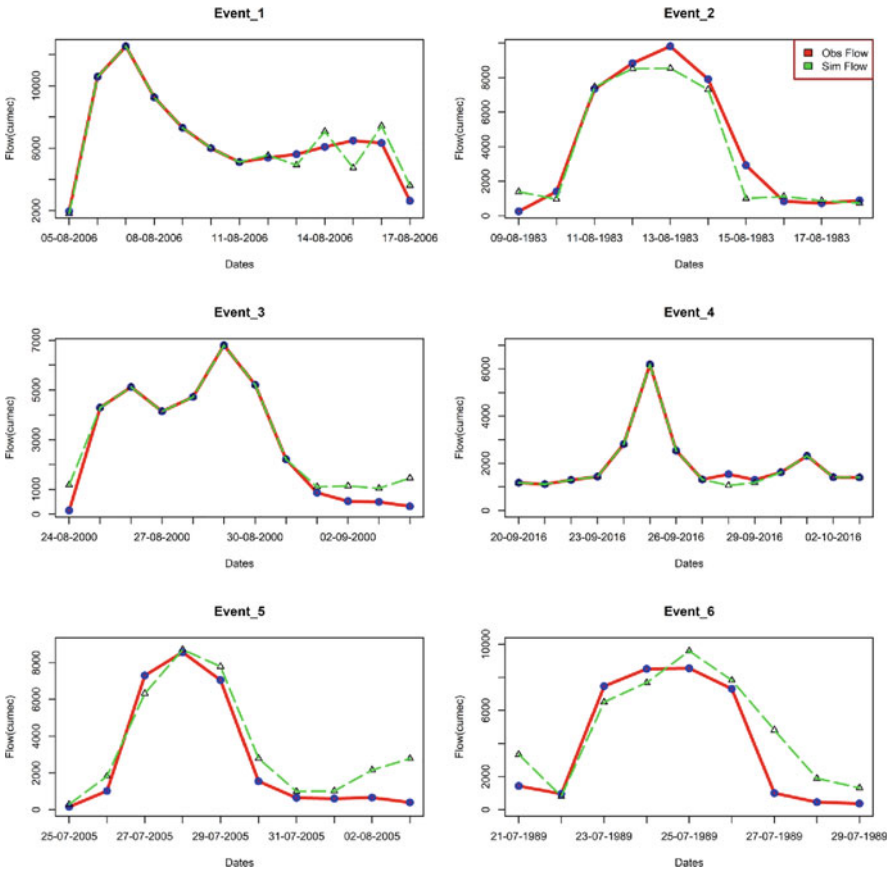

Fig. 20.4 Calibrated (1st and 2nd rows) and validated (3rd row) flood events at Yelli

20.13 Flood Hazard Map Generation

HEC-RAS 2D unsteady modelling was used to obtain the flood vulnerable areas under SSP245 and SSP585 scenarios. HEC-RAS 2D model was set up in such a way that the future flood events occurred at the same time in the basin. Water depth and velocity were simulated from the HEC-RAS model for flood events under both scenarios and in both rainfall cases. The simulated water depth and velocity of the MME mean flood events were given in Figs. 20.8, 20.9, 20.10, and 20.11. From Figs. 20.8 and 20.9, it was evident that flood inundation areas for the flood events were similar, but the water depth in the inundate areas were high under SSP585 scenario. From Figs. 20.10 and 20.11, velocity of the flooded water was similar under both the scenarios in the downstream of the channel. Velocity of the water is comparatively more in downstream side of channel under SSP585 scenario.

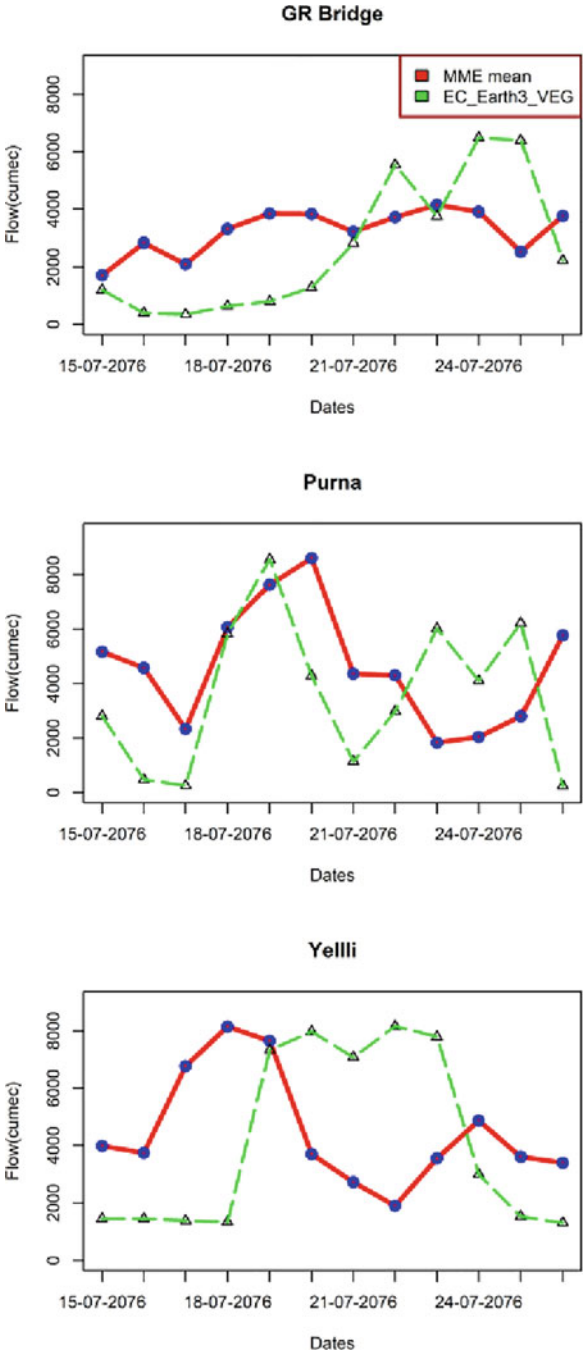

Fig. 20.5 Future flood events under SSP245

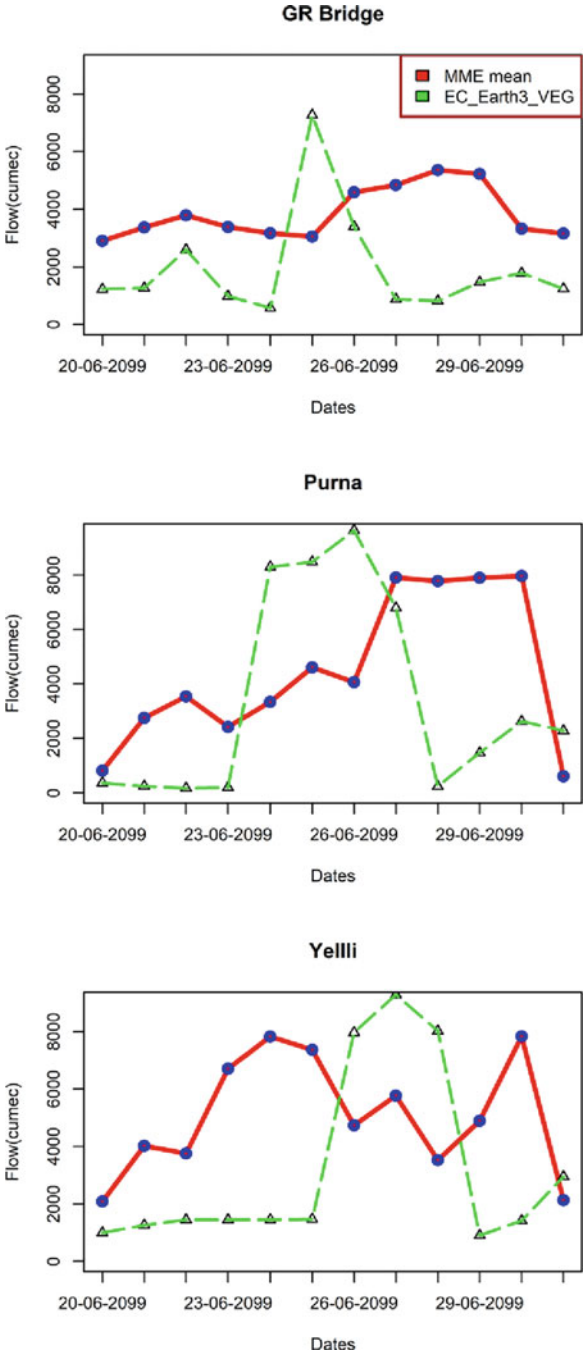

Fig. 20.6 Future flood events under SSP585

Table 20.5 Percentage of increment/decrement in the future flood peaks compared to historical maximum flood events (negative sign shows the decrease in percentage)

Gauging location	% change in flood peak with MME mean rainfall	% change in flood peak with EC-Earth3-Veg rainfall
SSP245		
GR Bridge	–33.35	4.19
Purna	–20.34	–20.75
Yelli	–35.02	–34.91
SSP585		
GR Bridge	–13.84	16.89
Purna	–26.27	–10.83
Yelli	–37.49	–25.94

Table 20.6 KS statistic values at gauging locations (bolded vales were accepted based on the KS test, *notated distribution was best fitted distribution)

Distribution	GR Bridge	Purna	Yelli
Normal	**0.20**	0.21	**0.17**
Log normal	**0.14***	**0.16***	**0.11***
GEV	**0.19**	**0.20**	0.40
GP	0.22	**0.17**	0.45
Gumbel	**0.17**	**0.20**	0.38
Cauchy	0.22	0.28	**0.18**
Logistic	**0.16**	**0.16**	**0.13**
Uniform	0.41	0.44	0.33
Pearson type III	**0.18**	**0.17**	0.26

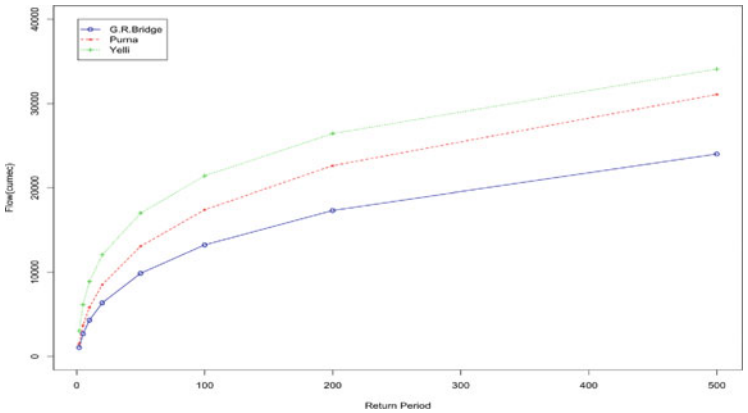

Fig. 20.7 Flood frequency analysis at G.R. Bridge, Purna and Yelli

From the analysis of future flood hazard maps, downstream area of the study area was found to be more vulnerable to future floods due to the low elevation and flat areas. Nanded town, on the bank of river Godavari is going to inundate for the above-mentioned flood under high emission scenario (SSP585). Flood mitigation

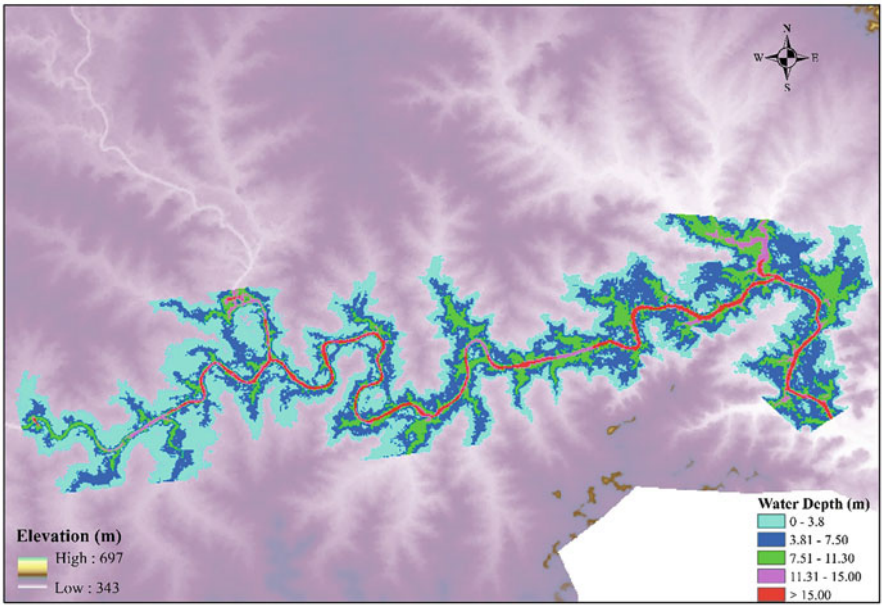

Fig. 20.8 Water depth map of future flood hazard from MME mean rainfall for the period 2070–2100 under SSP245

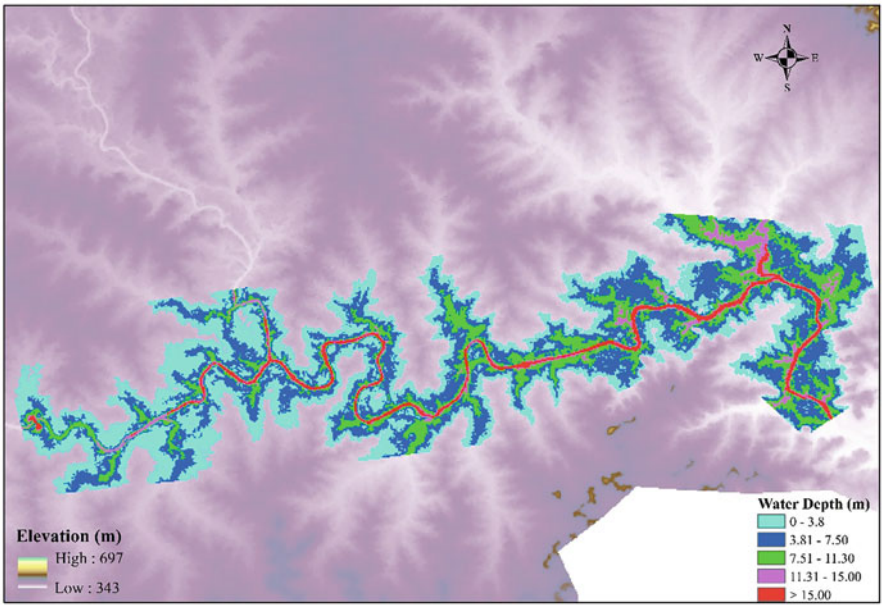

Fig. 20.9 Water depth map of future flood hazard from MME mean rainfall for the period 2070–2100 under SSP585

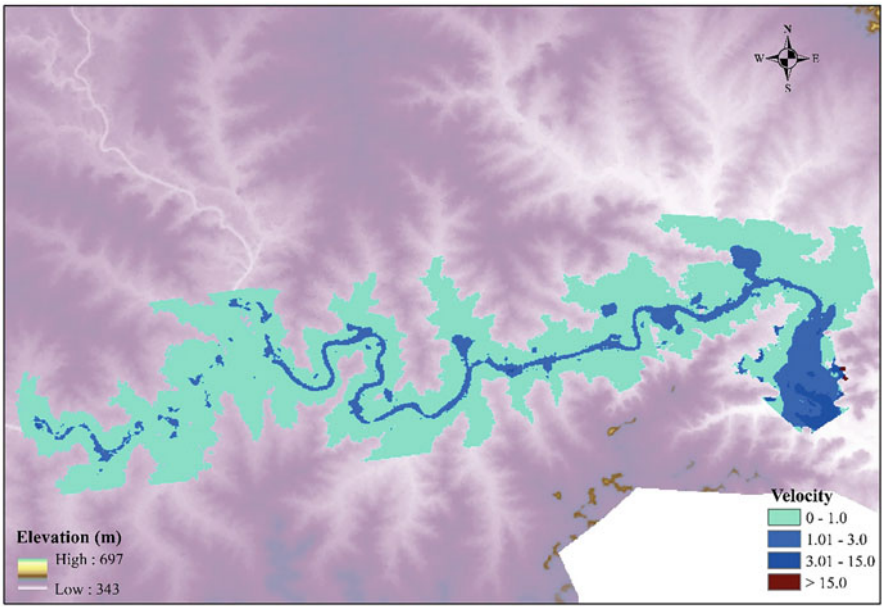

Fig. 20.10 Velocity map of future flood hazard from MME mean rainfall for the period 2070–2100 under SSP245

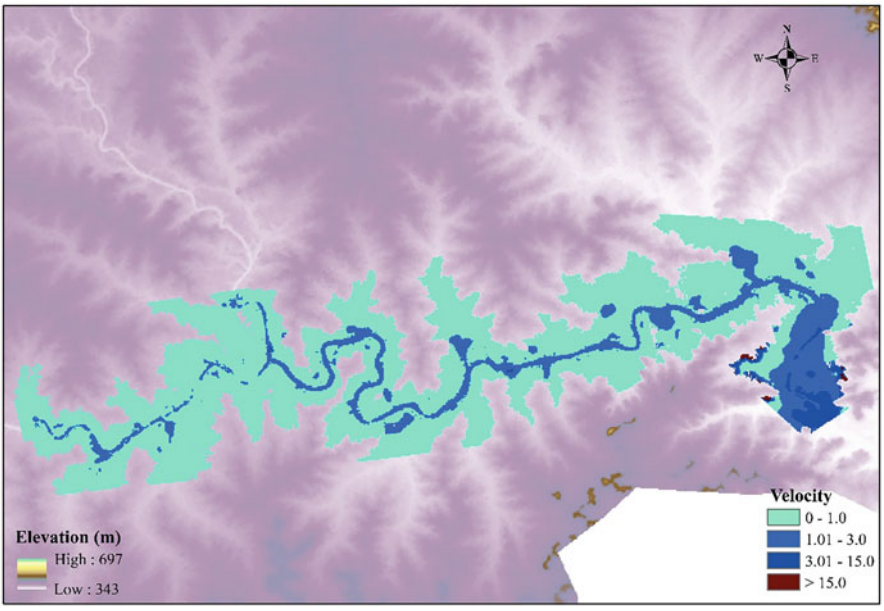

Fig. 20.11 Velocity map of future flood hazard from MME mean rainfall for the period 2070–2100 under SSP585

strategies like constructing dykes, bunds and flood protection structures need to be constructed along the river banks for better management of floods.

20.14 Conclusions

Floods are one of the most widespread natural hazards on this world. The flood prediction modelling is one of the important tools to mitigate the flood hazards. The ongoing improvement of the machine learning based flood models over the past decades, along with the available hydro-meteorological data, had increase the accuracy of predicted floods. The preparation of flood hazard maps was required for mitigating, planning and managing flood incidents. Floods were also identified as one of the major problems in the Godavari river basin. This study analysed the various aspects of floods like flood risk and flood inundation over Godavari river basin. The results show that:

1. The developed flood model is suitable for Godavari river basin, which shows a very high NSE values and low error in flood peak and error in time to peak for both the calibration and validation period. Therefore, the SVM model was suitably used for prediction of flood events in the study area.
2. Future flood events were generated by the developed SVM model with the MME mean rainfall and best performing GCMs rainfall (EC-Earth3-VEG).
3. Flood peak reduction around 10–37% was observed in future flood events compared to maximum historical flood peak in the study area due to the low rainfall in future.
4. The log normal distribution was found to be best fitted for all the gauging locations and flood frequency analysis was done by using the log normal distribution. The maximum flows occurred at each gauging location were in between 10- and 20-year return period flows with more flood volume.
5. The HEC-RAS model results show that the flood inundation areas were almost similar under SSP245 and SSP585. However, the extent is slightly more for SSP585. Flood water depth was more in most of the locations under SSP585 compared to SSP245.
6. The flood hazard maps also revealed that the flood related problems were more in the downstream side in comparison to the upstream side of the study area.
7. The future flood hazard map also revealed that the Nanded city which is on the banks of river Godavari will go under submergence for future flood events using both SSP245 and SSP585 for 2070–2100 time period.

The results of this study may help the organizations and stakeholders to manage flood risks and provide effective communication with the public.

References

Anandhi A, Srinivas VV, Kumar DN, Nanjundiah RS (2009) Role of predictors in downscaling surface temperature to river basin in India for IPCC SRES scenarios using support vector machine: role of predictors in downscaling temperature for IPCC scenarios using SVM. Int J Climatol 29:583–603. https://doi.org/10.1002/joc.1719

Costabile P, Costanzo C, Ferraro D, Macchione F, Petaccia G (2020) Performances of the New HEC-RAS version 5 for 2-D hydrodynamic-based rainfall-runoff simulations at basin scale: comparison with a state-of-the art model. Water 12:2326. https://doi.org/10.3390/w12092326

Das J, Umamahesh NV (2016) Downscaling monsoon rainfall over river Godavari basin under different climate-change scenarios. Water Resour Manag 30:5575–5587. https://doi.org/10.1007/s11269-016-1549-6

EC-Earth Consortium (EC-Earth) (2019a) EC-Earth-Consortium EC-Earth3 model output prepared for CMIP6 ScenarioMIP ssp585. DOI: 10.22033/ESGF/CMIP6.4912

EC-Earth Consortium (EC-Earth) (2019b) EC-Earth-Consortium EC-Earth3-Veg model output prepared for CMIP6 CMIP historical. DOI: 10.22033/ESGF/CMIP6.4706

Ghosh S (2010) SVM-PGSL coupled approach for statistical downscaling to predict rainfall from GCM output. J Geophys Res 115:D22102. https://doi.org/10.1029/2009JD013548

John CK, Pu JH, Pandey M, Hanmaiahgari PR (2021a) Sediment deposition within rainwater: case study comparison of four different sites in Ikorodu, Nigeria. Fluids 6(3):124

John CK, Pu JH, Moruzzi R, Pandey M (2021b) Health-risk assessment for roof-harvested rainwater via QMRA in Ikorodu area, Lagos, Nigeria. J Water Clim Change 12(6):2479–2494

Kim B, Sanders BF, Famiglietti JS, Guinot V (2015) Urban flood modeling with porous shallow-water equations: a case study of model errors in the presence of anisotropic porosity. J Hydrol 523:680–692. https://doi.org/10.1016/j.jhydrol.2015.01.059

Kishore P, Jyothi S, Basha G, Rao SVB, Rajeevan M, Velicogna I, Sutterley TC (2016) Precipitation climatology over India: validation with observations and reanalysis datasets and spatial trends. Clim Dyn 46:541–556. https://doi.org/10.1007/s00382-015-2597-y

Li S, Ma K, Jin Z, Zhu Y (2016) A new flood forecasting model based on SVM and boosting learning algorithms. In: 2016 IEEE congress on evolutionary computation (CEC). Presented at the 2016 IEEE congress on evolutionary computation (CEC). IEEE, Vancouver, pp 1343–1348. https://doi.org/10.1109/CEC.2016.7743944

Liu D, Mishra AK, Yu Z, Lü H, Li Y (2021) Support vector machine and data assimilation framework for Groundwater Level Forecasting using GRACE satellite data. J Hydrol 603:126929. https://doi.org/10.1016/j.jhydrol.2021.126929

Lovato T, Peano D (2020) CMCC CMCC-CM2-SR5 model output prepared for CMIP6 ScenarioMIP ssp585. https://doi.org/10.22033/ESGF/CMIP6.3896

Mekanik F, Imteaz MA, Gato-Trinidad S, Elmahdi A (2013) Multiple regression and artificial neural network for long-term rainfall forecasting using large scale climate modes. J Hydrol 503:11–21. https://doi.org/10.1016/j.jhydrol.2013.08.035

Melo I, Tomášik B, Torrieri G, Vogel S, Bleicher M, Korény S, Gintner M (2009) Kolmogorov-Smirnov test and its use for the identification of fireball fragmentation. Phys Rev C 80:024904. https://doi.org/10.1103/PhysRevC.80.024904

Mosavi A, Ozturk P, Chau K (2018) Flood prediction using machine learning models: literature review. Water 10:1536. https://doi.org/10.3390/w10111536

Nayak PC, Sudheer KP, Rangan DM, Ramasastri KS (2005) Short-term flood forecasting with a neurofuzzy model: flood forecasting with a neurofuzzy model. Water Resour Res 41:3562. https://doi.org/10.1029/2004WR003562

Pai DS, Sridhar L, Rajeevan M, Sreejith OP, Satbhai NS, Mukhopadhyay B (2014) Development of a new high spatial resolution (0.25° X 0.25°) long period (1901-2010) daily gridded rainfall data set over India and its comparison with existing data sets over the region. Mausam 65:1–18

Piani C, Haerter JO, Coppola E (2010) Statistical bias correction for daily precipitation in regional climate models over Europe. Theor Appl Climatol 99:187–192. https://doi.org/10.1007/s00704-009-0134-9

Pourghasemi HR, Yousefi S, Kornejady A, Cerdà A (2017) Performance assessment of individual and ensemble data-mining techniques for gully erosion modeling. Sci Total Environ 609:764–775. https://doi.org/10.1016/j.scitotenv.2017.07.198

Pu JH, Wallwork JT, Khan M, Pandey M, Pourshahbaz H, Satyanaga A, Hanmaiahgari PR, Gough T (2021) Flood suspended sediment transport: combined modelling from dilute to hyper-concentrated flow. Water 13(3):379

Quirogaa VM, Kurea S, Udoa K, Manoa A (2016) Application of 2D numerical simulation for the analysis of the February 2014 Bolivian Amazonia flood: application of the new HEC-RAS version 5. Ribagua 3:25–33. https://doi.org/10.1016/j.riba.2015.12.001

Raju KS, Kumar DN (2020) Review of approaches for selection and ensembling of GCMs. J Water Clim Change 11:577–599. https://doi.org/10.2166/wcc.2020.128

Rodi W (2017) Turbulence Models and Their Application in Hydraulics: a state-of-the-art review, 3rd edn. Routledge, London. https://doi.org/10.1201/9780203734896

Schupfner M, Wieners K-H, Wachsmann F, Steger C, Bittner M, Jungclaus J, Früh B, Pankatz K, Giorgetta M, Reick C, Legutke S, Esch M, Gayler V, Haak H, de Vrese P, Raddatz T, Mauritsen T, von Storch J-S, Behrens J, Brovkin V, Claussen M, Crueger T, Fast I, Fiedler S, Hagemann S, Hohenegger C, Jahns T, Kloster S, Kinne S, Lasslop G, Kornblueh L, Marotzke J, Matei D, Meraner K, Mikolajewicz U, Modali K, Müller W, Nabel J, Notz D, Peters-von Gehlen K, Pincus R, Pohlmann H, Pongratz J, Rast S, Schmidt H, Schnur R, Schulzweida U, Six K, Stevens B, Voigt A, Roeckner E (2019) DKRZ MPI-ESM1.2-HR model output prepared for CMIP6 ScenarioMIP ssp585. Earth Syst Grid Fed. https://doi.org/10.22033/esgf/cmip6.4403

Sharma VC, Regonda SK (2021) Two-dimensional flood inundation modeling in the Godavari River Basin, India—insights on model output uncertainty. Water 13:191. https://doi.org/10.3390/w13020191

Vapnik V (1999) The nature of statistical learning theory. Springer, Cham

Wallwork JT, Pu JH, Kundu S, Hanmaiahgari PR, Pandey M, Satyanaga A, Pandey M, Satyanaga A, Amir Khan M, Wood A (2022) Review of suspended sediment transport mathematical modelling studies. Fluids 7(1):23

Wang F, Wang X (2010) Fast and robust modulation classification via Kolmogorov-Smirnov test. IEEE Trans Commun 58:2324–2332. https://doi.org/10.1109/TCOMM.2010.08.090481

Xie Z, Chen G, Meng X, Zhang Y, Qiao L, Tan L (2017) A comparative study of landslide susceptibility mapping using weight of evidence, logistic regression and support vector machine and evaluated by SBAS-InSAR monitoring: Zhouqu to Wudu segment in Bailong River Basin. Environ Earth Sci 76:313. https://doi.org/10.1007/s12665-017-6640-7

Yukimoto S, Kawai H, Koshiro T, Oshima N, Yoshida K, Urakawa S, Tsujino H, Deushi M, Tanaka T, Hosaka M, Yabu S, Yoshimura H, Shindo E, Mizuta R, Obata A, Adachi Y, Ishii M (2019) The Meteorological Research Institute Earth System model version 2.0, MRI-ESM2.0: description and basic evaluation of the physical component. J Meteorol Soc Jpn Ser 97:931–965. https://doi.org/10.2151/jmsj.2019-051

Chapter 21
Field Study on Soil Organic Matter Content in Inundation Areas of Langol Catchment by "Loss-on-Ignition" Method

Moirangthem Siman Singh and Thiyam Tamphasana Devi

Abstract Organic matter content is an essential and distinguishing feature of soils that is commonly measured as a sink and source of carbon in the soil. Soil organic matter (SOM) is described as the total of vegetation and animal remains at different phases of decomposition, cells, and tissues of soil living systems, and substances that have decomposed well. It is a good measure of the fertility of the soil and is among the most vital agricultural soil components. It has a significant impact on soil physiochemical and biological features such as soil structure, water holding capacity, rate of water infiltration, and soil erodibility. The aim of this study is to find out the variation in soil organic content and its corresponding soil moisture content (SMC) for various land use and land cover types (agriculture, barren land, forest, built-up, and marshy land) in a frequently inundated region (Langol catchment situated in the North East region of India). The loss-on-ignition approach (LOI), which is a simple yet comprehensive method, is used for determining organic matter content in soil (measurement was recorded at a soil depth of 0–15 cm and 15–30 cm at each location of a total of ten sites (20 samples) from October 2021 to February 2022). It was observed that the organic matter content of the soil varies from 2.2% (moderately fertile) to 18% (highly fertile) depending on the type of land use and land cover. A higher value of SOM content (mean value) was observed in agriculture (15%) and forest land regions (17%), and its value reduced as the soil depth is increased. The higher SOM content in the top soil layer is due to the presence of appreciable plant and animal residues accumulated on the soil surface. Furthermore, there was no prominent co-relationship found between moisture content (17–57%) and its organic matter presence in the soil. Even though the study area lies in the low-lying region due to the presence of a higher built-up area (45%) and only 7% of agricultural land, the study location is not much used in agricultural activity at present. However, the soil in this study region is fertile and suitable for agricultural activity, but due to an increase in settlement (urbanisation) areas, in the future, organic matter presence may be drastically reduced, which affects the overall environment ecosystem in the region.

M. S. Singh · T. T. Devi (✉)
Department of Civil Engineering, National Institute of Technology, Manipur, India

M. Pandey et al. (eds.), *River Dynamics and Flood Hazards*, Disaster Resilience and Green Growth, https://doi.org/10.1007/978-981-19-7100-6_21

Keywords Ignition temperature · Langol catchment · Loss-on-ignition (LOI) · Soil organic matter (SOM)

21.1 Introduction

Carbon dioxide (CO_2) occurs naturally in the atmosphere and all animals, including humans, has long been exposed to CO_2 in the air. Humans, like other animals, are tolerant of CO_2 under normal circumstances. However, concentrations above the acceptable limit can be hazardous to plants and animals. In humans, it can lead to an increase in breathing rate and a rise in CO_2 concentration in the blood above normal levels, making the blood acidic. Under very high CO_2 concentrations, a significant increase in respiratory rate can happen. The effects can be very severe and loss of consciousness can also occur. However, soil organic content in soil plays an important role in reducing atmospheric CO_2. As a matter of fact, the increase in the content of organic matter in soil is a consequence of carbon sequestration carried out by terrestrial ecosystems. Therefore, high organic content in soil indicates a greater reduction in atmospheric CO_2 and is a step toward moderating global warming and climate change.

Soil organic matter is any product produced essentially by living organisms (plant or animal) that is brought back to the earth and passes through the decomposition action. At any instance, it features a variety of materials, extending from intact original plant and animal tissues to the significantly decomposed combination of substances referred to as humus. The amount of organic matter in any given soil is determined by different kinds of environmental, soil texture, and agronomic factors. Some of these, such as climate and soil texture happen naturally. Agricultural practices also have an impact on the quantity of organic matter in soil. Tillage, crop rotation and manuring practices can all have a significant impact on the SOM level. The percentage of organic matter present in soil is a result of all the organic material additions and losses that have occurred over time. We will look at why various soils have different levels of organic matter in this investigation. Anything that contributed a lot of organic residues to a soil might increase the amount of organic matter in it. And anything that causes soil organic matter to decompose more rapidly or to be removed by erosion, on the other side, may minimise organic matter.

Several soil characteristics are influenced by organic matter concentration such as (1) the ability of a soil to provide plants with nutrients such as nitrogen, phosphorus, and sulphur, as well as trace metals; (2) water infiltration rate and retention; (3) the extent of aggregation of soil material and overall structure that affects interactions between air and water; (4) capacity of the soil to hold exchangeable cations; (5) Friability and compaction properties; (6) adsorption or deactivation of chemical pesticides; (7) moisture holding capacity; and (8) the bonding or adhesion characteristics of organic materials ensure the stability of soil aggregates and pores (Pu et al. 2021; Shankar et al. 2021; Shivashankar et al. 2022),. Soils are the biggest stock of terrestrial organic carbon on Earth, containing an estimate of 2500 Pg C. Erosion of soil carbon and oxidation have contributed to the atmosphere

approximately 78 ± 12 Pg C ever since the industrial revolution, constituting around 29% of current global carbon emissions (Lal 2004). The top soil up to 1 m retains 1500 Gt SOC, with nearly half of that in the top 30 cm layer of soil (Batjes et al. 1996). Soil organic carbon (SOC) helps in the vertical accretion of wetland material, storing water, acting as plant nutrients source and sink, and stabilising the soil matrix (Lal 2004; DeLaune and White 2012). Quantifying SOC is useful for a range of diverse scientific applications, including understanding the concept of global carbon cycle, determining the importance of soils as an ecosystem service for management reasons, and carbon credits trading. Carbon is basically the most abundant element in the organic matter present in soil, accounting for 48–58% of the overall weight. As a result, organic matter measurements are frequently utilised as a way for organic carbon estimates by multiplying a certain factor to the organic matter value. Using this analytically derived conversion factor, the proportion of mass loss can subsequently be utilised to assess SOC. As mentioned, the LOI technique findings necessitate the use of a conversion factor to convert the measurement of soil organic matter into SOC estimation. The van Bemmelen value of around 1.724 has long been employed as a conversion coefficient, assuming that SOM constitute 58% carbon, 2% hydrogen, and 40% oxygen. On account of the significance of organic matter in delivering plant nutrients, chemical pesticides deactivation, etc., organic matter content determination is a regular technique undertaken in soil analysis and testing laboratory across the globe. But it is hard to assess the quantity of organic matter available in a soil. Furthermore, there is no entirely satisfactory method for quantifying the organic matter levels in the soil. However, LOI method presents a rational estimate of organic matter levels in soils. While several studies imply that LOI offers a great deal of promise for quickly and reliably measuring SOC, LOI method is not without its drawback. Some studies imply that since LOI can also breakdown inorganic elements, it is not always indicative of soil organic matter (SOM) and besides that, hardly every SOM ignites (Ball 1964). Furthermore, both these SOM and SOC were also calculated using LOI, leaving differentiation in the literature difficult (Konen et al. 2002). Some scholars have proposed that due to the difficulties of adequately assessing SOM and, more lately, greater attention in C cycling, SOC should essentially be calculated using LOI instead of SOM in most cases. If required, SOM can be obtained from SOC by utilising SOC/SOM ratios found from literature studies or from test samples (Schulte and Hopkins 2015). If SOC can be properly assessed using very affordable and convenient LOI, this might be useful for assessing the influence the impact of management on SOC as well as for ecological research. There are various ways for calculating SOM, each with its own set of benefits and drawbacks in terms of simplicity, cost, and accuracy (Nelson and Sommers 1982). For instance, wet oxidation process, the Walkley-Black (WB) method is a popular, routine, somewhat accurate, and low-cost method for determining SOM, although it uses chromate and produces toxic waste. Elemental carbon analysers are precise, yet they are costly to buy and maintain. Another approach, loss-on-ignition (LOI), has indeed been described as a low-cost and convenient way to estimate SOM. It includes igniting soil specimen at higher temperatures and calculating weight loss post-ignition (Konen et al. 2002). This

also eliminates the generation of chromic acid waste. The loss-on-ignition approach is straightforward, does not require highly trained personnel or sophisticated equipment, and may be used on reasonably large batches of samples on a regular basis. The LOI method's capacity to assess SOM content has been deemed credible (Abella and Zimmer 2007; Salehi et al. 2011; Wallwork et al. 2022). However, determining the ideal temperatures and duration to enhance ignition of SOM and simultaneously reducing inorganic C combustion is tough. Each of these factors can have a significant influence on LOI outcomes (Ben-Dor and Banin 1989; Schulte and Hopkins 2015). Heating at higher temperatures can also create structural water to be released from clays and inorganic elements. Nevertheless, the LOI procedure is nowadays extensively applied to calculate SOM using a muffle furnace at 360 °C for a duration of 2 h (Konen et al. 2002; Schulte and Hopkins 2015) and under temperature of 300, 450, and 600 °C for a duration of 2 h (Donkin 1991; Abella and Zimmer 2007) Furthermore, a muffle furnace temperature of 450 °C and heating time of 4 h is also used to determine SOM (Kumar et al. 2019). It was shown that such LOI approach was dependable and capable of providing accurate estimations of SOM for dry soils when compared to standard methods for SOC (Wet oxidation method) (Wang et al. 2013). The loss-on-ignition technique of quantifying SOM is based on determining the loss of weight from a dry soil specimen as a result of high temperature combustion. Ideally, complete oxidation would take place within a small temperature span where weight reduction from soil minerals is insignificant. Regrettably, as it is not the scenario, therefore choosing of ignition temperature is a little random yet crucial in order to reduce errors. Heating at high temperature (>500 °C) can generate inaccuracies due to carbon dioxide loss from carbonates, loss of structural water from clay minerals, and hydrated salt decomposition (Ball 1964; Ben-Dor and Banin 1989). Many of these errors will be eliminated by combustion of soil specimen under temperatures of 500 °C. Despite the fact that LOI is widely regarded as a basic method for estimating organic matter, findings suggest that variables such as time of exposure, crucible position in the furnace, sample amount, and the research facility that evaluates LOI may all have profound effect on the outcome. Also, sediment containing a large proportion of organic matter appeared to be more susceptible to inconsistencies compared to sediment containing a smaller percentage of organic matter. Normally, soil organic matter is limited only to the organic elements which pass through a 2-mm strainer with the soil particles.

The primary aim of this study is: (1) to estimate the organic matter content of the study area (Langol catchment) and (2) to compare these organic matter content among different land use types.

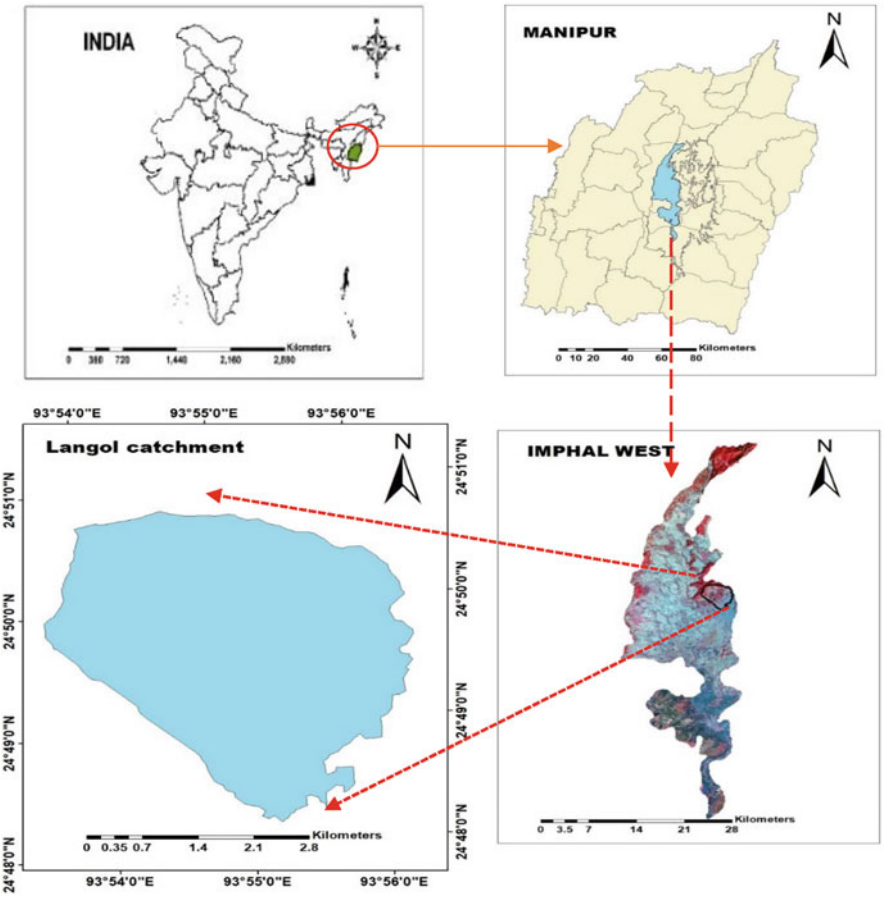

Fig. 21.1 Location of study area (Langol catchment)

21.2 Study Area

The Langol catchment is located in Lamphel Sub-Division of Imphal West District in the state of Manipur in North East India (Fig. 21.1) and is prominently covered by agricultural land. It is mostly a valley region with a small portion of hilly areas The study area covers an area of 14.01 km sq. It lies between a latitude of 24°50′50″N and 24°48′511″N and between a longitude of 94°53′37″E and 94°56′19″E.

The mean annual temperature in the state varies between 14.5 °C and 38 °C, with an average precipitation of 1250–2700 mm. In this region the soil mainly comprises ~~of~~ alluvium soil. With a territorial area of 22,327 km^2, Manipur is one of the country's hilly states, accounting for 0.68% of the country's geographical area. It is situated between the latitudes of 23°50′N and 25°42′N and the longitudes of 92° 59′E and 94°46′E, sharing an international boundary with Myanmar. It is

surrounded to the north, west, and southwest by the Indian states of Nagaland, Assam, and Mizoram, and to the southeast by Myanmar. Geographically, the state consists of a flat plateau with an alluvial valley and hilly terrain. The state's reported forest area is 17,418 km^2, accounting for 78.01% of the total land area. The population of the state is 2.72 million as per Census 2011 (Census 2011) which constitute 0.22% of the country's population. The average population density of the state is 122 persons per km^2. According to the Champion and Seth categorisation system, the state has ten forest types that fall into five forest type groups, namely: tropical semi-evergreen, subtropical broadleaved hill, tropical moist deciduous, subtropical pine, and montane wet temperate forest.

21.3 Rational of the Study

There is a significant change in the area covered by each land use classes. The study area is mostly occupied by settlement area (45%) and only 7% by agricultural land at present. Moreover, there might be reduction in the soil organic content from conversion of a vegetation cover to non-vegetation land cover. Therefore, there is a need to monitor the organic matter content of the soil. Since various soil properties is reliant on the organic content including the fertility of the soil, water holding capacity, permeability, nutrient availability, etc. Besides, Soil organic matter (SOM) is also an essential parameter in the estimation of carbon sequestration by the soil. The content of soil organic matter will be reflected in the carbon sequestration potential of soil which is one way to mitigate climate change by reducing atmospheric CO_2. A small increase of SOM over large areas in agricultural and pastoral land will significantly reduce atmospheric carbon dioxide. But due to increase in settlement area in the study site, there is a risk of decline in organic content of the soil. Therefore, there is a necessity to determine the SOM of the study site which can serve as a future reference for soil carbon sequestration studies and other related research. Moreover, since the carbon within the ecosystem can also be released into the atmosphere as carbon dioxide (CO_2), the soil organic matter must be carefully managed and maintained, hence it is crucial to be aware of the present organic matter availability of the region.

21.4 Limitations

Despite the benefits of utilising the LOI approach previously discussed, numerous researches have highlighted caution about using LOI estimations of OM or OC. The primary arguments focus on two major assumptions of the LOI method:

(a) Clay minerals do not lose a substantial amount of structural water; and
(b) CO_2 emissions from carbonate minerals are insignificant.

Soil organic matter (SOM) comprises a broad category of organic components, and accurate measurement of SOM is difficult for any analytical method. The most conventional method for determining SOM content is to measure mass loss on igniting at temperatures ranging from 450 °C to 900 °C. Besides the primary weight loss from the breakdown of organic matter, additional weight reduction occurs due to further loss of carbon dioxide from carbonates present in calcareous soils, to loss of elemental carbon, and to loss of structural water from clay minerals. The contribution from loss of structural water of clay minerals to the loss-on-ignition result varies depending on the proportion of clay present in the soil and the clay's mineralogical composition. In addition to these weight decrease, other small changes that may cause weight loss or gain, which include the oxidation of mineral components bound to the OM, are likely to occur at these high temperatures, namely the oxidation of iron (Fe) and manganese (Mn) containing minerals. However, evaporation of hygroscopic might cause mass loss, resulting in an overestimation of soil organic matter when there is incomplete removal of moisture before LOI ignition. In reality, these processes have a negligible impact on overall mass loss during ignition and may be ignored. It is also possible that not all OM gets oxidised at the temperatures employed in LOI experiments. Nonetheless, the mistakes induced by such factors in the proposed loss-on-ignition method's evaluation of organic matter content are deemed minor in comparison to the multiple assumptions and flaws associated in determining organic matter by other methods such as dichromate wet oxidation. In our perspective, the suggested loss-on-ignition method's convenience and technical simplicity may compensate the drawback of some ambiguity regarding mineral component contributions, especially if organic matter assessments for a great number of samples are required on a regular basis.

21.5 Materials and Methods

21.5.1 Data Used

For delineation of catchment area, satellite data (digital elevation model) is used which is acquired from the website of the Alaska Satellite Facility (ASF) of the ALOS PALSAR satellite. Using the watershed delineation procedure, the raster data is delineated using GIS (geographical information system) tools to obtain the required boundary of Langol catchment. The resolution of DEM used is 12.5 m. For land use and land cover map, Landsat 8 data is used which is obtained from the website of United States Geological Survey (USGS) Earth Explorer. The clarity of the image, particularly for those with restricted or minimal cloud cover, affected the decision of selection of the Landsat image dates. The Landsat image has a spatial resolution of 30 m. Using GIS tools, maximum likelihood supervised classification is performed. As a result, the study area is classified to six major divisions, i.e., forest, agriculture, barren, built-up, marshy, and water body. Table 21.1 lists the description of the satellite data used in this study.

Table 21.1 Description of the satellite data used

Sl. no.	Acquired date	Satellite	Source
1	08/11/2008	ALOS PALSAR	ASF
2	15/02/2021	LANDSAT 8	USGS

The GIS tool required is ArcGIS 10.3 and is geospatial software that can be used to demonstrate geographic information or, to put it another way, to create maps. It is a framework for gathering, organising, managing, analysing, communicating, and disseminating geographic data. As a matter of fact, the software essentially serves as a platform for connecting, sharing, and analysing geographic data. Remote sensing is a key tool that is essential for creating land use and land cover maps by a procedure known as image classification.

21.5.1.1 Delineation of Study Area

A digital elevation model (DEM) is defined as "any digital representation of the continuous variation of relief over space". Figure 21.2 shows how to use the spatial analyst hydrology tools in ArcGIS to delineate a watershed boundary from a digital elevation model (DEM): Firstly, the DEM were georeferenced to the WGS_84 datum and (UTM) Universal Transverse Mercator Zone 46 N coordinate system.

Fill sinks: The filling operation was carried to the DEM using fill tools of spatial analysts hydrology option. This technique fills up the depression in a grid. When cells of greater elevation surround a cell, the water in that cell becomes confined within and cannot flow. To resolve these issues, the fill sinks function alters the elevation value. When the procedure is finished, a completed DEM will be added to the map document.

Flow Directions: Flow direction is created using flow direction tools from the same spatial analysts hydrology option. This function determines the direction of flow for a specified grid. Using the eight directions pour point (D8) approach, the value in any given cell of the flow direction grid reflects the direction of the greatest fall out of that cell to one of its adjoining cells. The D8 flow model simulates flow direction from each pixel to its sharpest downhill slope neighbour. Once the procedure is completed, these D8 flow direction model produces an integer raster with values ranging from 1 to 255.

Flow Accumulation: Flow accumulation maps are generated using flow accumulation tools from the same spatial analysts hydrology option. The flow accumulation function specifies how many cells flow into each downslope cell. After the flow accumulation map is generated, cells which have significant concentration of flow are concentrated flow zones that can be utilised to identify stream courses. By using a threshold value, the outputs of flow accumulation are utilised to form a stream network to obtain cells with high accumulated flow.

Delineating Watershed: In order to delineate the watershed, a point shapefile is created and the proper location for the watershed outflow point is chosen in such a way that the area of interest is included after the delineation. Therefore, a number of

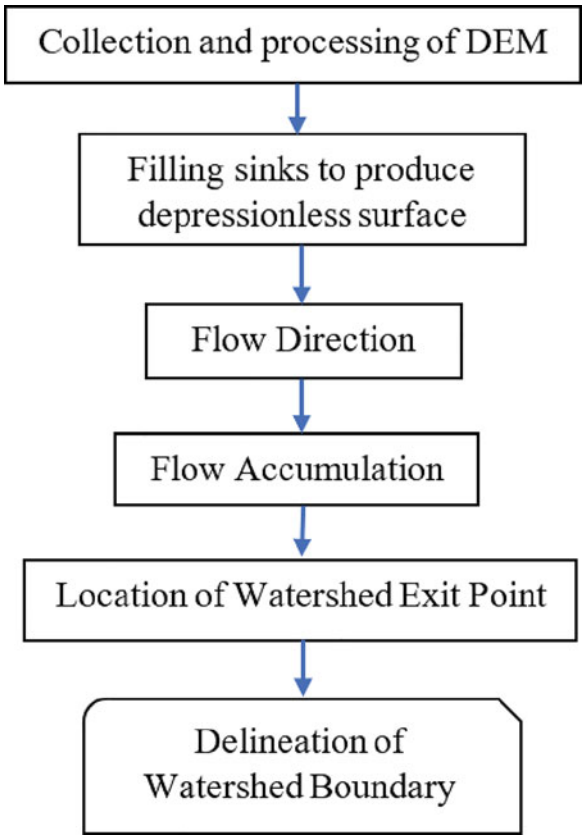

Fig. 21.2 Stepwise watershed delineation process using ArcGIS hydrology tool

outflow points is selected and delineated to pick the most suitable boundary of study area. Using the watershed delineation function, the catchment area is delineated and the boundary of the Langol catchment is obtained as shown in Fig. 21.3. The area of the catchment is calculated using the field calculator function and is obtained as 14.013 km^2.

21.5.1.2 Land Use and Land Cover Classification

Remote sensing is the key source of numerous types of thematic data that are crucial to GIS analysis, such as data on land use and land cover characteristics. The technique of allocating landcover classes to pixels of an image is known as image classification. For example, classes such as settlement area, forest, marshy area, and waterbody, etc. There are several benefits for image classification. It can often be used to differentiate various locations based on the kind of land usage type. Land use information are widely employed in urban development. During natural calamities like earthquakes, volcano eruptions, and severe droughts, high-resolution imagery is

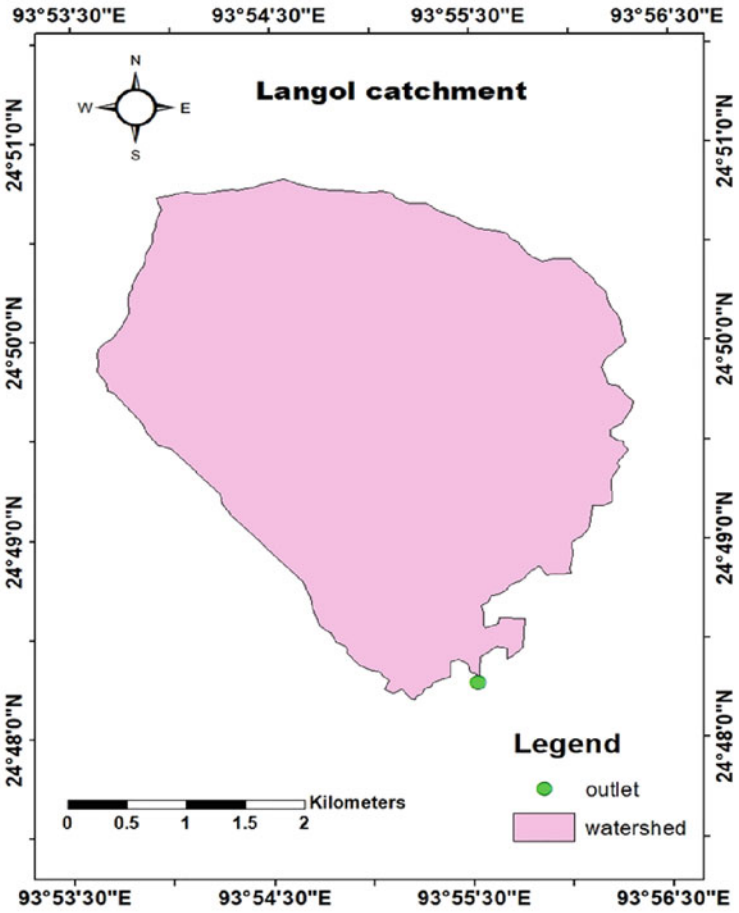

Fig. 21.3 Delineated watershed (Langol catchment)

also utilised to assess the effects and damage. The three common technique of image classification in remote sensing are as follows:

- Unsupervised image classification.
- Supervised image classification.
- Object-based image analysis.

The two most prevalent methodologies are technique of unsupervised and supervised image classification. Therefore, supervised and unsupervised classification are the two basic methods for classifying a multiband raster image. An image is categorised using the supervised classification approach by employing spectral signatures (i.e., reflectance values) collected from training samples (polygon corresponding to unique sample regions of the various land cover categories to be classified). These samples are collected by the image analyst, to classify the image.

However, in case of the unsupervised classification method, the software determines the spectral classes (or clusters) in the multiband picture without the assistance of an analyst. After finding the clusters, the analyst must determine what each cluster represents (e.g., forest, barren, agriculture, etc.). For this research, supervised classification was employed. Supervised classification is where "the user develops the spectral signatures of known categories and then the software assigns each pixel in the image to the cover type to which its signature is most comparable". The training locations were chosen in accordance with the Landsat image, map from Google Earth and Google Map. In supervised classification, the user "supervises" the process of classification. The analyst chooses what pixels values or spectral signatures should be associated with certain classes. This is accomplished by choosing representative sample locations of a recognised cover type referred to as Training sites. The software algorithm then applies the spectral signatures from these training areas to make classification of the whole image. Using maximum likelihood supervised classification, the whole areas is classified into six major divisions such as: forest, water body, built-up, marshy areas, agriculture, and barren land. The basic steps involved in this approach are presented in Fig. 21.4:

In QGIS software, the Semi-Automated Classification Plugin is installed. Semi-automatic Classification Plugin is a free open source plugin for QGIS, that may be used to do remote sensing analysis, and classification (either supervised or unsupervised). It is necessary to reduce the intensity of haziness effect in the satellite data caused by absorption and atmospheric scattering when image is taken through Earth's atmosphere. These two processes have an impact on image quality and are the driving force behind atmospheric correction. The dark object subtraction is the most basic and most widely employed atmospheric correction. This approach is based on the assumption of zero or low surface reflectance. The minimum DN value in the histogram from an entire scene is subtracted from all pixels. To get the surface reflectance, this atmospheric correction eliminates the scattering and absorption effects from the atmosphere.

- Image pre-processing: Using QGIS software, radiometric correction (DOS1 Atmospheric correction) is performed to remove the effects of absorption and atmospheric scattering. The metadata file and the raw Landsat band are fed as an input. After ensuring that all of the bands and metadata have been recognised by the plugin, the (Dark Object Subtraction) DOS1 atmospheric correction is performed. Thereafter, a multiband raster can be generated in ArcMap from the corrected Landsat 8 images in the previous step, either by using the Composite Bands (Data Management) tool or the Composite Bands button in the Image Analysis window. Therefore, using the composite band tool, the corrected Landsat 8 band 2, 4, 5, and 6 are combined to obtain a multiband image. Then, the multiband study area can be derived from these composite satellite images using Extract by Mask tool in ArcGIS 10.3 software.
- Defining of training sites: The initial stage in this classification process is to determine which sites will be served as training areas for each one of the land cover classes. This is commonly accomplished by employing visual image

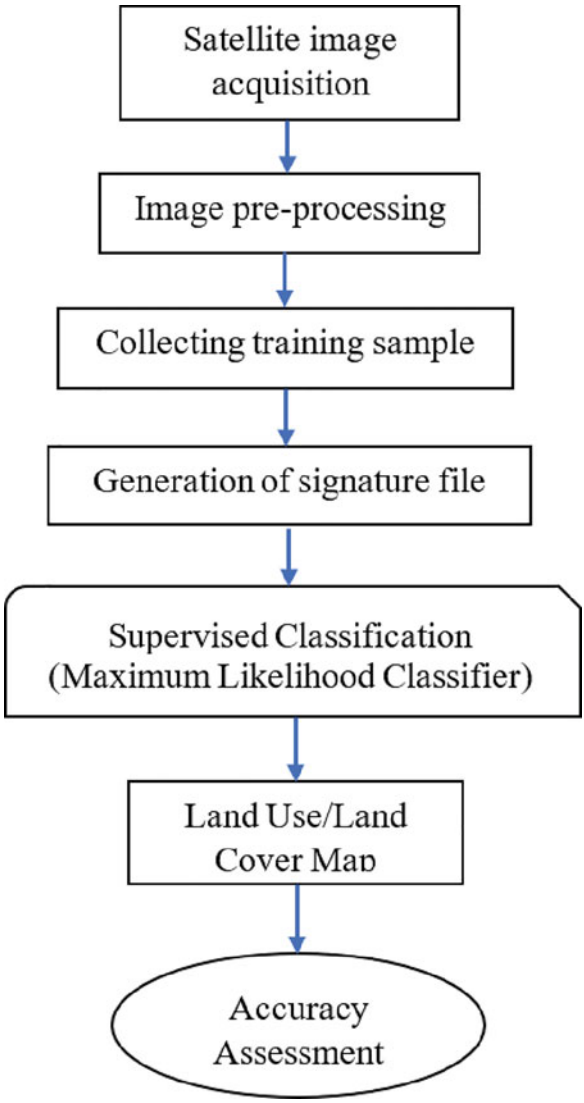

Fig. 21.4 Flowchart for generation of LULC Map

interpretation and Google Earth or Google Map. A number of training sites were chosen depending on regions that are clearly recognisable in valid image sources. For example, create a polygon for an urban area, such as a street or a building. Then add more urban areas that are representative of the whole image. For every land cover class, draw polygons. After that, combine all of them in a single class and doing the same for the rest of the classes. Finally, a total of 120 training sites were located.

- Extraction of signatures: Once we have got training samples for every class. Then the whole signature is generated and saved. The SIG files include various data

regarding the land cover types specified. All of the training sample data acquired up to this point is stored in the signature file. It is also a means of saving the samples so that we can work on them later.

- Classification of the image: The software then classifies the entire image based on the spectral signatures from these training sites. Therefore, using the supervised classification (maximum likelihood classifier) the whole area is classified into six major divisions, namely forest, agriculture, marshy areas, barren, built-up, and water body. Depending on the means and variances of the class signature, this technique allocates each pixel to one of the possible classes. Essentially, the classes should not or hardly overlap with one another. And the respective area of each land use and landcover class is determined. The areas are calculated by multiplying the area of a pixel to the number of pixels occupied by each landcover class and is given in the units of square kilometres.

21.5.1.3 Accuracy Assessment of LULC Map

Accuracy assessment is an essential part of any classification process. It compares the categorised image to a valid or ground truth data source. Ground truth can be gathered in the field, but it is time consuming and costly. Analysing high-resolution imagery, existing classified imagery, or GIS data layers can also yield ground truth data. An effective way for accessing the correctness of a classified map's is to create a series of random points from ground truth data and compare them to the classified data by generating a confusion matrix. There are three main steps in this procedure: Creation of Accuracy Assessment Points, Updating of Accuracy Assessment Points, and Computation of Confusion Matrix.

Accuracy Assessment Points: A popular method is to randomly choose hundreds of sites and identify their class categories using credible sources such as fieldwork or human interpretation of high resolutions imagery. The categorisation results at the same places are then compared to the reference points. The image which was used to create the classification is added. This image is considered to be the reference image or ground truth. A point shapefile is created. Using the elements of visual image interpretation, a set of accuracy evaluation points is created, with the same number of points for each class. i.e., 20 points for each class. These points are later assigned with "ID" concerning its class.

Update Accuracy Assessment Points: In this step, the accuracy assessment points are updated with values from the classified image. The classified image is added where the accuracy is to be assessed. Extraction of the pixel value for each point from the classified image was performed using extract multivalues to points tool. Then, both the values from the ground truth or reference and classified image are available along with the separate columns in the attribute table.

Compute Confusion Matrix: This step computes a confusion matrix using the random accuracy assessment points. The column of the confusion matrix represents the reference data while the row of the confusion matrix represents the remote sensed classification results. The accuracy assessment points are generated in the "Accuracy

Table 21.2 Rating criteria of kappa statistics

Kappa statistics	Strength of agreement
<0.00	Poor
0.00–0.20	Slight
0.21–0.40	Fair
0.41–0.60	Moderate
0.61–0.80	Substantial
0.81–1.00	Almost perfect

Assessment Points" and updated in the "Update Accuracy Assessment Points". This approach computes the user's accuracy and producer accuracy for each class along with an overall kappa index of agreement. The kappa index ranges from 0 to 1 where 1 represent 100% accuracy (Table 21.2).

$$\text{Overall accuracy} = \frac{\text{Number of correctly classified points}}{\text{Column total}} \tag{21.1}$$

$$K = \frac{\text{Observed Accuracy} - \text{Chance Agreement}}{1 - \text{Chance Agreement}} \tag{21.2}$$

For the field measurement of SOM at different locations (ten sites) within the catchment area, the required instruments are Hot air oven, muffle furnace, porcelain crucible, and portable GPS device. Figure 21.5 shows (a) hot air over, (b) over dried soil sample, (c) muffle furnace, and (d) core cutter used at field site for soil sampling.

21.5.1.4 Soil Sampling

The study area is divided uniformly into square grid of dimension 750 m using fishnet tool in the ArcGIS software. Therefore, the study area comprises of several square grid and one soil sample is taken for each respective grid which would represent the soil organic matter content of that particular grid area. Twenty soil samples (10 sites) from Langol catchment, depicting the various land use categories, were collected and analyse as a part of study of these soil attributes. Sampling was done for the top layer 0–15 cm and 15–30 cm depth. The basic approach of physical sampling entails collecting soil samples within a defined soil depth with a known volume soil corer equipment, allowing estimation of soil organic content**.** The soil is collected for two distinct depths: 0–15 cm, 15–30 cm by making use of soil corer for every sampling location. All samples were collected by driving a cylindrical core of 10 cm in diameter and 12.8 cm in length. A portable GPS device is used to locate each sample site where their respective latitude and longitude is noted. A total of 20 soil samples were obtained from ten soil sampling sites representing various land use types. The core technique requires weighing a predetermined volume of soil taken using a core. The core approach has emerged as the most preferred technique among ecologists, and it is suggested in several of the most generally recognised ecological methodology books. The core technique has numerous advantages: the

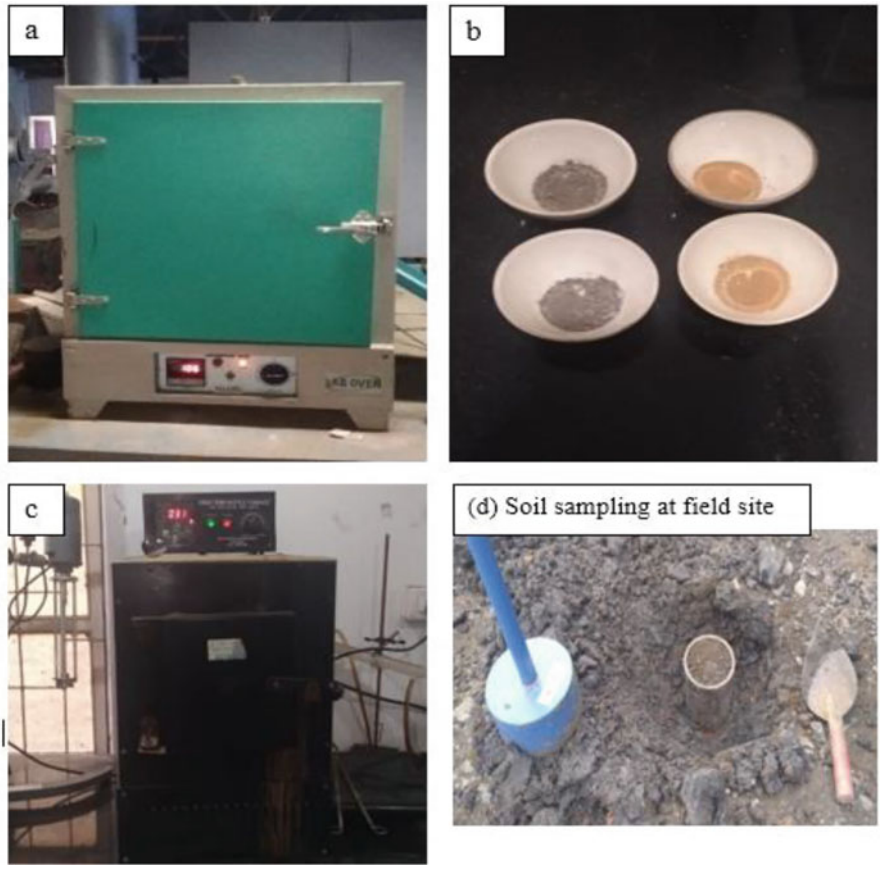

Fig. 21.5 Instruments used for the measurement (**a**) Hot air over (**b**) Over dried soil sample (**c**) Muffle furnace and (**d**) Core cutter at field site for soil sampling

soils acquired can be used for chemical analysis, sampling impact a comparatively small space, no sophisticated equipment is needed, and the portability and convenience of usage enables the collection of a huge number of cores. The soils were air dried, and larger organic materials were separated. A fraction of each sample was mashed further using a mortar and pestle to permit passing through a 2 mm sieve and kept for further analysis. The flowchart of methodology adopted for determination of Soil Organic Matter is presented in Fig. 21.6

21.5.1.5 Determination of Bulk Density

Bulk density is often measured in g/cm^3. The bulk density of soil is a measure of its compaction. It is computed by dividing the soil's dry weight by the volume of core which was used to take the sample. This volume includes the volume occupied by soil particles as well as the amount of space between soil particles. Bulk density is a

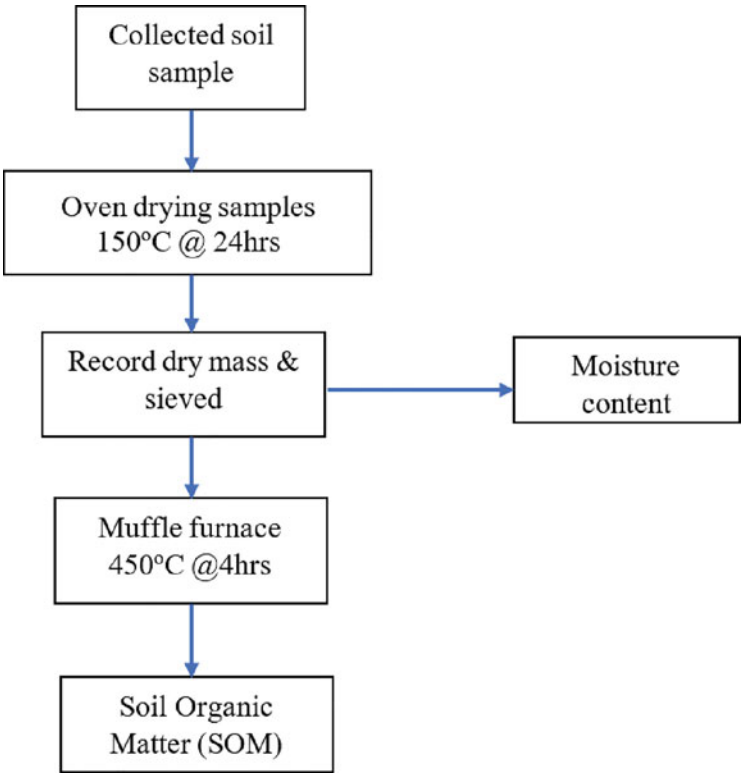

Fig. 21.6 Methodology adopted for determination of Soil Organic Matter in Langol catchment

reflection of soil structure and is influenced by the proportion and quality of mineral and organic soil components. It is a soil parameter with substantial spatial variability that is especially susceptible to extraneous substances in the samples (e.g., presence of coarse fragments, roots, etc.). Basically, the soil samples are oven-dried at 105° C for 24 h, cooled, and the soil's dry weight is recorded. Bulk density shows the soil's potential to withstand structures, transmit water and solutes, and aerate the soil.

$$\text{Bulk density} = \frac{\text{weight of soil after drying}}{\text{volume of the core}} \tag{21.3}$$

21.5.1.6 Loss-on-Ignition Method

For this experiment, the oven-dried soil is used where soil moisture has been removed. Firstly, the soils were dried for 24 h in a hot air oven at 105 °C, then weighed (W_{105}) after cooling for 20 min in a desiccator. After drying, soil samples are reduced to a small particle size by grinding. Then the sample is pass through a

2 mm sieve to filter out plant and root material, gravel, pebbles, and any other unwanted material in the samples. Then, a small amount of the dry soil nearly 5–8 g, which passes through 2 mm sieve is put in a porcelain crucible and placed inside a muffle furnace where it is heated to a temperature of 450 °C and kept for 4 h until the organic matter in the soil is removed. The temperature and duration for the LOI were chosen after reviewing a number of literatures. The weight loss during combustion was used to compute the soil organic matter. Basically, LOI was calculated by dividing the difference of the oven-dried soil mass and the soil mass obtained after combustion of the oven-dried soil mass. Weight (W_{450}) was computed after cooling in a desiccator as mentioned above. The organic matter content (OM) is evaluated by the following equation:

$$\text{SOM}\ (\%) = \frac{\text{W}\ (105\,^\circ\text{C}) - \text{W}\ (450\,^\circ\text{C})}{\text{W}\ (105\,^\circ\text{C})} \tag{21.4}$$

where

SOM (%) = Soil organic matter in percentage.
$W_{150^\circ C}$ = Weight of soil after drying in hot air oven.
$W_{450^\circ C}$ = Weight of soil after combustion at muffle furnace.

21.6 Results and Discussion

21.6.1 Land Use and Land Cover Classification Result

Supervised classification was performed for the study area using the maximum likelihood classifier algorithm. The study area is identified into six major classes (Fig. 21.7) i.e., forest, agriculture, built-up, barren, marshy, and water body. The area of each land use class was computed taking into consideration the pixel count of each respective class and total area of a pixel (900 m^2). Table 21.3 shows the percentage contributions for each classified area. The percentage areas of each category are: forest (16.85%), water body (2.22%), built-up (45.18%), marshy (11.38%), agriculture (7.66%), and barren land (16.69%) (Fig. 21.8). Among the various land use categories, the settlement area contributes the largest percentage area of 45%. It is followed by Forest and Barren areas with similar area distribution of 16% and Marshy area occupying an area of 11%. And the least occupied by agriculture (7%) and water body (2%). Therefore, the settlement area is the most predominant land cover of the study area occupying more than two-fifth of the study site.

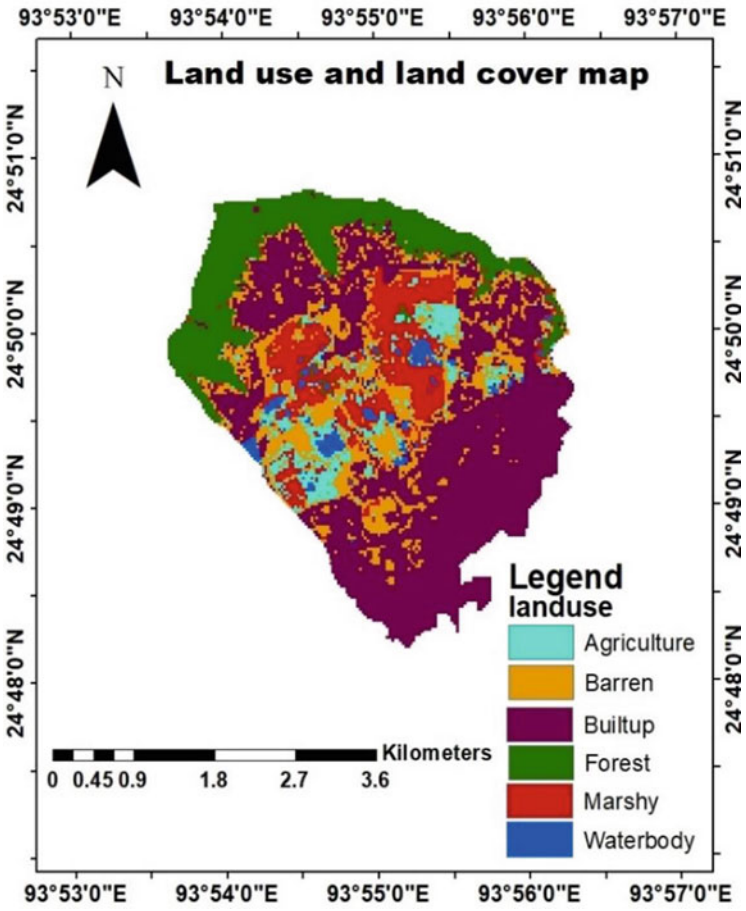

Fig. 21.7 Land use and land cover map of year (2021)

Table 21.3 Area distribution of Langol catchment in year 2021

Sl. no	Land cover	2021	
		Area (km^2)	Percentage (%)
1	Forest	2.3634	16.85
2	Water body	0.3114	2.22
3	Built-up	6.3342	45.18
4	Marshy	1.5857	11.38
5	Agriculture	1.0746	7.66
6	Barren	2.34	16.69

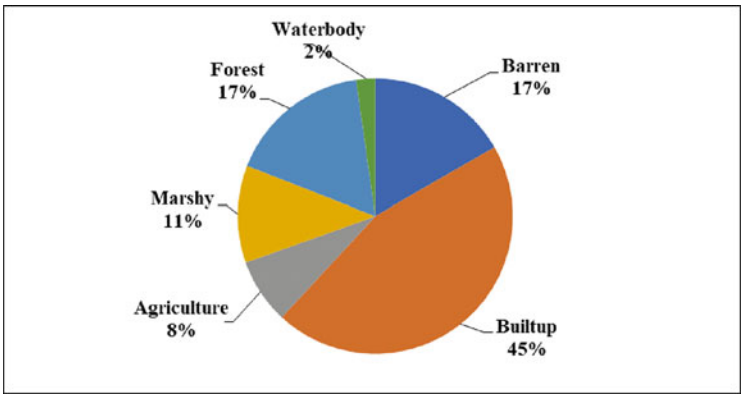

Fig. 21.8 Pie chart depicting percentage distribution of classified area

21.6.2 Accuracy Assessment Result

Accuracy assessment is a crucial technique to ensure that the classified image matches with the ground truth or reference data. The result of the accuracy assessment is presented in the form of an error matrix and is displayed in Table 21.4.

The outcome from accuracy evaluation revealed an overall accuracy of 83.33%. The user's accuracy ranged from 68% to 94% while producer's accuracy ranged from 75% to 85%. Table 21.3 depicts a conceptual confusion matrix for an LULC classification. The diagonal members of a matrix show the number of samples where the classification results match with the reference data source. The samples that were incorrectly identified or ignored by the classifier are represented by the off-diagonal member of the matrix. Pixels which have not been allocated to an appropriate class do not display along the diagonal of the matrix, indicating that the class assignment is confused between the several land cover classes. The commission error represents the points that are included in the category but do not actually belong there. For example, the commission error is largest in barren regions (32%), implying that a greater percentage of sites that do not belong ~~in~~to this category is labelled as barren. Likewise, the omission error represents those points which are not in a category despite the fact that they should be. Barren/bare land (35%) has the biggest omission error, implying that a greater percentage of sites that should be classified in this category are not. This research study yielded an overall Kappa index of 0.798. This coefficient value is considered to be substantially good. Aside from overall classification accuracy, parameter such as user accuracy, producer accuracy etc. provides the classifier with a much more precise explanation of performance of the model for a particular class or category in his subject of study or research.

Table 21.4 Error matrix of LULC classified map

	Reference data									
Classified data	Land cover	Forest	Water body	Built-up	Marshy	Agriculture	Barren	Row total	Commission error	User accuracy
	Forest	17	0	1	0	0	0	18	6	94
	Water body	1	17	0	1	0	0	19	11	89
	Built-up	1	1	15	2	0	0	19	22	78
	Marshy	1	1	2	16	0	3	23	31	69
	Agriculture	0	0	1	0	17	4	22	23	77
	Barren	0	1	1	1	3	13	19	32	68
	Column total	20	20	20	20	20	20	120		
	Omission error	15	15	25	20	15	35		Overall accuracy = 83.33%	Kappa index = 0.798
	Producer accuracy	85	85	75	80	85	65			

21.6.3 Soil Organic Matter Determination

The water content and the soil organic matter from ten location are listed in Table 21.5. The areas from which samples are collected include five land use classes which were taken during the month of October 2021 to February 2022.

Table 21.5 Field data and analysis result

Soil depth	Land use type	Lat & long	Climate	Water content (%)	SOM (g/kg)
1 (a) 0–15 cm (b) 15–30 cm	Barren	24°50′21″ N 93°54′18″ E	Cloudy(27 °C)	18.3 17.2	26.9 29.7
2 (a) 0–15 cm (b) 15–30 cm	Built-up	24°50′22″ N 93°54′47″ E	Cloudy (29 °C)	47.5 57.6	26.1 24.8
3 (a) 0–15 cm (b) 15–30 cm	Built-up	24°50′23″ N 93°55′38″ E	Rainy (26 °C)	17 18.3	24.3 22.4
4 (a) 0–15 cm (b) 15–30 cm	Agriculture	24°50′ 16”N 93°55’15″ E	Cloudy (29 °C)	37.5 44.1	133 123
5 (a) 0–15 cm (b) 15–30 cm	Agriculture	24°49′58″ N 93°54′23″ E	Sunny (29 °C)	40.6 42.3	146 146
6 (a) 0–15 cm (b) 15–30 cm	Marshy	24°49′59″ N 93°54′19″ E	Sunny (29 °C)	33.5 24.8	107 84
7 (a) 0–15 cm (b) 15–30 cm	Forest	24°50′2″ N 93°53′57″ E	Rainy (26 °C)	36.2 29.5	166 180
8 (a) 0–15 cm (b) 15–30 cm	Forest	24°50′21″ N 93°56′58″ E	Rainy (26 °C)	33.3 29.5	172 130
9 (a) 0–15 cm (b) 15–30 cm	Marshy	24°50′59″ N 93°55′33″ E	Cloudy (29 °C)	42.5 45.8	141 129
10 (a) 0–15 cm (b) 15–30 cm	Agriculture	24°50′6″ N 93°55′1″E	Cloudy (28 °C)	26.9 25.8	172 166

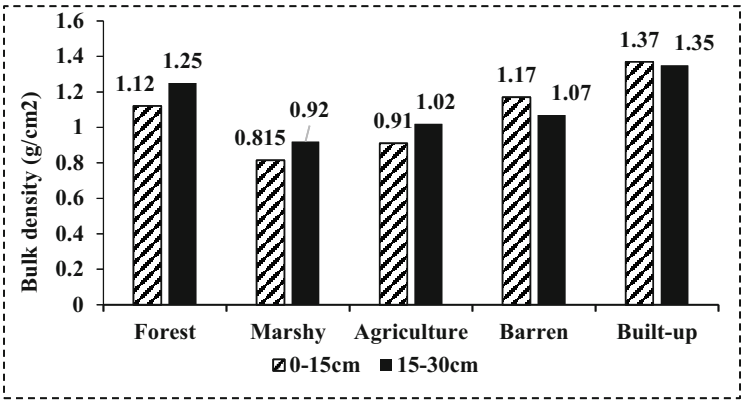

Fig. 21.9 Bulk density of various land use types

The bulk density of different land use types shows slight variation as depicted in Fig. 21.9. The lower soil layer is shown to have higher bulk density compared to the top layer. The bulk density rises with soil depth because of lesser presence of organic matter in the subsurface layer and reduces root penetration than top layers, and thus has less pore space. Also, the compacting weight of the soil above them affects the subsurface layers as well. The highest density was identified in built-up with a mean value of 1.36 g/cm^2 followed by forest area (1.185 g/cm^2), barren land (1.12 g/cm^2), and agriculture (0.965 g/cm^2). And the least value of bulk density was obtained from marshy areas with a mean value of 0.867 g/cm^2. The ranges of bulk density observed in the region falls within the ideal bulk densities for plant growth. This indicates that the soil is porous and less compacted. It will facilitate root growth, water, and air circulation through the soil. Hence, the study area is ideal for agricultural activities.

The water content and soil organic content value of 20 soil specimens in the study site (Langol catchment) varies from 17% to 57.6% and 22.4 g/kg to 180 g/kg. A total of 20 soil samples collected across the Langol catchment shows a wide range of organic content (Table 21.4) due to variances in vegetation patterns, water management, and soil properties, land use type, etc. From this practical study, we can infer that soil organic matter of forest soil has higher organic content which varies from 130 g/kg to 180 g/kg. It can be attributed to decaying of leaves, branches of trees, twigs, remains of insects, animal and their excreta, etc. so it is highly fertile. Moreover, the soil from agriculture areas also shows considerably high organic content and ranges from 123 g/kg to 172 g/kg. This is also due to decaying of crop residue, presence of living microbial biomass, remains of insects and their excreta, etc. The amount of moisture is also high in this type of soil. Lastly, those soil from barren and built-up areas results in presence of much lower organic content which varies from 26.9 g/kg to 29.7 g/kg and 22.4 g/kg to 26.1 g/kg, respectively.

From Fig. 21.10, we can infer that, mostly the top soil is found to have higher organic content compared to the deeper soil irrespective of land cover type since the top soil is where most of the Earth's biological soil activity occurs and accumulation

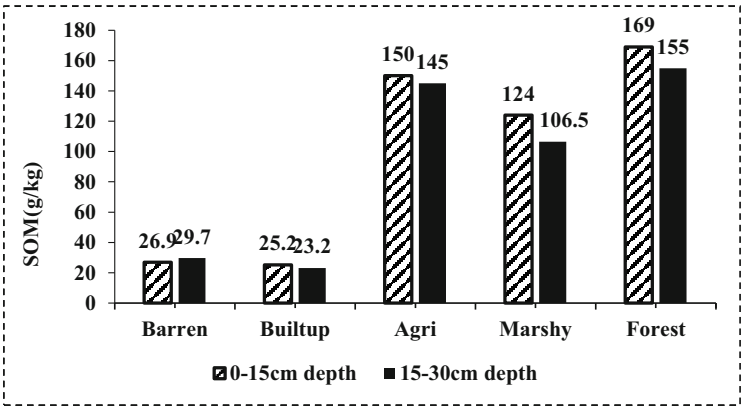

Fig. 21.10 Mean soil organic matter content of various land use type

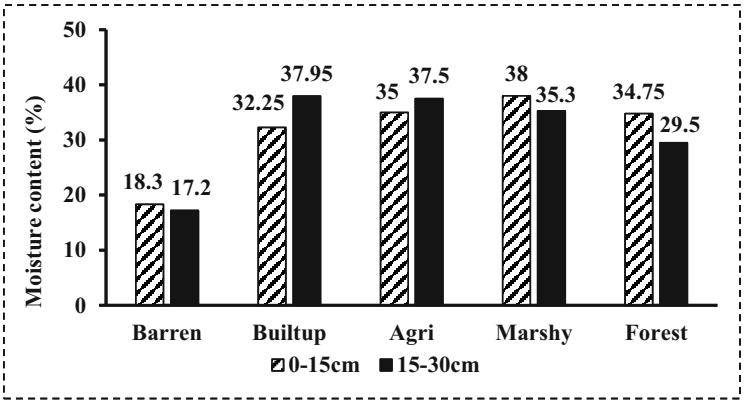

Fig. 21.11 Mean moisture content (%) of various land use type

of organic residue takes place. Moreover, the there is also good moisture content in the soil ranging from 17% to 57% as shown in Fig. 21.11, which account to appreciable rainfall occurring in the region. However, we did not find any significant co-relationship between the moisture content and its organic matter presence in the soil.

21.7 Conclusions

This approach can estimate soil organic matter with decent accuracy. For loss-on-ignition analysis, close attention should be given to the temperature and time of heating. Before weighing, samples are usually cooled in a desiccator for research reason. It is crucial to not allow samples to rehydrate following ignition.

Subsequently, we recommend taking weight shortly after the temperature has fallen beyond 150 °C but before it hits 105 °C. Table 21.3 displays the findings of SOC in the soil profile as assessed by mass loss by LOI (SOM). As expected, the SOM reduced as the depth increased. The higher SOM content in the top soil layers is the consequence of appreciable plant and animal residues accumulated on the soil surface. The suggested approach has the benefit of simplicity and provides a quick alternative for regular soil organic matter assessment. Since it was determined that soil organic matter content ranges from 2.4% (moderately fertile) to 18% (highly fertile) depending on the type of land use and land cover. We can see a great potential for expanding the agricultural area in the region which can also lead to further increase in the organic content level. Moreover, these increase in vegetation cover will help absorb atmospheric carbon dioxide thereby aiding carbon sequestration. Besides, the results obtained in this study can be used as a reference for other study areas with the similar soil type and landscape conditions.

21.8 Recommendations

In order to acquire consistent results in the determination of SOM, fine grinding of soil samples is crucial. Small uniform subsamples can only be generated from finely powdered, homogeneous materials. Poor sampling is frequently the cause of poor replication. When processing a large number of samples, a mechanised mortar and pestle device will save a lot of time and effort. A clay correction factor can be introduced, to avoid over-estimating the SOM content by correcting for structural water loss. Estimation of soil organic matter can be done using other methods such as wet oxidation method, elemental C analyser, etc. to compare their result and conclude which method is most suitable for determining SOM in soil containing considerable organic content.

Acknowledgments I extend my valuable thanks to Dr. Thiyam Tamphasana Devi for her valuable advice and suggestion for conducting this study. Thank are also to the Department of Civil Engineering and Department of Mechanical Engineering, NIT Manipur who provided the required laboratory equipment in the study.

References

Abella SR, Zimmer BW (2007) Estimating organic carbon from loss-on-ignition in northern Arizona forest soils. Soil Sci Soc Am J 71(2):545–550. https://doi.org/10.2136/sssaj2006.0136

Ball DF (1964) Loss-on-ignition as an estimate. J Soil Sci 15(1):84–92

Batjes NH (1996) Total carbon and nitrogen in the soils of the world. Eur J Soil Sci 47:151–163

Ben-Dor E, Banin A (1989) Determination of organic matter content in arid-zone soils using a simple "loss-on-ignition" method. Commun Soil Sci Plant Anal 20(15–16):1675–1695. https://doi.org/10.1080/00103628909368175

Census (2011) District census handbook, Imphal West, census of India, series 15, Part XIIB, directorate of census operation, Government of Manipur

DeLaune RD, White JR (2012) Will coastal wetlands continue to sequester carbon in response to an increase in global sea level?: a case study of the rapidly subsiding Mississippi river deltaic plain. Clim Change 110:297–314. https://doi.org/10.1007/s10584-011-0089-6

Donkin MJ (1991) Loss-on-ignition as an estimator of soil organic carbon in a-horizon forestry soils. Commun Soil Sci Plant Anal 22(3–4):233–241. https://doi.org/10.1080/00103629109368411

Konen ME, Jacobs PM, Burras CL, Talaga BJ, Mason JA (2002) Equations for predicting soil Organic carbon using loss-on-ignition for north central U.S. soils. Soil Sci Soc Am J 66(6):1878–1881. https://doi.org/10.2136/sssaj2002.1878

Kumar S, Ghotekar YS, Dadhwal VK (2019) C-equivalent correction factor for soil organic carbon inventory by wet oxidation, dry combustion and loss on ignition methods in Himalayan region. J Earth Syst Sci 128(3):1–10. https://doi.org/10.1007/s12040-019-1086-9

Lal R (2004) Soil carbon sequestration in India. Clim Change 65(3):277–296. https://doi.org/10.1023/B:CLIM.0000038202.46720.37

Nelson D, Sommers LE (1982) Matter methods of soil analysis. Part 2. Chemical and microbiological properties. In: Page AL (ed) Total carbon, organic carbon, and organic, vol 9, pp 539–579

Pu JH, Wallwork JT, Khan M, Pandey M, Pourshahbaz H, Satyanaga A, Hanmaiahgari PR, Gough T (2021) Flood suspended sediment transport: combined modelling from dilute to hyper-concentrated flow. Water 13(3):379

Salehi MH, Beni OH, Harchegani HB, Borujeni IE, Motaghian HR (2011) Refining soil organic matter determination by loss-on-ignition. Pedosphere 21(4):473–482. https://doi.org/10.1016/S1002-0160(11)60149-5

Schulte EE, Hopkins BG (2015) Estimation of soil organic matter by weight loss-on-ignition. In: Soil organic matter: analysis and interpretation, SSSA special publication number 46. SSSA, Madison, pp 21–31. https://doi.org/10.2136/sssaspecpub46.c3

Shankar MS, Pandey M, Shukla AK (2021) Analysis of existing equations for calculating the settling velocity. Water 13(14):1987

Shivashankar M, Pandey M, Zakwan M (2022) Estimation of settling velocity using generalized reduced gradient (GRG) and hybrid generalized reduced gradient–genetic algorithm (hybrid GRG-GA). Acta Geophys:1–11

Wallwork JT, Pu JH, Kundu S, Hanmaiahgari PR, Pandey M, Satyanaga A, Pandey M, Satyanaga A, Amir Khan M, Wood A (2022) Review of suspended sediment transport mathematical modelling studies. Fluids 7(1):23

Wang JP, Wang XJ, Zhang J (2013) Evaluating loss-on-ignition method for determinations of soil organic and inorganic carbon in arid soils of northwestern China. Pedosphere 23(5):593–599. https://doi.org/10.1016/S1002-0160(13)60052-1

Chapter 22
Agricultural Drought Assessment Using Satellite-Based Surface Soil Moisture Estimate

Hussain Palagiri and Manali Pal

Abstract Due to the lack of large scale, fine resolution, and accurate/quality soil moisture (SM) many agricultural drought studies are mostly based on ground-based SM observations having limited spatiotemporal variability. Microwave remote sensing showed capability in estimating geophysical properties like soil moisture. European Space Agency (ESA) under Climate Change Initiative (CCI) developed an active–passive multi-satellite merged ESA CCI SM dataset. In this study, to explore ESA CCI SM's potential in exploring drought monitoring, Empirical Standardized Soil Moisture Index (ESSMI) is derived to identify agricultural drought in Telangana state from 2001 to 2020. To evaluate ESSMI's efficiency it is compared to Standardized Precipitation Index (SPI) and Rainfall Anomalies (RFA) calculated from India Meteorological Department (IMD) daily gridded rainfall data. Temporal evolution of both indices showed ESSMI exhibiting a delayed response with SPI. The yearly drought identified by ESSMI showed consistency with SPI and RFA. Different classes of drought areas identified by ESSMI are compared with SPI which showed near normal and mild dry regions for most of the study period. SPI also showed extreme events in some months that ESSMI was unable to capture. Near normal to moderate droughts identified by ESSMI are generally larger than that of detected by SPI.

Keywords Agricultural drought · Soil moisture · Drought indices · Remote sensing · Empirical standardized soil moisture index (ESSMI) · European Space Agency (ESA) · Climate change initiative (CCI) SM (ESA CCI SM)

H. Palagiri · M. Pal (✉)
Department of Civil Engineering, National Institute of Technology Warangal, Warangal, India
e-mail: ph720022@student.nitw.ac.in; manalipal@nitw.ac.in

M. Pandey et al. (eds.), *River Dynamics and Flood Hazards*, Disaster Resilience and Green Growth, https://doi.org/10.1007/978-981-19-7100-6_22

22.1 Introduction

Hydrologic hazards are extreme events related to water occurrence, movement, and distribution (National Research Council 1999). They cause loss of life as well as economic, environmental, and social impacts that significantly slow the development process (Wilhite 2000). Hydrologic hazards include floods, droughts, landslides, and river scour and deposition. Drought is the most complex but least understood hazard and is distinct from other hazards. It affects more people than any other hazard (Hagman et al. 1984) spreading over a large geographical area. It is difficult to determine the onset and end of the drought event, as its effects occur slowly over time and may remain for years even after the end of the event. A drought can be short or long, continuing for few weeks to several years and can have devastating effects on water supplies and agriculture sector. In agriculturally dependent countries such as India, a severe drought can have a devastating effect on the economy. Given the major role of agricultural productivity in the economic development of India, identifying and assessing the agricultural drought is essential. An agricultural drought refers to a period with declining soil moisture (SM) content and consequent crop failure from water stress (Mishra and Singh 2010). Water stress is one of the major causes of agricultural drought (Narasimhan and Srinivasan 2005). SM plays an important role in indicating water stress and thereby identifying agricultural drought. Also, SM being interactive at the root zone, it is physically related to the growth and health of crops (Hunt et al. 2009). It is also capable in describing the effects of irrigation, precipitation, dry spells, and evapotranspiration (Padhee et al. 2017). Agriculture is the first sector to be affected by the onset of drought due to its dependence on SM reserves at various stages of crop growth (Narasimhan and Srinivasan 2005). Therefore, an agricultural drought index should be able to characterize the spatiotemporal variability of SM as it influences the agricultural drought propagation. But the operational agricultural drought monitoring studies are mostly based on indices based on precipitation, temperature, and other hydrological and meteorological variables without considering site specific soil properties (Torres et al. 2013). Standardized Precipitation Index (SPI) (McKee et al. 1993) and Standardized Precipitation Evapotranspiration Index (SPEI) (Vicente-Serrano et al. 2010) are meteorological drought indices frequently used for monitoring agricultural drought (Dai et al. 2020; Dutta et al. 2015; Mohammed et al. 2022). Atmospheric Water Deficit (AWD) (Purcell et al. 2003) is another frequently used agricultural drought index which assumes soil water balance using precipitation and evapotranspiration (Martínez-Fernández et al. 2016). Vegetation Condition index (VCI) (Kogan 2002), Vegetation Temperature Condition Index (VTCI) (Wang et al. 2001), and Vegetation Supply Water Index (VSWI) (Carlson et al. 1994) are other frequently used non-SM vegetation based drought indices to characterize agricultural drought. But these non-SM based indices lack the ability to assess/characterize agricultural droughts (Tirivarombo et al. 2018).

The agricultural drought is primarily caused by soil moisture content deficits and can be assessed more accurately by drought indices based on soil moisture

percentiles developed by drought assessment studies (Mukherjee et al. 2018). The first SM based agricultural drought indices include the Palmer Drought Severity Index (PDSI) developed by Palmer 1965, to use SM in identifying drought. The PDSI assesses water supply and water budget to provide soil moisture surplus/deficit. It has a timescale of 9 months and cannot identify short-term droughts. Another index namely Crop Moisture Index (CMI) was developed by Palmer in 1968 to monitor short-term moisture conditions that indicates more favourable moisture conditions over a particularly wet or dry month even in the middle of a serious long-term wet or dry period. Narasimhan and Srinivasan (2005) developed Soil Moisture Deficit Index (SMDI) using long-term soil moisture to determine agricultural drought at root zone depth. They also developed Evapotranspiration Deficit Index (ETDI) by combining soil moisture with evapotranspiration (Narasimhan and Srinivasan 2005). Both SMDI and ETDI exhibit short-term dry conditions and have no seasonality. Salvia et al. (2020) developed Soil Moisture Agricultural Drought Index (SMADI) by combining soil moisture and temperature conditions as a lagged response of vegetation. Based on actual water content and field capacity Hunt et al. (2009) developed Soil Moisture Index (SMI) and Martínez-Fernández et al. (2015) developed Soil Water Deficit Index (SWDI). But the need for availability of large scale wilting point and field capacity could compromise the usefulness of the index (Martínez-Fernández et al. 2015). The studies by Sheffield et al. (2004), Dutra et al. (2008), and Carrão et al. (2016) represented drought as percentiles of probability distribution function fitted to SM observations. Sheffield et al. (2004) and Dutra et al. (2008) fitted beta and normal Probability Density Functions (PDF) to SM observations, respectively, to represent drought. The study by Carrão et al. (2016) represented drought by fitting an empirical PDF (ePDF) to the long-term monthly soil moisture observations with a nonparametric Kernel Density Estimator (KDE) and developed spatially invariant and probabilistic year-round drought index Empirical Standardized Soil Moisture Index (ESSMI). They have used SM product developed by European Space Agency under the Climate Change Initiative (ESA CCI) programme to compute the ESSMI during the critical crop growth stages and found it was highly correlated with crop yield.

Ground-based SM agricultural drought indices are accurate but are of point-based nature with limited spatial variability and cannot be applied for large scale studies. With the advances made in remote sensing soil moisture can be retrieved globally using microwave sensors which helps in large scale agricultural drought monitoring. This builds the overall motivation of the current study that is explained in the following sections.

22.2 The Rationale of the Study

Microwave remote sensing showed capability in estimating geophysical properties like soil moisture using properties like backscatter and brightness temperature (Entekhabi et al. 2010; Jackson et al. 2011) and paved the way for a continuous

agricultural drought monitoring system by providing large scale, fine resolution, accurate/quality SM data. Active microwave sensors like European Remote Sensing Satellite Scatterometer (ERSCAT) and Advanced Scatterometer (ASCAT) have a higher spatial resolution but are very expensive. On the other hand, data provided by passive microwave sensors from Soil Moisture and Ocean Salinity (SMOS), Soil Moisture Active Passive (SMAP), and Advanced Microwave Scanning Radiometer-2 (ASMR2) have to deal with coarser spatial resolution but are inexpensive. ESA under Climate Change Initiative (CCI) programme developed a daily global SM dataset from 1978 to 2020 by merging several active and passive microwave SM data. This multi merged ESA CCI SM dataset was successfully used in several drought monitoring studies. Zhang et al. (2019) used this ESA CCI SM to derive Standardized Soil Moisture Index (SSI) to monitor agricultural drought over Yellow River Basin from 2000 to 2012. They compared the SSI with other drought indices such as SPI, SPEI, and PDSI. It showed a relatively higher consistency with PDSI and a significantly delayed response with SPI and SPEI. Again Zhang et al. (2021) compared the SSI derived from ESA CCI SM with SSI derived from Global Land Data Assimilation System (GLDAS)-Noah model, where both ESA CCI SM_SSI and GLDAS-Noah_SSI exhibit high consistencies in spatial patterns, showing their potential in drought monitoring across China. McNally et al. (2016) compared the ESA CCI SM with Noah SM/Variable Infiltration Capacity (VIC) SM over East Africa for the period of 1982–2013. They showed similar anomalies during extreme wet and dry years. The ESA CCI SM was able to monitor drought over moderately vegetated regions. Liu et al. (2019) used ESA CCI SM to derive Soil Moisture Anomaly Percentage Index (SMAPI) and compared it with GLDAS SM_SMAPI. The ESA CCI SM showed capability in identifying extreme drought events excluding densely vegetated regions and GLDAS SM is more effective in densely vegetated areas. Martínez-Fernández et al. (2017) used ESA CCI SM to derive Soil Water Deficit Index (SWDI) over Zamora province, Spain, for the period of 1978–2014 and compared it with Atmospheric Water Deficit index (AWD) and CMI. The SWDI showed correlation coefficients of 0.70 and 0.72 when compared with AWD and CMI. The ESA CCI SM was also utilized to develop alternative drought indicator by Carrão et al. (2016) where they used this product to develop a drought index ESSMI. Carrão et al. (2016) found ESSMI could accurately describe the severe and extreme drought intensities in north-eastern Brazil in 1993, 2012, and 2013. The ESSMI is based on SM alone and is computed by fitting a nonparametric ePDF to historical time series of SM observations and then transforming it into a normal distribution with a mean of zero and standard deviation of one. The nonparametric ePDF has been observed to be very flexible: the ESSMI provides a link between the observed SM and the respective probability of occurrence that is more accurate than with other proposed parametric distributions such as normal and beta for modelling SM (Carrão et al. 2016). However, the use of this index is very limited, especially in Indian drought monitoring studies. On the other hand, Telangana is a severely drought-prone state of India, with rainfall as its major water source. The Telangana government declared drought in 7 out of 10 districts in the year 2015 (Anuradha 2016). In last few years, almost 50% of the mandals in Telangana recorded scanty rainfall.

Additionally, the major occupation for two-thirds of the population in the state is agriculture-based that is heavily impacted by drought occurrences. This increases the need for accurate agricultural drought characterization in the state. Keeping in mind the necessity of drought monitoring system for Telangana and availability of large scale satellite soil moisture data from ESA CCI, the present study intends to employ the ESSMI using the nonparametric distribution of ESA CCI SM data, to characterize the agricultural drought in drought-prone Telangana. Then, ESSMI is compared with rainfall-based index Standardized Precipitation Index (SPI) and Rainfall Anomalies (RFA) as rainfall influences SM in the upper soil layer relative to the soil field capacity in deeper layers (Tigkas et al. 2019). The SPI is chosen over other meteorological-based indices to compare ESSMI as it needs rainfall data alone as input and SPI can also be calculated for short periods of record that contain missing data (Svoboda and Fuchs 2016). The SPI doesn't consider SM and evapotranspiration which are important components related to plant development. Still, due to its simple structure and low data requirements (Tigkas et al. 2019) SPI is the most widely used drought index worldwide for agricultural drought analyses. Another index namely SPEI takes evapotranspiration as input along with the rainfall requires a serially complete record of data with no missing months (Svoboda and Fuchs 2016) and the computations of evapotranspiration are complex. Hence, SPI and RFA are chosen to compare ESSMI for agricultural drought analyses in Telangana from 2001 to 2020.

22.3 Limitations of the Study

Microwave (MW) satellites provide SM at large spatial and temporal scale. However, they can only provide SM at surface level, whereas inputs of the agricultural drought index should well describe the moisture conditions in the root zone. The current study is restricted to using only surface SM based drought indices that may not always accurately characterize the SM dynamics at deeper layers. However, persistent stress in the surface SM is often indicative of severe SM deficit in the deeper soil profiles due to strong interconnection between the soil layers through advective and diffusive soil hydrologic processes (Sehgal et al. 2021). Some studies have shown a strong correlation between surface and root zone SM (Albergel et al. 2008; Hirschi et al. 2014; Pal et al. 2016; Pal and Maity 2019), although the coupling strength between soil layers decreases as depth increases (Ford et al. 2014; Wu et al. 2002; Pal et al. 2016; Pal and Maity 2019). Also, the surface SM is able to respond to transient drought conditions and captures the onset and spatial propagation of drought (Sehgal and Sridhar 2019). Hence, the authors attempt to utilize the above mentioned theories of mutual association of surface and deeper layers SM information to represent the agricultural drought only by surface SM information given by MW sensors. The satellite-based SM also have other uncertainties related to complex ground terrains with frozen land and dense forest cover along with uncertainties inherited from SM retrieval algorithms (Wu et al. 2021). These limitations add to

some missing data to the ESA CCI SM products. The inherent limitations of the source data to compute the drought index may result into some erroneous findings. Additionally, the study considers only the ESSMI values that represents drought based on soil moisture alone and doesn't consider other contributing hydro-climatological variables. The soil moisture alone may not reflect agriculture drought for all the prevailing hydro-meteorological conditions and land types. However, due to soil moisture being directly related to growth and health of crops, this study calculates SM based drought index ESSMI for drought characterization and compares it with rainfall-based index Standardized Precipitation Index (SPI) and Rainfall Anomalies (RFA).

22.4 Materials and Methods

22.4.1 Study Area

Telangana (Fig. 22.1) is located in the semi-arid region (15°46′–19°47′ N and 77° 16′–81°43′ E) with rainfall as its major water source. Drained by two major rivers, Godavari and Krishna, most of the land in the state is arid due to less rainfall and low ground water levels. The monsoon starts from June and ends in September with about 905.4 mm average annual rainfall. Telangana experiences dry conditions for

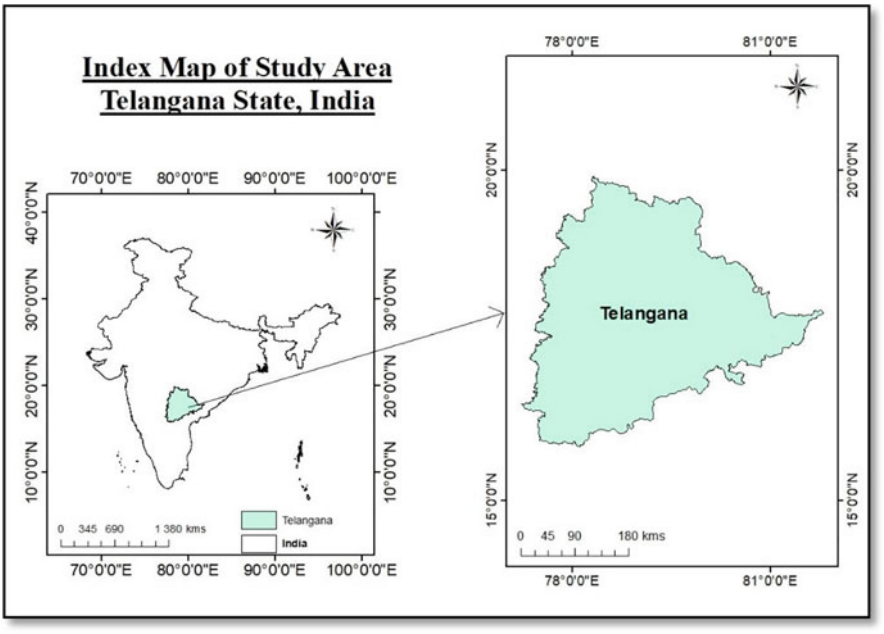

Fig. 22.1 Study area map

8–9 months across a year which worsens the agricultural crisis in the state. Total geographical area of the state is 276.95 lakh acres, of which the area under cultivation constitutes 49.07%. (Telangana State at a Glance 2021, Gov of Telangana). Red soils are predominant in Telangana accounting for 48% of the total area. Other soil types in the state are black cotton soils (25%), alluvium (20%), and rocks and boulders (7%). The major monsoon crops grown in the state are cotton, paddy, maize, soybean, and pulses and major rabi crops are paddy, groundnut, and bengal gram (Agriculture Action Plan 2021–22, Gov of Telangana).

22.4.2 Data

22.4.2.1 Soil Moisture Data

The European Space Agency (ESA) in the framework of Climate Change Initiative (CCI) has developed a daily global surface SM (ESA CCI SM) dataset for the time period from 1978 to 2020 at 0.25° × 0.25° spatial resolution (Gruber et al. 2019). This dataset ingests multiple satellite soil moisture data derived from four active and ten passive microwave sensors. The active C-band scatterometer instruments used to develop ESA CCI SM dataset are Active Microwave Instrument-Wind Scatterometer (AMI-WS), European Remote Sensing Satellite (ERS) 1 and 2, and Advanced Scatterometer (ASCAT) onboard Meteorological Operational satellite (MeTop). The passive multi-frequency radiometer instruments are Scanning Multichannel Microwave Radiometer (SMMR) onboard Nimbus-7, Special Sensor Microwave/Imager (SSM/I) onboard Defense Meteorological Satellite Programme (DMSP), TRMM Microwave Imager (TMI) onboard Tropical Rainfall Measuring Mission (TRMM), Advanced Microwave Scanning Radiometer-E (AMSR-E) onboard Aqua, Advanced Microwave Scanning Radiometer 2 (AMSR-2) onboard Global Change Observation Mission-Water (GCOM-W1), Microwave Imaging Radiometer using Aperture Synthesis (MIRAS) onboard Soil Moisture and Ocean Salinity (SMOS), SMAP L-band Radiometer onboard Soil Moisture Active Passive (SMAP), GPM Microwave Imager (GMI) onboard Global Precipitation Measurement (GPM), MicroWave Radiation Imager (MWRI) onboard Fengyun-3B (FY-3B), and WindSat onboard Coriolis. The temporal evolution of the complete product is shown in Fig. 22.2.

The current study uses ESACCI SM v06.1 daily surface data to retrieve SM data over Telangana State during 2001–2020 (https://esa-soilmoisture-cci.org/v06.1_release) The ESACCI SM provides surface SM in m^3/m^3 (Gruber et al. 2019).

The ESA CCI SM dataset have some missing observations, both temporally and spatially, because of the limitations of microwave remote sensing under frozen conditions, dense forest cover etc. In order to find out the amount of missing data for study area during the study period of 2001–2020, fraction of missing data at each grid is calculated. At each grid, the fraction is computed as the ratio of the sum of number of missing values present in complete time series length to the length of SM

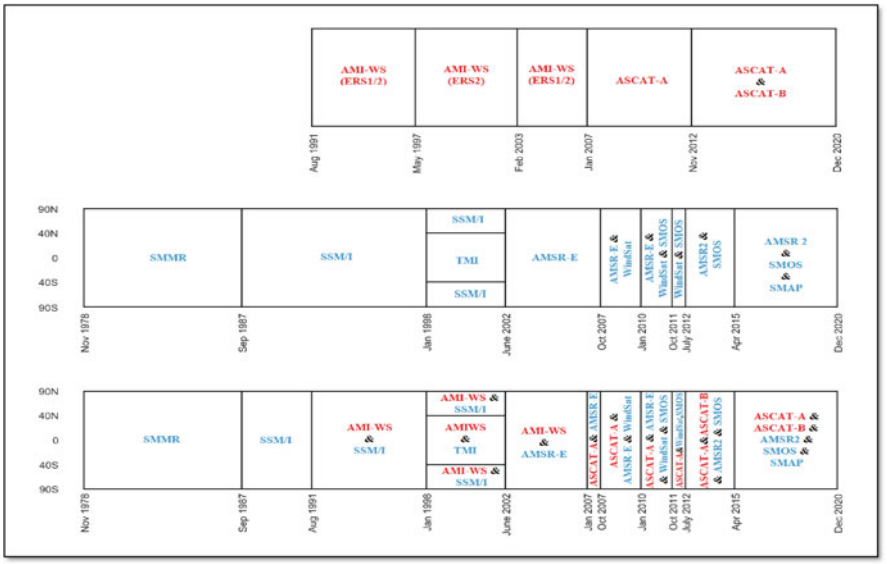

Fig. 22.2 The temporal evolution of sensors used in the Active (red), Passive (blue), and Combined (red and blue) ESA CCI SM product

time series data (Pal and Maity 2021). The fraction of missing data for the considered time period is shown Fig. 22.3. From the figure, it can be noted that the fraction of missing data is as low as 0.3 for most of the grids. The low fraction of missing data pledges nil or trivial amount of computational error thus assuring substantially accurate interpretation. Hence, the ESACCI SM is considered to be suitable enough to perform drought analysis for the chosen study area over the time period.

22.4.2.2 Rainfall Data

The India Meteorological Department (IMD) has provided a gridded daily rainfall dataset at a 0.25° × 0.25° spatial resolution covering a period of 121 years (1901–2021) over the Indian mainland. This dataset is recorded at IMD, Pune and is obtained from (https://www.imdpune.gov.in/Clim_Pred_LRF_New/Grided_Data_Download.html). In this study, the daily rainfall data is directly extracted for Telangana state from 2001 to 2020 to study the rainfall anomalies over Telangana from 2001 to 2020 (Table 22.1).

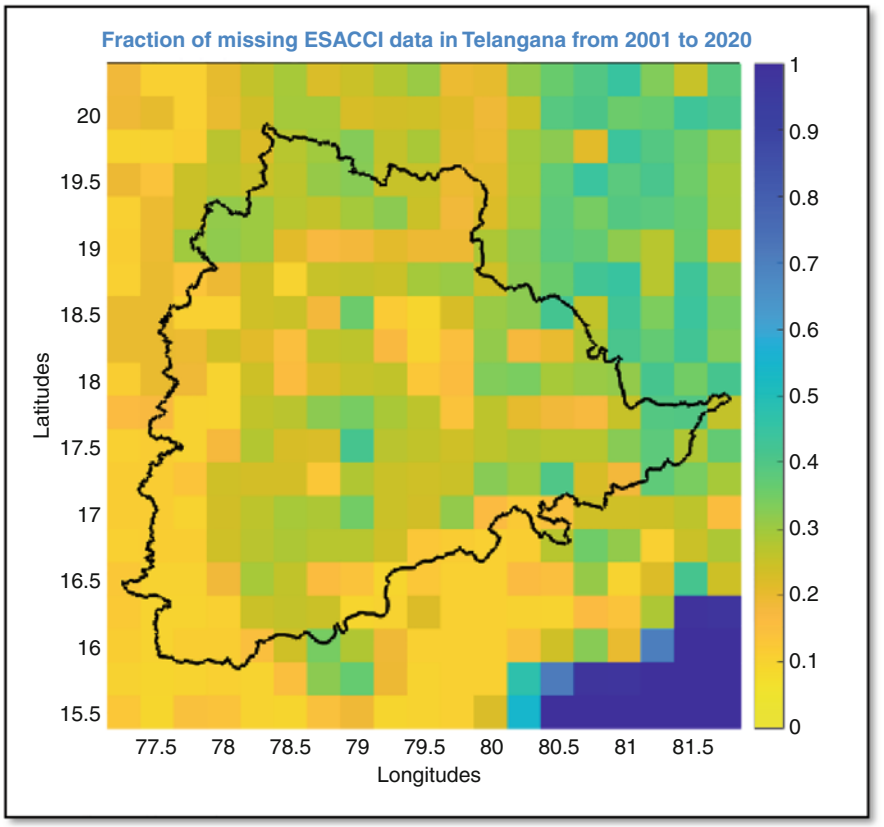

Fig. 22.3 Fraction of missing ESACCI SM data in Telangana from 2001 to 2020

Table 22.1 Datasets used in the study

Datasets used	Data Product	Spatial/ Temporal coverage	Source
ESA CCI	Soil moisture (~0–5 cm) (m^3/m^3)	0.25°/daily	https://esa-soilmoisture-cci.org/ Gruber et al. (2019)
IMD gridded rainfall	Rainfall (mm)	0.25°/daily	https://www.imdpune.gov.in/ Pai et al. (2014)

22.4.3 Empirical Standardized Soil Moisture Index (ESSMI)

The Empirical Standardized Soil Moisture Index (ESSMI) is developed by Carrão et al. (2016) that standardizes the observed SM for a particular time scale (e.g., month, season, year) with respect to the soil moisture climatology for the time scale.

The negative and positive ESSMI values correspond to drier periods and wetter periods than normal respectively. In this study, ESSMI is computed for Telangana with monthly SM, to identify drought from 2001 to 2020. The procedure to calculate ESSMI is described in the following steps.

(a) An empirical Probability Density Function (ePDF) is fitted to the long-term ESACCI SM observations, x_{t1}, x_{t2}, . . .x_{tn}; performed at an averaging timescale of $t = 1$ month (typically t is taken as 1, 3, 6, or 12 months) collected over n (=20) years from 2001 to 2020. Daily ESACCI SM observations over study region are averaged to monthly time scale for the study period. The ePDF is estimated by using a nonparametric Kernel density estimation KDE (Silverman 1986) defined as:

$$\widehat{f}_h(x) = \frac{1}{nh} \sum_{i=1}^{n} K \frac{(x - x_i)}{h}$$

where x_1, x_2, . . .x_n are random samples from an unknown distribution, which in this case are ESACCI monthly SM; n is the sample size (240), K is the kernel smoothing function, and h is the bandwidth. K and h control the smoothness of the density curve. K typically is chosen as the Gaussian function with mean 0 and variance 1 as (Silverman 1986; Wilks 2005):

$$K(x) = \frac{1}{\sqrt{2\pi}} e^{-\frac{x^2}{2}}$$

(b) The cumulative probability, $\widehat{F}(x_t)$ of the monthly averaged ESACCI SM observations x_t is computed related to the respective ePDF, which gives the non-exceedance probability of the monthly ESACCI SM observations.
(c) The non-exceedance probability is transformed to the standard normal variable Z with mean 0 and variance 1 and the ESSMI values are obtained.

The ESSMI ranges from −2 to +2 indicating extreme dry to extreme wet for different drought classes as provided in Table 22.2. The overall methodological concept for calculating the ESSMI is schematically represented in Fig. 22.4.

Table 22.2 Classification of ESSMI for different drought levels (Carrão et al. 2016)

Level of drought	ESSMI
Extreme wet	≥ 2.0
Severe wet	1.5–2
Moderate wet	1–1.5
Near normal	−1–1
Moderate dry	−1.5–−1
Severe dry	−2 to −1.5
Extreme dry	≤ − 2.0

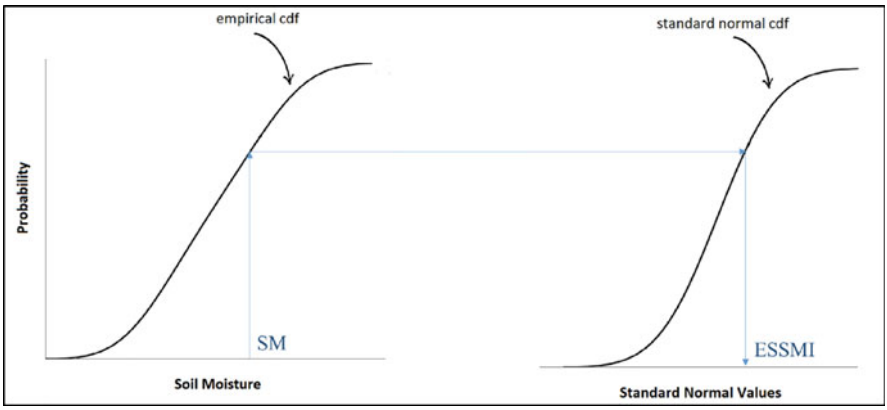

Fig. 22.4 Methodology adopted for deriving ESSMI over Telangana State

22.4.4 Standardized Precipitation Index (SPI)

The Standardized Precipitation Index (SPI) is a widely used meteorological drought index developed by McKee et al. 1993; McKee 1995). As the precipitation data is typically not normally distributed, a transformation has to be applied to the distribution (McKee et al. 1993). Computation of SPI is based on the probability of precipitation for any given time scale as an indicator to monitor the drought (Guttman 1998). It involves fitting a gamma PDF to a given frequency distribution of precipitation totals. In this study, 1-month, 12-month SPI over study period is calculated. Using the input precipitation rasters, monthly composites are generated for a set of averaging time periods of the required timescale (1, 12 in this study). The data set moves such that for each month a new value is determined from the previous months. For example, to generate a 3-month SPI for July, the precipitation values for the month of May, June and July are averaged for each year and used as the input. To transform the precipitation to SPI values, the mean and standard deviation of the precipitation are adjusted to 0 and 1; and the skewness of the existing data is readjusted to 0.

The pixelwise precipitation values are fitted to a gamma distribution which defines the relationship of probability to precipitation. After the fitting, the probability of any observed precipitation can be calculated. The gamma pdf is given as

$$G(x) = \frac{\int_0^x x^{a-1}\, e^{\frac{-x}{b}}\, dx}{b^a \top(a)}$$

These parameters are determined from the precipitation data, where a, b are the shape factor and scale factor, respectively, and x is the precipitation. $\top$ is the gamma function given as

Table 22.3 Classification of SPI for different drought levels (McKee et al. 1993)

Level of drought	SPI
Extreme wet	≥2.0
Severe wet	1.5–2
Moderate wet	1–1.5
Mild wet	0.5–1
Near Normal	−0.5 to 0.5
Mild dry	−1 to −0.5
Moderate dry	−1.5 to −1
Severe dry	−2 to −1.5
Extreme dry	≤ −2.0

$$\mathrm{T}(a) = \int_0^{\infty} y^{a-1}\, e^{-y} dy$$

Since the T is undefined for $x = 0$ and a precipitation distribution may contain 0 s, the cumulative probability becomes the function of probability of precipitation being 0 and the gamma pdf is given as

$$H(x) = q + (q - 1)\, G(x)$$

where q is the probability of the precipitation data being 0, calculated by dividing the number of days for which precipitation value is 0 by the total number of days. The cumulative probability is then transformed to the standard normal random variable Z, which is the value of SPI. Positive/negative SPI values represent that the precipitation values are greater/less than median precipitation. In this study, IMD daily gridded rainfall from 2001 to 2020 is used to calculate 1-month, 12-month SPI over Telangana to identify drought (Table 22.3).

22.4.5 Rainfall Anomalies

Rainfall anomaly (RFA) is used to investigate desiccation rather than drought (Agnew 2000). In this study, yearly/monthly rainfall anomalies in Telangana from 2001to 2020 are calculated. The RFA needs long-term rainfall data and rainfall data of the period for which anomalies are evaluated. IMD daily gridded rainfall data over a 32-year period from 1989 to 2020 are obtained to find rainfall anomalies. Using these long-term rainfall data, rainfall anomalies (R_t) for any time period t (yearly/monthly) is calculated as

$$R_t = \frac{P_t - \overline{P_T}}{\sigma_T}$$

where t is the time period (yearly/ monthly) for which rainfall anomalies are evaluated; P_t is the total rainfall for time period t; $\overline{P_T}$ and σ_T are the mean and standard deviation values of spatially averaged total rainfall across the study area, i.e. Telangana at any given month/year over the period of 1989–2020.

22.5 Results and Discussion

22.5.1 Spatiotemporal Distribution of ESSMI, SPI and RFA

Figure 22.5a, b shows the time series plot of spatially averaged monthly and yearly ESSMI, SPI and RFA in Telangana from 2001 to 2020. From Fig. 22.5a, a delay of month can be observed between ESSMI and SPI. This delay in response shows that in general the agricultural drought identified by ESSMI follows the meteorological drought identified by SPI. The monthly ESSMI couldn't identify any extreme events detected by SPI, but it is able to show inter seasonal variation with monsoons having highest ESSMI values compared to other seasons. The yearly ESSMI, SPI, and RFA are computed and plotted (Fig. 22.5b) to analyse the temporal variation of the drought in yearly scale. ESSMI showed drought in the years 2002–2004, 2009, 2012, 2014–2016, and 2018 with 2002, 2009, and 2015 showing moderate droughts and no severe and extreme yearly droughts which can be agreed by SPI and RFA. However, overall a consistent synchronous pattern is observed for all the indices such as the drought/wet ESSMI conditions are corresponding with the negative/

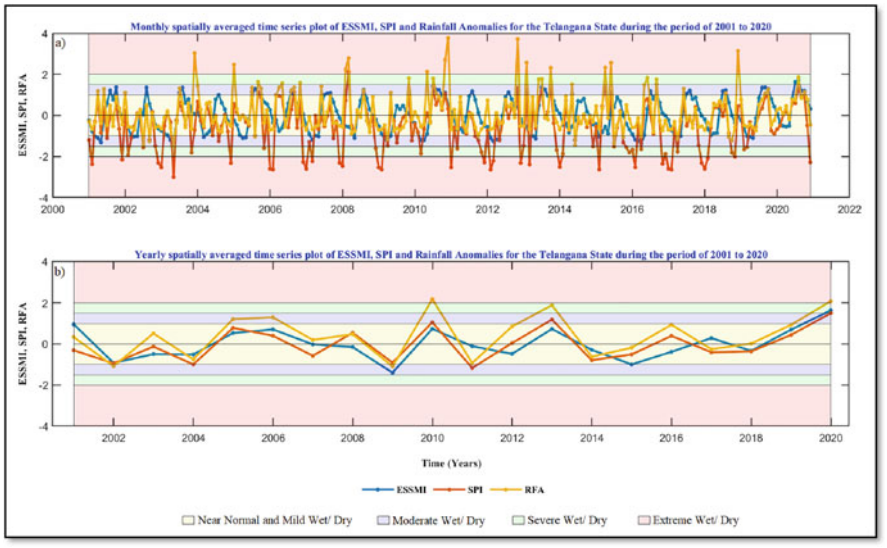

Fig. 22.5 Time series of spatially averaged monthly and yearly ESSMI, SPI and RFA in Telangana during the period of 2001 to 2020

positive SPI and RFA throughout the time period. The maximum value of ESSMI, i.e. 1.64 recognizes the 2020 as the wettest year. The finding is verified by the values of SPI and RFA, i.e. 1.49 and 2.08, respectively. Similarly, 2009 is marked as the driest year of the study period indicated by the minimum value of ESSMI, i.e. -1.39 and verified by the same observation by the values of SPI (−0.91) and RFA (−1.09). Also, India experienced its worst drought in 2009 with SPI −2.02 (Sarkar 2011a, b) and worst rainfall departure (Sarkar 2011a, b). Overall, the annual variation of the three indices, i.e. ESSMI, SPI, and RFA shows a coherent pattern throughout the study period.

Figure 22.6 shows the spatial distribution of yearly ESSMI, SPI, and RFA in Telangana for dry year 2009 and wet year 2020. The driest year 2009 and wettest year 2020 can be identified in temporal evolution of indices and is visualized in Fig. 22.6. For the dry year 2009, ESSMI, SPI, and RFA for most of the Telangana are in the range of 0 to−4 clearly indicating the drought experienced in that year. Similarly, for the wettest year 2020, both the indices exhibit positive values (0–4) along with the rainfall anomalies for the major portion of Telangana. Visually it can be seen at some grids where SPI and RFA showed extreme dry/wetness indicated by dark yellow/blue, ESSMI showed less dry/wetness indicated by light yellow/blue. It shows ESSMI's inability in detecting extreme events.

Although, a general spatiotemporal comparison (Figs. 22.5 and 22.6) among ESSMI, SPI, and RFA shows a good agreement in assessing the dry/wet conditions, a gridwise correlation between a) ESSMI and SPI and b) ESSMI and RFA are also assessed. The gridwise correlations are presented in Fig. 22.7 for the period of 2001 to 2020. As observed from Fig. 22.7, most of the grids of the study area show high correlations (CCs values are 0.73 with SPI, 0.77 with RFA) and some parts of the study area show weaker correlations (CCs values are 0.05 with SPI and RFA). The white grids in the Fig. 22.7 indicate ESA CCI missing data which shows the limitation of remote sensing retrievals. From the boxplots of CC values in Fig. 22.7, it is observed that the median of CC values are 0.47 and 0.52 for ESSMI with SPI and RFA respectively. That infers that more than 50% of the total available grids (some grids consist of missing ESSMI values) are having CCs higher than 0.47 and 0.52 with SPI and RFA.

22.5.2 Drought Area Analysis

Figure 22.8a–c describes the temporal variability of drought area ratio measured by ESSMI and SPI in four drought classes (i.e., near normal and mild, moderate, severe, and extreme) for the period during 2001 to 2020 in the Telangana. During the analysis, the near normal and mild class droughts are merged for SPI to match with the ESSMI drought classes and ESSMI does not have the mild drought class. From Fig. 22.8a, b, it can be noted that the 83.49% of the total drought area are inflicted by near normal and mild droughts as identified by ESSMI. The remaining 16.51% grids are affected with severe and extreme droughts. However, the SPI is

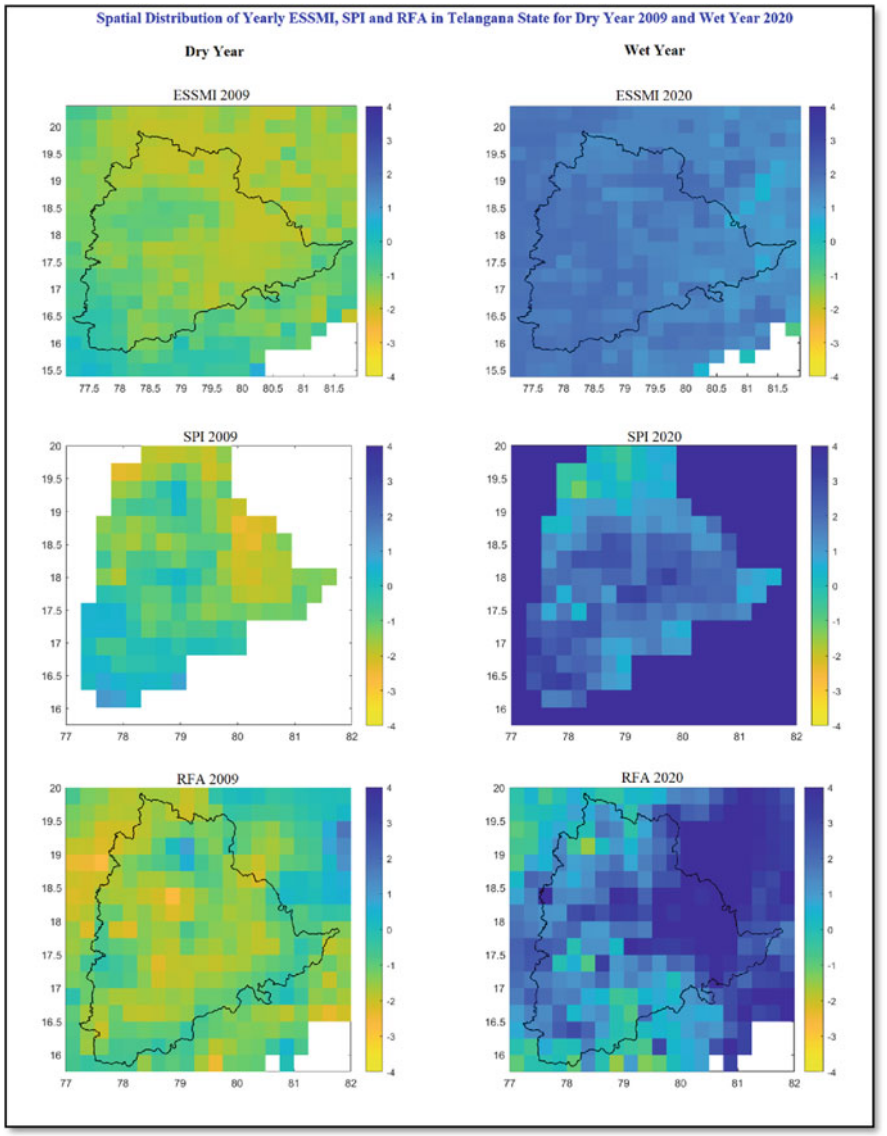

Fig. 22.6 Spatial Distribution of yearly ESSMI, SPI and RFA in Telangana for Dry Year 2009 and Wet Year 2020

able to characterize all the classes, i.e. severe, extreme, near normal, and mild droughts across the study area. According to SPI, the amount of near normal and mild, moderate, severe, and extreme droughts of total drought area are 56.75%, 11.17%, 7.22%, and 24.86%, respectively. To analyse the drought as a whole, total accumulated drought (near normal to extreme) area from 2001 to 2020 has been

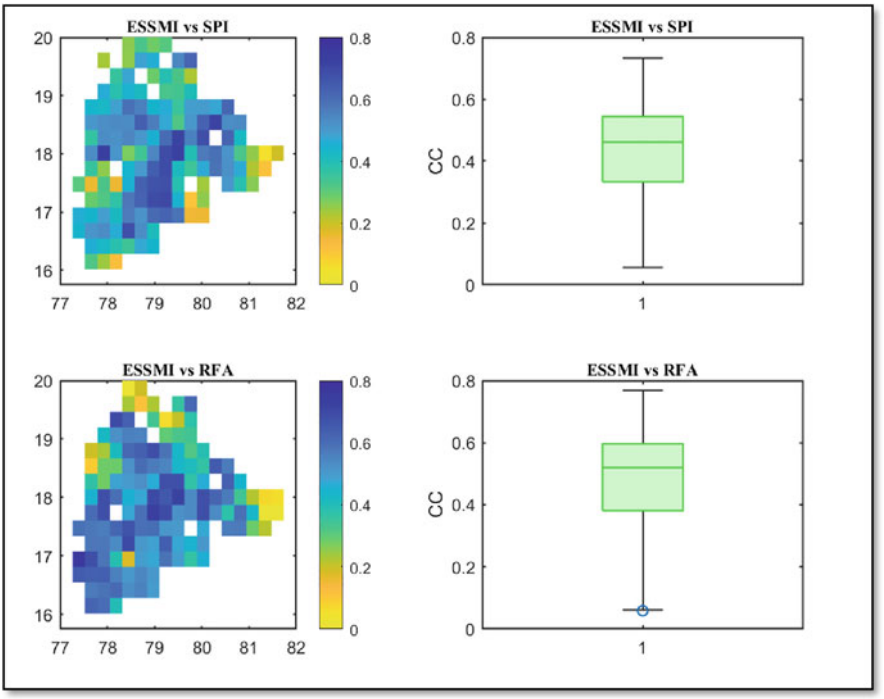

Fig. 22.7 Spatial Distribution and the box plots of the CC between ESSMI and SPI, RFA in Telangana during the period of 2001 to 2020

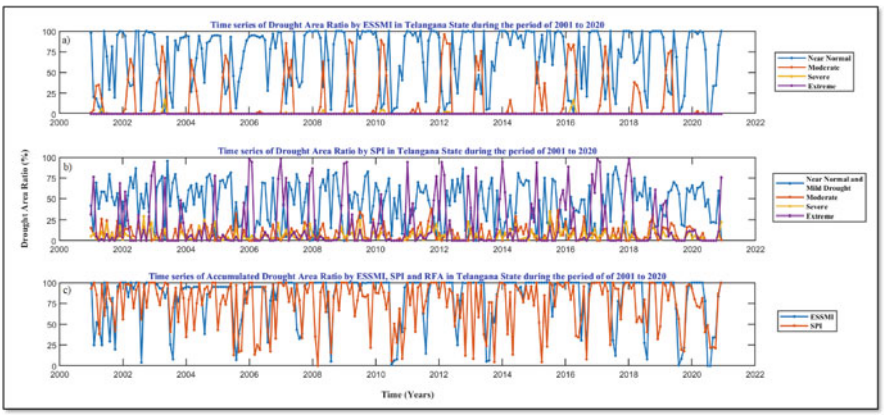

Fig. 22.8 Time series of Drought Area Ratio by (**a**) ESSMI (**b**) SPI in Telangana from 2001 to 2020 and (**c**) time series of Accumulated Drought Area Ratio in Telangana from 2001 to 2020

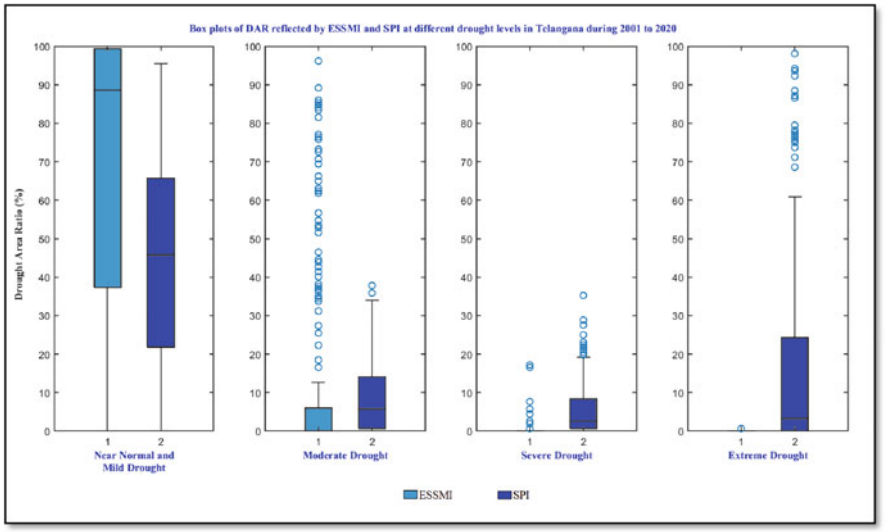

Fig. 22.9 Box plots of Drought Area Ratio reflected by ESSMI and SPI in Telangana from 2001 to 2020

Table 22.4 Proportion of DAR for different drought levels reflected by ESSMI and SPI in Telangana from 2001 to 2020

Drought index	Level of drought	Proportion of DAR			
		[0,10]	[10,20]	[20,30]	[30,∞]
ESSMI	Near normal and mild	0.09	0.05	0.06	0.79
	Moderate	0.77	0.02	0.02	0.2
	Severe	0.99	0.01	0	0
	Extreme	1	0	0	0
SPI	Near normal and mild	0.15	0.07	0.12	0.65
	Moderate	0.65	0.24	0.07	0.02
	Severe	0.79	0.14	0.05	0
	Extreme	0.64	0.07	0.04	0.24

calculated and shown in Fig. 22.8c. As shown in Fig. 22.8c, the variability of the accumulated drought area from 2001 to 2020 represented by ESSMI is mostly consistent with SPI. These results suggest that the drought as a whole is consistently indicated by both ESSMI and SPI.

It is noted from Fig. 22.9 that near normal, mild, and moderate drought areas are much larger than the severe and extreme drought area, represented by ESSMI and SPI. But ESSMI showed no severe and extreme droughts where SPI represented large number of extreme droughts. The detailed proportion of Drought Area Ratio (DAR) at near normal to extreme drought reflected by ESSMI and SPI are given in Table 22.4. The proportion of DAR is calculated as the ratio of sum of number of months with DAR present in the particular range to the number of months. From

Table 22.4, it can be observed that 79%, 65% of the total study period has the 30% and more near normal and mild drought area reflected by ESSMI and SPI, respectively. SPI shows, 65% of the total study period has only 0–10% extreme drought area and only 20% of total study period has extreme drought area more than 30% detected by SPI. Therefore, near normal to moderate droughts are the main types of drought levels with regard to drought area in Telangana from 2001 to 2020.

22.6 Conclusions

In this study, the potential of ESA CCI SM data product is explored to characterize the agricultural drought conditions in Telangana from 2001 to 2020, by computing the ESSMI. The efficiency of ESSMI in drought monitoring is evaluated by comparing it to the SPI. Temporal evolution of monthly ESSMI showed monthly delayed response when compared with SPI, whereas yearly ESSMI showed consistency with SPI and RFA. The monthly delayed response shown by ESSMI indicates that the agricultural drought follows the meteorological drought captured by SPI (Zhang et al. 2019). The analysis of different classes shows that ESSMI is able to identify more areas effected by near normal to moderate drought events when compared to SPI. However, no severe or extreme drought events are captured by ESSMI whereas, the SPI also identified some monthly extreme drought areas. The probable justification could be that the meteorological drought always does not translate to the same class of agricultural drought given some certain prevailing condition. Although, the current study is limited only to explore the ability of satellite derived soil moisture-based drought index (ESSMI using ESA CCI SM product) to identify the agricultural drought. The investigation of the probable physical reason for not coinciding all the classes of meteorological and agricultural drought is beyond the scope of this particular study. However, the overall performance of ESSMI is reliable for agricultural drought monitoring as it is able to effectively capture near normal to moderate drought events and shows a consistent association with the SPI and RFA both in short- and long-term (monthly and annual) temporal scale. The findings of the study also suggest the potential of ESA CCI SM product for characterizing the agricultural drought and thus can be used in higher spatial scales.

References

Agnew CT (2000) Using the SPI to identify drought. In: Drought Network News (1994–2001), p 1

Agriculture Action Plan (2021–22) Department of Agriculture, Government of Telangana. https://agri.telangana.gov.in/open_record_view.php?ID=959

Albergel C, Rüdiger C, Pellarin T, Calvet JC, Fritz N, Froissard F, Martin E et al (2008) From near-surface to root-zone soil moisture using an exponential filter: an assessment of the method based on in-situ observations and model simulations. Hydrol Earth Syst Sci 12(6):1323–1337

Anuradha UV (2016) Telangana Drought 2016. South Asia Network on Dams, Rivers and People, Delhi

Carlson TN, Gillies RR, Perry EM (1994) A method to make use of thermal infrared temperature and NDVI measurements to infer surface soil water content and fractional vegetation cover. Remote Sens Rev 9(1–2):161–173

Carrão H, Russo S, Sepulcre-Canto G, Barbosa P (2016) An empirical standardized soil moisture index for agricultural drought assessment from remotely sensed data. Int J Appl Earth Obs Geoinf 48:74–84

Dai M, Huang S, Huang Q, Leng G, Guo Y, Wang L, Zheng X et al (2020) Assessing agricultural drought risk and its dynamic evolution characteristics. Agric Water Manag 231:106003

Dutra E, Viterbo P, Miranda PM (2008) ERA-40 reanalysis hydrological applications in the characterization of regional drought. Geophys Res Lett 35(19):120

Dutta D, Kundu A, Patel NR, Saha SK, Siddiqui AR (2015) Assessment of agricultural drought in Rajasthan (India) using remote sensing derived vegetation condition index (VCI) and standardized precipitation index (SPI). Egypt J Remote Sens Space Sci 18(1):53–63

Entekhabi D, Njoku EG, O'Neill PE, Kellogg KH, Crow WT, Edelstein WN et al (2010) The soil moisture active passive (SMAP) mission. Proc IEEE 98(5):704–716

Ford TW, Harris E, Quiring SM (2014) Estimating root zone soil moisture using near-surface observations from SMOS. Hydrol Earth Syst Sci 18(1):139–154

Gruber A, Scanlon T, van der Schalie R, Wagner W, Dorigo W (2019) Evolution of the ESA CCI soil moisture climate data records and their underlying merging methodology. Earth Syst Sci Data 11(2):717–739

Guttman NB (1998) Comparing the palmer drought index and the standardized precipitation index 1. J Am Water Resour Assoc 34(1):113–121

Hagman G, Beer H, Bendz M, Wijkman A (1984) Prevention better than cure. Report on human and environmental disasters in the Third World, 2nd edn. Swedish Red Cross, Stockholm

Hirschi M, Mueller B, Dorigo W, Seneviratne SI (2014) Using remotely sensed soil moisture for land–atmosphere coupling diagnostics: the role of surface vs. root-zone soil moisture variability. Remote Sens Environ 154:246–252

Hunt ED, Hubbard KG, Wilhite DA, Arkebauer TJ, Dutcher AL (2009) The development and evaluation of a soil moisture index. Int J Climatol 29(5):747–759

Jackson TJ, Bindlish R, Cosh MH, Zhao T, Starks PJ, Bosch DD et al (2011) Validation of soil moisture and ocean salinity (SMOS) soil moisture over watershed networks in the US. IEEE Trans Geosci Remote Sens 50(5):1530–1543

Kogan F (2002) World droughts in the new millennium from AVHRR-based vegetation health indices. EOS Trans Am Geophys Union 83(48):557–563

Liu Y, Liu Y, Wang W (2019) Inter-comparison of satellite-retrieved and global land data assimilation system-simulated soil moisture datasets for global drought analysis. Remote Sens Environ 220:1–18

Martínez-Fernández J, González-Zamora A, Sánchez N, Gumuzzio A (2015) A soil water based index as a suitable agricultural drought indicator. J Hydrol 522:265–273

Martínez-Fernández J, González-Zamora A, Sánchez N, Gumuzzio A, Herrero-Jiménez CM (2016) Satellite soil moisture for agricultural drought monitoring: assessment of the SMOS derived soil water deficit index. Remote Sens Environ 177:277–286

Martínez-Fernández J, González-Zamora A, Sánchez N, Pablos M (2017) CCI soil moisture for long-term agricultural drought monitoring: a case study in Spain. In: 2017 IEEE International Geoscience and Remote Sensing Symposium (IGARSS). IEEE, Piscataway, NJ, pp 1985–1988

McKee TB (1995) Drought monitoring with multiple time scales. In: Proceedings of 9th Conference on Applied Climatology, Boston

McKee TB, Doesken NJ, Kleist J (1993) The relationship of drought frequency and duration to time scales. In: Proceedings of the 8th Conference on Applied Climatology, vol 17, pp 179–183

McNally A, Shukla S, Arsenault KR, Wang S, Peters-Lidard CD, Verdin JP (2016) Evaluating ESA CCI soil moisture in East Africa. Int J Appl Earth Obs Geoinf 48:96–109

Mishra AK, Singh VP (2010) A review of drought concepts. J Hydrol 391(1–2):202–216
Mohammed S, Alsafadi K, Enaruvbe GO, Bashir B, Elbeltagi A, Széles A et al (2022) Assessing the impacts of agricultural drought (SPI/SPEI) on maize and wheat yields across Hungary. Sci Rep 12(1):1–19
Mukherjee S, Mishra A, Trenberth KE (2018) Climate change and drought: a perspective on drought indices. Curr Clim Change Rep 4(2):145–163
Narasimhan B, Srinivasan R (2005) Development and evaluation of soil moisture deficit index (SMDI) and evapotranspiration deficit index (ETDI) for agricultural drought monitoring. Agric For Meteorol 133(1–4):69–88
National Research Council (1999) Hydrologic hazards science at the US geological survey. National Academies Press, Washington, DC
Padhee SK, Nikam BR, Dutta S, Aggarwal SP (2017) Using satellite-based soil moisture to detect and monitor spatiotemporal traces of agricultural drought over Bundelkhand region of India. GISci Remote Sens 54(2):144–166
Pai DS, Rajeevan M, Sreejith OP, Mukhopadhyay B, Satbha NS (2014) Development of a new high spatial resolution (0.25× 0.25) long period (1901-2010) daily gridded rainfall data set over India and its comparison with existing data sets over the region. Mausam 65(1):1–18
Pal M, Maity R (2019) Development of a spatially-varying statistical soil moisture profile model by coupling memory and forcing using hydrologic soil groups. J Hydrol 570:141–155
Pal M, Maity R (2021) Assimilation of remote sensing based surface soil moisture to develop a spatially varying vertical soil moisture profile database for entire Indian mainland. J Hydrol 601:126807
Pal M, Maity R, Dey S (2016) Statistical modelling of vertical soil moisture profile: coupling of memory and forcing. Water Resour Manag 30(6):1973–1986
Palmer WC (1965) Meteorological drought. In: U.S. Weather Bureau, Research Paper no 45, p 58
Palmer WC (1968) Keeping track of crop moisture conditions, nationwide: the new crop moisture index. Weatherwise 21(4):156–161
Purcell LC, Sinclair TR, McNew RW (2003) Drought avoidance assessment for summer annual crops using long-term weather data. Agron J 95(6):1566–1576
Salvia MM, Sanchez N, Piles M, Gonzalez-Zamora A, Martínez-Fernández J (2020) Evaluation of the soil moisture agricultural drought index (SMADI) and precipitation-based drought indices in Argentina. In: 2020 IEEE Latin American GRSS & ISPRS Remote Sensing Conference (LAGIRS). IEEE, Piscataway, NJ, pp 663–668
Sarkar J (2011a) Drought, its impacts and management: scenario in India. In: Droughts in Asian monsoon region, vol 8. Emerald Group, Bingley, pp 67–85
Sarkar J (2011b) Monitoring drought risks in India with emphasis on agricultural drought. In: Agricultural drought indices proceedings of an expert meeting, p 59
Sehgal V, Sridhar V (2019) Watershed-scale retrospective drought analysis and seasonal forecasting using multi-layer, high-resolution simulated soil moisture for southeastern US. Weather Clim Extrem 23:100191
Sehgal V, Gaur N, Mohanty BP (2021) Global flash drought monitoring using surface soil moisture. Water Resour Res 57(9):e2021WR029901
Sheffield J, Goteti G, Wen F, Wood EF (2004) A simulated soil moisture based drought analysis for the United States. J Geophys Res Atmos 109(D24)
Silverman BW (1986) Density estimation for statistics and data analysis. Chapman & Hall, London
Svoboda MD, Fuchs BA (2016) Handbook of drought indicators and indices. World Meteorological Organization, Geneva, pp 1–44
Telangana State at a Glance (2021) Telangana State at a Glance 2021 by Directorate of Economics and Statistics, Government of Telangana, https://www.telangana.gov.in/PDFDocuments/Telangana-State-at-a-Glance-2021.pdf
Tigkas D, Vangelis H, Tsakiris G (2019) Drought characterisation based on an agriculture-oriented standardised precipitation index. Theor Appl Climatol 135(3):1435–1447

Tirivarombo S, Osupile D, Eliasson P (2018) Drought monitoring and analysis: standardised precipitation evapotranspiration index (SPEI) and standardised precipitation index (SPI). Phys Chem Earth Parts A/B/C 106:1–10

Torres GM, Lollato RP, Ochsner TE (2013) Comparison of drought probability assessments based on atmospheric water deficit and soil water deficit. Agron J 105(2):428–436

Vicente-Serrano SM, Beguería S, López-Moreno JI (2010) A multiscalar drought index sensitive to global warming: the standardized precipitation evapotranspiration index. J Clim 23(7): 1696–1718

Wang PX, Li XW, Gong JY, Song C (2001) Vegetation temperature condition index and its application for drought monitoring. In: IGARSS 2001. Scanning the Present and Resolving the Future. In: Proceedings. IEEE 2001 International Geoscience and Remote Sensing Symposium (Cat. No. 01CH37217), vol 1. IEEE, New York, pp 141–143

Wilhite DA (2000) Drought as a natural Hazard: concepts and definitions. Drought Mitigation Center Faculty Publications, Lincoln, NE, p 69

Wilks DS (2005) Statistical methods in the atmospheric sciences, 2nd edn. Academic Press, San Diego, CA

Wu W, Geller MA, Dickinson RE (2002) The response of soil moisture to long-term variability of precipitation. J Hydrometeorol 3(5):604–613

Wu Z, Feng H, He H, Zhou J, Zhang Y (2021) Evaluation of soil moisture climatology and anomaly components derived from ERA5-land and GLDAS-2.1 in China. Water Resour Manag 35(2): 629–643

Zhang L, Liu Y, Ren L, Jiang S, Yang X, Yuan F, Wei L (2019) Drought monitoring and evaluation by ESA CCI soil moisture products over the Yellow River Basin. IEEE J Select Topics Appl Earth Observ Remote Sens 12(9):3376–3386

Zhang G, Su X, Ayantobo OO, Feng K (2021) Drought monitoring and evaluation using ESA CCI and GLDAS-Noah soil moisture datasets across China. Theor Appl Climatol 144(3):1407–1418

Chapter 23
A Review on Hydrodynamics of Vegetated Streams

Binit Kumar, Swagat Patra, Manish Pandey, and Prabhat Kumar Singh Dikshit

Abstract Vegetation such as submerged, emergent, and floating plays an essential role in altering the flow characteristics through a channel. Moreover, vegetation serves as a means for the ecological restoration of a river and the prevention of erosion. Hence, understanding the changes that take place in the flow as it flows through vegetation forms the crux of the river restoration and erosion prevention works to name a few. For understanding the hydrodynamics of vegetation, various experiments have been carried out throughout the years along with the arrangements of numerous models. Properties such as Flow velocity, Reynolds Shear Stress (RSS), and Turbulent Intensities, etc. are extensively studied to understand this complex flow-vegetation interaction in a much better way. This chapter aims to introduce the readers to the changes occurring in such properties due to vegetation; found by various experiments over the years, in a detailed manner. Studies and results based on the different experimental set-ups in terms of vegetation type, arrangement, etc. have been put forward in the study such that the readers can gain an insight into the comparative study in this field of research. The chapter concludes by highlighting the important results as well as the research gaps in this field of study.

Keywords Reynolds shear stress · Submerged · Emergent · Ecological river restoration · Erosion

B. Kumar (✉) · S. Patra · M. Pandey
Department of Civil Engineering, National Institute of Technology Warangal, Warangal, Telangana, India
e-mail: spce21405@student.nitw.ac.in; mpandey@nitw.ac.in

P. K. S. Dikshit
Department of Civil Engineering, IIT (BHU), Varanasi, India
e-mail: pksdikshit.civ@iitbhu.ac.in

M. Pandey et al. (eds.), *River Dynamics and Flood Hazards*, Disaster Resilience and Green Growth, https://doi.org/10.1007/978-981-19-7100-6_23

23.1 Introduction

Vegetation forms an integral part of a natural channel and its presence can be easily seen along the banks or in the channel itself. The vegetation found can be generally classified as emergent, submerged, and floating and each type has unique effects on the flow characteristics such as velocity, flow rate, etc. Over the years numerous experiments have been conducted to study the hydrodynamic characteristics in the presence of vegetation and it was found that vegetation can prove to be very helpful in reducing erosion, turbidity, and restoring the aquatic habitat/ecology. Previous investigations show that vegetation improves the quality of water (Schulz et al. 2003), maintains the stability of the channel bed (Wang et al. 2009), and increases the diversity of the aquatic life (Crowder and Diplas 2002). This was further substantiated by the study of James and Makoa (2006) which showed that emergent vegetation hinders the conveyance capacity of the channels. Siniscalchi et al. (2012) observed that a strong shear layer is formed at the top of the vegetation zone that augments the turbulent transport in the vertical direction.

Moreover, to mitigate hydrologic and sediment hazards, vegetation can be considered a useful tool (Aamir et al. 2022; Chaudhuri et al. 2022). With the increase of hydrological uncertainties due to both climatic and anthropogenic reasons, the probability of major hydrological hazards occurring is on the rise, and past studies have shown that vegetation can efficiently act as a tool to ensure that these uncertainties do not result in large-scale hazards. For instance, if the example of mass sediment movement occurring due to a sudden eruption or rainfall is considered, vegetation along river banks can significantly aid in trapping the excess debris and mud, thus preventing the deposition of large amounts of those materials in downstream areas. This will help in averting a possible catastrophe (Garcia et al. 2008). Figure 23.1a, b illustrates the extent of large-scale destructions due to hydrological extremes.

Fig. 23.1 (**a**) Deposition of debris and mud due to mass sediment movement. (Source: https://www.cbecoeng.com/service-area/post-fire-hydrologic-hazard-assessments) (**b**) Aerial view of flooding in Grand Forks, ND, during spring of 1997. (Source: U.S. Geological Survey)

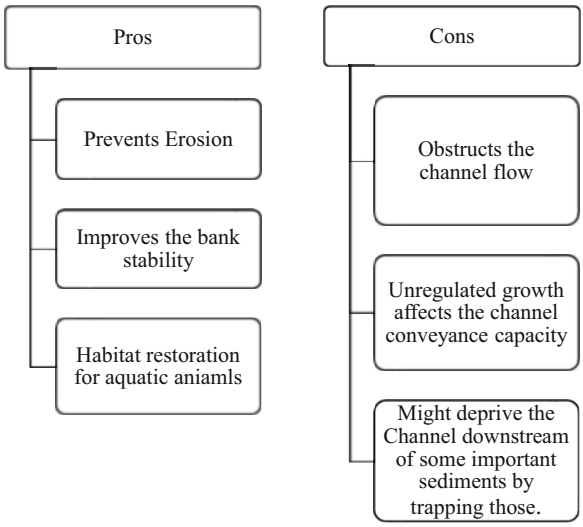

Fig. 23.2 Effect of vegetation in a channel

However, over-stressing its importance might result in its uncontrollable growth throughout the channel length, which will cause considerable effects on the performance of the channel. For instance, vegetation, especially emergent, provides large obstructions to the channel flow and if not controlled, affects the conveyance capacity of the channel; decreasing the efficiency (in terms of water distribution) of the channel (Montakhab et al. 2015; Khan et al. 2021, 2022; John et al. 2021). Thus, if controlled, vegetation has the full potential to be an integral part of river restoration and erosion prevention works. A brief insight into the advantages and disadvantages is presented below in Fig. 23.2 for a better understanding of the effects of vegetation in a channel.

Therefore, it is seen that vegetation can decrease the erosion of the river banks, which in turn, increases the bank stability (David 2008; Pandey et al. 2021, 2022; Singh et al. 2022). In addition to that, vegetation can also be used for the attenuation of floods, breaking wake energy, and preventing coastal erosion (Nepf and Vivoni 2000; Wilson et al. 2003), to name a few.

Figure 23.3 can further help to strengthen the reader's understanding of the different vegetation types found in natural river streams through visualization:

In the present chapter, an extensive study of the effects of vegetation on flow characteristics in a channel has been presented. An attempt has been made to review the various studies carried out throughout the years in this field of research to enhance our understanding. The chapter discusses the research gap that needs to be addressed which is followed by a comprehensive summary highlighting the key points of the study.

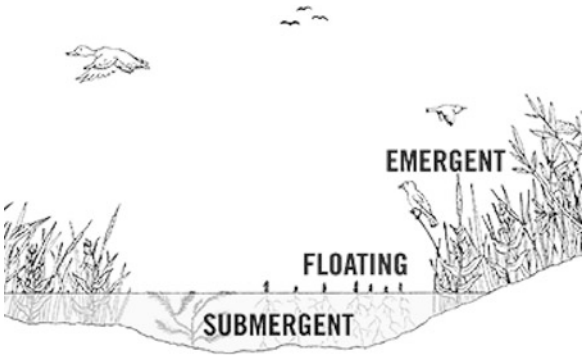

Fig. 23.3 Different vegetation types (Emergent, Floating, and Submerged) found in natural river streams. (Source: https://sge.wonderville.ca/wetlands/thebasics.html)

23.2 Effect of Vegetation on the Ecology of the Channel

The presence of vegetation improves the overall ecology of a channel. It helps in providing substrate for fish spawning and covers for fish (House and Boehne 1986; Gortz 1998). With time, these vegetations are broken down through various biological and physical processes and converted into Fine Particulate Organic Matter (FPOM), Dissolved Organic Matter (DOM), and finally CO_2 (Campbell et al. 2011; Shankar et al. 2021; Shivashankar et al. 2022). These changes affect the biological properties and structure of the channel and depending on the prevailing conditions, different organisms thrive in the channel, thus creating a change in the channel ecology.

Moreover, floating vegetation has been found to be very beneficial in the assimilation of excess nutrients from natural river systems (Winton et al. 2020). They are extensively used in the construction of wetlands for wastewater treatment as they have the capacity to absorb nutrients directly from surface water (Brix 1997). In addition to that, studies carried out by Winton et al. 2020 also found that the importance of floating vegetation in the assimilation of excess nutrients is relatively more in urbanized and industrial areas. One more aspect where floating vegetation can play a vital role is in the transfer of nutrients from water to land. Floating vegetation gets transported through wind-induced currents and later gets stranded on exposed flood plains, thus transferring nutrients from aquatic to terrestrial settings (Winton et al. 2020).

23.3 Research Interest and Gaps

To understand the hydrodynamic characteristics such as flow velocity, turbulence intensity, etc. various experiments have been carried out in the past years. Most of the earlier works were concentrated on the study of flow characteristics in the presence of vegetation by simulating vegetation with the help of artificial cylindrical rods or flexible plastic materials. For instance, Wilson et al. (2003) examined the

flow through vegetation by using two different forms of cylindrical rods representing vegetation with and without foliage. However, with time it was found that the response of natural vegetation is different in many aspects from those of the simulated rigid cylindrical rods or flexible plastic materials. Caroppi et al. (2021) carried out a study using both natural vegetation and wooden cylindrical rods and it was found that the use of rigid cylinders gives an inadequate explanation of the shear layers induced by foliated reconfiguring vegetation.

Then, further studies were conducted using different configurations of vegetation as well as using emergent, floating, and submerged vegetation at the same time. Moreover, studies were also conducted to understand the channel hydrodynamics in the presence of vegetation in combination with downward seepage. It helped in strengthening our understanding of the flow characteristics in a natural vegetated channel as a natural setting involves various types of vegetations and configurations. Chen et al. (2011) studied the flow characteristics by using three different plant configurations; staggered, columnar, and aligned to simulate vegetation in a channel. On the other hand, Devi and Kumar (2016) examined the hydrodynamics of a channel in the presence of submerged flexible vegetation in combination with downward seepage. Devi et al. (2018) used natural rice stems to simulate flexible emergent vegetation and compared the results with and without the presence of downward seepage.

Finally, it is seen that numerous attempts have been made to understand the flow characteristics in the presence of vegetation but even then, there are several areas that are being left out. For example, very few or no experiments have been carried out to compare emergent, flexible, and floating vegetation in the presence of downward seepage. Hence, if these areas are covered in future studies, it would certainly enhance our understanding of the hydrodynamics of the vegetated streams.

23.4 Experimental Set-Ups

The experimental set-ups adopted by the various researchers over the years were wide-ranging, depending on their study interests. For instance, Chen et al. (2011) used flexible plastic materials to simulate vegetation in a rectangular glass-walled flume whereas Devi et al. (2018) carried out their study in a Tilting flume with natural rice stems depicting the vegetation aspect.

The following table attempts to give a summary of some of the experimental conditions so that the readers can gain important insights into the developments taking place in this area (Table 23.1).

Table 23.1 Different experimental set-ups adopted over the years

Author	Flume type	Flume dimensions L × W × H (m)	Vegetation type	Velocity measurement
Dunn et al. (1996)	Tilting flume	19.5 × 0.91 × 0.61	Cylindrical wooden dowels	Acoustic Doppler Velocimeter (ADV)
Nezu and Onitsuka (2001)	Tilting flume	10 × 0.4 × 0.3	Bronze cylindrical rods	Laser Doppler anemometer (LDA) and particle image Velocimeter (PIV)
Järvelä (2003)	Recirculating glass-walled	50 × 1.1 × 1.3	Natural wheat stems	3D acoustic Doppler Velocimeter (ADV)
Chen et al. (2011)	Rectangular glass walled	8 × 0.3 × 0.6	Flexible plastic	3D sideways 16 MHz macro ADV
Devi and Kumar (2016)	Tilting flume	20 × 1 × 0.72	Flexible rubber cylinders	3D acoustic Doppler Velocimeter (ADV)
Devi et al. (2018)	Tilting flume	20 × 1 × 0.72	Natural Rice stems	3D acoustic Doppler Velocimeter (ADV)
Caroppi et al. (2021)	1st case: Glass walled recirculating 2nd case: Acrylic walled recirculating	1st case: 20 × 0.6 × 0.8 2nd case: 8 × 0.4 × 0.4	1st case: Reconfiguring natural plants in a grass underlining 2nd case: Rigid cylinders	Acoustic Doppler Velocimeter (ADV)

23.5 Effect of Vegetation on Flow Characteristics

Vegetation affects the flow characteristics like velocity and discharges significantly. It is seen that the time-averaged velocity decreases in the vegetated region and this velocity reduction gets diverted towards the non-vegetated region (Devi et al. 2018). The velocity profile gets retarded with respect to the upstream free zone in the presence of emergent vegetation in a fully vegetated channel (Devi et al. 2018). The time-averaged velocity mentioned above in stream-wise and vertical directions, respectively, was found using the following equations:

$$U = \left(\frac{1}{n}\right) * \sum_{i=1}^{n} U_i \tag{23.1}$$

$$W = \left(\frac{1}{n}\right) * \sum_{i=1}^{n} W_i \tag{23.2}$$

where U_i and W_i are the instantaneous velocities in the stream-wise and vertical direction, respectively.

The velocity profile in an unvegetated channel was assumed to be logarithmic (Nezu and Nakagawa 1993) and it was observed that in the presence of vegetation, there is a change in the universal logarithmic velocity profile (Järvelä 2003). However, the velocity profile was found to be uniform over the depth for emergent vegetation (Stone and Shen 2002; Tsujimoto and Kitamura 1990) whereas, for submerged vegetation, the velocity profile was found to be somewhat S-shaped (Carollo et al. 2002; Ikeda and Kanazawa 1996). The presence of downward seepage is found to increase the velocity near the bed region which is characterized by the movement of the velocity profile in the downward direction (Devi et al. 2018). However, in the presence of vegetation the flow velocity in the vegetated region decreases; even with the presence of downward seepage (Devi et al. 2018). The flow in a vegetated channel is also characterized by an inflection point near the top of the vegetation stem (Poggi et al. 2004; Carollo et al. 2005; Chen et al. 2011). This inflection point is developed because of the velocity difference in the upper and the lower flow region (Zong and Nepf 2012).

Further studies were carried out to determine the effect of plant form on the velocity profile and it was found that the presence of frond-foliage reduces the mean velocity and induces larger drag forces (Wilson et al. 2003). Moreover, with a decrease in velocity in the vegetated region, fine grain sediments and organic matter starts accumulating and with an increase in velocity in the unvegetated region, coarse grain sediments are left between patches, thereby promoting erosion (Sand-Jensen and Madsen 1992).

23.6 Effect of Vegetation on Turbulent Characteristics

The turbulence in a natural vegetative channel differs greatly from that in an unvegetated channel. The turbulent intensity was found to be caused by the variation of the instantaneous velocity due to the presence of vegetation and change in bed roughness, which is then suppressed by the emergent vegetation (Devi et al. 2018). The Turbulent Kinetic Energy (TKE) generated is developed due to the shear present at the interface of the vegetated and unvegetated region and three fluctuating velocity components; viz. $u\supseteq$, $v\supseteq$ and $w\supseteq$, contribute to this based on whether the vegetation is flexible or rigid (Caroppi et al. 2021). Nezu and Onitsuka (2001) studied the turbulence characteristics using Laser Doppler Anemometer (LDA) and Particle Image Velocimeter (PIV) and found that the horizontal vortices generated near the free surface are because of the shear instability, which further increases with vegetation density. The presence of an extra superficial zone of fronds affects the momentum exchange between the vegetated zone and the upper flow zone and it was found that the presence of such superficial zones decreases the shear-induced turbulence (Wilson et al. 2003). Moreover, the momentum exchange in the presence of flexible vegetation is found to be 40% more efficient than that of rigid vegetation

(Caroppi et al. 2021). On the other hand, the turbulence close to the water surface is transferred from the unvegetated zone towards the vegetated zone with the help of secondary currents (Nezu and Onitsuka 2001).

The presence of vegetation can help in damping the Reynolds Shear Stress (RSS) and eventually the sediment transport downstream; even with the presence of downward seepage in the channel (Devi et al. 2018). Earlier investigations found that the flow within an aquatic canopy occurs in two regions; viz. the "vertical exchange zone or the upper canopy" and "longitudinal exchange zone or the lower canopy" (Nepf and Vivoni 2000). The first zone, i.e., the vertical exchange zone, is characterized by the vertical exchange of turbulence with the overlying water whereas in the longitudinal exchange zone, turbulence is found to be generated by the canopy elements locally and hence the momentum budget involves balancing the pressure gradient and vegetative drag (Nepf and Vivoni 2000). Moreover, experiments conducted to compare hydrodynamic characteristics in the presence of flexible and rigid vegetation revealed that the development of shear layers is different for different vegetation types (Caroppi et al. 2021). In the case of flexible natural vegetations, the shear layer is found to be developed within the vegetation, with the position of the peak in RSS progressively moving towards the main channel, whereas for the rigid case, most of the shear layer developed into the main channel and because of the sudden change in drag, there was an asymmetry of the distribution relative to the peak (Caroppi et al. 2021).

23.7 Effect of Vegetation on Erosion

The presence of vegetation in a channel reduces the erosion rate in the channel significantly. Previous studies found that the quantity of erosion in a partly emerged vegetative channel is much higher than that of a partly submerged vegetative channel because of a higher flow momentum transfer in the previous case (Devi et al. 2018). Lower vegetation density is found to promote sandification because of the occurrence of more turbulence, which in turn, increases the risk of erosion (Van Katwijk et al. 2010; Zong and Nepf 2012).

However, the presence of partial vegetation in a channel affects its stability. Due to the lateral exchange of flow momentum from the vegetated to the unvegetated region, there are higher chances of erosion taking place downstream of the unvegetated region (Devi et al. 2018) and hence proper caution should be taken while formulating an erosion prevention work using vegetation.

23.8 Conclusion

Vegetation in a channel plays a crucial role in maintaining the ecology and stability of a channel. Vegetation helps in decreasing the flow velocity in a channel, thereby decreasing the chances of erosion taking place in the channel. Moreover, vegetation also plays a crucial role in inhibiting turbulence in a channel, which again helps in reducing the erosion process. Numerous studies suggested that the effect of vegetation on the hydrodynamics of a channel can only be efficiently studied if we use natural plants to stimulate vegetation rather than using artificial rods. The presence of fronds has also been found to affect the flow characteristics and it was found that fronds are more efficient in reducing the flow velocity, turbulence, Reynolds Shear Stress, and hence erosion. However, the velocity profile in a vegetated channel deviated from the universal logarithmic velocity profile and studies suggested that the profile in most cases is a S-shaped curve. The presence of downward seepage along with vegetation has also been studied and it was found that even with the presence of downward seepage, vegetation was able to reduce flow velocity and turbulent intensity.

However, the presence of vegetation does not always portray a positive picture. It has been found that the presence of vegetation on one-half of the channel causes erosion to take place in the unvegetated zone, thereby acting as a challenge in river restoration and erosion prevention works. Hence, due importance should be given to understanding the hydrodynamics in such a scenario to design or restore a natural channel. Moreover, studies should be carried out in comparing the composite case of the presence of emergent, floating and submerged vegetation in the presence of downward seepage so that the processes taking place in the natural setting are understood more efficiently. Thus, from the above study, the readers can get a better idea of how vegetation can prove to be efficient in tackling the menace of river bank erosion as well as aiding in restoring a polluted river. From the present chapter, the readers can gain insights into the hydrodynamics like flow velocity, turbulence characteristics, etc. of a channel in the presence of vegetation, thereby enhancing their understanding of the study area.

References

Aamir M, Ahmad Z, Pandey M, Khan MA, Aldrees A, Mohamed A (2022) The effect of rough rigid apron on scour downstream of sluice gates. Water 14(14):2223. https://doi.org/10.3390/w14142223

Brix H (1997) Do macrophytes play a role in constructed treatment wetlands? Water Sci Technol 35(5):11–17. https://doi.org/10.2166/wst.1997.0154

Campbell C, Butts KD, Gariglio F, Reeder WJ (2011) Effects of vegetation in channels; a summary of findings regarding vegetation interactions with channel processes and potential application to the lower Boise River, Boise River Flood Control report

Carollo F, Ferro V, Termini D (2002) Flow velocity measurements in vegetated channels. J Hydraul Eng 128(7):664–673

Carollo FG, Ferro V, Termini D (2005) Flow resistance law in channels with flexible submerged vegetation. J Hydraul Eng 131(7):554–564
Caroppi G, Västilä K, Gualtieri P, Järvelä J, Giugni M, Rowiński PM (2021) Comparison of flexible and rigid vegetation induced shear layers in partly vegetated channels. Water Resour Res 57: e2020WR028243. https://doi.org/10.1029/2020WR028243
Chaudhuri S, Pandey M, Debnath K, Oliveto G (2022) A comparative study on equilibrium scour volume around circular cylinders in clay-sand mixed cohesive beds, at near threshold velocity of sand–an experimental approach. Water Supply 22(8):6777–6791. https://doi.org/10.2166/ws.2022.250
Chen SC, Kuo YM, Li YH (2011) Flow characteristics within different configurations of submerged flexible vegetation. J Hydrol 398(2011):124–134. https://doi.org/10.1016/j.jhydrol.2010.12.018
Crowder DW, Diplas P (2002) Vorticity and circulation: spatial metrics for evaluating flow complexity in stream habitats. Can J Fish Aquat Sci 59(4):633–645
David L (2008) Flow through rigid Vegetation Hydrodynamics. Thesis of Master of Science, Virginia Polytechnic Institute and State University
Devi TB, Kumar B (2016) Channel hydrodynamics of submerged, flexible vegetation with seepage. J Hydraul Eng 142(11):04016053. https://doi.org/10.1061/(ASCE)HY.1943-7900.0001180
Devi TB, Sharma A, Kumar B (2018) Flow characteristics in a partly vegetated channel with emergent vegetation and seepage. Ecohydrol Hydrobiol 19(2019):93–108. https://doi.org/10.1016/j.ecohyd.2018.07.006
Dunn C, Lopez F, García M (1996) Mean flow and turbulence in a laboratory channel with simulated vegetation. In: Hydraulic engineering series, vol 51. University of Illinois at Urbana-Champaign, Urbana, IL
Garcia HM, MacArthur CR, French R, Miller J (2008) Sedimentation hazards. In: Sedimentation engineering, pp 885–936. https://doi.org/10.1061/9780784408148.ch19
Gortz P (1998) Effects of stream restoration on the macroinvertebrate community in the river Esrom, Denmark. Aquat Conserv Mar Freshwat Ecosyst 8:115–130
House RA, Boehne PL (1986) Effects of instream structures on salmonids habitat and populations in Tobe Creek, Oregon. N Am J Fish Manag 6:38–46
Ikeda S, Kanazawa M (1996) Three dimensional organized vortices above flexible water plants. J Hydraul Eng 122(11):634–640
James, C.S., Makoa, M.J. (2006). Conveyance estimation for channels with emergent vegetation boundaries. Proceedings of the ICE-Water Management Thomas Telford London 159 (4), 235–243
Järvelä J (2003) Effect of submerged flexible vegetation on flow structure and resistance. J Hydrol 307(2005):233–241. https://doi.org/10.1016/j.jhydrol.2004.10.013
John CK, Pu JH, Moruzzi R, Pandey M (2021) Health-risk assessment for roof-harvested rainwater via QMRA in Ikorodu area, Lagos, Nigeria. J Water Clim Change 12(6):2479–2494
Khan MA, Sharma N, Pu J, Aamir M, Pandey M (2021) Two-dimensional turbulent burst examination and angle ratio utilization to detect scouring/sedimentation around mid-channel bar. Acta Geophys 69(4):1335–1348
Khan MA, Sharma N, Pu JH, Pandey M, Azamathulla H (2022) Experimental observation of turbulent structure at region surrounding the mid-channel braid bar. Mar Georesour Geotechnol 40(4):448–461
Montakhab, A., Yusuf, B., Folkard, A.M. (2015). Flow and turbulence in vegetation in a channel. Proceedings of the ice-water management Thomas Telford London168 (1), 16–23
Nepf HM, Vivoni ER (2000) Flow structure in depth-limited, vegetated flow. J Geophys Res 105 (C12):28547–28557
Nezu I, Nakagawa H (1993) Turbulence in open channel flows. J Fluid Mech 269:373–375. https://doi.org/10.1017/S0022112094211618
Nezu I, Onitsuka K (2001) Turbulent structures in partly vegetated open-channel flows with LDA and PI V measurements. J Hydraul Res 39(6):629–642. https://doi.org/10.1080/00221686.2001.9628292

Pandey M, Jamei M, Karbasi M, Ahmadianfar I, Chu X (2021) Prediction of maximum scour depth near spur dikes in uniform bed sediment using stacked generalization ensemble tree-based frameworks. J Irrig Drain Eng 147(11):04021050

Pandey M, Jamei M, Ahmadianfar I, Karbasi M, Lodhi AS, Chu X (2022) Assessment of scouring around spur dike in cohesive sediment mixtures: a comparative study on three rigorous machine learning models. J Hydrol 606:127330

Poggi D, Porporato A, Ridolfi L (2004) The effect of vegetation density on canopy sub-layer turbulence. Bound-Lay Meteorol 111(3):565–587

Sand-Jensen K, Madsen TV (1992) Patch dynamics of the stream macrophyte, *Callitriche cophocarpa*. Freshw Biol 27:277–282. https://doi.org/10.1111/j.1365-2427.1992.tb00539

Schulz M, Kozerski HP, Pluntke T, Rinke K (2003) The influence of macrophytes on sedimentation and nutrient retention in the lower river spree (Germany). Water Res 37(3):569–578

Shankar MS, Pandey M, Shukla AK (2021) Analysis of existing equations for calculating the settling velocity. Water 13(14):1987

Shivashankar M, Pandey M, Zakwan M (2022) Estimation of settling velocity using generalized reduced gradient (GRG) and hybrid generalized reduced gradient–genetic algorithm (hybrid GRG-GA). Acta Geophys:1–11

Singh UK, Jamei M, Karbasi M, Malik A, Pandey M (2022) Application of a modern multi-level ensemble approach for the estimation of critical shear stress in cohesive sediment mixture. J Hydrol 607:127549

Siniscalchi F, Nikora VI, Aberle J (2012) Plant patch hydrodynamics in streams: mean flow, turbulence and drag forces. Water Resour Res 48:W01513

Stone BM, Shen HT (2002) Hydraulic resistance of flow in channels with cylindrical roughness. J Hydraul Eng 128(5):500–506

Tsujimoto T, Kitamura A (1990) Velocity profile of flow in vegetated-bed channels, KHL Progressive Report No. 1, Kanazawa University, Japan

Van Katwijk M, Bos A, Hermus D, Suykerbuyk W (2010) Sediment modification by seagrass beds: muddification and sandification induced by plant cover and environmental conditions. Estuar Coast Shelf Sci 89:175–181. https://doi.org/10.1016/j.ecss.2010.06.008

Wang C, Yu JY, Wang PF, Guo PC (2009) Flow structure of partly vegetated open channel flows with eelgrass. J Hydrodyn 21(3):301–307

Wilson CAME, Stoesser T, Bates PD, Pinzen, Batemann A (2003) Open channel flow through different forms of submerged flexible vegetation. J Hydraul Eng 129(11):847–853. https://doi.org/10.1061/(ASCE)0733-9429(2003)129:11(847)

Winton RS, Kleinschroth F, Calamita E et al (2020) Potential of aquatic weeds to improve water quality in natural waterways of the Zambezi catchment. Sci Rep 10:15467. https://doi.org/10.1038/s41598-020-72499-1

Zong L, Nepf H (2012) Vortex development behind a finite porous obstruction in a channel. J Fluid Mech 691:368–391. https://doi.org/10.1017/jfm.2011.479

Chapter 24
Analysis of Stormwater Drainage Network of the Central Zone in the Surat City by Using SWMM 5.1 Software

M. Kusha Kumar, Ganesh D. Kale, and Arpit Sharma

Abstract In recent years, urban flooding events in the India have increased, which affected major cities. Flooding events occurred in: Srinagar in year 2014, Chennai in year 2015, and Hyderabad in 2016 were the most catastrophic ones. Urban flooding primarily occurs because of rapid urbanization, low rates of infiltration, and inadequate stormwater drainage network (SWDN) infrastructure. Stormwater drainage plays a crucial role in transporting rainfall from urban areas to the outlet site. Thus, the assessment of SWDN in urban areas is important. Many software packages are existing, which are proficient in simulating urban floods. SWMM is extensively utilized across the globe for analysis, design, and planning associated with combined sewers, sanitary sewers, storm water runoff, and other systems of drainage in urban areas. None of the reviewed studies have analyzed urban SWDN of the Central Zone (CZ) in the Surat City. Thus, analysis of SWDN of the CZ in the Surat City is performed in the current study by using SWMM software. From the aforesaid analysis, it is found that corresponding to 2 and 5 years return periods (RPs), numbers of junction nodes flooded are found to be 72 and 99, respectively. The maximum flooding discharge and duration of flooding are observed at the J145 junction corresponding to 2- and 5-year RPs. Other junctions are also got flooded but maximum flooding discharge and duration of flooding at these junctions are found to be less as compared to the J145 junction.

Keywords Urban flood · Stormwater · Drainage · SWMM 5.1

24.1 Introduction

Commonly, the term "flooding" refers to temporary inundation of typically dry areas, either partially or completely, that is caused by an unusual or rapid accumulation of water or by the runoff of inland or tidal waters. Flooding is a natural event

M. Kusha Kumar · G. D. Kale (✉) · A. Sharma
Department of Civil Engineering, Sardar Vallabhbhai National Institute of Technology, Surat, Gujarat, India
e-mail: gdk@ced.svnit.ac.in; ds17ce009@ced.svnit.ac.in

M. Pandey et al. (eds.), *River Dynamics and Flood Hazards*, Disaster Resilience and Green Growth, https://doi.org/10.1007/978-981-19-7100-6_24

that cannot be avoided. The only practical course of action for it is to reduce the damaging and detrimental effects of floods. Urban flood is characterized by abrupt, intense flood as a result of short-term high-intensity rainfall (Seenu et al. 2019). For urban flood management, primary task is identifying the urban regions that are vulnerable to flooding along with their respective hazard scale. This could lead to the zoning of probable urban flood hazard areas by using a probabilistic methodology (Akter and Tanim 2016). The process of collecting and conveying waste water, rain/stormwater or an integration of both is defined as the urban drainage. A part of urban infrastructure is urban stormwater. Urban flooding mainly happens because of rapid urbanization, low infiltration rates, and insufficient stormwater drainage network (SWDN) infrastructure (Kumar et al. 2018).

At present, over half of the world's population resides in urban areas and more than one million people are residing in 500 cities worldwide. The requirement of existing global engineers and urban planners is to stop the inconvenience of recurrent floods during the rainy season by designing an effective stormwater drainage system. Owing to the increased trend of urban floods lately, there are a variety of challenges faced by urban planners across the world. India is facing flooding at recurrent intervals in recent times. Out of 329 million ha, an overall geographical area of 48 million ha is vulnerable to floods, rendering India highly prone to flooding. Due to diverse losses like damage to houses, other public utilities and agriculture, on an average, India loses 18.05 billion INR and 1600 human lives per year (Bisht et al. 2016).

In recent years, urban flooding events in India have raised affecting major cities. Ahmedabad (2001), Hyderabad (2000), Delhi (2002, 2003, 2009 and 2010), Surat (2006), Kolkata (2007), Chennai (2004), Mumbai (2005), Guwahati (2010), and Jamshedpur (2008) are the most prominent among them. Flooding events occurred in: Hyderabad in 2016, Srinagar in 2014, and Chennai in 2015 were the most catastrophic ones (Rangari et al. 2019).

Many software packages are existing, which are competent of simulating urban floods. Software packages for instance Storm Water Management Model (SWMM), Hydrologic Engineering Center-River Analysis System (HEC-RAS), Hydrologic Engineering-Center Hydrologic Modeling System (HEC-HMS), MIKE Flood generate easily explicable outputs (Rangari et al. 2019). SWMM is widely utilized across the globe for analysis, design, and planning associated with combined sewers, sanitary sewers, storm water runoff, and other systems of drainage in urban areas. SWMM is being used in thousands of stormwater and sewer studies across the world. Applications that are distinctive include: (1) design and dimensioning of components of the drainage system for flood mitigation; (2) flood plain mapping of natural channel systems; and (3) development of control strategies to minimize combined sewer overflows, etc. (Rossman 2015).

Storm water drainage plays a vital role in transporting rainfall of urban areas to outlet site, generally a water body such as lake or river. Therefore, management of storm water plays a prime role in the quick removal of excess runoff from different catchments to the outlet. Nearly all stormwater drains are incapable to take excessive runoff as a consequence of urbanization, so flash floods took place even during short

period rainfall of high intensity (Rangari et al. 2019). Thus, analysis of urban drainage system is important. The number of overflow events in a given time period can be determined by using statistical analysis of the United States Environmental Protection Agency (US EPA) SWMM with a threshold value of maximum depth at each node of the link network (Akter and Tanim 2016).

Outside of India, various studies were performed on the topic of analysis of urban drainage system (Qin et al. 2013; Moore et al. 2016; Li et al. 2017; Martínez et al. 2018; Duan and Gao 2019; Arjenaki et al. 2020; Cardoso et al. 2020; Dell et al. 2021, etc.). In India also studies were performed on the topic of analysis of urban drainage system, which are discussed in the following paragraphs.

Bisht et al. (2016) have employed Mann-Kendall and Sen's slope tests to carry out trend analysis of rainfall events by utilizing daily rainfall time series data from 1956 to 2012. They have also evaluated design storms for a limited developed region in the West Bengal, India by using frequency analysis methods based on L-moments and daily cumulative annual rainfall data for the period of 1975–2013. MIKE URBAN and SWMM were used to develop an appropriate drainage system for the study area. The MIKE URBAN model simulation results were presented for a severe rainfall event that took place on July 29th, 2013. A multi-utility detention lake was also designed to recharge groundwater and decrease the peak value of outflow hydrograph at the posterior end during the rainfall of high intensity. From the trend analysis of rainfall data, it was discovered that, there were no significant trends in 2-, 3-, and 1-day annual maximum precipitation as well as in accumulated monsoon precipitation. It was also found that, by ensuring adequate connectedness in stormwater drains and keeping drains clean in the rainy season, a large number of drainage issues can be solved.

Kumar et al. (2018) have evaluated SWDN by using the PCSWMM model for the southern part of Delhi, India. For the study, 15-min time interval precipitation data obtained from the India Meteorological Department (IMD) corresponding to the period of 2008–2012 was used for simulation purpose and storm water drains were transformed into conduit layers and manhole layers with the aid of ArcGIS 10.2. These data were then imported into Personal Computer SWMM (PCSWMM) in order to create a hydrology-hydraulic model for surface runoff. For August 20th, 2010, the model was simulated and evaluated, corresponding to the 109.2 mm maximum rainfall record. The waterlogging locations were identified by the model and these were compared with the previous record to validate the model performance. The study found that, waterlogging was caused by an improper drain gradient, which meant that the invert levels of the drains were not uniform, preventing the flow from moving forward and causing backflow.

An attempt was made by Kansal et al. (2019) to identify the urban flooding hotspots in Gurugram, which is located in Haryana, India. The hotspots were identified by rainfall-runoff modeling performed by using the SWMM developed by the EPA. The data of annual maximum daily rainfall corresponding to hourly steps was collected from the New Delhi Regional Meteorological Centre (RMC) Palam Station, which was used as a modeling input. In the study, 3500 ha was taken as the drainage area threshold contributing to a specific confluence site, as more than

this area was regarded as a higher risk spot. Similarly, it was observed that, places near train lines, highways, administrative facilities, etc. are more important as these can cause greater public inconvenience. In this study, five hotspots in the Gurugram City were identified in the context of urban flooding by performing rainfall-runoff modeling by using SWMM software. By using the multicriteria decision analysis (MCDA) technique, namely choosing by disadvantage, the prioritization of potential hotspots was performed to commence actions for its management.

Vemula et al. (2019) have evaluated and assessed the effects of future extreme rainfall events on the Hyderabad City's urban stormwater network (SWN) conveyance capability, along with flood risk analysis and flood mapping. They have used historical and future extreme rainfall events for the runoff simulation process. They have simulated catchment runoff by using SWMM software. They have used the non-linear regression-based mathematical downscaling approach to extract regional rainfall corresponding to Representative Concentration Pathways (RCPs) 2.6, 4.5, 6, and 8.5. They have forecasted heavy rainfall of 282, 431, 564, and 693 mm for the years 2040, 2098, 2068, and 2088 corresponding to RCPs 6.0, 4.5, 8.5, and 2.6, respectively. Results obtained from SWMM showed that, extreme rainfall of future can contribute to increased runoff quantities leading to flood in the Hyderabad City. The prevailing SWN was found to be capable of managing RCP 6 with 82% runoff. For the transmission of runoff corresponding to RCPs 2.6, 4.5, and 8.5, the SWN was found to be insufficient. From simulation findings, it was observed that, carrying capacity of storm drains can be improved by 25–30% by desilting large drains and outlets.

In the metropolitan city of Hyderabad, India, Kadaverugu et al. (2020) have assessed flood mitigation utility of green spaces and evaluated tangible economic damage to the built infrastructure by using Integrated Valuation of Ecosystem Services and Trade-offs (InVEST) model. For 5- and 2-year design precipitation corresponding to 1 h. duration, they have carried out their study. For the study, Quantum Geographic Information System (QGIS) was used to assess the historical variations in the built up area in the study area and InVEST model was used to estimate retention of runoff and economic damage. The findings showed that, urban green and open areas have retained around 44–50% of precipitation. With an increment of 13% in the rainfall rate, the runoff volume was observed to be incremented by 21%, whereas the retained runoff was found to be improved by just 5%. This indicated that, a slight increment in the rainfall intensity was resulted in large runoff generation. They have also estimated the economic loss due to flood inundation by using the unit cost method, which was found to be 1.39 million USD. Study concluded that, the sharp increment in runoff generation can be minimized by increasing the green cover in the study area and turning open fields into rain gardens.

None of the reviewed studies have analyzed urban SWDN of the Central Zone (CZ) in the Surat City. Thus, the analysis of SWDN in the CZ of the Surat City is performed in the present study by using SWMM software.

24.2 Study Area and Data

24.2.1 Study Area

Surat City is situated on the banks of the Tapti River. The city is located at latitudes 21°06' N to 21°15' N and longitudes 72°45′ E to 72°54′ E and has a shoreline of the Arabian Sea on its west. Surat, situated in Gujarat state of India, is well-known for its textile market, polishing industries, and diamond cutting (Joshi et al. 2012). Surat is typically impacted by two kinds of floods, namely Khadi flood and the Tapi River flood. Tapi River flood occurs because of the heavy inflow of rainfall in the basin, while the Khadi flood occurs because of heavy rainfall in the city and the tidal impact of the sea (Vanjara 2020). The summers are pretty hot, with temperatures varying from 37.78 °C to 44.44 °C. The mean annual rainfall of the city is 1143 mm (https://www.suratmunicipal.gov.in/TheCity/Weather). The entire Surat city is divided into seven administrative zones by the Surat Municipal Corporation (SMC) (Joshi et al. 2012). These are CZ, East Zone, West Zone, South Zone, North Zone, Southeast Zone, and Southwest Zone (https://www.suratmunicipal.gov.in/Services/CityCivicCenterListOfCenters). The present study is mainly focused on the CZ of the Surat city.

The CZ is having an area of about 8.18 sq. km with a population of about 408,760 as per the 2011 census (https://www.suratmunicipal.gov.in/TheCity/City/Stml3). The walled city of Surat is positioned at the geographical center of the Surat, which is called as the CZ. The CZ comprises of 12 (1–12) administrative wards. The problem related to stormwater drainage of the CZ is that water logging occurs in some areas (Jariwala and Bhagat 2020). Hence, this zone is selected as the study area in the current study. The CZ is very close to the Tapi River as shown in the Fig. 24.1. The present study is performed to assess whether the existing SWDN is sufficient enough to carry the stormwater or not.

24.2.2 Data Used

The necessary data for the analysis of urban SWDN of the CZ, Surat City is collected from the Drainage Department of the SMC, Surat. The collected data consisted of: SWDN plan in AutoCAD, storm drainage design details like: dimensions of pipes, RLs of junctions, and pipe material details. Daily rainfall data for developing Intensity Duration Frequency (IDF) curves is obtained from the IMD, Pune.

Fig. 24.1 The CZ, Surat City. (Source: Google Earth Pro-Version (2022), Central Zone of the Surat City. Terrain Layer. [Software])

24.3 Methodology

In the present study, SWMM 5.1 software is used for the analysis of existing SWDN of the study area.

24.3.1 IDF Curve Construction

Gumbel's extreme value (GEV) distribution method is used for the preparation of IDF curves and intensity of rainfall is calculated by using Bernard equation given in Central Public Health and Environmental Engineering Organisation (CPHEEO) (2019).

24.3.2 Gumbel Extreme Value Distribution

It is an extensively used probability distribution function corresponding to extreme values in meteorological and hydrologic studies for predicting maximum rainfall and

flood peak, etc. Gumbel distribution is extensively used in the Indian sub-continent (CPHEEO 2019). The process of the analysis is given below.

The value of the variable x corresponding to recurrence interval T is evaluated by using Eq. (24.1) (Subramanya 2008).

$$x_T = \overline{x} + K\sigma_{n-1} \tag{24.1}$$

where

σ_{n-1} = Standard deviation corresponding to sample size $N = \sqrt{\frac{\sum (x-\overline{x})^2}{N-1}}$.
K = Frequency factor = $\frac{y_T - \overline{y}_n}{S_n}$.
y_T = Reduced variate, which is function $T = -\left[\ln . \ln \frac{T}{T-1}\right]$.
$\overline{x}$ = Mean of the variable.
$\overline{y}_n$ = Reduced mean which is a function of sample size N and whose value can be referred from table.
S_n = Reduced standard deviation, which is a function of sample size N and whose value can be referred from table.

24.3.3 Establishing IDF Association

IDF relationship formulae are empirical ones, which were developed on the basis of observation that, as the time duration of storm increments the intensity of storm declines. Bernard equation, i.e., $i = \frac{a}{t^n}$ is usually adopted for estimating intensity of rainfall for Indian conditions. The constants of this equation are estimated by using curve fitting technique, which is described as follows (CPHEEO 2019).

The equation $I = \frac{a}{t^n}$ on logarithmic scale turns into the following form, which is a straight-line equation given in Eq. (24.2) (CPHEEO 2019).

$$\log I = \log a - n \log t \tag{24.2}$$

where.

I = Rainfall intensity in mm/h.
T = Duration of rainfall in minutes.
a and n = Constants.

Therefore, by plotting I and t on the log–log graph, corresponding trend line can be approximated to a straight line of best fit. The slope of this line will be the value of "n" and its intercept on Y-axis will be the value of "a." After determination of constants, the intensities corresponding to various durations such as 5, 10, 15, 20, and so on can be estimated by using the Bernard equation shown in Eq. (24.3) (CPHEEO 2019).

$$i = \frac{a}{t^n}. \tag{24.3}$$

24.4 SWMM Description

The EPA SWMM is a dynamic model of rainfall-runoff utilized for simulation of a single event or simulation of long-term (continual) runoff quality and quantity, mainly from urban areas. The SWMM runoff segment operates on a succession of sub-catchment areas which take precipitation and produce runoff and pollutant loads. By means of a system of channels, pipes, treatment/storage devices, regulators and pumps, the routing segment of SWMM conveys this runoff. During the simulation period, which is made up of several time steps, SWMM monitors the quality and amount of runoff produced by every sub-catchment, as well as the discharge, depth of flow, and quality of water in each pipe and channel (Rossman 2015).

SWMM was originally developed in year 1971 and has gone through many key upgrades since then. It continues to be extensively used across the world for design, planning, and analysis associated with combined sewers, storm water runoff, sanitary sewers and other systems of drainage in urban areas, with several applications in non-urban areas also (Rossman 2015).

SWMM, since its inception, has been utilized in thousands of sewer and stormwater investigations across the world. Some typical applications consists of: sizing and design of drainage system constituents for flood control, natural channel system's flood plain mapping, designing control policies for reducing combined sewer overflows, assessing the impact of infiltration and inflow on sanitary sewer overflows, etc. (Rossman 2015). Steps for the analysis of SWDN in SWMM software are shown in the form of flow chart in Fig. 24.2 and these steps are referred from Rossman (2015).

24.5 Results and Discussions

The intensity of rainfall is used as an input in the SWMM model to evaluate the SWDN performance and this input is obtained from the IDF curves. IDF curves for various durations and return periods (RPs) are derived from the Gumbel's method. Daily rainfall data is obtained from the IMD, Pune, India. To develop the IDF curve, firstly, the annual maximum depth of rainfall is derived from the daily rainfall data, which is transformed into rainfall depth corresponding to different durations such as 5 min, 10 min, 20 min, 30 min, etc. Gumbel's method is applied and the rainfall depth is converted into the intensity and then constants "a" and "n" of the Bernard equation are calculated by plotting the intensity of rainfall vs. duration for RPs of 2 and 5 year on a log–log graph. Then, the rainfall intensity is derived by using the Bernard equation for different durations and IDF curves are plotted. Design details of the CZ SWDN, which are required for evaluation of its performance, are obtained from the Drainage Department of the SMC, Surat.

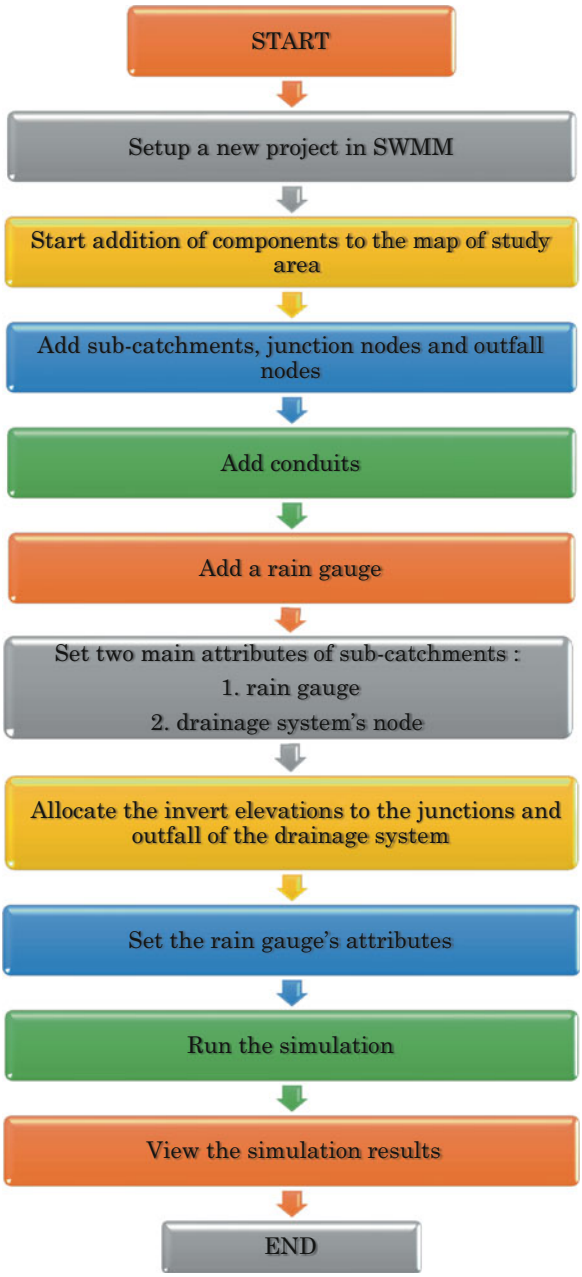

Fig. 24.2 Steps for the analysis of SWDN in SWMM software

24.5.1 Development of IDF Curves

Daily annual maximum rainfall data is derived from daily rainfall data. Annual maximum rainfall depths correspondent to different short durations are given in Table 24.1 and these are determined by using the Reduction formula given by the IMD (Rashid et al. 2012). The Gumbel frequency factor (K) correspondent to 2- and 5-year RPs and rainfall depths for different durations corresponding to 2- and 5-year RPs are shown in Tables 24.2 and 24.3, respectively. The intensities of rainfall shown in Table 24.4 are corresponding to different short durations and 2- and 5-year RPs and these are estimated by using the Gumbel's distribution. By using the Bernard equation, intensities of rainfall for different durations are calculated, which are given in Tables 24.5 and 24.6 and these are corresponding to 2- and

Table 24.1 Annual maximum rainfall depths (P_t) correspondent to short durations of different years for the Surat City

Year	Peak annual rainfall (mm)	Rainfall depths (P_t in mm) for short durations							
		5 min	10 min	15 min	20 min	30 min	40 min	50 min	60 min
1995	166.5	25.18	31.72	36.36	40.01	45.81	50.43	54.31	57.72
1996	190.4	28.79	36.28	41.58	45.75	52.39	57.67	62.11	66.01
1997	82.6	12.49	15.74	18.04	19.85	22.73	25.02	26.94	28.64
1998	208.6	31.55	39.74	45.56	50.13	57.40	63.19	68.04	72.32
1999	187.8	28.40	35.78	41.01	45.13	51.68	56.89	61.26	65.11
2000	96.4	14.58	18.37	21.05	23.16	26.53	29.20	31.45	33.42
2001	82	12.40	15.62	17.91	19.70	22.56	24.84	26.75	28.43
2002	146.6	22.17	27.93	32.02	35.23	40.34	44.41	47.82	50.82
2003	261.5	39.55	49.82	57.11	62.84	71.95	79.21	85.30	90.66
2004	245	37.05	46.68	53.51	58.87	67.41	74.21	79.92	84.94
2005	199.9	30.23	38.09	43.66	48.03	55.00	60.55	65.21	69.30
2006	144.1	21.79	27.46	31.47	34.63	39.65	43.65	47.00	49.96
2007	200.3	30.29	38.16	43.74	48.13	55.11	60.67	65.34	69.44
2008	128.4	19.42	24.46	28.04	30.85	35.33	38.89	41.88	44.51
2009	148.6	22.47	28.31	32.45	35.71	40.89	45.01	48.47	51.52
2010	143	21.63	27.25	31.23	34.36	39.35	43.32	46.65	49.58
2011	131.7	19.92	25.09	28.76	31.65	36.24	39.89	42.96	45.66
2012	137.4	20.78	26.18	30.01	33.02	37.81	41.62	44.82	47.63
2013	316	47.79	60.21	69.01	75.93	86.95	95.72	103.08	109.55
2014	111.6	16.88	21.26	24.37	26.82	30.71	33.80	36.40	38.69
2015	215.3	32.56	41.02	47.02	51.74	59.24	65.22	70.23	74.64
2016	126.4	19.11	24.08	27.61	30.37	34.78	38.29	41.23	43.82
	Average	25.23	31.78	36.43	40.09	45.90	50.53	54.42	57.83
	SD	8.97	11.31	12.96	14.26	16.33	17.98	19.36	20.58

Table 24.2 Gumbel frequency factor (K) for 2- and 5-year RPs

RP (years)	Gumbel frequency factor (K)
2	−0.162
5	0.719

Table 24.3 Rainfall depths for different durations and correspondent to 2- and 5-year RPs

	Rainfall depths (P_T in mm) for different durations							
RP (P_T) ↓	5 min	10 min	15 min	20 min	30 min	40 min	50 min	60 min
P_2	23.76	29.93	34.31	37.75	43.22	47.58	51.24	54.46
P_5	31.68	39.92	45.75	50.34	57.64	63.46	68.34	72.63

Table 24.4 Intensities of rainfall for different short durations corresponding to 2- and 5-year RPs

Duration (min)	Intensity of rainfall (mm/h) for 2-years RP	Intensity of rainfall (mm/h) for 5-years RP
5	286.19	381.80
10	180.29	240.52
15	137.24	183.00
20	114.03	152.13
30	86.44	115.32
40	71.84	95.84
50	61.73	82.36
60	54.45	72.65

Table 24.5 Intensities of rainfall correspondent to various durations for 2-year RP

Duration (min)	Value of constant 'a'	Value of constant 'n'	Intensity (mm/h)
5	836.77	0.667	286.02
10	836.77	0.667	180.14
20	836.77	0.667	113.45
30	836.77	0.667	86.57
40	836.77	0.667	71.45
50	836.77	0.667	61.57
60	836.77	0.667	54.52

5-year RPs, respectively. Rainfall intensity duration curve (logarithmic graph) and IDF curves for 2- and 5-year RPs are shown in Figs. 24.3 and 24.4, respectively.

24.5.2 Analysis of Storm Drainage System

Figure 24.5 depicts the SWDN of Surat City's CZ after input of all required parameters such as sub-catchments, junction nodes, outfall nodes, conduits, and rain gauge. Figure 24.6 shows the maximum flooded junction (J145 junction) in the SWDN of the CZ, Surat City. Simulation is performed by using dynamic wave routing method and its results are given in Tables 24.7 and 24.8, respectively. The

Table 24.6 Intensities of rainfall for various durations corresponding to 5-year RP

Duration (min)	Value of constant '*a*'	Value of constant '*n*'	Intensity (mm/h)
5	1116.00	0.667	381.46
10	1116.00	0.667	240.25
20	1116.00	0.667	151.31
30	1116.00	0.667	115.46
40	1116.00	0.667	95.30
50	1116.00	0.667	82.12
60	1116.00	0.667	72.72

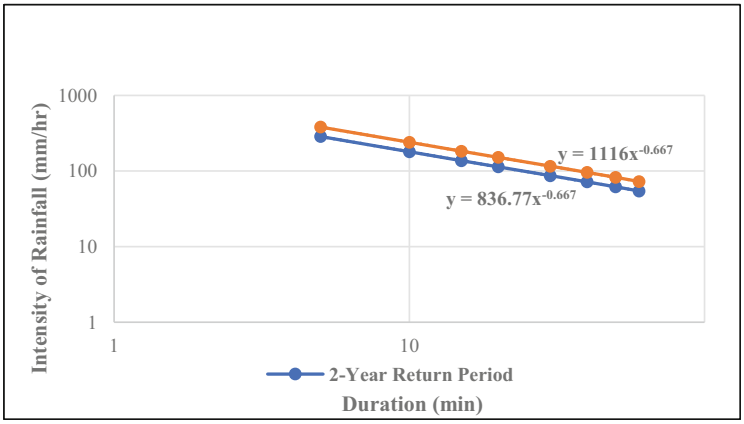

Fig. 24.3 Rainfall intensity duration curve corresponding to 2-year RP for the Surat City

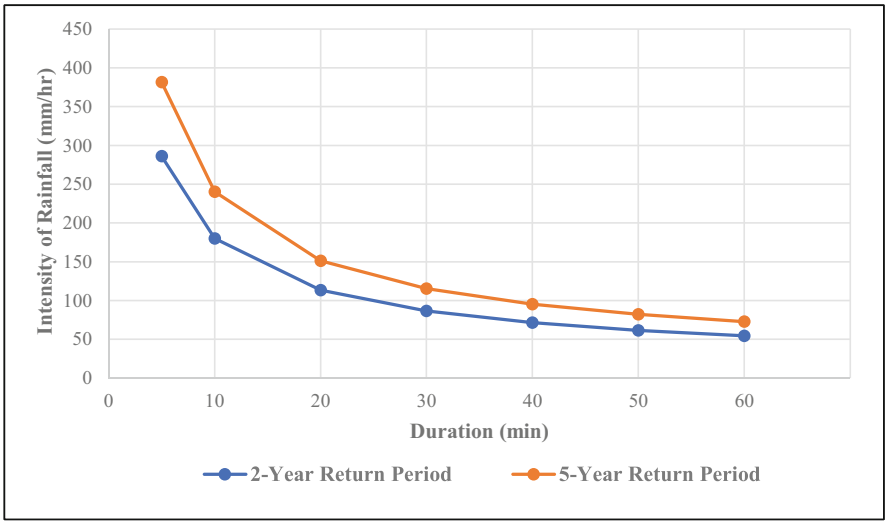

Fig. 24.4 IDF curves correspondent to 2 and 5-year RPs

Fig. 24.5 SWDN of the CZ, Surat City

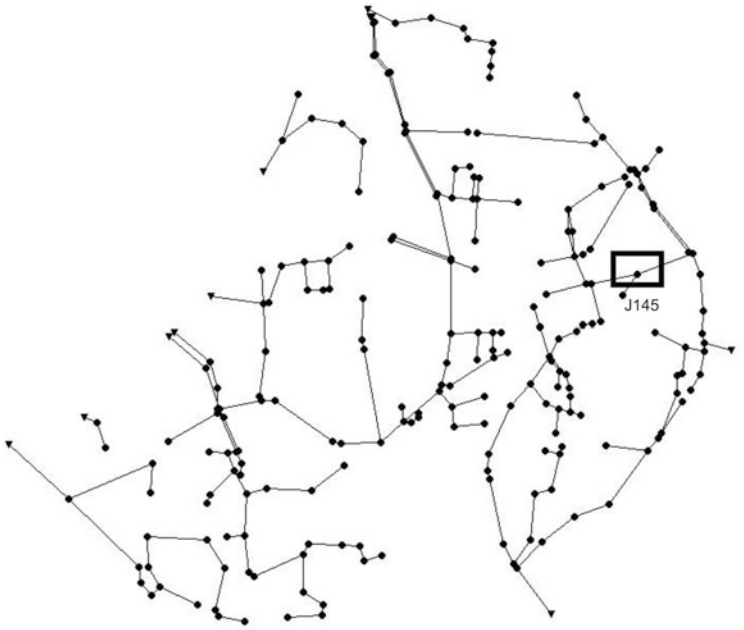

Fig. 24.6 The maximum flooded junction (J145 junction) in SWDN of the CZ, Surat City

Table 24.7 Node flooding summary corresponding to 2-year RP

Node	Hours flooded	Maximum flooding discharge (m^3/s)	Node	Hours flooded	Maximum flooding discharge (m^3/s)
J1	0.01	0.145	J87	0.75	0.59
J2	0.01	0.335	J88	0.01	0.308
J3	0.7	0.424	J89	0.71	0.379
J4	0.61	0.468	J90	0.3	0.105
J5	0.32	0.343	J91	0.01	0.117
J6	0.15	0.145	J92	0.01	0.007
J7	0.01	0.135	J93	0.47	0.188
J10	0.26	0.097	J94	0.28	0.158
J11	0.01	0.04	J95	0.26	0.212
J12	0.01	0.084	J101	0.09	0.098
J13	0.01	0.192	J111	0.25	0.121
J14	0.01	0.66	J127	0.08	0.054
J15	0.77	0.646	**J145**	**0.49**	**3.778**
J18	0.62	0.932	J147	0.73	0.177
J19	0.01	0.204	J148	0.01	0.05
J22	0.03	0.381	J163	0.11	0.083
J24	0.22	0.056	J170	0.13	0.043
J28	0.01	1.049	J171	0.01	0.005
J29	0.03	0.754	J176	0.09	0.036
J30	0.01	0.493	J177	0.11	0.054
J32	0.37	1.248	J178	0.01	0.056
J33	0.2	0.076	J184	0.64	0.172
J34	0.65	0.093	J185	0.72	0.316
J38	0.07	0.035	J186	0.73	0.632
J39	0.1	0.023	J187	0.01	0.16
J57	0.03	0.114	J188	0.01	0.08
J58	0.01	0.124	J189	0.13	0.199
J59	0.22	0.138	J190	0.02	0.262
J61	0.01	0.095	J191	0.01	0.212
J62	0.01	0.038	J194	0.57	0.666
J74	0.33	0.274	J197	0.01	0.093
J76	0.12	0.238	J206	0.01	0.171
J77	0.01	0.095	J207	0.01	0.237
J78	0.05	0.034	J208	0.75	0.36
J85	0.01	0.211	J212	0.01	0.374
J86	0.01	0.156	J213	0.01	0.397

Table 24.8 Node flooding summary corresponding to 5-year RP

Node	Hours flooded	Maximum flooding discharge (m^3/s)	Node	Hours flooded	Maximum flooding discharge (m^3/s)
J1	0.01	0.148	J85	0.02	0.84
J2	0.14	0.376	J86	0.01	0.51
J3	0.75	0.523	J87	0.79	0.925
J4	0.76	0.501	J88	0.01	0.267
J5	0.52	0.38	J89	0.77	0.606
J6	0.38	0.352	J90	0.47	0.243
J7	0.07	0.083	J91	0.07	0.134
J10	0.46	0.2	J92	0.01	0.12
J11	0.35	0.147	J93	0.66	0.215
J12	0.09	0.102	J94	0.47	0.225
J13	0.01	0.28	J95	0.74	0.383
J14	0.01	0.849	J101	0.43	0.237
J15	0.81	1.213	J102	0.06	0.055
J16	0.24	0.163	J107	0.01	0.287
J18	0.71	1.426	J108	0.01	0.546
J19	0.01	0.459	J111	0.49	0.445
J20	0.01	0.168	J119	0.02	0.612
J22	0.19	0.752	J120	0.01	0.715
J24	0.54	0.409	J121	0.01	0.287
J28	0.01	1.284	J122	0.01	0.157
J29	0.04	1.255	J127	0.29	0.279
J30	0.01	1.25	**J145**	**0.58**	**6.635**
J32	0.53	1.882	J147	0.78	0.289
J33	0.38	0.196	J148	0.34	0.122
J34	0.78	0.229	J151	0.22	0.189
J38	0.41	0.19	J152	0.19	0.482
J39	0.41	0.087	J158	0.01	0.451
J57	0.26	0.375	J161	0.01	0.535
J58	0.01	0.341	J162	0.01	0.97
J59	0.41	0.393	J163	0.34	0.287
J60	0.01	0.034	J164	0.01	0.074
J61	0.1	0.282	J170	0.51	0.216
J62	0.35	0.598	J171	0.06	0.066
J63	0.01	0.716	J172	0.01	0.018
J64	0.02	0.414	J173	0.36	0.115
J74	0.49	0.367	J176	0.33	0.202
J75	0.01	0.122	J177	0.6	0.135
J76	0.28	0.279	J178	0.01	0.091
J77	0.18	0.132	J183	0.28	0.416
J78	0.23	0.149	J184	0.78	0.31
J84	0.01	0.235	J185	0.78	0.568
J186	0.77	0.876	J197	0.11	0.103

(continued)

Table 24.8 (continued)

Node	Hours flooded	Maximum flooding discharge (m^3/s)	Node	Hours flooded	Maximum flooding discharge (m^3/s)
J187	0.01	0.246	J199	0.01	0.29
J188	0.04	0.124	J206	0.01	0.182
J189	0.32	0.489	J207	0.01	0.184
J190	0.11	0.281	J208	0.79	0.591
J191	0.01	0.243	J212	0.01	0.757
J193	0.01	0.19	J213	0.01	0.602
J194	0.66	1.315	J218	0.19	0.308
J195	0.01	0.15			

quality of simulation results is found to be good as continuity errors corresponding to surface runoff and flow routing are −2.18% and 0.16%, respectively, for a 2-year RP and these for a 5-year RP are −2.21% and 0.12%, respectively. Node flooding summaries corresponding to rainfall of 2- and 5-year RPs for the SWDN of the study area are given in Tables 24.7 and 24.8, respectively.

From Tables 24.7 and 24.8, it is observed that, hours of flooding are less and the quantity of maximum flooding discharge is also less for majority of the junctions corresponding to 2- and 5-year RPs. Corresponding to 2- and 5-year RPs, the numbers of junction nodes flooded are 72 and 99, respectively. For a 2-year RP, maximum flooding discharge is observed at the junction number J145 and its magnitude is 3.778 m^3/s while its duration is found to be 0.49 h. Similarly, for a 5-year RP, maximum flooding discharge is observed at the same junction (J145) but maximum flooding discharge and duration of flooding are greater as compared that of 2-year RP (magnitude 6.635 m^3/s and duration 0.58 h). Other junctions are also flooded but maximum flooding discharge and duration of flooding is less for these junctions as compared to J145 junction. In this study, an evaluation of the SWDN of study area is performed. This evaluation will help decision makers in formulating strategies for controlling and managing floods in the study area. SWMM is found to be useful for the assessment of SWDN of the study area.

24.6 Conclusions

Analysis of SWDN of the CZ in the Surat City is performed in the current study by using SWMM software. From the aforesaid analysis, it is found that, corresponding to 2- and 5-year RPs, numbers of junction nodes flooded are 72 and 99, respectively.

The maximum flooding discharge and duration of flooding is observed at the J145 junction corresponding to 2- and 5-year RPs. Thus, there is a need to increase the size of the conduits at this junction in order to avoid the flooding at the given junction. Other junctions are also got flooded but maximum flooding discharge and duration of flooding are less for these junctions as compared to J145 junction.

In addition to this, the research demonstrates how the system reacts to varying levels of rainfall intensity corresponding to 2- year 5-year RPs. SWMM is found to be useful for the assessment of SWDN of the study area. In this study, an evaluation of the SWDN of study area is performed. This evaluation will help decision makers in formulating strategies for controlling and managing floods in the study area. An ensemble of latest GCMs corresponding to different RCP scenarios can be used in the future study to evaluate the impact of climate change on the performance of SWDN of the study area.

References

Akter A, Tanim AH (2016) Estimating urban flood hazard zones using SWMM in Chittagong City. Tech J River Res Ins 13(1):87–101

Arjenaki MO, Sanayei HRZ, Heidarzadeh H, Mahabadi NA (2020) Modeling and investigating the effect of the LID methods on collection network of urban runoff using the SWMM model (case study: Shahrekord City). Model Earth Syst Environ 7:1–16

Bisht DS, Chatterjee C, Kalakoti S, Upadhyay P, Sahoo M, Panda A (2016) Modeling URBAN floods and drainage using SWMM and MIKE URBAN: a case study. Nat Hazards 84(2): 749–776

Cardoso MA, Almeida MC, Brito RS, Gomes JL, Beceiro P, Oliveira A (2020) 1D/2D stormwater modelling to support urban flood risk management in estuarine areas: hazard assessment in the Dafundo case study. J Flood Risk Manag 13(4):1–15

Central Public Health and Environmental Engineering Organisation (CPHEEO) (2019) Manual on stormwater drainage systems. Volume-I, Part-A: Engineering Design, Ministry of Housing and Urban Affairs, Government of India

Dell T, Razzaghmanesh M, Sharvelle S, Arabi M (2021) Development and application of a SWMM-based simulation model for municipal scale hydrologic assessments. Water 13(1644):1–16. https://doi.org/10.3390/w13121644

Duan HF, Gao X (2019) Flooding control and hydro-energy assessment for urban stormwater drainage systems under climate change: framework development and case study. Water Resour Manag 33(10):3523–3545

Google Earth Pro (2022) Central Zone of the Surat City. Terrain Layer. [Software]

Jariwala PB, Bhagat SS (2020) A study of existing scenario based on reconnaissance survey: a case of walled city, Surat. Int Res J Eng Technol 7:5491–5497

Joshi PM, Sherasia NK, Patel DP (2012) Urban flood mapping by geospatial technique a case study of Surat City. IOSR J Eng 2:43–51

Kadaverugu A, Rao CN, Viswanadh GK (2020) Quantification of flood mitigation services by urban green spaces using InVEST model: a case study of Hyderabad city, India. Model Earth Syst Environ 7:1–14

Kansal ML, Osheen, Tyagi A (2019) Hotspot identification for urban flooding in a satellite town of national capital region of India. In: World environmental and water resources congress 2019: emerging and innovative technologies and international perspectives. American Society of Civil Engineers, Reston, VA, pp 12–24

Kumar S, Kaushal DR, Gosain AK (2018) Assessment of stormwater drainage network to mitigate urban flooding using GIS compatible PCSWMM model. In: Urbanization challenges in emerging economies: energy and water infrastructure; transportation infrastructure; and planning and financing. American Society of Civil Engineers, Reston, VA, pp 38–46

Li J, Deng C, Li Y, Li Y, Song J (2017) Comprehensive benefit evaluation system for low-impact development of urban stormwater management measures. Water Resour Manag 31(15): 4745–4758

Martínez C, Sanchez A, Toloh B, Vojinovic Z (2018) Multi-objective evaluation of urban drainage networks using a 1D/2D flood inundation model. Water Resour Manag 32(13):4329–4343

Moore TL, Gulliver JS, Stack L, Simpson MH (2016) Stormwater management and climate change: vulnerability and capacity for adaptation in urban and suburban contexts. Clim Change 138(3–4):491–504

Qin HP, Li ZX, Fu G (2013) The effects of low impact development on urban flooding under different rainfall characteristics. J Environ Manage 129:577–585

Rangari VA, Sridhar V, Umamahesh NV, Patel AK (2019) Floodplain mapping and management of urban catchment using HEC-RAS: a case study of Hyderabad city. J Inst Eng (India) A 100(1): 49–63

Rashid M, Faruque SB, Alam JB (2012) Modeling of short duration rainfall intensity duration frequency (SDRIDF) equation for Sylhet City in Bangladesh. ARPN J Sci Technol 2(2):92–95

Rossman L (2015) Stormwater management model user's manual version 5.1—manual. US EPA Office of research and development, EPA, Washington, DC

Seenu PZ, Venkata Rathnam E, Jayakumar KV (2019) Visualisation of urban flood inundation using SWMM and 4D GIS. Spat Inf Res 28:459–467. https://doi.org/10.1007/s41324-019-00306-9

Subramanya K (2008) Engineering hydrology. McGraw-Hill, New Delhi

Vanjara JA (2020) Mitigation of urban flooding by using green infrastructure in Surat, India. Int J Environ Res Dev 10(1):1–17

Vemula S, Raju KS, Veena SS, Kumar AS (2019) Urban floods in Hyderabad, India, under present and future rainfall scenarios: a case study. Nat Hazards 95(3):637–655

Chapter 25
Review of State-of-the-Art Research on River Hydrological Hazards, Restoration, and Management

Deeksha Nayak and Anoop Kumar Shukla

Abstract River's health and self-sufficiency are depending on a variety of factors. One of the most important components for a steady supply of clean water is the surrounding lands known as the watershed, storm water/sewage water disposal practises, local temperature, and yearly precipitation. Rivers provide residential and industrial water supplies, hydroelectricity generation, inland fishing, and are responsible for the deposition of fertile soil in the plains as well as the construction of deltas. Climate change is changing the scale and frequency of river risks, and governments and communities are under increasing pressure to limit and adapt to these potentially disastrous consequences. This comes to the point where it is important to understand the river and the hazards associated. This chapter provides us an overview of river hazards and its types, ecological restoration associated with the river plains and river hazard management strategies.

Keywords River pollution · River flooding · River biodiversity · River restoration · River hazards

25.1 Introduction

River has played an important role in humans' life ever since history can be traced. Rivers have been important to human settlements since the beginning of civilisation, providing water for irrigation, houses, and industry, as well as rich ground for agriculture, as well as functioning as transit routes and leisure activities (Güneralp and Marston 2012; John et al. 2021a, b). There are researchers empirically proving the human way of life was guided by the river from the ancient times (Jain et al. 2021). As the time advanced the we find the river once which was considered as boon to the human life started becoming the bane (Rudari 2017). In the recent past due to the increase in human population we find the major human activities still

D. Nayak · A. K. Shukla (✉)
Manipal School of Architecture and Planning, Manipal Academy of Higher Education, Manipal, Karnataka, India
e-mail: deeksha.msapma@learner.manipal.edu

M. Pandey et al. (eds.), *River Dynamics and Flood Hazards*, Disaster Resilience and Green Growth, https://doi.org/10.1007/978-981-19-7100-6_25

dependent on the river. These activities have a diverse effect on ecosystems, be it on environment impacted by land use changes, which ultimately leads to change in climatic condition of the area, deforestation, air, soil, and water pollutions. These changes are directly linked with various geomorphological hazards (Chakraborty 2013). According to (Scheidegger 1994), hazards are the sudden changes in the long-term behaviour caused by minute changes in the initial conditions.

25.1.1 Importance of River Biodiversity

River ecosystems are supported by the underlying geology and climate. Such characteristics govern how steep and swiftly a river runs, how much material it moves and dumps, and whether its water is generally acidic or alkaline. Rivers are extremely variable settings within this inherent framework, where physical, chemical, and biological processes interact to generate a patchwork of connected habitats known as a 'habitat mosaic' (Addy et al. 2016). Rivers and streams are connected with a wide range of environments. These comprise places characterised by the type of flow, like waterfalls, rapids, and pools, morphological characteristics, such as gravels and river banks, or controlling plants, such as woods, aquatic plants. River surroundings include adjacent wetland regions, swamps and fens, floodplain meadows, and wet woods. From a grain of sand to a floodplain meadow, ecosystem may be investigated at various sizes. Moderate habitat is frequently described, so these units serve as the 'building blocks' for a habitat mosaic. A river reach, on a broader scale, described as the stretch of river which provisions a certain assembly of various habitat components. The reaches are nestled inside the bigger river sections that comprise the river (Frissell et al. 1986).

The characteristics of a river's sedimentation and flow movement have an impact on the layout of river-bed ecosystem. Some sections of the river see significant changes in flow velocity, whereas others offer protection from increasing or diminishing flows. Throughout the summer, areas such as shingle bars and marginal zones are sometimes dry.

The process through which plants grow through early colonisation by pioneer species to become a diverse ecosystem is referred to as vegetation succession. River bank vegetation commonly grow scrub and forest, which is important for integrating surface and groundwater and supplying woody debris to the stream. Rapids and cascades have a somewhat steep gradient, causing torrential circumstances due to tremendous water velocity. Large rocks protect invertebrates and fish from strong speeds. Larvae of blackflies like chute flow, which occurs in waterfalls where water clings the surface of rocks and stones. Riffles form when fast-moving shallow water collides with gravel debris, resulting in a fragmented water surface. Riffles offer habitat to clinging animals and are chosen by fish as a feeding spot, for predator protection due to the broken surface of the water, and for salmon, lamprey, or trout egg nests due to water.

Glides are underwater zones with a textured surface and medium flow speeds, generally along riverbeds of pebbles or sand. The region is generally populated by aquatic plants and have a lower species richness and variety than riffles. Pools are places of substantially deeper water with slower currents. Because of the organic materials that collect on the river bed, they offer animals with deep-water protection and food. Backwaters are moist places that are linked to the primary river but have minimal or no waterflow throughout seasonal fluctuations. Adult fish use them for protection, dragonflies use them for breeding, and lampreys use them as nursery places.

In the stream, tree roots and woody debris affect water quality, maintain sediments, and work with a variety of natural habitat. Wood debris slows the flow of water, forming pools and eddies within which fish can relax, shelter from predators, and evade natural sun. It can serve as a growing medium for algae, fungus, bacteria, plants, and insects. Plants and animals (particularly ground beetles, spiders, and craneflies) benefit from exposed silt. Since it supports a diverse variety of species, along with some specialised and many critically endangered species, this environment is critical for conservation. Banks of the river deliver specialised ecosystems which is sparse in environment elsewhere. Sand martin gatherings nest on worn river banks. The plant communities along riverbanks (riparian) range from mature woods to species-rich meadows. They provide food and refuge to water animals as well as various terrestrial critters with variety of bird types. Floodplain water landscapes support varied variety of ecosystems, including wading birds, amphibians, as well as bats and reptiles.

Floodplain meadows originated from hay pastures, which were once prevalent in river valleys. They have plummeted over the previous 50 years as a result of agricultural expansion, construction growth, and poor management. Those that survive are important flood storage areas, have great preservation importance due to floral diversification, provide nectar for a variety of species especially pests, and act as initial aspects of ecological modification.

25.2 River Hazards

There are three types of hazards that could be associated with:

(i) The hazards that occur when in contact with the water is termed as Primary hazards.
(ii) Hazards caused due to the flooding, health impacts like famine and diseases, along with disruptive services are termed as Secondary hazards.
(iii) Hazards caused due to the change in position or flow of river is termed as Tertiary hazards.

25.2.1 Types of River Hazards

25.2.1.1 Primary Hazards

25.2.1.1.1 Strainers

In general, a strainer is caused by a man-made or natural impediment such as a tree, roots, fence, or a guard railing. The obstruction enables water to travel through while stopping and holding items like boats and people. Bouncing twigs might suggest a partially submerged strainer, and vehicles in the water are undercut strainers.

25.2.1.1.2 Sieves

Obstructions caused by the rocks or the riverbed, which is similar to that of strainers I called as sieves. They're usually boulder-clogged places that allow water to move through but would obstruct a human or boat. Obstacles usually push water around them, forming a pillow over their face. Sieves, on the other hand, allow water to pass through but not humans. Water will just disappear into groupings of rocks rather than being disturbed, which can be difficult to see.

25.2.1.1.3 Holes

There are many different kinds of holes. Ledge hole, river broad hole, little hole, giant hole, recirculating hole, and big macking holes are all examples of different types of holes. These are all generated when water rushes over a rock, travels to the river's bottom, and then turns back on itself. The hole's strength is determined by the water's elevation change and the amount of water that can flow out and away from the rock.

25.2.1.1.4 Undercuts

Rocks or rock walls with pockets for water to flow through, although not usually with people or boats. These are particularly hazardous since we never know where the water goes once it has vanished. Another feature is that they can appear and vanish as the water level changes.

25.2.1.1.5 Flow

What a river will be like can be greatly influenced by the amount of water. Some rivers get more challenging as the water level rises. Additional impediments from the

list above may be present and pose a threat. Also, less eddies to slow down and regroup generally results from more water. You could believe a river will become simpler when the water level falls. That is not always the case, though. Less water could result in unforeseeable challenges. Local run may lose its identity when the water level drops. Unexpected undercut rocks, strainers, and sieves can occur and present some challenges.

Larger hanging loads can be carried by streams travelling at faster speeds. In addition to rocks and sediment, these huge particles may also include large things such as cars, homes, and bridges during a flood.

- Flood waters have the ability to cause significant erosion. Levees, buildings, and bridges can all be compromised by this erosion, leading to their eventual collapse.
- Water damage is caused by water invading human-made structures. Even with minor floods, anything that comes into touch with the water, including floors, walls, and furniture, is likely to be lost or damaged. Typically, flooding causes automotive damage that is difficult to repair.
- Because of their fast velocity, floodwaters can carry a greater suspended weight of silt. When flood waters retreat, the velocity is normally much reduced, and silt is deposited. When the floodwaters recede, everything, including the interior of buildings, is generally coated in a thick layer of stream-deposited mud.
- Crop loss typically occurs when cropland is flooded. Animals such as livestock, pets, and other creatures frequently get lost and drown.
- The water frequently drowns those who are caught in the high-velocity flood waters.
- Floodwaters can concentrate trash, waste, and hazardous substances, which can have a negative impact on health.

25.2.1.2 Secondary Hazards

25.2.1.2.1 Pollution

Water is necessary for survival. It comprises 70% of the Earth's surface. However, only a tiny portion of this important resource is appropriate for our use. Seas hold 97% of the world's total water, which is unfit for human consumption. The remaining 3% is stored in diverse sources such as rivers, lakes, and underground aquifers (Wallwork et al. 2022).

Only 2.5% is fresh water, with 98.8% of the fresh water frozen and only 0.3% in lakes and rivers. Finally, living bodies contain 0.003% of fresh water (Chaturvedi 2019).

River ecology is more prone to external contamination due to the flow properties of river water. Furthermore, once pollution occurs, it can quickly spread throughout the river basin. In recent years, due to the rapid development of the urban economy, the rapid increase of the population, the deepening of the degree of industrialisation, the increase of the urban water consumption and the discharge of river pollutants, the

river self-purification and ecological compensation of the regulation ability of decline, and the water quality significantly deteriorated (Wang et al. 2020).

There is no evidence of river contamination abating. It is growing by the day. Water pollution can occur due to a number of factors, all of which lead to poor water quality. Manufacturers discharge liquid effluent into river systems. Because precipitation brings these pollutants into waterways, our agricultural practises, which include the use of agricultural chemicals, add to water contamination. Domestic waste dumped into rivers adds to pollution levels. The development of towns and cities grows in parallel with population growth. As a result, the quantity of domestic garbage we discharge into rivers rises. Municipal sewers in most towns and cities transport our garbage to waterways. Rivers have caught fire as a result of excessive pollution levels. This demonstrates how severely contaminated our waterways are.

We may immediately detect signs of river contamination in our daily lives. Floating dead animal in our water, coloured river water, or a bad odour emanating from the river are all indicators of water contamination. Whenever you see or feel either of these qualities in a waterway, you may be sure it has been contaminated.

There are three different types of river pollutions:

- Physical pollution.
- Chemical pollution.
- Biological pollution.

Physical pollution: Waste and other composite materials are the most apparent forms of contamination. Metal containers and plastic packaging, for example, are unsightly and endure in the environment. If ingested or become intertwined in waterways, they can obstruct them and damage bird and fish life.

Stormwater brings sand, grit, and other fine elements into the river, where they collect. Total suspended solids (TSS) siltation can block waterways and have a severe influence on invertebrate population and fish egg survival.

Chemical pollution: Damaging pollutant could enter waterways out of a multitude of sources, including the obvious, such as industrial effluents, while the less obvious, like agricultural and roadway runoff. Such chemicals can inflict immediate and disastrous damage to the environment, or they might accumulate slowly, building in plant and animal life in such a way that human and environmental health consequences do not become apparent for several years. Nutrient pollution can cause ecological disruption by causing growth of algae, which could also produce toxins and damage various aquatic organisms.

Extensive use of agricultural chemicals, such as fertilisers and pesticides, has contaminated rivers and streams by heavy metals. These heavy metals enter the human through the things we eat, and most of these cause serious health problems including cancer. The quantity of oxygen in rivers diminishes when pollutants or liquid manure enter the water. If there is insufficient oxygen in a body of water, no living thing can live. It also permanently changes the nature of the river. Nitrate, in addition to heavy metals, is a major agricultural contaminant. Nitrate is an agricultural chemical. Nitrate enters streams from agricultural crop runoff. When our

drinking water originates from a river, we also get nitrate. Some researchers believe that excessive levels of nitrate in drinking water are harmful.

Biological pollution: Pathogens are more likely to infiltrate a creek if hygiene is poor, treatment of wastewater is inadequate or non-existent, or people are living near a river. Certain bacteria and parasites carried by man and animal waste may endanger human wellbeing in locations wherever river water is being used for cooking, washing, or consuming.

Drinking water sources could become contaminated, particularly if wastewater treatment facilities are swamped. Disease and other negative health repercussions could result from this, particularly in developing nations.

- Electrical and gas service may be interrupted.
- Transportation networks may be interfered with, leading to a lack of food and cleaning materials.
- Food shortages frequently result in hunger in less developed nations.

25.2.1.2.2 Bank Erosion

Bank erosion is a fundamental geomorphological process in the alluvial floodplain that can be caused by both natural and artificial sources (Chaudhuri et al. 2022; Pandey et al. 2022a, b). Anthropogenic activity altering river flows can alter river shape and regime, as well as the rate of sediment deposition (Roksandic et al. 2011; Singh et al. 2022; Wallwork et al. 2022). River bank erosion affects millions of people each year. That is damaging our resources such as agricultural land, homes, transportation routes, and crops, among others. Riverbank erosion has an influence not only on human lives but also on the ecosystem. There are several examples of long-term human suffering caused by these issues, such as economic, health, education, transportation, and settlement issues.

Erosion is the process that occurs in a river channel. The riverbank erosion process may be visualised in two ways like, (i) mechanical erosion and (ii) chemical erosion. We find mechanical erosion due to corrosion or abrasion, as well as hydraulic action and attrition, and chemical erosion is caused by corrosion, solution, and carbonation. There are two parts into which bank erosion can be divided, (i) lateral erosion, (ii) vertical erosion or down cutting.

Facts show that river bank erosion happens in two ways: physical and human. Rivers and streams are continually changing dynamic systems. Natural riverbank erosion can result in beneficial effects such as the establishment of fertile floodplains and alluvial terraces. Some rivers contain a healthy degree of erosion; nevertheless, unstable rivers and the erosion that occurs on their banks are reason for concern. Some of the physical factors are poor soil drainage, wave action, excessive sand extraction, intense precipitation, etc. while human factors include deforestation, dam and bridge construction, and unscientific river boundary (Tripathy and Mondal 2020).

Predicting future rates and directions of river bank erosion is a complex topic that appears in many engineering applications. A local study of previous patterns in natural rivers is the greatest pointer to future patterns of bank erosion. The finest sources of information are generally topographic maps and satellite photographs from several years ago, complemented by local witnesses. However, due to scale and resolution constraints, satellite photos provide qualitative outcomes to some extent. Although bank erosion is a complex process, a variety of approaches for predicting bank erosion rates have been developed throughout the years (Pandey et al. 2022a, b).

There are several strategies for controlling bank erosion. The bank protection measures have been classified as structural, non-structural, and biological. However, long-term protection is provided by structural measures.

Structural measures: Hard material protection and river barrier are the two basic types of structural measures used.

Hard material protection is also known as resistive bank stabilisation method. It operates by resisting the flow's power. This is a discontinuous bank protection approach; expect bank scalloping between hard spots. The main goal of this strategy is to defend the bank toe with boulders, stones, cc blocks, and so on. (i) Revetment is an example of a hard material protection. C.C. blocks are put on the slope to continually protect the bank from erosion, and geotextile filters are installed beneath the blocks to defend against seepage failure. (ii) Guide bunds built at bridge crossings to safeguard bridge abutments, as well as their upstream and downstream sections, against erosion. Boulders. (iii) To lower shear stress and near-bank flow velocity, graded boulders are put at the bank's toe. (iv) Brick mastication On the sloped bank slope, brick mattresses are laid.

Barrier across the river is also known as redirection bank stabilisation method. The goal is to shift stream flow and energy away from eroding banks. (i) By wasting flow energy, groynes redirect flow away from the bank and diminish near-bank flow velocity.

Groynes are often made of RCC or an earth-boulder mix. (ii) Spurs are often made of clay, RCC, or wooden logs. Spurs can be solid or porous, submerged or non-submerged. (iii) Vanes are built at river bends to disperse flow velocity. (iv) Submerged bend way weirs located upstream of the bend divert water flowing down the eroding bank at an angle perpendicular to the weir.

Non-structural measures: Short-term protection is achieved by non-structural means. Examples are (i) flow area increase by dredging, (ii) flow diversion at the upstream of the problem area by channelization, and (iii) geo-bag dumping.

Biological protection measures: Bioengineering practises are strategies that are used in addition to traditional ways and are used all around the world. The following biological protection strategies are routinely used (i) bank vegetation, (ii) wooden piling, (iii) willow post, (iv) bandallings, (v) crisscross porcupines, (vi) long hard points.

25.2.1.3 Tertiary Hazards

25.2.1.3.1 Flood

Flooding may be caused by a variety of meteorological and related phenomena, including tropical cyclones, low pressure systems, thunderstorms, snowmelt, and debris flows. These events can cause a wide range of floods, from stream flooding to urban flooding to flash flooding. Because all flooding is potentially lethal, it is vital to be aware of impending flood scenarios and ready to respond promptly to mitigate risk.

There are three major types of floods:

- Fluvial floods (river floods).
- Pluvial floods (flash floods and surface water).
- Coastal flood (storm surge).

Fluvial Floods (River Floods)

Once the level of water in a stream, lake, or river rises, it rushes onto the banks, beaches, and neighbouring land, causing a fluvial flood. Significant rain or melting of snow might be the blame for the surge in water levels (Fig. 25.1).

A river flood may create widespread damage since the overflow affects minor rivers downstream, forcing dams and dikes to break and flooding to occur. Both duration and severity (volume) of precipitation with in river's basin region influence flood hazard. Additional factors to take into account are soil water saturation from previous rains and the geography surrounding the water resource. Floodwater rises slower and is deeper in flatter areas, where that might remain for days. Floodwaters in steep or hilly terrain can form minutes after a heavy rain, drain quickly, and cause significant damage due to debris movement. To estimate the possibility of river

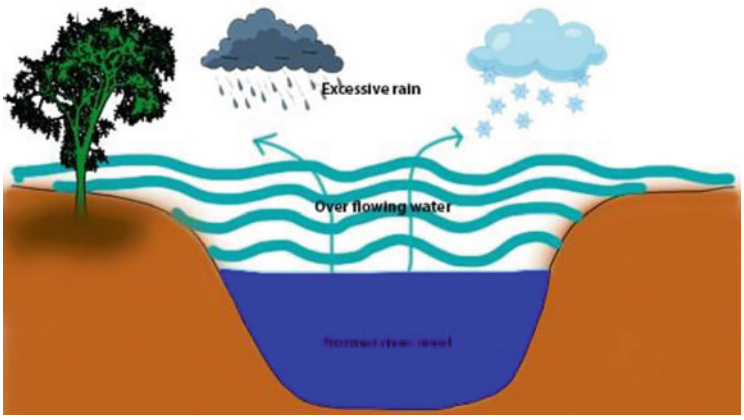

Fig. 25.1 Fluvial floods

flooding, models combine historical precipitation, predicted precipitation, current river levels, along with soil and terrain parameters.

River floods are often characterised hydrologically in terms of a river's water level or discharge(Merz et al. 2010). There are researchers who point out weak relationship between hydrological and damaging floods: even if we know a lot about hydrological floods in one area, we may know nothing about damaging floods in another (Pielke et al. 2000). Floods are caused by a combination of physical and cultural causes.

Pluvial Floods

A pluvial flood occurs when heavy rain generates a flood that is not produced by an overflowing water body (Fig. 25.2). A common misconception regarding floods is that you should always be near a body of water to be impacted. However, pluvial flooding could happen everywhere, urban or country, and also in areas where there are no adjacent bodies of water.

- Flash floods: A flash flood is described as a powerful, high-velocity raging river created by heavy rain falling in such a brief span of time in the local vicinity or on higher ground nearby. They can also occur as a result of a fast release of water out of a levee or dam upstream. Because of the speed of the water and the hurling debris that is usually caught up in the rush, flash floods are extremely dangerous and harmful.
- Surface water: If an urban sewage system gets overworked, water rushes onto streets and neighbouring structures, resulting in surface water flooding. It happens slowly, giving people opportunity to relocate to safer locations, as well as the water level is usually low. It offers minimal imminent risk to individuals, and it has the potential to do significant economic devastation.

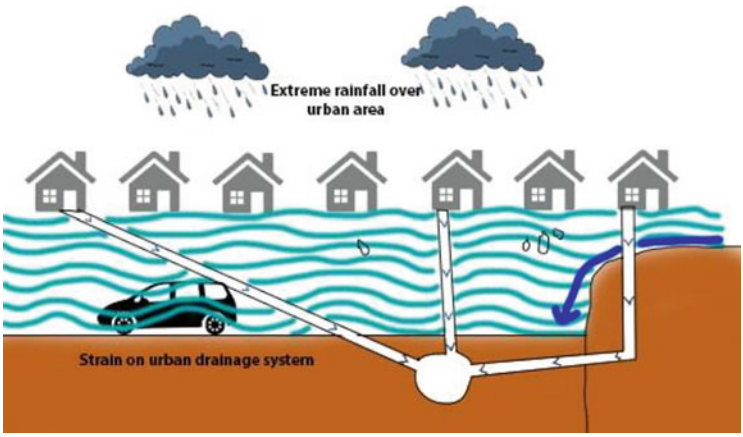

Fig. 25.2 Pluvial floods

Coastal Flood

The inundation of land regions near the coast by seawater is known as coastal flooding. Windstorms that occur at the same time as high tide (storm surge) and tsunamis are common sources of coastal flooding (Fig. 25.3).

Storm surge occurs when strong breezes from a windstorm carry water onshore; this is the most common cause of coastal flooding and it is also the deadliest threat associated with a windstorm. Windstorms that occur during high waves cause significant storm surge floods, and the intensity of the consequences rises with the tide. In this type of flood, water overwhelms low-lying terrain, resulting in tragic loss of lives and properties.

Several other factors influence the strength of a coastal flood, including the windstorm's force, amplitude, speed, and trajectory. Onshore and offshore topography also are important. Coastal flood models employ this data, and also data from prior storms in the region, to determine the likelihood and intensity of the storm surge.

Flood risks account for around one-third of all natural-hazard damages. Floods have a high societal cost; they are very disruptive and can have a considerable impact on the poor, exacerbating the divide between affluent and poor.

Because of flooding, river channels may move or form new channels while the old ones become dry. Flood sediment may ruin agricultural land (though floodwater silt might also aid to boost agricultural production). Jobs could be lost as a result of service interruptions, business closures, etc. (however, work in the construction industry may be obtained to assist restore or repair flood damage).

- Insurance premiums could rise.
- The misuse of humanitarian resources may lead to corruption.
- Destroying a habitat for wildlife.

Fig. 25.3 Coastal Flood

Traditional ecological system management focuses on goods or services that people want, with an emphasis on marketable commodities. Resource managers understand just enough about ecosystems to optimise commodity output. As a result, ecosystems are over-utilised and under-appreciated (Apfelbaum 2014).

A new point of view and strategy to ecosystem management are necessary. Resource managers have only lately begun to recognise the link between an ecosystem's health and its viability for human use. According to researchers, regional ecosystem deterioration can lead to a decrease in natural resource commodity output (Himalayas et al. 1991). The rising number of vulnerable plant and animal species globally is evidence of widespread ecological deterioration. Reduced species and collapse in ecosystem structure, services, and processes are examples of decline (Sweeney et al. 1990).

Species often decrease and perish over a few years. Ecological restoration should ideally focus on mosaics of ecosystems and ecotones across huge landscapes, while also paying particular attention to localised species populations, isolated habitats, and lower levels of ecological structure. In this chapter we deal with ecological restoration of river water.

Water is the foundation of life and, perhaps, the most important prerequisite for economic and social progress. Rivers, streams, creeks, springs, lakes, ponds, and other associated habitats have developed over time to sustain a wide range of plant and animal species. Freshwater habitats provide valuable cultural and recreational resources to people all around the world (Asaeda et al. 2009).

Water covers more than 70% of the earth's surface, while freshwater resources available for direct human use account for less than 1%. This is the water found in lakes, reservoirs, rivers and streams, and shallow subsurface aquifers that may be accessed at a reasonable cost. The atmosphere cannot contain a considerable fraction of the Earth's freshwater at any given moment, and vast amounts of water are constantly cycling through the atmospheric reservoir on extremely short periods. Water cycling through the atmosphere is critical for replenishing freshwater supplies on which all life depends.

Every year, water scarcity becomes more prevalent, and rivalry between diverse water users intensifies. Because of rising human activity, water quality is decreasing at an alarming rate, and aquatic ecosystems are being irreparably disrupted. As more water is removed and utilised for human consumption, there is rising worry over whether the decreased water supply to lakes, rivers, estuaries, and adjacent wetlands is sufficient to sustain the health of these ecosystems. Freshwater scarcity is caused by the unequal distribution of water on Earth, as well as water pollution, which renders water useless. Global water use is quickly increasing, according to the World Resources Institute, and water availability is set to become one of the most serious and controversial resource challenges of the twenty-first century. One-third of the world's population now lives in nations with moderate to severe water stress, and this figure might climb to two-thirds in the next 30 years unless substantial water conservation measures and integrated watershed planning are implemented.

25.2.2 River Habitat Problems

River modification is routinely undertaken with the best of intentions but with little awareness about the potential repercussions. Population increase and technological improvement have resulted in significant changes to the freshwater, wetland, and terrestrial environments within waterways since the industrial revolution. There are no longer really natural habitats that have evaded both direct and indirect human change.

It is critical to identify the types and effects of physical modification in order to establish a successful restoration approach. Strategies should also include additional stresses; i.e., deteriorating quality of water is essential to be addressed with physical repair to assure retrieval. Several forms of change are frequently existing, raising the overall amount of deterioration. Increased stream sedimentation intake from a livestock grazing riverbank that is already generating sediment deposition, for example, might exacerbate channel siltation.

25.2.2.1 Direct Degradation

- River Channelisation and Dredging: Channelisation includes the straightening, diversion, and deepening of natural rivers, as well as the construction of man-made channels. This enhances farmland drainage and reduce the occurrence of floods in the area. The legacy of significant river channelisation has resulted in profoundly altered naturally complex rivers. Channelised rivers contain similar shapes and sediments of river bed, resulting in poor stream flow diversity essential to offer diverse environment for different invertebrate species (Harrison et al. 2004) and juvenile fish (Millidine et al. 2012). Another effect of channelization is the isolation of waterways from the floodplains that reduces the regularity of freshwater and material interchange with the floodplain. Dredging is used to keep channelized rivers in good shape. Dredging can have long-term repercussions, in addition to the acute impact on habitat.
- Gravel Extraction: River gravel extraction to furnish material for building. Gravel mining has the ability to alter natural particle sizes and river shape. Depending on flow and sediment supply regimes, the related habitat may take a long time to recover. In severe circumstances, extraction can cause the river bed and banks to deteriorate (Kondolf 1997).
- Removal of in-stream Woods: Earlier to human influence, large wood deposition would indeed be a regular part of rivers, since riparian woods were considerably more widespread. Only until late 1990s, when such environmental necessity of preserving wood became accepted, ‘de-snagging’ was a normal practice to enhance routing, help minimise flood danger, help fish movement, and aid discharge. Rivers with less timber tend to be broader, straighter, and less biologically diverse.

- Weirs and Locks: Weirs were constructed to create ponds that would provide water to industrial set up, and agriculture. River navigation gates work in the same way as weirs do. Weirs often cause river profiles to be artificially 'plain' or terraced, which causes sediment accumulation and other difficulties which includes increased nutrient storage. Additional impact of weirs is that they limit upstream and downstream species migration.
- Additional in-stream structures: Recognising the physically damaged condition of waterways, as well as the reduction of fish species, has led to the formation of facilities which includes flow deflectors and debris mats aimed at improving fish habitat.
- Bank Reinforcement: Artificial bank reinforcement with stones, lumber, rubble, or concrete seeks to restrict channel movement to preserve land, communities, or infrastructure like bridges and highways, as well as to control sediment influx by disintegrating banks.
- Flood Embankments: Flood embankments or levees made of soil or cement are designed to keep rivers from flooding onto nearby floodplains. Flood barriers have also been erected and sustained for generations, but as need for floodplain infrastructure rose, such as urban population, so did the elevation and length of flood embankments during the twentieth century.
- Alteration of Riparian and Floodplain Areas: Floodplain development for farmland, urban settlement, and commerce diminishes these regions' genuine character and is typically accompanied by channelization, riverbank strengthening, and flood berms.

25.2.2.2 Indirect Degradation

- Land Use: Aside from river corridors, way the ground is maintained will have a brief influence on suspended sediment input into waterways. Increased evapotranspiration and soil moisture storage can come from intensive agriculture or development, resulting in higher peak flows and lower baseflows. Accelerated runoff can cause river channel erosion and expansion in severe circumstances, particularly where impermeable surfaces associated with urban growth exist, resulting in unnatural river shape and ecology.
- Physical modification caused by non-native flora and fauna: Obtrusive non-native species will have an influence on the physical environment in addition to harming local flora and fauna through opposition or virus transmission.
- Climate Change: Waterways are particularly sensitive to variations in rainfall and temperature regimes, rendering them prone to climate change consequences. Increased frequency of severe floods may have an influence on both natural ecosystem viability and quality of water. Such factors alter ecosystem, species richness, structure, and dispersion, as well as the interconnectedness of water bodies. Global warming estimates can aid in high-level conversations about when and where water habitat and biodiversity might alter.

- Dams and flow regulation: The nineteenth century saw an increase in dam construction to provide reserves for drinking purposes, energy generation, and flood control. Among the consequences is the disturbance of the natural flow variability required to activate specific ecological behaviours.

25.2.3 River Restoration Benefits

Rivers provide various advantages and services to people in addition to the rich biodiversity they sustain. The advantages of naturally functioning rivers include products like clean drinking water (Arthington et al. 2010) and ecosystem services like water purification and flood management, all of which are critical for human life (Fig. 25.4). Water's vital significance is mirrored in our modern towns and cities, many of which sprang up near rivers. Characterising the 'natural capital' offered by waters is good beginning idea for developing plans to protect, restore, and employ the ecosystem services they provide in the long run. Considering the products and

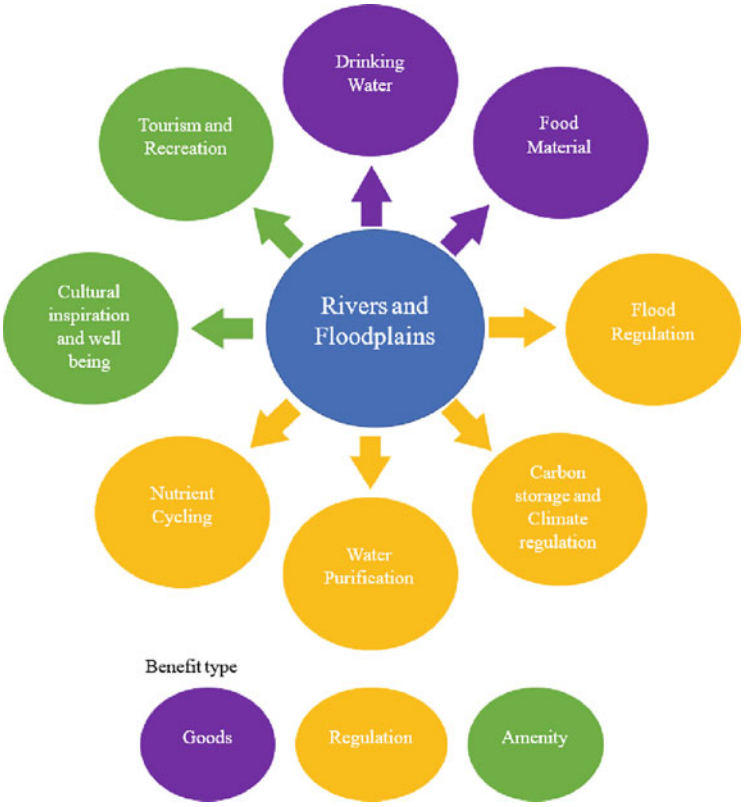

Fig. 25.4 Importance of river restoration

services provided by waterways and floodplains gives insight into the myriad benefits that their restoration may bring.

25.2.4 River Hazards Management

There are steps that can be taken to manage the hazards, these steps aim at lengthening the amount of time taken by the water to reach the river channel, that increases the lag time providing space to take necessary actions. River hazard management has two major strategies followed across the globe:

(i) Hard Engineering Techniques: The creation of artificial constructions to manage rivers is known as hard engineering. They are frequently more expensive. Every hard design approach has advantages and disadvantages.

- Dam construction: Dams and reservoirs are commonly built along the river channel to regulate the amount of water discharge. The dam stores water and discharges it in a controlled manner. This controls flooding. Water is frequently stored beside the dam in a reservoir. This water can be subsequently utilised to generate electricity or intended for usage. A dam can be fairly costly to build. Sediment is regularly caught behind the dam's barrier, triggering downstream erosion. Dwellings and farmland could be destroyed if the river valley is inundated to create a reservoir. The benefits of dam construction are obvious; the dam's water can be used to create electricity by passing it through a turbine. Reservoirs may attract tourists. The drawbacks of dam building include that it is incredibly expensive to build. Dams trap silt, enabling the reservoir to hold less water. Flooding commonly occurs in areas, leading to rotting plants. This results in the production of methane, a greenhouse gas. When settlements are destroyed, people are impacted. Locals in disadvantaged countries are rarely contacted and have little say over where they are sent.
- River Management: To accommodate more water, the river channel might be enlarged or deepened. Straightening a river channel pushes the water faster along its path. The river's channel route can also be changed, moving flooding away from communities. A reservoir is frequently used to store water behind a dam. Such water could also be used to generate power or for recreation. Since river flows faster downstream, modifying the river system may raise the risk of flooding. Also, these channels are very expensive to be build.
- River straightening and dredging: Straightening the riverbank speeds up the water flow, enabling enormous volumes of water to move quickly through an area. Dredging makes the stream deeper, enabling it to hold more water. The canal is constructed to store more water, which is one of the benefits of this technology. It is used to reduce flood risk in highly populated areas. The

downside is that dredging must be performed on a frequently. As when the river runs faster, the flood risk downstream increases.
- Embankments: Elevating the banks of a river enables it to hold sufficient water. With a one-time cost, it is inexpensive. The advantages of this strategy include the possibility of capturing flood water inside the waterway. It looks to be artificial. The downsides of this technology are that water accelerates, creating a risk of floods downstream.

(ii) Soft Engineering Techniques: This does not include the development of man-made infrastructure, rather takes a more environmentally friendly and organic strategy to lower the danger of river flooding. Every strategy has its own benefits and drawbacks.

- Afforestation: Trees are being planted along the river. It implies that more rainfall is intercepted while river outflow is reduced. This is a moderate option that enhances the environmental quality of the drainage basin.
- Managed Floods: The river is allowed to run organically in some places to minimise flooding in other areas, such as near settlements.
- Flood warning and preparation: The EPA monitors rivers and issues flood warning signals through digital media so that people are equipped. People can protect their properties by using items such as sacks. The advantages of this strategy are that more goods may be saved, which implies less compensation claims. Warnings may not be shown to all users. Warnings are worthless when flash floods come at such fast speeds. The downsides of this strategy are that they do not protect land from flooding; rather, they inform the public that a flood is impending.
- Floodplain zoning: Allowing only specific land uses on the floodplain decreases the danger of flooding to homes and vital structures. The advantages of this techniques are that its more costly structures and land uses are further away from the river and hence have a lower flood risk. Less damage is incurred, which results in fewer insurance claims. The disadvantages of this techniques is that it is not always possible to alter existing land usage. Planners must select which sort of flood to prepare for.
- Planning: Regulations are put in place by government agencies to prohibit urban expansion near or on the floodplain. It reduces the possibility of flooding as well as the danger of destruction of property. There may be opposition to development restrictions in areas where housing is scarce. Flood management strategies are seen differently by various interest groups:
- Governments agencies and developers usually choose large hard technical solutions, such as construction of dams. Revenue can be generated by the constructing of a dam and reservoir. Profits may be created by either producing electricity or earning money leisurely. Environmental organisations and local communities frequently choose gentler methods, such as tree planting. Soft solutions create less environmental impact and do not require community migration. Flood management solutions that are effective must

be economically, ecologically, and socially sustainable. Sustainable solutions enable management without jeopardising future generations' demands.

25.3 Conclusion

The deterioration of river function is becoming increasingly serious in the rapid pace of urbanisation, putting significant strain on the sustainable exploitation of rivers and further limiting the healthy growth of cities (Choi et al. 2008). Human-caused ecological disruption has resulted in changes to the river channel, water, sediment, and nutrient flows (Singh and Awasthi 2011). Understanding river dynamics is required for disaster mitigation along rivers. Damage consequences can be reduced by better floodplain and river valley management, flood and lateral erosion prevention techniques, increased disaster preparedness, and the establishment of a forecasting and warning system. It is useful to investigate the catastrophic state of urban waterways and the methods of hazard control. Government and non-government organisations must work together to develop regulations for river restoration, and people must be informed about the river's deteriorating health and the need to repair it for their current lives and the sustainability of future generations.

The Earth's future environment, especially in the wake of global warming, will be distinct from the past (Choi et al. 2008). As a result, restoration aiming at replicating historical ecosystems will be impossible, or at the very least unsustainable, in the future environment. Restoration plans should contain a number of goals and approaches that recognise the dynamic nature underlying biological communities in an unpredictable and changing future environment. There are several restoration approaches available to help in the repair of river ecosystem functions and structures. For improved forecast and understanding of restoration results, an inter-disciplinary approach is required. Water ecosystem restoration is an area of applied science with a direct link to human values; as a result, restoration efforts require public support. Rehabilitation strategies and goals must be economically, ethically, morally, and politically feasible and justifiable in order to gain such support.

References

Addy, Stephen., Cooksley, S., Dodd, N., Waylen, K., Stockan, J., Byg, A., & Holstead, K. (2016). River restoration and biodiversity: nature based solutions for restoring rivers in the UK and Republic of Ireland. CREW reference: CRW2014/10

Apfelbaum SI (2014) Ecological Restoration. Ecol Restor 32(1):104–105. https://doi.org/10.3368/er.32.1.104

Arthington AH, Naiman RJ, McClain ME, Nilsson C (2010) Preserving the biodiversity and ecological services of rivers: new challenges and research opportunities. Freshw Biol 55(1): 1–16. https://doi.org/10.1111/j.1365-2427.2009.02340.x

Asaeda T, Manatunge J, Priyadarshana T, Park BK (2009) Problems, restoration, and conservation of lakes and Rivers. In: Oceans and aquatic ecosystems. Kluwer Academic Publishers, Netherlands

Chakraborty S (2013) Causes and consequences of fluvial hazards-A hydro-geomorphic analysis in Duars region, India. Indian Streams Res J 3(1) https://www.researchgate.net/publication/306057537

Chaturvedi AK (2019). River water pollution-A new threat to India: A case study of river ganga. Vivekananda International Foundation wwwvifindiaorg

Chaudhuri S, Pandey M, Debnath K, Oliveto G (2022) A comparative study on equilibrium scour volume around circular cylinders in clay-sand mixed cohesive beds, at near threshold velocity of sand–an experimental approach. Water Supply 22(8):6777–6791. https://doi.org/10.2166/ws.2022.250

Choi YD, Temperton VM, Allen EB, Grootjans AP, Halassy M, Hobbs RJ, Naeth MA, Torok K (2008) Ecological restoration for future sustainability in a changing environment. Ecoscience 15(1):53–64. https://doi.org/10.2980/1195-6860(2008)15[53:ERFFSI]2.0.CO;2

Frissell CA, Liss WJ, Warren CE, Hurley MD (1986) A hierarchical framework for stream habitat classification: viewing streams in a watershed context. Environ Manag 10:199–214. https://doi.org/10.1007/BF01867358

Güneralp I, Marston RA (2012) Process-form linkages in meander morphodynamics: bridging theoretical modeling and real world complexity. Prog Phys Geogr 36(6):718–746. https://doi.org/10.1177/0309133312451989

Harrison SSC, Pretty JL, Shepherd D, Hildrew AG, Smith C, Hey RD (2004) The effect of instream rehabilitation structures on macroinvertebrates in lowland. In source. J Appl Ecol 41(6):1140–1154. http://www.jstor.org, http://www.jstor.org/stable/3505789

Himalayas N, Yonzon PB, Hunter ML (1991) Cheese, tourists, and red pandas in the Nepal Himalayas. Conserv Biol 5(2):196–202. http://www.jstor.org, http://www.jstor.org/stable/2386193, http://www.jstor.org/page/info/about/policies/terms.jsp

Jain R, Lodhi AS, Oliveto G, Pandey M (2021) Influence of cohesion on scour at piers founded in clay–sand–gravel mixtures. J Irrig Drain Eng 147(10):04021046

John CK, Pu JH, Pandey M, Hanmaiahgari PR (2021a) Sediment deposition within rainwater: case study comparison of four different sites in Ikorodu. Nigeria Fluids 6(3):124

John CK, Pu JH, Moruzzi R, Pandey M (2021b) Health-risk assessment for roof-harvested rainwater via QMRA in Ikorodu area, Lagos, Nigeria. J Water Climate Change 12(6):2479–2494

Kondolf GM (1997) PROFILE hungry water: effects of dams and gravel mining on river channels. Environ Manag 21:533–551. https://doi.org/10.1007/s002679900048

Merz B, Hall J, Disse M, Schumann A (2010) Fluvial flood risk management in a changing world. Nat Hazards Earth Syst Sci 10(3):509–527. https://doi.org/10.5194/nhess-10-509-2010

Millidine KJ, Malcolm IA, Gibbins CN, Fryer RJ, Youngson AF (2012) The influence of canalisation on juvenile salmonid habitat. Ecol Indic 23:262–273. https://doi.org/10.1016/j.ecolind.2012.04.004

Pandey M, Jamei M, Ahmadianfar I, Karbasi M, Lodhi AS, Chu X (2022a) Assessment of scouring around spur dike in cohesive sediment mixtures: A comparative study on three rigorous machine learning models. J Hydrol 606:127330

Pandey M, Pu JH, Pourshahbaz H, Khan MA (2022b) Reduction of scour around circular piers using collars. J Flood Risk Manag 15:e12812. https://doi.org/10.1111/jfr3.12812

Pielke RA, And JR, Downton MW (2000) Precipitation and damaging floods: trends in the United States, 1932–1997. J Clim 13(20):3625–3637. https://doi.org/10.1175/1520-0442(2000)013<3625:PADFTI>2.0.CO;2

Roksandic M, Dragicevic S, Zivkovic N, Kostadinov S, Zlatic M, Martinovic M (2011) Bank erosion as a factor of soil loss and land use changes in the Kolubara River basin. Serbia African J Agric Res 6(32):6604–6608. https://doi.org/10.5897/AJAR11.736

Rudari R (2017) Words into action guidelines: National Disaster Risk Assessment Hazard Specific Risk Assessment 4. Flood Hazard Risk Ass

Scheidegger AE (1994) IMllMI hazards: singularities in geomorphic systems. Geomorphology I0: 19–25. https://doi.org/10.1016/0169-555X(94)90005-1

Singh D, Awasthi A (2011) Natural hazards in the Ghaghara River area, ganga plain, India. Nat Hazards 57(2):213–225. https://doi.org/10.1007/s11069-010-9605-7

Singh UK, Jamei M, Karbasi M, Malik A, Pandey M (2022) Application of a modern multi-level ensemble approach for the estimation of critical shear stress in cohesive sediment mixture. J Hydrol 607:127549

Sweeney JM, Hart JH, Jaquish HS (1990) Structure and dynamics of Midwest oak savannas. In: Sweeney JM (ed) Managetnent of dynamic Ecosystetns. North Central Section, The Wildlife Society, pp 19–30

Tripathy B, Mondal T (2020) River Bank erosion and environmental degradation. Int J Res 7(7): 302–313. https://www.researchgate.net/publication/343797515

Wang Y, Liu Y, Huang J, Wu T, Huang J (2020) Analysis and prevention of Urban River pollution. J Phys Conf Ser 1549(2):022056. https://doi.org/10.1088/1742-6596/1549/2/022056

Wallwork JT, Pu JH, Kundu S, Hanmaiahgari PR, Pandey M, Satyanaga A, Pandey M, Satyanaga A, Amir Khan M, Wood A (2022) Review of suspended sediment transport mathematical modelling studies. Fluids 7(1):23

Chapter 26
Erosion Susceptibility Mapping Based on Hypsometric Analysis Using Remote Sensing and Geographical Information System Techniques

Padala Raja Shekar and Aneesh Mathew

Abstract Geomorphological processes inside a river basin have an impact on water supply and scarcity. Identifying the effect of geomorphological processes on basin hydrology, necessitates a quantitative evaluation of river basin morphology. The Maner River basin's nine sub-watersheds (SWs) were chosen for this present chapter study. The Shuttle radar topography mission (SRTM) digital elevation model (DEM) was utilized for hypsometric analysis. The catchment's volume of rock mass and the quantity of erosion occurring there in relation to the remaining mass are both expressed by the catchment's hypsometric curve. The area under a hypsometric curve was utilized to determine the hypsometric integral (HI). In a geographical information system (GIS) context, the HI value was calculated using the elevation-relief ratio method. These variables were statistically examined by classifying them into distinct groups using the natural break interval method. The erosion process is divided into three stages: the old period, when the catchment is completely stabilized; the equilibrium or mature period; and the in-equilibrium or early period, when the catchment is extremely susceptible to erosion of soil. The HI values for all of Maner's sub-catchments range between 0.39 and 0.64. As a result, higher priority has been assigned to SW3 and SW5, medium priority to SW1, SW2, SW4, and SW6, and lower ranking to SW7, SW8, and SW9. The high priority represents the sub-catchments that are most susceptible to soil erosion. These findings will aid in the development of proper water and soil conservation measures to decrease soil erosion throughout the catchment.

Keywords Hypsometric integral · Soil erosion · GIS · SRTM · DEM

P. R. Shekar (✉) · A. Mathew
Civil Engineering Department, National Institute of Technology, Tiruchirappalli, Tamil Nadu, India
e-mail: 403121003@nitt.edu

M. Pandey et al. (eds.), *River Dynamics and Flood Hazards*, Disaster Resilience and Green Growth, https://doi.org/10.1007/978-981-19-7100-6_26

26.1 Introduction

Water resource management and development have faced huge substantial challenges due to erosion and related problems. Water regularly erodes silt from the reach's bed and banks and transports it through the catchment downstream. Different hazards like landslides or ground deformations may cause silt to overflow into the river system, causing an unanticipated build- up of sediment deposition (Amundson et al. 2015). In addition to naturally occurring silt, activities including agriculture, deforestation, mining, urbanization, and road construction will inevitably have an impact on soil erosion rates (Hassan et al. 2017).

A catchment or watershed is an area where all rainfall flows to a common outlet. A catchment, in other words, is a geological dynamic component that contains all soil that adds discharge to a common outfall (Sharma et al. 2007a, 2015; John et al. 2021). Population growth has also reduced the accessibility of water and land resources (Sharma et al. 2007b; Wallwork et al. 2022). A variety of quantitative analyses are used to calculate the topography of the catchment, and the analyses can range from a single catchment to the entire country. Without a suitable technique, it would be tough to distinguish findings from various catchments. The HI and hypsometric curve are the best methods for analysing drainage basin topography (Ramu and Mahalingam 2012; Shivashankar et al. 2022).

The assessment and evaluation of the link between altitude and catchment region is known as hypsometry, and it is done in an effort to know the level of disequilibrium and also the stage of geomorphologic evolution. It aids in determining the impact of geologic and tectonic factors. The goal of hypsometric analysis is to create a dimensionless connection between both the catchment's horizontal cross-sectional region and elevation, allowing for catchment comparison regardless of scale problems (Dowling et al. 1998). Hysometry was traditionally utilized to determine the geomorphological structure of landmasses and catchment areas. The channel network and catchment shape have an important impact on it. It is the process of calculating the elevation allocation as a component of the region occupied by every contour interval inside a terrain unit. Langebein and Basil proposed the concept of hypsometry in 1947. Strahler (1952) added the HI and the percentage hypsometric curve (area–elevation curve).

Non-dimensional measurements of the percentage of the catchment area above the given height are called hypsometric curves (Strahler 1952). The geomorphic and tectonic development of river catchments, according to Hurtrez et al. (1999a), Schumm (1956), and Strahler (1964), is related to hypsometric curves in terms of their forms. Landform ages have also been determined using hypsometric curves (Strahler 1952, 1964; Schumm 1956). The integral and hypsometric curve is key aspects of catchment environments (Ritter et al. 2002). The difference between the shape of the hypsometric curve and integral values is what is used to determine the level of disequilibrium in the balance of erosive as well as tectonic forces (Weissel et al. 1994). The shape of the hypsometric curve for distinct river systems under identical hydrologic factors can provide a relative knowledge of past soil movement

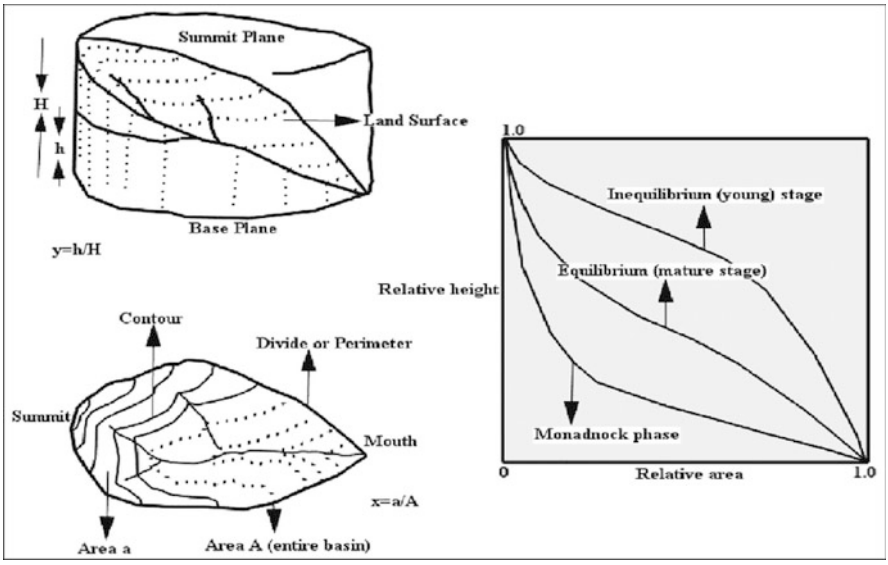

Fig. 26.1 Shows hypsometric curves and the concept of hypsometric analysis (Ritter et al. 2002)

in the catchments (Singh and Sarangi 2008; Shankar et al. 2021). The shape of the hypsometric curve thus represents differences in the gradient of the initial catchment. Based on the shapes of their hypsometric curves, Strahler (1952) categorized river catchments as young, mature, distorted or peneplain. According to Singh and Sarangi (2008), these hypsometric curve shapes portray the periods of landscape evolution and also indicate the status of erosion of the catchment. Hypsometric curve morphologies fluctuate often throughout the initial geomorphic periods of development, but after the catchment reaches maturity, there is little variation. Concave hypsometric curves, on the other hand, suggest that the catchment is more susceptible to erosion operations and that the catchment has achieved a stable state (Hurtrez et al. 1999b).

The HI is a geomorphic aspect categorized by geologic phases of catchment development. It is crucial for assessing a catchment's erosion condition and, as a result, aids in the prioritization of catchments for suggesting water and soil preservation activities. In addition, the HI denotes the erosion cycle (Garg 1983; Strahler 1952). The erosion cycle is the overall amount of time taken to decrease a land region to its initial level (Fig. 26.1). This overall time frame, or erosion cycle, can be grouped into three categories: old (HI is less than 0.30), when the catchment is fully stabilized; mature (HI is between 0.30 and 0.60), when the catchment is highly vulnerable to erosion; and young (HI is greater than 0.60), when the catchment is highly susceptible to erosion (Strahler 1952). The hypsometric integral clarifies erosion in the catchment during its safety.

Watershed prioritizing has gained the attention of scientists and planners from all around the world in recent years for the catchment development and management

plan. In order to determine the most susceptible area, researchers used a variety of elements and approaches to define the watershed priority level. Among them, soil loss, runoff potential, sediment generation and transport, morphology, slope, etc., are the most crucial. They are sometimes referred to as erosion hazard parameters (Rai et al. 2017; Shekar and Mathew 2022b). A particular sub-catchment may be given high priority for a number of issues; however, the severity of land degradation is frequently used as the primary factor for prioritization. Prioritizing catchments becomes difficult in unguaged or inadequately gauged situations. As a result, hypsometric analysis is used to prioritize those catchments (Farhan et al. 2016).

Recent improvements in remote sensing (RS) and GIS approaches have made it possible to present correct, well-timed, and real-time data on numerous features of the catchment (Shekar and Mathew 2022a; Sarp et al. 2011). Owing to the time-consuming nature of information gaining and also the analysis involved in assessment, there is a scarcity of hypsometric analysis-based research for minor river basins to analyse catchment health. However, with the introduction of RS data and GIS tools, the estimation process has become simpler than traditional approaches. Taking into account the foregoing, this present chapter study was conducted in the Maner catchments to prioritize their sub-catchments for erosional susceptibility mapping based on hypsometric analysis for soil and water conservation.

26.2 Study Area

The Maner River catchment area is 2056 km^2 in Maharashtra state, India, and is surrounded by 76°30′0′′ and 77°45′0′′ east longitudes and 17°45′0′′ and 19°00′0′′ north latitudes (Fig. 26.2). The outlet of the Maner River can be located at longitudes 77°32′ 42′′ east and latitudes 18°42′ 18′′ north. The catchment's maximum and minimum elevations range from 352 to 706 m above mean sea level. According to FAO (1988), the main soil units in the area are vertic cambisols and chromic vertisols. The slope varies between 0 and 29.15°. The Maner catchment consists of nine sub-watersheds in that SW8 is in the fifth order, while SW1, SW3, SW4, SW5, SW6, SW7, and SW9 are in the fourth order, and SW2 is in the third order in the Maner catchment. The catchment has a dendritic to sub-dendritic drainage structure. The study region features significant rock, according to the United States Geological Survey's (USGS) World Geologic Maps. The types of rock that were seen in the study region were paleocene cretaceous extrusive rocks, as shown in Fig. 26.3.

26.3 Methodology

The present chapter study's methodology employs automatic extraction techniques for evaluating the parameters of the Maner River basin using a DEM. To understand the morphological parameters, ArcGIS 10.8.2 was used to derive the basin

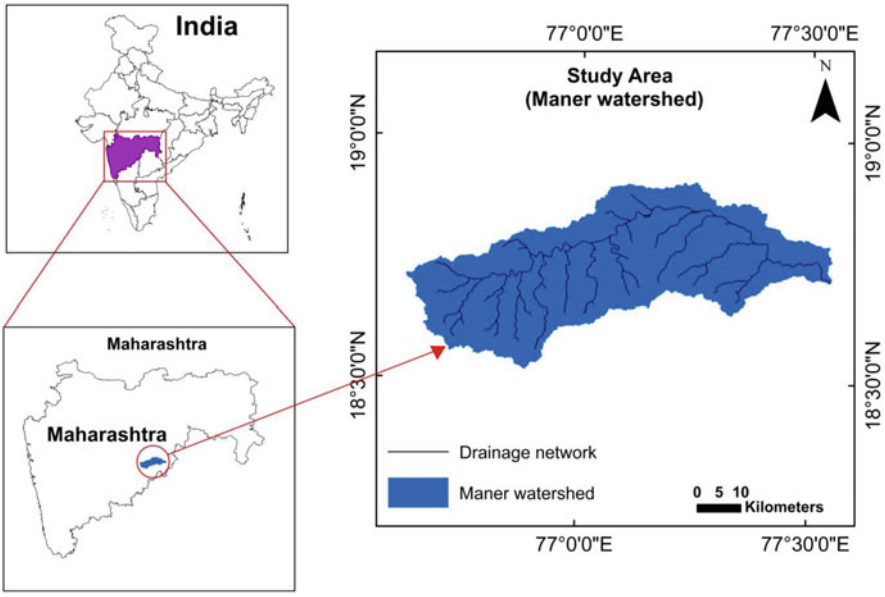

Fig. 26.2 Study area of Maner catchment

boundary, drainage pattern, and catchments within the basin. The process of determining the morphometric analysis begins with filling the sinks in the DEM. The flow direction was determined after the DEM was filled. Flow accumulation has been taken into consideration based on the flow direction of each cell in order to generate a drainage network. Figure 26.4 depicts the delineation of the sub-catchments. The goal of hypsometric analysis is to establish a relationship linking the catchment's horizontal cross-sectional area as well as elevation. GIS tools are used to perform the hypsometric analysis for the Maner area. The hypsometric curve is normally depicted as a provision of relative height (h/H) versus relative area (a/A) (Strahler 1952). The line feature class in ArcGIS 10.8.2 was used to produce the contours, which were then subjected to the hydrology tool's processing. The attribute tables of the geo-referenced feature classes that represented the contours and their contained region with the catchment boundary were used to store the contours' elevation, perimeter values, area, and length. The hypsometric curve for the catchment was plotted using the attribute feature classes that had these values. The hypsometric curves for the basin were generated using Strahler's (1952) approach. An elevation-relief ratio was utilized to determine the basins' hypsometric integrals (HI) using an empirical formula (Pike and Wilson 1971) (Eq. 26.1).

$$E = \frac{E_{\text{mean}} - E_{\text{maximum}}}{E_{\text{maximum}} - E_{\text{minimum}}} \tag{26.1}$$

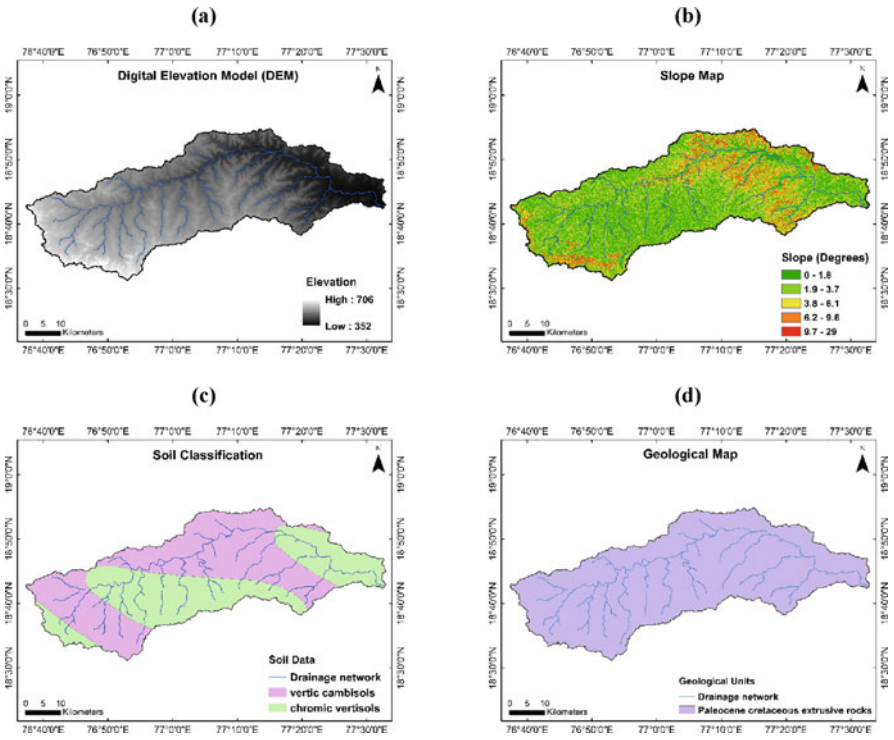

Fig. 26.3 (**a**) Digital elevation model (DEM); (**b**) Slope map; (**c**) Soil classification; (**d**) Geological map

where E is the elevation-relief ratio equivalent to the HI; E_{mean} is the catchment's weighted mean elevation estimated from the delineated catchment's identifiable contours; and E_{max} and E_{min} are the maximum and minimum elevations within the sub-catchments. In percentage units, the hypsometric integral is expressed. Catchment prioritization is the process of ranking different areas of a catchment in order of importance for adopting appropriate soil conservation measures.

26.4 Results and Discussions

The nine sub-watersheds of the Maner watershed's generated hypsometric curve coordinates were plotted and shown in Fig. 26.4. The drainage system is reaching the mature stage for ten of these sub-watersheds and the young stage for one of them (SW5), according to the hypsometric curves of these sub-watersheds. The comparison of these curves in Fig. 26.5 revealed a slight variation in the amount of mass removed from the research area's sub-watersheds. For the sub-watersheds under research, it was also noted that the hypsometric curves had an S-shaped and convex

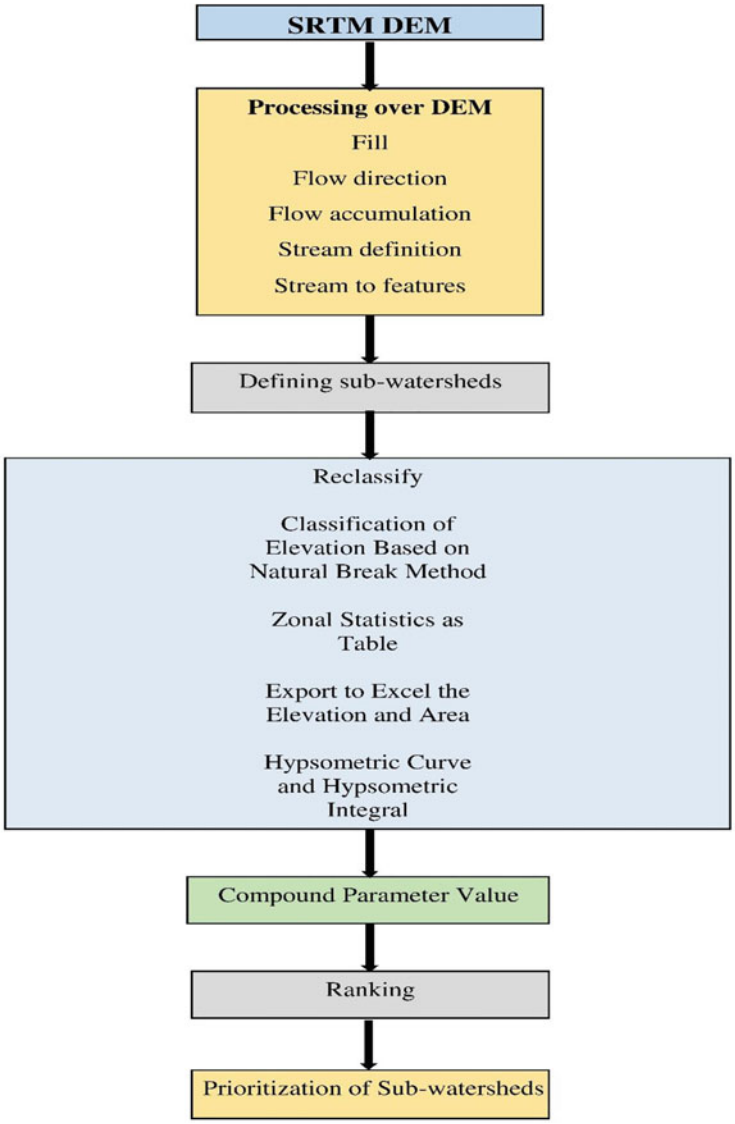

Fig. 26.4 Methodology of hypsometric analysis

upward combination, as illustrated in Table 26.1. This could be as a result of erosion of soil from these sub-watersheds brought on by cutting into channel beds, bedrock materials moving down slope, and so on.

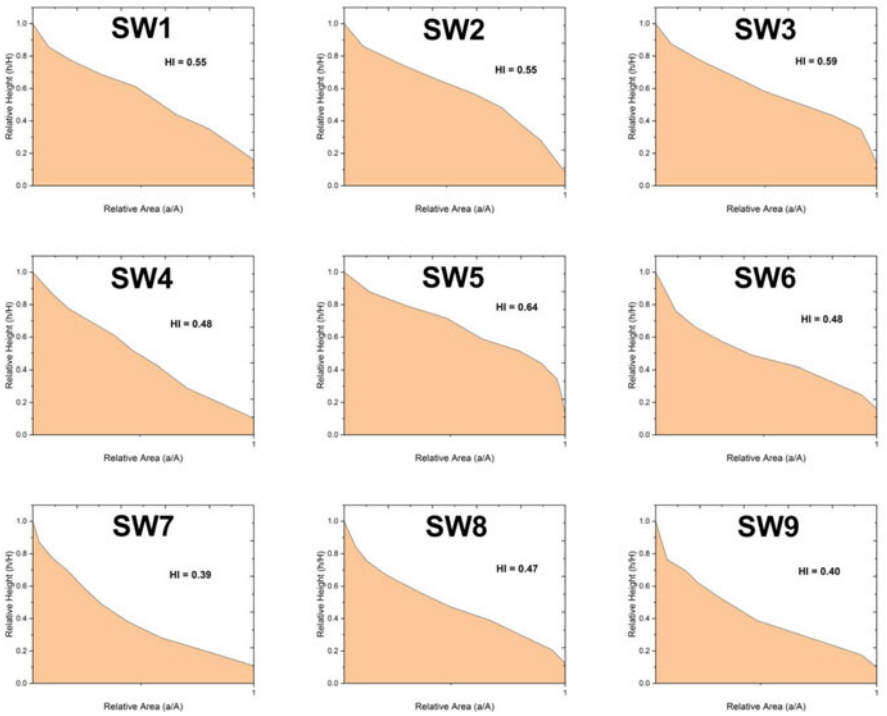

Fig. 26.5 hypsometric curve and hypsometric integral

Table 26.1 Stage of catchment

HI	Stage	Shape
HI $\geq$ 0.6	Young or in-equilibrium	Convex upward
HI: 0.30 $\leq$ HI $<$ 0.6	Mature or equilibrium	S-shaped
HI $<$ 0.30	Old or monadnock	Concave upward

26.5 Estimation of Hypsometric Integral Values

Table 26.2 displays the HI values calculated using the Elevation-Relief Ratio (E) Relationship approach for the nine sub-watersheds of the study area. The HI is calculated using the hypsometric curve and is equal to the ratio of the square's total area to the area under the curve. It is calculated by measuring the area under the % hypsometric curve, and it is represented in percentage units. The hypsometric integral is obtained by integrating the hypsometric curve. The elevation-relief ratio (E), which is defined as the integration of the hypsometric curve and is provided in Eq. (26.1), was mathematically demonstrated by Pike and Wilson in 1971. An indirect estimator of the erosion from river basin systems is the HI value. It also gives a very good understanding of how the land surface is distributed at different

Table 26.2 Calculation of hypsometric integral, ranking and prioritization

SW	Area (km^2)	Perimeter (km)	Maximum elevation (m)	Minimum elevation (m)	Hypsometric integral (HI)	Ranking	Final priority
SW1	313.80	122.00	543	373	0.546	6	Medium
SW2	98.06	89.31	562	388	0.548	7	Medium
SW3	274.67	127.97	590	416	0.590	8	High
SW4	240.33	122.37	551	366	0.478	4	Medium
SW5	127.91	78.41	563	419	0.642	9	High
SW6	325.37	141.18	665	445	0.483	5	Medium
SW7	275.38	140.57	527	352	0.393	1	Low
SW8	276.56	126.69	666	491	0.471	3	Low
SW9	124.14	89.74	706	492	0.401	2	Low

km^2 kilometre square, *km* kilometre, *m* metre

elevations. As given in Table 26.2, the HI values of the sub-watersheds of the Maner river basin ranged from 0.393 to 0.642.

26.6 Relevance of Hypsometric Integral on Watershed Hydrological Responses

The two key hydrological reactions to rainfall events over watershed systems are surface runoff and sediment losses. The HI value could be used to indirectly predict erosion from catchment systems. The sub-watersheds of the Maner watershed were found to be in a young and mature stage based on the HI values (Table 26.2). This showed that the main causes of erosion of soil in these sub-watersheds were cutting into channel beds, bedrock materials moving down slope, bedrock material moving down slope, and so on. These changes in landforms were also visible in the present chapter study watershed's many sub-watersheds.

Figure 26.4 illustrates the HI values of the sub-watersheds of the Maner watershed, which varied from 0.393 to 0.642. There were three groups identified: low (0.39–0.48), medium (0.48–0.56), and high (0.56–0.64) (Farhan et al. 2016). Sub-catchments with compound parameter values in the range of (0.39–0.48) have received low priority. The sub-catchment has been given a medium priority with a compound parameter value in the range of (0.48–0.56). Sub-catchments with compound parameter values in the range of (0.56–0.64) have been given high priority. As given in Table 26.2, SW3 and SW5 are high priority sub-catchments; SW1, SW2, SW4, and SW6 are medium priority sub-catchments; and SW7, SW8, and SW9 are low priority sub-catchments, as shown in Fig. 26.6.

The SW7, SW8, and SW9 have been found to have low priority or to be less susceptible to erosion rate. However, the SW1, SW2, SW4, and SW6 have medium priority, which indicates the sub-watersheds' hydrologic response will have a

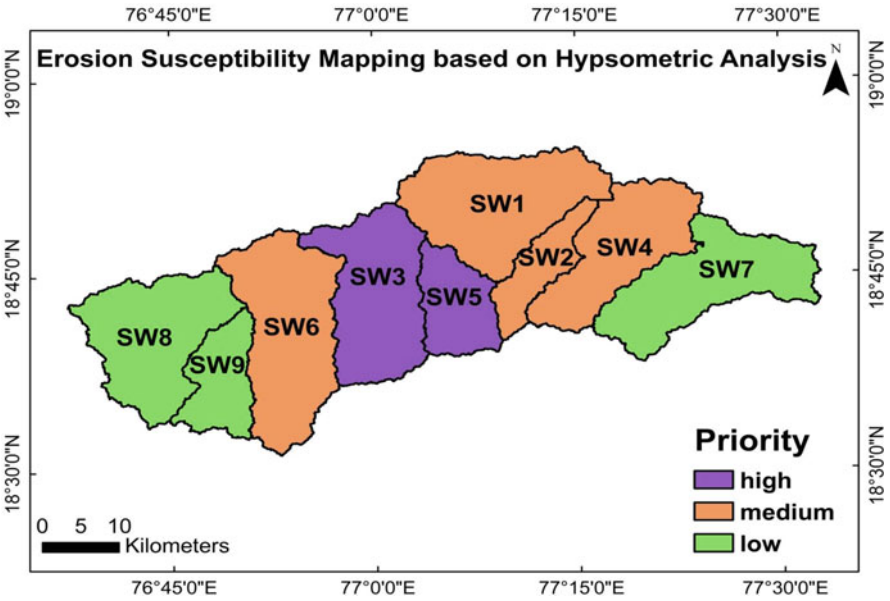

Fig. 26.6 Priority of sub-watersheds based on hypsometric analysis

modest rate of erosion unless there are really high intensity storms that cause large runoff peaks. Additionally, SW3 and SW5 have a high priority, making them particularly susceptible to degradation. Therefore, proper water and soil conservation measures are required for the sub-watershed with the highest priority.

26.7 Conclusions

The complexity of denudational processes and the rate of morphological changes are expressed through hypsometric studies of watersheds. Understanding the erosion status of watersheds will help to prioritize them for water and soil conservation efforts. However, due to the complicated computation involved in hypsometric curves, extreme caution must be used when interpreting and comparing them. In this present chapter, hypsometric analysis is used to demonstrate how RS and GIS approaches can be used to prioritize sub-catchments. The hypsometric integral values are shown for the nine sub-catchments (0.393–0.642). According to the results of hypsometric analysis-based prioritization, the SW3 and SW5 sub-catchments are of high priority. As a result, the SW3 and SW5 sub-catchments are highly susceptible to soil erosion. As a result, hypsometric analysis values can be utilized as an estimator of catchment status of erosion, which is significant to catchment prioritization for water and soil conservation measures.

Acknowledgements The authors appreciate the insightful comments provided by the anonymous reviewers, which helped to make this paper better. The US Geological Survey (USGS) is also acknowledged by the authors for providing the satellite data.

Data Availability The corresponding author can be contacted for access to the datasets created for and/or used in the analysis of the present chapter study.

Conflict of Interest The authors say they have no conflicting interests.

References

Amundson R, Berhe A, Hopmans J, Olson C, Sztein AE, Sparks D (2015) Soil and human security in the 21st century. Science 80:348. https://doi.org/10.1126/science.1261071

Dowling TI, Richardson DP, O'Sullivan A, Summerell GK, Walker J (1998) Application of the hypsometric integral and other terrain based metrices as indicators of the catchment of health: a preliminary analysis technical report 20/98. CSIRO Land and Water, Canberra

FAO (1988) FAO Soil Map of the world, Revised Legend With Corrections and Updates World Soil Resource Food and agricultural organization. FAO, Rome, Italy, Report 60

Farhan Y, Elgaziri A, Elmaji I, Ali I (2016) Hypsometric analysis of Wadi Mujib Wala catchment (southern Jordan) using remote sensing and GIS techniques. Int J Geosci 7:158–176. https://doi.org/10.4236/ijg.2016.72013

Garg SK (1983) Geology—the science of the earth. Khanna Publishers, New Delhi

Hassan MA, Roberge L, Church M, More M, Donner SD, Leach J, Ali KF (2017) What are the contemporary sources of sediment in the Mississippi river? Geophys Res Lett 44:8919–8924. https://doi.org/10.1002/2017GL074046

Hurtrez JE, Sol C, Lucazean F (1999a) Effect of drainage area on hypsometry from an analysis of small scale drainage basins in the Siwalik hills (Central Nepal). Earth Surf Process Landf 24: 799–808

Hurtrez JE, Lucazean F, Lava J, Avouac JP (1999b) Investigation of the relationship between basin morphology, tectonic uplift and denudation from the study of an active fold belt in Siwalik hills (Central Nepal). J Geophys Res 104:799–796

John CK, Pu JH, Pandey M, Moruzzi R (2021) Impacts of sedimentation on rainwater quality: case study at Ikorodu of Lagos, Nigeria. Water Supply 21(7):3356–3369

Langebein WB, Basil W (1947) Topographic characteristics of drainage basins. USGS Water supply paper

Pike RJ, Wilson SE (1971) Elevation—relief ratio hypsometric integral and geomorphic area-altitude analysis. Geol Soc Am Bull 82:1079–1084

Rai PK, Mohan K, Mishra S, Ahmad A, Mishra VN (2017) A GIS based approach in drainage morphometric analysis of Kanhar river basin, India. Appl Water Sci 7(1):217–232

Ramu, Mahalingam B (2012) Hypsometric properties of drainage basin in Karnataka using geographical information system. N Y Sci J 5(12):156–158

Ritter DF, Kochel RC, Miller JR (2002) Process geomorphology. McGraw Hill, Boston

Sarp G, Toprak V, Duzgun S (2011) Hypsometric properties of the hydraulic basins located on Western part of Nafz. In: 34th International symposium on remote sensing of environment theme: water a limited and degraded resource, Sydney, Australia

Schumm SA (1956) The evolution of drainage systems and slopes in badlands at Perth Amboy, New Jersey. Geol Soc Am Bull 67:597–564

Shankar MS, Pandey M, Shukla AK (2021) Analysis of existing equations for calculating the settling velocity. Water 13(14):1987

Sharma SK, Mishra N, Gupta A (2007a) Morphometric analysis of Uttala Nala catchment using GIS technique. Sci Front 1:178–185

Sharma SK, Kujur S, Suriya S (2007b) GIS based morphometric analysis of Sarphanala catchment. Geogr Obs 37:50–54

Sharma SK, Gajbhiye S, Tignath S (2015) Application of principal component analysis in grouping geomorphic parameters of a catchment for hydrological modelling. Appl Water Sci 5(1):89–96

Shekar PR, Mathew A (2022a) Morphometric analysis for prioritizing sub-catchments of Murredu river basin, Telangana state, India, using a geographical information system. J Eng Appl Sci 69: 44

Shekar PR, Mathew A (2022b) Evaluation of morphometric and hypsometric analysis of the Bagh River basin using remote sensing and geographic information system techniques. Energy Nexus 7:100104

Shivashankar M, Pandey M, Zakwan M (2022) Estimation of settling velocity using generalized reduced gradient (GRG) and hybrid generalized reduced gradient–genetic algorithm (hybrid GRG-GA). Acta Geophys:1–11

Singh O, Sarangi A (2008) Hypsometric analysis of the lesser Himalayan catchments using geographical information system. Indian J Soil Cons 36(3):148–154

Strahler AN (1952) Hypsometric (area-altitude) analysis of erosional topography. Geol Soc Am Bull 63:1117–1141

Strahler AN (1964) Quantitative geomorphology of drainage basins and channel networks. In: Chow VT (ed) Handbook of applied hydrology, vol 63. McGraw Hill, New York, pp 1117–1141

Wallwork JT, Pu JH, Kundu S, Hanmaiahgari PR, Pandey M, Satyanaga A, Pandey M, Satyanaga A, Amir Khan M, Wood A (2022) Review of suspended sediment transport mathematical modelling studies. Fluids 7(1):23

Weissel JK, Pratson LF, Malinverno A (1994) The length scaling properties of topography. J Geophys Res 99:13997–14012

Part IV
Climate Change and Global Warming Issues

Chapter 27
Climate Change Implication and Adaptation for River Systems

Fatima Amin and Anil Kumar Gupta

Abstract Climate change the greatest threats to peace in the twenty-first century to date. Extreme events are causing more and more damage, loss, and consequence around the globe. Global climate change has been affecting different regions of the planet. Rivers provide a diverse variety of natural amenities to mankind. Human activity, on the other hand, causes diverse stress on river ecosystems. Climate change is a result of human behaviour, and it is something we need to be concerned about. Several studies have projected the major impacts of climate change. The potential for negative consequences, as well as the cost and complexity of adaptation, will increase the degree and intensity as global climate change increases. Climate change is already impacting communities in river basins' livelihoods, health, and other social indices, particularly those who live on resource-poor riverbanks. As disasters become more frequent, evacuation, challenges, and migration become more common, posing significant physiological, psychological, social, and economic consequences. Extreme hydrological extremes are one of the consequences of climate change. As a result, hotspots and vulnerable sites emerge, demanding challenging adaptation.

Keywords Climate Change impact · River system · Resilience · Adaptation · Mitigation

27.1 Introduction

Climate change is already inflicting disruption in the world with simply 1.1 °C (2 °F) of warming (Legg 2021). Half the world' population currently experiences water insufficiency for a minimum of 1 month every year. Currently, over three billion individuals live in nations that are extraordinarily sensitive to climate change, with international hotspots centred on small Island Developing States, the Arctic, South Asia, Central and South America, and far of Sub-Saharan Africa. Climate change, as

F. Amin · A. K. Gupta (✉)
National Institute of Disaster Management, New Delhi, India

M. Pandey et al. (eds.), *River Dynamics and Flood Hazards*, Disaster Resilience and Green Growth, https://doi.org/10.1007/978-981-19-7100-6_27

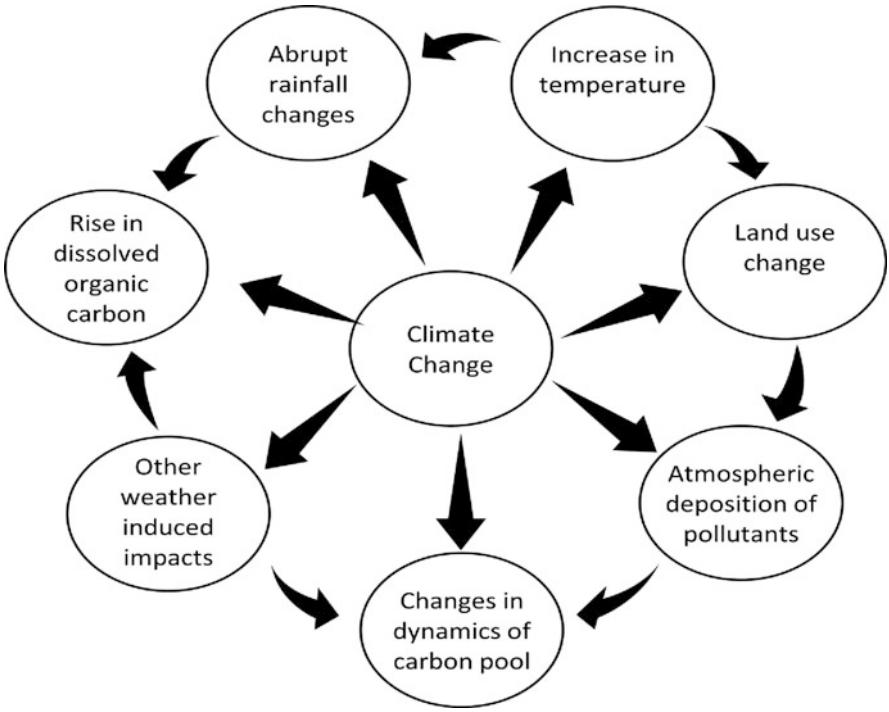

Fig. 27.1 Impact of climate change

per the IPCC, will push 32–132 million humans into severe poverty with inside the subsequent couple of years. More effect may be on food safety due to climate change, so one can additionally boom the incidence of deaths due to heat, cardiovascular disease, and mental health difficulties. Many glaciers at some point of the globe will either melt or lose maximum in their bulk if global temperatures rise simply 1.5 °C, and an about 350 million humankinds will face water scarcity by the end of 2030 (Levin et al. 2022).

The impact of climate change on river systems as a paradigm of hunger or distress, temperature increase is impacting the hydrological cycle and leading climate variability to shift (Fig. 27.1). Rainfall has been extremely excessive or severely scarce in various locations; compared to long-term trends. Severe droughts, floods, and waterborne diseases will be the first and worst effects of climate change on river systems and river communities. River monitoring and rehabilitation must be part of the change, along with reducing climate change impact. Major changes in the planning, structure, and utilization of water resources have increased throughout the world over the last 30 years (Teegavarapu et al. 2020). Rivers have been key resources in the world since the beginning of human history, which explains why they have taken on such a prominent role in economic and social development (Downs and Gregory 2014). Climate change can induce allogenic channel adjustment, but it is hard to predict which climate changes will be considerable over short,

historic, or paleohydrologic periods. The most significant climate changes were assumed to be related with glaciations at first, but it has lately been recognized that other aspects of climate change throughout the Holocene post-glacial period were also relevant (Gregory and Benito 2003).

27.2 Assessment of Changes and Trends in River System Under Climate Change

The science is clear and concise: climate change jeopardizes people's and the planet's well-being. Delaying action risks causing climate change repercussions that are so severe that our entire world would be unrecognizable. The upcoming years provide a limited window for attaining a stable and successful, secure future for all. Changing course will involve immediate, optimistic, and synchronized initiatives to minimize disbursements, build strength, safeguard environments, and significantly boost back for adaptation and gravitating to misfortune and damage. Climate change is now accepted as a genuine, pressing, and globally connected issue, and logical evidence for global climate change is considered permanent (Allison et al. 2009) (Fig. 27.2).

A river channel, its river basin, and floodplain shape a river course formed by nature over millions of years of development. Water is a vital asset and plays an important role in human civilization that is primarily influenced by climate change. The impact of climate change on river systems is possible because dripping climate conditions promote surface dryness and put additional stress on rivers to meet water demand. Precipitation is also expected to change as a result of temperature variations

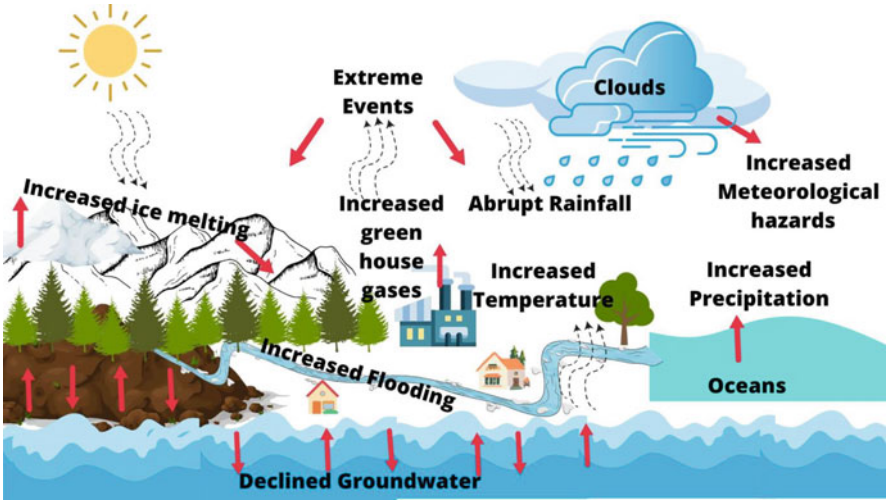

Fig. 27.2 Impact of Climate change on River System

(Shrestha et al. 2017). Hydro-morphological modifications have been made in numerous swamp river systems to improve stream utilization, including channel rectifying, embankment development, dam control, groyne development, and stream detachment from its floodplain. In a roundabout way, these changes have a significant impact on stream and dregs regimes. The response of water course structure to engineering and stream direction of alluvial flows has been evaluated in a variety of ways, demonstrating significant large-scale morphological changes (Hiemstra et al. 2022). These patterns have an impact on river capacity by influencing both outflow conditions and the stability of infrastructure. Extreme weather conditions caused by climate change result in larger elements in marsh river streams, changes in stream and silt control initiated by climate change and river pattern triggers longitudinal (long channel cut) and horizontal morphological changes as the river looks for progressive stability contingency (Arbos et al. 2020).

The strengthening of river monitoring systems and climate forecasting systems is critical for far better preparedness and rapid response activity. Regular monitoring of river flows is essential to identify climate change-induced changes in flow of river system (Palmer et al. 2009). Furthermore, efforts should be made to manage adjacent land zones, and anthropogenic activities should be mitigated. In order to reduce the contamination stack within the river, infrastructure development and mechanical agglomeration along the river should be mitigated. For years human kind has ruthlessly tampered with river systems. Floodplains have been encroached upon, suffocating their flow with tragic results. Catchments have been destroyed, and forests have been cut down. Over-extraction has had an impact on their stream, and a few perennial rivers have now become regular. A few have indeed disappeared completely. Dams and floods have had an impact on river ecology and the environment of river species, resulting in disasters and relocation. Sand mining has altered river beds, causing a river's course to change and surges to occur. Water quality has been impacted by contamination from residential, sewer, and industrial sources and water bodies have become receptacles for human-created waste (Grillakis et al. 2011).

27.3 Develop Structural and Non-structural Measures for Disaster Mitigation Under Climate Change Scenarios

According to the Intergovernmental Panel on Climate Change. Climate change dominances the change in temperature and precipitation around the living world, due to these changes the water flow will increase stress on the water supply in some areas and will reduce pressure in others (Sivakumar 2011). To maintain optimal efficiency, hydropower operators need to adapt changes in the areas where more runoff is expected, structural and non-structural (or a combination of the two)

Table 27.1 Structural and Non-structural Mitigation Strategies

STRUCTURAL AND NON STRUCTURAL MITIGATION STRATEGIES

Structural Measures	Non- Structural Measures
❖Construction of Dams for risk reduction.	❖Advanced Hydro-dynamic techniques for Early warning system.
❖Construction of Embankments and earth berms for reduction of vulnerability.	❖Disaster Management plans and policies for mitigation strategies.
❖Widening and deepening of river bed, tributaries and natural drains.	❖Improved land-use planning and soil bioengineering.
❖River corridor rehabilitation and restoration	❖Relocation of buildings from the hazard prone area according to the extreme value analysis.

Fig. 27.3 Shipra River, Padli Village, Nainital District, Uttarakhand (PC: Dr. Manish Pandey)

measures need to be implemented to maximize control yields while degrading other constraints (Table 27.1).

There has been arise of climate change impact studies on hydrology substantially over the past decade (Minville et al. 2010). This increased understanding of future hydrological conditions and vulnerability has lately prompted studies focusing on the stewardship of water resources in climate changes (Barnett et al. 2005). Increased variability in time in thawing caused an increase in futile spills (Fig. 27.3). On the grounds that operation rules were optimized to presume long-term climate, ineffective spills can be reduced through structural measures. It is frequently necessary to

adjust the existing infrastructure, either through upgrading/redevelopment or by making strides in operation (Nohara et al. 2006).

Non-structural measures are crucial in addition to improving and optimizing the effectiveness of existing infrastructures. Nearly 60,000 dams have been built around the world, with another 3700 currently under construction or planned. River health has deteriorated as the number of interventions in the name of development has increased. Some streams and rivers have even vanished as a result of this decline, which has resulted in an increase in chronic diseases. As species become extinct and the food chain is disrupted, the threat of new diseases and even pandemics looms large. While rivers provide good adaptation measures, they are also under threat from shifts to hydropower as a source of renewable energy.

27.4 Discussion

27.4.1 Adaptive and Coping Capacities for Risk Prevention

According to the United Nations Framework Convention on Climate Change (UNFCC), Adaptation refers to changes in biological, social, or financial structure in consideration of actual or anticipated climatic stimuli, as well as the consequences of those changes. Climate resilience can be broadly described as a socio-ecological framework's adaptable ability to retain stresses and continue working in the face of external stresses caused by climate change. Climate resilience and adaptation are currently extremely crucial, and the role of rivers in this must be understood.

The concussion of a disaster is determined further more by the magnitude of the risk, but also by a variety of socioeconomic and natural factors (Bahadur et al. 2013). Disaster resilience assessment using a record and component indicators are commonly a critical component of natural risk management. The resilience approach to dealing with natural disasters has grown in popularity recently, and it contends that individuals have the institution to plan, adjust, and change in the presence of social cohesion, community association, and trust. Adaptive competence integrates preventative techniques, such as making decisions to keep a strategic distance from an event, and impact-minimization methodologies, which encourage and promote recovery (Jabeen et al. 2010).

Risk assessment at the unrestricted level presents distinctive objections related to a data deficiency, as well as a profoundly impenetrable and competent exchange among communities' capacities and the challenges they face. To proclaim risk evaluation, it is intriguing that risk assessments be conducted locally, resulting in increased awareness and a sense of local participation of the process and the alternatives that will be used to address the risks. In order to integrate climate change, a balance must be struck between the necessity for a modern assessment that includes prime scientific consultation and thorough analysis of participatory conclusion and the exigency to keep the method basic, participatory, and effective. Hazard assessments are thus expected to be planned, predicting experimental

measurements conceivable risk events that will occur in the future. To improve disaster risk management and climate change adaptation, risk identification and vulnerability assessment can be attempted at various stages, namely before, during, and after disasters occur (Ylla Arbós et al. 2021).

Climate change scenarios and disaster risk reduction strategies necessitate open high technological initiative, and acknowledgement. According to disaster loss data analysis, frequent low-obscurity underline an assemblage of hazards, that is recognized when an extraordinary risk event occurs. Comparable hazard accretion may occur at substantial proportion in volatile regions, specifically within the context of conflict and forced migration. Nations and their peoples must now strengthen their adaptation capacities and build resilience to the unusual challenges posed by climate change. Recognizing appropriate risk management techniques requires a context-based considering of these risks. This would include a much better collection of sub-national disaster data that allows perception of sophisticated designs of local risk, as well as locally owned forms of risk identification and reduction. Climate change adaptation and resilience, on the other hand, must be taken seriously. Another example is climate finance, which focuses on this. Rich countries promised to provide USD 100 billion per year beginning in 2020 to assist poorer countries in handling climate change through relief including adaptation efforts in the Paris Agreement on Climate Change.

27.4.2 Policy Development and Implementation at National, Regional and Global Levels

Climate change due to unpredictable changes within the worldwide environment might not be subject to the well-known 'stationarity' (Kundzewicz et al. 2007). The main challenge is with the existing organization and administrative system, particularly with the implementation of policy perspectives, rather than with hydrologic vulnerability. As a result, policymakers face the challenge of understanding these climate change impacts and developing and implementing policies and measures to ensure an optimal level of adaptation. Adaptation can include both national and regional plans, as well as practical steps that can be implemented at both the bottom-up and top-down levels of an organization.

A total of 170 countries include adaptation policies for climate change as for now, but many are still or in phase of planning and implementation of the policies. Assuming the hypothetical impacts of prevailing and projected climate conditions on hydrological forms is gaining more impetus in the present day since of the social and political implications of river systems. Modern instructional and administration models should be implemented with collaboration and coordination at various levels of administration, as well as recognition and consideration in policy formulation and implementation. Controls should also include a hydraulic and hydrologic plan for sustainable water and land use in order to reduce water-related risks.

27.5 Climate Change and Adaptive Mitigation Strategies

Adapting to climate change is frequently a challenge in decision-making processes; climate change decision-making methodology should be vigorous and adaptive considering the viability of climate change: non-stationarity and large uncertainty. One common strategy for adaptation is to heighten the adaptability of how metrological conditions are managed. Climate change, as well as mitigation and adaptation strategies include critical levels as well as various types of vulnerabilities and risks.

Climate change risks must be pushed to be regarded methodically in all levels of improvement planning progressive incorporate adaptation initiative. There is dire demand of collaboration with Ministries of Planning and Finance to involve incorporating climate change aspects into National Development Plans, integrating Poverty Reduction Strategies (PRSs), joint assistance strategies, and related programmes and projects justified to improve climatic resilience. Including practical climate change adaptation measures will significantly improve the benefits and sustainability of a wide range of development activities (Wallwork et al. 2022).

The national level is critical for integrating climate change adaptation. At this level, critical decisions are made that build an empowering environment for different sectors of societies. Needs at the national level study of climate change susceptibleness are incorporated into stable visions, decline in poverty, and sustainable progressive techniques. At the sectoral level, raise awareness of the effects of climate change on specific sites of work among both organizers and their partners within giver organizations. Embrace additionally in capacity enhancement and the direction of capability that can assist project managers and decision introducers to transcendent deduce the contents of climate change on counterstrategy and to be far better prepared to integrate adaptation considerations into their decision systems.

As a result, decisions to integrate adaptation should not keep unsettled due to the availability of fundamentally advanced climate information. There is need for resembling attempt to require conclusion to the extent that people are justified, and also making the necessary investments in improved data for future planning and implementation.

27.6 Conclusion and Way Forward

New research indicates that integrating developed approaches like inundations with nature-based solutions could dramatically reduce vulnerabilities associated with water and the shoreline, especially in urban areas. Analysing the better specialized technologies, such as resilient crop varieties, advanced livestock breeding or solar and wind power that help to strengthen resilience. In any case, a few of these climate adaptation reactions can be harmful if poorly planned or executed. Expanding water system frameworks can help to address short-term climate risks, but it can also deplete rare groundwater reserves.

There are two types of rise to significance and diverse orientation measures to deal with the impact of climate change on river systems. Mitigation strategies aim to reduce greenhouse gas emissions, whereas adaptation strategies aim to reduce vulnerability to climate change. Mitigation thus addresses the causes of climate change, whereas adaptation addresses its consequences. Towards this end, adaptation is regarded as the most appropriate approach, i.e. activities and measures for anticipating the unexpected and unfavourable effects of climate change. As a result, adaptation encourages measures and actions that avoid or mitigate the damage caused by climate change. Adaptation measures and activities should be integrated into a broader development context rather than being treated as separate viable measures. Adoption of adaptation measures should be supported by sound water governance, astute innovation, and adaptable institutions, followed by improved data collection on climate and newly emerging risks.

As illustrated in this chapter the large-scale morphological patterns and climate change has suggestions on numerous capacities, putting weight on the multi-functionality of a marsh river system. As a result, coordinated river management is essential, with quantitative data emphasizing the importance in evaluating various policy alternatives. Nature-based solutions are a promising and difficult approach to river management that necessitates an integrated assessment of legal, social, climatic, and hydrological factors.

Rivers can fundamentally help in adaptation and resilience development. Rivers, on the other hand, are rarely accorded the attention they deserve. Rivers and floodplains have the ability to act as climate change sponges, holding extra water and pushing it into groundwater 'banks', as well as advertising water during drought seasons. When rivers are allowed to flow continuously, water is available all year. Rivers transport silt to the sea. Healthy habitats, of which rivers are an important part, help to enhance climate resilience. A river is more than just water. Understanding a river and establishing a connection with it will lead to proper action.

References

Allison EH, Perry AL, Badjeck MC, Neil Adger W, Brown K, Conway D et al (2009) Vulnerability of national economies to the impacts of climate change on fisheries. Fish Fish 10(2):173–196

Arbos CY, Blom A, Goldaracena FA, Van Vuren S, Schielen RMJ (2020) Bed level change in the upper Rhine Delta and Niederrhein. In: River Flow 2020: The 10th Conference on Fluvial Hydraulics. CRC Press/Balkema-Taylor & Francis Group, Boca Raton, Florida, pp 680–684

Bahadur AV, Ibrahim M, Tanner T (2013) Characterising resilience: unpacking the concept for tackling climate change and development. Clim Dev 5(1):55–65

Barnett TP, Adam JC, Lettenmaier DP (2005) Potential impacts of a warming climate on water availability in snow-dominated regions. Nature 438(7066):303–309

Downs P, Gregory K (2014) River channel management: towards sustainable catchment hydrosystems. Routledge, London

Grillakis MG, Koutroulis AG, Tsanis IK (2011) Climate change impact on the hydrology of Spencer Creek watershed in southern Ontario, Canada. J Hydrol 409(1–2):1–19

Gregory KJ, Benito G (2003) Potential of palaeohydrology in relation to global change. In: Gregory KJ, Benito G (eds) Palaeohydrology: Understanding global change. Wiley, Chichester, pp 3–15
Hiemstra KS, Van Vuren S, Vinke FSR, Jorissen RE, Kok M (2022) Assessment of the functional performance of lowland river systems subjected to climate change and large-scale morphological trends. Int J River Basin Manag 20(1):45–56
Jabeen H, Johnson C, Allen A (2010) Built-in resilience: learning from grassroots coping strategies for climate variability. Environ Urban 22(2):415–431
Kundzewicz ZW, Mata LJ, Arnell NW, Doll P, Kabat P, Jimenez B, Miller K, Oki T, Zekai S, Shiklomanov I (2007) Freshwater resources and their management:173–210
Legg S (2021) IPCC, 2021: Climate Change 2021-the Physical Science basis. Interaction 49(4): 44–45
Levin K, Boehm S, Carter R (2022) 6 Big Findings from the IPCC 2022 Report on Climate Impacts, Adaptation and Vulnerability
Minville M, Krau S, Brissette F, Leconte R (2010) Behaviour and performance of a water resource system in Québec (Canada) under adapted operating policies in a climate change context. Water Resour Manag 24(7):1333–1352
Nohara D, Kitoh A, Hosaka M, Oki T (2006) Impact of climate change on river discharge projected by multimodel ensemble. J Hydrometeorol 7(5):1076–1089
Palmer MA, Lettenmaier DP, Poff NL, Postel SL, Richter B, Warner R (2009) Climate change and river ecosystems: protection and adaptation options. Environ Manag 44(6):1053–1068
Sivakumar B (2011) Global climate change and its impacts on water resources planning and management: assessment and challenges. Stoch Env Res Risk A 25(4):583–600
Shrestha NK, Du X, Wang J (2017) Assessing climate change impacts on fresh water resources of the Athabasca River basin, Canada. Sci Total Environ 601:425–440
Teegavarapu RS, Kolokytha E, de Oliveira Galvão C (2020) Climate change-sensitive water resources management. CRC Press, Boca Raton, Florida
Wallwork JT, Pu JH, Kundu S, Hanmaiahgari PR, Pandey M, Satyanaga A, Khan MA, Wood A (2022) Review of suspended sediment transport mathematical modelling studies. Fluids 7(1):23
Ylla Arbós C, Blom A, Viparelli E, Reneerkens M, Frings RM, Schielen RMJ (2021) River response to anthropogenic modification: channel steepening and gravel front fading in an incising river. Geophys Res Lett 48(4):e2020GL091338

Chapter 28
Non-parametric Approaches to Identify Rainfall Pattern in Semi-Arid Regions: Ranipet, Vellore, and Tirupathur Districts, Tamil Nadu, India

Venkatesh S., T. Kirubakaran, R. Mohammed Ayaz, S. Mohamed Umar, and S. Parimalarenganayaki

Abstract Rainfall is a complex natural occurrence with a wide range of patterns and intensities that can cause flooding and drought and it is critical to track these variances. In this research, the annual wetness, dryness, long-term seasonal rainfall pattern, and intensity were determined using rainfall data from 17 observed gridded rain gauge locations in Ranipet, Vellore, and Tirupathur for a 35-year period (1986–2020). The Rainfall Anomaly Index (RAI) results revealed that all three districts experienced meteorological drought from 2001 to 2004. The outcomes of the non-parametric tests Mann-Kendall (MK), modified Mann-Kendall (mMK), and Sen's slope estimator revealed that the station 3 in Vellore has a 95% confidence level, and the station 4 in Ranipet district has a 90% confidence level with the raising pattern of rainfall. The remaining stations in the study area involve a combination of rising and falling patterns. In the research region, the intensity of the rainfall pattern varies from −3.61 to 4.58 mm/month. The outcomes of this research will be extremely useful for government agencies and policy makers for rainwater conservation planning.

Keywords Rainfall pattern · Rainfall Anomaly Index (RAI) · Mann-Kendall (MK) · Modified Mann-Kendall (mMK) · Sen's slope estimator

28.1 Introduction

Understanding the distribution of rainfall with respect to time and space is important, as climatic change erratically modifies the rainfall pattern. Extreme rainfall events cause floods and low rainfall causes drought. The hazards associated with flood and drought includes loss of livelihood such as damage to residential and agricultural land, loss of livestock, and psychological imbalance (Wallwork et al. 2022; Pandey

Venkatesh S. · T. Kirubakaran · R. M. Ayaz · S. M. Umar · S. Parimalarenganayaki (✉)
School of Civil Engineering, Vellore Institute of Technology, Vellore, Tamil Nadu, India

M. Pandey et al. (eds.), *River Dynamics and Flood Hazards*, Disaster Resilience and Green Growth, https://doi.org/10.1007/978-981-19-7100-6_28

et al. 2021; John et al. 2021a, b). Therefore, it is important to understand the distribution of rainfall with respect to time and space (Pu et al. 2021). According to Rahman et al. (2017), of all the meteorological variables, rainfall is the highly influencing factor on agricultural planning, flood vulnerability assessment, hydrological processes, water managements, global climate change, and other environmental evaluations. The study on rainfall pattern is very essential in the arid or semi-arid region as it is very inconsistent, insufficient, and unpredictable (Pal et al. 2000). Water management of such regions will be successful, only with the scientific knowledge on the past rainfall pattern (Belay et al. 2021; Costa and Rodrigues 2017; Das et al. 2021; Jayanta et al. 2020; Gemeda et al. 2021; Hamed and Ramachandra Rao 1998; Park and Singh 1996). Rainfall pattern can be studied by pie and bar chart analysis (Pavithra et al. 2021), histogram analysis (John 2018), surfer (Basnet and Poudel 2021), and innovative graphical analysis (Rathnayake 2019). All the analysis mentioned above only gave us the basic results whether the rainfall is increased or decreased. Whereas, the scientific analysis requires confidence level or significant level of rainfall pattern, intensity of rainfall and correlation effects in temporal series data. Non-parametric tests are commonly used for the above mentioned analysis (Pandey and MdAzamathulla 2021; Cruz et al. 2013; Das and Bhattacharya 2018; Yue et al. 2002a). The Mann-Kendall (MK), Auto Correlation Function (ACF), modified Mann-Kendall (mMK), and Sen's Slope (SS) analyzer are non-parametric tests that are particularly useful in identifying the linear pattern and intensity in long-term hydrological temporal series data (Yue et al. 2002b; Gemeda et al. 2021; Praveen et al. 2020). MK and mMK test were used to find the rainfall pattern, ACF is used to fine the auto correlation. SS analyzer is applied to find the intensity of the rainfall pattern (Shankar et al. 2021; Caloiero et al. 2020; Khaniya et al. 2019; Mondal et al. 2012; Pandit 2016; Saini et al. 2020). The Rainfall Anomaly Index is utilized to calculate the frequency and intensity of dry and wet years (Hansel et al. 2016; Keyantash and Dracup 2002).

In this research, an attempt was made to examine the quantity of dry and wet years, pattern of rainfall, intensity of the pattern in three districts of semi-arid region of Tamil Nadu, namely Ranipet, Vellore, and Tirupathur from 1986 to 2020, using the Rainfall Anomaly Index (RAI), MK test, mMK test, and SS analyzer.

28.2 Materials and Methods

28.2.1 Study Area

A report on "Observed Rainfall Variability and Changes over Tamil Nadu State is prepared by the India Meteorological Department, Ministry of Earth Sciences" indicated that the average annual frequency of dry days and average maximum temperature is increasing in northern part of Tamil Nadu (Guhathakurta et al. 2020). Hence it is essential to understand the rainfall trend of the Ranipet, Vellore, and Tirupathur districts of northern Tamil Nadu, India (Fig. 28.1). Agriculture is the

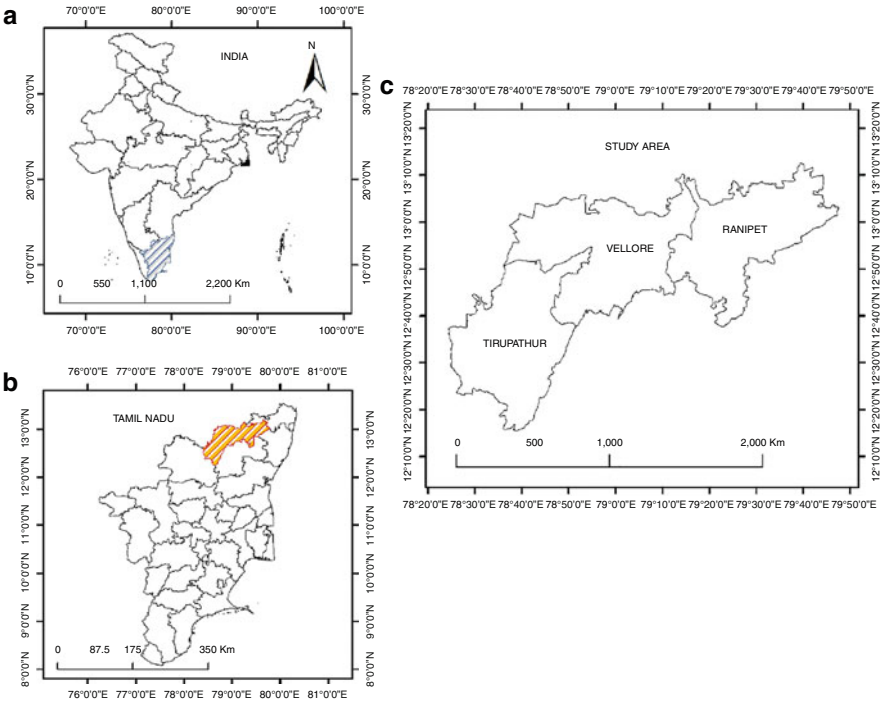

Fig. 28.1 Map showing study area of Ranipet, Vellore, and Tirupathur districts

major occupation in the research region, which majorly depends on rainfall as well as groundwater. The study area map is prepared from the Open Street Map (OSM) place search plugin using QGIS software. The geographical extent of 6155 km^2 ranges from latitude 12° 14′ 58.7436″ N to 13° 12′ 28.3068″ N and longitudes 78° 23′ 58.524″ E to 79° 47′ 33.7812″ E. The districts are divided into 16 taluks with 842 revenue villages, and the majority of the district's water needs are satisfied by groundwater (CGWB 2009). The mean temperature in the research region between 18.2 and 36.80 °C, with mean yearly rainfall of 969 mm for the last 35 years (1986–2020). The Palar and Ponnai rivers are the two primary rivers in this area. The northeastern and southern parts are influenced by hills and elevated areas, and the eastern side is covered by plains.

28.2.2 Data Collection

The daily rainfall data was gathered from the India Meteorological Department (IMD Pune) website during a 35-year period (1986–2020) using the procedure provided by Pai et al. 2021; Jayanta et al. 2020. The procedure of obtaining IMD gridded observation data includes installation of Python IMDlib in OSGeo4W shell

packed with QGIS platform and running the python code. This allows for the retrieval of daily rainfall data in excel format for the study duration.

The data was analyzed and interpreted using a variety of approaches, including RAI, MK test, mMK test, and SS analyzer.

28.2.3 Rainfall Anomaly Index

Van Rooy (1965), introduced the RAI, which is a ranking-based drought indicator that gives both positive and negative intensities of rainfall. It is also regarded as a noteworthy procedural simplicity index (similar to Standard Precipitation Index) because it simply requires precipitation data (Hansel et al. 2016; Keyantash and Dracup 2002). The RAI index is determined as follows:

$$RAI = +3\frac{R-\overline{A}}{\overline{B}-\overline{A}}$$

$$RAI = -3\frac{R-\overline{A}}{\overline{b}-\overline{A}}$$

where

R—The current rainfall (monthly, seasonal, and annually);
$\overline{A}$—The historic series mean monthly, seasonal and annual rainfall;
$\overline{B}$—10 largest monthly/seasonal/annual rainfall averaged;
$\overline{b}$—10 lowermost monthly/seasonal/annual rainfall averaged;
$A-\overline{A}$—The positive and negative anomaly based on positive or negative values.

The degree of severity for the RAI index consist of nine classes, varying from incredibly dry (RAI $\leq$ -3) to incredibly wet (RAI $\geq$ 3) (Van Rooy 1965). In this research these nine classes are reclassified into three classes, namely dry years (≤ -0.5), near normal years (-0.49 to 0.49), and wet years (≥ 0.5), to calculate number dry, wet, and near normal years.

28.2.4 Mann-Kendall Test

The MK test was performed to examine if the amount of rain in the research area had any monotonic trends (Kendall 1975; Mann 1945). The MK statistic (S) (Das et al. 2020; Das and Bhattacharya 2018) of the series x is calculated as

Table 28.1 Significance level for MK test

S. No.	Z-Value	α (level of significance)	Confidence level (SL)
1	± 1.645 to ± 1.960	10%	90% CL
2	± 1.960 to ± 2.575	5%	95% CL
3	$> \pm 2.575$	1%	99% CL

Where, if $Z > 0$: Raising pattern, and if $Z < 0$: Falling pattern

$$S = \sum_{b=1}^{a-1} \sum_{c=b+1}^{a} sign\left(m_j - m_k\right)$$

where a is the quantity of data points, sign denotes the signum work, and m_j and m_k are the data points of time b and c, respectively.

The variance of S (VAR (S)) is computed using the following formula:

$$\text{VAR}\ (S) = \frac{1}{18}\left\{a\ (a-1)(2a+5) - \sum_{r=1}^{f} v_r(v_r-1)(2v_r+5)\right\}$$

where 'f' denotes the number of tied groups (a collection of sample data with comparable values), and v_r denotes the extent of the rth ties number.

To estimate the standardized test measurement Z, the estimation of (S) and VAR (S) are utilized as follows:

$$Z = \begin{cases} \dfrac{(S-1)}{\sqrt{\text{Var}(S)}} & if\ S > 0 \\ 0 & if\ S = 0 \\ \dfrac{(S+1)}{\sqrt{\text{Var}(S)}} & if\ S < 0 \end{cases}$$

The positive and negative values of Z represent rising and falling tendencies, respectively. The confidence level of null and alternative hypothesis was used according to Pearson and Hartley's (Pearson and Hartley 1966) and Jayanta et al. 2020. Table 28.1 gives a full discussion of the confidence level of various z-value ranges.

28.2.5 Autocorrelation Function

ACF is generally described as the most challenging issues in temporal series data analysis and pattern discovery. The variance of the MK test result enhances serial dependence (autocorrelation). In addition, positive serial correlation in temporal

series analysis increases type one error and identifies a clear pattern, if there was no realistic pattern. Therefore, the lag-1 ACF coefficient (r_k) was applied to test for serial correlation in all datasets at a 0.05 level of significance for a 2-tailed (upward and downward) test (Das et al. 2020; Das and Bhattacharya 2018; Hamed and Ramachandra Rao 1998).

$$r_k = \frac{\sum_{k=1}^{N-K} \left(x_t - \overline{x_t}\right)\left(x_{t+k} - \overline{x_{t+k}}\right)}{\left[\sum_{k=1}^{n-k} \left(x_t - \overline{x_t}\right)^2 \left(x_{t+k} - \overline{x_{t+k}}\right)^2\right]^{0.5}}$$

where r_k is the ACF component of the temporal series data x_t at lag k, x is the mean of the temporal series data (x_t), N is the entire distance of the x_t temporal series, and k is the maximum lag.

28.2.6 Modified Mann-Kendall Test

The mMK test is an altered form of the MK test that is said to be more resistant to autocorrelation (Hamed and Ramachandra Rao 1998). It is suggested based on the altered variance of S given by equation

$$\mathrm{VAR}(S) = \left[\frac{a(a-1)(2a+5)}{18}\right]\left[\frac{a}{a_e^*}\right]$$

The auto correlated data is used to alter the correlation factor $\left[\frac{n}{n_e^*}\right]$.

$$\left[\frac{a}{a_e^*}\right] = 1 + \left[\frac{2}{a^3 - 3a^2 + 2a}\right] \sum_{a-1}^{f=1} (a-p)(a-p-1)(a-p-2)\rho_e(p)$$

$\rho_e(p)$ is the autocorrelation factor within observation ranks and can be calculated as

$$\rho(p) = 2\sin\left[\frac{\pi}{6}\,\rho_e(p)\right]$$

28.2.7 Sen's Slope Estimator

The real intensity of gradient in a hydro-meteorological data set was determined using Sen's slope estimator (Sen 1968). To determine the value of gradient Q, the gradients of N sets of data were determined using the following equation:

$$Q_i = \frac{b_l - b_m}{l - m}, i = 1,2,\ldots\ldots N, l > m$$

where b_l and b_m are data values at l and m, respectively, and Q_i is the median gradient.

28.3 Results and Discussion

The obtained daily rainfall data was verified for flaws or incomplete data in the temporal series, and it was concluded that less than 1% of the data was incomplete, according to the multiple imputation approach assessed by SPSS software. A broad solution to the issue of missing data is multiple imputation, by constructing multiple separate plausible imputed data sets to account for the uncertainty around the missing data (Jayanta et al. 2020). Several research studies (Poonia et al. 2016; Yadav et al. 2018) used such data because the quality of data was guaranteed by the competent body.

Using the Thiessen polygon approach, 17 rain gauge locations were found in the research region, which includes six stations from Vellore, six stations from Ranipet, and five stations from Tirupathur (Fig. 28.2). The rainfall data from these stations was used to figure out the RAI, pattern, and intensity in the research region.

The mean yearly rainfall was 969 mm for the 35-year research period (1986–2020). The year 2005 had the maximum yearly mean rainfall of 2346 mm, while the lowest mean yearly rainfall was 85 mm in 2003. When compared to the

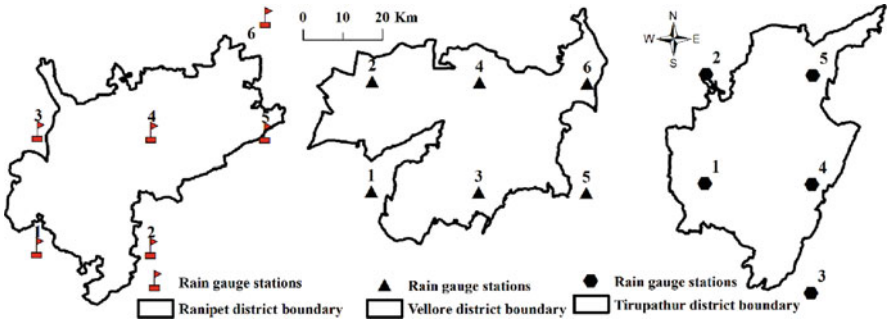

Fig. 28.2 Selected rain gauge locations in Ranipet, Vellore, and Tirupathur districts

other two districts (Vellore and Tirupathur), Ranipet had the most and least rain during the study period.

28.3.1 Analysis of Wet and Dry Years Using Rainfall Anomaly Index

In Ranipet district, a total of six rain gauge locations were used to calculate the RAI. During the research period, the annual RAI of Ranipet district showed a higher quantity of dry years than wet years (Fig. 28.3). Continuous dry years were observed during 2001–2004 (Fig. 28.4). According to the results from Fig. 28.4, the driest year in the 35-year period (1986–2020) was 2003 (station 5), with a severity index of −6.405, and the year with the highest positive value was 2015, with a RAI value of 7.493 (station 4).

In Vellore district, a total of six rain gauge locations were used to calculate the RAI. During the research period, the annual RAI of the Vellore district shows a

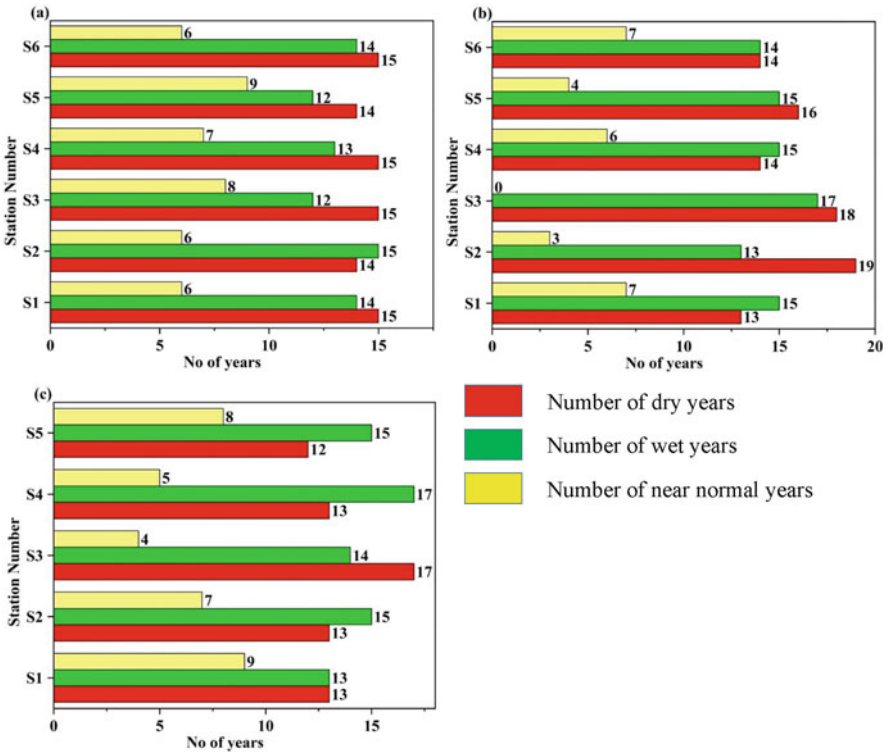

Fig. 28.3 Number of dry and wet years for all stations in three districts: (**a**) Ranipet, (**b**) Vellore, (**c**) Tirupathur

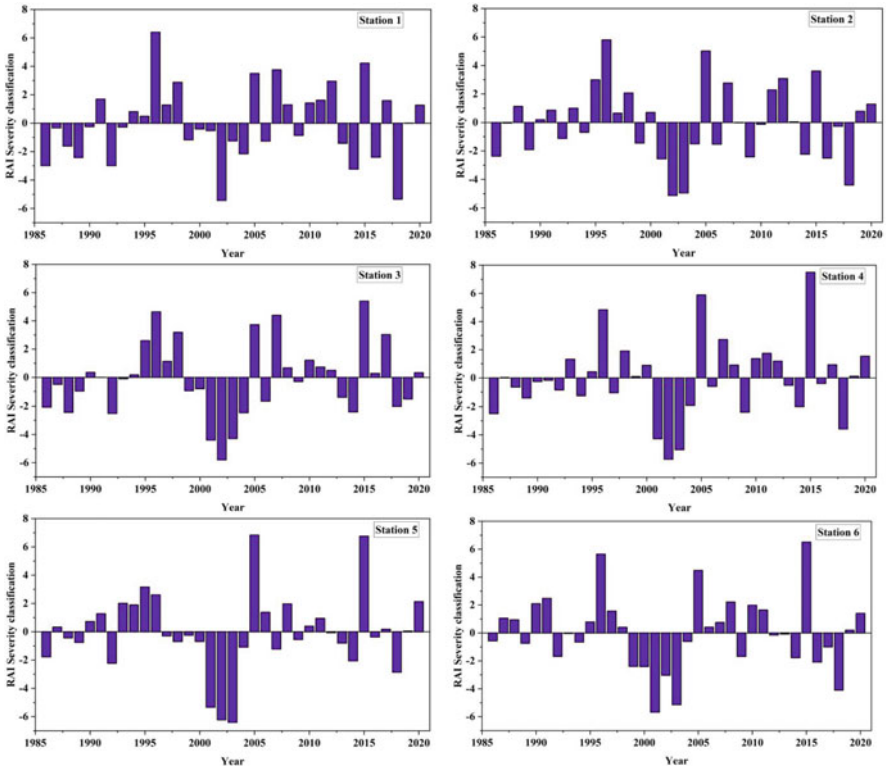

Fig. 28.4 RAI severity classification for all stations in Ranipet district

higher quantity of dry years than wet years (Fig. 28.3). Continuous dry years were observed during 2001–2004 (Fig. 28.5). According to the results from Fig. 28.5, the driest year in the 35-year period (1986–2020) was 2002 (station 4), with an index of −6.174, and the year with the highest positive value was 1996, with a RAI of 6.371 (station 5), making it an extremely wet year.

Similarly, five rain gauge locations in Tirupathur district were used to calculate the RAI. During the research period, the yearly RAI of Tirupathur district showed a higher quantity of wet years than dry years (Fig. 28.3). Continuous dry years were observed during 2001–2004 (Fig. 28.6). According to the results from Fig. 28.6, the driest year in the 35-year period (1986–2020) was 2002 (station 3), with a RAI of −6.938, and the year with the highest positive value was 1996, with a RAI of 5.448 (station 3). As a result, droughts were more severe in years with negative anomaly index values than in years with positive anomaly index values. Drought will result from a long duration of dry years (Signarbieux and Feller 2012). From 2001 to 2004, all three districts had consecutive dry years, as shown in Figs. 28.4, 28.5, 28.6. During this time period (2001–2004), there was a drought across India (Anandharuban and Elango 2021).

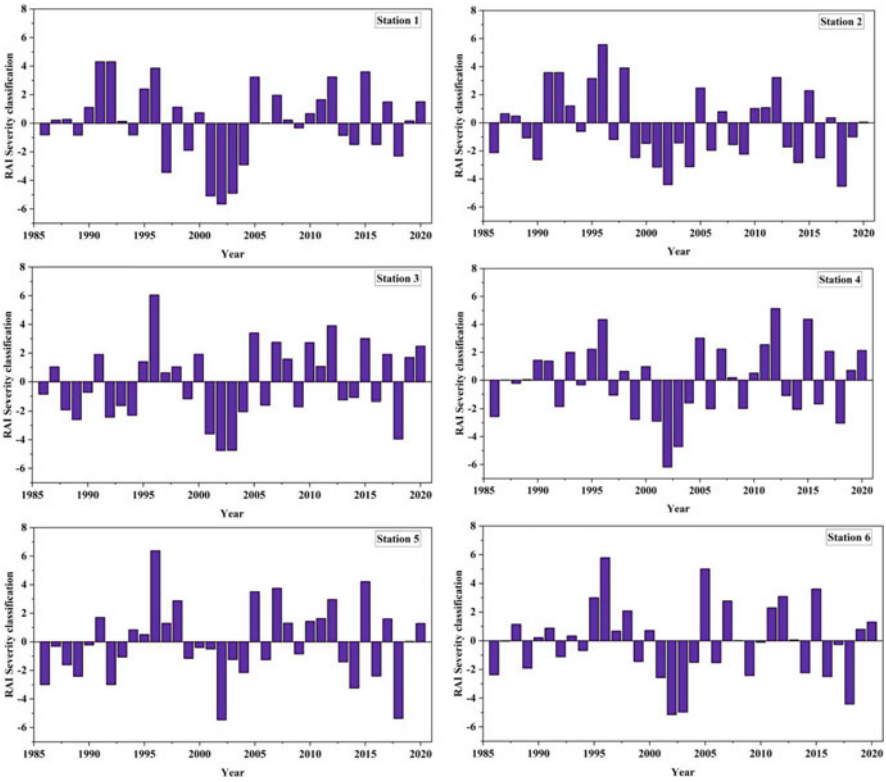

Fig. 28.5 RAI severity classification for all stations in Vellore district

28.3.2 Pattern and Intensity of Rainfall Using Non-parametric Approaches

The MK test and SS analyzer were used to analyze temporal series data for the research region from 1986 to 2020. During pattern analysis, the Hamed and Ramachandra Rao (1998) technique was utilized to deal for autocorrelation. The pattern analysis has been done for all four seasons according to Das et al. 2020. Figures 28.7, 28.8, 28.9, 28.10, 28.11, 28.12, 28.13, 28.14, 28.15, 28.16, 28.17 and 28.18 show the MK test and SS analyzer results for seasonal rainfall data for all three districts. A positive Z-value shows a raising pattern, and a negative *Z*-value shows a falling pattern, and a mixed pattern indicated a combination of positive and negative *Z*-values. As there are no repeating values in the rainfall data, there are no changes in the MK statistics calculation.

Figures 28.7, 28.8, 28.9, 28.10 show the rainfall pattern and intensity of Ranipet district for all four seasons. During winter, a mixed pattern varying from −0.27 to 0.49 with intensity varying from −0.59 to 0.83 was observed. During summer, a mixed pattern varying from −1.08 to 0.46 with intensity varying from −0.54 to 0.21

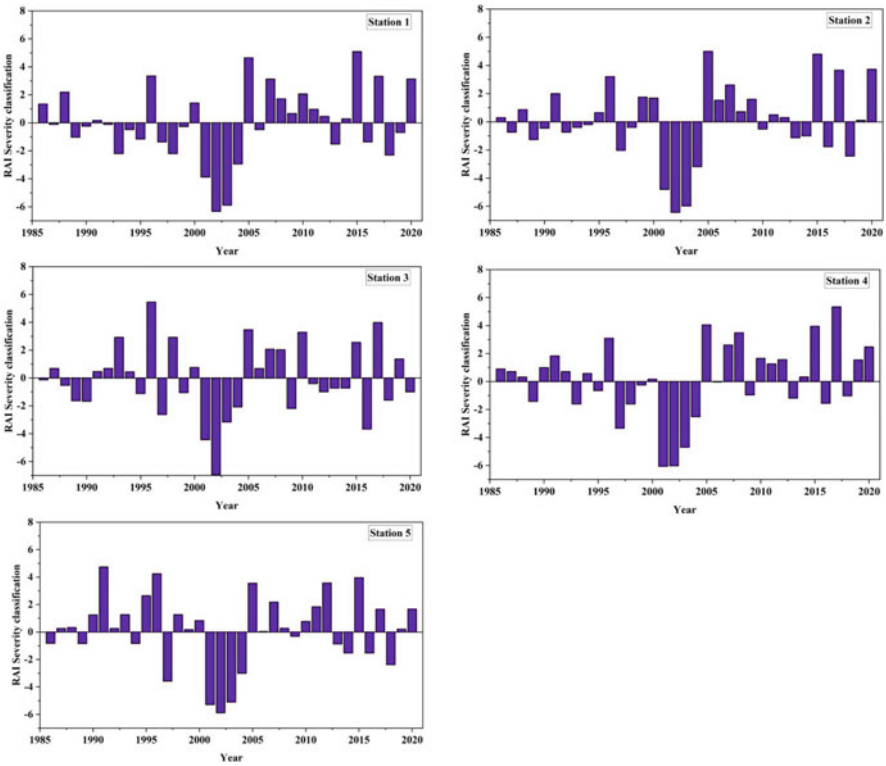

Fig. 28.6 RAI severity classification for all stations in Tirupathur district

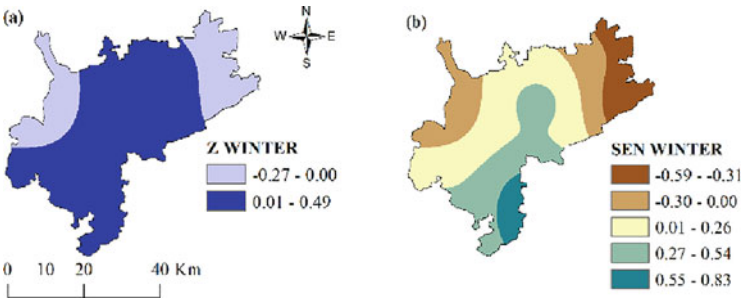

Fig. 28.7 (**a**) Rainfall trend and (**b**) Intensity maps for Ranipet in winter

was observed. During rainy season, five stations (stations 1, 2, 3, 5, and 6) showed a raising pattern varying from 0.36 to 1.64 with intensity varying from 0.99 to 4.58 and a 90% confidence level of raising pattern varying from 1.645 to 1.761 with intensity varying from 0.54 to 0.21 was observed in station 4. In the post-rainy season, a mixed pattern varying from −0.82 to 1.01 with intensity varying from −3.61 to 2.71 was observed. Figures 28.11, 28.12, 28.13, 28.14 shows the rainfall

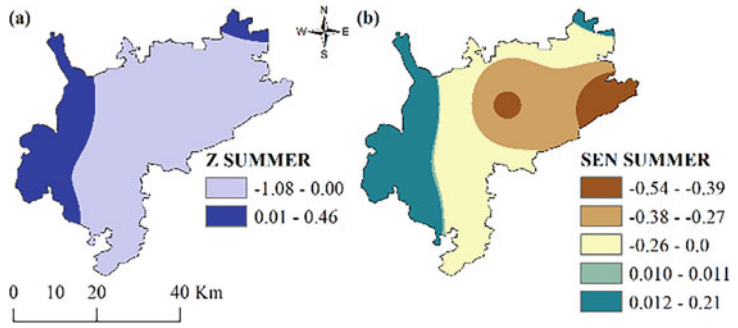

Fig. 28.8 (**a**) Rainfall trend and (**b**) Intensity maps for Ranipet in summer

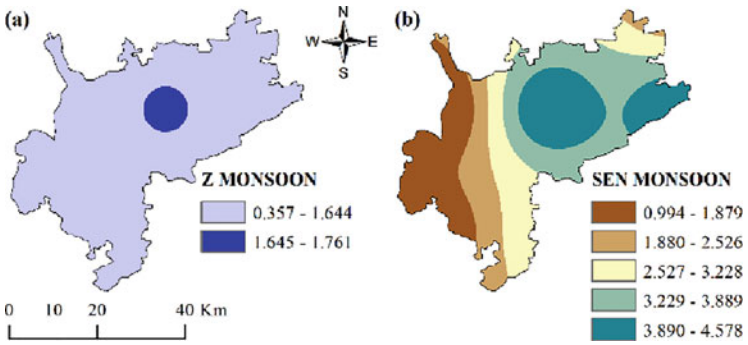

Fig. 28.9. (**a**) Rainfall trend and (**b**) Intensity maps for Ranipet in monsoon

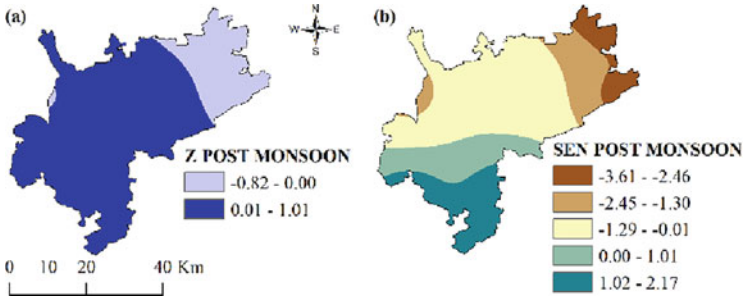

Fig. 28.10. (**a**) Rainfall trend and (**b**) Intensity maps for Ranipet in post-monsoon

pattern and intensity of Vellore district for all four seasons. During winter, a mixed pattern varying from −0.028 to 0.82 with intensity varying from −0.14 to 1.29 was observed. During summer, a raising pattern varying from 0.14 to 0.57 with intensity varying from 0.15 to 0.63 was observed. During rainy season five stations (stations 1, 2, 4, 5 and 6) shows a mixed pattern varying from −0.526 to 1.644 with intensity varying from −2.07 to 3.73, and station 3 had a 95 percent confidence level of

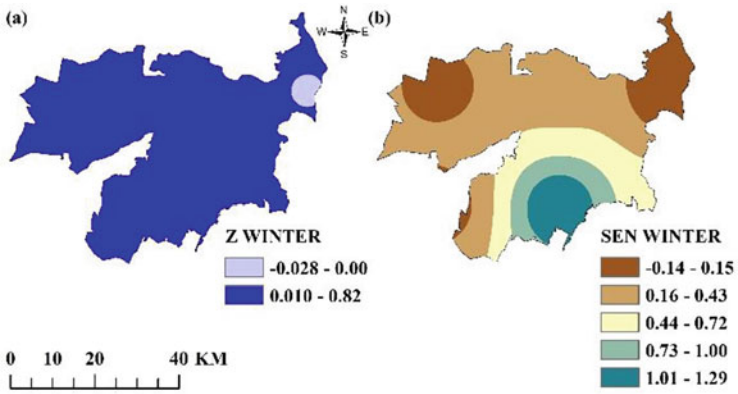

Fig. 28.11 (**a**) Rainfall trend and (**b**) Intensity maps for Vellore in winter

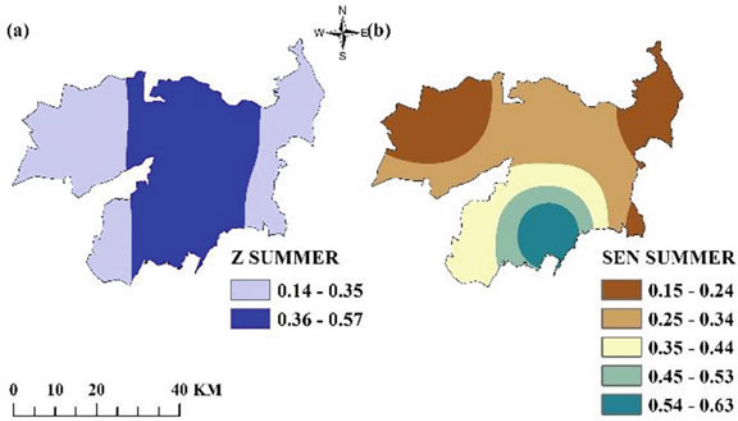

Fig. 28.12 (**a**) Rainfall trend and (**b**) Intensity maps for Vellore in summer

raising pattern varying from 1.645 to 2.114 with intensity varying from 2.58 to 3.72. In the post-rainy season, a mixed pattern varying from −0.67 to 0.79 with intensity varying from-1.63 to 1.40 was observed. Figures 28.15, 28.16, 28.17, 28.18 shows the rainfall pattern and intensity of Tirupathur district for all four seasons. During winter, a mixed pattern varying from −0.43 to 0.40 with intensity varying from −0.29 to 0.22 was observed. During the summer, a mixed pattern varying from −0.90 to 0.37 with intensity varying from −0.90 to 0.37 was observed. During the rainy season, a mixed pattern varying from −0.14 to 0.99 with intensity varying from 0.12 to 1.95 was observed. During the post-rainy season, a raising pattern was found with intensity varying from 0.12 to 1.95.

On the basis of gauged data, a pattern analysis was undertaken. The overall pattern analysis revealed that, with the exception of two stations (station 3 in Vellore and station 4 in Ranipet), all of the remaining rain gauge locations displayed

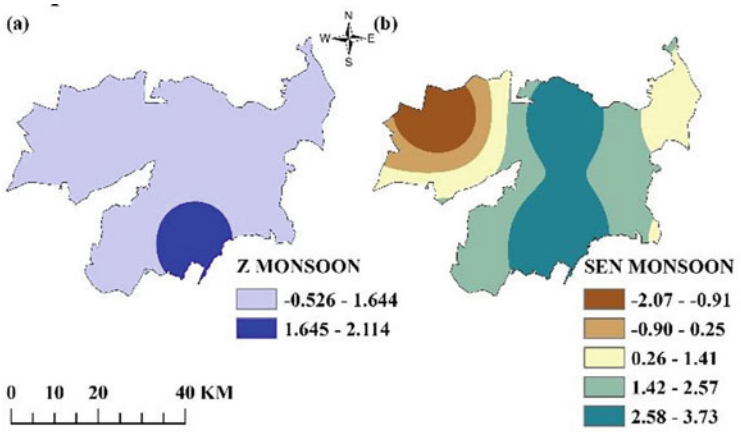

Fig. 28.13 (**a**) Rainfall trend and (**b**) Intensity maps for Vellore in monsoon

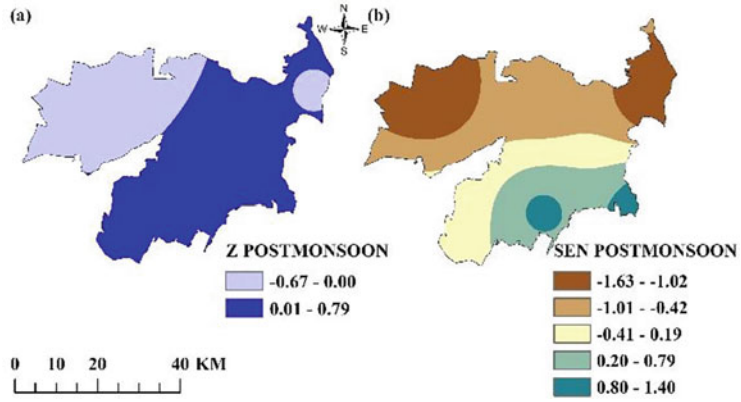

Fig. 28.14 (**a**) Rainfall trend and (**b**) Intensity maps for Vellore in post-monsoon

non-significant raising or falling pattern. Except for Tirupathur, the remaining two districts (Vellore and Ranipet) experienced a falling pattern in rainfall throughout the rainy season, which is an ominous call for those two districts.

28.4 Conclusion

Non-parametric statistical analysis was carried out to examine the quantity of dry and wet years, pattern of rainfall, intensity of the pattern in three districts of semi-arid region of Tamil Nadu, namely Ranipet, Vellore, and Tirupathur from 1986 to 2020, using the Rainfall Anomaly Index (RAI), MK test, mMK test, and SS analyzer. The

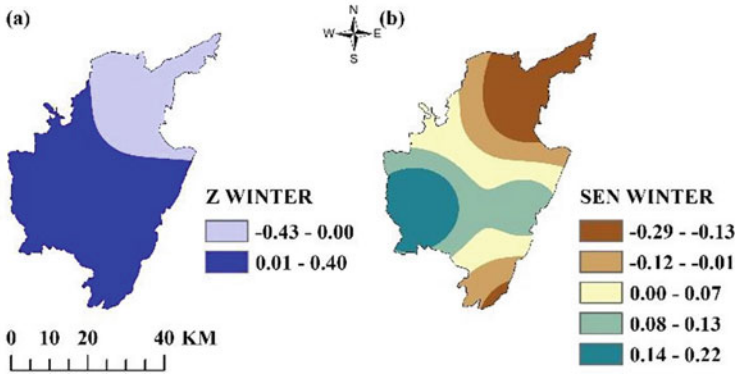

Fig. 28.15 (**a**) Rainfall trend and (**b**) Intensity maps for Tirupathur in winter

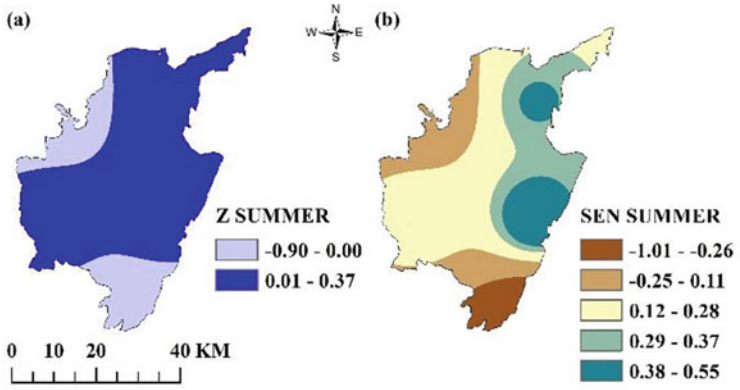

Fig. 28.16 (a) Rainfall trend and (**b**) Intensity maps for Tirupathur in summer

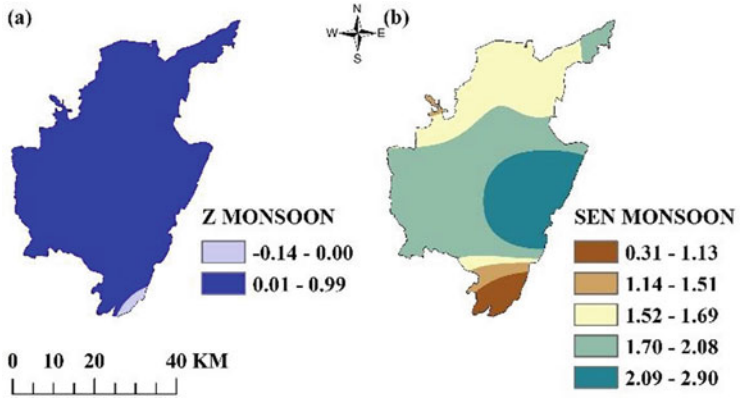

Fig. 28.17 (**a**) Rainfall trend and (**b**) Intensity maps for Tirupathur in monsoon

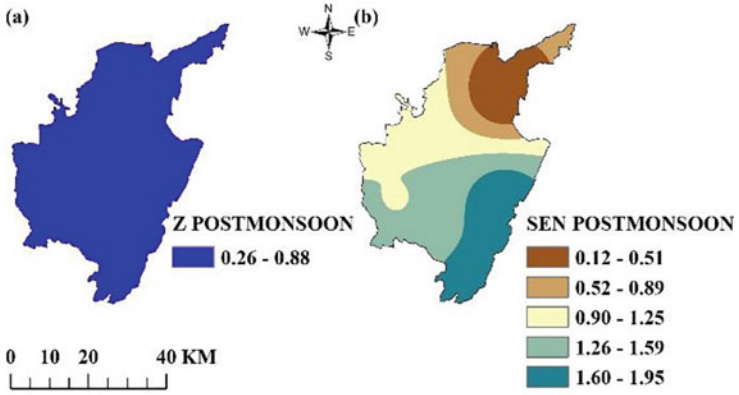

Fig. 28.18 (**a**) Rainfall trend and (**b**) Intensity maps for Tirupathur in post-monsoon

data from 17 rain gauges were used to figure out the RAI, rainfall pattern analyses, and intensity of rainfall pattern.

According to RAI findings, drought was observed in all three areas from 2001 to 2004. In Vellore and Ranipet districts, the quantity of dry years is larger than the quantity of wet years. The quantity of wet years in Tirupathur district surpasses the quantity of dry years.

The seasonal rainfall pattern in the region was studied using non-parametric approaches such as MK and mMK. The station 3 in Vellore has a 95% confidence level with the raising pattern of rainfall, and the station 4 in Ranipet district has a 90% confidence level with the raising pattern of rainfall. All remaining stations in three districts have a combination of both raising and falling patterns with a non-significant confidence level, indicating an irregular rainfall pattern in the research region. The overall intensity of the rainfall pattern in the entire research region varying from −3.61 to 4.58. Since the research region is heavily reliant on groundwater to meet its varying demands and also the rainfall pattern in the research region is irregular, it is important for the government and policymakers to take the necessary steps to effectively harvest rainfall in order to improve groundwater levels.

References

Anandharuban P, Elango L (2021) Spatio-temporal analysis of rainfall, meteorological drought and response from a water supply reservoir in the megacity of Chennai, India. J Earth Syst Sci 130(1). https://doi.org/10.1007/s12040-020-01538-2

Basnet K, Poudel K (2021) Developing a formula to estimate precipitation at ungauged location and analysis of rainfall pattern: case study for Rastra Bank chowk, Pokhara, Nepal. Himalayan J Appl Sci Eng 2(2):1–13

Belay A, Demissie T, Recha JW, Oludhe C, Osano PM, Olaka LA, Solomon D, Berhane Z (2021) Analysis of climate variability and trends in southern Ethiopia. Climate 9(6):1–17. https://doi.org/10.3390/cli9060096

Caloiero T, Filice E, Coscarelli R, Pellicone G (2020) A homogeneous dataset for rainfall trend analysis in the Calabria region (southern Italy). Water 12(9):2541

CGWB (2009) Central ground water board, district groundwater brochure Vellore district. Tamil Nadu Technical report series, pp 1–20

Costa JA, Rodrigues GP (2017) Space-time distribution of rainfall anomaly index (Rai) for the Salgado Basin, Ceará state - Brazil. Ciência e Natura 39(3):627. https://doi.org/10.5902/2179460x26080

Cruz FT, Narisma GT, Villafuerte MQ, Cheng Chua KU, Olaguera LM (2013) A climatological analysis of the southwest monsoon rainfall in the Philippines. Atmos Res 122:609–616. https://doi.org/10.1016/j.atmosres.2012.06.010

Das J, Bhattacharya SK (2018) Trend analysis of long-term climatic parameters in Dinhata of Koch Bihar district, West Bengal. Spatial Inform Res 26(3):271–280. https://doi.org/10.1007/s41324-018-0173-3

Das J, Gayen A, Saha P, Kumar S (2020) Meteorological drought analysis using standardized precipitation index over Luni River basin in Rajasthan, India. SN Appl Sci 2:1530. https://doi.org/10.1007/s42452-020-03321-w

Das J, Rahman ATMS, Mandal T, Saha P (2021) Exploring driving forces of large-scale unsustainable groundwater development for irrigation in lower Ganga River basin in India. Environ Dev Sustain 23(5):7289–7309. https://doi.org/10.1007/s10668-020-00917-5

Gemeda DO, Feyssa DH, Garedew W (2021) Meteorological data trend analysis and local community perception towards climate change: a case study of Jimma City, southwestern Ethiopia. Environ Dev Sustain 23(4):5885–5903. https://doi.org/10.1007/s10668-020-00851-6

Guhathakurta P, Krishnan U, Menon P, Prasad AK, sable S T & Advani, S. C. (2020) Observed rainfall variability and changes over Tamil Nadu state, India. Meteorological Department, Pune, India

Hamed KH, Ramachandra Rao A (1998) A modified Mann-Kendall trend test for autocorrelated data. J Hydrol 204(1–4):182–196. https://doi.org/10.1016/S0022-1694(97)00125-X

Hansel S, Schucknecht A, Matschullat J (2016) The modified rainfall anomaly index (mRAI)—is this an alternative to the standardised precipitation index (SPI) in evaluating future extreme precipitation characteristics? Theor Appl Climatol 123(3):827–844

Jayanta D, Mandal T, Saha PIU, Bhattacharya SK (2020) Variability and trends of rainfall using non-parametric approaches: A case study of semi-arid area. Mausam 71(1):33–44. https://doi.org/10.54302/mausam.v71i1.4

John SK (2018) Rainfall pattern analysis over India in relation to the state of Kerala. In: Engineering and Mathematical Topics in Rainfall. IntechOpen, London

John CK, Pu JH, Pandey M, Hanmaiahgari PR (2021a) Sediment deposition within rainwater: case study comparison of four different sites in Ikorodu, Nigeria. Fluids 6(3):124

John CK, Pu JH, Pandey M, Moruzzi R (2021b) Impacts of sedimentation on rainwater quality: case study at Ikorodu of Lagos, Nigeria. Water Supply 21(7):3356–3369

Kendall MG (1975) Rank correlation methods. Charles Griffin. Oxford Univ. Press, London, UK, p 202

Keyantash J, Dracup JA (2002) The quantification of drought: an evaluation of drought indices. Bull Am Meteorol Soc 83(8):1167–1180

Khaniya B, Jayanayaka I, Jayasanka P, Rathnayake U (2019) Rainfall trend analysis in Uma Oya basin, Sri Lanka, and future water scarcity problems in perspective of climate variability. Adv Meteorol 2019:1–10

Mann HB (1945) Nonparametric tests against trend. Econometrica 13:245–259

Mondal A, Kundu S, Mukhopadhyay A (2012) Rainfall trend analysis by Mann-Kendall test: A case study of north-eastern part of Cuttack district, Orissa. Int J Geol Earth Sci 2(1):70–78

Pai D, Rajeevan M, Sreejith O, Mukhopadhyay B, Satbha N (2021) Development of a new high spatial resolution (0.25° × 0.25°) long period (1901–2010) daily gridded rainfall data set over India and its comparison with existing data sets over the region. Mausam 65(1):1–18. https://doi.org/10.54302/mausam.v65i1.851

Pal JS, Small EE, Eltahir EAB (2000) Simulation of regional-scale water and energy budgets: representation of subgrid cloud and precipitation processes within RegCM. J Geophys Res Atmos 105(D24):29579–29594

Pandit DV (2016) Seasonal rainfall trend analysis. Int J Eng Res Appl 6(7):69–73

Pandey M, MdAzamathulla H (2021) Discussion of "gene-expression programming, evolutionary polynomial regression, and model tree to evaluate local scour depth at culvert outlets" by Mohammad Najafzadeh and Ali Reza Kargar. J Pipeline Syst Eng Pract 12(2):07021001

Pandey M, Jamei M, Karbasi M, Ahmadianfar I, Chu X (2021) Prediction of maximum scour depth near spur dikes in uniform bed sediment using stacked generalization ensemble tree-based frameworks. J Irrig Drain Eng 147(11):04021050

Park JI, Singh VP (1996) Temporal and spatial characteristics of rainfall in the Nam River dam basin of Korea. Hydrol Process 10(9):1155–1171. https://doi.org/10.1002/(SICI)1099-1085(199609)10:9<1155::AID-HYP367>3.0.CO;2-U

Pavithra CJ, Balakrishna HB, Shivakumar Naiklal HS (2021) Rainfall pattern analysis in the three Major Valley Systems of Bengaluru. Appl Ecol Environ Res 9(7):687–694

Pearson ES, Hartley HO (1966) Biometrika tables for statisticians, vol 1, 3rd edn. Cambridge University Press, London

Poonia S, Rao AS, Singh DV (2016) Rainfall characteristics and meteorological drought in Hanumangarh district of arid Rajasthan. Mausam 67(2):505–512

Praveen B, Talukdar S, Shahfahad, Mahato S, Mondal J, Sharma P, Islam ARMT, Rahman A (2020) Analyzing trend and forecasting of rainfall changes in India using non-parametrical and machine learning approaches. Sci Rep 10(1):1–21. https://doi.org/10.1038/s41598-020-67228-7

Pu JH, Wallwork JT, Khan M, Pandey M, Pourshahbaz H, Satyanaga A, Hanmaiahgari PR, Gough T (2021) Flood suspended sediment transport: combined modelling from dilute to hyper-concentrated flow. Water 13(3):379

Rahman MA, Yunsheng L, Sultana N (2017) Analysis and prediction of rainfall trends over Bangladesh using Mann–Kendall, Spearman's rho tests and ARIMA model. Meteorog Atmos Phys 129(4):409–424. https://doi.org/10.1007/s00703-016-0479-4

Rathnayake U (2019) Comparison of statistical methods to graphical methods in rainfall trend analysis: case studies from tropical catchments. Adv Meteorol 2019

Saini A, Sahu N, Kumar P, Nayak S, Duan W, Avtar R, Behera S (2020) Advanced rainfall trend analysis of 117 years over west coast plain and hill agro-climatic region of India. Atmos 11(11):1225

Sen PK (1968) Estimates of the regression coefficient based on Kendall's tau. J Am Stat Assoc 63(324):1379–1389

Signarbieux C, Feller U (2012) Effects of an extended drought period on physiological properties of grassland species in the field. J Plant Res 125(2):251–261. https://doi.org/10.1007/s10265-011-0427-9

Shankar MS, Pandey M, Shukla AK (2021) Analysis of existing equations for calculating the settling velocity. Water 13(14):1987

Van Rooy MP (1965) A rainfall Anomally index independent of time and space. NOTOS

Wallwork JT, Pu JH, Kundu S, Hanmaiahgari PR, Pandey M, Satyanaga A, Pandey M, Satyanaga A, Amir Khan M, Wood A (2022) Review of suspended sediment transport mathematical modelling studies. Fluids 7(1):23

Yadav SK, Nath S, Gautam S (2018) Analysis of rainfall variability in western Rajasthan. India 7(4):1592–1595

Yue S, Pilon P, Cavadias G (2002a) Erratum: power of the Mann-Kendall and Spearman's rho tests for detecting monotonic trends in hydrological series (journal of hydrology (2002) 259 (254-271) PII: S0022169401005947). J Hydrol 264(1–4):262–263. https://doi.org/10.1016/S0022-1694(02)00078-1

Yue S, Pilon P, Phinney B, Cavadias G (2002b) The influence of autocorrelation on the ability to detect trend in hydrological series. Hydrol Process 16(9):1807–1829

Chapter 29
Decadal-Based Analysis of Hydrological Components in the Kesinga Sub-Catchment in Mahanadi Basin: An Assessment of Climate Variability Impact

Pooja Agarwal, M. A. Alam, and Pramod Kumar Sharma

Abstract The annual distribution of rainfall is highly concentrated in specific months over the Indian sub-catchment. Monsoon rainfall constitutes about 80% of total rainfall received in a year. In such a case, variability in climate parameters directly affects the runoff patterns and subsequently water availability within a region. The present work aims to evaluate the impact of climate variability on various hydrological components on a decadal basis in the Kesinga river basin (humid region). The SWAT model was developed separately for the period 1981–1990, 1991–2000, and 2001–2010 using land use/land cover maps of respective periods, and various hydrological components were analyzed over the three decades. Calibration and validation were done using the SUFI-2 algorithm. The results show that annual runoff has experienced an increase whereas no significant change can be observed in ET estimates over the study period. In addition, a significant change has been identified in different land use and land cover categories of the region over a specified time interval, thus, the observed increase in runoff leading to flash floods may be attributed to changes in climate variables, especially rainfall. Lastly, SWAT simulated ET was compared to GLDAS Noah global datasets of ET. A systematic positive bias has been observed in Noah ET estimates as compared to SWAT simulated ET time series.

Keywords SWAT · Climate variability · Runoff · ET · GLDAS Noah

P. Agarwal (✉) · P. K. Sharma
Department of Civil Engineering, Indian Institute of Technology, Roorkee, India

M. A. Alam
Department of Civil Engineering, Punjab Engineering College, Chandigarh, India

M. Pandey et al. (eds.), *River Dynamics and Flood Hazards*, Disaster Resilience and Green Growth, https://doi.org/10.1007/978-981-19-7100-6_29

Abbreviations

ET	Evapotranspiration
GLDAS	Global land data assimilation system
LULC	Land use land cover
SUFI	Sequential uncertainty fitting
SWAT	Soil and water assessment tool
SWAT-CUP	Calibration and uncertainty programs

29.1 Introduction

Hydrological hazards of various types pose a plethora of technical and public policy issues around the world. Droughts, flooding, and other related events are examples of hydrological hazards, which are defined as extreme events associated with the occurrence, movement, and distribution of water (e.g., landslides and river scour and deposition). Climate variability, demographic trends, land cover change, and other causative factors all contribute to hydrological hazards and their consequences, which may be exacerbated by global climate change. The continued increase in greenhouse gases in the atmosphere will result in global warming and an intensification of the hydrological cycle, making hydrological extreme studies more arduous and challenging. Because of the enormous impacts of hydrological hazards on society and its economies, novel approaches, techniques, or methods for predicting, preventing, and mitigating hydrological extremes must be considered. Given the complexities of nonstationary hydro-meteorological and hydro-climatological processes, it is critical to apply recent technological advances and scientific knowledge to improve our understanding of hydrological hazards and our ability to cope with droughts and floods (Trajkovic et al. 2016).

Flooding is a massive ecological hazard in urban areas, causing death and destroying property and infrastructure. One of the primary causes of urban floods can be associated with increased precipitation which further can be linked to global changes in climate, changes in the usage of the land, and their impact on the region's hydrology. Recent studies have indicated alterations in the hydrological parameters such as rainfall, runoff, ET, etc., at global and regional levels. These hydrological parameters of a region are influenced either by climatic variations or human activities or a combination of both. In order to assess the prevailing changes in hydrological characteristics, it is important to investigate the factors responsible for these changes. In order to deal effectively with the problems associated with the alterations in the hydrological parameters of a region, it is also necessary to determine the major factors responsible for a particular variation in a particular region. Several studies have been conducted to investigate the impacts of climatic variations and human activities on hydro-meteorological parameters at global and regional scales using various techniques such as the Budyko framework, statistical methods, time-trend

analyses (Zhang and Lu 2009), hydrological modeling using SWAT model (Ghaffari et al. 2010; Singh et al. 2013; Rajib and Merwade 2016; Zuo et al. 2016; Chandra et al. 2016; Wu et al. 2017).

An extensive analysis of land use land cover changes between 1966 and 2009 using toposheets and satellite images was presented by Zope et al. 2017 for the Poisar River catchment in Mumbai, India comprising a catchment area of 20.19 km^2. It was observed that there was an increase in built-up area from 16.64% to 44.08% and a decrease in open space from 43.09% to 7.38% of the total catchment area between 1966 and 2009. For flood assertion, a comprehensive approach of Hydrological Engineering Center-Hydrological Modeling System (HEC-HMS), HEC-GeoHMS, and HEC-River analysis system with HEC-GeoRAS was applied. These models were combined with GIS and remote sensing data to develop a model at the regional level for estimating the extent of the flood plain and analyzing flood hazards. To create flood plain maps, the implications of detention ponds and land use land cover change on runoff water and flood plain extent were studied for different return periods. The peak discharge was observed to increase from 2.6% to 20.9% for LULC change between 1966 and 2009 for return periods of 200, 100, 50, 25, 10, and 2 years. The establishment of a detention pond for LULC in 2009 reduced flood extent from 4.5% for the 25-year return period to 7.7% for the 100-year return period, and the total flood hazard area decreased by 14.9%. The results indicated that the hydrological impacts of low return period rainfall events were greater due to the geographic characteristics of the region. Detention ponds also reduced peak discharges along with the extent of the flooded area, flood depth, and flood hazard. The integration of available software models with GIS and remote sensing proved to be extremely effective for flood disaster and mitigation management planning and measures. In another study, Idowu and Zhou (2021) the issue of persistent flooding in Lagos State, Nigeria, which occurs in tandem with increased urbanization and urban expansion rates was addressed. As a result, to determine the potential causative factors of flood raise in the state, an estimation of LULC variations along with the passed time in regards of flood hazard mapping was required. Over the course of 35 years, four major kinds of land coverage in the study area were mapped and studied: water, wetland, vegetation, and developed. The researchers then created a map-matrix-based, post-classification LULC change recognition technique to determine multi-year land cover changes between 1986 and 2000, 2000 and 2016, 2016 and 2020, and 1986 and 2020. Seven criteria were recognized as potential contributors to the study area's increasing flood hazards. Their weights were calculated by calculating the Analytical Hierarchy Process (AHP) and the Shannon Entropy weighting approach. The eventual results were categorized as flood hazard ranging from very high, high, moderate, low, and very low. According to an analysis of LULC development in regard to flood hazard, the majority of LULC changes result in the transformation of wetland areas into urban areas and uncontrolled urbanization in flood hazard zones ranging since very high to moderate. During the 35-year period, wetland areas decreased by 69% while developed areas increased by 94%. Wetland was a predominant land coverage type in 1986, but it will be the least common by 2022. These LULC changes may be to blame for the region's increased

flooding. Adnan et al. (2020) investigated and discovered that the construction of polders on Bangladesh's coast has pointedly altered flooding trends and resulted in significant LULC changes. The analysis provided a Spatio-temporal assessment of deficiency in relation to LULC variation and pluvial overflow risk in Bangladesh's south-western embankment area. A combination of logistic regression (LR), cellular automata (CA), and Markov Chain models were used on the basis of historical data to forecast LULC. Flood risk assessment was carried out for current and forthcoming LULC set-ups. A spatial regression model with multiple parameters was generated to guesstimate the wealth index (WI) for current and imminent scenarios. Agricultural land cover in the specified area is condensed from 34% to 8%, while aquaculture land coverage augmented from 17% to 39% during the study period, i.e. 2005 to 2010, respectively. Between 2010 and 2019, the variation rate in LULC was comparatively gradual. A prediction was made explaining LULC for the year 2030 based on recent trends.

SWAT is one of the most extensively used hydrological models used to assess the impacts of land use and climate changes on runoff and sediment yields in a watershed (Ghaffari et al. 2010; Singh et al. 2013; Rajib and Merwade 2016; Zuo et al. 2015; Chandra et al. 2016 and Wu et al. 2017). It is a semi-distributed hydrological model and is an outcome of USDA Agricultural Research Service (ARS) modeling conducted over a period of 30 years at the Texas agricultural experimental station. A considerable amount of work has been carried out implementing hydrologic modeling using the SWAT model in India and other countries. Ghaffari et al. 2010, investigated the hydrological effects of and use change in Zanjanrood Basin in Iran using the SWAT model. The results indicated an increase in a runoff with respect to changes in land use (overgrazing and replacing of rangelands) in the region. Baker and Miller 2013, assessed the hydrological model for water resources in an East African watershed which showed an increase in surface runoff and a decrease in groundwater recharge due to changes in land use. Dhar and Mazumdar 2009, exercised a SWAT model over the Kangsabati river watershed in the Bankura district of West Bengal, India to evaluate various parameters such as evapotranspiration, potential evapotranspiration, and lateral flow. Pradhan et al. 2015, studied climate change impact on water availability in the Indrawati basin, Nepal using SWAT. Chandra et al. 2016, applied SWAT to model sediment yield in the Upper Tapi Basin, India. Erosion-prone areas in the catchment were demarcated to provide better soil conservation measures such as filter strips and stone bunds. Singh et al. 2013, used the SWAT model to estimate the streamflow in the Tungabhadra catchment in India. SUFI-2 and GLUE techniques were used to calibrate the distributed model. Although a lot of literature is available at a large river basin scale, there is still a lot of scope of work that can be done on a sub-catchment scale. Mahanadi is one of the major rivers in India, but there is a lack of regional studies in this area. The study area for this study is Kesinga, which is a sub-catchment in the Mahanadi basin, India.

Many studies have been conducted for analyzing variations and their causes in hydrological parameters on basin levels. Not much of such work is present on a regional basis. Regional studies are important to plan better management practices

considering the varying climatic characteristics of the area. The main focus of this work is to analyze the influence of climatic variations on temporal patterns of overflow and evapotranspiration in the Kesigna sub-catchment over the period 1981to 2010. The objectives of the study can be defined as (1) Developing a SWAT model for Kesinga sub-catchment incorporating LULC change for three decades, i.e. 1981–1990, 1991–2000, and 2001–2010; (2) Detecting temporal variations prevailing in runoff and ET during the study period; (2) Comparison of GLDAS Noah model and SWAT simulated values of ET for the region; (3) Investigating the effect of climate variability on observed variations.

29.2 Study Area

The study area chosen for this study is the Kesinga sub-catchment in the Mahanadi Basin, as shown in the Fig. 29.1. The latitudinal and longitudinal extent of the area ranges from 83.13 to 83.22 in East and from 20.12 to 20.20 in North, respectively. It is a semi-arid region covering an area of 11,856 km^2 at an average elevation of 187 m and experiences tropical climatic conditions. Mahanadi basin comprises fertile soil, resulting in the development of agricultural practices in the region, thereby converting most of the land cover into croplands.

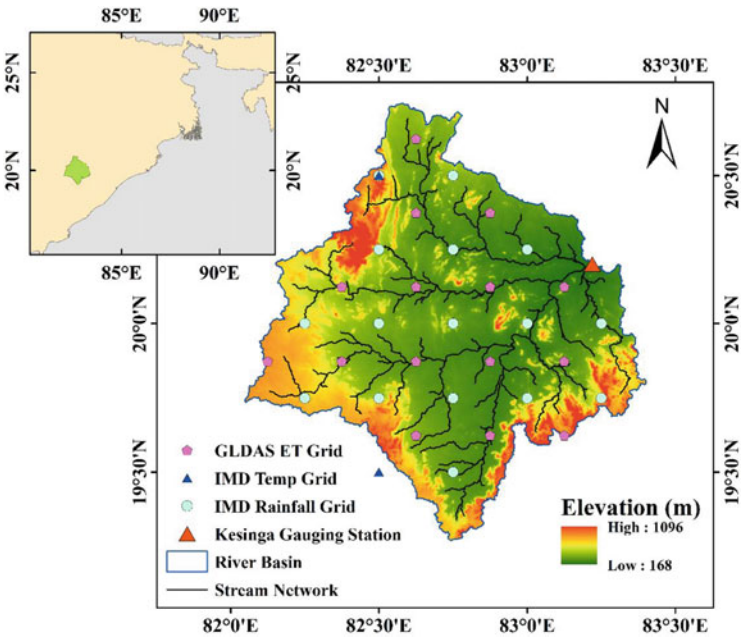

Fig. 29.1 Location map of the study area

29.3 Datasets

The datasets used in this study are observed daily records of rainfall and runoff, and GLDAS Noah model-simulated global estimates of ET at a monthly time step. Gridded rainfall dataset is collected from Indian Meteorological Department (IMD) at 0.25° × 0.25° resolution for the period 1981to 2010. A total of 16 rainfall grids are found to fall within the study area. The Basin average of daily temperature and rainfall is calculated using the Thiessen polygon method. The daily runoff dataset was downloaded from Water Resources Information System: India (WRIS: India) portal for the period 1979–2011. Satellite imageries were acquired to prepare LULC maps to study the variations in the land use/ land cover and to use as input for developing the SWAT model. The sources and other properties of the aforementioned datasets are summarized in Table 29.1.

The DEMs are collected from SRTM elevation data with absolute vertical accuracy of the 30 m. The vertical accuracy of SRTM-derived DEMs indicates that they can be used to create a topographic map with contour intervals greater than 16 m (Elkhrachy 2018). Because the vertical accuracy standard requires that 90% of all points tested have their elevation within half of the contour interval as stated in scientific findings. The results clearly show that the SRTM data has regional variations in accuracy and has thus been widely used worldwide.

29.4 Methodology

29.4.1 Development of the SWAT Model

The methodology adopted in this study is presented as a flowchart in Fig. 29.2. Various datasets were collected and data inputs were prepared as required for the development of the SWAT model. Thereafter, the SWAT model was developed for

Table 29.1 Details of the datasets obtained from various sources

Input data	Resolution	Duration	Source
Rainfall	0.25° × 0.25°	1981–2010	India meteorological department (IMD)
Runoff		1981–2010	WRIS: India
Evapotranspiration	0.25° × 0.25°	1981–2010	GLDAS
Digital elevation model (DEM)	30 m		SRTM
Soil type	1:5000000		FAO
LANDSAT images	30 m		LANDSAT 5, LANDSAT 7 and LANDSAT 8

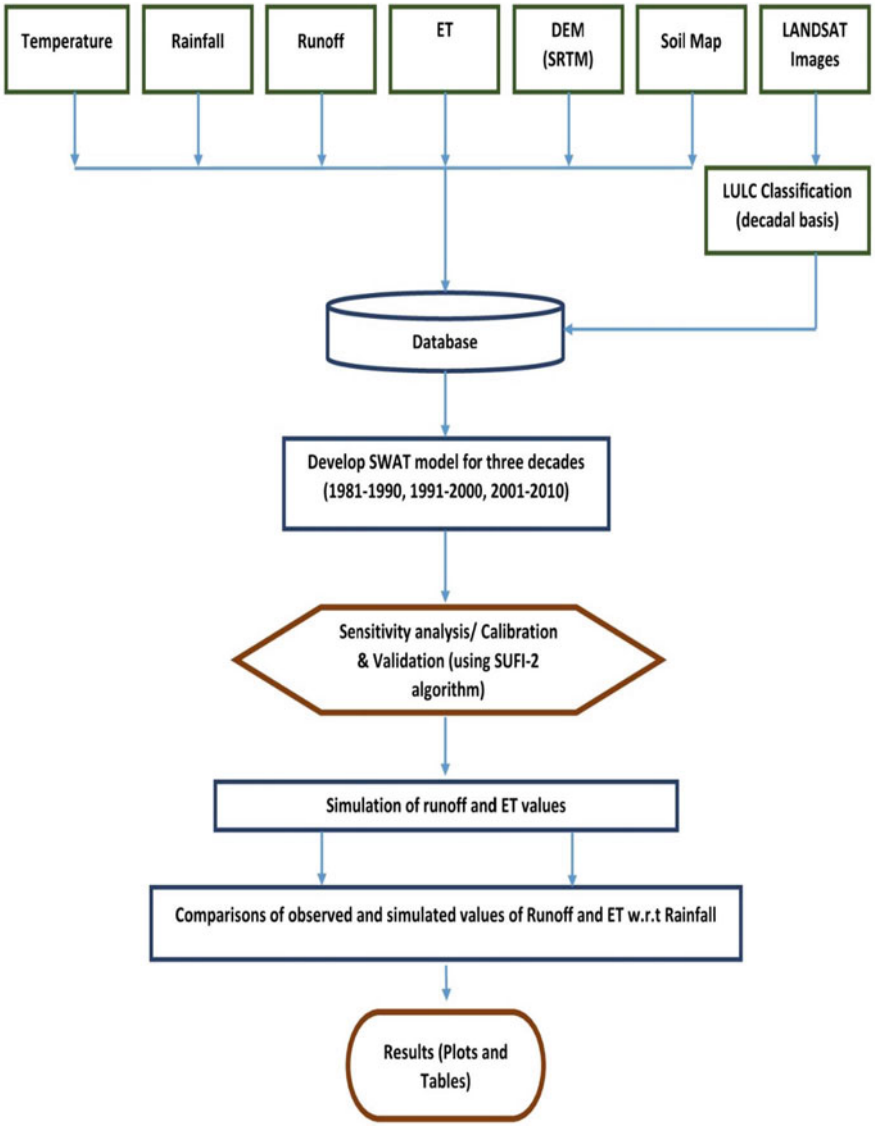

Fig. 29.2 Flowchart of the methodology adopted in the present study

each decade separately, viz. 1981–1990, 1991–2000, 2001–2010 using LULC map of each decade. LULC maps were prepared for each decade, which indicated significant changes in the land use patterns during the study period. Sensitivity analysis was conducted to identify the sensitive parameters. Calibration and validation were carried out using the SUFI-2 technique. Thereby, values of runoff and ET were simulated and analyzed. The variations in simulated values of hydrologic

parameters were compared against the variations found in rainfall time series to investigate their dependency on climate variability.

29.4.2 Model Calibration and Validation Using SUFI-2 Algorithm

The SUFI-2 algorithm was used for parameter optimization with the help of SWAT-CUP which is a public domain program linking the SUFI-2 procedure to SWAT. Table 29.2 shows the results of the sensitivity analysis of SWAT model parameters for a runoff with the statistics and ranking of parameters in terms of their sensitivity. Curve Number (CN2) is found to be the most sensitive parameter, followed by soil available water capacity (SOL_AWC) and then other parameters. These sensitive parameters are mostly responsible for the model calibration and parameter changes during the model iteration process. The remaining parameters have no or very negligible effects on streamflow simulation. The goodness-of-fit and efficiency of each model have been evaluated using five objective functions, viz. P-factor, R-factor, R^2, NS, and PBIAS, which are specified in Table 29.3, represent model efficiency to a satisfactory level.

Table 29.2 Parameter sensitivities for SUFI-2

Parameter	Ranking	*t*-stat	*P*-value
r__CN2.Mgt	1	−7.772	0
r__SOL_AWC.SOL	2	3.515	0.0007
v__GW_REVAP.GW	3	1.475	0.143
v__ESCO.Hru	4	−0.991	0.324
v__ALPHA_BF.Gw	5	0.696	0.488
r__SOL_K.SOL	6	−0.679	0.498
r__OV_N.hru	7	0.307	0.759

Table 29.3 Stream flow results of calibration and validation for each decade

	1981–1990		1991–2000		2001–2010	
Variables	Cal	Val	Cal	Val	Cal	Val
P-factor	86%	75%	86%	74%	82%	77%
R-factor	0.7	0.56	0.74	0.52	0.68	0.56
R^2	0.88	0.84	0.88	0.85	0.84	0.81
NS	0.88	0.81	0.88	0.83	0.84	0.80
PBIAS	6.4	−8.3	6.4	−7.8	6.1	−5.6

29.5 Results and Discussions

29.5.1 Comparison of Monthly Observed and Simulated Values of ET on a Decadal Basis

In Fig. 29.3, the GLDAS Noah and SWAT simulated values for ET are plotted on monthly basis for each decade. As evident from the figure, the values simulated by the SWAT model for each decade are in good agreement with that of GLDAS Noah ET values. However, the ET data series obtained by GLDAS Noah experiences an overall positive bias over the SWAT simulated values, as depicted in Fig. 29.4. This bias can be accounted to the alterations in data used as input for the SWAT model or any discrepancies incurred during the development or execution of the SWAT model. Nevertheless, the bias can be reduced by improving the precision of the model.

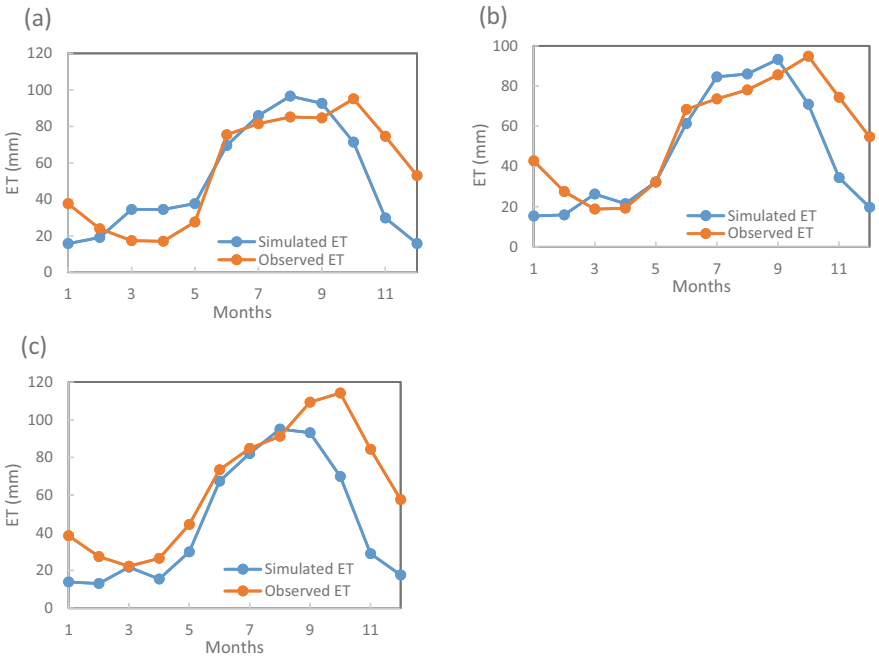

Fig. 29.3 Comparison of observed and simulated ET values for the decade (**a**) 1981–1990; (**b**) 1991–2000; and (**c**) 2001–2010

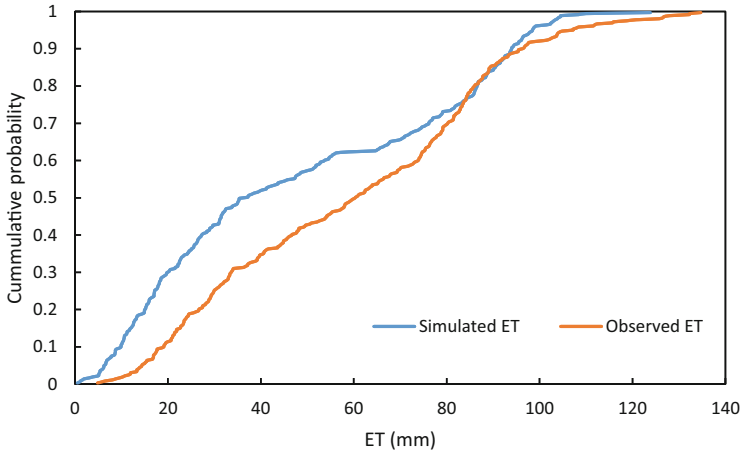

Fig. 29.4 Comparison of CDF of observed and simulated ET values

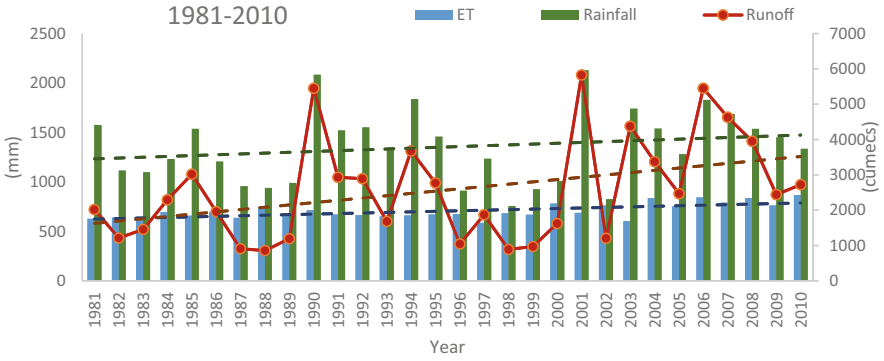

Fig. 29.5 Variation in annual runoff and ET during the study period (1981–2010)

29.5.2 Variation in Annual Rainfall, Runoff, and Evapotranspiration (ET)

Variation in the annual series of rainfall, runoff, and ET for the entire study period (1981–2010) has been illustrated in Fig. 29.5. The bar graphs represent rainfall and ET, whereas runoff is denoted as a line graph. It is evident from the figure that annual rainfall is increasing during the study period. Similarly, the annual runoff is increasing significantly during the study period. The presence of similar variation in both the parameters time series strongly indicates the impact of climatic parameters such as rainfall on hydrological components such as runoff for the sub-catchment. The annual ET has been observed to be slightly increasing with time, however, the change is not significant over the study period.

29.5.3 *Variation in the Annual Runoff, Evapotranspiration, and Rainfall on a Decadal Basis*

Figure 29.6 shows the variations in the annual runoff, ET, and rainfall during each decade of the study period. During the first decade, 1981–1990, the annual rainfall tends to increase and similar variation can be seen in the annual runoff. On the contrary, rainfall series show a decrement in the annual values for the next decades of the study period, viz. 1991–2000, however, the runoff values still show slight increment throughout the decade. During the third decade, 2001–2010, a significant decreasing pattern can be seen in the annual series of rainfall as well as the runoff. Going through the variations plotted for each decade it can be said that variations in the runoff patterns are highly influenced by the variability exhibited by the rainfall during that decade. Similar variations can be observed in the ET time series, however, the variations are not significant in comparison to the variations in runoff values. From Figs. 29.5 and 29.6, it can be inferred that the hydrological components of the Kesinga sub-catchment are highly dependent on the climatic variations prevailing in the region.

29.6 Conclusion

The impacts of climate variability have not been much investigated at a regional scale in India. In this study, a region-based analysis of hydrological components (runoff and evapotranspiration) has been carried out for the Kesinga sub-catchment in the Mahanadi basin from 1980 to 2010. SWAT model was developed for each decade to study the variations in annual runoff and ET values on a decadal basis, using observed data series of annual rainfall, thereby taking into account the climatic variability.

A significant dependence of variations in runoff pattern on the rainfall variability was seen throughout the study period as well as on a decadal basis. The annual rainfall increased by about 23% which denoted a major impact of climate variation on the increment of annual runoff. However, ET showed insignificant variations throughout the study period and on a decadal basis. In the comparison of GLDAS Noah and SWAT simulated ET values, GLDAS Noah modeled ET values are found to consist of a systematic positive bias. Going through all the results, it can be concluded that the hydrologic parameters in the Kesinga sub-catchment are majorly influenced by climatic variations. The findings of the present study provide a useful platform for further hydro-meteorological process-based studies in the region. Factors leading to an increase in rainfall and runoff can be investigated to facilitate better management practices in the region.

The effect of urbanization is recognized as the primary cause of the raised flood peak discharge and decrease in holdup time. Natural areas that were previously used as detention or retention ponds are now being retrieved to meet the needs of urban inhabitants due to the rapid development of the area's infrastructure. Installing

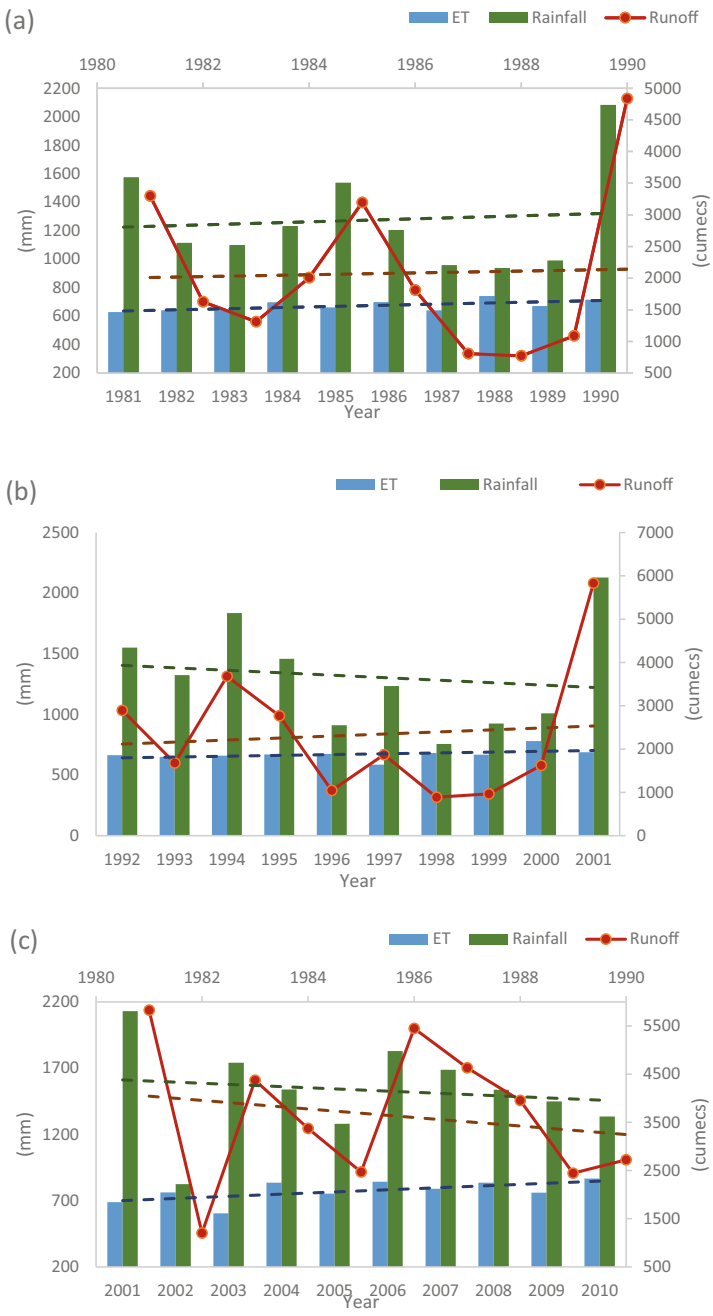

Fig. 29.6 Variation in annual rainfall, runoff and ET during (**a**) 1981–990; (**b**) 1991–2000; (**c**) 2001–2010 in Kesinga sub-catchment

detention ponds is one of the better mitigation measures because it significantly reduces peak outflow, the range of flood, and the extent of destroyed area. The floodplain and flood hazard maps produced in the present paper will be useful to the Municipal Corporation for flood extenuation, attentiveness, and supervision development. Flood hazard maps will also help insurance companies determine premium criteria for structures in flood and hazard zones.

References

Adnan MSG, Abdullah AYM, Dewan A, Hall JW (2020) The effects of changing land use and flood hazard on poverty in coastal Bangladesh. Land Use Policy 99:104868

Baker TJ, Miller SN (2013) Using the soil and water assessment tool (SWAT) to assess land use impact on water resources in an east African watershed. J Hydrol 486:100–111

Chandra P, Patel PL, Porey PD (2016) Prediction of sediment erosion pattern in upper Tapi Basin, India. Curr Sci 110:00113891

Dhar S, Mazumdar A (2009) Hydrological modelling of the Kangsabati River under changed climate scenario: case study in India. Hydrol Process 23(16):2394–2406

Elkhrachy I (2018) Vertical accuracy assessment for SRTM and ASTER digital elevation models: a case study of Najran city. Saudi Arabia Ain Shams Eng J 9(4):1807–1817

Ghaffari G, Keesstra S, Ghodousi J, Ahmadi H (2010) SWAT-simulated hydrological impact of land-use change in the Zanjanrood basin, Northwest Iran. Hydrol Process 24(7):892–903

Idowu D, Zhou W (2021) Land use and land cover change assessment in the context of flood Hazard in Lagos state, Nigeria. Water 13(8):1105

Pradhan NS, Sijapati S, Bajracharya SR (2015) Farmers' responses to climate change impact on water availability: insights from the Indrawati Basin in Nepal. Int J Water Resour Dev 31(2): 269–283

Rajib MA, Merwade V (2016) Improving soil moisture accounting and streamflow prediction in SWAT by incorporating a modified time-dependent Curve Number method. Hydrol Process 30 (4):603–624

Singh V, Bankar N, Salunkhe SS, Bera AK, Sharma JR (2013) Hydrological stream flow modelling on Tungabhadra catchment: parameterization and uncertainty analysis using SWAT CUP. Curr Sci 104:1187–1199

Trajkovic S, Kisi O, Markus M, Tabari H, Gocic M, Shamshirband S (2016) Hydrological hazards in a changing environment: early warning, forecasting, and impact assessment. Adv Meteorol 2016:1–2

Wu L, Wang S, Bai X, Luo W, Tian Y, Zeng C, Luo G, He S (2017) Quantitative assessment of the impacts of climate change and human activities on runoff change in a typical karst watershed, SW China. Sci Total Environ 601:1449–1465

Zhang S, Lu XX (2009) Hydrological responses to precipitation variation and diverse human activities in a mountainous tributary of the lower Xijiang, China. Catena 77(2):130–142

Zope PE, Eldho TI, Jothiprakash V (2017) Hydrological impacts of land use–land cover change and detention basins on urban flood hazard: a case study of Poisar River basin, Mumbai. India Nat Hazards 87(3):1267–1283

Zuo D, Xu Z, Peng D, Song J, Cheng L, Wei S et al (2015) Simulating spatiotemporal variability of blue and green water resources availability with uncertainty analysis. Hydrol Process 29 (8):1942–1955

Zuo D, Xu Z, Yao W, Jin S, Xiao P, Ran D (2016) Assessing the effects of changes in land use and climate on runoff and sediment yields from a watershed in the loess plateau of China. Sci Total Environ 544:238–250

Chapter 30
Prediction of Future Rainfall in the Upper Godavari Basin Using Statistical Downscaling Model

B. Deepthi and A. B. Mirajkar

Abstract Climate change is a complex phenomenon with serious consequences for both nature and humanity. Given the upper Godavari basin's significant vulnerability to climate change, the current study tries to forecast future precipitation over the basin for the years 2021–2100. This is the first study to use a GCM from the Coupled Model Intercomparison Project Phase 5 (CMIP5) to project the future precipitation over the basin. The daily precipitation from the Canadian Earth System Model (CanESM2) is downscaled using a statistical downscaling model (SDSM) under three different representative concentration pathway scenarios (RCP 2.6, RCP 4.5, and RCP 8.5). The study also attempts to compare the observed monthly rainfall from 1961 to 2005 to the changes in mean monthly rainfall under three RCP scenarios. Large-scale atmospheric variables using reanalysis data from the National Centers for Environmental Prediction (NCEP) from 1961 to 1990 and 1991 to 2005 are used to calibrate and validate SDSM, respectively. When using statistical parameters such as correlation coefficient (CC), Nash–Sutcliffe efficiency (NSE), and root-mean-square error (RMSE), the data generated during the calibration and validation of SDSM shows high accuracy with observed rainfall, indicating that the SDSM can replicate observed rainfall of the basin very well. Except for June, July, and August, the percentage change in mean monthly rainfall suggested an increase in future rainfall relative to observed rainfall in all three RCP scenarios. However, the average annual rainfall under RCP 4.5 and RCP 8.5 scenarios show a decreasing trend compared to the observed rainfall. While considering the near future (the 2030s), the increase in average annual rainfall in the 2030s for the RCP 2.6 scenario is about 4% compared to the baseline period (1961–2005). For the RCP 4.5 scenario, the projected precipitation indicates a decrease in average annual rainfall for the 2030s of about 13% compared to the baseline period (1961–2005). In the RCP 8.5 scenario, the mean annual rainfall is decreasing is about 7.5% as compared to the baseline period (1961–2005). The findings of this study are critical for proper

B. Deepthi
Department of Civil Engineering, Indian Institute of Technology Bombay, Mumbai, India

A. B. Mirajkar (✉)
Department of Civil Engineering, Visvesvaraya National Institute of Technology, Nagpur, India

M. Pandey et al. (eds.), *River Dynamics and Flood Hazards*, Disaster Resilience and Green Growth, https://doi.org/10.1007/978-981-19-7100-6_30

planning and management of water resources in the basin in the face of changing climatic circumstances.

Keywords Climate change · General circulation model · SDSM · RCP · Rainfall

30.1 Introduction

Floods and droughts can be caused by changes in precipitation frequency, intensity, and timing. Climate change is a complex process with far-reaching implications for our environment, water supplies, ecosystems, and economic development. Several studies have looked at the effects of climate change on water resources over the last few decades (e.g., Wilby et al. 2000; Milly et al. 2005; Kundzewicz et al. 2008; Obeysekera et al. 2011; Asadi Zarch et al. 2015; Sunil et al. 2020; Cao et al. 2021; Shankar et al. 2021; Wallwork et al. 2022). The Intergovernmental Panel on Climate Change (IPCC) assessment reports go into great detail about the impacts of climate change on water resources (IPCC 2014) and show that the hydrological cycle is intensifying globally, affecting both surface and groundwater supplies.

India is most vulnerable to river and flood dangers. The population is subject to floods and disasters associated with silt and flooding in varying degrees, intensities, and patterns due to the geo-climatic variability of the country (Pu et al. 2021). The community has come to view extreme weather events like floods, droughts, and cyclones as normal occurrences that have been made worse by the effects of climate change. Riverine erosion, deposition scour, and sediment movement is among the most dangerous hydrological processes. To lessen the risks, it is crucial to estimate the erosion accurately (John et al. 2021a, b). Sediment transport in rivers is one of the main causes of scouring and deposition. As a result, a thorough understanding of climate change and its consequences is essential for effective water resource management and planning and addressing ineffective adaptation and mitigation efforts.

In most research analyzing the influence of climate change on water supplies, two key processes are used. GCMs (General Circulation Models) simulate the current and future climates under various scenarios in the first step (e.g., Leung et al. 2004; Chu et al. 2008; Anandhi and Nanjundiah 2015; Raju and Kumar 2018; Deepthi et al. 2020; Hunt et al. 2020). This step mainly focuses on simulating/ projecting climate variables like precipitation, temperature, etc., at GCM scale/resolution. However, most of the GCMs have coarser resolution emphasizing the need for downscaling of GCMs, so that the analysis can be done at the catchment scale. This constitutes the second step, in which the coarse-scale GCMs are downscaled to the catchment scale (e.g., Prudhomme et al. 2002; Fowler et al. 2007).

Statistical downscaling and dynamic downscaling are two types of downscaling approaches. In statistical downscaling, a statistical relationship is formed between large-scale predictors and predictands (climate variables). Statistical downscaling has the advantage of being computationally inexpensive. A regional climate model (RCM) is layered inside a global climate model (GCM) in dynamic downscaling, making it computationally expensive. According to Wilby and Wigley (2000),

statistical downscaling involves only a few assumptions. The key assumption is that the relationship between predictors and predictands that we are developing will remain the same in the future. The predictors can also keep the predictand's statistical properties. In recent years numerous studies have used the statistical downscaling technique to downscale the GCMs to the catchment scale and further study the impact of climate change on water resources (Abbaspour et al. 2009; Chu et al. 2010; Huang et al. 2011; Wang et al. 2012; Sigdel and Ma 2016; Gebremedhin et al. 2018)

Among such studies, the most widely used example of statistical downscaling is the empirical statistical downscaling model (SDSM). SDSM is a hybrid of a multiple linear regression model and stochastic weather generator (Hassan et al. 2014). It is a widely used tool to assess the impact of climate change on water resources. For instance, Hassan et al. (2014) used SDSM to statistically downscale the output from the model, HadCM3 over Peninsular Malaysia. The precipitation and temperature outputs from the model under two different scenarios were downscaled. They concluded that all the three climatic variables show an increasing trend in the future under all the scenarios. Saraf and Regulwar (2016) used SDSM to statistically downscale the weather data in the Upper Godavari River basin. They used two GCMs from CMIP3, CGCM3, and HadCM3 to project the future maximum temperature, minimum temperature, and precipitation under four scenarios. They found that the downscaled precipitation and maximum temperature show an increasing trend in the future under all the scenarios. Siabi et al. (2021) explore the applicability of SDSM in the Black Volta section of Ghana. They have considered two GCMs, HadCM3 from CMIP3 and CanESM2 from CMIP5, to project the future maximum temperature, minimum temperature, and precipitation in the basin under five different scenarios. Munawar et al. (2022) used SDSM for statistically downscaling maximum temperature, minimum temperature, and precipitation from five CMIP5 GCMs over the Jhelum River basin. They have considered two future scenarios, RCP 4.5 and RCP 8.5, and concluded that winter and pre-monsoon seasons are potentially affected in terms of warming and precipitation.

Encouraged by the applications of SDSM, the present study investigates the applicability of the statistical downscaling model (SDSM) in downscaling precipitation for the Upper Godavari basin. Although Saraf and Regulwar (2016) used SDSM for statistically downscaling the climatic variables in the Upper Godavari basin, they limited the study by using only the GCMs from CMIP3. To address this issue, the present study has considered a GCM from the latest CMIP5 to project the future precipitation in the basin. To our knowledge, this is the first study to use a model from CMIP5 to project the future climate in the Upper Godavari basin. The study also examines the effects of three alternative concentration pathway scenarios on mean monthly rainfall: RCP 2.6, RCP 4.5, and RCP 8.5. This research provides a valuable dataset for climate change impact applications in the water resources of the studied region.

30.2 Study Area and Data

30.2.1 Study Area

The susceptibility of India's Upper Godavari River basin to climate change is investigated in this study. The Godavari basin is India's second largest basin in terms of length and water supply. The Godavari basin spans Andhra Pradesh, Odisha, Chhattisgarh, and Maharashtra, as well as minor sections of Karnataka, Madhya Pradesh, and the Union Territory of Puducherry. The latitude and longitude of the Godavari River basin range from 16.3° to 22.56° N and 73.4° to 83° E, respectively. The Upper Godavari River basin lies entirely within the western and central parts of the state of Maharashtra. The Upper Godavari region is enclosed between 19° to 20.75° N latitude and 73° to 75.75° E longitude. Figure 30.1 shows the location map of the Upper Godavari River basin. The region receives ample rainfall throughout the monsoon season (June to September). Because the basin receives so much rain during the southwest monsoon season, it is nearly dry for the rest of the year.

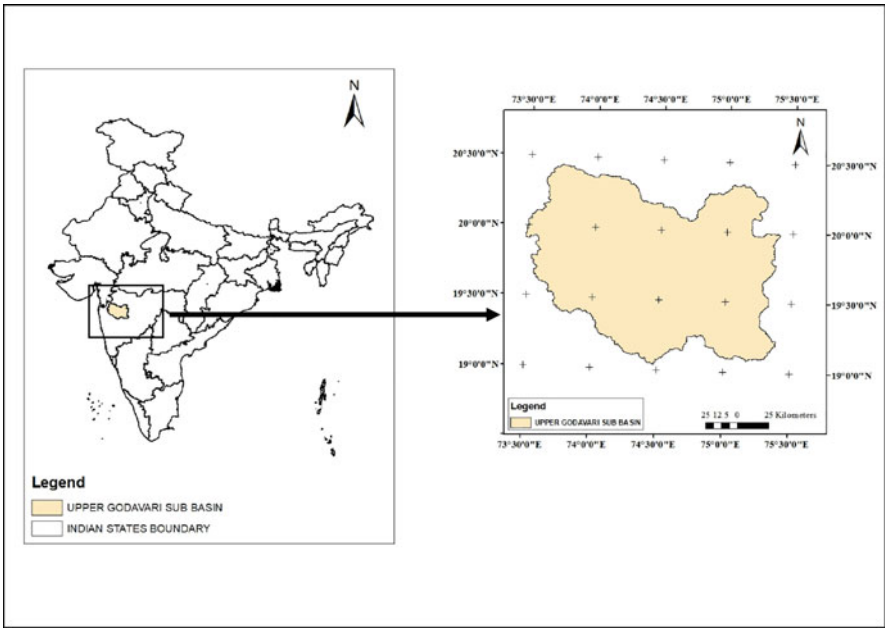

Fig. 30.1 Location map of the Upper Godavari River basin

30.2.2 Data

30.2.2.1 NCEP/NCAR Reanalysis Data

The NCEP/NCAR reanalysis data from 1961 to 2005 are used. The horizontal resolution for NCEP/NCAR data is 2.5° × 2.5°. The variables or the predictors used in this study from NCEP/NCAR Reanalysis data are presented in Table 30.1. A total of 17 predictors from NCEP/NCAR Reanalysis data are used for this study.

30.2.2.2 GCM Data

The second-generation Canadian Earth System Model (CanESM2) developed by the Canadian center for climate modeling and analysis (CCCma) is used in this study. The model is a part of the CMIP5, and the resolution of the model is 3.75° × 3.75°. The historical and future simulated predictors required for the SDSM model are derived from the GCM. The future predictors are available for RCP 2.6, RCP 4.5, and RCP 8.5, and all these scenarios are addressed in this study. The historical data is available from 1961 to 2005, and the future predictor variables are available till 2100. CanESM2 was chosen after an assessment of the literature and the availability of data in SDSM-compatible format. The gridded predictor variables of NCEP/NCAR and CanESM2 for the nearest grid in the study area are downloaded from the site (https://climate-scenarios.canada.ca/?page=pred-canesm2).

In this study, daily gridded rainfall data at 1° × 1° resolution in the upper Godavari river basin over the period 1961–2005 are used. The data were obtained from the India Meteorological Department (IMD); see Rajeevan et al. (2008) for details of gridded rainfall data in India. The average gridded rainfall data over the basin is used for analysis.

Table 30.1 Predictors selected from NCEP/NCAR Reanalysis data

Relative humidity at 1000 hPa	Air temperature at 1000 hPa
Relative humidity at 850 hPa	Air temperature at 850 hPa
Relative humidity at 500 hPa	Air temperature at 500 hPa
Specific humidity at 1000 hPa	Northward wind at 1000 hPa
Specific humidity at 850 hPa	Northward wind at 850 hPa
Specific humidity at 500 hPa	Northward wind at 500 hPa
Geopotential height at 1000 hPa	Eastward wind at 1000 hPa
Geopotential height at 850 hPa	Eastward wind at 850 hPa
Geopotential height at 500 hPa	Eastward wind at 500 hPa
Mean sea level pressure	

30.3 Methodology

This study uses the Statistical Downscaling Model (SDSM) 4.2.9 to downscale and projects future climate data. Wilby et al. (2002) created SDSM as a downscaling method to analyze the implications of local climate change using a statistical downscaling technique. SDSM is a hybrid of multiple linear regression (MLR) and stochastic weather generator (SWG) (Meenu et al. 2013; Mahmood and Babel 2014).

30.3.1 Statistical Downscaling Model Setup

Some essential model parameters must be adjusted before constructing the link between given station weather data (predictand) and large-scale atmospheric variables to have the best statistical agreement between observed and simulated climate data (predictors). The model configuration is based on the SDSM 4.2 manual and is explained in the following.

- Year length: when dealing with predictand and NCEP reanalysis data, the Gregorian calendar is used, which has 366 days in a leap year. However, when working on scenario creation using CanESM2 GCM output, a 365-day year length is chosen because this model has a 365-day model year.
- Standard start and end date: the start date 1 January 1961 and the end date 31 December 2005 are used in the model as the available NCEP-NCAR reanalysis and GCM output data are available for the period 1961–2005.
- Allow negative values: the negative values are not allowed for precipitation.
- Event threshold: for precipitation, the event threshold is set to 0.1. It indicates that days with less than or equal to 0.1 mm of precipitation per day are classified as dry.
- Missing data identifier: the missing data is given as –999 for all the input data sets. The model skipped this value whenever it found this value in the input data during model calibration and calculating the summary statistics.

30.3.2 Quality Control and Data Transformation

The quality control function aids in the verification of input data mistakes by providing general statistics such as mean, maximum, and minimum values, the number of missing data, the total number of values, and so on. The data transformation procedure allows you to transform either the predictor variable or the predictand by choosing amongst logarithm, power, inverse, lag, and binomial transformations. This study, however, does not undergo any such transition.

30.3.3 Selection of Predictor Variables

The selection of predictor variables is the most crucial step in the statistical downscaling model. The screen variables feature in SDSM is a powerful tool for identifying the most important predictor variables. It gives you the option of making the correlation between predictor factors and predictand monthly, seasonal, or annual. You may also utilize partial correlation and scatter plots to determine which predictor variables to use.

30.3.4 Model Calibration

The 53 years of historical data sets observed between 1961 and 2005 are grouped into two groups. The first 30 years of data (1961–1990) are used for calibration, while the subsequent 15 years (1991–2005) are utilized for validation. The predictor variables collected after the screening procedure are used for calibration and validation.

30.3.5 Weather Generator

Using the regression model weights or parameter files created during model calibration and large-scale atmospheric predictor variables from the NCEP/NCAR reanalysis dataset, the weather generator option generates ensembles of synthetic daily weather data for the selected period. The length of the record to be synthesized and the number of ensembles wanted can be modified as needed. For all variables and stations, 20 ensembles of synthetic daily weather data series are constructed from 1991 to 2005 to compare with observed station data.

30.3.6 Validation of SDSM Results

Data from observed rainfall and NCEP reanalysis are separated into two groups: data from 1961 to 1990 is used to train SDSM, while data from 1991 to 2005 is used to validate SDSM. SDSM includes a summary statistics function that summarizes the observed and simulated data results, allowing you to compare the two sets of data. To summarize, you can use a variety of statistical alternatives such as mean, variance, autocorrelation, mean dry spell length, and mean wet spell length. The summary statistics result can then be plotted using SDSM's comparison results technique. Visualizing and comparing two data sets helps quickly analyze simulated data against observed data.

30.3.7 Scenario Generation

The future data is downscaled using the same parameter file or regression weight obtained during the weather generator once the model has been verified. This time, rather than NCEP/NCAR reanalysis data, model output is employed as large-scale atmospheric predictor variables. The three emission scenarios in the model are called Representative Concentration Pathways (RCPs) 2.6, 4.5, and 8.5. For each emission scenario, 20 ensembles of synthetic daily time-series data will be produced from 2021 to 2100.

30.3.8 Statistical Evaluation of the Model

The correlation coefficient (CC), Nash–Sutcliffe efficiency (NSE), and root-mean-square error (RMSE) are the quantitative statistics used to evaluate the SDSM's effectiveness. The correlation coefficient (CC) measures how closely observed and simulated data are linked. It has a –1 to 1 range. The greater or lower the CC value from 0, the better the positive or negative association, whereas 0 indicates that there is no linear relationship. The NSE determines the relative size of the residue as well as the variance of the observed data. Its value ranges between –1 and 1, with 1 being the best. Values less than 0 indicate poor performance, whereas those between 0 and 1 indicate adequate performance. One of the error indices used to measure the difference between observed and simulated values is the root mean square error (RMSE). The perfect fit is represented by an RMSE value of 0.

30.4 Results and Discussion

30.4.1 Calibration and Validation of SDSM

Among the 17 predictor variables of NCEP, five predictor variables are selected based on high explained variance, partial correlation, and scatter plot. Five predictor variables are specific humidity at 850 hPa (shum850), eastward wind at 500 hPa (uwind500), northward wind at 1000 hPa (vwind1000), relative humidity at 1000 hPa (rhum1000), and northward wind at 850 hPa (vwind850). Table 30.2

Table 30.2 Partial correlation value of five predictor variables with the predictand

Selected predictors	Partial correlation value
Relative humidity at 1000 hPa	0.45
Specific humidity at 850 hPa	0.53
Eastward wind at 500 hPa	0.56
Northward wind at 1000 hPa	0.43
Northward wind at 850 hPa	0.42

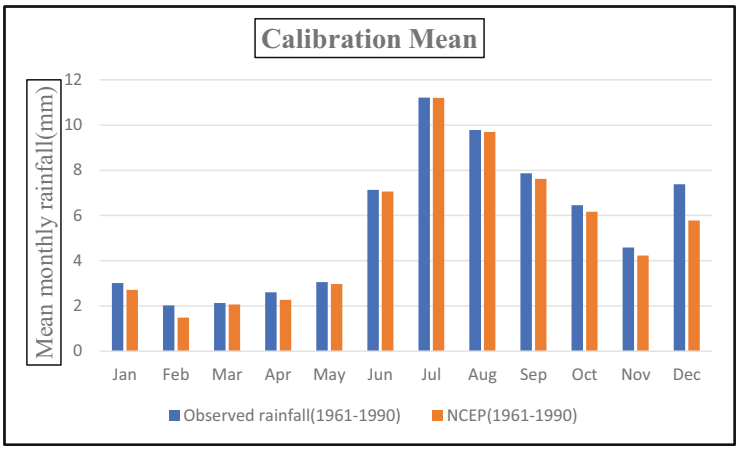

Fig. 30.2 Mean obtained during calibration period for NCEP and observed rainfall

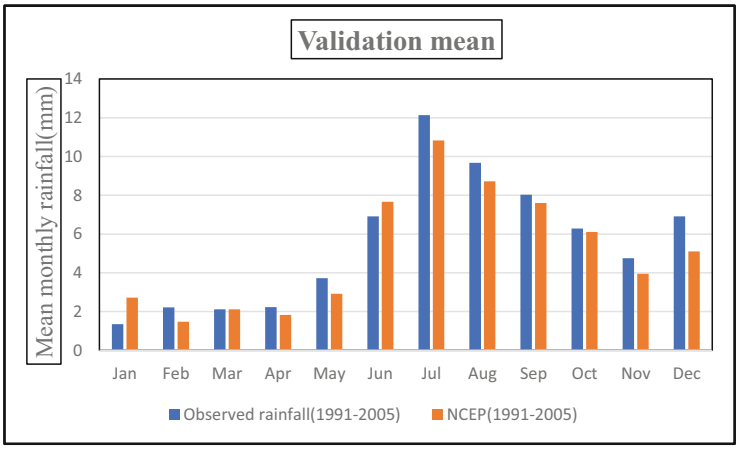

Fig. 30.3 Mean obtained during validation period for NCEP and observed rainfall

shows the partial correlation value obtained for the selected predictor variables. These five variables are used for calibrating the model. The data simulated by the model during the calibration and validation period is compared with observed rainfall data.

Mean during the calibration and validation period is compared to determine whether the SDSM can predict the rainfall data. Figures 30.2 and 30.3 show the values obtained during calibration and validation.

Figure 30.2 indicates that both the NCEP and observed rainfall have the same mean during the calibration period, but during the validation period, NCEP has less mean as compared to observed rainfall data (Fig. 30.3). During the validation period, July month shows the maximum mean value for both the NCEP and observed

rainfall. Figure 30.3 shows that during the validation period, the model simulates 11% less mean rainfall for July than the observed rainfall.

30.4.2 Statistical Evaluation of Models

For statistical evaluation of SDSM software, the parameters such as correlation coefficient (CC), Nash–Sutcliffe efficiency (NSE), and root-mean-square error (RMSE) are determined for the calibration and validation period. Table 30.3 shows the values obtained for these statistical parameters during the calibration and validation.

These statistical parameters are also obtained from the historical rainfall data generated by the GCM for the study area. These statistical characteristics were calculated using observed rainfall data from 1961 to 2005. By examining these statistical metrics, it is feasible to establish whether this GCM is acceptable for future rainfall prediction in the research area. The values of these statistical parameters are given in Table 30.4.

From Table 30.4, it is clear that the CanESM2 model is better for future rainfall prediction in the study area.

30.4.3 Change in Future Monthly Precipitation

30.4.3.1 RCP 2.6 Scenario

Figure 30.4 shows the mean monthly change in projected rainfall for the RCP 2.6 scenario. The mean monthly rainfall simulated by the CanESM2 model during 2021–2020 is more than the observed mean rainfall for some months such as September, October, November, and December. Downscaled precipitation obtained by the CanESM2 model for the study area for the scenario RCP 2.6 shows a decrease in future mean rainfall for the 2030s period except for September. In September, for the 2030s, it shows an increase in mean rainfall by 3 mm. For January, mean rainfall is increasing slightly by 0.29 mm. Then for the remaining months, except for September, the mean rainfall decreases for all months for all the periods. For RCP

Table 30.3 Statistical evaluation of SDSM model

Parameters	CC	NSE	RMSE
Calibration	0.75	0.66	4.13
Validation	0.78	0.72	3.83

Table 30.4 Statistical evaluation of the GCM

Parameters	*R*	NSE	RMSE
Year	1961–2005	1961–2005	1961–2005
CanESM2	0.78	0.56	3.12

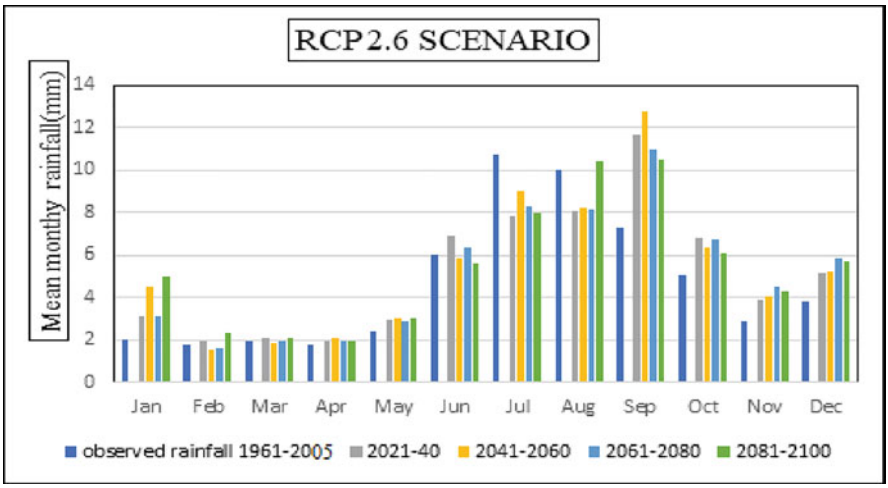

Fig. 30.4 Mean monthly change in projected rainfall for the RCP 2.6 scenario

2.6, it can be seen that for September, the percentage increase in mean rainfall compared to the baseline period is 41%, and for July, it shows a decrease of 33% for the 2030s. Compared to the 2030s, in the 2050s, RCP 2.6 scenario shows an increase in mean rainfall for all months except June, offering a decrease of 26% for the period 2050s. Now for the period, the 2070s, mean rainfall keeps on decreasing compared to the 2050s for all the months except October, November, and December, where there is a slight increase in rainfall, but the amount is less than that of the mean of the baseline period. For the 2090s, compared to the 2030s, 2050s, and 2070s, the increase in mean rainfall is observed only in January and August. However, in the 2090s, the increase in mean rainfall for January is 39% more than the mean rainfall obtained for the baseline period for January. Only for September the mean rainfall shows an increase compared to the baseline period for the 2030s, 2050s, 2070s, and 2090s. The increase in mean rainfall for January in the 2050s and 2090s shows a possibility of shifting the rainy season.

30.4.3.2 RCP 4.5 Scenario

Figure 30.5 shows the mean monthly change in projected rainfall for the RCP 4.5 scenario. The mean monthly rainfall simulated by the CanESM2 model during 2021–2040 is more than the observed mean rainfall for months such as September, October, November, and December. For the 2030s, there is a decrease in mean rainfall for all the months except September compared to the mean rainfall obtained for the baseline period. The amount of increase is only 33%, while for RCP 2.6, it is around 41%. For the period the 2050s, the mean rainfall for all months is more than 2030s but less than that of the mean rainfall obtained for the baseline period except September. In September, the mean rainfall is more than the baseline period by 25%

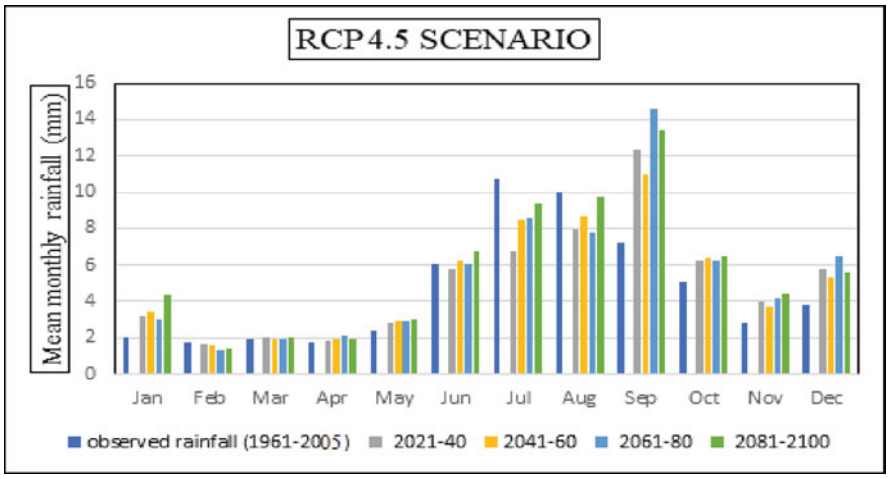

Fig. 30.5 Mean monthly change in projected rainfall for the RCP 4.5 scenario

for the period of the 2050s. For the period the 2070s, mean rainfall for all months is less than 2050s but less than that of the mean rainfall obtained for the baseline period except September. For September in the 2070s, the maximum increase in mean rainfall is obtained as compared to the 2030s, 2050s, and 2090s, and the increase in amount as compared to the baseline period is about 43%, but in all these periods, the amount of increase is less than that obtained for the RCP 2.6 scenario. For the 2090s, the increase in mean rainfall is more than the mean rainfall received for all other periods. But for September in the 2090s, the mean rainfall is less than in the 2070s. We can conclude that the study area will receive comparatively less rainfall in the future. The increase in rainfall is obtained for September followed by January, so there is a possibility of shifting the rainy season as observed in the RCP 2.6 scenario.

30.4.3.3 RCP 8.5 Scenario

Figure 30.6 shows the mean monthly change in projected rainfall for the RCP 8.5 scenario. The mean monthly rainfall simulated by the CanESM2 model during 2021–2040 is more than the observed mean rainfall for some months such as September, October, November, and December. In this scenario, for the period of the 2030s, the mean rainfall for all the months is less than the mean rainfall obtained for the baseline period except for September. In September, the mean rainfall is more than the observed mean rainfall by an amount equal to 38% for the 2030s. For the period the 2050s, the mean monthly rainfall is more as compared to 2030s for all months but less than the baseline period except for September. For the 2050s, mean rainfall is more than the observed mean rainfall by 46% in September. For the period the 2070s, the mean monthly rainfall is more than the 2030s and 2050s period for all months except for August, September, and October. For these months, mean rainfall

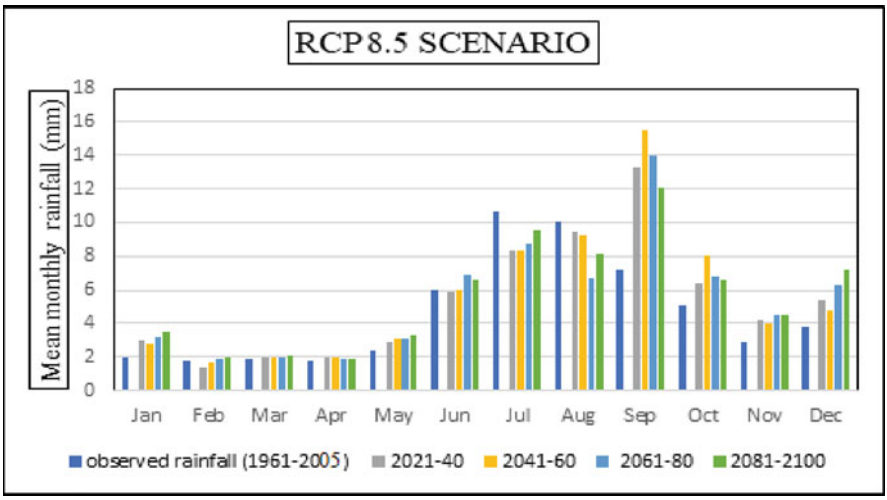

Fig. 30.6 Mean monthly change in projected rainfall for the RCP 8.5 scenario

is decreasing. For the period the 2090s, the mean rainfall is more than 2030s, 2050s, and 2070s for all months except for August, September, and October. For these months, mean rainfall for the period of the 2090s is less as compared to other periods.

30.4.4 Change in Dry and Wet Spell Length

30.4.4.1 RCP 2.6 Scenario

Figures 30.7 and 30.8 show the maximum dry spell and wet spell length days obtained for the RCP 2.6 scenario. The maximum dry spell days simulated by the CanESM2 model during the period 2021–2020 are less than the observed maximum dry spell days for the monsoon period. The wet day threshold is set as 0.1 mm/day for this analysis. For this scenario, the maximum dry spell length is less than the observed maximum dry spell length for June, July, August, September, October, November, and December for all the periods. For the remaining months maximum, the dry spell length is the same as the baseline period for all the periods. The maximum decrease in maximum dry spell length is observed for September for the period of the 2070s. For the 2070s, the maximum decrease compared to the baseline period is about 72%.

The maximum wet spell length with rainfall more than the wet day threshold is less than that of the baseline period for all the months except July, August, and September for all the periods. From Fig. 30.8, it is clear that we are getting an increase in rainfall only for these months. We are experiencing a decrease in rainfall

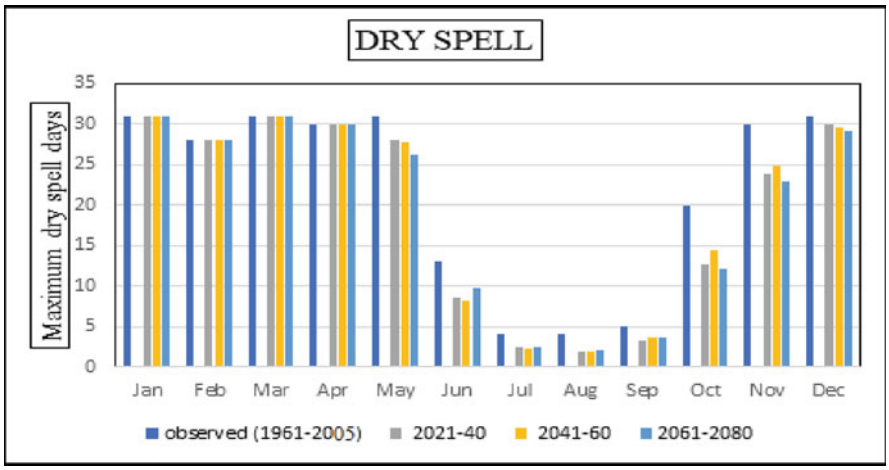

Fig. 30.7 Maximum dry spell length obtained for RCP 2.6 scenario

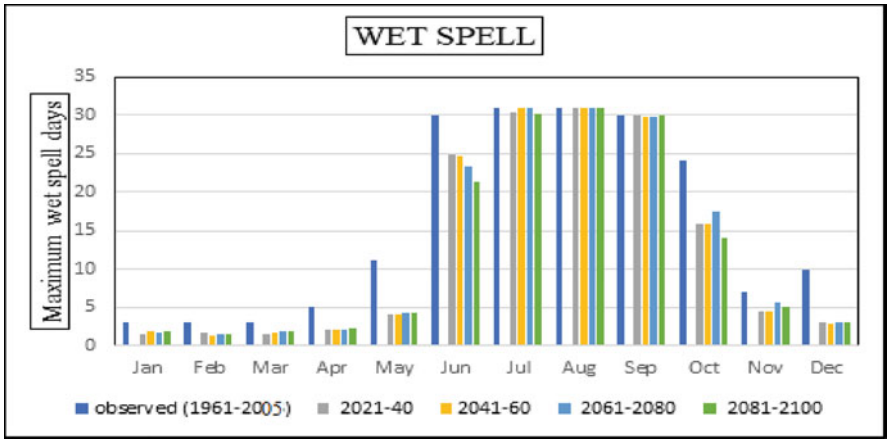

Fig. 30.8 Maximum wet spell length obtained for RCP 2.6 scenario

for the remaining months of all the periods. Also, there is a decrease in maximum wet spell length for June when the period increases.

30.4.4.2 RCP 4.5 Scenario

Figures 30.9 and 30.10 show the maximum dry spell and wet spell length days obtained for the RCP 4.5 scenario. The maximum dry spell days simulated by the CanESM2 model during 2021–2040 are less than the observed maximum dry spell days for the monsoon period. From Fig. 30.9, it is clear that the maximum dry spell observed for the 2030s, 2050s, 2070s, and 2090s is less than the baseline period for

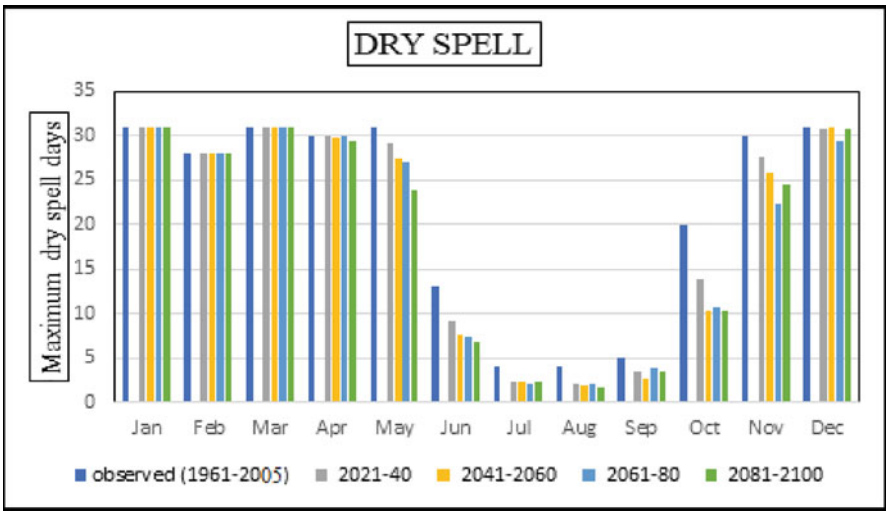

Fig. 30.9 Maximum dry spell length obtained for RCP 4.5 scenario

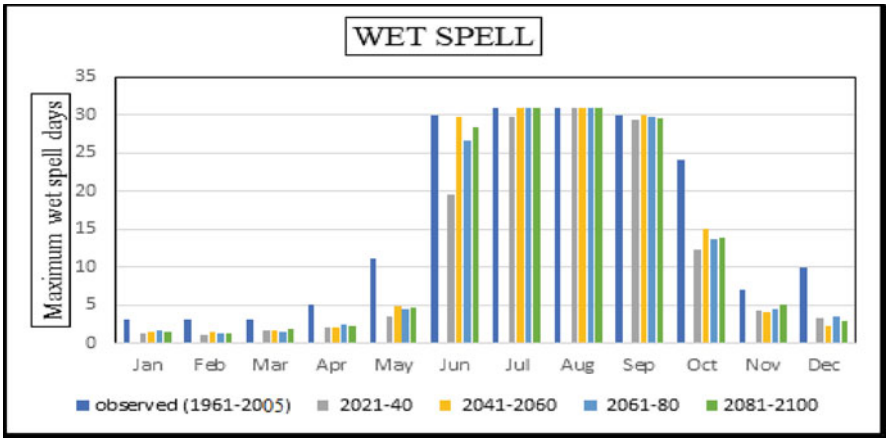

Fig. 30.10 Maximum wet spell length obtained for RCP 4.5 scenario

May, June, July, August, September, and November. For the remaining months, the maximum dry spell length is the same as that of the baseline period for all the periods. The maximum decrease in maximum dry spell length is observed for September for the period of the 2050s. For the 2070s, the maximum decrease compared to the baseline period is about 80%. For October also, there is a considerable decrease in maximum dry spell length for all the periods, and the maximum decrease is obtained for the period of the 2090s.

The maximum wet spell length with rainfall more than the wet day threshold is less than that of the baseline period for all the months except July, August, and September for all the periods. From Fig. 30.10, it is clear that we are only getting an

increase in rainfall for these months. We are experiencing a decrease in rainfall for the remaining months of all the periods. But compared to the RCP 2.6 scenario, there is an increase in maximum wet spell length for the June month with the increase in the period. In the 2070s, the maximum wet spell length observed for June month is the same as that of the baseline period. So as compared to the RCP 2.6 scenario, there is an increase in rainfall for June in the RCP 4.5 scenario.

30.4.4.3 RCP 8.5 Scenario

Figures 30.11 and 30.12 show the maximum dry spell and wet spell length days obtained for the RCP 8.5 scenario. The maximum dry spell days simulated by the

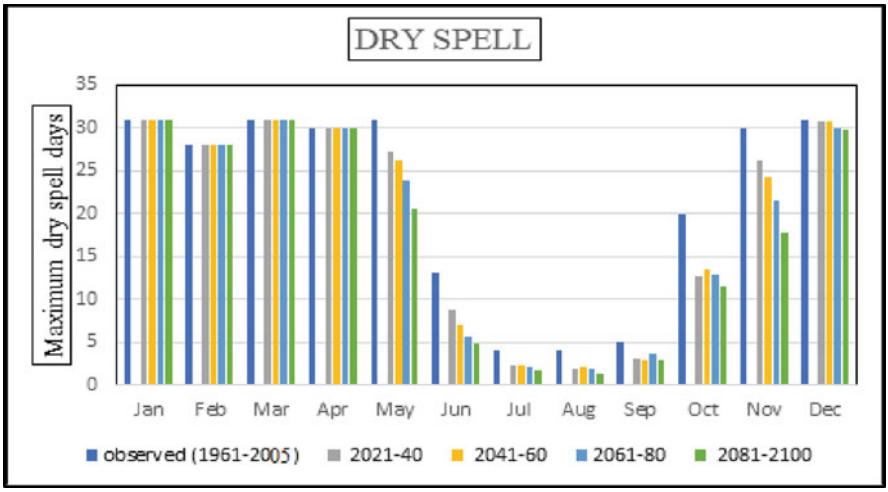

Fig. 30.11 Maximum dry spell length obtained for RCP 8.5 scenario

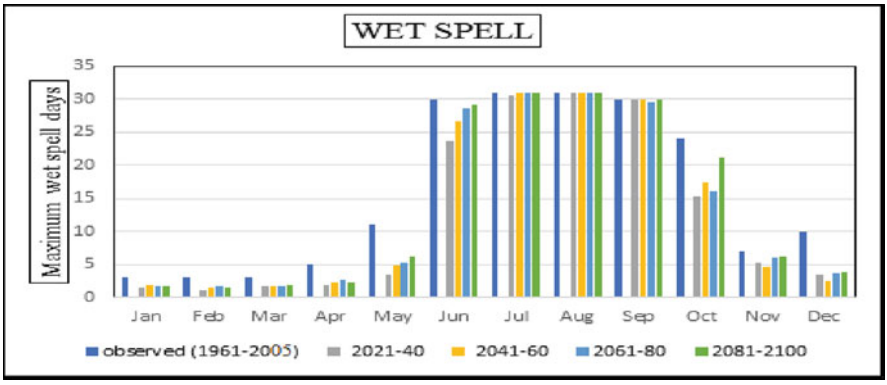

Fig. 30.12 Maximum wet spell length obtained for RCP 8.5 scenario

CanESM2 model from 2021 to 2040 are less than the observed maximum dry spell days for the monsoon period. From Fig. 30.11, it is clear that the maximum dry spell observed for the 2030s, 2050s, 2070s, and 2090s is less than the baseline period for May, June, July, August, September, October, and November. For the remaining months, the maximum dry spell length is the same as the baseline period for all the periods. The maximum decrease in maximum dry spell length is observed for September for the period of the 2090s. For the 2090s, the maximum decrease compared to the baseline period is about 78%. For October, there is a considerable decrease in maximum dry spell length for all the periods, and the maximum decrease is obtained for the 2090s.

The maximum wet spell length with rainfall more than the wet day threshold is less than that of the baseline period for all the months except July, August, and September for all the periods. From Fig. 30.12, it is clear that only for these months we are getting an increase in rainfall. We are experiencing a decrease in rainfall for the remaining months of all the periods. But as compared to the RCP 2.6 scenario, there is an increase in maximum wet spell length for the June month with the increase in the period. So as compared to the RCP 2.6 scenario, there is an increase in rainfall for the June month in the RCP 8.5 scenario also, whereas, for the RCP 4.5 scenario, rainfall shows a decreasing trend after the 2050s and then increases for the June month.

30.5 Conclusion

This study investigates the upper Godavari basin's vulnerability to climate change by forecasting future rainfall in the basin for the years 2021–2100. The daily precipitation from the general circulation model CanESM2 was downscaled using the statistical downscaling model (SDSM) under three different representative concentration pathway scenarios (RCP 2.6, RCP 4.5, and RCP 8.5). The study also compares the observed monthly rainfall from 1961 to 2005 to the changes in mean monthly rainfall under three RCP scenarios.

The data collected during SDSM's calibration and validation revealed that the model accurately replicated observed precipitation. As a result, the SDSM model is appropriate for this research. Looking at the data for past rainfall simulated by the GCM, it can be inferred that the CanESM2 model is a good fit for forecasting future rainfall in the upper Godavari river basin. Except for June, July, and August, the percentage change in mean monthly rainfall suggested an increase in future rainfall relative to observed rainfall in all three RCP scenarios. However, the average annual rainfall under RCP 4.5 and RCP 8.5 scenario shows a decreasing trend compared to the observed rainfall. While considering the near future (the 2030s), the increase in average annual rainfall in the 2030s for the RCP 2.6 scenario is about 4% compared to the baseline period (1961–2005). For the RCP 4.5 scenario, the projected precipitation indicates a decrease in average annual rainfall for the 2030s of about 13 % compared to the baseline period (1961–2005). In the RCP 8.5 scenario, the mean

annual rainfall is decreasing is about 7.5 % as compared to the baseline period (1961–2005). The findings of this study are critical for planning and managing water resources in the basin in the face of changing climatic circumstances.

The outcomes from the present study lead to some important future directions of research. It would be interesting to use different statistical downscaling techniques like change factor of mean (CFM), quantile perturbation (QP), etc. among others to examine whether the future climate projections vary according to the downscaling techniques. Further the study has considered only one GCM, ensemble of GCMs from the latest phase CMIP6 can be incorporated. Moreover, the future climate projections from this study can be used to study the impact of climate change on runoff generation in basin by using hydrological models.

References

Abbaspour KC, Faramarzi M, Ghasemi SS, Yang H (2009) Assessing the impact of climate change on water resources in Iran. Water Resour Res 45(10):W10434. https://doi.org/10.1029/2008WR007615

Anandhi A, Nanjundiah RS (2015) Performance evaluation of AR4 climate models in simulating daily precipitation over the Indian region using skill scores. Theor Appl Climatol 119:551–566. https://doi.org/10.1007/s00704-013-1043-5

Asadi Zarch MAA, Sivakumar B, Sharma A (2015) Droughts in a warming climate: a global assessment of standardized precipitation index (SPI) and reconnaissance drought index (RDI). J Hydrol 526:183–195

Cao C, Yan B, Guo J, Jiang H, Li Z, Liu Y (2021) A framework for projecting future streamflow of the Yalong River basin to climate change. Stoch Env Res Risk A. https://doi.org/10.1007/s00477-021-02009-w

Chu J-L, Kang H, Tam C-Y, Park C-K, Chen C-T (2008) Seasonal forecast for local precipitation over northern Taiwan using statistical downscaling. J Geophys Res 113:D12118. https://doi.org/10.1029/2007JD009424

Chu JT, Xia J, Xu CY, Singh VP (2010) Statistical downscaling of daily mean temperature, pan evaporation and precipitation for climate change scenarios in Haihe River China. Theor Appl Climatol 99(1–2):149–161. https://doi.org/10.1007/s00704-009-0129-6

Deepthi B, Sunil A, Saranya CN, Mirajkar AB, Adarsh S (2020) Ranking of CMIP5-based general circulation models using compromise programming and TOPSIS for precipitation: a case study of Upper Godavari basin, India. Int J Big Data Mining Global Warming 2(1):2050007. https://doi.org/10.1142/S2630534820500072

Fowler HJ, Blenkinsop S, Tebaldi C (2007) Linking climate change modelling to impact studies: recent advances in downscaling techniques for hydrological modelling. Int J Climatol 27:1547–1578. https://doi.org/10.1002/joc.1556

Gebremedhin MA, Abraha AZ, Fenta AA (2018) Changes in future climate indices using statistical downscaling model in the upper baro basin of Ethiopia. Theor Appl Climatol 133(1–2):39–46. https://doi.org/10.1007/s00704-017-2151-4

Hassan Z, Shamsudin S, Harun S (2014) Application of SDSM and LARS-WG for simulating and downscaling of rainfall and temperature. Theor Appl Climatol 116(1–2):243–257. https://doi.org/10.1007/s00704-013-0951-8

Huang J, Zhang J, Zhang Z, Xu C, Wang B, Yao J (2011) Estimation of future precipitation change in the Yangtze River basin by using statistical downscaling method. Stoch Environ Res Risk A 25(6):781–792. https://doi.org/10.1007/s00477-010-0441-9

Hunt KMR, Turner AG, Shaffrey LC (2020) The impacts of climate change on the winter water cycle of the western Himalaya. Clim Dyn 55:2287–2307. https://doi.org/10.1007/s00382-020-05383-3

IPCC (2014) Climate change 2014: synthesis report. In: Pachauri RK, Meyer LA (eds) Contribution of working groups I, II and III to the fifth assessment report of the intergovernmental panel on climate change. IPCC, Geneva, p 151

John CK, Pu JH, Moruzzi R, Pandey M (2021a) Health-risk assessment for roof-harvested rainwater via QMRA in Ikorodu area, Lagos, Nigeria. J Water Clim Change 12(6):2479–2494

John CK, Pu JH, Pandey M, Moruzzi R (2021b) Impacts of sedimentation on rainwater quality: case study at Ikorodu of Lagos, Nigeria. Water Supply 21(7):3356–3369

Kundzewicz ZW, Mata LJ, Arnell N, Doll P, Jimenez B, Miller K, Oki T, Sen Z, Shiklomanov I (2008) The implications of projected climate change for freshwater resources and their management. Hydrol Sci J 53:3–10. https://doi.org/10.1623/hysj.53.1.3

Leung LR, Qian Y, Bian X, Washington WM, Han J, Roads JO (2004) Mid-century ensemble regional climate change scenarios for the Western United States. Clim Chang 62:75–113

Mahmood R, Babel MS (2014) Future changes in extreme temperature events using the statistical downscaling model (SDSM) in the trans-boundary region of the Jhelum river basin. Weather Clim Extremes 5:56–66. https://doi.org/10.1016/j.wace.2014.09.001

Meenu R, Rehana S, Mujumdar PP (2013) Assessment of hydrologic impacts of climate change in Tunga-Bhadra river basin, India with HEC-HMS and SDSM. Hydrol Process 27(11): 1572–1589. https://doi.org/10.16943/ptinsa/2018/49506

Milly PCD, Dunne KA, Vecchia AV (2005) Global pattern of trends in streamflow and water availability in a changing climate. Nature 438:347–350. https://doi.org/10.1038/nature04312

Munawar S, Rahman G, Moazzam MFU, Miandad M, Ullah K, Al-Ansari N, Linh NTT (2022) Future climate projections using SDSM and LARS-WG downscaling methods for CMIP5 GCMs over the transboundary Jhelum River basin of the Himalayas Region. Atmos 13:898. https://doi.org/10.3390/atmos13060898

Obeysekera J, Irizarry M, Park J, Barnes J, Dessalegne T (2011) Climate change and its implications for water resources management in south Florida. Stoch Env Res Risk A 25:495–516. https://doi.org/10.1007/s00477-010-0418

Prudhomme C, Reynard N, Crooks S (2002) Downscaling of global climate models for flood frequency analysis: where are we now? Hydrol Process 16:1137–1150. https://doi.org/10.1002/hyp.1054

Pu JH, Wallwork JT, Khan M, Pandey M, Pourshahbaz H, Satyanaga A, Hanmaiahgari PR, Gough T (2021) Flood suspended sediment transport: combined modelling from dilute to hyper-concentrated flow. Watermark 13(3):379

Rajeevan M, Bhate J, Jaswal AK (2008) Analysis of variability and trends of extreme rainfall events over India using 104 years of gridded daily rainfall data. J Geophys Res 35:L18707. https://doi.org/10.1029/2008GL035143

Raju KS, Kumar DN (2018) Impact of climate change on water resources –with modeling techniques and case studies. Springer, Cham

Saraf VR, Regulwar DG (2016) Assessment of climate change for precipitation and temperature using statistical downscaling methods in Upper Godavari River Basin, India. J Water Resour Prot 8:31–45. https://doi.org/10.4236/jwarp.2016.81004

Shankar MS, Pandey M, Shukla AK (2021) Analysis of existing equations for calculating the settling velocity. Watermark 13(14):1987

Siabi EK, Kabobah AT, Akpoti K, Anornu GK, Amo-Boateng M, Nyantakyi EK (2021) Statistical downscaling of global circulation models to assess future climate changes in the Black Volta basin of Ghana. Environ Chall 5:100299. https://doi.org/10.1016/j.envc.2021.100299

Sigdel M, Ma Y (2016) Evaluation of future precipitation scenario using statistical downscaling model over humid, subhumid, and arid region of Nepal. Theor Appl Climatol 123(3–4): 453–460. https://doi.org/10.1007/s00704-014-1365-y

Sunil A, Deepthi B, Mirajkar AB, Adarsh S (2020) Modeling future irrigation water demands in the context of climate change: a case study of Jayakwadi command area, India. Model Earth Syst Environ. https://doi.org/10.1007/s40808-020-00955-y

Wallwork JT, Pu JH, Kundu S, Hanmaiahgari PR, Pandey M, Satyanaga A, Pandey M, Satyanaga A, Amir Khan M, Wood A (2022) Review of suspended sediment transport mathematical modelling studies. Fluids 7(1):23

Wang X, Yang T, Shao Q, Acharya K, Wang W, Yu Z (2012) Statistical downscaling of extremes of precipitation and temperature and construction of their future scenarios in an elevated and cold zone. Stoch Environ Res Risk A 26(3):405–418. https://doi.org/10.1007/s00477-011-0535-z

Wilby RL, Wigley TML (2000) Precipitation predictors for downscaling: observed and general circulation model relationships. Int J Climatol 20:641–661. https://doi.org/10.1002/(SICI)1097-0088(200005)20:63.0.CO;2-1

Wilby RL, Hay LE, Gutowski WJ, Arritt RW, Takle ES, Leavesley GH, Clark M (2000) Hydrological responses to dynamically and statistically downscaled general circulation model output. Geophys Res Lett 27:1199–1202

Wilby RL, Dawson CW, Barrow EM (2002) SDSM — a decision support tool for the assessment of regional climate change impacts. Environ Model Softw 17:147–159

Chapter 31
Projecting Future Maximum Temperature Changes in River Ganges Basin Using Observations and Statistical Downscaling Model (SDSM)

Nitesh Gupta, Jitendra Patel, Shivani Gond, Ravi Prakash Tripathi, Padam Jee Omar, and P. K. S. Dikshit

Abstract Climate change is the most considerable peril to the environment and a significant concern for humans of twenty-first century, which affects life all around the globe. River Ganges basin is highly vulnerable to climate change, which plays a vital role in socio-economic activities and the water supply for livelihood and irrigation in the northern part of India. A statistical downscaling model (SDSM) is used to forecast future changes in the maximum temperature of the Ganges basin (India) due to climate change under the 2.6, 4.5, and 8.5 RCPs scenarios of the CanESM2 model outputs for the forthcoming annual change (2006–2099) as well as monthly changes in maximum temperatures. In addition to that, the use of 26 large-scale climatic variables that were produced using data from the NCEP reanalysis (1961–2005) and the Canadian Earth System Model (CanESM2, 1961–2100) is employed. It is critical to identify the best predictors to use for the simulation phase for each location using SDSM. The investigation revealed that there was an increase of between 0.4 and 3.4 °C in the maximum average temperature over the basin at study stations. Furthermore, according to the RCP 8.5 scenario of the CanESM2 model, these maximum temperature changes will be raised to a greater extent than

N. Gupta
Department of Civil Engineering, Institute of Technology, Nirma University, Ahmedabad, Gujarat, India

J. Patel
Department of Civil Engineering, National Institute of Technology, Calicut, Kerala, India

S. Gond · P. K. S. Dikshit
Department of Civil Engineering, Indian Institute of Technology (BHU), Varanasi, Uttar Pradesh, India

R. P. Tripathi
Department of Civil Engineering, Rajkiya Engineering College, Sonbhadra, Uttar Pradesh, India

P. J. Omar (✉)
Department of Civil Engineering, Motihari College of Engineering, Motihari, Bihar, India

M. Pandey et al. (eds.), *River Dynamics and Flood Hazards*, Disaster Resilience and Green Growth, https://doi.org/10.1007/978-981-19-7100-6_31

under the RCP 2.6 and RCP 4.5 circumstances. The months of March–July were predicted to have significant raise temperature (maximum) in all scenarios and the least variation in maximum temperature projection during August and September. According to an uncertainty analysis linked to model scenarios, the CanESM2 model under scenario RCP 4.5 performed the best in the simulation of future maximum temperatures of all scenarios. The downscaled data provide better management of projected temperature and, ultimately finer scale adaptation plans in the basin.

Keywords Climate projection · GCM · Statistical downscaling · SDSM · Predictors · Maximum temperature

31.1 Introduction

The "climate change" is a term used for a long-term statistically changed behavior of climatic variables for a specific region or the earth as a whole; these changes are persistent and sometimes irreversible. Stratospheric Green House Gases (GHG) concentrations being perturbed appear to be the primary driver of recent climate change. Anthropogenic activities by human beings have been affecting the environment predominantly for centuries (Jana et al. 2021; Ashiq et al. 2010). However, the worldwide industrial revolution was the point when the consequences of human activities began to appear on a global scale (Baede et al. 2001); along with that, uncontrollable urbanization caused the degradation of forests and trees and has increased GHGs emissions. According to experts, global warming is one element that significantly impacts regional and global rainfall patterns (Omar et al. 2017; Gupta et al. 2021a, b). According to the fifth Assessment Report of the IPCC (2013), a report based on scientific assessment (Alexander 2016) indicated the rise of mean global (ocean and land) average temperature by 0.85 °C during 1800–2012. Rising carbon dioxide concentrations are causing the planet to heat up. It would further increase between 1.4 °C and 5.8 °C by the last quarter of the twenty-first century. Along with that, there has been an increment in the concentration of CO_2 by twofold in the environment. CO_2 has the property of trapping the heat provided by sun's rays. The higher the level of CO_2, the greater is the amount of heat trapped (Horton 1995). This results in an increase in atmospheric temperature leading to global warming. Global warming can result in many serious changes in the environment, which can ultimately affect human health (Wallwork et al. 2022). It can also cause sea level rise, which can lead to loss of coastal land, changes in rainfall patterns, increased risk of drought and floods, and threats to biodiversity (Singh et al. 2022). The effects are already evident in some areas such as Nunavut, Canada. The World Health Organization (WHO) reports that climate change is responsible for at least 150,000 deaths per year, a number that is expected to double by 2030 (Kasotia 2007). As a result of rising global surface temperatures, hazards such as droughts (Gupta et al. 2022), floods (Omar and Kumar 2021), high intensity storms, sea level rise are likely to increase. Flash floods will carry heavy sediment load (Omar et al. 2022), which may

impact the performance of any stormwater management system (Pandey et al. 2022; Almasalmeh et al. 2022).

The trend analysis technique aids in the examination of shifting rainfall and temperature patterns (Jones and Moberg 2003; Omar et al. 2019). A method for estimating the quantity of stream flows, soil moisture, and groundwater reserves, as well as a framework for decision-makers who want to ensure that enough water is available to all users at all times (Saddique et al. 2020; Omar et al. 2020; Gupta et al. 2021a, b; Shekhar et al. 2021). Revadekar et al. (2011) and Sheikh et al. (2015) both found an increasing tendency in warm temperature extremes over South Asia, despite a mixed trend in precipitation. Indian subcontinent in South Asia is one of the regions experiencing frequent and sharp increment in the minimum surface temperature, and extreme hot and cold events have shown the climatic inclination towards the warmer side (Jones 1994; Kothawale and Rupa Kumar 2005). The obtained results in the present study for the Ganga river basin are alarming. They show a strong coincidence (Krishnan et al. 2019), in which it is concluded that if the increment in global mean temperature happens to be retained at 1.5 °C, then there will be an elevation in temperature by 0.3–0.7 °C in Hindu Kush Himalaya (HKH) region, along with the change in the projected temperature by 2.5 ± 1.5 °C for RCP4.5 and 5.5 ± 1.5 °C for RCP8.5 by the end of the twenty-first century.

In order to have a better scientific knowledge of large-scale climate change (Dixon et al. 2016) and global warming effects during future periods, General Circulation Models (GCMs) runs can be used (Semenov and Stratonovitch 2010; Shankar et al. 2021). GCMs provide information that increasing GHGs concentrations will have significant effects on global as well as regional scale. One of the drawbacks of GCMs owing to the more coarse resolution is that they face significant biases and a high level of uncertainties in the representation of the current as well as future climate (Shrestha et al. 2021; Meenu et al. 2013). Therefore, the utility of GCMs is unfortunately restricted for local impact studies (Lutz et al. 2016). Moreover, it is all because of their spatial resolution (50,000 km^2) and incapability of resolution of significant sub-grid scale features such as topography and clouds (Shivashankar et al. 2022; Akhter et al. 2018). Recently, the dynamical (i.e., the regional climate model), as well as statistical techniques of downscaling, have been extensively developed (Dibike and Coulibaly 2005) to facilitate the information based on climate change at a refined resolution than that obtained through GCMs (Meher et al. 2017). Observation of data outcome of significant fine resolution for the daily climate is efficient to facilitate these types of impact studies for decades from the past but insufficient to do so for the future. Although GCMs are the conventional sources for the prediction of future climate such as models-scenarios output, these model outputs with substantial coarser spatial resolution cannot be directly implemented for fine-scale impact studies (Wilby and Dawson 2004). All of these model outputs are time-dependent and numerically simulated in three dimensions heat exchanges, atmospheric motions, and interactions among ice, ocean, and land (Dracup and Vicuna 2005). Moreover, the large extents of biases are comprised of all model outputs that, if not taken care of will definitely cause the impact assessments to involve significant errors. Which makes it compulsory for GCM to go through

bias correction and spatial downscaling before they are used for impact analysis on a regional/local scale (Wilby et al. 2002; Fowler et al. 2007). In order to provide the best possible information, downscaling of data is compulsorily done, the predictor selection, which is the foremost important step in downscaling, a number of techniques have been analyzed by the data scientists for the improvement of predictor selection (Hashemi-Ana et al. 2015). Therefore, due to economical, computationally compatible, flexible, and quickly transferable aspects, downscaling methods have gained the publicity in recent years and have been used enormously for a number of impact assessments of change in climate (Goubanova et al. 2011; Wang et al. 2014). One of them particularly is predicted hydrologic impact studies under the consequences of climate changes (Kure et al. 2013; Zuo et al. 2015). At the regional and national levels, this information is critical to long-term planning of mitigation and adaptation measures (Munawar et al. 2022; Frias et al. 2012; Gu et al. 2012). For the majority of statistical downscaling strategies, the assumption that the statistical link between large-scale GCM outputs and fine-scale observational data for the future climate is the same as for the present-day climate change is critical (Pandey et al. 2019; Boe et al. 2006; Fowler et al. 2007; Maraun et al. 2018). In the last few decades, some simple downscaling methods are developed that straight away involve GCM precipitation as a predictor and their model outputs include bias correction too (Iizumi et al. 2011). Several hydro-climatological investigations found that outputs from climate models that have been bias-corrected and statistically downscaled performed well (Li et al. 2017) and basin scales (Su et al. 2016; Chaudhary et al. 2019).

A number of studies has proposed different methods of statistical downscaling in the past two decades. These recently developed methods are based on the non-conventional algorithms which include Support vector machine (SVM), statistical downscaling model (SDSM), nonhomogeneous hidden Markov model (NHMM), and so on are all examples of automated statistical downscaling (ASD) (Hessami et al. 2008; Chen et al. 2012). Statistical methods such as correlation analysis, distribution functions, and uncertainty analysis have been used by a number of researchers for a comparative study of performance in apprehending the basic characteristics of climate change on a local scale. As a result, it was discovered that SDSM algorithms had a significant impact on downscaled outcomes (Tryhorn and Degaetano 2010; Gutmann et al. 2014). When it comes to downscaling results, picking a predictor is as important as SDSM (Kidson and Thompson 1998). Other researchers have found that the performance of predictors is dependent on the season and the region, and the combination of predictor variables outperforms the single variable predictors (Hessami et al. 2008). In addition to that, the downscaled results and number of predictors are related to each other as reported in some literature (Timbal et al. 2003; Meher and Das 2019). Predictors can be selected using p-values, correlation (CA), stepwise regression analysis (SRA), and partial correlation (PCA) (Huang et al. 2011; Mahmood and Babel 2013; Tripathi and Pandey 2021). However, this is still unclear how different methods for predictor selection affect the downscaled results by predictor combination and the process of predictor combination itself. According to a few studies, climate change has an impact on temperature trends (Rahmstorf and Ganopolski 1999; Goyal and Ojha 2012; Toros et al. 2015;

Whan et al. 2014; Abbasnia and Toros 2016) in the coming decades. The outputs from GSM and the requisite information on hydro-climatic conditions at the watershed level present the greatest obstacles in studies of the influence of climate change on hydrology and water resources (Salon et al. 2008; Willems and Vrac 2011). The accuracy of the downscaling methods that depend on applying the relationships between large-scale predictors (i.e., GCM results) and local scale predict ands over the Ganges River Basin, India is yet scanty. In view of the need for high-resolution projections to establish a baseline for subsequent climate impact studies, accordingly, this study aimed to determine the potential applicability of SDSM in the daily downscaling of maximum temperature (T_{max}) for selected stations of the River Ganges Basin, India. In SDSM uncertainty assessment, the selection of appropriate predictor variables is critical for NCEP reanalysis data sets. It also includes an application of SDSM for climate change scenario generation and comparing downscaled daily maximum temperature series for 1969–2005 with three future periods during near future (2011–2040, 2041–2070), and far future (2071–2099) while downscaling CanESM2 model output in current conditions using the statistical downscaling approach (2.6, 4.5, and 8.5 RCPs). Therefore, the findings of this study will aid in the development of long-term climate change adaptation and mitigation plans to counteract the negative effects of climate change in the basin.

31.2 Study Area and Data Description

Ganges River Basin (Uttar Pradesh, Uttarakhand, and West Bengal), India, Nepal, Tibet, and Bangladesh, are all included in the watershed zone of the Ganges River's east longitudes of 73°30′–89°0′ and north latitudes of 22°30′–31°30′. The Ganges sub-basin (Fig. 31.1) covers an area of 1,086,000 km^2, with a drainage area of

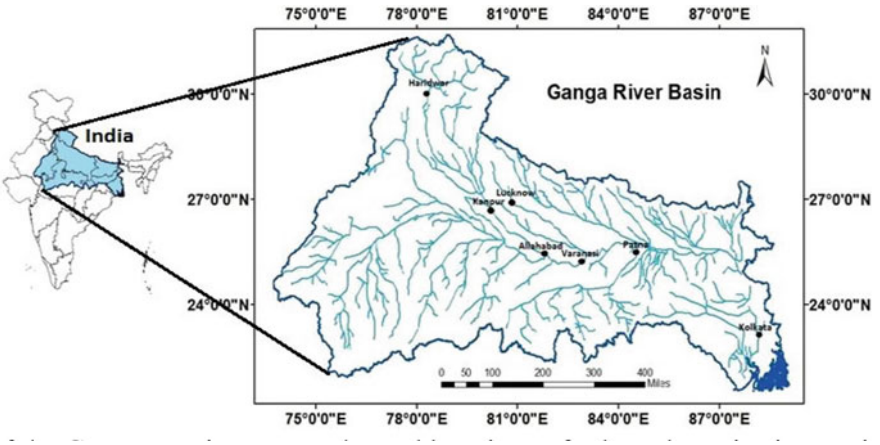

Fig. 31.1 Map of the Ganges Basin topography and locations of selected monitoring stations in India

861,404 km^2 in India, accounting for 26.2% of the country's total land area. This basin is surrounded by the Himalayas and Aravallis, the ridge that separates it from India's Indus basin, Vindhya and Chhota Nagpur plateaus, and the Brahmaputra ridge. Sub-basin is bordered by the Himalayas, the Aravallis, a ridge dividing it from the Indus basin, Vindhya and Chhota Nagpur plateaus, and the Brahmaputra ridge.

Seven meteorological stations in India, namely Allahabad, Haridwar, Kanpur, Kolkata, Lucknow, Patna, and Varanasi also the heavenly cities of River Ganges Basin employed in the downscaling trials. The sites were selected to reflect as many distinct climatic conditions as feasible for the basin, which is predominantly classified as humid subtropical with dry winter (CWa) and semi-arid (BS) in areas of the Western U.P. The occurrences of temperature fluctuate anywhere from 0 °C to 50 °C, with cyclical droughts and floods due to unpredictable rains making it a state of extremes in India. Summers are scorching hot, winters are freezing cold, and the rainy season can be either exceedingly wet or incredibly dry. The monsoon season is when most of the year's precipitation falls (annual rainfall ranges from 948 to 2986 mm).

31.3 Data Sets

The SDSM model can be used to statistically downscaling data from GCM model outputs (Table 31.1) in order to assess future temperature changes.

Daily data of maximum temperature (T_{max}), data records has been used as predict and variables, sourced India Meteorological Department (IMD), Pune, for different periods, mainly from 1971 to 2005, more details of seven stations from IMD (http://www.imd.gov.in/pages/obs_network.php?id=01) are provided in Table 31.2.

In downscaling studies, the 850-hPa level predictor variables for station Haridwar may not be used because Kolkata is located at a lower altitude than Haridwar. The graphical variation of maximum monthly temperature for different study stations has been illustrated in Fig. 31.2.

Furthermore, for the predictor variables, the reanalysis results are used as surrogates for observed data (Shashikanth et al. 2014). A total of 26 standardized surface and atmospheric predictor variables for the GCM model were acquired from NCEP reanalysis data for the same time period (1971–2005) on the SDSM (http://co-public.lboro.acwd/cocwd/SDSM/).

Table 31.1 GCM model and their characteristics as SDSM input

GCM	IPCC	Representative concentration pathways	Resolution	Reference
CanESM2	IPCC5	RCP2.6, RCP4.5 and RCP8.5	2.81° × 2.81°	AR5, Canadian Centre for Climate Modelling and Analysis (CCCma), Canada

Table 31.2 Geographic and climatic information of studied meteorological stations

Station index	Name	Latitude	Longitude	Altitude (m)	Geographical and Climatic Details
42475	Allahabad	25°27′	81°44′	98	Subtropics; humid; hot summer
99918	Haridwar	29°56′	78°09v	295	Humid
42366	Kanpur	26°26′	80°22′	126	Tropical; warm and temperate
42807	Kolkata	22°34′	88°21′	14	Tropical wet and dry/savanna
42369	Lucknow	26°45′	80°53′	128	Extreme type of continental; humid subtropical
42492	Patna	25°36′	85°06′	60	Humid subtropical; extreme type of continental
42483	Varanasi	25°18′	83°01′	90	Humid subtropical; large variations between summer and winter

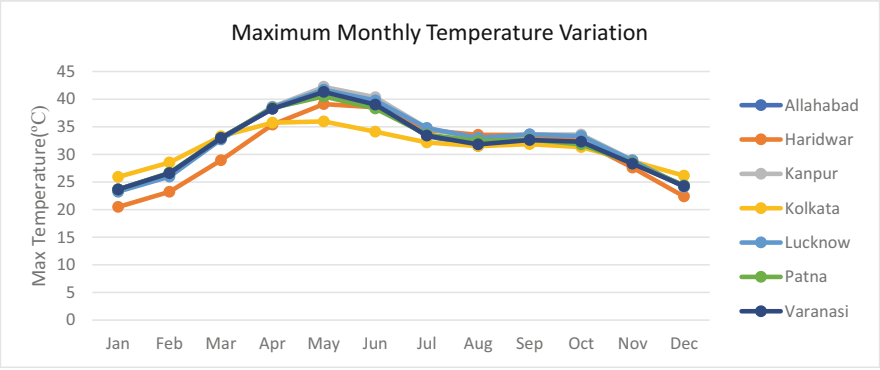

Fig. 31.2 The monthly maximum temperature variance at weather stations of the River Ganges Basin over the baseline period (1971–2005)

31.4 Data Outputs

Simulated daily maximum temperatures (T_{max}) for the current scenarios (1971–2005) and future scenarios (2.6, 4.5, and 8.5 RCPs) are analyzed statistically downscaled. The following outputs were obtained during the process.

- Predictors of the site's daily maximum temperature are stored in the T_{max}. PAR file.
- Model output of daily maximum temperature produced by the weather generator is T_{max}-syn.OUT for the current time (1971–2005).
- T_{max}-RCP 2.6 OUT: daily maximum temperature estimates under RCP2.6 (2006–2100).
- T_{max}-RCP 4.5 OUT is the daily maximum temperature for 2006–2100 under the RCP4.5 scenario.
- T_{max}-RCP 8.5 OUT is a daily maximum temperature forecast for RCP 8.5 (2006–2100).

31.5 Methodology

For impact assessment and adaptation research, GCM-based climate change estimations are only accessible at a coarser spatial resolution. It is required to downscale the GCMs to regional or local scale in order to better comprehend the change in climate variables.

31.6 Description of Statistical Downscaling Model (SDSM)

The basic principle of statistical downscaling was to identify statistical relationships between an observed small-scale predict and variable and larger-scale predictor variables for a baseline period and then applied these relationships to downscale future climate scenarios using a global climate model (GCM) output predictor (Wilby and Dawson 2013, 2007). SDSM makes use of atmospheric circulation indicators and regional moisture factors (e.g., the occurrence of rainfall or daily mean temperatures) to estimate daily weather features at specific locations, A conditional weather generator is used (Wilby et al. 2002). Due to its ability to replicate observed data properties, it was utilized in this situation. In that case, the downscaling process is either unaffected by an event (such as the occurrence of a wet day or the air temperature) or is dependent on an event (as with rainfall amounts).

Predictor (*Ui*) and predictor (*Xij*) have a direct linear relationship for conditions like temperature:

$$U_i = \gamma_0 + \sum_{j=1}^{n} \gamma_j X_{ij} + \varepsilon_i \tag{31.1}$$

On the day *i* the selected NCEP predictors are *Xij* and *Ui*, respectively, and *Ui* is the temperature. *j* is the least squares regression coefficient for each month. The deterministic component model error is rationalized on a daily basis, and the stochastically generated *i* is assumed to have a Gaussian distribution.

In order to downscale the maximum temperature (predictand), the following major steps were taken: (1) Data quality check and screening of predictors; (2) Calibration and validation of predictand data; (3) Generation of current and future time series data for *Tmax*; and (4) statistical analysis of downscaled current and projected *Tmax* for various scenarios, (5) Analysis of uncertainty.

31.7 Data Quality Check and Screening of Predictors

The vital stage of statistical downscaling was the screening and selection of appropriate predictors for downscaling predictands. The maximum temperature time series is considered an unconditional variable because it is normally distributed. SDSM software takes into account the direct association between observed maximum temperature and large-scale predictors as independent variables when choosing a multivariate regression model. When validating a model with regression parameters and NCEP and GCM predictors, it is common practice to construct a maximum of one hundred daily time series. However, twenty time series is regarded as the standard precedent, as it was established by previous study (Stern and Kaufmann 2000; Chu et al. 2010).

Although, the consensus is that a combination of variables is superior to individual variables in statistical downscaling, but finding a suitable combination of predictor variables is still a challenge because predictor choice can be complicated by the region, season, and predictands. There are many indicators that can be used to pick some effective atmospheric predictors from a large number of atmospheric predictors, such as partial correlation, correlation matrix, explained variance, P-value, histograms, and scatterplots. Multiple co-linearity, which can lead to incorrect end outcomes among predictors, must be taken into account while picking predictors. SDSM can be optimized using two methods: ordinary least squares (OLS) or dual simplex (DS). OLS is more efficient than DS and gives comparable outcomes. The Super Predictor, the first and most appropriate predictor, is easy to select; however, the second, third, fourth, and subsequent predictors are much more difficult (Mahmood and Babel 2013). According to Pu et al. (2021), a correlation coefficient less than 0.7 between two predictors is acceptable. With the coefficients of absolute and partial correlation between the predictor and predictand, the following equation can be used to figure out the percentage reduction in absolute partial correlation (*PRP*) (*R* and *Pr*, respectively).

$$PRP = \left(\frac{\mathrm{Pr} - R}{R}\right) \tag{31.2}$$

Consequently, the second-best predictor was determined by looking at the predictor with the lowest PRP score. The same method is used to select the third, fourth, and subsequent predictors, as described above.

Predictand variability can be described using one to three large-scale variables during calibration (Chu et al. 2010; Mahmood and Babel 2013). More predictors in the regression equation mean a greater chance of multiple co-linearity, hence using fewer predictors during calibration is preferred. There are decreased chances of experiencing multiple co-linearity during calibration when there are fewer predictors.

31.8 Calibration of Predictand Data and Validation

Measuring error results from the validation of the SDSM model while evaluating the multivariate regression model's performance for calibration of prediction outcomes. The first half of daily temperature data (1971–1995) was used to calibrate the model, while the second half (1995–2005) was used to validate the model. A monthly and annual sub-model of the SDSM was developed using NCEP predictors that were selected during screening at each location in the River Ganges basin in the current study. The performance indicators such as spatial-temporal standard error (SE), R squared, Durbin–Watson statistics, and mean bias error (MBE) were employed to calibrate SDSM (Chu et al. 2010; Huang et al. 2011; Mahmood and Babel 2014).

31.9 Weather Generator

Calibrating output and observed NCEP re-analyzed atmospheric variables were used to generate daily synthetic data for the historical time period. Using independent data, it validates the calibrated model and generates false time series for present climate conditions, allowing for a comparison between observed and model outcomes. Charts were plotted using graphical outputs from the statistical models. The statistical outputs that were utilized were the sum, mean, maximum, and minimum of the generated and observed meteorological data, respectively.

31.10 Climatic Scenarios Generation

Since climate change will be highly dependent on human activities in the future, the Intergovernmental Panel on Climate Change has released its fifth assessment report, which is referred to as AR5 (IPCC 2007), which evaluates various concentration scenarios based on Representation Concentration Pathways (RCPs), which are linked to the concentration of greenhouse gases rather than emissions. Four possible climatic futures have been selected for climate modelling and research, each of which is based on the amount of greenhouse gas emissions that can be expected in the following years. Radiative forcing levels in 2100 are the inspiration for the names of the three RCPs: RCP2.6, RCP4.5, and RCP8.5 (2.6, 4.5 and 8.5 W/m^2 respectively). The RCPs are consistent with a wide range of possible changes in future anthropogenic (i.e., human activities) greenhouse gas (GHGs) emissions, and aim to represent their atmospheric concentrations.

In this stage of the study, according to final regression equations and calibrated multivariate regression models between various predictors of large-scale variables with maximum temperature variables at study station scales in the observation period, the process of downscaling will be done on outputs of the CanESM2

model under various concentration scenarios during future periods. Thus, the daily maximum temperature time series at the station scale is simulated and produced for future periods.

31.11 Results and Discussion

There are two types of daily time series that are necessary for the SDSM model to be developed. The NCEP predictor and observed daily time series are shown here.

31.12 Selection of Predictors

The very first and appropriate predictor (super predictor) is crucial, whereas the second, third, fourth, and soon predictors are considerably more subjective. Table 31.3 summarizes the results of partial correlation between chosen CanESM2 model predictor variables and the maximum temperature variable at each study station.

31.13 Calibration and Validation

To evaluate the performance of multivariate regression models that is resulted from validation step of SDSM model, there are some measurement errors for calibration of predictions outputs. The 35 years of accessible temperature data were divided into two daily datasets; the first half (1971–1955) used 25 years of daily data for model calibration, while the second half (1995–2005) used model validation. In the present study, SDSM was developed a monthly and annual sub-model, with the NCEP predictors that were chosen throughout the screening procedure at each location in the river Ganges basin. Spatio-temporal standard error (SE) of predictions, R square (R^2), and Durbin–Watson statistics were used as performance indicators during the calibration of SDSM.

Overall results of different statistical measurement showed that the final regression equations have acceptable accuracy to predict daily maximum temperature during future decades based on large-scale atmospheric variables from each GCM model (Table 31.4). Also, statistical analysis of t-tests in any time scale like monthly and annually, showed that there is no significant difference in the critical level of 0.05 between final observational values of maximum temperature and final prediction variables at each study station during the period (1971–2005).

Table 31.3 CanESM2 model's partial connection between maximum temperatures observed at various stations over time

Predictor	Description	Station						
		Haridwar	Kanpur	Lucknow	Allahabad	Varanasi	Patna	Kolkata
Mslp	Mean sea level pressure	–0.009	0.01	0.005	–	–	0.033	0.032
p5_z	500 hPa vorticity	0.215	0.241	0.251	0.192	0.193	–	0.145
s850	850 hPa specific humidity	–	–	–	0.137	-0.165	–	–
P850	850 hPa geopotential height	–	–	–	–	–	0.054	–
Temp	Mean temperature at 2 m	0.228	0.29	0.269	0.388	0.365	0.372	0.294

Table 31.4 Results of SDSM model's calibration and validation phase in observed period (1971–2005)

Station	SE	R squared	Durbin–Watson
Haridwar	3.166	0.690	0.252
Kanpur	3.114	0.721	0.285
Lucknow	3.114	0.721	0.280
Allahabad	3.183	0.711	0.311
Varanasi	2.864	0.727	0.320
Patna	2.738	0.705	0.304
Kolkata	2.095	0.581	0.357

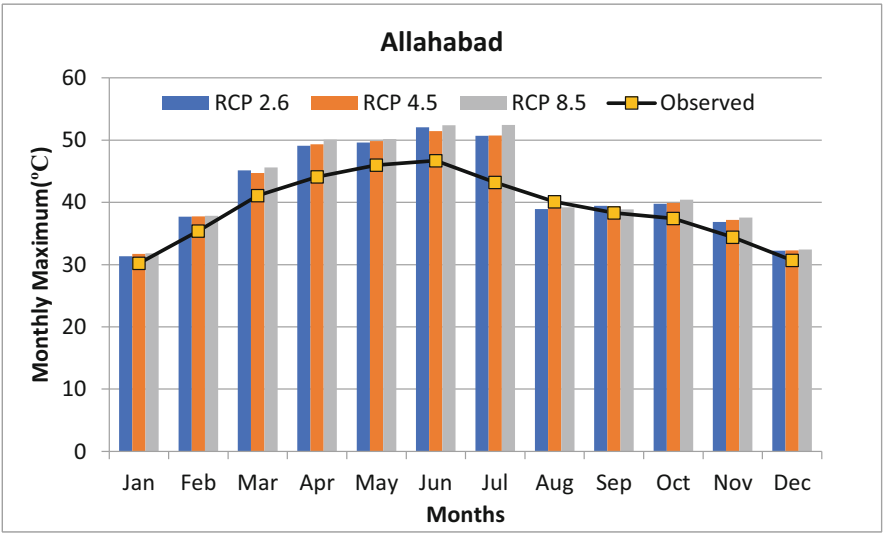

Fig. 31.3 Comparison between projected maximum temperature of different scenarios with observed temperature trend for Allahabad district

31.14 Changes in Future Monthly Temperature (T_{max})

After assessing the capabilities of SDSM to simulate the climate of the basic period (1971–2005), by establishing a statistical link between large- and small-scale climate factors, the daily maximum temperature (T_{max}) for future decades was calculated and analyzed. The local climates were forecast using the same set of predictors, but CanESM2 gave the time. According to Figs. 31.3, 31.4, 31.5, 31.6, 31.7, 31.8, 31.9, and 31.10, all of the RCPs agreed that the long-term maximum temperature in all of the study stations might be higher than the observed/historical maximum temperature. The months of March–July were predicted to have significant raise temperature (maximum) in all scenarios and the least variation in maximum temperature projection during August and September.

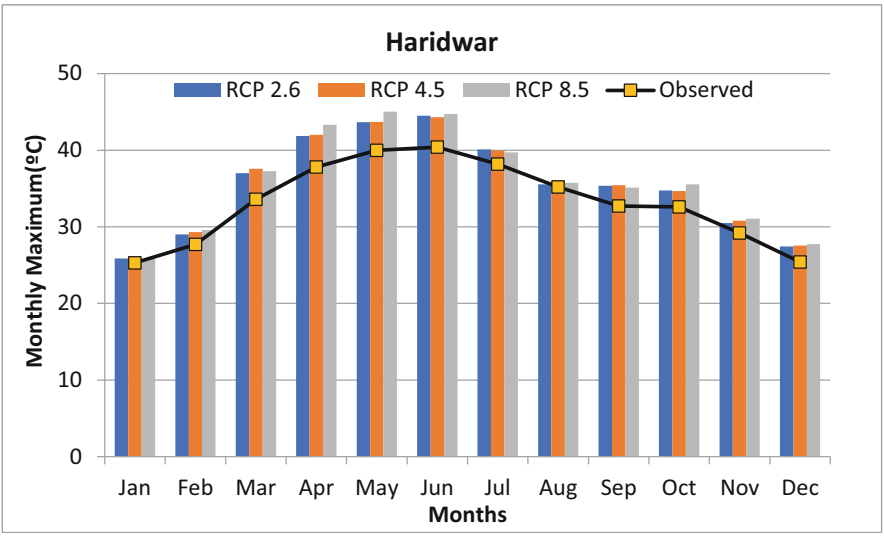

Fig. 31.4 Comparison between projected maximum temperature of different scenarios with observed temperature trend for Haridwar district

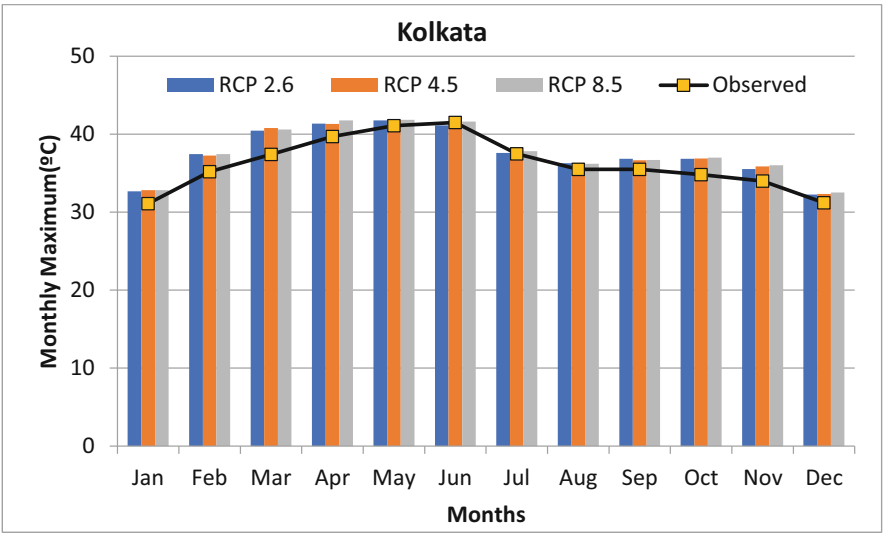

Fig. 31.5 Comparison between projected maximum temperature of different scenarios with observed temperature trend for Kolkata district

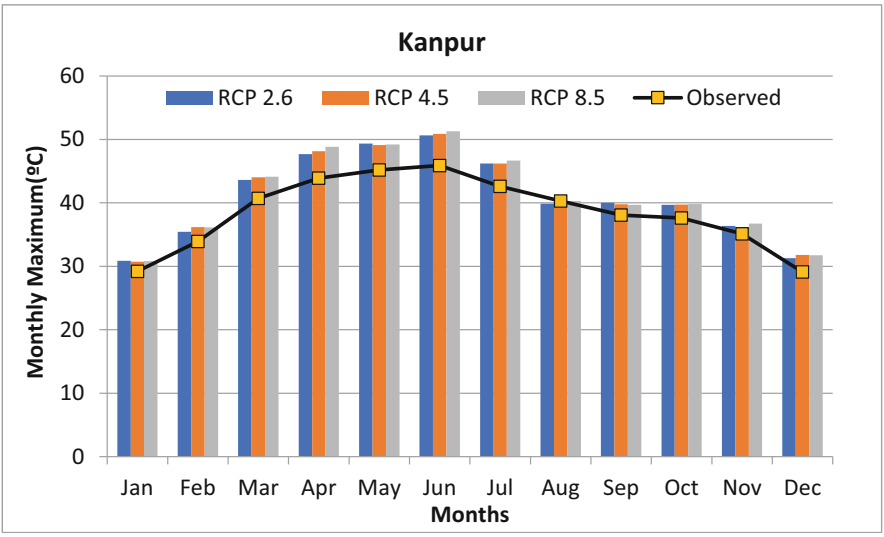

Fig. 31.6 Comparison between projected maximum temperature of different scenarios with observed temperature trend for Kanpur district

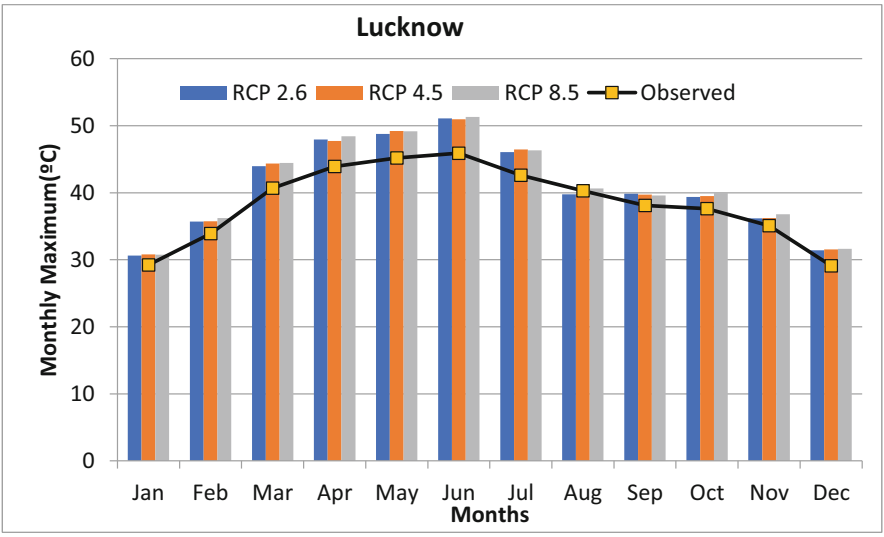

Fig. 31.7 Comparison between projected maximum temperature of different scenarios with observed temperature trend for Lucknow district

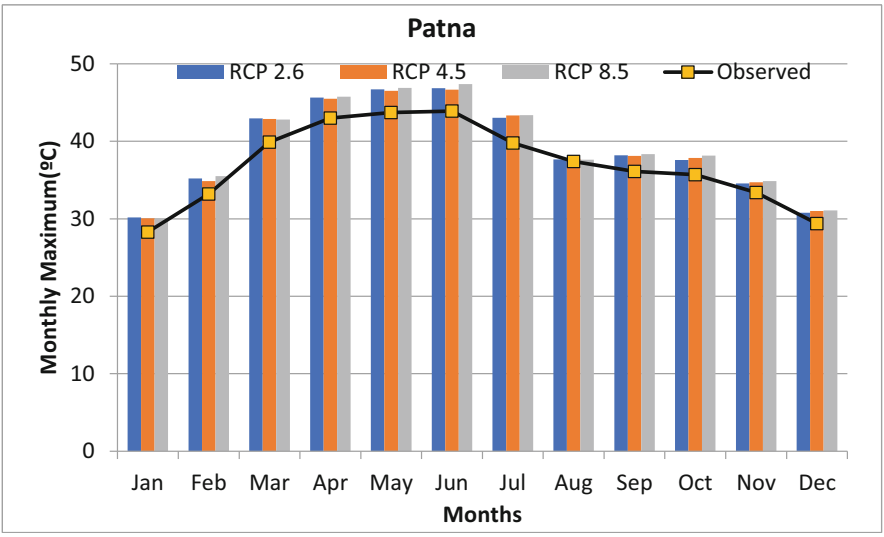

Fig. 31.8 Comparison between projected maximum temperature of different scenarios with observed temperature trend for Patna district

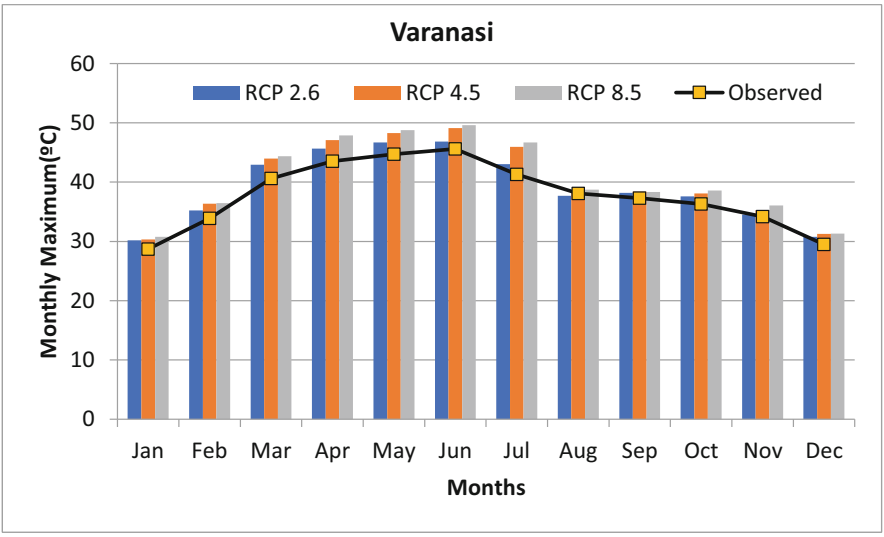

Fig. 31.9 Comparison between the projected maximum temperature of different scenarios with observed temperature trend for Varanasi district

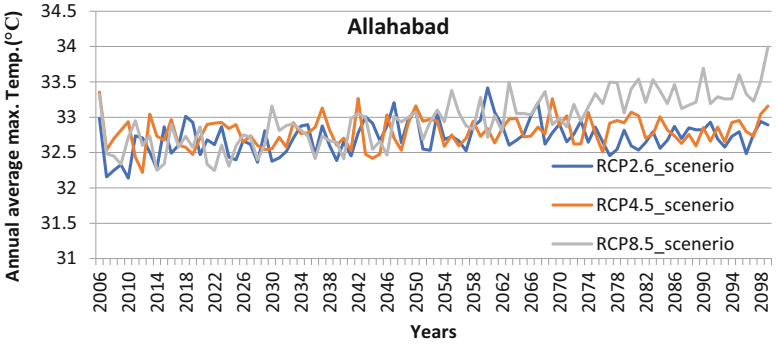

Fig. 31.10 Future projected scenarios of maximum temperature for period of 2006–2100 for Allahabad district

31.15 Changes in Future Annual Temperature (T_{max})

The daily maximum temperature (T_{max}) for future decades was estimated and examined after evaluating SDSM's capacity to simulate the climate of the base period (1971–2005) and creating a statistical connection between large- and small-scale climate parameters. The CanESM2 model outputs at a station size were used to downscale daily maximum temperatures for future decades in the river Ganges basin utilizing SDSM model capability. For two future eras, 2041–2070 and 2071–2099, temperature data was collected from each scenario's uncertainty analysis. Finally, each model scenario was used to compare predicted maximum temperature changes to those seen between 1971 and 2000. A rise in the maximum temperature is expected at all research sites over the next several decades, regardless of the model scenario that was used. The increase in the maximum temperature, on the other hand, varies from station to station and over time (Figs. 31.10, 31.11, 31.12, 31.13, 31.14, 31.15, and 31.16).

The projected T_{max} values are predicted for Allahabad, Haridwar, Kanpur, Kolkata, Lucknow, Patna, and Varanasi and results indicate an increase in temperature in coming years (as shown in Figs. 31.10, 31.11, 31.12, 31.13, 31.14, 31.15, and 31.16). However, GCM for the three scenarios indicated different increases in temperature for the period 2006–2099. The maximum increase in temperature indicated by the GCM was about 9% with respect to the base period (1971–2005). Figures 31.10, 31.11, 31.12, 31.13, 31.14, 31.15, and 31.16 illustrate the annual variations of the temperature of Ganges River basin under different RCPs scenarios. The maximum change in maximum temperature was in the range of 3.00 °C. The maximum temperature will approach to near range 32.5–34 °C in the twenty-first century, i.e., will increase in the range of 1.6 °C for Allahabad (Fig. 31.10), whereas for Haridwar, T_{max} will rise in the range 26.4–28.1 °C (Fig. 31.11). There is also a significant difference in maximum temperature between the stations in the north-western mountainous River Ganges Basin (Haridwar) and the plain region of the

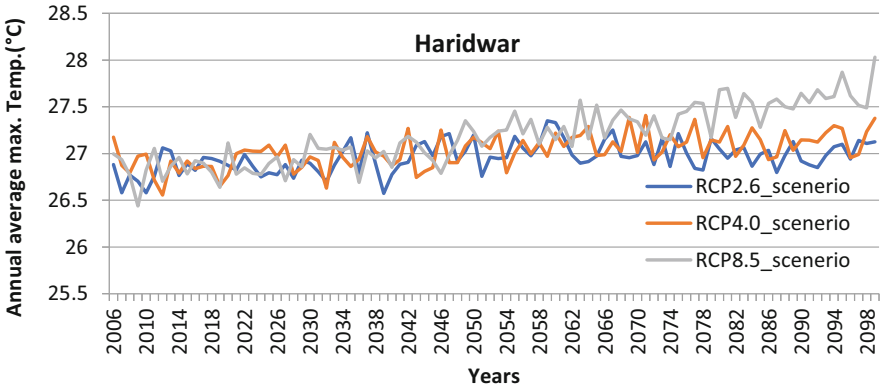

Fig. 31.11 Future projected scenarios of maximum temperature for period of 2006–2100 for Haridwar district

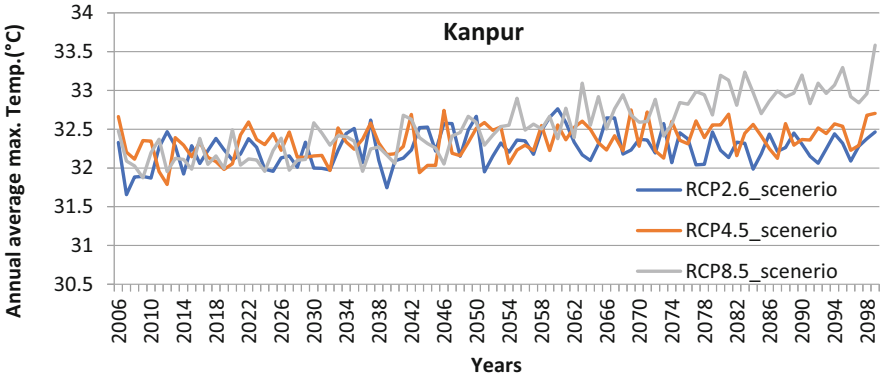

Fig. 31.12 Future projected scenarios of maximum temperature for period of 2006–2100 for Kanpur district

River Ganges Basin (Allahabad), which are both located in India. The maximum temperature varies in the range of 32.1–33.6 °C in Kanpur (Fig. 31.12), whereas for Kolkata, there is a small range of variation 31.4–32 °C (Fig. 31.13). There is also a significant difference in maximum temperature between the plain region of the River Ganges Basin (Kanpur), and the eastern shore of the River Ganges Basin (Kolkata). Lucknow and Varanasi are demonstrating the same range of variation in maximum temperature (Figs. 31.14 and 31.16), i.e., 31.9–33.5 °C, whereas Patna illustrates the variation in range of 31.4–32.6 °C (Fig. 31.15).

According to model projections, if we reduce greenhouse gas emissions, there will be about a degree of warming over this century (the orange line). If we do not reduce greenhouse gases as much, Earth will warm much more (gray line). The representation around the lines indicates the range of model results from these three scenarios. At the end-of-century, the increase in the temperature have a similar

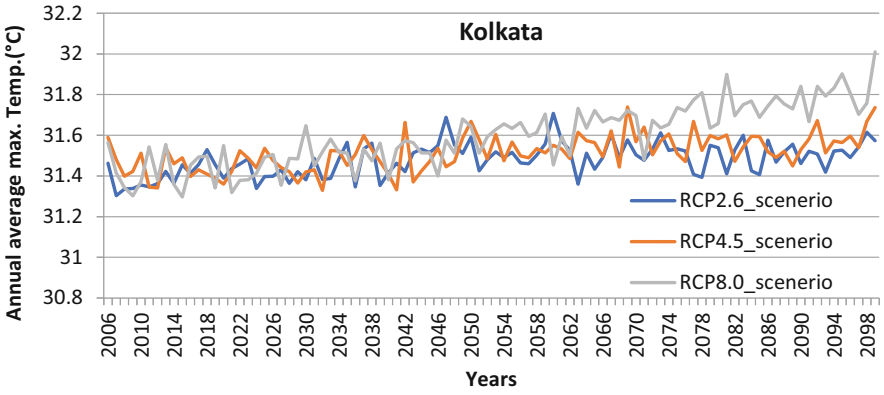

Fig. 31.13 Future projected scenarios of maximum temperature for period of 2006–2100 for Kolkata district

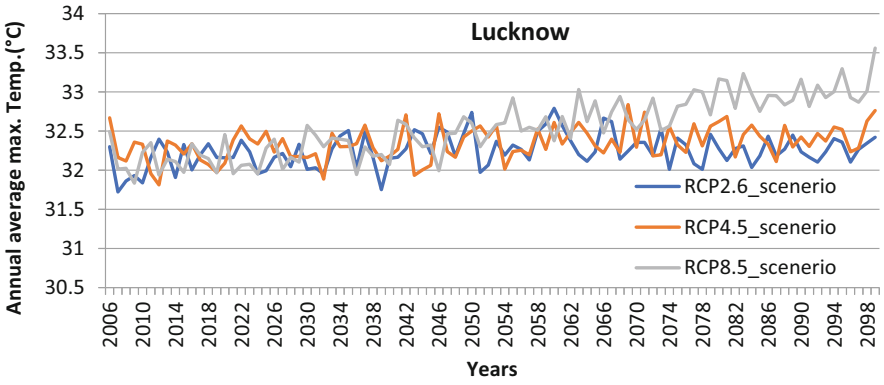

Fig. 31.14 Future projected scenarios of maximum temperature for period of 2006–2100 for Lucknow district

regional distribution to mid-century temperature increases (2041–2070). What matters in comparisons between two future dates when it comes to maximum temperature changes are changes in intensity levels. This means that maximum temperatures will rise by 0.42–4.42 °C between now and the end of the twenty-first century as intensity values of rising maximum temperatures are added. Furthermore, the scenario predicts the highest rise in T_{max} at the end of the twenty-first century (2071–2199). As a consequence of the simulation findings of scenario RCP 8.5 vs. scenario RCP 2.6, the future trend of maximum temperature has grown greatly, while scenario RCP 4.5 agreed to produce an analogous pattern to RCP 2.6 with minute increase in maximum temperature over the river Ganga basin. The temperature increases are expected to be greater on land than over oceans and greater at high latitudes than in the tropics and mid-latitudes. Warmer temperatures cause

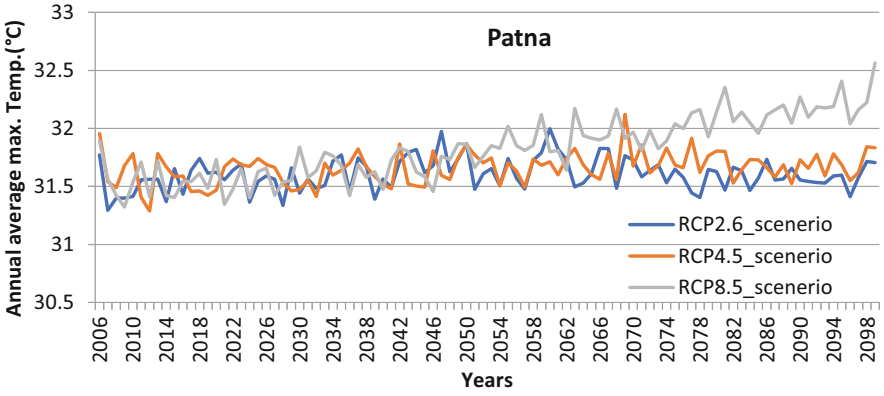

Fig. 31.15 Future projected scenarios of maximum temperature for period of 2006–2100 for Patna district

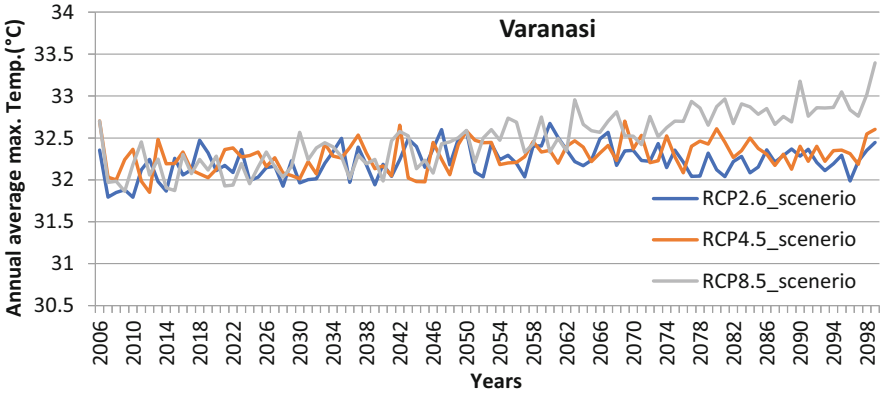

Fig. 31.16 Future projected scenarios of maximum temperature for period of 2006–2100 for Varanasi district

changes to other aspects of climate, such as rain, snow, and clouds. They are also causing changes to the ocean, life, ice, and all other parts of the Earth system.

31.16 Conclusion

Anthropogenic activities made by human beings create an environmental threat in society in the form of climate change, especially meteorological variables like rising temperature in recent years have allocated numerous investigations. Thus, in the present study for necessity recognition and reasonable comparative evaluation of change in the climate that affects the occurrence of daily maximum temperatures

during the two future periods (2041–70 and 2071–2099) along with the base period (1971–2000), it has been tried that the data of CanESM2 model under existing scenarios (RCP 2.6, RCP 4.5, RCP8.5) are downscaled by using of the decision support tool, the Statistical Downscaling Model (SDSM) model. At the study stations, the SDSM offered a long-term climate pattern with a lower percentage of MAE and a closer R-value to 1.0. The results demonstrate that the increase in future maximum temperature changes will be more exacerbated under scenario RCP 8.5 compared to other CanESM2 scenarios. Therefore, the range of uncertainty taken related to the output of other model scenarios, assemble scenario results indicated that the average rising maximum temperature variation will be increased between 0.17 and 2.1 °C for a near-future period (2041–2070) and between 0.7 and 3.2 °C for a far-future period (2071–2099) in study stations of River Ganga Basin. According to the model's simulations of all possible scenarios, the maximum temperature in the Ganges Basin will rise by an average of 0.3–3.5 °C between the middle and end of the twenty-first century, compared to the observed timespan (1971–2005). There is also a significant difference in maximum temperature between the stations in the northwestern mountainous River Ganges Basin (Haridwar) and the eastern shore of the River Ganges Basin (Kolkata), which are both located in India. However, the maximum temperature will occur at Allahabad overall study stations of the basin. Mountainous areas in northern latitudes with drier climates was predicted to be more sensitive to rising maximum temperatures in the next decades, according to this study's survey results. In addition, the plain area of the basin will also be adversely affected by climate change.

References

Abbasnia M, Toros H (2016) Future changes in maximum temperature using the statistical downscaling model (SDSM) at selected stations of Iran. Model Earth Syst Environ 2:68

Akhter J, Das L, Meher JK, Deb A (2018) Evaluation of different large-scale predictors based statistical downscaling models in simulating zone-wise monsoon precipitation over India. Int J Climatol 39:465–482

Alexander LV (2016) Global observed long-term changes in temperature and precipitation extremes: a review of progress and limitations in IPCC assessments and beyond. Weather Clim Extrem 11:4–16

Almasalmeh O, Saleh AA, Mourad KA (2022) Soil erosion and sediment transport modelling using hydrological models and remote sensing techniques in Wadi Billi, Egypt. Model Earth Syst Environ 8(1):1215–1226

Ashiq M, Zhao C, Akhtar J, Ni M (2010) GIS-based high-resolution spatial interpolation of precipitation in mountain–plain areas of Upper Pakistan for regional climate change impact studies. Theor Appl Climatol 99(3):239–253

Baede APM, Ahlonsou E, Ding Y, Schimel D (2001) The climate system: an overview. In: Houghton JT, Ding Y, Griggs DJ, Noguer M, van der Linden PJ, Dai X, Maskell K, Johnson CA (eds) Climate change 2001: the scientific basis. Contribution of Working Group I to the third assessment report of the Intergovernmental Panel on Climate Change. Cambridge University Press, Cambridge

Boe J, Terray L, Habets F, Martin E (2006) A simple statistical' dynamical Iieme based on weather types and conditional resampling. J Geophys Res 111:D23106

Chaudhary S, Agarwal A, Nakamura T (2019) Rainfall projection in Yamuna River Basin, India, using statistical downscaling, water resources and environmental engineering II. Springer, Singapore

Chen HP, Sun JQ, Chen XL, Zhou W (2012) CGCM projections of heavy rainfall events in China. Int J Climatol 32:441–450

Chu JT, Xia J, Xu CY, Singh VP (2010) Statistical downscaling of daily mean temperature, pan evaporation and precipitation for climate change scenarios in Haihe River. Theor Appl Climatol 99(1–2):149–161

Dibike YB, Coulibaly P (2005) Hydrologic impact of climate change in the Saguenay watershed: comparison of downscaling methods and hydrologic models. J Hydrol 307(1-4):145–163

Dixon KW, Lanzante JR, Nath MJ, Hayhoe K, Stoner A, Radhakrishnan A, Balaji V, Gaitán CF (2016) Evaluating the stationarity assumption in statistically downscaled climate projections: is past performance an indicator of future results? Clim Chang 135:395–408

Dracup JA, Vicuna S (2005) An overview of hydrology and water resources studies on climate change: the California experience. In: World Water Congress, Anchorage, Alaska, pp 1–12

Fowler HJ, Blenkinsop S, Tebaldi C (2007) Linking climate change modelling to impacts studies: recent advances in downscaling techniques for hydrological modelling. Int J Climatol 27:1547–1578

Frias MD, Minguez R, Gutierrez JM, Mendez FJ (2012) Future regional projections of extreme temperatures in Europe: a nonstationary seasonal approach. Clim Chang 113(2):371–392

Goubanova K, Echevin V, Dewitte B, Codron F, Takahashi K, Terray P, Vrac M (2011) Statistical downscaling of sea-surface wind over the Peru–Chile upwelling region: diagnosing the impact of climate change from the IPSLCM4 model. Clim Dyn 36:1365–1378

Goyal MK, Ojha CSP (2012) Downscaling of surface temperature for lake catchment in an arid region in India using linear multiple regression and neural networks. Int J Climatol 32(4): 552–566

Gu H, Wang G, Yu Z, Mei R (2012) Assessing future climate changes and extreme indicators in east & south Asia using the RegCM4 regional climate model. Clim Chang 114(2):301–317

Gupta N, Banerjee A, Gupta SK (2021a) Spatio-temporal trend analysis of climatic variables over Jharkhand, India. Earth Syst Environ 5(1):71–86

Gupta SK, Gupta N, Singh VP (2021b) Variable-sized cluster analysis for 3D pattern characterization of trends in precipitation and change-point detection. J Hydrol Eng 26(1):04020056

Gupta N, Gond S, Gupta SK (2022) Spatiotemporal trend characteristics of rainfall and drought jeopardy over Bundelkhand region, India. Arab J Geosci 15:1155

Gutmann E, Pruitt T, Clark MP, Brekke L, Arnold JR, Raff DA, Rasmussen RM (2014) An intercomparison of statistical downscaling methods used for water resource assessments in the United States. Water Resour Res 50:7167–7186

Hashemi-Ana SK, Khosravi M, Tavousi T (2015) Validation of AOGCMs capabilities for simulation length of dry spells under the climate change in Southwestern area of Iran. Open J Air Pollut 4(02):76–85

Hessami M, Gachon P, Ouarda TBMJ, St-Hilaire A (2008) Automated regression-based statistical downscaling tool. Environ Model Softw 23(6):813–834

Horton B (1995) Geographical distribution of changes in maximum and minimum temperatures. Atmos Res 37(1):101–117. https://doi.org/10.1016/0169-8095(94)00083-P

Huang J, Zhang J, Zhang Z, Xu C, Wang B, Yao J (2011) Estimation of future precipitation change in the Yangtze River basin by using statistical downscaling method. Stoch Env Res Risk A 25(6):781–792. https://doi.org/10.1007/s00477-010-0441-9

Iizumi T, Nishimori M, Dairaku K, Adachi SA, Yokozawa M (2011) Evaluation and intercomparison of downscaled daily precipitation indices over Japan in present-day climate: strengths and weaknesses of dynamical and bias correction-type statistical downscaling methods. J Geophys Res Atmos 116:D01111

IPCC (2007) Climate change: the physical science basis. Contribution of working group I to the fourth assessment, report of the intergovernmental panel on Climate change. Cambridge University Press, Cambridge, p 996

IPCC (2013) Climate change 2013: the physical science basis. Contribution of working group I to the fifth assessment, report of the intergovernmental panel on Climate change. Cambridge University Press, Cambridge, p 1550

Jana P, Pandey R, Semeraro T, Alatalo JM, Areteno R, Todaria NP, Tripathi R (2021) Community perspectives on conservation of water sources in Tarkeshwar sacred groves Himalaya India. Water Supply 21(8):4343–4354. https://doi.org/10.2166/ws.2021.181

Jones PD (1994) Hemispheric surface air temperature variations: a reanalysis and an update to 1993. J Clim 7(11):1794–1802

Jones PD, Moberg A (2003) Hemispheric and large-scale surface air temperature variations: an extensive revision and an update to 2001. J Clim 16(2):206–223

Kasotia P (2007) The health effects of global warming: developing countries are the most vulnerable. UN Report, Vol. XLIV, No. 2, Green Our World!"

Kidson JW, Thompson CS (1998) A comparison of statistical and model-based downscaling techniques for estimating local climate variations. J Clim 11:735–753

Kothawale DR, Rupa Kumar K (2005) On the recent changes in surface temperature trends over India. Geophys Res Lett 32(18)

Krishnan R, Shrestha AB, Ren G, Rajbhandari R, Saeed S, Sanjay J, Ren Y (2019) Unravelling climate change in the Hindu Kush Himalaya: rapid warming in the mountains and increasing extremes, The Hindu Kush Himalaya Assessment. Springer, Cham, pp 57–97

Kure S, Jang S, Ohara N, Kavvas ML, Chen ZQ (2013) Hydrologic impact of regional climate change for the snow-fed & glacier-fed river basins in Republic of Tajikistan: statistical downscaling of global climate model projections. Hydrol Process 27:4071–4090

Li LD, O'Leary GJ, Christy B, Macadam I, Wang B, Anwar MR, Weeks A (2017) Effects of different climate downscaling methods on the assessment of climate change impacts on wheat cropping systems. Clim Chang 144(4):687–701

Lutz AF, ter Maat HW, Biemans H, ShresthaA B, Wester P, Immerzeel WW (2016) Selecting representative climate models for climate change impact studies: an advanced envelope-based selection approach. Int J Climatol 36(12):3988–4005

Mahmood R, Babel MS (2013) Evaluation of SDSM developed by annual and monthly sub-models for downscaling temperature and precipitation in the Jhelum basin, Pakistan and India. Theor Appl Climatol 113(1–2):27–44

Mahmood R, Babel MS (2014) Future changes in extreme temperature events using the statistical downscaling model (SDSM) in the trans-boundary region of the Jhelum river basin. Weather Clim Extremes 5:56–66

Maraun D, Widmann M, Gutierrez JM (2018) Statistical downscaling skill under present climate conditions: a synthesis of the VALUE perfect predictor experiment. Int J Climatol. https://doi.org/10.1002/joc.5877

Meenu R, Rehana S, Mujumdar PP (2013) Assessment of hydrologic impacts of climate change in Tunga–Bhadra river basin, India with HEC-HMS & SDSM. Hydrol Process 27:1572–1589

Meher JK, Das L (2019) Selection of suitable predictors and predictor domain for statistical downscaling over the Western Himalayan region of India. Theor Appl Climatol 139:431–446

Meher JK, Das L, Akhter J, Benestad RE, Mezghani A (2017) Performance of CMIP3 and CMIP5 GCMs to simulate observed rainfall characteristics over the Western Himalayan region. J Clim 30(19):7777–7799

Munawar S, Tahir MN, Baig MHA (2022) Twenty-first century hydrologic and climatic changes over the scarcely gauged Jhelum river basin of Himalayan region using SDSM and RCPs. Environ Sci Pollut Res 29(8):11196–11208

Omar PJ, Kumar V (2021) Assessment of damage for dam break incident in Lao PDR using SAR data. Int J Hydrol Sci Technol. https://doi.org/10.1504/IJHST.2021.10040874

Omar PJ, Gupta N, Tripathi RP, Shekhar S (2017) A study of change in agricultural and forest land in Gwalior city using satellite imagery. SAMRIDDHI 9(2):109–112
Omar PJ, Bihari DS, Kumar DP (2019) Temporal variability study in rainfall and temperature over Varanasi and adjoining areas. Disaster Adv 12(1):1–7
Omar PJ, Dwivedi SB, Dikshit PKS (2020) Sustainable development and management of groundwater in Varanasi, India. In: Advances in water resources engineering and management. Springer, Singapore, pp 201–209
Omar PJ, Shivhare N, Dwivedi SB, Dikshit PKS (2022) Identification of soil erosion-prone zone utilizing geo-informatics techniques and WSPM model. Sustainable Water Resour Manage 8(3):1–13
Pandey KK, Abhash A, Tripathi RP, Dayal S (2019) Flow-field Near Forty-Five Degree Dividing Open Channel
Pandey M, Pu JH, Pourshahbaz H, Khan MA (2022) Reduction of scour around circular piers using collars. J Flood Risk Manage 3:e12812. https://doi.org/10.1111/jfr3.12812
Pu JH, Wallwork JT, Khan M, Pandey M, Pourshahbaz H, Satyanaga A, Hanmaiahgari PR, Gough T (2021) Flood suspended sediment transport: combined modelling from dilute to hyper-concentrated flow. Watermark 13(3):379
Rahmstorf S, Ganopolski A (1999) Long-term global warming scenarios computed with an efficient coupled climate model. J Clim Change 43(2):353–367
Revadekar JV, Patwardhan SK, Rupa KK (2011) Characteristic features of precipitation extremes over India in the warming scenarios. Adv Meteorol 21:25
Saddique N, Khaliq A, Bernhofer C (2020) Trends in temperature and precipitation extremes in historical (1961–1990) and projected (2061–2090) periods in a data scarce mountain basin, northern Pakistan. Stoch Env Res Risk A 34(10):1441–1455
Salon S, Cossarini G, Libralato S, Gao Solidoro XC, Giorgi F (2008) Downscaling experiment for the Venice lagoon. I. Validation of the present-day precipitation climatology. J Clim Res 38(1): 31–41
Semenov MA, Stratonovitch P (2010) Use of multi-model ensembles from global climate models for assessment of climate change impacts. J Clim Res 41(1):1–14
Shankar MS, Pandey M, Shukla AK (2021) Analysis of existing equations for calculating the settling velocity. Watermark 13(14):1987
Shashikanth K, Salvi K, Ghosh S, Rajendran K (2014) Do CMIP5 simulations of Indian summer monsoon rainfall differ from those of CMIP3? Atmos Sci Lett 15(2):79–85
Sheikh MM, Manzoor N, Ashraf JM, Adnan D, Collins S, Hameed NI (2015) Trends in extreme daily rainfall and temperature indices over South Asia. Int J Climatol 35(7):1625–1637
Shekhar S, Chauhan MS, Omar PJ, Jha M (2021) River discharge study in river Ganga, Varanasi using conventional and modern techniques. In: The Ganga river basin: a hydrometeorological approach. Springer, Cham, pp 101–113
Shivashankar M, Pandey M, Zakwan M (2022) Estimation of settling velocity using generalized reduced gradient (GRG) and hybrid generalized reduced gradient–genetic algorithm (hybrid GRG-GA). Acta Geophys 2022:1–11
Shrestha D, Sharma S, Bhandari S, Deshar R (2021) Statistical downscaling and projection of future temperature and precipitation change in Gandaki Basin. J Inst Sci Technol 26(1):16–27
Singh UK, Jamei M, Karbasi M, Malik A, Pandey M (2022) Application of a modern multi-level ensemble approach for the estimation of critical shear stress in cohesive sediment mixture. J Hydrol 607:127549
Stern DI, Kaufmann RK (2000) Detecting a global warming signal in hemispheric temperature series: a structural time series analysis. J Clim Change 47(4):411–438
Su BJ, Huang M, Gemmer D, Jian H, Tao T, Jiang CZ (2016) Statistical downscaling of CMIP5 multi-model ensemble for projected changes of climate in the Indus River Basin. Atmos Res 178:138–149
Timbal B, Dufour A, McAvaney B (2003) An estimate of future climate change for western France using a statistical downscaling technique. Clim Dyn 20:807–823

Toros H, Tek A, Solum S, Yeniceri DN, Sogut AS, Oguzhan B, Caglar ZN, Okcu D, Kalafat AG, Giden F, Koyuncu H (2015) Climate trends and variations between 1912–2014 in Kandilli, Istanbul, VII, Atmospheric Science Symposium, Istanbul, pp 978–987

Tripathi RP, Pandey KK (2021) Experimental study of local scour around T-shaped spur dike in a meandering channel. Water Supply 21(2):542–552

Tryhorn L, Degaetano A (2010) A comparison of techniques for downscaling extreme precipitation over the Northeastern United States. Int J Climatol 31:1975–1989

Wallwork JT, Pu JH, Kundu S, Hanmaiahgari PR, Pandey M, Satyanaga A, Pandey M, Satyanaga A, Amir Khan M, Wood A (2022) Review of suspended sediment transport mathematical modelling studies. Fluids 7(1):23

Wang H, Long L, Kumar A, Wang W, Schemm J-KE, Zhao M, Vecchi GA, LaRow TE, Lim Y-K, Schubert SD, Shaevitz DA, Camargo SJ, Henderson N, Kim DY, Jonas JA, Walsh KJE (2014) How well do global climate models simulate the variability of Atlantic tropical cyclones associated with ENSO? J Clim 27(15):5673–5692

Whan K, Alexander LV, Imielska A, McGree S, Jones D, Ene E, Finaulahi S, Inape K, Jacklick L, Kumar R, Vaiimene M (2014) Trends and variability of temperature extremes in the tropical Western Pacific. Int J Climatol 34(8):2585–2603

Wilby RL, Dawson CW (2004) sdsm—a decision support tool for the assessment of regional climate change impacts. Environ Model Softw 17:145–157

Wilby RL, Dawson CW (2007) SDSM 4.2—a decision support tool for the assessment of regional climate change impacts. In: Version 4.2 user manual. Lancaster University, Lancaster, pp 1–94

Wilby RL, Dawson CW (2013) The statistical downscaling model: insights from one decade of application. Int J Climatol 33(7):1707–1719

Wilby RL, Dawson CW, Barrow EM (2002) SDSM-A decision support tool for the assessment of regional climate change impacts. J Environ Model Softw 17(2):145–157

Willems P, Vrac M (2011) Statistical precipitation downscaling for small-scale hydrological impact investigations of climate change. J Hydrol 402(3):193–205

Zuo DP, Xu ZX, Zhao J, Abbaspour KC, Yang H (2015) Response of runoff to climate change in the Wei River basin, China. Hydrol Sci J 60(3):508–522

Chapter 32
Trend Assessment of Rainfall Over Mumbai and Pune Cities

Garv Saini, P. Jagadeesh, and G. Saikumar

Abstract The yearly rainfall trend for an area would be important in planning irrigation patterns, reservoir management, storm water drainage, and so on, as well as understanding the influence of climate change on rainfall in a region. Mumbai and Pune are two metropolitan cities in Maharashtra state that have developed in the last 20–30 year. The present study intends to examine the precipitation pattern in Mumbai and Pune. Monthly and yearly precipitation data values from the years 2000–2020 were utilized for the study. Basic statistical tests are used to assess the trend of rainfall or its absence, and rainfall trend analysis is done using linear regression analysis, Mann-Kendall analysis, and Sen's Slope estimator. The results of trend analysis have shown an increasing trend in the Annual rainfall, non-monsoon, southwest monsoon, and northeast monsoon in both Mumbai and Pune. In both cities, a decreasing trend has been observed during the pre-monsoon season. Reliability analysis is performed to provide statistics for drinking water scheme design (90% dependability) and irrigation requirement calculation (75% dependability).

Keywords Trend analysis · Rainfall · Hydrologic hazards

32.1 Introduction

India's agriculture and allied sectors, food security, and energy security are critically dependent on the timely availability of water and a favorable environment. Rainfall plays a significant role in satisfying needs of agriculture, residential water supply, hydroelectric power generation, and industries (Gandhre et al. 2020; John et al.

G. Saini · P. Jagadeesh
School of Civil Engineering, VIT, Vellore, India
e-mail: garv.saini2018@vitstudent.ac.in

G. Saikumar (✉)
Department of Civil Engineering, National Institute of Technology Warangal, Warangal, India
e-mail: gs712006@student.nitw.ac.in

M. Pandey et al. (eds.), *River Dynamics and Flood Hazards*, Disaster Resilience and Green Growth, https://doi.org/10.1007/978-981-19-7100-6_32

2021a, b). Global climate change may alter long-term rainfall patterns that affect water supply, as well as the risk of increased droughts and floods (Pu et al. 2021; Singh et al. 2022; Wallwork et al. 2022). The south west (S-W) monsoon, which provides for approximately 80% of the total precipitation in the nation, is crucial for the supply of freshwater for drinking and irrigation (Jagadeesh and Agrawal 2015). Changes in climate across the Indian region, particularly the S-W monsoon, will have a huge influence on agricultural productivity, water resource management, and the country's general economy (Kumar et al. 2010; Potdar et al. 2019). Nowadays metropolitan cities have encountered severe water scarcity and declined groundwater levels a result of rapid urbanization. Several studies reported that the frequency of natural calamities such as floods and droughts was found to be increasing in the Indian region (Joshi and Pandey 2011; Mondal et al. 2015). Normal rainfall is required for appropriate agricultural productivity in order to keep food prices stable, as food prices are dependent on agricultural yields. As agriculture accounts for 16% of India's GDP, a proper monsoon is also required for economic development (Rana et al. 2013). Other economic activities like fishing and forestry are also directly affected by the amount of precipitation. India's population growth and modernization have resulted in increased water consumption. As a result, it is vital to investigate the features of these events as well as the scientific reasons behind them.

Numerous researches have been conducted to investigate the long-term pattern of rainfall over the Indian subcontinent. Mooley and Parthasarathy (1984) has studied an analysis of the All-India summer monsoon rainfall (June–September) from 1871 to 1978. Parthasarathy et al. (1994) have taken all India monthly, seasonal, and yearly homogenous data series from 1871 to 1993. They examined some data facts and long-term trends in monsoon rainfall in India. Patil et al. (2013) studied the trend of rainfall in Pune district using 47 years data from 1958 to 2004. Mann-Kendall (MK) and modified MK tests for detecting trends and Sen's slope estimator was utilized for quantifying the change. There was a noticeable alteration in the spatial and temporal rainfall pattern over the Pune region during the time of analysis. Rana et al. (2012) have done trend analysis for rainfall in Delhi and Mumbai cities of India. The results showed that a slight significant decreasing trend for long-term S-W monsoon rainfall in Mumbai and both stations' average maximum daily rainfall has decreased. Jagadeesh and Agrawal (2015) investigated trends and their magnitude using Mann-Kendall test and Sen slope methods. The overall analysis shows an increasing trend in the east and a more decreasing trend in the south and west compared to the north of the catchment from eight rain gage stations in Kerala's Bharathapuzha catchment from 1975 to 2009. Gandhre et al. (2020) conducted a precipitation trend analysis for Maharashtra's coastal districts from 1901 to 2000, which revealed an increasing trend for Sindhudurg and Mumbai metropolis. There is no discernible trend for Thane, Raigad, Ratnagiri, or Mumbai Suburban districts. Rainfall in Mumbai has increased by 6.25 mm each year. Potdar et al. (2019) conducted a Trend Analysis of Rainfall Data for Maharashtra and Goa from 1901 to 2015, and the findings show that the long-term trend in annual period and southwest monsoon season across Maharashtra as a whole, Konkan and Goa, and

Madhya Maharashtra is increasing, while it is decreasing in Marathwada and Vidarbha.

Maharashtra state has the second largest population in India and the third largest surface area. The two largest metropolitan cities in Maharashtra are Mumbai and Pune. The population of these two cities is rapidly growing as people migrate for jobs and education. Such cities have a higher population density than towns or rural regions. A significant portion of Mumbai was built through the process of land reclamation, which is the removal of water to raise the level of the land, it is highly susceptible to hydrological hazards such as flooding (Rana et al. 2012; Shankar et al. 2021; Pandey et al. 2022). This emphasizes the need of rainfall trend analysis so that stormwater drains may be designed to drain excess precipitation or groundwater from impermeable cemented constructions such as roadways, sidewalks, and parking lots. Water consumption is increasing as a result of urbanization and economic growth. This rainfall trend analysis study will aid in water management by determining how rainfall has changed in previous years in order to meet escalating water needs.

The aim of the research was to examine the rainfall trend in Mumbai and Pune cities from 2000 to 2020 and identify overall increasing or decreasing trends, as well as to learn how the basic statistical data has changed over the given time period for the annual period, non-monsoon season, pre-monsoon season, southwest monsoon season, and northeast monsoon season. Find out the fundamental statistics about rainfall such as maximum and minimum rainfall, mean, standard deviation, skewness, and kurtosis of data gathered in various years based on the monsoon seasons. In addition, the Mann-Kendall and Sen Slope methods will be used to analyze rainfall trends.

32.2 Data and Methodology

This research looks at rainfall changes in Mumbai and Pune, two major cities in the Indian state of Maharashtra, from 2000 to 2020. Precipitation data was analyzed by categorizing it into four seasons: (1) non-monsoon (January, February, March), (2) pre-monsoon (April, May), (3) southwest monsoon (June, July, August, September), and (4) northeast monsoon (October, November, and December) then basic statistical analysis of the data is done to find out the maximum and minimum rainfall, mean, standard deviation, skewness, and Kurtosis.

Trend is defined as the long-term change in the dependent variable over a lengthy period of time or as the overall movement of a series over an extended period of time (Panda and Sahu 2019). According to recent research, the nonparametric Mann-Kendall (MK) trend test is the most extensively used approach for detecting trends. Mann (1945) developed the test first, Kendall (1975) subsequently developed the test static known as the Kendall's tau statistic. It was discovered to be a great tool for trend identification in a variety of applications (Burn and Elnur 2002).

32.3 Mann–Kendall's Test

The M-K test is a statistical nonparametric test that is commonly used for trend analysis in climatological and hydrological time series data. There are two benefits to using this test. First, it is a nonparametric test that does not need the data to be distributed regularly. Second, due to inhomogeneous time series, the test has limited sensitivity to sudden breaks. The null hypothesis H0, according to this test, suggests that there is no trend (the data is independent and randomly ordered). This is compared to the alternative hypothesis H1, which expects a trend. The M-K statistic may be calculated as follows:

$$S = \sum_{j=1}^{n-1} \sum_{k=j+1}^{n} \operatorname{sign}\left(x_k - x_j\right) \tag{32.1}$$

where

$$\operatorname{sign}\left(x_k - x_j\right) = \begin{matrix} +1, & x_k - x_j > 0 \\ 0, & x_k - x_j = 0 \\ -1, & x_k - x_j < 1 \end{matrix} \tag{32.2}$$

and tau is estimated as

$$\tau = \frac{2S}{N(N-1)} \tag{32.3}$$

Variance of S is calculated by the formula:

$$\text{VAR (S)} = \frac{1}{18}[n(n-1)(2n+5)] \tag{32.4}$$

where n is the number of value points in the set, the value of test statistic Z is calculated by

$$\begin{aligned} \text{Z} &= \frac{\text{S}-1}{\sqrt{\text{VAR(S)}}} \quad \text{if } \text{S} > 0 \\ &= 0, \text{if } S = 0 \\ &= \frac{\text{S}+1}{\sqrt{\text{VAR(S)}}} \quad \text{if } S < 0. \end{aligned}$$

32.4 Sen's Slope Estimator Test

Sen's estimate is a nonparametric approach for determining the size of a trend in a time series (Sen 1968). Sen's nonparametric method is used to determine the true slope of an existing trend, such as the amount of change every year. A positive Sen's slope value shows an upward or growing trend in the time series, whereas a negative value suggests a downward or decreasing trend.

The Sen's method can be used in cases where the trend can be assumed to be linear that is

$$f(t) = Qt + B \tag{32.6}$$

where Q is the slope, B is the constant, and t is the time.

To get the slope estimate Q, the slopes of all the data value pairs are calculated using the equation:

$$Q_i = \frac{x_j - x_i}{j - i} \tag{32.7}$$

where x_j and x_i are the data values at time j and i ($j >$ i), respectively, $i = 1, 2, 3, \ldots N$.

The Sen's estimator of slope is the median of all the values of Q_i.

$$Q = Q_{\left[\frac{(N+1)}{2}\right]}, \text{if N is odd,or}$$

$$Q = \frac{1}{2}\left(Q_{\left[\frac{(N)}{2}\right]} + Q_{\left[\frac{(N+2)}{2}\right]}\right), \text{if } N \text{ is even}$$

To obtain an estimate of B in equation $f(t)$ the values of difference $x_i - Qt_i$ are calculated. The median of these values gives an estimate of B.

32.5 Results and Discussion

32.5.1 Statistical Analysis

The arithmetic mean was used to compute the average annual and seasonal rainfall in Mumbai and Pune. The mean annual rainfall in Mumbai is more than in Pune since it is closer to the shore and is in the windward direction, or on the side facing the wind. It is lower in Pune because it is located in the leeward direction, which is shielded from the wind. The average seasonal rainfall in these cities are shown in Figs. 32.1 and 32.2. Both Mumbai and Pune have a similar rainfall pattern, with the majority of

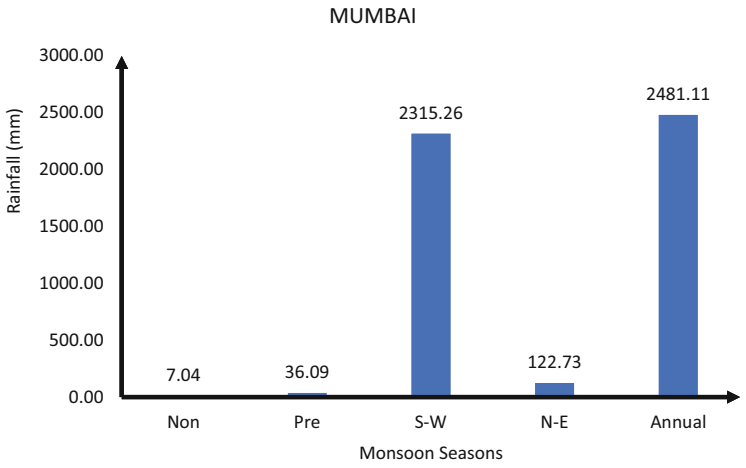

Fig. 32.1 Mean rainfall data of Mumbai

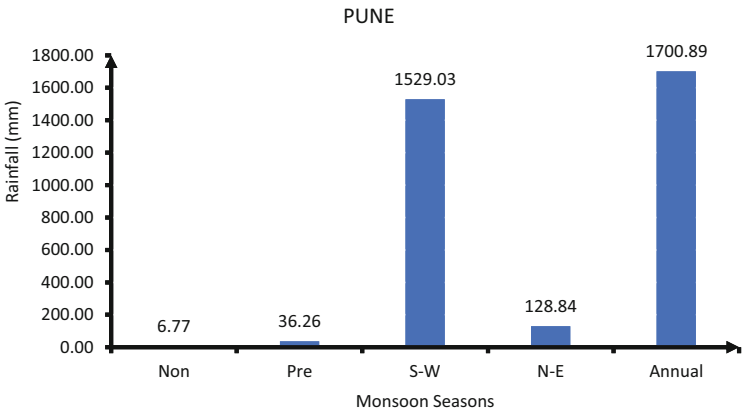

Fig. 32.2 Mean annual rainfall data of Pune

the yearly rainfall falling during the southwest monsoon season and the least falling during the non-monsoon season from January to March.

In Mumbai, where the mean annual rainfall is considerably high, the southwest monsoon rainfall becomes the most significant, accounting for 93.3 percent of the annual rainfall. Pre-monsoon and northeast monsoon both contribute 1.4% and 4.9%, respectively. The non-monsoon contributes the least, on average, 0.28%.

The analysis of mean rainfall distribution reveals that the southwest monsoon rainfall contributes the most, accounting for 89.9% of total annual rainfall whereas, the pre-monsoon rainfall and the northeast monsoon rainfall provide 2% and 7.5%, respectively. Similar to Mumbai, the smallest contribution is from non-monsoon rainfall, which accounts for only 0.3%. Both places have a similar tendency, with

Table 32.1 Statistical analysis of rainfall in Mumbai

Period	Mean (mm)	Maximum (mm)	Minimum (mm)	Standard Deviation	Coeff of Variation	Skewness	Kurtosis
Non	7.04	52.89	0	11.91	1.69	3.24	11.70
Pre	36.09	271.16	0.43	68.63	1.90	2.78	7.46
S-W	2315.26	3133.26	1295.19	564.82	0.24	-0.22	-1.18
N-E	122.73	260.91	12.72	87.05	0.71	0.67	-0.45
Annual	2481.11	3387.31	1326.58	587.23	0.24	0.11	-0.91

Table 32.2 Statistical analysis of rainfall in Pune

Period	Mean (mm)	Maximum (mm)	Minimum (mm)	Standard Deviation	Coeff of Variation	Skewness	Kurtosis
Non	6.77	41.23	0	9.33	1.38	2.71	9.26
Pre	36.26	166.17	2.56	46.49	1.28	1.95	3.06
S-W	1529.03	2462.62	823.02	476.95	0.31	0.21	-0.95
N-E	128.84	286.71	18.92	85.06	0.66	0.63	-0.72
Annual	1700.89	2729.43	890.96	509.23	0.30	0.29	-0.82

greatest rainfall occurring during the southwest and northeast monsoon seasons, followed by decreased rainfall during the pre- and non-monsoon seasons.

The statistical parameters maximum (Max) and minimum (Min) rainfall, mean, standard deviation, skewness, and Kurtosis of rainfall data for both Mumbai and Pune have been computed and are given in Tables 32.1 and 32.2 for seasonal monsoon and annual rainfall data.

The highest mean rainfall value is observed in the S-W monsoon season of 2315.26 mm. In the non-monsoon season, the greatest rainfall was 52.89 mm in 2015, while the smallest rainfall was 0 mm in 2012. The greatest rainfall in the pre-monsoon season was 271.16 mm in 2000, while the smallest rainfall was 0.43 mm in 2013 and the average annual rainfall over the years 2000–2020 in Mumbai is observed to be 2481.11 mm. The maximum rainfall overall annually of 3387.31 mm was recorded in 2019, and minimum annual rainfall of 1326.58 mm was recorded in the year 2002.

The values of skewness are positive in the non-monsoon, pre-monsoon, northeast monsoon, and annual seasons, indicating that it is positively skewed, i.e. the number of observations fewer than the center point (or mean) is greater than the number of values after the center point. In contrast, during the southwest monsoon season, the skewness score is negative, indicating that the data is negatively skewed.

Very high Kurtosis values obtained in non-monsoon and pre-monsoon periods suggest that the data set has a Leptokurtic distribution (with a high degree of peakedness), with a very prominent peak and heavy tails, indicating a dramatic contrast between the peak value and the other values. Negative Kurtosis values in the southwest monsoon, northeast monsoon, and yearly period imply a Platykurtic distribution for the data set (having a low degree of peakedness). They have a flat top around the mean rather than a high peak, implying that the gap between the peak value and the other values in the time period is less.

The highest mean rainfall value is observed in the S-W monsoon season of 1529.03 mm. The maximum rainfall in the non-monsoon season of 41.23 mm was recorded in 2015, and the minimum rainfall of 0 mm in 2012. The maximum rainfall in pre-monsoon season of 166.17 mm was recorded in 2006, and the minimum rainfall of 2.56 mm in 2013. The maximum rainfall overall annually of 2729.43 mm was recorded in 2019, and minimum annual rainfall of 890.96 mm in 2002.

The values of skewness are positive in all the rainfall periods which indicates that they are positively skewed. Very high Kurtosis values in non- and pre-monsoon periods as observed in Mumbai indicate that the data set is Leptokurtic distribution, they have a very distinct peak and the tails are heavy, i.e. sharp difference between the peak value and the other values. Whereas, negative values of Kurtosis in S-W monsoon season, N-E monsoon season, and annual period indicate that the data set is a Platykurtic distribution, they have a flat top around the mean instead of a sharp peak so there is less difference between the peak value and the other values. This exact same trend was observed in Mumbai also.

The percentage of coefficient of variation of rainfall in Mumbai as shown in Fig. 32.3. The S-W monsoon season contributes the most to yearly rainfall, the numbers are closer together, resulting in a comparable coefficient of variation, 24.40%for S-W and 23.67%for the annual period. In contrast, there is a wide range of values for pre-monsoon (190.15%), non-monsoon (169.25%), and northeast monsoon (70.93%) (Fig. 32.4).

Similar to Mumbai, the S-W monsoon period contributes the bulk of yearly rainfall in Pune, and the values are closer to each other, resulting in a similar coefficient of variation, 31.19% for the S-W monsoon season and 29.94% for the annual period. Higher values are observed during the non-monsoon season (137.84%), pre-monsoon season (128.21%), and N-E monsoon season (66.02%).

The graphs and the numbers generated in the table show that when the coefficient of variation is low, the skewness is also low, as both represent how the distribution is with regard to the mean value and provide insight into the pattern of data values over time. As a result, the coefficient of variation and skewness values are both low for the S-W monsoon season and the yearly period, whereas they are high for the non-, pre-,

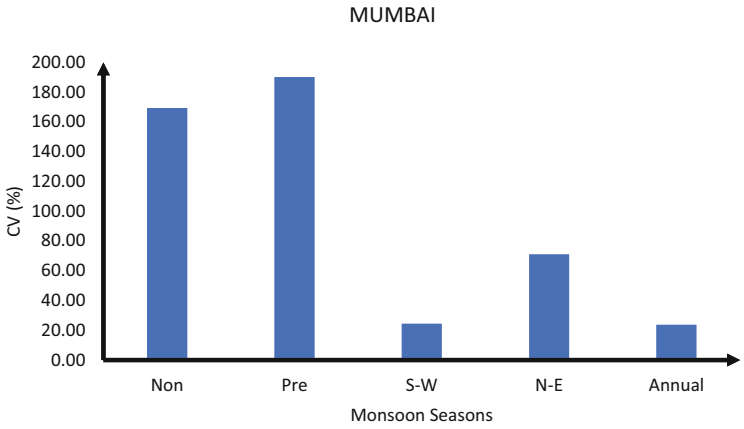

Fig. 32.3 Coefficient of variation (%) of rainfall in Mumbai

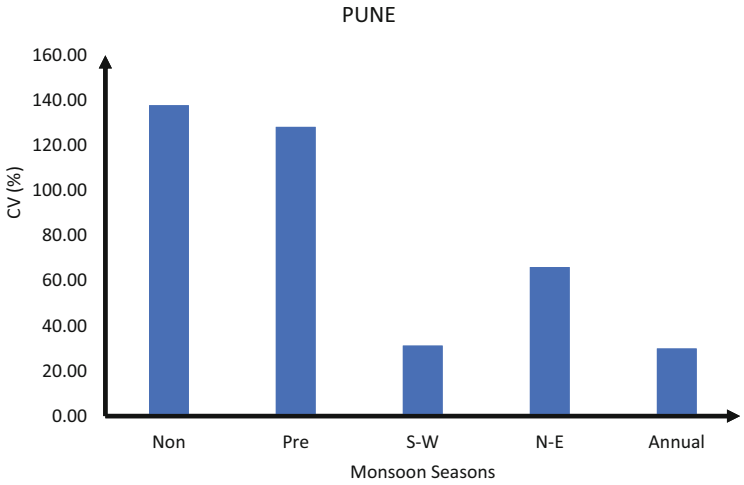

Fig. 32.4 Coefficient of variation (%) of rainfall in Pune

and N-E monsoon seasons. The standard deviation of seasonal and annual rainfall in both cities are shown in Fig. 32.5.

32.5.2 Rainfall Trend Analysis

The rainfall trends from the year 2000–2020 for Mumbai and Pune using monthly rainfall data have been analyzed by Mann-Kendall, Sen's Slope Estimator, and Linear Regression Analysis. Figures 32.6, 32.7, 32.8, 32.9, and 32.10 show the

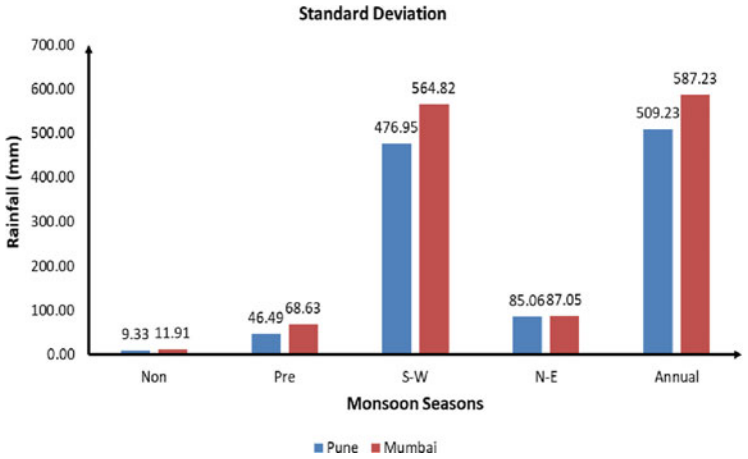

Fig. 32.5 Standard deviation of annual and seasonal rainfall in Pune and Mumbai

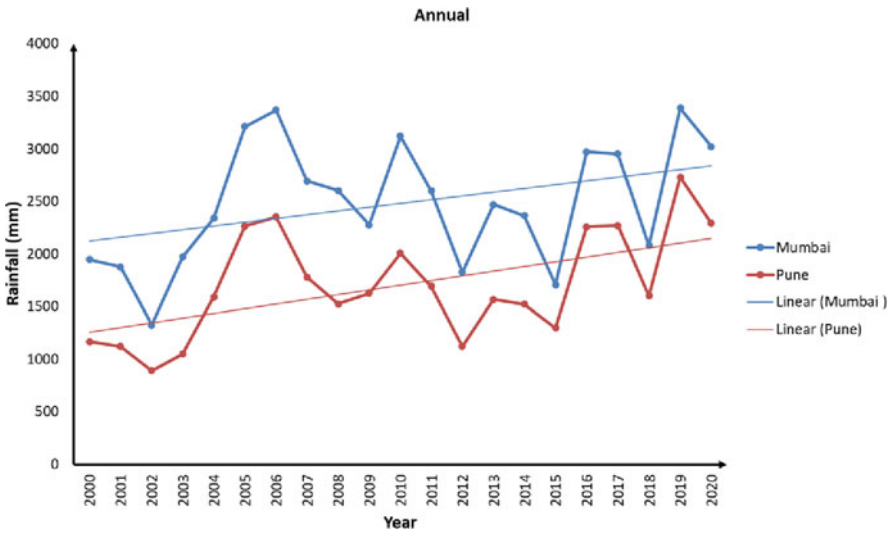

Fig. 32.6 Annual rainfall trend in Mumbai and Pune

trend of rainfall for annual, non-monsoon, pre-monsoon, S-W monsoon, and N-E monsoon over the period 2000–2020. In both Mumbai and Pune, the total annual rainfall rise. This might be attributable to a number of factors, including climate change, which raises overall temperatures and increases precipitation. During the non-monsoon season in the provided time period, a rising tendency has been noted. During the pre-monsoon season (April–May), both Mumbai and Pune had a declining tendency, but the southwest monsoon period in both cities saw an increase.

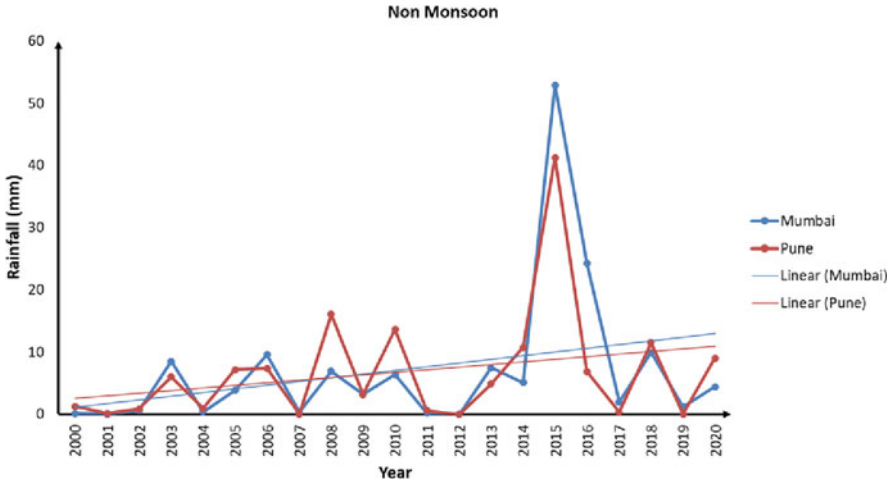

Fig. 32.7 Non-monsoon rainfall trend in Mumbai and Pune

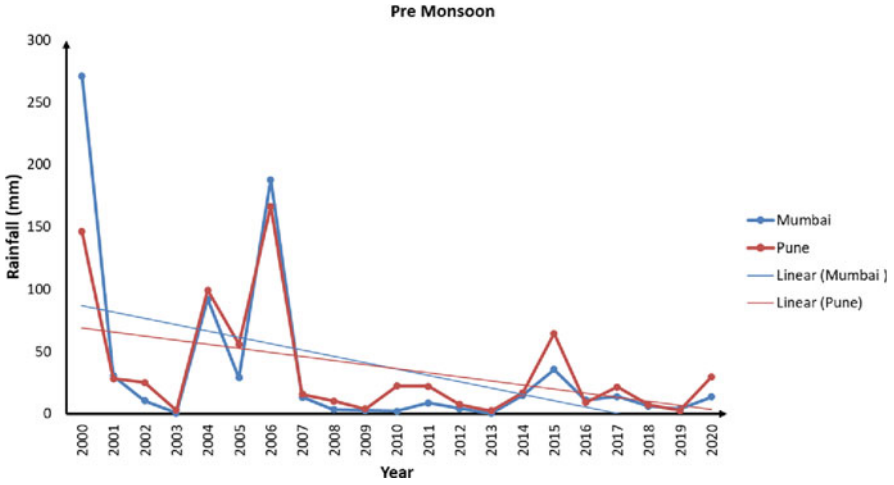

Fig. 32.8 Pre-monsoon rainfall trend in Mumbai and Pune

During the northeast monsoon season, a rising tendency has been noted in both Mumbai and Pune.

32.5.3 Mann-Kendall Analysis

This test just identifies the direction of the trend, not the amount of the trend, therefore it does not need presuming normality and is entirely dependent on the

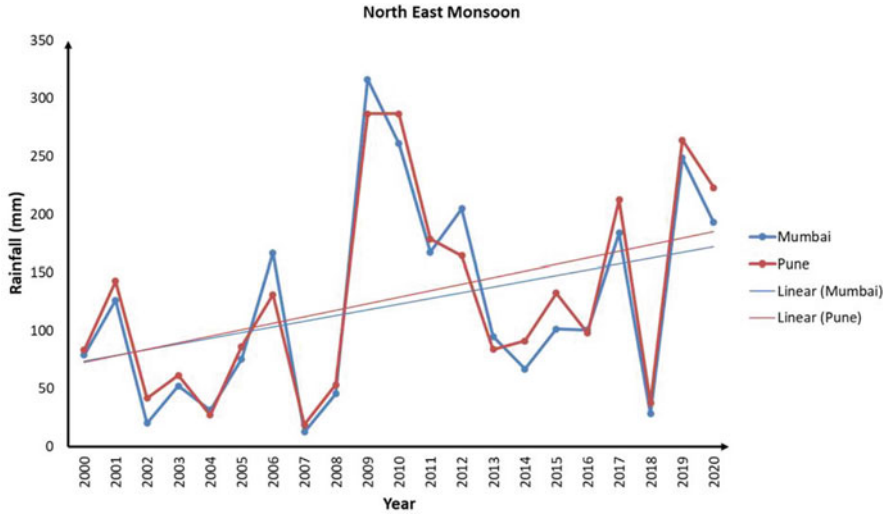

Fig. 32.9 Southwest monsoon rainfall trend in Mumbai and Pune

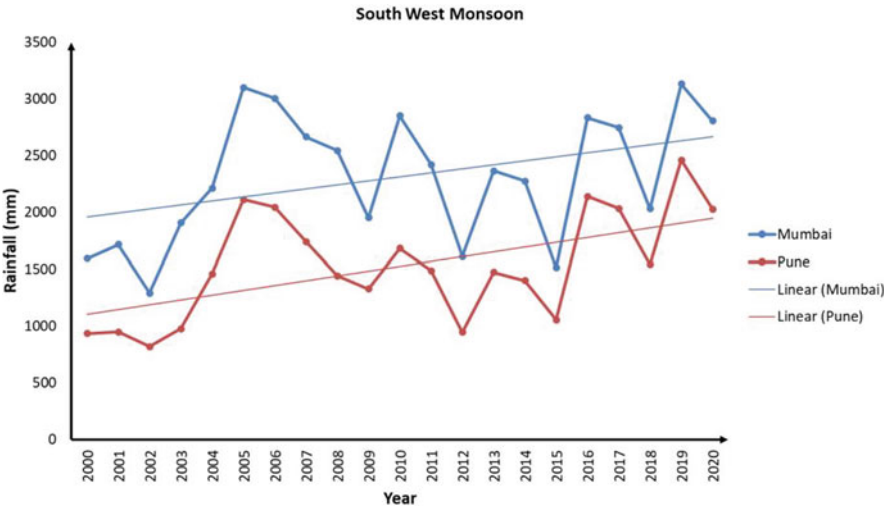

Fig. 32.10 Northeast monsoon rainfall trend in Mumbai and Pune

numbers that have been recorded and utilized for the computation. If the Z value is negative, the trend is said to be falling; if the Z value is positive, the trend is said to be advancing. The results of Mann-Kendall analysis are given in Table 32.3

The results suggest that rainfall in Mumbai and Pune is increasing in the non-monsoon season, S-W monsoon season, N-E monsoon season, and yearly period. During the pre-monsoon season, it has been declining. Mann-Kendall analysis of seasonal and annual rainfall of Mumbai and Pune are shown in Fig. 32.11.

Table 32.3 Mann-Kendall—Z values

Area/Season	Annual	Non	Pre	S-W	N-E
Mumbai	1.358861	1.479649	-1.17768	1.479649	1.600437
Pune	2.204375	0.875711	-1.84201	2.204375	1.902406

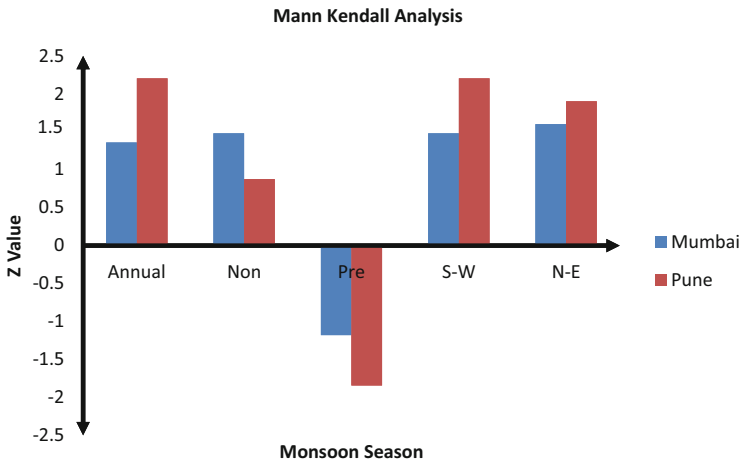

Fig. 32.11 Mann-Kendall analysis of annual and seasonal rainfall

32.5.4 Sen's Slope Estimator

Sen's Slope estimator findings are given in Table 32.4. Sen's Slope method analysis for annual, non-monsoon season, pre-monsoon season, S-W monsoon season, N-E monsoon season indicates rising patterns in annual, non-, S-W, N-E monsoon seasons, and declining trends in pre-monsoon season, comparable to Mann-Kendall Analysis. The S-W monsoon season has the most yearly growth in Mumbai, with 39.44 mm and 40.08 mm in Pune, followed by the N-E monsoon season's 4.18 mm/year in Mumbai and 0.28 mm/year in Pune, and the non-monsoon season's 0.21 mm/year rise. However, there has been a 0.8 4 mm/year reduction in Mumbai and a 1.40 mm/year decline in Pune during the pre-monsoon season. On an annual basis, Mumbai has had a rise of 41.31 mm/year, while Pune has seen a rise of 46.21 mm/year.

Table 32.4 Sen's slope estimator

Rainfall Season	Mumbai		Pune	
	Slope	Constant	Slope	Constant
Annual	41.31353	2102.728	46.20932	1137.668
Non	0.214917	1.050833	0.280769	0.969231
Pre	-0.84053	22.22	-1.40403	34.06653
S-W	39.44528	1948.687	40.08409	1009.871
N-E	4.185417	50.3275	5.762083	51.7175

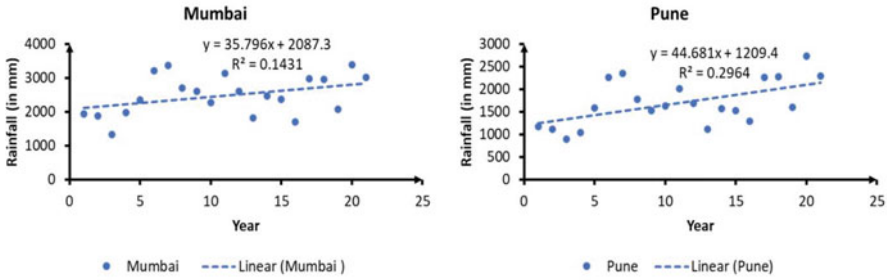

Fig. 32.12 Linear regression analysis of annual rainfall

32.5.5 Linear Regression Analysis (Figs. 32.12, 32.13, 32.14, 32.15, and 32.16)

The slope and intercept values of the linear regression analysis graphs are given in Tables 32.5 and 32.6. The slope values in Mumbai and Pune have a negative sign in the pre-monsoon season, indicating that there has been an overall declining tendency throughout the years. Similarly, slope values in Mumbai and Pune have a positive sign in the non-monsoon, S-W, N-E monsoon seasons, and the yearly period, showing an overall growing tendency (Fig. 32.17).

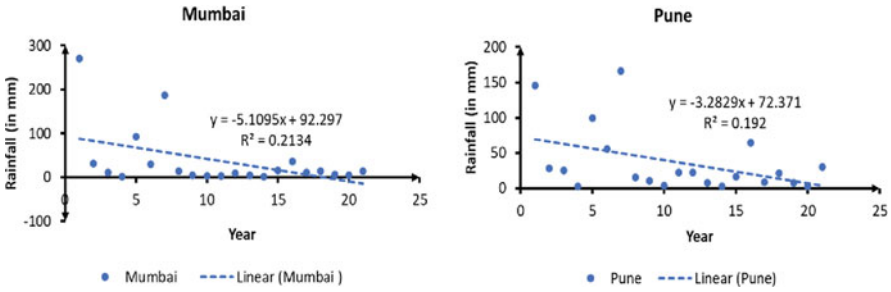

Fig. 32.13 Linear regression analysis of non-monsoon season

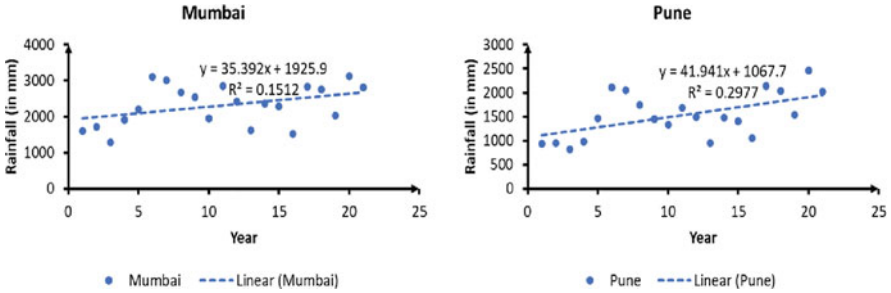

Fig. 32.14 Linear regression analysis of pre-monsoon season

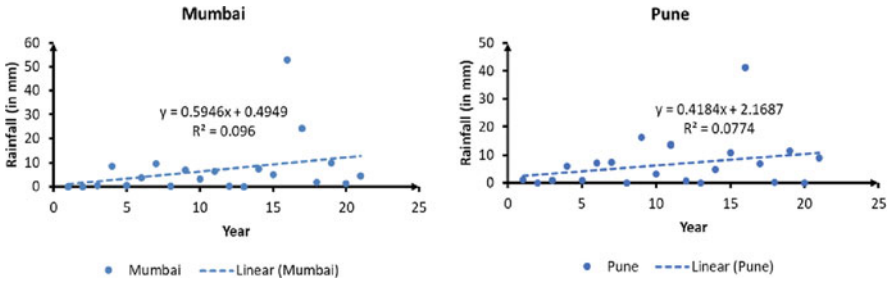

Fig. 32.15 Linear regression analysis of S-W monsoon season

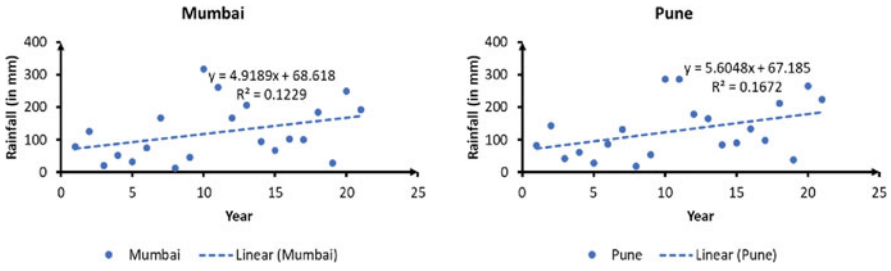

Fig. 32.16 Linear regression analysis of N-E monsoon season

Table 32.5 Linear regression analysis for annual and seasonal rainfall

Rainfall Season	Mumbai		Pune	
	Slope	Intercept	Slope	Inercept
Annual	35.8	2087	44.68	1209
Non	0.59	0.49	0.42	2.17
Pre	-5.11	92.3	-3.28	72.37
S-W	35.39	1926	41.94	1068
N-E	4.919	68.62	5.605	67.18

Table 32.6 Comparison between Sen slope and regression analysis

Slope/Monsoon Season	Annual	Non	Pre	S-W	N-E
Mumbai					
Sen Slope	41.31353	0.214917	-0.84053	39.44528	4.185417
Regression Slope	35.8	0.59	-5.11	35.39	4.919
Pune					
Sen Slope	46.20932	0.280769	-1.40403	40.08409	5.762083
Regression Slope	44.68	0.42	-3.28	41.94	5.605

32.5.6 Reliability Analysis

Internal consistency means the amount to which test measurements stay consistent across repeated trials under the same conditions is referred to as dependability. The design of drinking water schemes is based on 90% dependability, whereas irrigation requirements are calculated using 75% dependability. The results are shown in Figs. 32.18, 32.19, 32.20, 32.21, and 32.22. The results showed that the rainfall during non-monsoon and pre-monsoon period would not be having any significant contribution in the annual rainfall. S-W monsoon has significant contribution in annual rainfall.

90% dependable annual rainfall in Mumbai and Pune is 1824.6 mm and 1121 mm, 75% dependable annual rainfall in Mumbai and Pune is around 1970 mm and 1295 mm. During non-monsoon period 90% dependable rainfall for Mumbai and Pune is 0.12 mm and 0.03 mm. While 75% dependable rainfall is approximately 0.4 mm for Mumbai and 0.62 mm for Pune. In pre-monsoon season 90% dependable

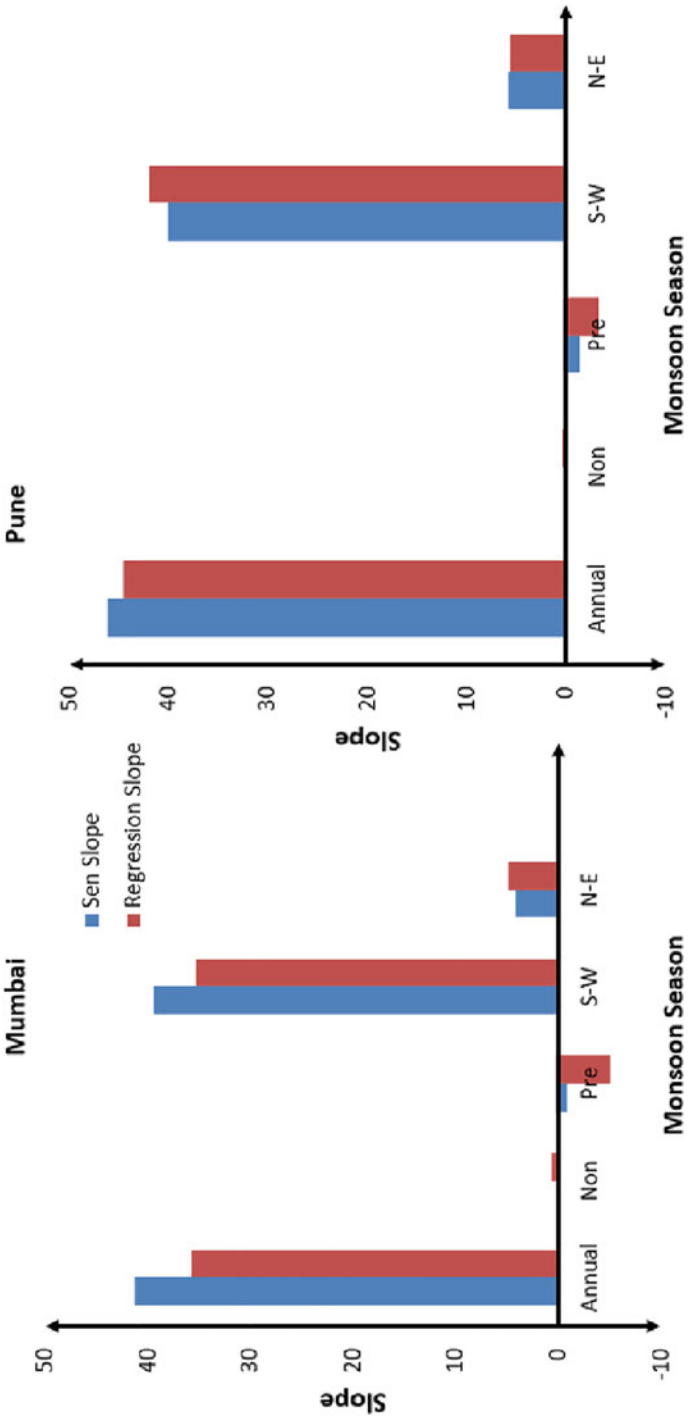

Fig. 32.17 Comparison of Sen slope and regression analysis

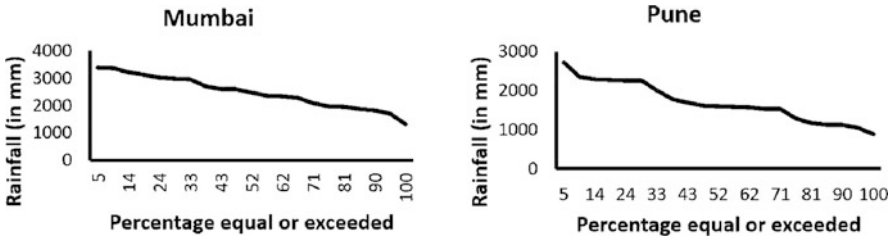

Fig. 32.18 Reliability curve for annual rainfall

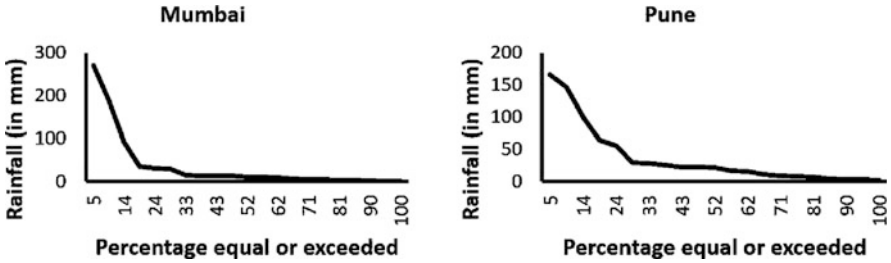

Fig. 32.19 Reliability curve for non-monsoon season

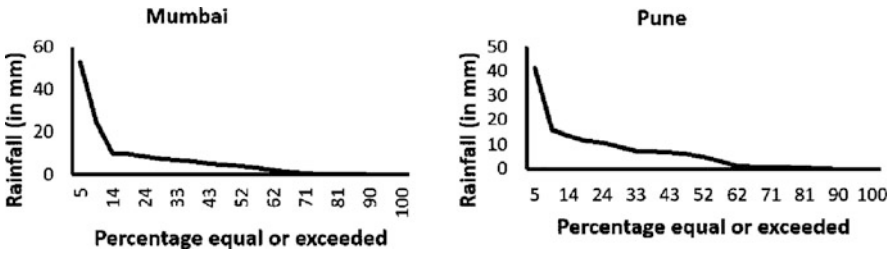

Fig. 32.20 Reliability curve for pre-monsoon season

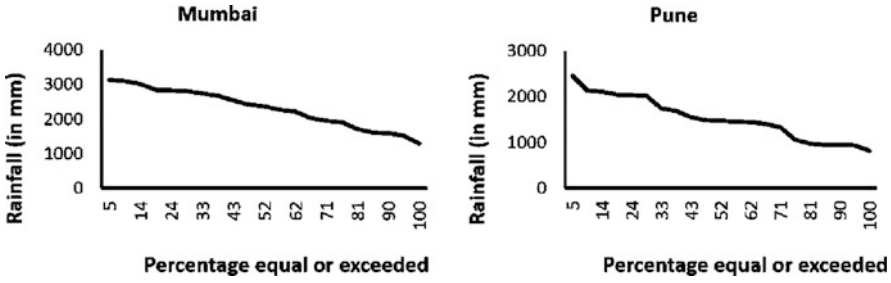

Fig. 32.21 Reliability curve for southwest monsoon season

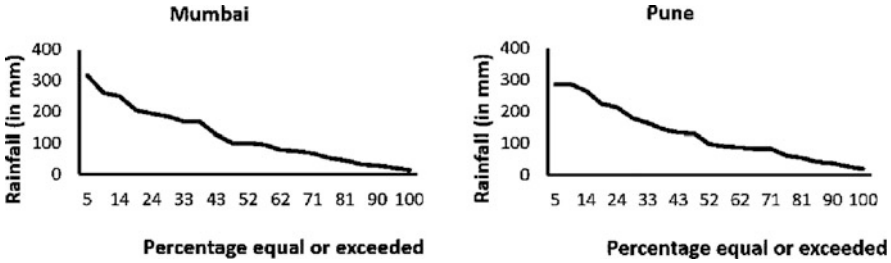

Fig. 32.22 Reliability curve for northeast monsoon season

rainfall for Mumbai and Pune are 2.2 mm and 2.9 mm and 75% dependable rainfall is around 4.2 mm and 7.5 mm for Mumbai and Pune.

During S-W monsoon the 90% dependable rainfall in Mumbai and Pune is 1594.4 mm and 947.9 mm. In northeast monsoon season the 90% dependable rainfall for Mumbai is 28.4 mm and for Pune around 36.7 mm.

32.6 Conclusion

Monthly rainfall data of Mumbai and Pune cities from 2000 to 2020 were analyzed in this study. Annual and seasonal rainfall are statistically analyzed. The outcomes are as follows: In Mumbai and Pune, the average annual rainfall is 2481.11 mm and 1700.89 mm, respectively. The southwest monsoon has contributed the most to both cities, accounting for 93.3%in Mumbai and 89.9 percent in Pune. In both Mumbai and Pune, a rising tendency has been noted in the annual period, non-monsoon, southwest monsoon, and northeast monsoon. In both locations, however, a diminishing tendency has been noted throughout the pre-monsoon season.

The highest rise per year in Mumbai is 39.44 mm/year in the S-W monsoon season, 4.18 mm/year in the N-E monsoon season, and 0.21 mm/year in the non-monsoon season. During the pre-monsoon season, there was a 0.84 mm/year reduction. A rise of 41.31 mm/year has been noted on a yearly basis.

The annual rise in Pune is 40.08 mm/year in the S-W monsoon season, followed by a 5.76 mm/year increase in the N-E monsoon season and a 0.28 mm/year increase in the non-monsoon season. During the pre-monsoon season, there was a 1.40 mm/year decline. A rise of 46.21 mm/year has been noted on a yearly basis.

The dependable rainfall (90% or 75%) varies widely between the months and it is the highest in the southwest monsoon season. These values slightly decrease in the following months during northeast monsoon season. Thereafter, the rainfall reduces drastically and 90% and 75% rainfall are almost nil for non-monsoon and pre-monsoon season. Thus, this shows the need for very careful planning in the design of water related schemes for drinking, irrigation or industry. This also highlights the need for creation of storage to meet the demand in these months.

References

Burn DH, Elnur MAH (2002) Detection of hydrologic trends and variability. J Hydrol 255(1–4): 107–122

Gandhre N, Dauji S, Londhe S (2020) Analysis of precipitation extremes for coastal districts of Maharashtra. In: Proceedings of the international conference on recent advances in computational techniques (IC-RACT)

Jagadeesh P, Agrawal S (2015) Investigation of trends and its magnitude by non-parameteric Mann-Kendall and Sen's slope methods. Int J Hydrol Sci Technol 5(1):83–94

John CK, Pu JH, Pandey M, Hanmaiahgari PR (2021a) Sediment deposition within rainwater: case study comparison of four different sites in Ikorodu, Nigeria. Fluids 6(3):124

John CK, Pu JH, Moruzzi R, Pandey M (2021b) Health-risk assessment for roof-harvested rainwater via QMRA in Ikorodu area, Lagos, Nigeria. J Water Clim Change 12(6):2479–2494

Joshi MK, Pandey AC (2011) Trend and spectral analysis of rainfall over India during 1901–2000. J Geophys Res Atmos 116:D6

Kendall MG (1975) Rank correlation methods. Google Scholar, London

Kumar V, Jain SK, Singh Y (2010) Analysis of long-term rainfall trends in India. Hydrol Sci J 55(4):484–496

Mann HB (1945) Nonparametric tests against trend. Econometrica 13:245–259

Mondal A, Khare D, Kundu S (2015) Spatial and temporal analysis of rainfall and temperature trend of India. Theor Appl Climatol 122(1):143–158

Mooley DA, Parthasarathy B (1984) Fluctuations in all-India summer monsoon rainfall during 1871–1978. Clim Chang 6(3):287–301

Panda A, Sahu N (2019) Trend analysis of seasonal rainfall and temperature pattern in Kalahandi, Bolangir and Koraput districts of Odisha, India. Atmos Sci Lett 20(10):e932

Pandey M, Pu JH, Pourshahbaz H, Khan MA (2022) Reduction of scour around circular piers using collars. J Flood Risk Manage 3:e12812. https://doi.org/10.1111/jfr3.12812

Parthasarathy B, Munot AA, Kothawale DR (1994) All-India monthly and seasonal rainfall series: 1871–1993. Theor Appl Climatol 49(4):217–224

Patil JP, Sarangi A, Singh DK, Chakraborty D, Rao MS, Dahiya S (2013) Rainfall trend analysis: a case study of Pune district in Western Maharashtra region. J Soil Water Conserv 12(1):35–43

Potdar SS, Kulkarni S, Patil P, Pawar RP, Jakhalekar VV, Nade DP (2019) The long-term trend analysis of rainfall data from 1901 to 2015 for Maharashtra and Goa region from India. Int J Water 13(3):293–309

Pu JH, Wallwork JT, Khan M, Pandey M, Pourshahbaz H, Satyanaga A, Hanmaiahgari PR, Gough T (2021) Flood suspended sediment transport: combined modelling from dilute to hyper-concentrated flow. Watermark 13(3):379

Rana A, Uvo CB, Bengtsson L, Parth Sarthi P (2012) Trend analysis for rainfall in Delhi and Mumbai, India. Clim Dyn 38(1):45–56

Rana N, Singh S, Sundriyal YP, Juyal N (2013) Recent and past floods in the Alaknanda valley: causes and consequences. Curr Sci 105(9):1209–1212

Sen PK (1968) Estimates of the regression coefficient based on Kendall's tau. J Am Stat Assoc 63(324):1379–1389

Shankar MS, Pandey M, Shukla AK (2021) Analysis of existing equations for calculating the settling velocity. Watermark 13(14):1987

Singh UK, Jamei M, Karbasi M, Malik A, Pandey M (2022) Application of a modern multi-level ensemble approach for the estimation of critical shear stress in cohesive sediment mixture. J Hydrol 607:127549

Wallwork JT, Pu JH, Kundu S, Hanmaiahgari PR, Pandey M, Satyanaga A, Pandey M, Satyanaga A, Amir Khan M, Wood A (2022) Review of suspended sediment transport mathematical modelling studies. Fluids 7(1):23

Chapter 33
Evaluation of Potential Lakes Susceptible to GLOF Using Multicriteria Assessment in Jhelum Sub-basin of Indus Basin

Nibedita Guru

Abstract The successive glacial lake outburst floods (GLOFs) are a major threat to lives and livelihoods in deglaciation environments in the Indian Himalayan Region (IHR) as they are the source of catastrophic damage downstream. It has been stated that the rapid expansion of glacial lakes (GL) is expected to increase due to climate change and imposing the development of flood hazards and risks. This study analyses a total of nine different parameters associated with glacial lakes and glaciers that can be obtained from high-resolution remote sensing satellites and empirical formula to identify potential lakes in the Jhelum sub-basin. In this sub-basin, a total of 202 glacial lakes were identified, and only 77 lakes of the total lakes have a glacier association. To determine potential glacial lakes in the sub-basin multicriteria analysis (MCA) was applied and compared with some other weighting methods to assess its vulnerability. The vulnerability index has been computed to classify the different stages of vulnerability through probability distribution for meaningful characterization. It has been observed that the analytic hierarchy process (AHP) method has the potential to identify potential lakes.

Keywords MCA · Potential lakes · Jhelum sub-basin · Vulnerability · High-resolution satellite data

33.1 Introduction

The number, size, and dense distribution of glacial lakes in the Himalayan region are increasing due to the impact of climate change on glaciers and surrounding environments (Kumar and Murugesh Prabhu 2012; Zhang et al. 2015; Maharjan et al. 2018; Chaudhuri et al. 2022). Glacial Lake Outburst Floods (GLOF) event could be extremely disastrous and create long-term degradation in the valleys, may occur due to rapid discharge of substantial amount of water retained in glacial lakes, that

N. Guru (✉)
Forest Ecology and Climate Change Division, Rain Forest Research Institute, Jorhat, India
e-mail: gurun@icfre.org

M. Pandey et al. (eds.), *River Dynamics and Flood Hazards*, Disaster Resilience and Green Growth, https://doi.org/10.1007/978-981-19-7100-6_33

happens due to erosion process, increase in water pressure, merging of an avalanche/rock into the lake, nature of the damming materials, etc. (ICIMOD 2001; Ashraf et al. 2012; Hakeem et al. 2018; John et al. 2021a, b).

However, a hazard is mainly defined as a natural potential event/phenomenon that may have a negative impact in terms of damaging property, loss of life, and injury to the downstream society. Hazards are the origin of disasters. Hence, disaster risk scientists mainly focus on the study of hazard classification and its causes, also the spatio-temporal patterns are based on a different perspective. The GLOF events may also have a transboundary hazardous effect causing loss of lives, destruction of houses, bridges, agriculture, forests, hydro-power stations, roads, etc. Hence, regular monitoring of both glacial lakes and glaciers is necessary along with the adaptation of suitable mitigation measures like early warning systems (Bajracharya et al. 2006; Wallwork et al. 2022). Due to its hazardous nature, GLOF is considered a catastrophic event worldwide. For an instance, during the last century, approximately ~32,000 people in Peru passed away due to GLOFs, in Iceland, seven numbers of people died, the European Alps recorded 393 deaths, and South America and Central Asia recorded 5745 and 6300 deaths (Carrivick and Tweed 2016). Thus, around the world, GLOF has the potential to cause a severe hazard, mainly in high mountain regions. Thus, it required high attention in recent years to assess and reduce its impact on damages and fatalities (Mool et al. 2001; Nie et al. 2013; Westoby et al. 2014). In July 1959, a massive "glacial" flood triggered in the Jhelum River due to 4 days of continuous rains lashing the valley and Srinagar (Bhatt et al. 2017). Recently, thousands of people have lost their lives in the last event that happened in Kedarnath, India (Allen et al. 2015; Das et al. 2015; Carrivick and Tweed 2016). Due to these past GLOF events, monitoring of glacial lakes associated with glaciers is required to identify potential lakes that can lead to downstream area destruction. Hence, to prevent such hazardous events, identification and documentation of critical glacial lakes from different inventories are needed.

As majority of glacial lakes can be found in the high mountainous region under inclement weather conditions, which are unapproachable for detailed investigation and continuous monitoring. In that case, satellite remote sensing technology is found to be one of the best tools for rapid and qualitative hazard assessment of glacier and glacial lakes (Raj 2010) and had also been widely accepted in inventorying glacial lakes and glaciers, and also in identifying potential lakes by using Landsat Multispectral Scanner (MSS), Thematic Mapper (TM), Enhanced Thematic Mapper Plus (ETM+), and Resourcesat-1 (IRS P6) Linear Imaging Self-Scanning (LISS) III satellite data. Worni et al. (2013) carried out a study of identification and mapping of glacial lakes based on Landsat series data over the Indian Himalayas and found a total of 251 glacial lakes having areas >0.01 km^2 using remote sensing techniques. Bhagat et al. (2004) mapped 156 glacial lakes >0.01 km^2 and identified seven potential lakes which can create GLOF in the Himalayan region using Landsat data. Various glacial lake inventories are available for the Himalayan region using LISS IV data (Gupta et al. 2019; Guru et al. 2019). Criteria for defining a potential glacial lake are based on various factors such as previous GLOF events, geomorphology of the area, and geotechnical features of the lake and its environments and

also based on the condition of lakes, dams, associated glaciers, and topographic features around the glaciers and lakes (ICIMOD 2010). To assess the potentially dangerous glacial lakes across the Himalayan region various methods have been used (Raj 2010; Worni et al. 2013; Prakash and Nagarajan 2017; Khadka et al. 2021).

The main objective of this study is to map and identify potential lakes susceptible to GLOF in the Jhelum sub-basin of the Indus basin, by selecting more influential parameters obtained from high-resolution remote sensing satellite data as fewer studies have been documented in this selected region by considering low to medium resolution data with minimum parameters. For this purpose, an analytical hierarchical process multicriteria approach was applied along with other weighting methods for assigning their weight to assess vulnerability followed by beta distribution for meaningful characterization of vulnerability which is not addressed in this study region yet.

33.2 Study Area

Jhelum sub-basin of the Indus basin is located in the Western Himalayan Region in Jammu and Kashmir state of India. It is shaped by the water of a spring, viz. Cheshma Verinag, located at the foot of Pir Panjal range in the Southeastern part of Kashmir valley, flows through India and Pakistan extending about 725 km (Mehnaza 2017). It is situated geographically between latitudes of 33.00° to 34.75° N and longitudes 73.25° to 75.75° E, covering an area of 21,937.03 km^2 (excluding the Kishanganga river catchment) within the Indian region, shown in Fig. 33.1. Three major tributaries, viz. Sandran River, Bringi River, and Arapath join in the course up to Anantnag town on its right side. Lidder forms the headwaters of the Jhelum river which is fed by several glaciers and consider the biggest River. Poonch River is one of the tributaries of the Jhelum River flows from India in the southwest direction and confluence with the Jhelum River in Pakistan. The temperature and rainfall of the study area range from 5 °C to 40.7 °C and 11 mm to 234 mm, respectively. The elevation of the sub-basin ranges from 5346 m to 205 m above mean sea level. South Asia Network on Dams, Rivers and People (2017) reported that the glacier area in the Jhelum sub-basin has depleted by 27.47% by reducing from 46.09 km^2 in 1962 to 33.43 km^2 in 2013 over the last 51 years.

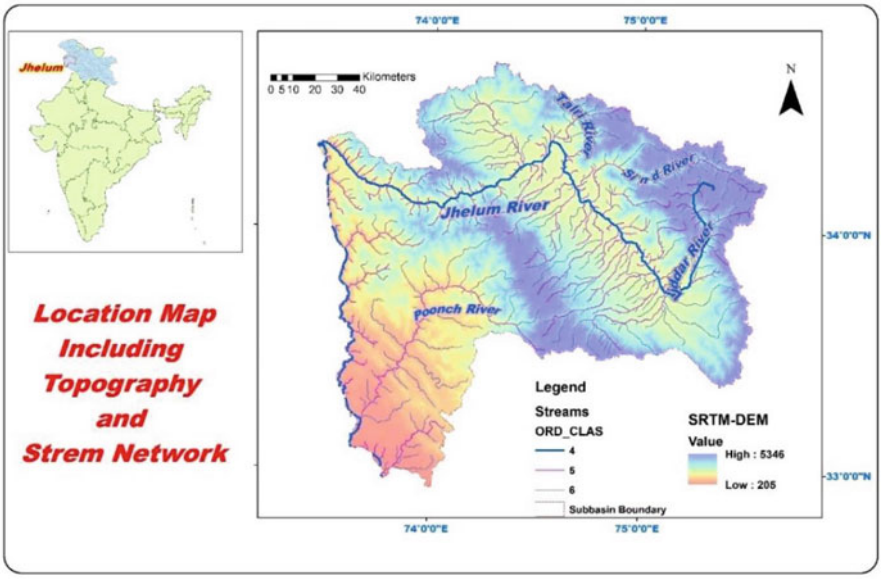

Fig. 33.1 Location map of the study area along with topography and stream network

33.3 Materials and Methods

33.3.1 Data Sets used for Mapping and Inventory of Glacial Lakes

For identification of glacial lakes from satellite imagery, images should be cloud-free and with least or no snow cover, which in the Himalayas occurs generally between August and December. There is various earth observation (EO) satellite data having different spatial and radiometric resolution available, but for mapping of GL, it has been found that medium to high-resolution EO datasets is robust. In most of the previous studies Landsat data have been widely used for this purpose because of its wide coverage and free accessibility (Bolch et al. 2010; Wang et al. 2013); Zhang et al. 2015). SAR data has also been found to be useful for mapping GL but along with it auxiliary datasets such as DEM, normalized vegetation index (NDVI), and manual corrections are also needed for the removal of noise lies within/around the GLs (Wangchuk et al. 2019; Miles et al. 2017). Orthorectified Resourcesat-2 Linear Imaging Self-Scanning Sensor-4 (LISS-IV) images from 2014, 2016, and 2017 were used to delineate the boundary of the glacial lake in the Jhelum sub-basin due to its high resolution of 5.8 m (Fig. 33.2). Whereas, more cloud obstruction and snow coverage have been found in the 2015 year datasets which are not suitable for mapping GL. Topographic information of the study area was derived from the Shuttle Radar Topography Mission (SRTM) digital elevation model (DEM) (30 m) and was downloaded from the data portal (https://urs.earthdata.nasa.gov/).

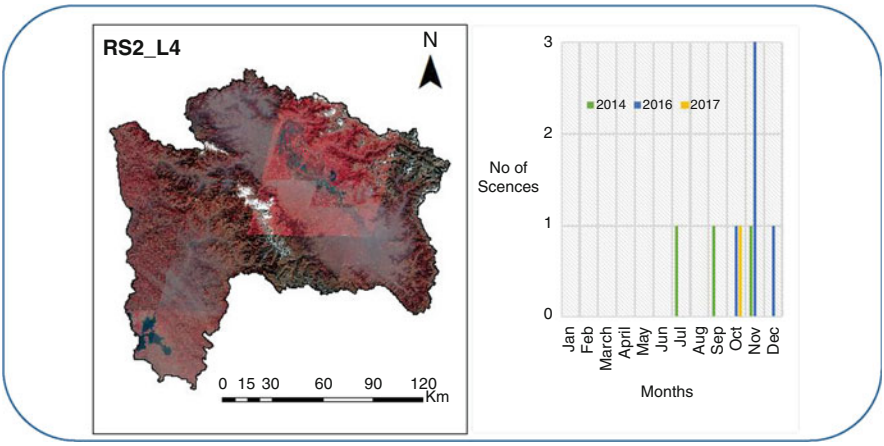

Fig. 33.2 Month-wise number of RS-2 LISS-IV scenes used in the study

For better visualization and identification of lakes, especially for lakes under shadow and/or snow-covered areas, DEM and Google Earth were also used. Furthermore, to identify the nature of glacial lakes, Randolph Glacier Inventory v6.0 has been used (RGI Consortium 2017). For a few glacial lake attributes like river and lake name, Toposheet at 1:250,000 scale was used, which were downloaded from the University of Texas Toposheet Library.

The glacial lakes boundary was delineated by consistent manual digitization through the visual interpretation method which includes spectral band combinations in false color composite (FCC) of near infra-red (NIR), Red, and Green bands in Red, Green, and Blue channels, respectively, along with the knowledge of image interpretation keys such as size, tone, texture, pattern, association, shape, shadow, and orientation. In FCC, glacial lakes seem dark blue to a black color and frozen lakes seem white color. To identify a glacial lake and demarcate its boundaries clearly, appropriate image enhancement techniques, i.e. histogram equalization, a nonlinear contrast stretching technique along with google earth were used, which improves the interpretation by highlighting the lake as well as helps to eliminate the effect of shading in lake identifications. Furthermore, the inventoried glacial lakes were broadly categorized into four classes based on their dam types, such as a moraine-dammed lake, ice-dammed lake, glacier erosion dammed lake, and other glacial lakes fed by glacial melt. They are briefly described in Table 33.1.

Altogether 19 different attributes were generated in the glacial lake inventory, hydrological information, which includes basin, sub-basin, river, and lake; geometric information, which includes elevation, maximum length, mean width, surface area, aspect; lake information, which includes feature types, glacial lake type, lake ID; other information, which includes latitude, longitude, Topo grid 250 k, Topo grid 50 k, source of the database, source of elevation, and date of the pass. Typically, lake ID is set in 12-digit format like "0142H0300080," where "01" denotes to Basin code which is Indus, "42H03" denotes to the 1:50,000 scale Toposheet number, and

Table 33.1 Glacial lake types and their description

S. No.	Lake type	Lake subtype	Code	Identification
1	Moraine-dammed lake	End-moraine dammed lake	M(e)	Lake dammed by end (terminal) moraines
2		Lateral-moraine dammed lake	M(I)	Lake dammed by lateral moraine(s), not in contact with glacial ice
3		Lateral-moraine dammed lake (with ice)	M (Ig)	Lake dammed by lateral moraine(s) in contact with glacial ice
4		Other-moraine dammed lake	M(o)	Lake dammed by other moraines
5	Ice-dammed lake	Supra-glacial lake	I(s)	Pond or lake on the surface of a glacier
6		Glacier ice-dammed lake	I(d)	Lake dammed by glacier ice with no lateral moraines
7	Glacier erosion dammed lake	Cirque erosion lake	E(c)	A small pond occupying a cirque
8		Glacier trough valley lake	E(v)	Lakes formed in the glacier trough as a result of the glacier erosion process
9		Other glacier erosion dammed lake	E(o)	Bodies of water occupying depressions formed by the glacial erosion process
10	Other glacial lake	Other glacial lake	O	Lakes formed in a glaciated valley and are fed by glacial melt, but damming material is not directly part of the glacial process

the last five digits denote the chronological number for each lake within the study area.

33.3.2 GLOF Susceptibility

For this purpose, the multicriteria decision-based method was designed and applied to assess the potential glacial lakes and their GLOF susceptibility in the Jhelum sub-basin. The complete procedures trailed in the assessment of GLOF are shown in Fig. 33.3. Based on different literature studies, various factors prevailing the mechanism of GLOF potential have been identified and compiled. A total of nine different parameters, viz., glacial lake type, the glacial lake area, distance from associate glacier snout to glacial lake inlet, the expansion rate of glacial lakes, series of upstream glacial lakes, glacial lake volume, the slope between associated glacier snout and glacial lake inlet, glacier retreat, and drainage outflow have used. Glacial lake types are related to susceptibility based on their potential to outburst nature. Lake area affects the volume of stored water and maximum outburst flood volume. It has been considered that a larger lake area along with high-intensity precipitation is reasonable enough to cause damage downstream, which provides plenty of water sources for GLOFs. Distance and slope of GL with glacier snout are less than considered as high potential lakes as the glacier area generally reflects the area of

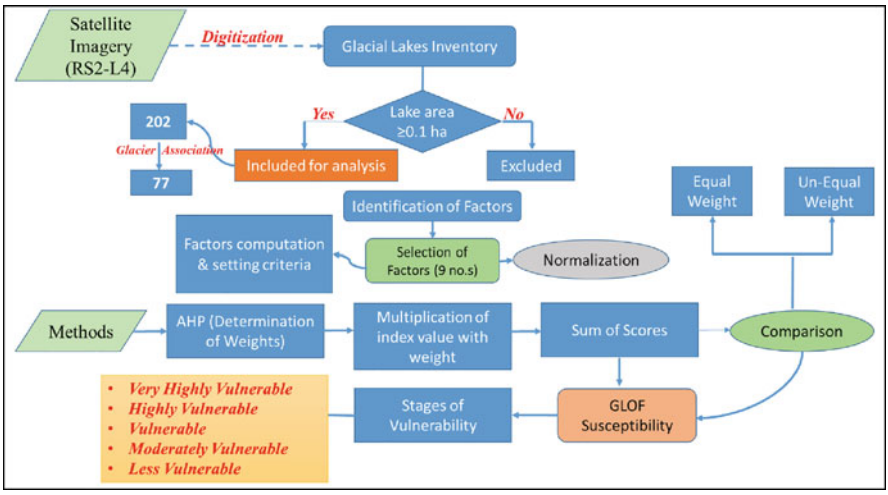

Fig. 33.3 Flowchart of GLOF assessment process

accumulation that suggests the magnitude of snow/ice avalanches into the lake which could also generate overtopping waves. Glacier retreat has a direct impact on the sudden increase in volume with GLOF potential. An increase in drainage outflow may have the potential to increase the volume and rate of flow to nearby settlements and the chance of washing out the area due to high velocity along with debris flow. Out of those, four parameters such as type, area, distance from snout to the lake, and expansion rate of lakes are considered to be most important due to glacial lake surrounding characteristics, condition of associated glaciers, and topographic features. Based on the importance of each type of lake, weight has assigned such as the highest rank is given to end-moraine dammed lake as 7, lateral moraine-dammed lake as 6, another moraine-dammed lake as 5, supra-glacial lake as 4, cirque erosion lake as 3, other glacier erosion dammed lake as 2, and other glacial lakes as 1. Likewise, glacial lakes are considered if they are in direct contact or proximity to their parent glacier. Furthermore, to estimate the expansion rate of mapped lakes, we have taken the glacial lake inventory prepared by International Centre for Integrated Mountain Development (ICIMOD) in 2005 (ICIMOD 2010).

33.3.3 Methods to Identify Potential Glacial Lakes

To identify the potential glacial lakes three different weighting methods have been used, viz., equal, unequal, and AHP methods. Then quantitative assessment has been done by determining the vulnerability index which has an important role to identify potential lake vulnerability based on different criteria. The details of each parameter are explained below in different sections. The Intergovernmental Panel on Climate

Change (IPCC 2007) has done a quantitative assessment of vulnerability by constructing a vulnerability index, based on numerous set of parameters that results in vulnerability. Whereas, each parameter used is having different scales and units, therefore they need to be normalized based on two types of functional relationships (UNDP 2006), viz., Eq. (33.1): $+^{ve}$ (lake type, area, expansion rate, series of u/s lakes, volume, and slope b/w snout and lake,) and Eq. (33.2): $-^{ve}$ (distance from snout to lake, glacier retreat, and drainage outflow), using the following equation:

$$x_{ij} = \frac{X_{ij} - \mathrm{Min}X_{ij}}{\mathrm{Max}X_{ij} - \mathrm{Min}X_{ij}} \tag{33.1}$$

$$y_{ij} = \frac{\mathrm{Max}X_{ij} - X_{ij}}{\mathrm{Max}X_{ij} - \mathrm{Min}X_{ij}} \tag{33.2}$$

where x_{ij} is the normalized value of the indicator (j) concerning region (i), X_i is the actual value of the indicator concerning region (i), and Min X_{ij} and Max X_{ij} are the minimum and maximum values, respectively, of indicator (j) among all the regions (i).

33.3.3.1 AHP Method

The AHP method was first developed (Saaty 1980) and is used to solve problems having multiple criteria with a decision-making matrix shown in Fig. 33.4. In the AHP method, a pairwise comparison matrix at a scale of 1–9 was designed where 9 specifies the extreme significance and 1 specifies the equal significance of the in-between criterion of the matrix (Feizizadeh et al. 2014). Then, relative weights/eigenvectors are determined using Saaty's method. Finally, the consistency relationship/ratio (CR) is calculated to check the efficiency of the analytic hierarchy process as:

$$\mathrm{CR} = \frac{\mathrm{CI}}{\mathrm{RI}} \tag{33.3}$$

where CI = consistency index, RI = random index.

Generally, a randomly generated pairwise comparison matrix is used to obtain the random index (RI) (Saaty 1980), and its value for matrices 1–9 are taken from Saaty's and given in Table 33.2. Saaty's, chosen method involves the comparison of the CI of decision data with the RI, i.e. the CI expected from a matrix of that order. For 1 and 2 order RI values are 0, i.e. these must be consistent and increases with an increase in the order of the matrix.

Consistency relationship supports defining the possible procedures and evaluations of logical anomalies of the decision-making (Chen and Zhu 2010). It signifies the likelihood that the matrix judgments were formed randomly (Saaty 1997). The

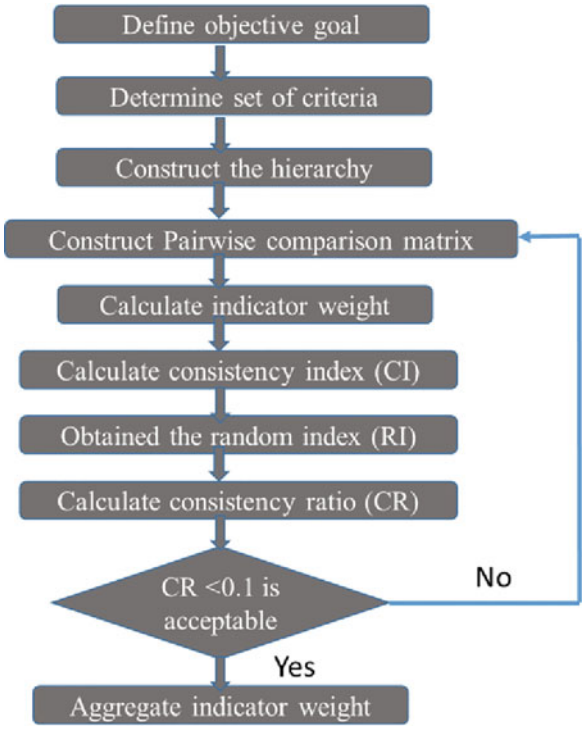

Fig. 33.4 Flowchart of analytic hierarchy process

Table 33.2 Scale of pairwise AHP comparison

n	1	2	3	4	5	6	7	8	9
RI	0	0	0.58	0.9	1.12	1.24	1.32	1.41	1.45

CR mostly be determined by the consistency index and random index. The CR value should be <0.10, for consistency and a meaningful result.

$$CI = \frac{\lambda_{\max} - n}{n - 1} \tag{33.4}$$

where $\lambda_{\max}$ = principle or highest eigenvector of the computed matrix, n = order of the matrix.

The advantage of this method is that it can deal with both qualitative and quantitative data effectively. It supports decision-makers in accepting the decision-making model structure while dealing with a given complex decision problem, especially those are having subjective judgment by breaking down it into a simpler, smaller, and more understandable decision. Which is mainly associated with a multilevel hierarchical structure of criteria, sub-criteria, and so on.

33.3.3.2 Equal Weight Method

In this method, the simple averages of all the normalized scores of parameters are used to calculate the vulnerability index (VI) and then rank it:

$$\mathrm{VI} = \frac{\sum_j x_{ij} + \sum_j y_{ij}}{K} \tag{33.5}$$

where K is the parameters.

33.3.3.3 Unequal Weight Method

For this method, Iyengar and Sudarshan (1982) formula has been used as it is statistically sound and well appropriate for the improvement of the composite index of vulnerability:

$$\overline{y}_i = \sum_{j=1}^{K} w_j x_{ij} \tag{33.6}$$

where $\overline{y}_i$ is a linear sum of normalized score, i.e. x_{ij}, and w is the weight determined by

$$w_j = \frac{c}{\sqrt{\mathrm{var}_i\left(x_{ij}\right)}} \tag{33.7}$$

where c is a normalizing constant and determined by

$$c = \left[\frac{\sum_{j=1}^{j=K} 1}{\sqrt{\mathrm{var}_i\left(x_{ij}\right)}} \right]^{-1} \tag{33.8}$$

The computed vulnerability index using both methods, lies between 0 and 1, with 1 indicating maximum vulnerability and 0 representing no vulnerability. The advantage of this method is that it captures the large variation among the parameters without dominating the impacts of small variation parameters.

33.3.3.4 Vulnerability Assessment

For this purpose, the beta distribution is a suitable fractional classification for probability distribution to obtain a meaningful characterization of the different stages of vulnerability. The probability density is given by

$$f(z) = \frac{z^{a-1}(1-z)^{b-1}}{B(\alpha, \beta)}, 0 < z < 1 \text{ and } a,b > 0 \tag{33.9}$$

where $B(\alpha, \beta) = \int_0^1 x^{a-1}(1-x)^{b-1}dx$, a represents the lower bound and b represents the upper bounds of the vulnerability index, and α, β are beta functions. A linear division is applied to beta distribution values to maintain the same probability weight interval of 20%, which can be used to describe the five stages of vulnerability (%), viz., less vulnerable (0–20), moderately vulnerable (20–40), vulnerable (40–60), highly vulnerable (60–80), and very highly vulnerable (80–100).

33.4 Results and Discussion

33.4.1 Lake Inventory of Jhelum

A total of 392 features of size greater than 0.0025 km^2 (0.25 ha) were mapped having a total area of 263.04 km^2 spread in an elevation ranging from 205 m to 4500 m. Out of 392 glacial lakes, 202 glacial lakes have a total area of 16.75 km^2 and 190 are water bodies having a total area of 246.29 km^2, as shown in Fig. 33.5. Whereas, 77 lakes are found to be associated with their parent glacier. In this study, seven different subtypes (M(e), M(I), M(o), I(s), E(c), E(o), and O) out of a total of ten glacial lakes have been found (Fig. 33.5). The distribution of different types of GL along with their number and area are summarized in Fig. 33.6.

Figure 33.6a depicted that glacier erosion dammed lake types (94.5%) (i.e., other glacier erosion dammed lakes (85.6%) and cirque erosion lakes (8.9%)) are the dominant lakes among others. The size of glacial lakes in the Jhelum sub-basin ranges from a minimum of 0.0025 km^2 to a maximum of 1.610 km^2. The majority of glacial lakes in the total lakes mapped are less than 0.05 km^2 in size, and they cover a total area of 2.02 km^2. Most of the lakes are located within the elevation range of 3800–4000 m amsl, whereas only other glacier erosion dammed lakes are distributed along with all the elevation ranges. From the analysis, it has been shown that 50% (39 lakes) of 77 glacial lakes are associated with the parent glacier.

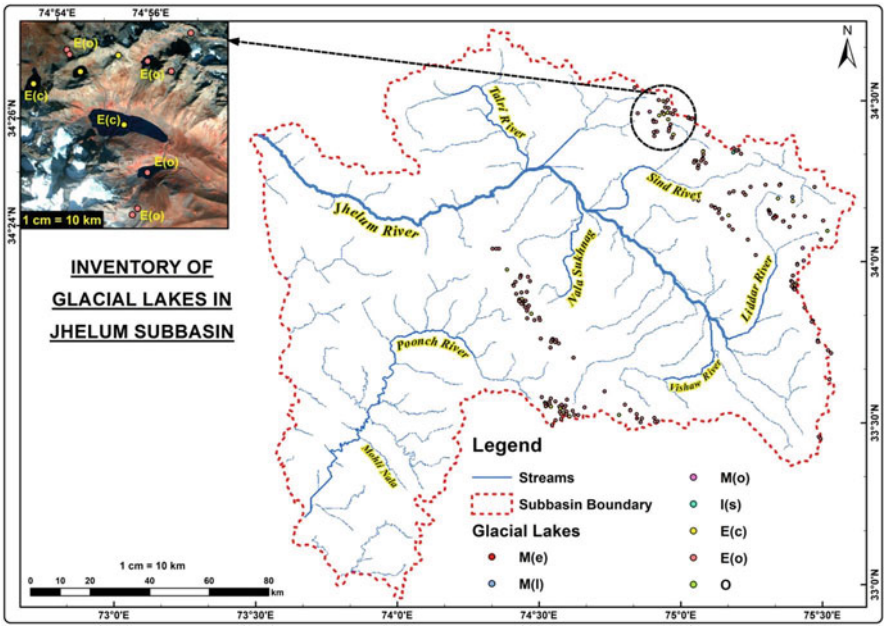

Fig. 33.5 Glacial Lake Inventory in Jhelum Sub-basin shows different types and its distribution

33.4.2 GLOF Susceptibility Assessment

For this purpose, a pairwise comparison matrix was designed at a scale of 1–9 for each parameter as per their susceptibility toward potential GLOF events. Then, relative weights of each nine parameters were computed using Saaty's method followed by both equal and unequal weighting methods given in Table 33.3. The weights obtained from AHP and Unequal weights are not consistent because of their different approaches to weight estimation. Unequal weights determine the weight based on the variance between the parameters while AHP considers both qualitative and quantitative approaches effectively by building a decision-making model. Also, it can deal with complex matrices by simplifying them into hierarchy form. The CR value was determined to check the efficiency of the analytic hierarchy process and obtained as 0.09 which is <0.10 represents consistency with meaningful results. The vulnerability index (y_i) for each lake, within the lower bound and upper bound, was estimated. Later, probability density variable such as alpha (α) (1.839) and beta (β) (2.186) using the vulnerability index range is calculated to obtain the beta distribution value for each lake. This beta distribution value ranges between 0 and 1 and falls under five categories of vulnerability (under Sect. 33.3.3.4), where values near 1 are in the very high vulnerable category and vice versa.

The vulnerability assessment depicted that five lakes were found under the very highly vulnerable category (80–100%) which can be considered as potentially vulnerable to GLOF shown in Fig. 33.7, whereas in unequal weight methods six

Fig. 33.6 Distribution of glacial lakes in the Jhelum sub-basin as per (**a**) type-wise, (**b**) area range-wise, (**c**) elevation range-wise, and (**d**) GL area of different types of lake

Table 33.3 Weight obtained from AHP and Unequal weighting methods

Sl. No.	Criteria	Weight_AHP	Weight_unequal
1	GL type	0.28	0.17
2	GL area	0.20	0.13
3	Distance_GS_GL	0.13	0.07
4	Expansion rate of GL	0.13	0.15
5	Series of us GL	0.08	0.13
6	Volume	0.07	0.15
7	Slope_GS_GL	0.05	0.06
8	Glacier retreat	0.04	0.12
9	Drainage outflow	0.03	0.03

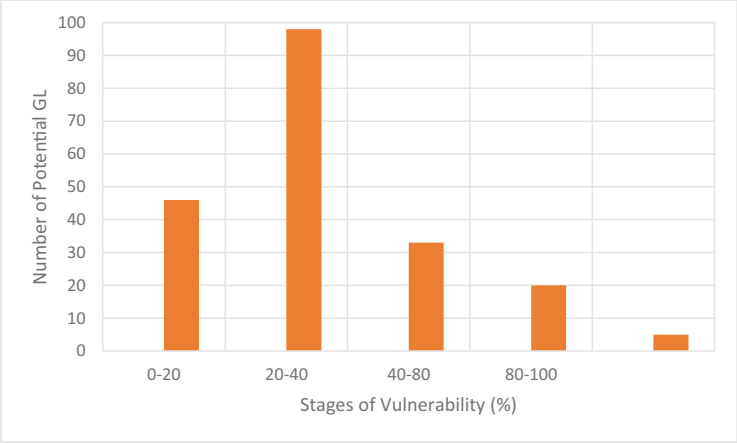

Fig. 33.7 Number of potential glacial lakes under different stages of vulnerability (AHP method)

Table 33.4 List of potential glacial lakes falling under the very high vulnerable category obtained from AHP method

Rank	ID No	Glacial lake	Lake name	River	Area (km^2)	Elevation (m)
1	0143J1500189	E(c)	Gangabal Lake	Kankanaz Nar	1.610	3571
2	0143K1400286	M(e)	Chir Sar – 1	Zali Nar	0.040	3639
3	0143N0800349	M(e)	Katar Nag	Liddar River	0.072	3856
4	0143J1500193	E(o)	Lolgul Gali Lake	Salnai N	0.367	3846
5	0143K0500227	E(o)	Bod Sar	Sinwar	0.454	3954

lakes were found under the same category. The details of five potential GL are given in Table 33.4 along with their rank. These lakes are lying between the elevation ranges of 3500 and 4000 m amsl and are shown in Fig. 33.8.

It has been also found that, in comparison with the area of all glacier erosion dammed lakes, end-moraine dammed lakes are small, but yet found to be potential because the weight assigned to expansion rate is high which in this case is an average of +20% and also due to their proximity (0–200 m) with its parent glacier. While, other glacier erosion dammed lakes are less in rank because both are lying within 250–500 m range from the glacier and experience less change in the area of ±2%. Whereas cirque erosion lakes are decreasing in size with an average rate of –5%, higher-ranked have a very large area.

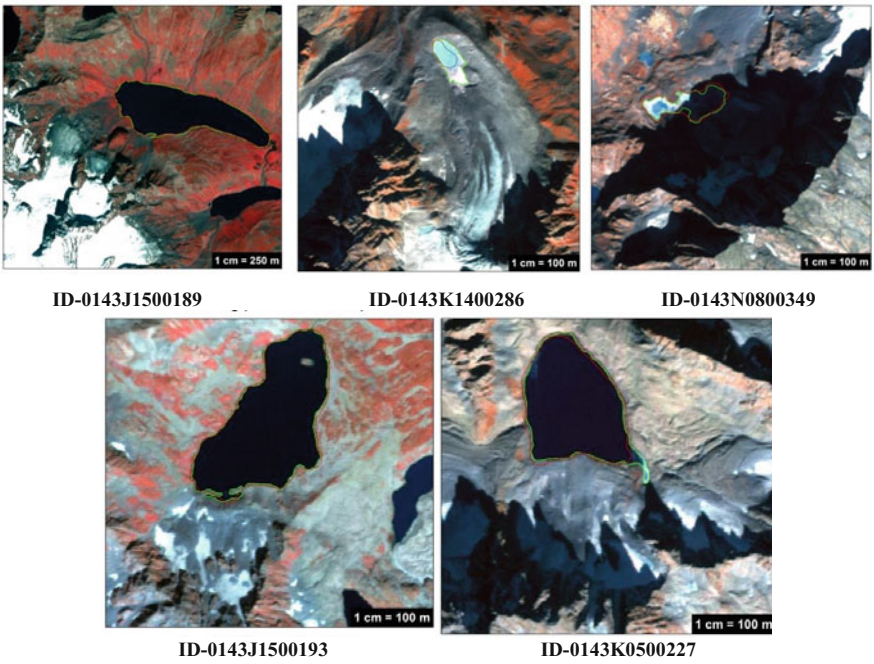

Fig. 33.8 Identified potentially glacial lakes susceptible to GLOF

33.5 Conclusions

This study was performed to examine the glacial lakes and GLOF susceptibility in the Jhelum sub-basin of the Indus basin. Also, to demonstrate the effectiveness of remote sensing data for inventorying glacial lakes in the Jhelum sub-basin of the Indus basin in the Indian Himalayas. A total of 392 features were mapped (>0.0025 km^2), which contains 202 lakes; out of which 77 lakes are associated with its parent glacier. A GLOF susceptibility assessment was done by considering nine influential criteria using AHP method integrated with the vulnerability index through beta distribution and compared with other weighting methods. AHP weighting method is considered an effective method for assigning weights to different parameters and quantifying its vulnerability as it deals with the decision-making matrix very well in both qualitative and quantitative ways. The results show that out of 202 glacial lakes, five lakes were found under the very highly vulnerable category, which may cause a threat to the livelihood downstream while the remaining range of vulnerability may provide a better understanding of GLOF susceptibility in the region. The obtained results are important to the decision-makers and scientists for integrated disaster risk reduction. Furthermore, for future recommendation, the lakes under the very high vulnerable category must be prioritized for detailed GLOF susceptibility studies using hydrodynamic models. Also, it is recommended that similar studies using

high-resolution satellite data can be done in other sub-basins/basins of the Indian Himalayas Region for determining the potential GLOF induce lakes, and reduce its impact in the downstream valley. To better assess the vulnerability, more glacier as well as triggering parameters can be considered.

Acknowledgments The author acknowledge the National Remote Sensing Centre, ISRO, Dept. of Space, Govt. of India, Hyderabad for the supports. The author acknowledge the Editor-in-Chief and the anonymous reviewers for their insightful comments.

References

Allen SK, Rastner P, Arora M, Huggel C, Stoffel M (2015) Lake outburst and debris flow disaster at Kedarnath, June 2013: hydrometeorological triggering and topographic predisposition. Landslides 2015:1–13. https://doi.org/10.1007/s10346-015-0584-3

Ashraf A, Naz R, Roohi R (2012) Glacial lake outburst flood hazards in Hindu Kush, Karakoram and Himalayan Ranges of Pakistan: implications and risk analysis. Geomatics 3(2):113–132. https://doi.org/10.1080/19475705.2011.615344

Bajracharya SR, Mool PK, Shrestha BR (2006) The impact of global warming on the glaciers of the Himalaya. In: Proceedings international symposium on geo-disasters, infrastructure management and protection of world heritage sites. Nepal Engineering Collage, Nepal, pp 231–242

Bhagat RM, Kalia V, Sood C, Mool PK, Bajracharya S (2004) Inventory of glaciers and glacial lakes and the identification of potential glacial lake outburst floods (GLOFs) affected by global warming in the mountains of the Himalayan region: Himachal Pradesh Himalaya, India

Bhatt CM, Rao GS, Farooq M, Manjusree P, Shukla A, Sharma SVSP, Kulkarni SS, Begum A, Bhanumurthy V, Diwakar PG, Dadhwal VK (2017) Satellite-based assessment of the catastrophic Jhelum floods of September 2014, Jammu & Kashmir, India. Geomatics 8(2):309–327. https://doi.org/10.1080/19475705.2016.1218943

Bolch T, Menounos B, Wheate R (2010) Landsat-based inventory of glaciers in western Canada, 1985–2005. Remote Sens Environ 114(1):127–137. https://doi.org/10.1016/j.rse.2009.08.015

Carrivick JL, Tweed FS (2016) A global assessment of the societal impacts of glacier outburst floods. Glob Planet Chang 144:1–16. https://doi.org/10.1016/j.gloplacha.2016.07.001

Chaudhuri S, Pandey M, Debnath K, Oliveto G (2022) A comparative study on equilibrium scour volume around circular cylinders in clay-sand mixed cohesive beds, at near threshold velocity of sand–an experimental approach. Water Supply. https://doi.org/10.2166/ws.2022.250

Chen J, Zhu Q (2010) Uncertainty and decision strategy analysis of GIS-based ordered weighted averaging method. In: IEEE 2010 International conference on information, networking and automation (ICINA), 375–379. ISBN:978-1-4244-8106-4.

Das S, Kar NS, Bandyopadhyay S (2015) Glacial lake outburst flood at Kedarnath, Indian Himalaya: a study using digital elevation models and satellite images. Nat Hazards 77:769–786. https://doi.org/10.1007/s11069-015-1629-6

Feizizadeh B, Jankowski P, Blaschke T (2014) A GIS based spatially-explicit sensitivity and uncertainty analysis approach for multi-criteria decision analysis. Computers and Geosciences. https://doi.org/10.1016/j.cageo.2013.11.009

Gupta A, Guru N, Maheshwari R, Sweta RBS (2019) Inventory of glacial lakes in gilgit subbasin of indus basin using high resolution satellite imagery. J Indian Natl Cartogr Assoc 2019:38

Guru N, Gupta A, Sweta MR, Rao BS, Raju PV, Rao VV (2019) Identification of potential lakessusceptible to GLOF in Jhelum Subbasin of Indus Basin. Hydraulics 155:1452–1462. https://doi.org/10.6084/m9.fig-share.14686860.v1

Hakeem AK, Abirami S, Rao VV, Diwakar PG, Dadhwal VK (2018) Updated inventory of glacial lakes in teesta basin using remote sensing data for use in GLOF risk assessment. J Indian Soc Remote Sens 46(3):463–470. https://doi.org/10.1007/s12524-017-0699-1

ICIMOD (2001) Mountain environment and natural resource information systems. Inventory of glaciers, glacial lakes and glacial lake outburst floods, monitoring and early warning systems in Hindu Kush-Himalayan Region Bhutan

ICIMOD (2010) Formation of glacial lakes in the Hindu Kush-Himalayas and GLOF Risk Assessment

IPCC (2007) IPCC fourth assessment report – climate change 2007: working group 1, the physical science basis, summary for policymakers. http://ipcc-wg1.ucar.edu/wg1/wg1-report.html

Iyengar NS, Sudarshan P (1982) A method of classifying regions from multivariate data. Econ Polit Weekly 1982:2048–2052

John CK, Pu JH, Pandey M, Hanmaiahgari PR (2021a) Sediment deposition within rainwater: case study comparison of four different sites in Ikorodu, Nigeria. Fluids 6(3):124

John CK, Pu JH, Pandey M, Moruzzi R (2021b) Impacts of sedimentation on rainwater quality: case study at Ikorodu of Lagos, Nigeria. Water Supply 21(7):3356–3369

Khadka N, Chen X, Nie Y, Thakuri S, Zheng G, Zhang G (2021) Evaluation of glacial lake outburst flood susceptibility using multi-criteria assessment framework in Mahalangur Himalaya. Front Earth Sci 8:601288. https://doi.org/10.3389/feart.2020.601288

Kumar B, Murugesh Prabhu TS (2012) Impacts of climate change: glacial lake outburst floods (GLOFs). Climate Change 6:81–102

Maharjan SB, Mool PK, Lizong W, Xiao G, Shrestha F, Shrestha RB (2018) The status of glacial lakes in the Hindu Kush Himalaya. International Centre for Integrated Mountain Development (ICIMOD), Kathmandu

Mehnaza A (2017) Projection of future temperature and precipitation for Jhelum river basin in India using multiple linear regression. Int J Eng Res Appl 7(6-4):89–10. https://doi.org/10.9790/9622-07060489101

Miles KE, Willis IC, Benedek CL, Williamson AG, Tedesco M (2017) Toward monitoring surface and subsurface lakes on the greenland ice sheet using Sentinel-1 SAR and Landsat-8 OLI imagery. Front Earth Sci 5:58

Mool PK, Wangda D, Bajracharya SR, Kunzang K, Gurung DR, Joshi SP (2001) Inventory of glaciers, glacial lakes and glacial lake outburst floods. Monitoring and early warning systems in the Hindu Kush-Himalayan Region. International Centre for Integrated Mountain Development, Bhutan

Nie Y, Liu Q, Liu S (2013) Glacial lake expansion in the Central Himalayas by Landsat images, 1990-2010. PLoS ONE 9(3):e92654. https://doi.org/10.1371/journal.eone.0092654

Prakash C, Nagarajan R (2017) Outburst susceptibility assessment of moraine dammed lakes in Western Himalaya using an analytic hierarchy process. Earth Surf Process Landf 42:2306–2321. https://doi.org/10.1002/esp.4185

Raj KB (2010) Remote sensing based hazard assessment of glacial lakes: a case study in Zanskar basin, Jammu and Kashmir, India. Geomatics 1(4):339–347. https://doi.org/10.1080/19475705.2010.532973

RGI Consortium (2017) Randolph glacier inventory – a dataset of global glacier outlines: version 6.0. Technical report, global land ice measurements from space, Colorado, USA, Digital Media

Saaty TL (1980) The Analytic Hierarchy Process: Planning, Priority Setting, Resource Allocation, Mcgraw-Hill, New York, NY. McGraw-Hill, New York.

Saaty TL (1997) A scaling method for priorities in hierarchical structure J. Math. Psychol., 15(3), pp. 34–39

South Asia Network on Dams, Rivers and People (2017). https://sandrp.in/2017/06/08/jammu-and-kashmir-rivers-profile-jhelum-and-chenab-basins

UNDP (2006) Human development report. United Nations Development Program. Available at http://hdr.undp.org/hdr2006/statistics

Wallwork JT, Pu JH, Kundu S, Hanmaiahgari PR, Pandey M, Satyanaga A, Pandey M, Satyanaga A, Amir Khan M, Wood A (2022) Review of suspended sediment transport mathematical modelling studies. Fluids 7(1):23

Wang X, Ding Y, Liu S, Jiang L, Wu K, Jiang Z, Guo W (2013) Changes of glacial lakes and implications in Tian Shan, central Asia, based on remote sensing data from 1990 to 2010. Environ Res Lett 8:044052

Wangchuk S, Bolch T, Zawadzki J (2019) Towards automated mapping and monitoring of potentially dangerous glacial lakes in Bhutan Himalaya using Sentinel-1 synthetic aperture radar data. Int J Remote Sens 40(12):4642–4667

Westoby MJ, Glasser NF, Brasington J, Hambrey MJ, Quincey DJ, Reynolds JM (2014) Modelling outburst floods from moraine-dammed glacial lakes. Earth Sci Res 134:137–159. https://doi.org/10.1016/j.earscirev.2014.03.009

Worni R, Huggel C, Stoffel M (2013) Glacial lakes in the Indian Himalayas - from an area-wide glacial lake inventory to on-site and modeling based risk assessment of glacial lakes. Sci Total Environ 468-469:71–84. https://doi.org/10.1016/j.scitotenb.2012.11.043

Zhang G, YaoT XH, Wang W, Yang W (2015) An inventory of glacial lakes in the third pole region and their changes in response to global warming. Glob Planet Chang 131:148–157. https://doi.org/10.1016/j.gloplacha.2015.05.013